CONTENTS

Part I

PREFACE . . . . iii 1/A6

REGULATIONS

1. HELICOPTER EXTERNAL NOISE REQUIREMENTS - FAA PERSPECTIVE 1 1/A8
Charles R. Foster

2. HELICOPTER NOISE REGULATIONS: AN INDUSTRY PERSPECTIVE 17 1/B10
R. A. Wagner

3. NOISE REQUIREMENTS FROM A MILITARY POINT OF VIEW 33 1/C12
Charles C. Crawford, Jr.

4. THE IMPACT OF URBAN OPERATIONS ON HELICOPTER NOISE REQUIREMENTS . . . 45 1/D10
Stanley R. Spector

ROTOR NOISE

5. PREDICTION AND REDUCTION OF ROTOR BROADBAND NOISE 61 1/E12
Richard E. Hayden and Krishna S. Aravamudan

6. THEORETICAL MODELS OF HELICOPTER ROTOR NOISE 89 1/G12
D. L. Hawkings

7. NOISE DUE TO ROTOR-TURBULENCE INTERACTION 109 2/B6
R. K. Amiet

8. THEORY ON ACOUSTIC SOURCES 127 2/C10
S. E. Wright

9. POTENTIAL ACOUSTIC BENEFITS OF CIRCULATION CONTROL ROTOR 149 2/E5
Robert M. Williams and Ian C. Cheeseman

10. HELICOPTER NOISE RESEARCH AT THE LANGLEY V/STOL TUNNEL 181 2/G9
Danny R. Hoad and George C. Greene

11. EXPLORATORY WIND-TUNNEL INVESTIGATION OF THE EFFECT OF THE MAIN ROTOR WAKE ON TAIL ROTOR NOISE 205 3/B7
Robert J. Pegg and Phillip A. Shidler

12. WIND TUNNEL INVESTIGATIONS OF MODEL ROTOR NOISE AT LOW TIP SPEEDS . . . 221 3/C9
K. S. Aravamudan, A. Lee, and W. L. Harris

13. HELICOPTER EXTERNAL NOISE PREDICTION AND CORRELATION WITH FLIGHT TEST 263 3/F11
Bharat P. Gupta

14. FULL-SCALE TESTING OF AN OGEE TIP ROTOR 277 3/G11
Wayne R. Mantay, Richard L. Campbell, and Phillip A. Shidler

15. HOVERING IMPULSIVE NOISE - SOME MEASURED AND CALCULATED RESULTS 309 4/C4
D. A. Boxwell, Y. H. Yu, and F. H. Schmitz

16. IMPROVED METHODS FOR CALCULATING THE THICKNESS NOISE 323 4/B4
Yoshiya Nakamura and Akira Azuma

17. THE IMPORTANCE OF QUADRUPOLE SOURCES IN PREDICTION OF TRANSONIC TIP SPEED PROPELLER NOISE 339 4/E6
Donald B. Hanson and Martin R. Fink

18. BOUNDS ON THICKNESS AND LOADING NOISE OF ROTATING BLADES AND THE FAVORABLE EFFECTS OF BLADE SWEEP ON NOISE REDUCTION 373 4/G12
F. Farassat, Paul A. Nystrom, and Thomas J. Brown

19. A STUDY OF THE NOISE RADIATION FROM FOUR HELICOPTER ROTOR BLADES . . . 387 5/A14
Albert Lee and Marianne Masher

Item 830-H-10
NAS 1.55:2052/pt.1

COMPLETED

ORIGINAL

NASA Conference Publication 2052
Part I

Helicopter Acoustics

Proceedings of an International
Specialists Symposium held at
NASA Langley Research Center
Hampton, Virginia
May 22-24, 1978

DEPARTMENT OF DEFENSE

AMERICAN HELICOPTER SOCIETY INC.

415

Item 830-H-10 NAS 1.55:2052/pt.1

NASA Conference Publication 2052
Part I

Helicopter Acoustics

Proceedings of an International
Specialists Symposium sponsored
by the American Helicopter Society,
Washington, D.C.; the U.S. Army
Research Office, Durham, North
Carolina; and the Langley Research
Center, Hampton, Virginia, and
held at Langley Research Center
May 22-24, 1978

NASA
National Aeronautics
and Space Administration

**Scientific and Technical
Information Office**

1978

Blank Page

PREFACE

The papers included herein were presented at the International Specialists Symposium on Helicopter Acoustics which was held at the NASA Langley Research Center on May 22-24, 1978. The symposium was jointly sponsored by the American Helicopter Society, the U.S. Army Research Office, and the NASA Langley Research Center. Exterior and interior noise problems were addressed both from the physics and engineering as well as the human factors points of view.

The objective of the symposium was to explore the role of technology in closing the gap between what the customers and the regulating agencies would like to have and what is currently available. In this regard, papers were presented on noise regulation concepts, human factors and criteria, rotor noise generation and control, design, operations and testing for noise control, helicopter noise prediction and research tools and measurements. There was active participation by attendees from a number of foreign countries.

The included papers are largely as submitted as camera-ready copy at the time of the symposium. Only minor editorial changes have been performed and a title page and abstract have been added. The assistance of the Scientific and Technical Information Programs Division of the NASA Langley Research Center in publishing these proceedings is gratefully acknowledged.

Use of manufacturers or identification of commercial products in this report does not constitute an official endorsement of such manufacturers or products, either expressed or implied, by the National Aeronautics and Space Administration.

Blank Page

HELICOPTER EXTERNAL NOISE REQUIREMENTS--FAA PERSPECTIVE

Charles R. Foster
Federal Aviation Administration

INTRODUCTION

Helicopter noise certification was formally initiated by the Federal Aviation Administration (FAA) with the issuance in December 1973 of an Advance Notice of Proposed Rule Making No. 73-32 entitled "Noise Standards for Short Haul Aircraft." Concurrently, the International Civil Aviation Organization's Committee on Aircraft Noise (ICAO/CAN) at its second meeting in November 1971 established a working group to investigate the problems of noise certification of vertical and short takeoff and landing aircraft. In those time frames, the dramatic growth of the helicopter industry to its present status was not anticipated--nor that the contribution of helicopters to community noise would grow correspondingly. Since helicopter operations over populated areas are becoming more frequent, public awareness of their noise intrusion is receiving more attention. In this context, enactment of helicopter noise certification standards for the control of noise impact contributing to community annoyance is necessary to ensure the future development of helicopters as an environmentally compatible air transportation mode.

REQUIREMENTS FOR NOISE STANDARDS

As a result of the unique operational capabilities of helicopters, approximately 20 different helicopter types are currently used in commercial operations. The operations include business and executive use, resources monitoring and exploration, firefighting, and a variety of emergency applications. The number of operational heliports has increased from a few hundred in the early 1960's to more than 3400 at present, while the number of helicopters using those heliports has grown to more than 7000 aircraft and is forecast to exceed 9000 by the year 1980. Faced with this past and projected growth of the helicopter industry as well as the increase of the public's awareness of aircraft noise, it is apparent that the development of helicopter noise standards will be necessary both for the protection of the environmental interest of the community and to ensure the orderly growth of the helicopter industry itself.

It is fortunate that the ICAO and FAA developments of noise standards are proceeding concurrently in view of the desirability of achieving consistency between domestic and international standards. Both efforts have developed complementary data bases, and certification concepts under consideration are being reviewed cooperatively. With the combined data base, it will be possible to develop standards which reflect more varied technical approaches to helicopter design. This, in turn, should provide a broader application of available noise control techniques and lead to acoustically improved helicopters. An additional, but not inconsequential, aspect of the commonality of domestic and international noise standards will result from the assurance that a manufacturer's product would have worldwide acceptability and will not be constrained in a few countries because of more restrictive environmental requirements.

REGULATORY BACKGROUND

The FAA issued subsonic transport category aircraft noise standards in 1969 under the provisions of the 1968 Amendments to the Federal Aviation Act. These standards, which were the first aircraft noise certification standards, were incorporated in the Federal Aviation Regulations (FAR's) as the now well-known Part 36 entitled "Noise Standards, Aircraft Type and Airworthiness Certification." The FAA, working with industry and the public through the administrative procedures process, developed the noise certification concept over approximately a 4-year period. The measurement concept consisted of measuring the aircraft noise at three locations as shown in figure 1, which provided an approximation of the expected noise impact at a typical airport runway. Associated with the choice of measurement locations, the certification test operational procedures and power settings were selected to be representative of those which might be used in normal aircraft/airport operation. The development of the certification concept required selection of a noise unit which was identified as the Effective Perceived Noise Decibel (EPNdB). This unit applies a frequency weighting to the noise spectra for consistency with human perception and also provides correction factors to encourage the elimination of objectional tonal characteristics and excessively long flyover time histories.

Using these measurement and evaluation techniques, the required noise levels were established for takeoff, sideline and approach measurement locations. The takeoff noise level requirements are shown in figure 2 along with noise measurement data for aircraft in the current commercial fleet. The initial standards are identified by the curve labeled December 1969, which varies from 93 EPNdB at low gross weights to 108 EPNdB at the higher takeoff weights. An additional set of curves labeled October 1977 for two-, three- and four-engine aircraft is shown to indicate an increase in stringency in the noise level requirements which has become possible as a result of approximately 9 years of noise certification and control experience.

This extensive background of certification experience with subsonic fixed-wing aircraft is logically being used in the development of the noise certification standards for helicopters. It was initially obvious, however, that the large technical and operational differences between helicopters and fixed-wing aircraft should be considered before finalization on noise standards for this unique class of aircraft. Accordingly, the approach to helicopter noise certification is based on an in-depth evaluation of the helicopter acoustic technology and consideration of regulatory concepts which could be considered appropriate for helicopters.

HELICOPTER ACOUSTIC TECHNOLOGY

Noise Sources

The acoustic technology of helicopters differs considerably from that of fixed-wing aircraft. One of the fundamental reasons for this difference is the introduction of several new noise sources resulting from the unsteady aerodynamics of rotary-wing aircraft (fig. 3). The main rotor noise results from the periodic and random loads on the primary lifting surfaces which usually are associated with a blade passing frequency varying between 10 and 20 Hz. This rotor noise source is strongly influenced by the blade tip Mach number, which if sufficiently high can introduce adverse compressibility effects. The main rotor loading, which contributes to the broadband noise, can also be dominated by air flow interactions resulting from the intersection of the wake or vortex generated by the preceding blade. The well-known phenomena of blade slap result from both interaction and compressibility effects. At lower speeds, the slap results primarily from dynamic pressure deficiencies, whereas at high speeds the slap can be related to shock-stall phenomena.

For single main rotor helicopters, the requirement for a tail rotor introduces a unique noise source. The tail rotor introduces rotational noise components and associated harmonics which occur in the frequencies range of 50 to 100 Hz. In addition to these basic components, since the tail rotor operates in a complex flow field, it produces fluctuating noises as a result of interaction with the flow field of the main rotor. Contributing further to this complexity, in some configurations there is also a tail rotor component introduced by the effect of the flow field distortions from shrouds or other fixed surfaces. The presence of the main rotor and tail rotor as noise sources tends to dominate the noise generation of the basic powerplant in many configurations. This, however, may not be the case for piston engine powerplants or for gas turbine engines which produce strong compressor tones or exhaust noises. Noise sources such as gear trains, aerodynamic noise or structural vibrations are generally not major contributors and can be treated on an individual component basis.

Technology Trends

In the interest of developing more versatile aircraft for the commercial field, many new technology innovations are being introduced in advanced helicopter designs. Advances in the field of materials, especially the use of plastics and in composite materials, have resulted in the ability to design and manufacture rotor blades with controlled thickness and twist distributions which provide both structural and aerodynamic advantages. These advantages can contribute to reduced configuration weight and hence less power required for a given operational speed with a corresponding noise reduction. The concept of reduced power requirements may also be realized by an extensive helicopter drag reduction effort. These improvements, which have a direct noise reduction potential, also have a secondary noise reduction potential since the advance designs will have improved specific fuel consumption, require less fuel for a given range, and, therefore, could operate at reduced weights. These technology advances could be incorporated in the future generation of high performance helicopters and their judicious use can provide quieter designs while minimizing performance penalties associated with noise control.

Design Noise Control

In addition to the broad technology advances which can result in quieter helicopter designs, specific concepts are currently being explored which are fundamental to the control of helicopter noise. In designing main rotors for noise control, the basic parameters for consideration are rpm, number of blades, airfoil selection, thickness distribution, aerodynamic loading, tip shape, sweep and/or tilt. Proper selection of these parameters can control broadband noise and can be used to delay the onset of compressibility effects with the resultant decrease in main rotor noise. Control of tail rotor noise is, in general, more complex; however, the same basic design parameters can also reduce the magnitude of this source. The tail rotor noise may also be controlled by changing blade numbers and by configurational rearrangement to avoid interactions. Many of the helicopter noise control techniques are configuration specific and, therefore, limited in application.

HELICOPTER REGULATORY CONCEPTS

In the approximately 6 years that the helicopter noise certification standards have been in an evolutionary process, many different concepts of certification have been suggested. One of the first proposals suggested for conducting the certification noise test was to simply measure the total acoustic radiation of a helicopter in a 1.5-meter (5-foot) wheel height hover as shown in figure 4. Using this concept, it was considered that noise sources could be identified and treated individually, thereby eliminating high noise level radiation in any direction. In the hover test, the pilot was to locate the aircraft centrally with respect to a circular array of microphones and rotate the aircraft in 45° steps to identify the lateral noise radiation in all directions. Unfortunately, when this technique was explored it was found to be highly susceptible to the influence of variations in wind velocity and was not effective in providing repeatable test data. The next proposal for certification paralleled the FAR Part 36 Appendix F requirements for small propeller-driven airplanes which consisted of a single horizontal overflight test over a single microphone (fig. 5). For helicopters, the basic concept of the level flyovers appeared attractive since it produced repeatable data under a condition corresponding to community overflights. The technique is still currently under active consideration for helicopter noise certifica-cation and, as shown in figure 6, consists of a 150-meter altitude overflight over an array of three microphones spaced perpendicular to the ground track. The current recommendation is that the three microphones aligned 150 meters apart would be averaged to develop a single flyover noise value from a minimum of six overflights with the helicopter stabilized at a speed of no less than 90 percent of the maximum speed in level flight with maximum continuous power (V_H) or of the never exceed speed (V_{NE}). The rotor speed would be stabilized at the maximum normal operating rpm and the flyover tests should be conducted at weights within +5 or -10 percent of the maximum certificated takeoff weight. These test speeds were chosen because they were considered to be approximately equal to the speed for best range in cruise which is not currently a defined airworthiness parameter. Since, in general, increased flyover speeds result in increased noise, regulatory consideration must be given to the control of noise in this operational mode.

At one time the flyover test alone was considered as the only test required. However, it later became apparent that the addition of an approach test might also be desirable to identify low speed blade wake interaction noise generated by most helicopters during approach (fig. 7). It was suggested that the approach test be conducted with a steady angle of 6° during six approaches at maximum normal operating rpm and speed for best rate of climb (V_Y) airspeed (fig. 8). The noise levels would be established by again averaging the readings of three microphones aligned 150 meters apart and perpendicular to the flight path. The microphones are positioned such that the overflight altitude is 120 meters below the approach path, which provides the opportunity for direct comparison with CTOL approach noise measurements. Experience to date has shown these tests to be repeatable and relatively easy to conduct.

The incorporation of a takeoff test has been a controversial concept that is also under consideration. While a takeoff test was considered desirable, it had previously been rejected as being too difficult to define and as too dependent on the pilot's operational technique. Recently, an expediency to avoid these complications was introduced; namely, a takeoff test utilizing the flight path intercept technique was proposed (fig. 9). This procedure is currently being evaluated. Using this technique, the test aircraft would establish the speed V_Y for best rate of climb in steady level flight at an altitude of 20 meters above ground level (AGL) prior to reaching a target point 500 meters before the three-microphone measurement area. The aircraft would then apply full power and initiate a steady climb at V_Y intersecting the climb path which has its apex at the target point. Some investigators have tried this technique and found it to be relatively simple and repeatable. The test should reward those aircraft which achieve quieting in the takeoff mode because of improved performance characteristics. It is believed to give a reliable measure of relative acoustic benefit attributable to good takeoff performance.

The current consensus on the noise evaluation unit is that the Effective Perceived Noise Level (EPNL) used in FAR 36 and ICAO Annex 16 should be retained. At this point in time there is, however, no consensus on the use of a correction to the unit for impulsiveness. The International Standards Organization in Technical Committee 43 has advanced a draft proposal #356 to ISO 3891 for the measurement of noise from helicopters including a blade-slap correction. Alternative proposals of considerably less complexity, having approximately the same correlation with psychoacoustic study results have been advanced. It is also considered that the duration correction, which is increased in magnitude because of impulsivity, may adequately correlate with psychoacoustic studies. This issue has recently been the subject of a joint NASA/FAA psychoacoustic overflight program and is also an issue which will be addressed during the present meeting in the Human Factors and Criteria Session this afternoon.

AVAILABLE NOISE LEVEL TEST DATA

The United States and other ICAO member nations have conducted helicopter test programs in accordance with the flight procedures outlined above. The resulting noise level measurements are presented in figures 10 to 12 for the flyover, approach, and takeoff tests, respectively. The FAA has a flight test program scheduled for June to complement this test data base. In the figures, approximate corrections for helicopter impulsivity are indicated. These data do not define proposed noise level limits but are considered indicative of noise levels that would be realized under certification conditions for in-service aircraft. In setting the noise level limits for certification standards, it is necessary to evaluate the economic implications as well as the technological practicability of meeting prescribed standards. In finalizing these standards it will be necessary to evaluate reasonable noise control design requirements and also to identify noise floors which are lower bounds for technically achievable limits.

An intermediate proposal suggested for the treatment of aircraft which exceed specified noise levels by a given amount would be to limit their operations to remote regions. Utilizing this concept would avoid the enforcement of environmental constraints on designs of specific purpose helicopters, if the benefit of those constraints was not made available to the public. For example, there are currently hundreds of flights daily transporting thousands of people to their jobs on off-shore oil rigs which take off from and return to remotely located heliports. The economic impact of noise control requirements on these operations probably would be excessive and it is considered reasonable to explore the development of concepts which would prevent this potential application of noise control requirements. The establishment of new limited use certification categories through the definition of restricted operational use, placarding, or through airport and/or airways use restrictions may be one way of accomplishing this objective.

CONCLUSION

The development of U.S. domestic helicopter noise standards is a process which will proceed in accordance with the requirements of the Administrative Procedures Act. It is believed that rationally developed standards will help the helicopter to realize its growth potential as an environmentally compatible transportation mode.

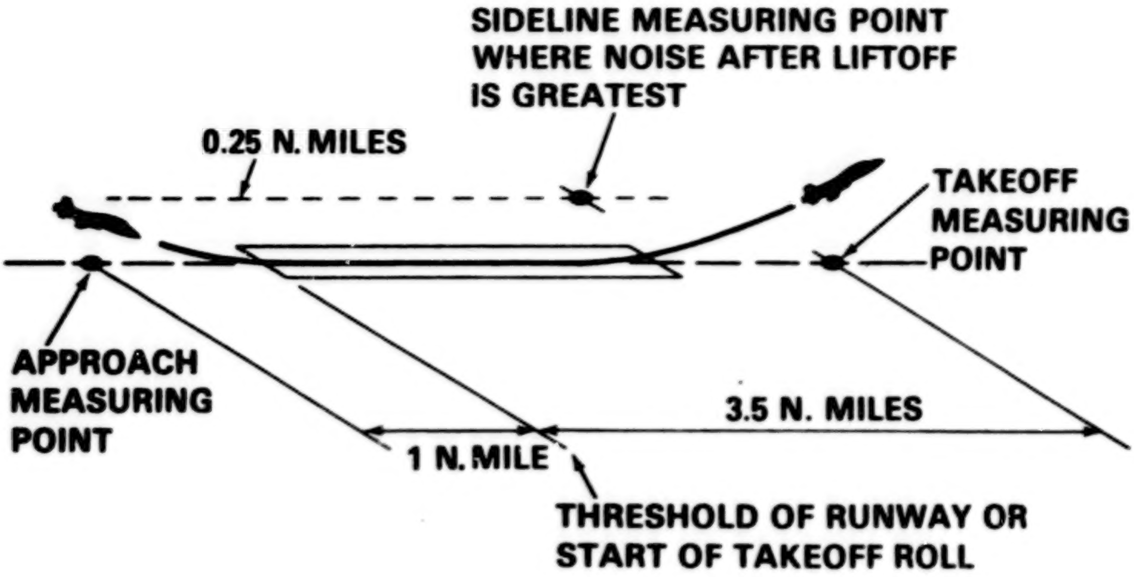
SIDELINE MEASURING POINT WHERE NOISE AFTER LIFTOFF IS GREATEST
0.25 N. MILES
TAKEOFF MEASURING POINT
APPROACH MEASURING POINT
3.5 N. MILES
1 N. MILE
THRESHOLD OF RUNWAY OR START OF TAKEOFF ROLL

Figure 1.- Noise measuring points for airplane type certification.

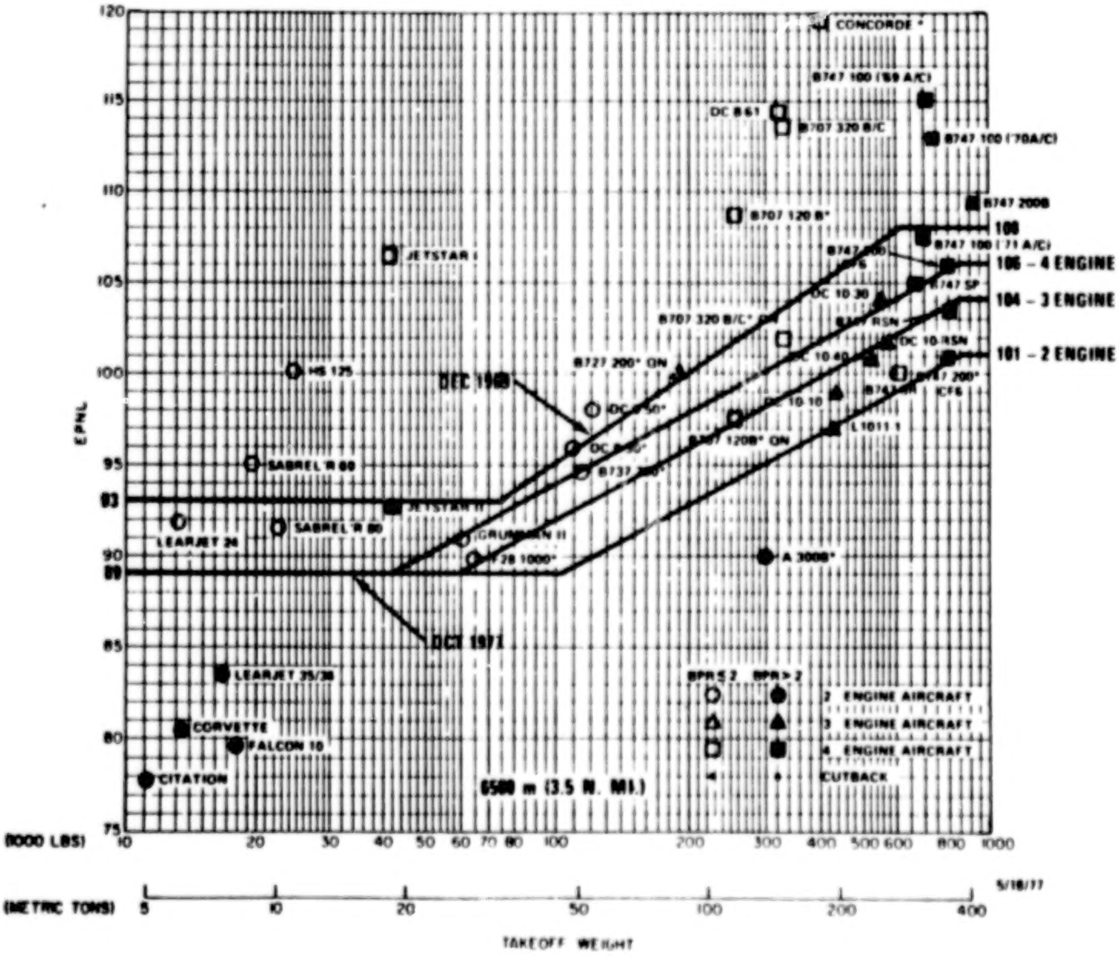

Figure 2.- FAR-36 takeoff noise.

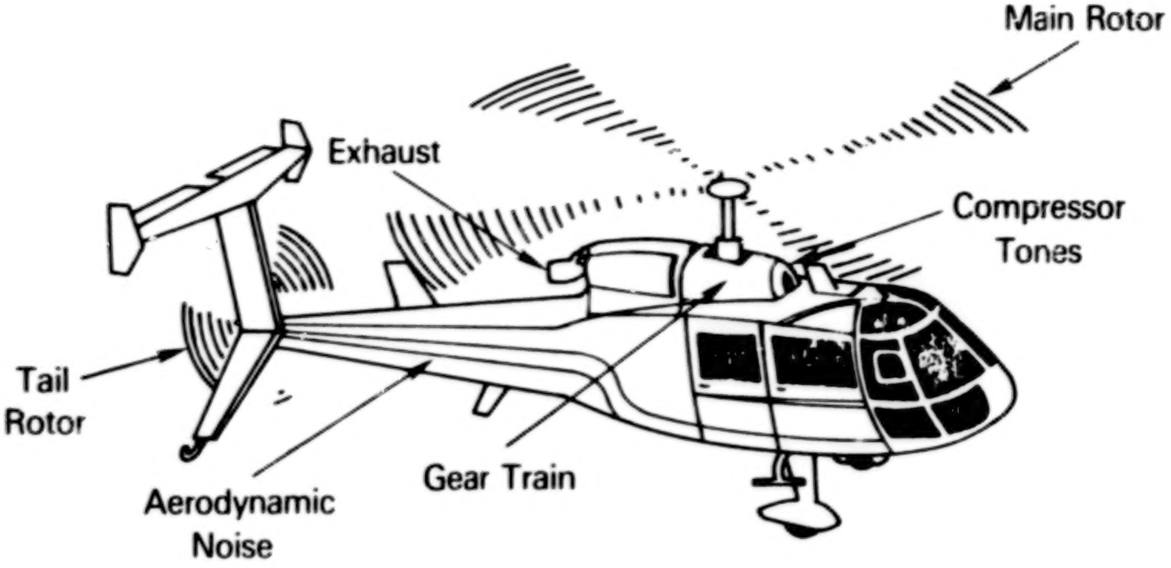
Main Rotor
Exhaust
Compressor Tones
Tail Rotor
Gear Train
Aerodynamic Noise

Figure 3.- Helicopter noise sources.

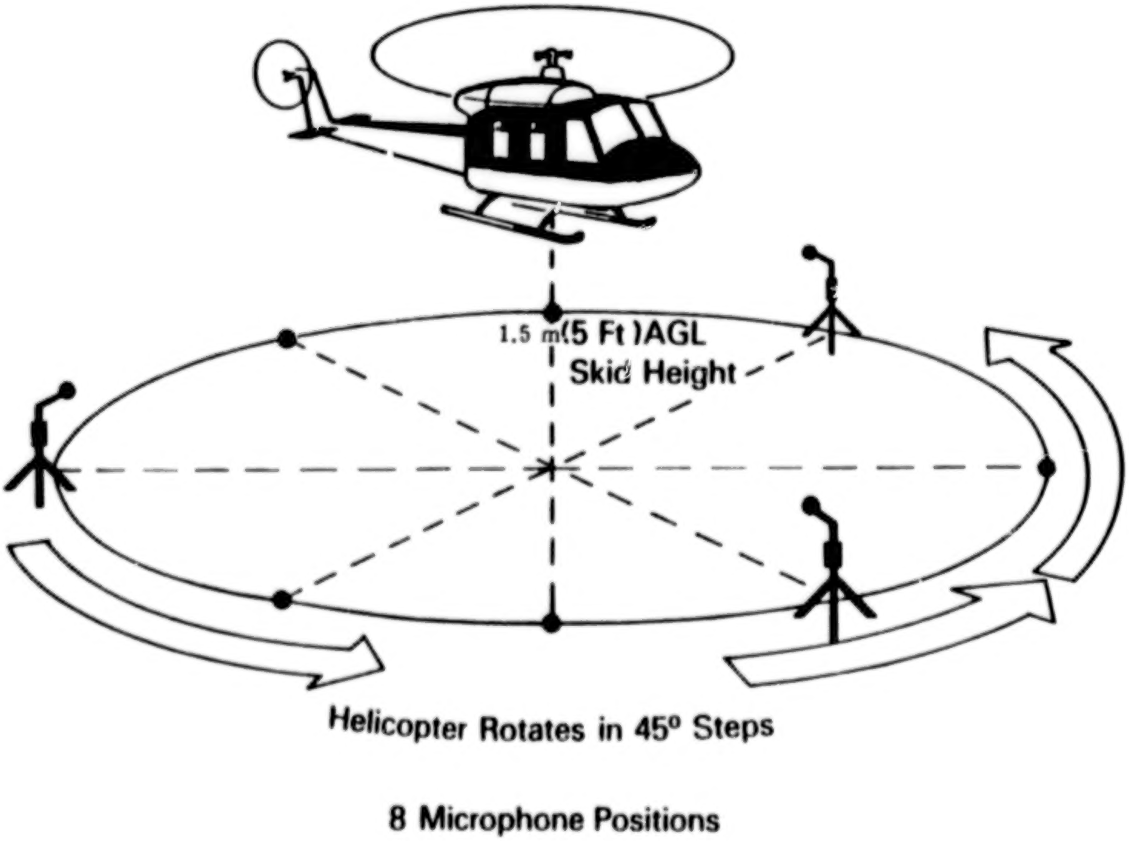
1.5 m(5 Ft)AGL Skid Height
Helicopter Rotates in 45° Steps
8 Microphone Positions

Figure 4.- Helicopter hover noise test.

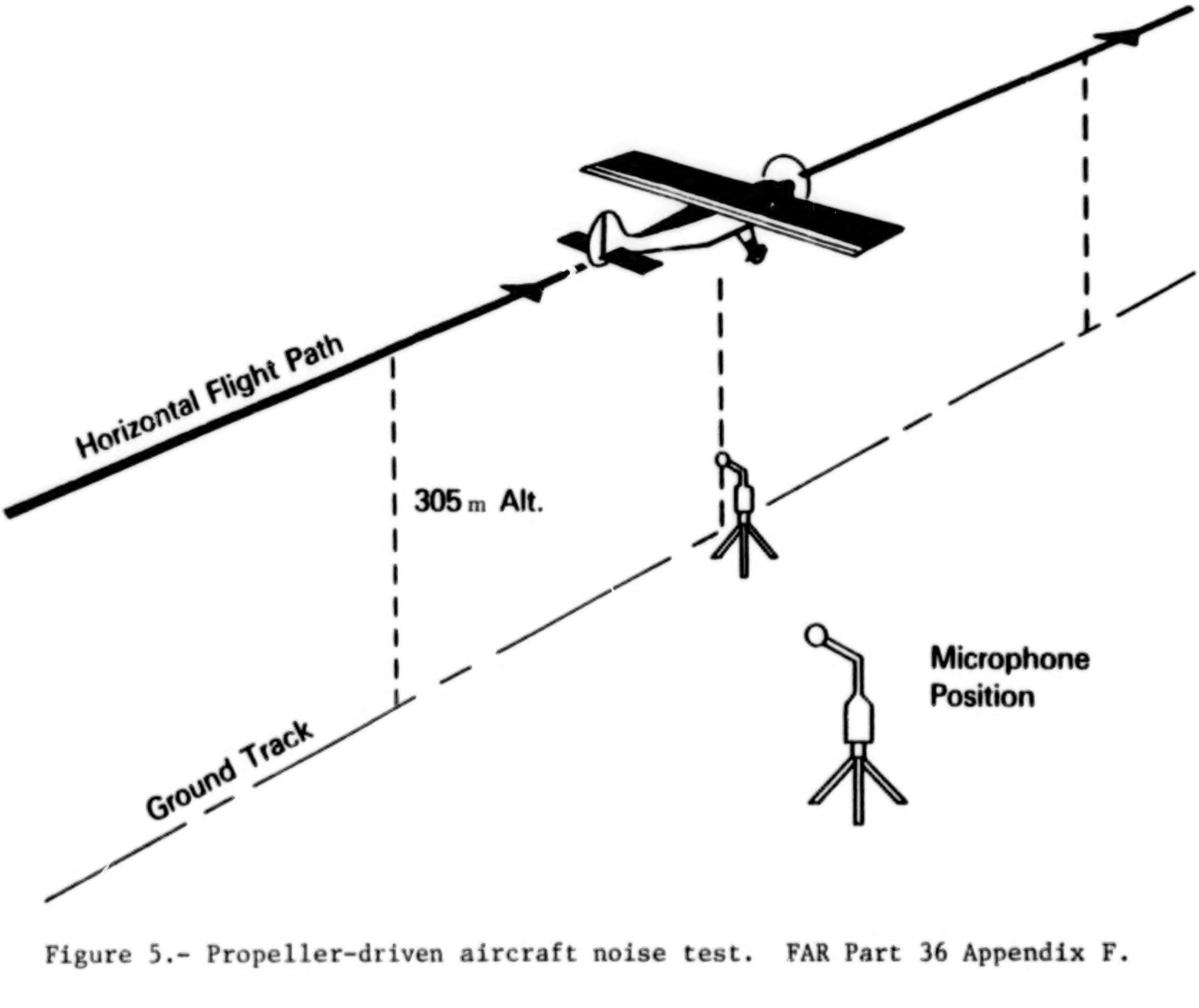
Horizontal Flight Path
305 m Alt.
Ground Track
Microphone Position

Figure 5.- Propeller-driven aircraft noise test. FAR Part 36 Appendix F.

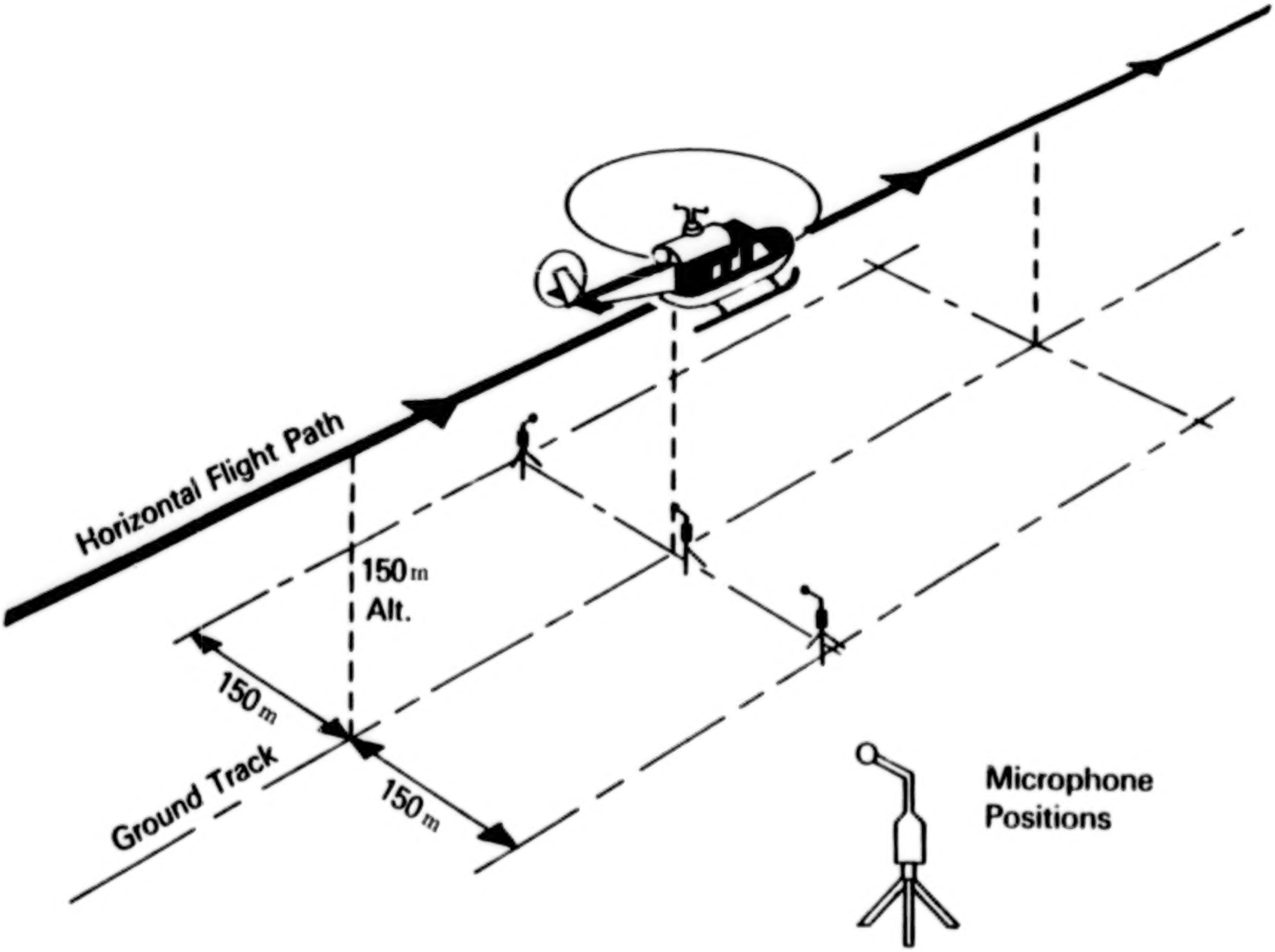
Horizontal Flight Path
150 m Alt.
150 m
150 m
Ground Track
Microphone Positions

Figure 6.- Helicopter flyover noise tests.

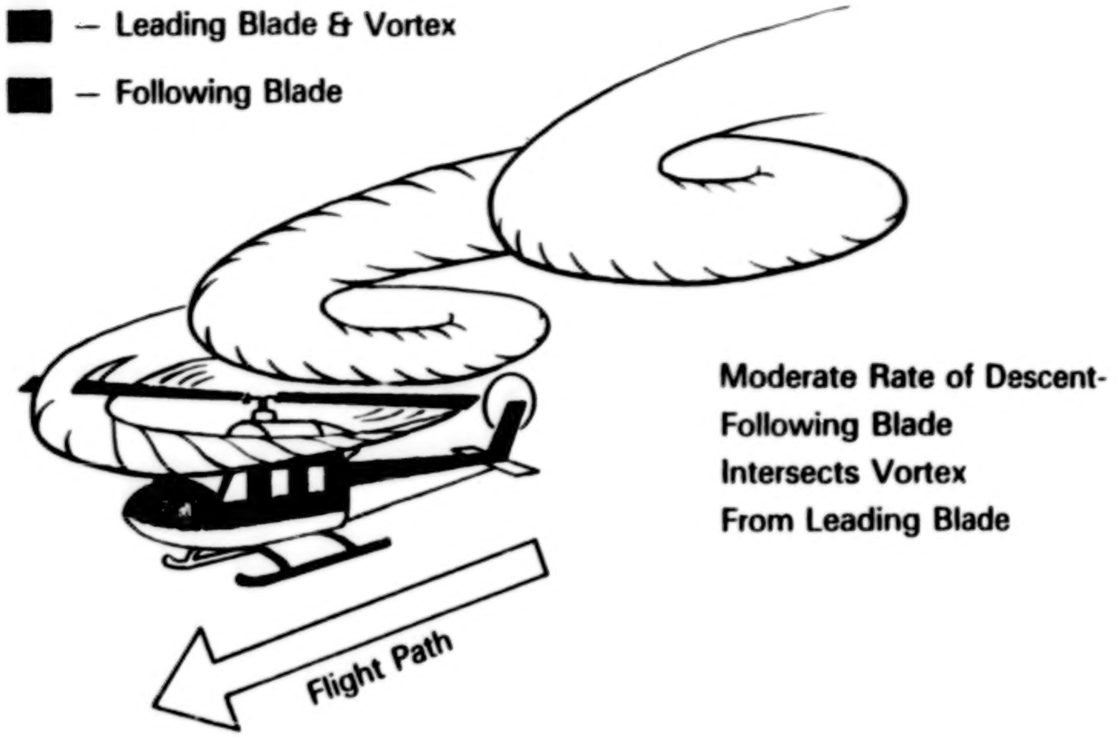
■ – Leading Blade & Vortex
■ – Following Blade
Moderate Rate of Descent-
Following Blade
Intersects Vortex
From Leading Blade
Flight Path

Figure 7.- Tip vortex interaction.

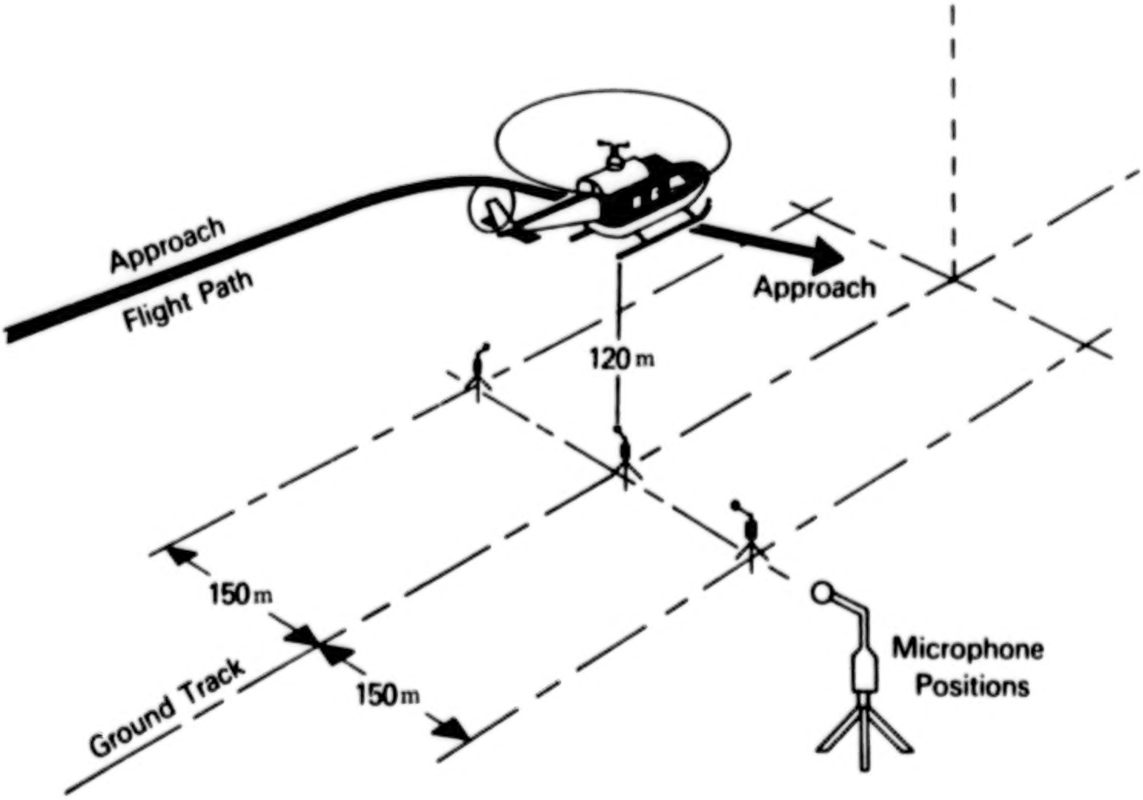
Approach
Flight Path
Approach
120 m
150 m
150 m
Ground Track
Microphone
Positions

Figure 8.- Helicopter approach noise tests.

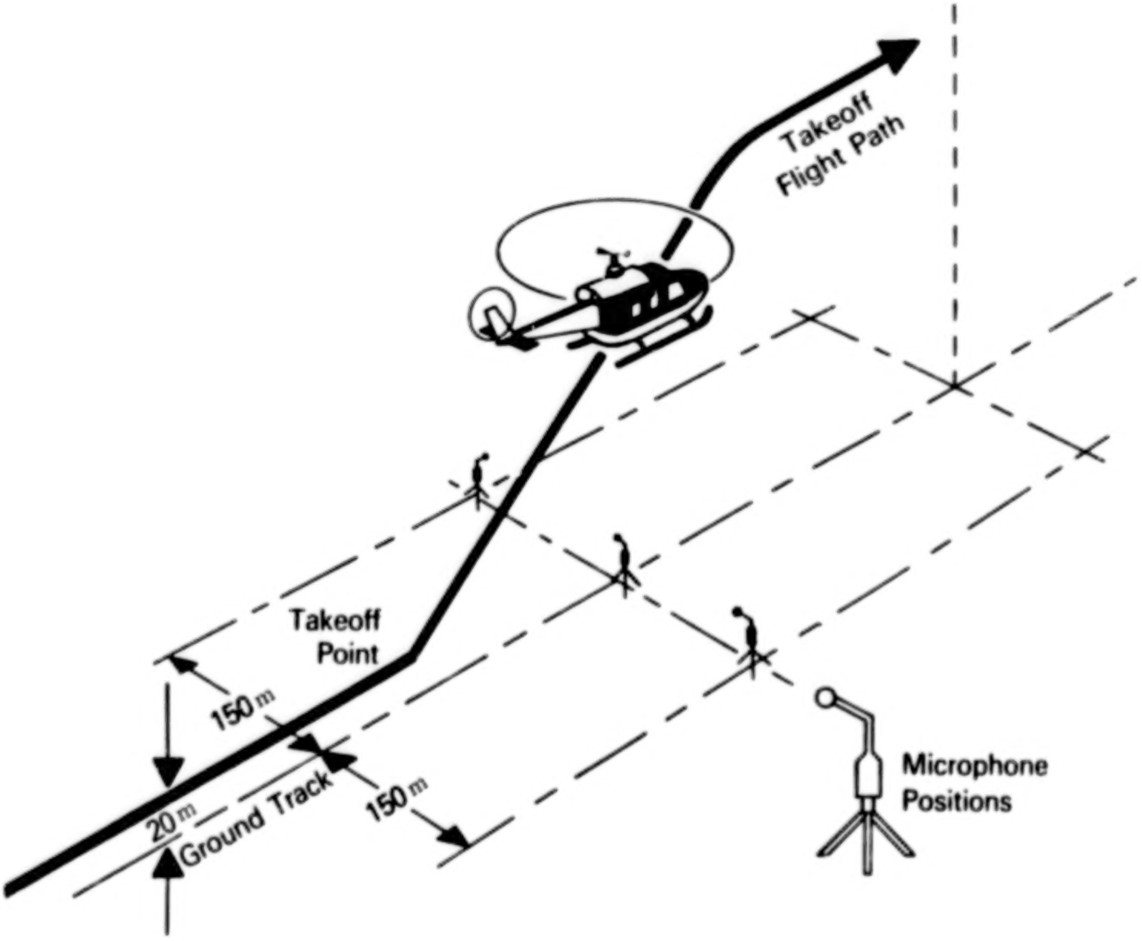
Takeoff
Flight Path
Takeoff
Point
150 m
20 m
Ground Track
150 m
Microphone
Positions

Figure 9.- Helicopter takeoff noise tests.

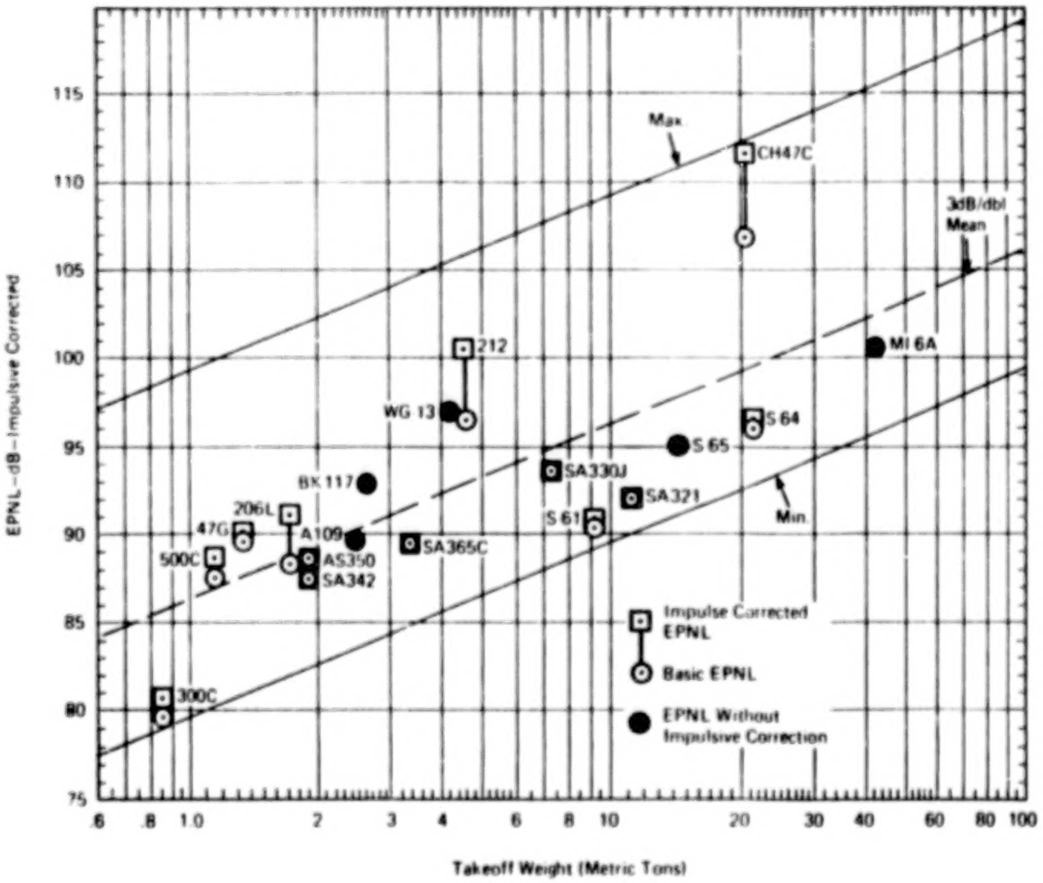

Figure 10.- Helicopter flyover noise levels.

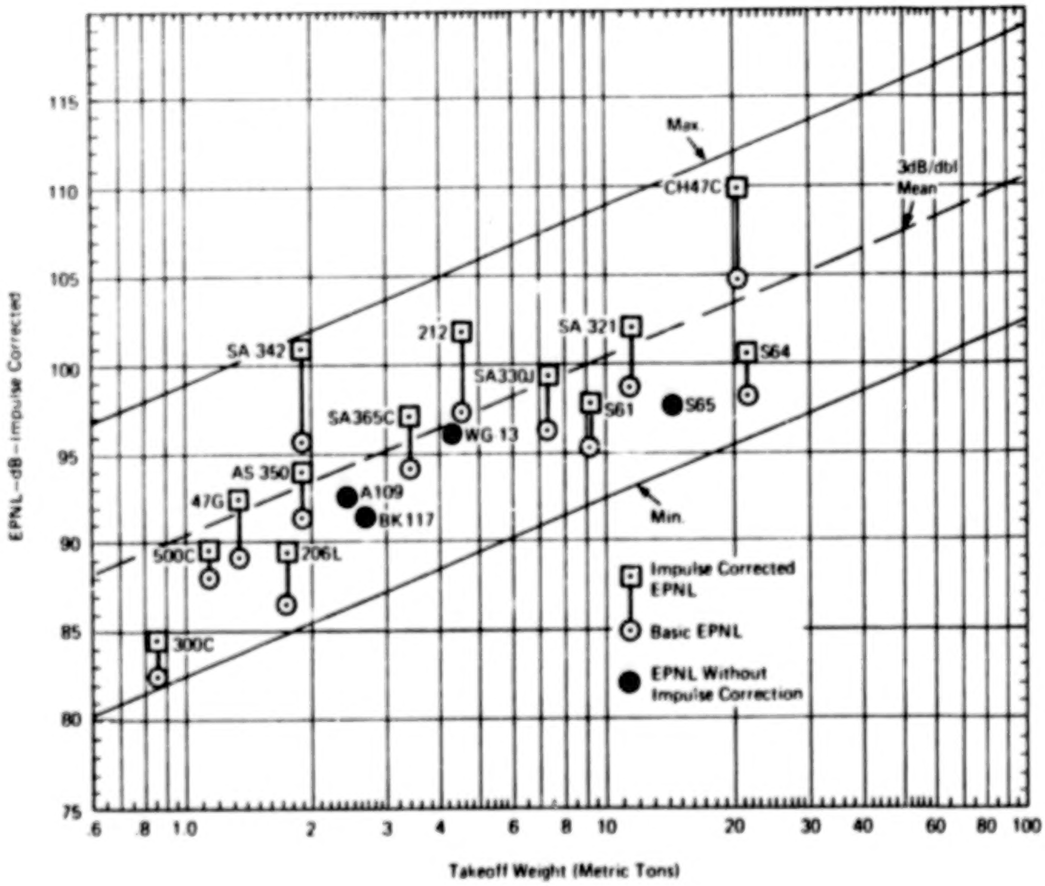

Figure 11.- Helicopter approach noise levels.

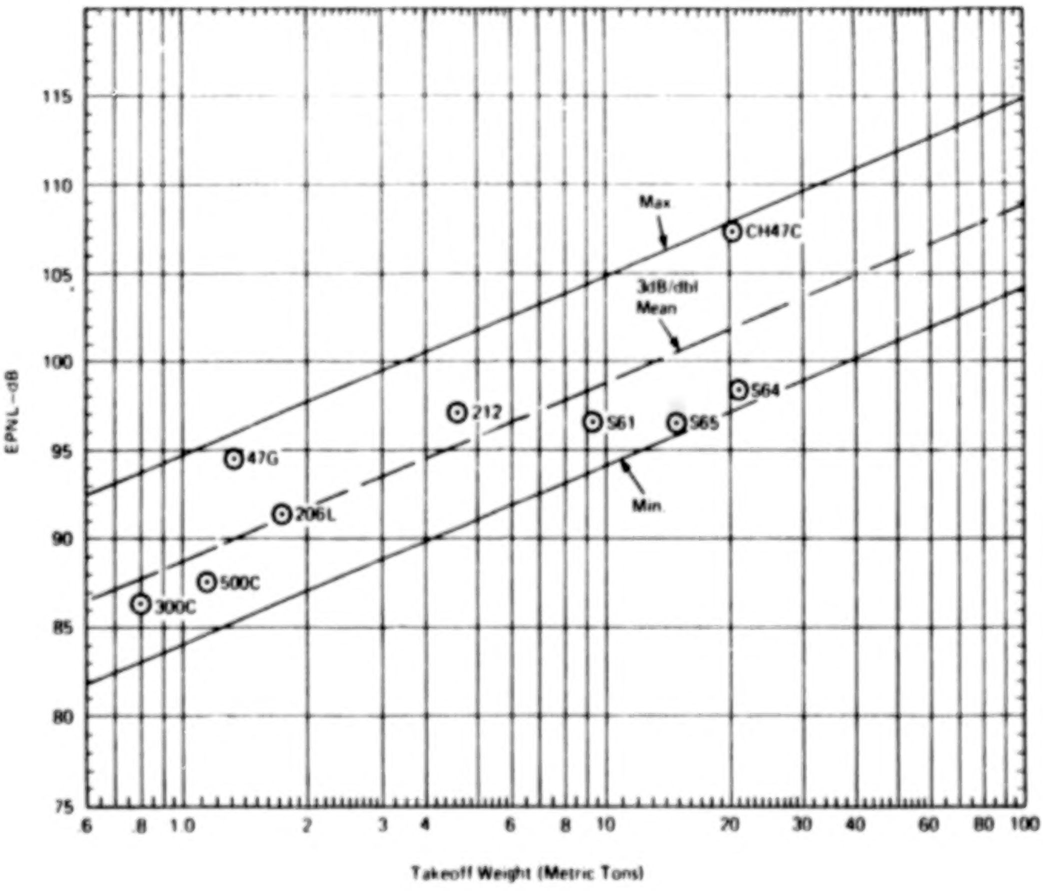

Figure 12.- Estimated takeoff noise levels.

HELICOPTER NOISE REGULATIONS: AN INDUSTRY PERSPECTIVE

R. A. Wagner
Chairman, HAA Committee on Helicopter
Acoustic Certification Standards

SUMMARY

Regulation standards for external noise of helicopters are being developed. In the United States, the Federal Aviation Agency (FAA) and, on the international scene, the International Civil Aviation Organization (ICAO) are active in this work.

The U.S. helicopter industry has been coordinating its acoustics certification views through the Helicopter Association of America (HAA). Its Committee* on Helicopter Acoustic Certification Standards has prepared this paper.

Helicopter noise measurement programs have been conducted by FAA and ICAO. Noise reduction/economic studies have been prepared and some helicopters have been modified for noise reduction. The problems of new design helicopters meeting a prescribed noise limit have been studied and probable design margins assessed. Laboratory and field studies have been, and are continuing to be, pursued in an attempt to determine appropriate units to measure annoyance associated with blade "slap." Lastly, there is a discussion in progress involving the unique operational capabilities of helicopters and the implications relative to noise regulations and certification.

BASELINE DATA

It is obvious that, before quantitative regulations can be written, data for the current state of the art must be assembled. Programs were undertaken by FAA and ICAO for acoustic measurements. The FAA/Department of Transportation (DOT) tests are reported in reference 1. The noise characteristics of eight helicopters are described in level flyovers, simulated approaches, and hover. Takeoff tests are currently being scheduled on these machines and others that may be available.

Certain conclusions are noted in reference 1 which illustrate differences in noise characteristics of several types of helicopters.

Three general noise classes were apparent depending upon noise-time history during flyover:

---

*Especially acknowledging C. Cox, R. Schlegel, and H. Sternfeld, Jr.

(a) Maximum noise at the overhead position and appearing to be tail rotor noise propagated downward.

(b) Maximum noise before the overhead position and caused by main rotor compressibility.

(c) Maximum noise after the overhead position caused by unmuffled reciprocating engines.

A lesson to be learned from this is that there are several noise-making elements in helicopters whose levels, directional aspects, and techniques for modifying are different. Since operation parameters for main rotor, tail rotor, and engine are all intimately interrelated in helicopters, a change in any of the elements involves changes in all the elements. The implications of this interrelatedness must be taken into account in the economic reasonableness, technologically practicable doctrine.

Noise levels during approaches varied with glide slope, and no particular glide slope gave the maximum noise for all helicopters. This suggests that if a particular glide slope is selected for measuring approach noise during certification tests, helicopter A might be benefited and helicopter B could be penalized. It would appear more equitable to allow the applicant to select an approach technique within the airworthiness envelope of his helicopter and use this measured noise as the approach level. This concept is appropriate to helicopters because of the unique flight characteristics.

Current U.S. thinking is to require flyover, approach and takeoff tests to demonstrate compliance with noise levels. The method considered would be to average arithmetically all the data from at least six passes at each test condition after correction and adjustment.

The Committee recommends that before the limit lines are drawn at least the following should be accomplished:

- All available data be adjusted for impulsive noise correction if any adjustment is found necessary.
- Data be adjusted for whatever weather and atmospheric parameters are called for.
- Data should be handled according to whatever test procedures and processing are called for.
- The limits should consider all of the existing fleet.
- All presently scheduled and subsequent tests whose purpose is for data base should be done within the meteorological limits of wind, humidity, etc., and distances proposed for certification testing.

- Correction methods for off-standard conditions should be completely verified before inclusion in the regulations.

- Predictive accuracy (or inaccuracy) must be taken into account.

NOISE REDUCTION/ECONOMIC STUDIES

In a recent working paper of the U.S. Representative to ICAO, the following statements appear:

"In setting a noise level limit, ICAO has previously attempted to determine what is 'economically reasonable, and technologically practicable.'....it has been felt that successful commercial application of a technology by at least one company was prima facie evidence of meeting the ICAO requirements." Our Committee's position is that, for helicopters, it is not true that successful commercial application of a technology by at least one company is prima facie evidence of meeting ICAO requirements for Economic Reasonableness and Technological Practicability (ERTP). Unlike jet transports, which are all designed to pretty much one general requirement - i.e., move people or goods so far, so fast - helicopters are designed to many varied requirements. As examples, external load-industrial category helicopters emphasize sling or hoist payload at low airspeeds. Corporate/executive category helicopters emphasize airspeed in addition to payload. Air taxi operations require high speed, payload and fuel efficiency. Still other helicopters can be designed specifically for high altitude-hot day conditions.

Hence, noise technology in one helicopter type does not guarantee successful application to other types, even those produced by the same company. Tradeoffs between helicopter noise and productivity are not as well understood and predictable as some regulatory agencies' personnel believe.

The only study published to date by the FAA which addresses the economic impact of noise reduction on helicopter noise is reference 2. This study concluded that a vehicle noise reduction of 2.5 EPNdB could be achieved on most helicopters by engine duct treatments with only a 2 to 3 percent increase in vehicle life cycle cost. It was additionally concluded that rotor noise reduction methods were not cost-effective means for reducing helicopter noise.

A detailed review by the Committee has shown the study to be technically lacking in several important areas, resulting in the incorrect conclusions that not only engine noise reductions can measurably reduce helicopter noise, but also that 2-3 dB reductions can be made with a modest increase in life cycle cost. The Committee's findings did substantiate the conclusion that means for reducing rotor noise were generally very costly to the vehicle's life cycle cost. The results of some actual aircraft noise reduction programs are herein presented to substantiate these findings.

CRITIQUE OF REFERENCE 2*

The study has its major weaknesses in (a) the incorrect identification and reduction of helicopter predominant sound sources, (b) an inaccurate cost analysis, particularly for light helicopters, (c) an incomplete weight trending analysis, (d) the exclusion of impact analysis of some major factors such as range, payload, marketability and vehicle suitability and (e) non-applicability to tandem helicopters.

Relative to the noise analyses used: (1) Tail rotor noise is shown to be significantly underpredicted, resulting in its exclusion as a major noise source. In fact, many helicopters flying today have predominant contributions of their tail rotor to the vehicle's PNL and EPNL. (2) The main rotor noise analysis assumes an unrealistically rapid rolloff of rotor broadband noise. This incorrectly emphasizes the importance of other noise sources such as the engine in the important mid-frequency region. A recently completed study for NASA (ref. 3) substantiates this conclusion. (3) The engine analysis used significantly overpredicts engine noise by underpredicting the rolloff of core engine noise above 1000 Hz by 7-8 dB per octave.

All of the above result in the incorrect conclusion that turbine exhaust treatments, rather than rotor noise reduction (main and tail) are required to reduce the perceived noise level of helicopters.

As far as the cost analysis is concerned: (1) Quantity of aircraft is not considered. (2) Adjustments to cost data, such as inflation, changing overhead rates, new technology costs, development costs and recertification cost are not stated and/or included. (3) Estimates are not correlated with statistical data. (4) Using the study's estimates, the costs for nine current models was underpredicted by 15 to 350 percent, while the costs for five other models were overpredicted by from 23 to 83 percent. Inaccuracies of over ± 2 to 1 were therefore seen.

With regard to the weight analysis used: (1) The selection of driving weight parameters is incomplete and the majority of the trending equations are incorrect. (2) The significant influence of mission requirements (such as altitude/temperature criteria and single engine ceiling requirements) is ignored. (3) Far too much dependence is placed on main rotor size and power rating. (4) Input data used are for older military aircraft. No data are included for light helicopters which represent the bulk of the fleet. (5) Engines are assumed to be "rubberized" such that engine weight is incorrectly considered a linear function of small power changes. In reality an engine cannot generally be resized in small increments, requiring the next larger size available engine to be used.

Relative to the performance analysis used: (1) Installed power relationships are too generalized, as they do not account for installation losses which can be significant. (2) Forward flight power required relationships are very much dependent on individual manufacturer's design philosophy and, therefore, cannot be generalized in the manner of reference 2. (3) The specific fuel consumption data used does not apply to modern-day turboshaft engines.

---

*The views expressed are those of the Committee and are not necessarily those of NASA.

SPECIFIC NOISE REDUCTION CASES

Analysis

A Sikorsky S-61N 8840 kg (19 500 lb) gross weight helicopter was analyzed by Committee members to determine the impact on direct operating cost of applying state-of-the-art noise reduction technology to reduce its cruise flyover noise. The best analytical techniques available to Sikorsky were used for this study and were updated with actual weights, performance and cost data to provide the most realistic models possible.

The result of this study is shown in figure 1 as the dotted line and is compared with the reference 2 results (normalized to Direct Operations Cost (DOC)) for main rotor reductions and engine silencers. It should be noted that the engine silencing curve of reference 2 demonstrating the limited penalty associated with noise reduction, shows no correlation with the total vehicle curve. Rather, the total vehicle results more closely correlate with the reference 2 rotor curve (which was concluded to be impractical) even though tail rotor, main rotor and engine noise reduction was generally required to achieve the required noise reductions. A 2-dB noise reduction resulted in a 13-percent increase in DOC while a 3-dB noise reduction resulted in a 70-percent increase in DOC.

Hardware

Several helicopters have been modified for reduced noise and demonstrate the economic impact of the application of current state-of-the-art technology.

In the case of Boeing Vertol model 347 helicopter, which resutled from modifications to the CH-47 helicopter, a noise reduction in the order of 12 PNdB was achieved. The following changes were incorporated:

Changed from three- to four-bladed rotors.
Reduced rotor rpm.
Increased height aft pylon 0.76 m (30 in.).
Increase length fuselage 2.79 m (110 in.).

The total increase in weight empty was approximately 1590 kg (3500 lb). Since the aerodynamic performance of both aircraft is similar, this weight comes directly out of payload. Allowing 75 kg (165 lb) per passenger plus 15.9 kg (35 lb) baggage, the reduction comes to 18 passengers. At a maximum seating density of 52 passengers, the reduction in potential passengers, and hence, revenue, is 35 percent.

Another helicopter modified for reduced noise, the Hughes OH-6, will also be addressed here. In reference 4, a reduction of 10 dB (OASPL) (from

90 to 80) is stated as being accompanied by a reduction in payload from 295 kg (650 lb) to 267 kg (590 lb), or 28 kg (60 lb) for 10 dB. This is a reduction of noise of 10 dB with a payload reduction of about 10 percent. However, the report states that it was an idealized "perfect" muffler; i.e., it did not reduce power, it did not increase fuel consumption, it did not weigh anything, but it did reduce noise. A practical case in the same reference shows that for 10 dB noise reduction, the payload drops from 295 kg (650 lb) to 159 kg (350 lb) which is a reduction of 46 percent. A large part of the penalty is in the power-robbing aspect of the muffler, but it does represent the real world.

Another helicopter to be considered is the Hughes 269C as modified for police work. The standard version has a gross weight of 930 kg (2050 lb), and a payload of 286 kg (630 lb) with full fuel. The never-exceed speed V_{NE} for the standard version is 175 km/h (109 mph). The quieted version has a gross weight of 873 kg (1925 lb) and a payload of 229 kg (505 lb) with full fuel; V_{NE} in the quiet mode is 113 km/h (70 mph). Thus, the quieted version payload is about 60 percent of the standard version. This is for a reduction in noise of from 3 to 8 dB (either dBA or PNdB) for the various flight conditions. Further, the quieted version has a minimum operating speed and a minimum operating altitude over the terrain of 152 m (500 ft). These latter limitations come about because of the reduced rotor rpm. Here again, the real world is more severe than theory.

Two major points result from the above: (1) One cannot generalize noise-economic studies, which must be made on specific models by the respective manufacturers, and (2) The cost of noise reduction is significant, and has shown a range of payload and DOC penalty from 3 to 23 percent impact per PNdB of reduction. The payload reduction associated with reduction in noise for the CH-47C and the OH-6A is 35 to 46 percent and on another aircraft this reduction in payload exceeds 70 percent for a reduction as low as 3 PNdB.

As a result, noise standards must not be established which require significant reductions over current design helicopters until such time as the technology is developed to economically achieve the required reductions. This technology development requires a substantial financial commitment comparable to that spent to develop economically viable quieting means for fixed-wing aircraft.

NOISE TRENDS AND POSSIBLE NOISE LIMITS

Figure 2 shows noise levels of 16 current helicopters and possible noise limits under consideration in the United States and internationally. The levels are taken from DOT/FAA noise measurements, ICAO/CAN Working Group B data, and U.S. industry supplied data. Several trends are evident. Helicopter noise levels vary directly with gross weight. Larger variations in noise level occur in cruise flyover than in a 6° approach for a given size helicopter. Also, noise levels of the quieter designs are generally higher during approach than in cruise flyover.

Possible noise limits under consideration by the FAA and within ICAO Committee on Aircraft Noise (CAN) Working Group B differ in stringency and variation with gross weight. The FAA's possible limits are the most stringent, particularly for the approach condition. If such limits were in effect, one-half of the helicopters shown in figure 2 would not comply for the flyover condition. For the approach condition, over 70 percent would not comply.

The upper line, labeled HAA, in figure 2 has been proposed by U.S. industry as a possible noise standard. It represents levels that "place a lid" on the noise of future designs and derivative versions. At the same time, the standard penalizes those helicopter types which are the noisiest. With such a standard, 25 to 30 percent of the helicopters shown in figure 2 would not comply. In view of the present understanding of rotor sound generation, the accuracy of noise prediction, and the limited change possibilities of derivative helicopters, this standard is believed a more rational initial step.

PREDICTION ACCURACY

The development of standards and the establishment of noise limits must consider the accuracy of helicopter noise prediction as well as the repeatability of the data. The manufacturer must have a high level of confidence of meeting these limits since the certification test is conducted near the end of the development program. This has been recognized by DOT/FAA (refs. 5 and 6) in the development of noise standards for fixed-wing aircraft. For these aircraft, the confidence level of noise prediction is high because of the extensive resources expended over the past decade. Tolerances range from 2 EPNdB up to 5 or 6 EPNdB.

Such is not the case for helicopters. The state of technology of helicopter noise prediction is not as advanced as that for jet transports and propeller-driven airplanes. To assure compliance, a helicopter manufacturer's design would have to be targeted below the noise rule requirement by tolerance margins of up to 5 EPNdB for derivative and growth versions, and 10 to 12 EPNdB for new designs that are substantially different for current experience. This is illustrated in figure 3. Coupled with this is the fact that no prediction method exists for the approach and takeoff conditions.

LIMITED CHANGE POSSIBILITIES OF DERIVATIVES

Under the acoustical change provision of FAR Part 36 aircraft noise standards, the noise level of derived versions must not exceed that of the "parent" aircraft if the parent's noise level is above the limits. This provision is being considered for the helicopter noise rule. This means that future derivatives of the helicopters exceeding the limits in figure 2 cannot "grow" in the traditional manner.

The helicopter industry follows a unique design/product improvement cycle in developing derived versions and in designing new ones. Since the helicopter derives its lift and control from constantly powered rotating blades, a continuous flow of power is required from the engine to the rotors. This flow is accomplished by means of a complex transmission/drive train system which must transmit high torque loads during all helicopter flight regimes. The expense of developing and testing the components of this transmission/drive train/rotor system represents a significant factor in the overall cost of the helicopter. For this reason the design/development cycle many times calls upon previously developed components to meet the requirements of a newly designed helicopter.

After a new helicopter type is certificated and in production, new or updated requirements of the helicopter operator must be met. The manufacturer must decide on a new product or modification of an existing one. Because of the high cost of components and qualification testing of a helicopter, the decision to modify an existing product is more often the choice. Thus, derived versions of a helicopter design are constantly being developed, using as many of the original drive train/rotor system components as possible.

Typically, helicopter derivatives are growth versions with higher payload and/or range capability and increased gross weight. For the same rotor tip speeds, the gross weight effect increases the noise level. To offset this, rotor tip speeds of all growth versions, if the parent design is noncompliant, would have to progressively decrease.

Reducing rotor tip speeds has several very practical limits. Torque levels in the transmission and drive train increase. With previously developed components, torque limits can be quickly reached. Hence, in those designs that are torque-limited, derivative versions would not be possible under the acoustical change provision. Lowering rotor tip speeds also directly affects the lifting capability and control of the vehicle. It is not possible to generalize this effect since each design starts from a different baseline. However, experience has shown that performance and controllability tend to be degraded.

Any retroactive provisions which apply to current helicopters or to future production of existing designs would curtail the growth of the helicopter industry. Unlike fixed-wing aircraft noise control, it has been demonstrated that retrofit and modifications to existing helicopter designs result in unacceptable performance and safety degradation (refs. 2, 4, 7, and 8).

ROTOR IMPULSIVE NOISE

The matter of rotor impulsive noise generates quite a bit of controversy due to the very subjective nature of people's response to it. The term, as used here, applies to any rotor signature having as one of its characteristics a high crest factor, regardless of the physical cause of the noise. It should be understood that impulsive noise is not associated with any one helicopter configuration or flight condition. It may be due to intersections between blades and vortices shed by other blades or rotors. Examples of this are tandem rotor helicopters, or single rotor helicopters in descent. Impulsive noise may also be associated with high advancing tip Mach Number on any configuration.

Figure 4 illustrates typical spectra of impulsive rotors. It is the preponderance of high-amplitude higher harmonics that create the sound often referred to as "bang" or "slap."

There is no question that an impulsive rotor is more annoying than a non-impulsive rotor. There is considerable room for debate, however, as to the units which best measure the annoyance. The unit of Effective Perceived Noise Level (EPNL) has been selected by both FAA and ICAO as the basic unit for helicopter noise regulation. The debate centers on whether EPNL adequately measure impulsive noise, or whether an additional adjustment, in the form of a penalty, is required.

Several descriptors for impulsive rotor noise have been proposed and some of these were evaluated in an FAA report (ref. 9).

One of the leading contenders is

$$\Delta = -6.875 + 13.75 \log CI \qquad 0 \geq \Delta \geq 5.5 \qquad (1)$$

where

$$CI = \frac{\frac{1}{N} \sum_{j=1}^{n} V_i^{4}}{\left[\frac{1}{N} \sum_{j=1}^{n} V_i^{2}\right]^2} \qquad (2)$$

and

N = the number of samples of V_i obtained in each 0.5 second by high-speed digitizing of the signal

V_i = voltage sampled at ith time increment

Two forms of the above have been proposed: one in which the signal is low-pass filtered at 2000 Hz prior to high speed digitizing, and one in which the signal is "A"-weighted prior to digitizing.

Another proposed approach uses the difference between the maximum peak A-weighted sound pressure level and the maximum A-weighted sound pressure level as measured by analog devices. These measurements may be based on the peak values during the run, or performed every 0.5 second as in the previous method.

A conclusion of the reference 9 study is: "All of the impulsiveness descriptors...when applied to the EPNL values for actual flyovers, improve correlation with the average judged response. None, however, provides a correlation that is statistically significantly different from zero at the 1-percent level...."

Reference 9 further states that: "Correlation between main rotor blade passage frequency (the pulse repetition rate) and averaged judged response is higher than that provided by all of the impulse measures except the French method" (eqs. (1) and (2).)

Reference 9 also concludes: "Descriptors formed by combining repetition rate with each of the impulsiveness measures are all significant at the 1-percent level accounting for 75 to 87 percent of the variance in averaged judged response."

So, we even see a disagreement among proponents of the impulse penalty as to whether impulse level or repetition rate is more important. This latter position is at variance with at least two other studies (refs. 10 and 11) which find repetition rate to be barely significant.

Use of methods such as those described above implies that the data analysis for helicopter certification may be considerably more involved than that required for airplanes. Such complexities should not be introduced unless the current method is clearly proven to be inadequate. This is not the case. Figure 5 shows the EPNLs of successively impulsive flybys obtained by increasing the advancing tip Mach Numbers of a helicopter while holding the airspeed relatively constant. Figure 5 also presents the time histories of the first and last runs showing that the EPNL of the impulsive data is greater than that of the non-impulsive data because the levels are higher and the time duration greater.

The results indicate that the last run had an increase of 8 PNdB due to level, and 5 PNdB due to exposure time, for a total increase of 13 EPNdB over the first run.

The HAA Committee finds that EPNL, by itself, is a realistic and sensitive enough measure of blade impulse noise without further embellishment.

CERTIFICATION TO OPERATIONAL CATEGORIES

The Noise Control Act of 1972 relates, among other things, to the promotion of "an environment for all Americans free from noise that jeopardizes their health and welfare." Thus, the thrust of the Act is toward the protection of people.

The philosophies of present aircraft certification standards establish a noise limit which may not be exceeded if type certification is to be achieved. This philosophy was developed in conjunction with fixed-wing aircraft. Such aircraft are generally operated from airports, and airports are generally located in centers of population.

Helicopters, however, can operate from totally unprepared fields and perform much of their useful work in sparsely populated areas. HAA statistics show that over 70 percent of helicopter operations are conducted in areas occupied by few, if any, people. The search for and production of new energy sources, and other raw materials, are prominent in these non-noise sensitive regions.

While all studies to date do not show the same penalties for quieting, all studies show that some penalties result when helicopters are made quieter. Fuel economy is worsened, power is reduced, weight increases, greater costs are incurred, all in various degrees, when quieting is required.

Therefore, the Committee feels that it is rational to direct attention to the unique operational abilities of helicopters when writing noise regulations. The regulations should not preclude certification on the sole basis of inability to meet noise criteria. Rather, inability to meet noise criteria should result in limitation of operational areas. The regulations should permit "dual" certification if requested: a quiet mode, complying with all regulations, including noise, and a more efficient mode (not meeting the noise criteria) having operational constraints as part of the certification.

HAA is in the process of questioning the helicopter operating members as follows:

Do you favor a helicopter noise certification criterion which, all other aspects considered equal,

( ) Requires all helicopters to be certificated with a performance which produces noise levels based upon operation in congested areas?

or

( ) Uses a certification noise level based on operation in congested areas but allows relaxation when operations are to be conducted in sparsely populated areas?

Fifty-eight responses have been received of which 57 favored the second criterion. The other respondent favored the first for new designs and the second for existing designs.

FAR 36 now has a statement: "No determination is made, under this part, that these noise levels are, or should be, acceptable for operation at, into, or out of any airport." This certainly recognizes the probable existence of local opinion and local regulations about the operations of noisy vehicles. It further appears that administrative channels are in existence for implementing local controls and approval of helicopter operations. FAR 133 Rotorcraft External-Load Operations, Para. 133.31(f) allows rotorcraft external load operations over congested areas if those operations are conducted without hazard to persons or property on the surface. The operator must develop a plan and coordinate the plan with the FAA district office, and get agreement with local officials relative to air traffic control, etc.

If, in the above, "hazard" is construed to include noise damage or annoyance, the "plan" of FAR 133.31(f) can include, for example, a minimum altitude and a path so as to minimize noise on the ground.

CONCLUSIONS

(1) Helicopters, as noise generators, are more complicated than fixed-wing aircraft. This fact does in no way excuse helicopters from noise regulations. The fact does, however, indicate that there should be a different regulatory and operational attitude toward helicopters than to fixed-wing aircraft.

(2) These differences impact upon the ERTP doctrine making generalizations unreliable when applied to a variety of helicopters.

(3) Hardware experience has indicated greater performance and economic penalties than published theory would indicate.

(4) The relatively primitive and incomplete state of the art of helicopter noise prediction methods, particularly for new designs, cries out for generous noise limits, and increased funding for further study.

(5) If the traditional, successful industry policy of derivative design is not recognized by the regulatory agencies, there will be severe economic implications, curtailing industry growth.

(6) The question of rotor impulsive noise and the units with which it shall be expressed promises to make testing and data reduction more complicated and costly than is necessary, at least for the initial body of regulations. EPNL, by itself, appears to be an adequate and practical descriptor for this decade.

(7) The ability of helicopters to operate where no other vehicle can demands reasoned consideration. If we insist upon levels of quiet (appropriate for cities) when operating in the wilderness, we shall be needlessly, and inefficiently, constrained by a man-made wall of unreason.

REFERENCES

1. True, H. C.; and Rickley, E. J.: Noise Characteristics of Eight Helicopters. Report No. FAA-RD-77-94, July 1977.

2. Bowes, Michael A.: Helicopter Noise Reduction Design Trade-Off Study. DOT/FAA Report FAA-AEQ-4, Jan. 1977.

3. Sternfeld, Harry, Jr.; Doyle, Linda B.: The Effects of Engine Noise and Rotor Broad Band Noise on Civil Helicopter Operations. NASA-CR-145085, 1976.

4. Wagner, R. A.: Noise Levels of Operational Helicopters of the OH-6 Type Designed for the L.O.H. Mission. NASA CR-14760, 1974.

5. Foster, Charles R.: Aircraft Noise Standards, A Government Point of View. SAE West Coast Meeting, August 9-12, 1976.

6. Working Paper of U.S. Representative to ICAO: The Use of Noise Data in the Development of Aircraft Noise Standards. ICAO/CAN Working Group D, April 3-6, 1978.

7. Brown, E. L.; Cox, C. R.; Halwes, D. R.: A Preliminary Design Study of a Quiet Light Observation Helicopter. TR 69-99, U.S. Army Aviation Materiel Laboratories, 1969.

8. Halwes, D. R.; Cox, C. R.: Noise Reduction Possibilities for a Light Helicopter. SAE Paper 690683, Bell Helicopter Textron, 1969.

9. Galloway, William J.: Evaluation of Acoustical Descriptors for Assessing Subjective Response to Helicopter Impulse Noise. Bolt, Beranek and Newman Report 3572, 8 November 1977.

10. Sternfeld, Harry, Jr.; Doyle, Linda B.: Evaluation of the Annoyance Due to Helicopter Rotor Noise. NASA CR-3001, 1978.

11. Lawton, Ben W.: Subjective Assessment of Simulated Helicopter Blade-Slap Noise. NASA TN D-8359, December 1976.

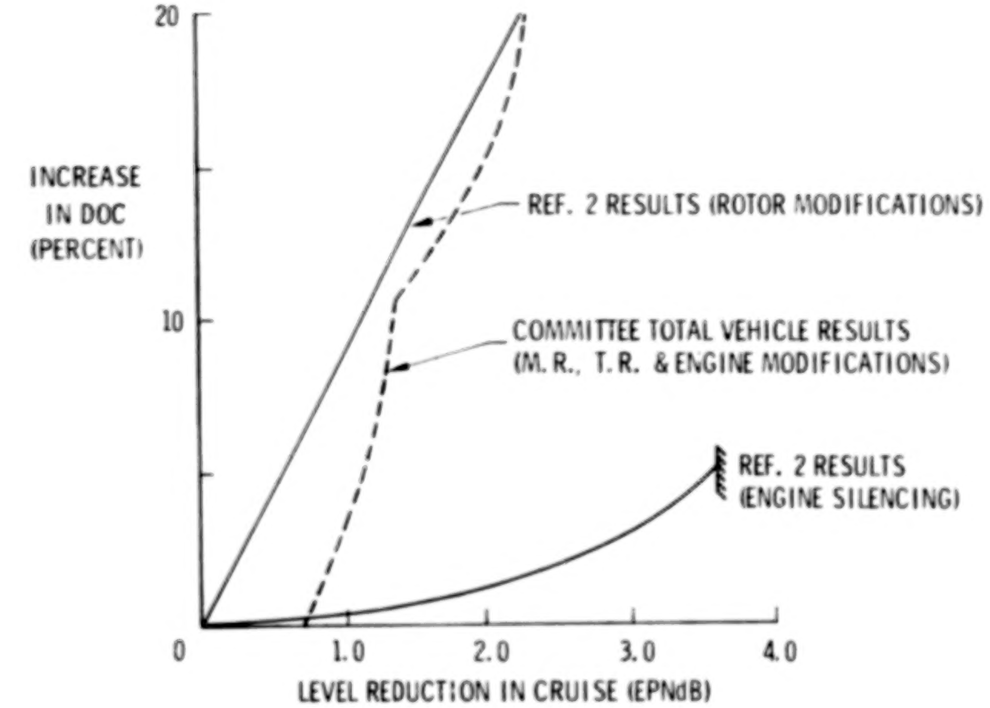

Figure 1.- Comparative trade-off results.

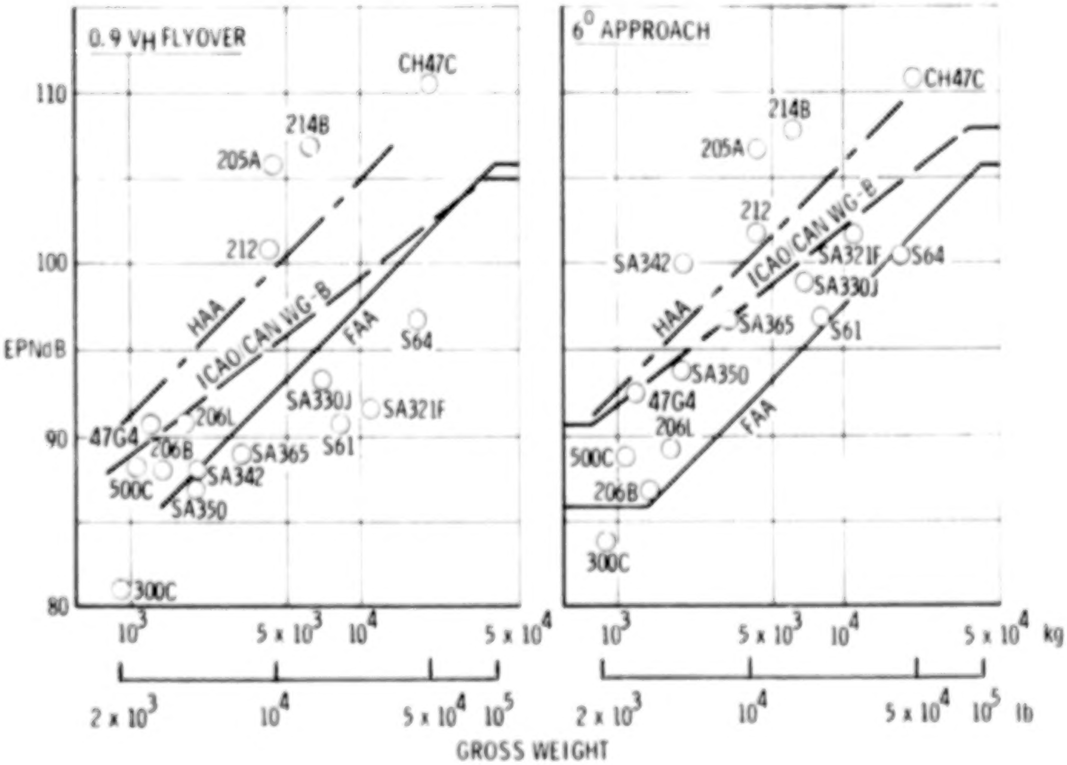

Figure 2.- Helicopter external noise trends and noise limits under consideration (ISO impulsivity included).

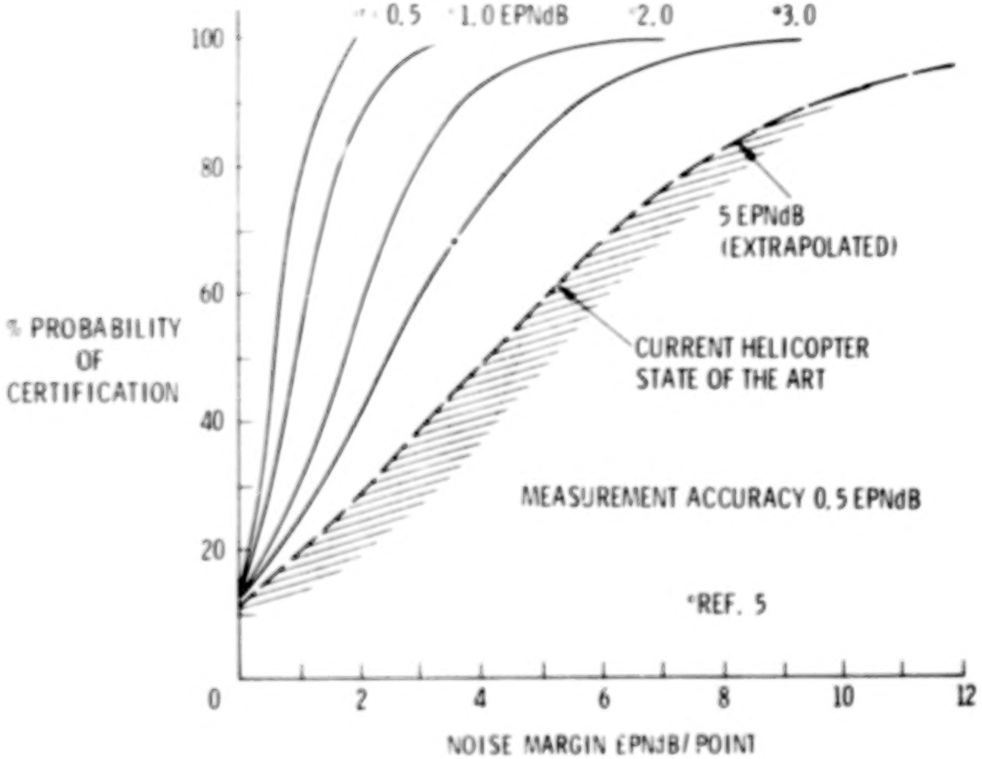

Figure 3.- Required design noise margin EPNdB/point.

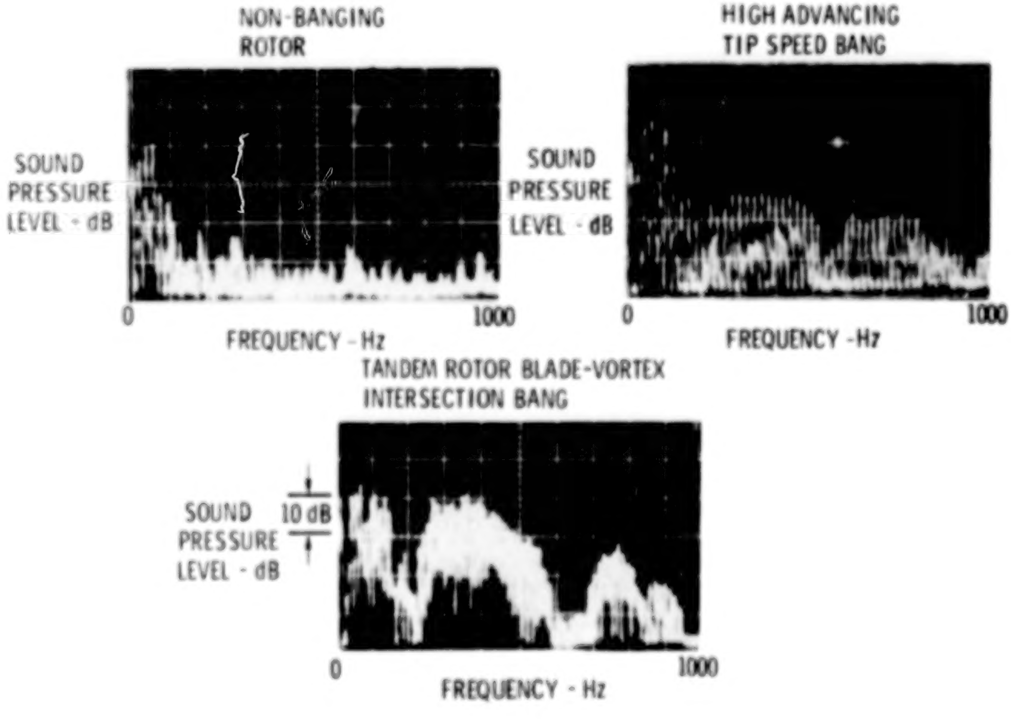

Figure 4.- Narrow band spectra - rotor noise.

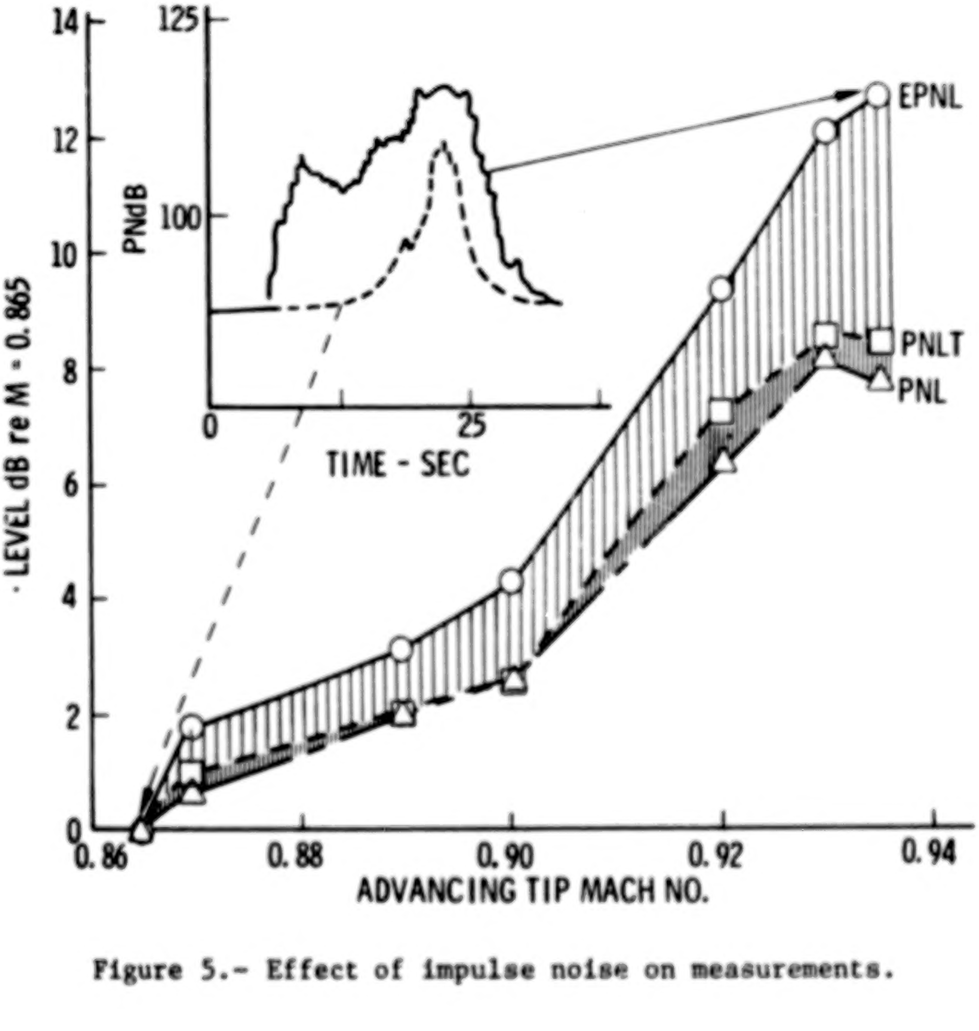

Figure 5.- Effect of impulse noise on measurements.

3

NOISE REQUIREMENTS FROM A MILITARY POINT OF VIEW

CHARLES C. CRAWFORD, JR.
U.S. Army Aviation Research and Development Command

SUMMARY

Little effort has been expended by the military to establish external noise standards for helicopters. Prior to UTTAS/AAH, specific requirements were nonexistent. Recent requirements which have been used for these designs generally have not been met. The military must cooperate with the Federal Aviation Administration (FAA) in establishing such requirements to minimize public annoyance; however, the FAA should use simple criteria which do not excessively impact overall design. Military internal noise requirements, while not generally met in the past, must be stiffened and enforced if realistic acoustical treatment, good speech intelligibility, and hearing conservation are to be achieved. Without significant additional research, an aggressive attack on external noise will significantly impact cost and flight performance; therefore, jeopardizing performance margins needed for overall helicopter reliability improvements.

INTRODUCTION

Establishing realistic external noise requirements for military helicopters is an extremely difficult task. This results in a diverse range of needs, for example, the battlefield is an extremely noisy environment. During peacetime operation, military helicopters are frequently criticized because of the noise they generate. The task of avoiding public annoyance is extremely important in order to attain support of the public, particularly in the face of our all-volunteer fighting forces. Some specific missions require the helicopter to operate as far as possible behind enemy lines without detection. Most of us are aware of operating features developed by Hughes Helicopters for a prototype OH-6A to make this type of mission possible; however, the Army prefers to avoid dedicated mission aircraft as much as possible to minimize our total logistical support problem.

On the technical side of the issue, the range of noise sources significantly complicates the problem. The predominant source of external noise from the main and tail rotor are drastically affected by the number of blades, blade design, and operating tip speeds of the rotors. Fundamental gear meshing frequencies for present day transmission gearboxes range from 40 to 22 000 Hz. Engine noise at its relatively high frequency (5000 Hz and above) can also be an important factor. The impulse noise from aircraft ordinance, blade slap phenomenon, and other wake vortices effects are also important.

The military is hard-pressed to meet current design-to-cost requirements; therefore, a significant amount of money is not available to apply to noise reduction during the full-scale engineering development effort. Currently, only those techniques may be used that do not adversely effect operating cost.

EXTERNAL NOISE DISCUSSION

It is first important to consider the noise levels of our current helicopters. A summary of sound exposure levels using A-weighted averaging techniques for a large range of Army helicopters from the two place TH-55 trainer to the CH-54B crane are contained in Table I. The dispersion in this noise is shown at distances of 30.5, 305 and 3050 meters (100, 1000 and 10000 feet). The data are taken from Ref. 1 which is a summary of noise measurements obtained during helicopter operation at our Aviation Center, Ft. Rucker, AL. Eight manuevers, which include level flight at 91.4 meters (300 feet), turns over the middle of the runway, ascent and descent to the runway, takeoff and landings, and hover in and out of ground effort are averaged from an array of microphones positioned at 61 meters (200 feet), intervals perpendicular to the aircraft's flight path. As you can see, the noise levels are quite high, ranging from 97 to 107 SELdB(A) at 30.5 meters (100 feet), reducing to only 86 to 97 SELdB(A) at 305 meters (1000 feet). None of the aircraft listed in this table were required to meet specific external noise requirements during their design.

Our first quantitative noise requirements were initiated with the UTTAS airframe and engine development programs. Figures 1(a) and 1(b) show the original airframe requirements which were crudely based on noise measurements made using the Lockheed XH-51 experimental helicopter. The noise levels of the winning prototype are shown to significantly exceed these requirements. It should be pointed out that there were no significant noise differences between the two competing prototypes relative to this requirement. With some improvement in the production configuration, production specification values taken from Ref. 2 still exceed the requirement; therefore, the objective of keeping the detectability of this larger helicopter down to the levels of the XH-51 could not be met without a significant additional expenditure. Aircraft development costs and schedule trade-offs negated achievement of the noise level objectives. A similar picture exists for the Advanced Attack Helicopter as shown in Figure 2. Specification values are from Ref. 3.

PROPOSED COMMERCIAL STANDARDS

Much work has been done by the FAA and working parties of the International Civil Aviation Organization (ICAO) in preparing standards that would be a prerequisite for civil type certification. An Effect Perceived Noise level range of 88 to 105 EPNdB for a fly-over at 150 meters and for takeoffs and approaches at the same height is envisioned. This does not include the 3 EPNdB correction for rotor impulse noise. For the fly-over case, the speed of 90% of the maximum speed in level flight or 90% of the Never Exceed Speed, whichever is less, would be used. The familiar flight profile for these test conditions are shown in Figure 3. It is the Army's understanding that the flight elevations and other test conditions remain open for negotiation and may not necessarily be 150 meters for all conditions.

The concept of an external noise requirement to prevent public annoyance is certainly valid; however, the demonstration technique appears unduly complicated. Variations in pilot techniques should not be allowed to meet ultimate external noise requirements. The Army has consistently held to this position in the demonstration of flight performance which has kept such demonstrations relatively straight forward. For example, hover, maximum speed and manuever commitments must all have been demonstrated at 100% rotor rotational speed because a combat flight crew may well forget to adjust main rotor speed for a critical manuever, thus losing performance when it is most important.

The Army does not believe that any of its current helicopters could meet the new proposed requirements; and even with current technology, the natural tendency would be to lower design tip speed in order to reduce noise. This approach has many disadvantages in that high speed retreating blade stall will result at lower forward speeds, high speed manueverability will be reduced and entry into autorotation will be compromised by rotor decay from a lower potential energy condition.

Scout and Attack helicopters during tactical operations will spend a predominant amount of time in hover or near hover flight; therefore, external noise under these conditions is also important to the military to minimize detectability in combat environment.

Any attempt to make existing helicopters, or those designs currently in development, conform to existing FAA thinking will divert funds needed for long-range research to insure that our next generation of helicopters will probably be optimized for detectability and performance at an affordable cost.

INTERNAL NOISE REQUIREMENTS

Most of our current helicopters do not meet the internal noise requirements of Ref. 4. Hearing damage risk criteria is being determined for personnel who operate our aircraft for long periods of time. Aircraft internal aided and unaided communications are less than optimum. As a result, the Army has established a working group to develop the helicopter requirements for MIL-A-8806A, under the chairmanship of the U.S. Army Aviation Research and Development Command (AVRADCOM). Government membership includes representatives from U.S. Army Health Services Command, U.S. Army Avionics Research and Development Activity, U.S. Army Aeromedical Research Laboratory, U.S. Army Human

Engineering Laboratory, U.S. Army Training and Doctrine Command (TRADOC), U.S. Army Troop Support and Aviation Materiel Readiness Command (TSARCOM), Department of the Army--Office of the Surgeon General, U.S. Army Environmental Hygiene Agency, as well as four major U.S. helicopter manufacturers (Bell Helicopter Textron, Boeing Vertol, Hughes Helicopters, and Sikorsky Aircraft). This working group will emphasize requirements for crew hearing conservation in terms of mission times, duty cycles, ground exposure time and troop temporary threshold shifts resulting during helicopter transit to the assault area. Speech intelligibility, both aided and unaided, with emphasis on reduced background noise in avionic equipment will be addressed. Impulse noise requirements of weapons as well as impulsive rotor near field noise will be considered during revision of the specification. The working group is chartered to have a draft revised specification by mid-1979.

The seriousness of the current situation is well illustrated by reviewing Figure 4 (obtained from Ref. 5). The sound pressure levels between 250 and 8000 Hz, which covers the normal hearing range, are largely above the specification requirements in the cabins of our current helicopters. Figures 5 and 6 (also from Ref. 5) show the reductions that must be necessary for effective communication at speech intelligible levels of 50% and 80% respectively. To date, the working group is projecting an adjustment to the military specification as shown in Figure 7 for unaided communication with a significant relaxation where aided communication is available. Peak pressure levels for impulse noise currently presented in MIL-STD-1474 (Ref. 6) appear acceptable. These are illustrated in Figure 8 for no ear protection and for various combinations of ear plugs and muffs, depending upon the daily exposures rate. In developing such criteria, the exposure duration to steady noise is quite important. Standards obtained from Ref. 7 are shown in Table II.

TRADE-OFF IMPACTS RE NOISE REDUCTION

If specification external noise requirements exist, new designs will be based on significant margins due to relatively poor prediction techniques. For example, analysis by others has shown that for a small 1361 kilogram (3000 pound) class helicopter, a 3 to 4 dB margin will require a 45 kilogram (100 pound) margin in weight, as well as a 20 knot decrement in forward speed. If the inability to achieve specific requirements will block the production of a design, industry is forced to take such conservatisms due to the poor accuracy of noise predictions. Although vehicle flight performance can be predicted quite accurately, most organizations use a 5% conservatism to insure achieving flight performance objectives.

The most significant technique in reducing rotor noise is reduction of tip speed, as previously discussed. This has been quantified to show (see Figure 9) that a reduction in tip speed of 230 m/sec (750 ft/sec) to 200 m/sec (650 ft/sec) results in an increase in design gross weight of approximately 160 kg (350 lb) (5%) for an Advanced Scout Helicopter of a 3402 kg (7500 lb) class with all other performance requirements remaining fixed. This 5% increase in helicopter size will also represent a 5% increase in helicopter cost.

CONCLUDING REMARKS

Establishing realistic external noise requirements for military aircraft is an extremely difficult task. Cooperating with the FAA to generate and enforce such requirements is extremely important to minimize public annoyance; however, a cautious path must be followed to insure that unnecessary payload penalties and cost impacts, which are built into the basic design are minimized. High performance margins are needed for combat effectiveness and weight allowance for innovative reliability improvements. Reliability improvements are the key to reducing life cycle operating costs. The demonstration of compliance with extreme noise requirements should be kept extremely simple, and avoid gimmicks in piloting techniques. Before such requirements become regulatory, much research is needed to develop innovative techniques for noise reductions without unduly affecting performance and cost.

REFERENCES

1. Rotary Wing Operational Noise Data. Report TRN #38, U.S. Army Construction Engineering Research Laboratory, Champaign, IL, February 1978.

2. UH-60A Utility Tactical Transport Aircraft System Prime Item Development Specification. AMC-CP-2222-S1000B, Sikorsky Aircraft, Division of United Technologies, Stratford, CT, 1 November 1976.

3. Advanced Attack Helicopter System Specification. AMC-SS-AAH-H10000A, Hughes Helicopters, Culver City, CA, 23 November 1976.

4. Military Specification: Acoustical Noise Level in Aircraft, General Specification For. MIL-A-8806A, Department of Defense, 11 July 1966.

5. Doyle, L. Bukowski; Sternfeld, H.: Evaluation of Current Helicopter Internal Noise Level Design Criteria. Contract DAAJ01-74-C-10544, The Boeing Vertol Company, Philadelphia, PA, December 1976.

6. Military Standard: Noise Limits for Army Materiel. MIL-STD-1474(MI), Department of Defense, 1 March 1973.

7. Noise and Conservation of Hearing. Technical Bulletin MED 251, U.S. Army, 7 March 1972.

TABLE I.- HOW NOISY ARE OUR CURRENT HELICOPTERS

		SOUND EXPOSURE LEVEL dB(A) AT		
HELICOPTER	LOADING	30.5 m	305 m	3050 m
OH-58A	NORMAL MISSION	97	86	69
UH-1H	MAX WT	106	94	79
UH-IB	MAX WT	101	90	73
AH-IG	NORMAL MISSION	105	93	76
CH-47C	MAX WT	107	97	82
CH-54B	MAX WT	106	95	78
TH-55	PILOT/STUDENT	99	87	67

DATA AVERAGE FROM 8 SPECIFIC MANEUVERS & 6 PICKUPS AT FORT RUCKER BY US ARMY CONSTRUCTION ENGINEERING RESEARCH LAB (RPT TRN-38)

TABLE II.- MAXIMUM RECOMMENDED SOUND LEVEL EXPOSURE

	MAXIMUM STEADY NOISE dB(A)	
EXPOSURE DURATION PER DAY IN HOURS	TB MED 251 7 MARCH 1972	WALSH-HEALY CRITERIA
8	85	90
6	87	92
4	90	95
3	92	97
2	95	100
1-1/2	97	102
1	100	105
1/2	105	110
1/4 OR LESS	110 (CEILING)	115 (CEILING)

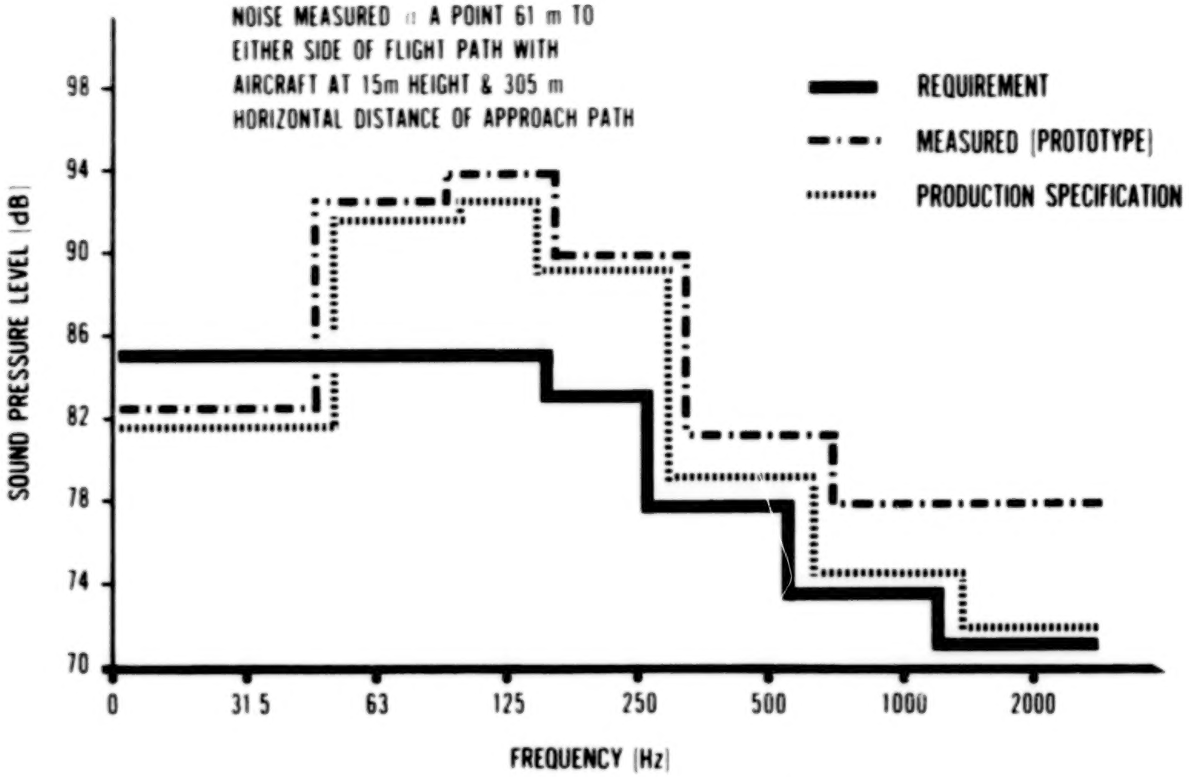

(a) Black Hawk in out-of-ground-effect hover.

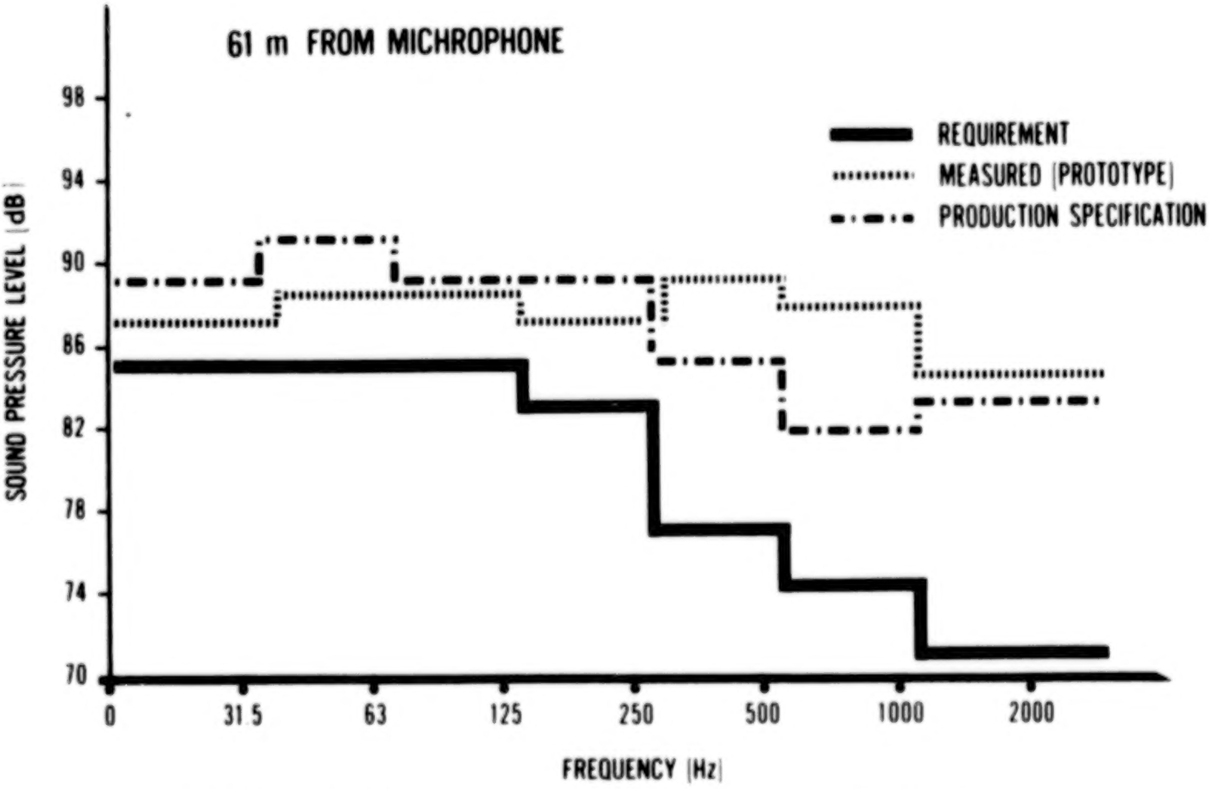

(b) Black Hawk in cruise at true airspeed of 150 knots.

Figure 1.- External noise.

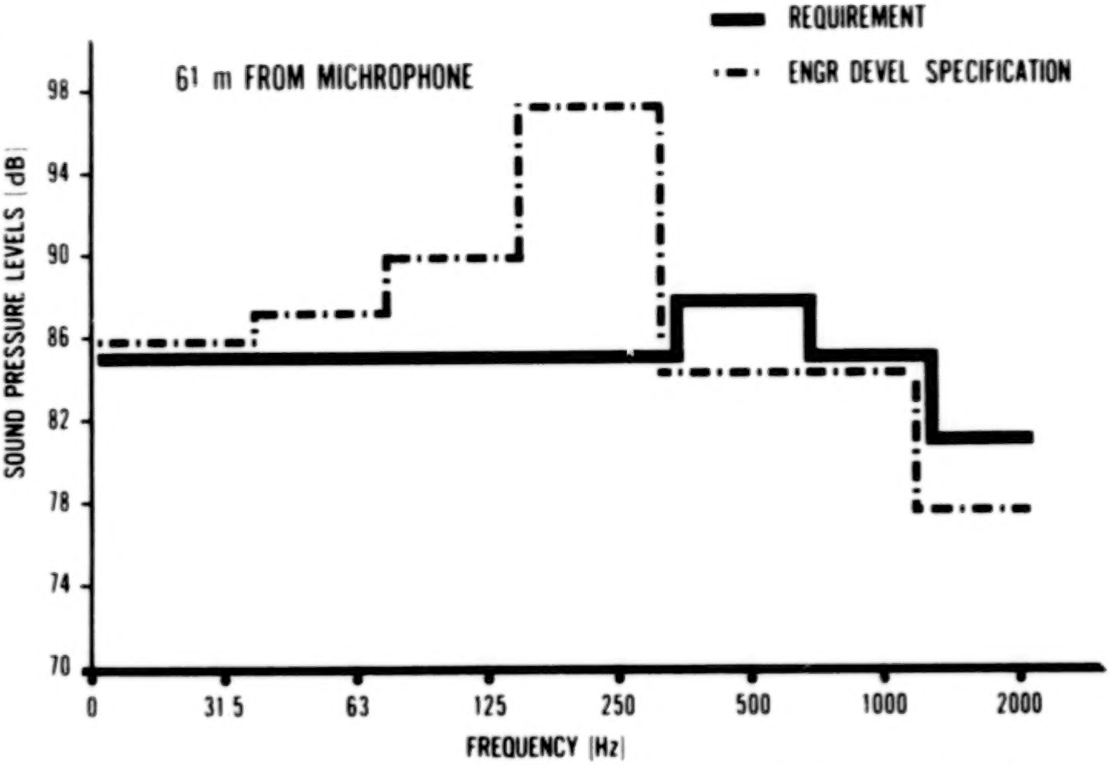

Figure 2.- External noise for advanced attack helicopter in out-of-ground-effect hover.

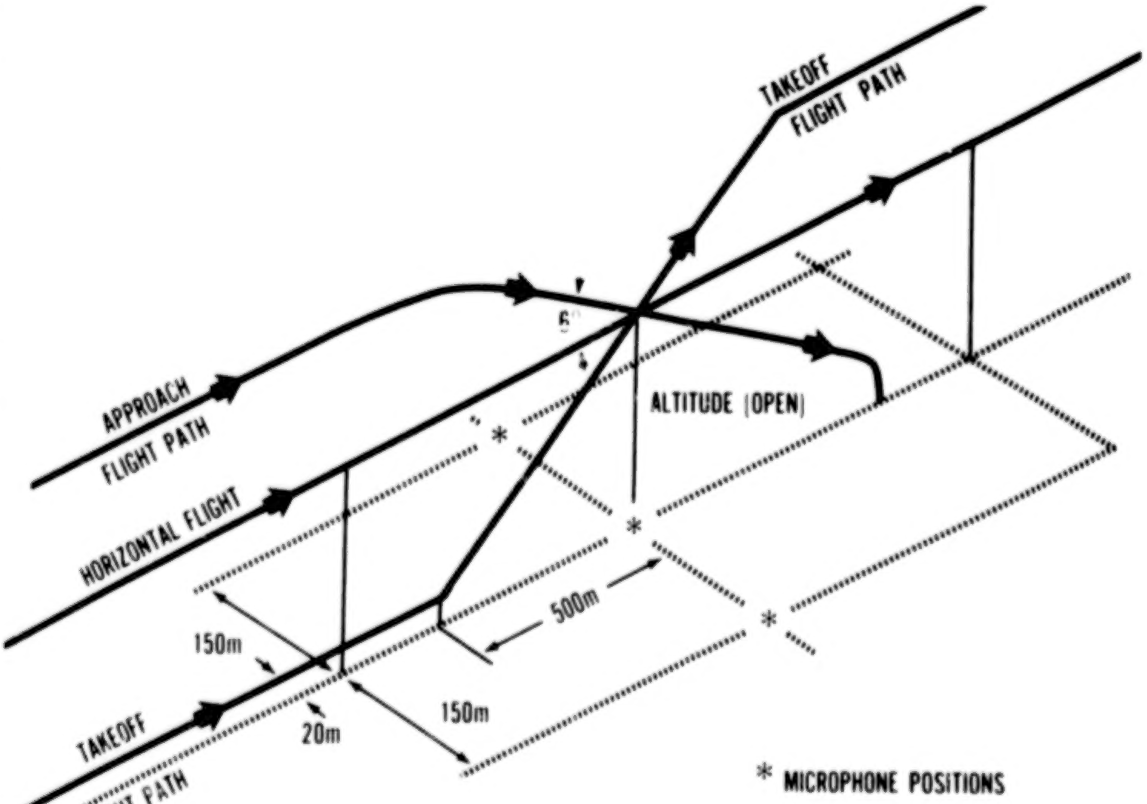
TAKEOFF FLIGHT PATH
APPROACH FLIGHT PATH
HORIZONTAL FLIGHT
ALTITUDE (OPEN)
500m
150m
150m
20m
TAKEOFF FLIGHT PATH
* MICROPHONE POSITIONS

Figure 3.- Proposed helicopter noise tests.

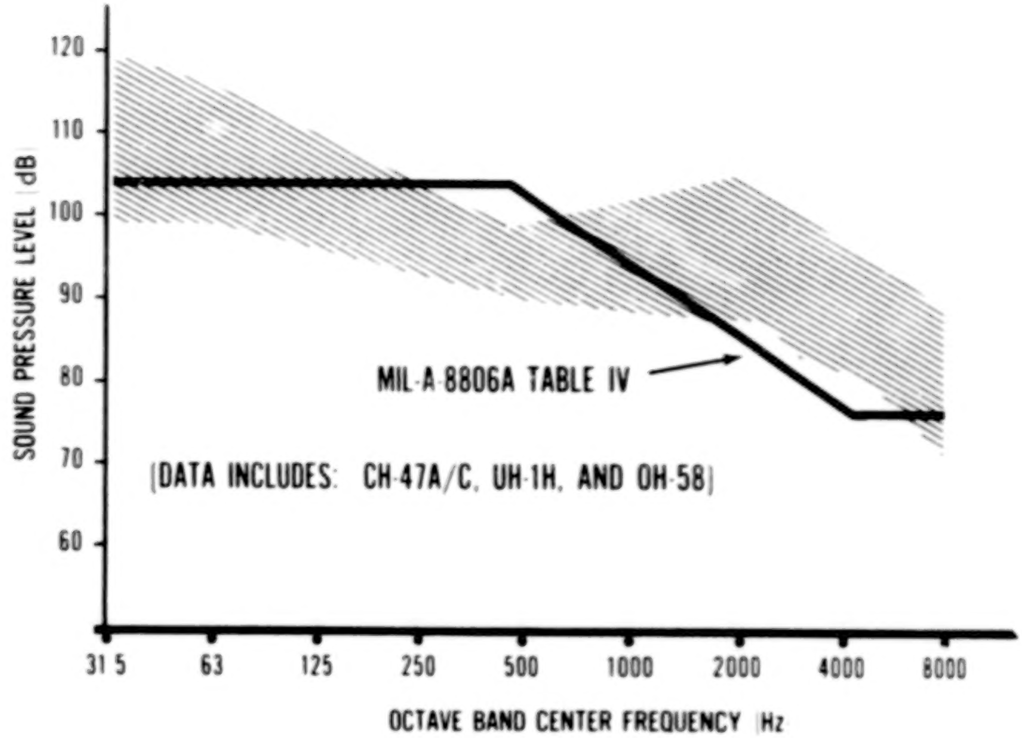

Figure 4.- Scatter of center cabin noise data in army helicopters during cruise flight.

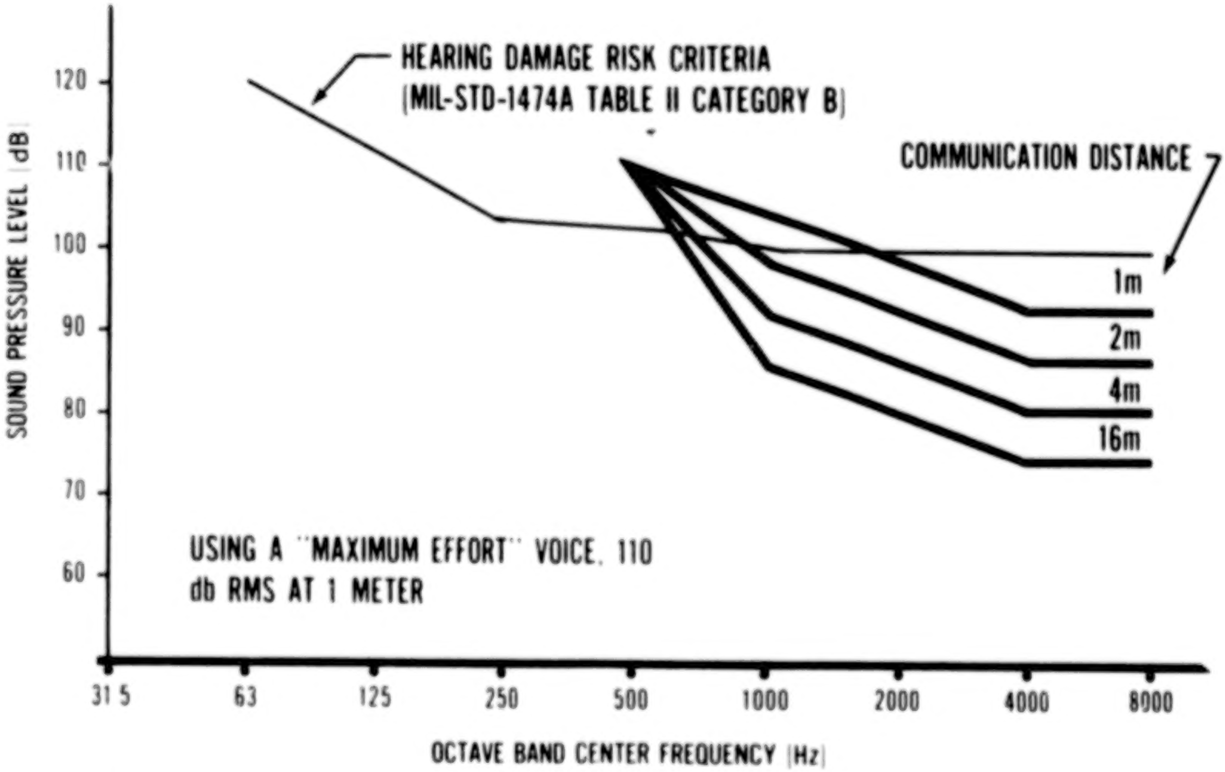

Figure 5.- Helicopter interior noise levels required for emergency commands. 50% speech intelligibility.

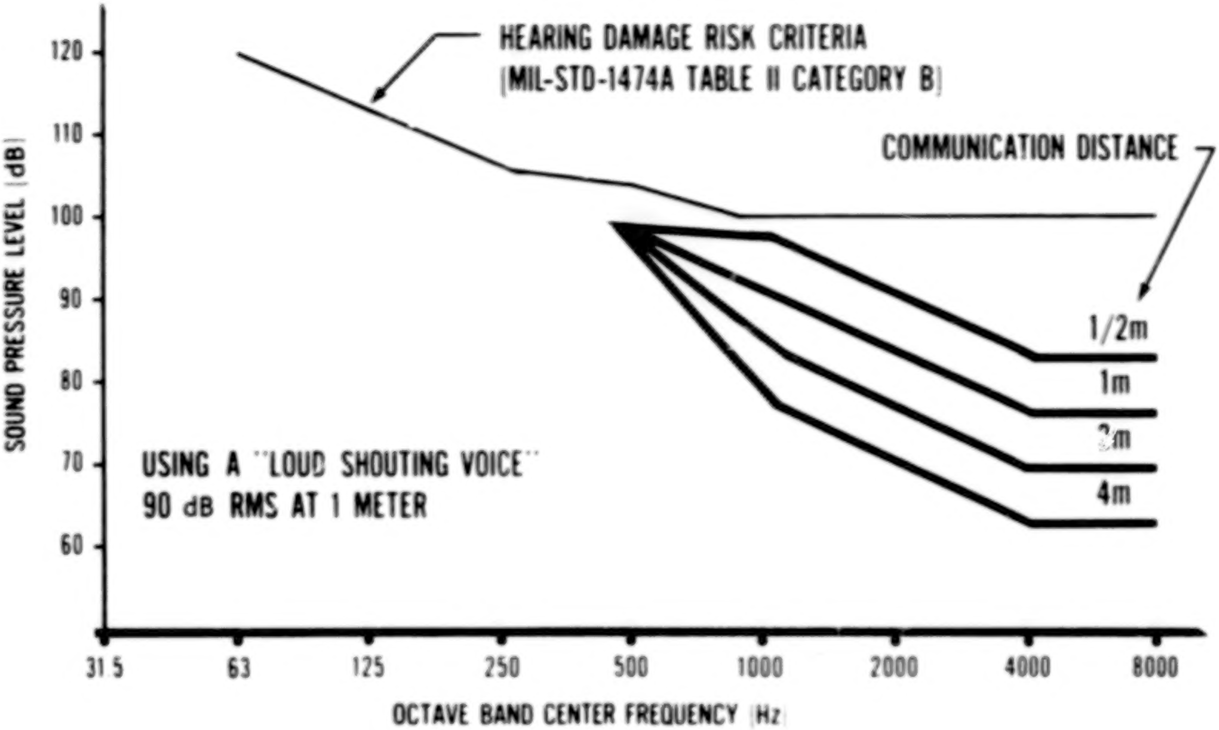

Figure 6.- Helicopter interior noise levels required for instructing troops. 80% speech intelligibility.

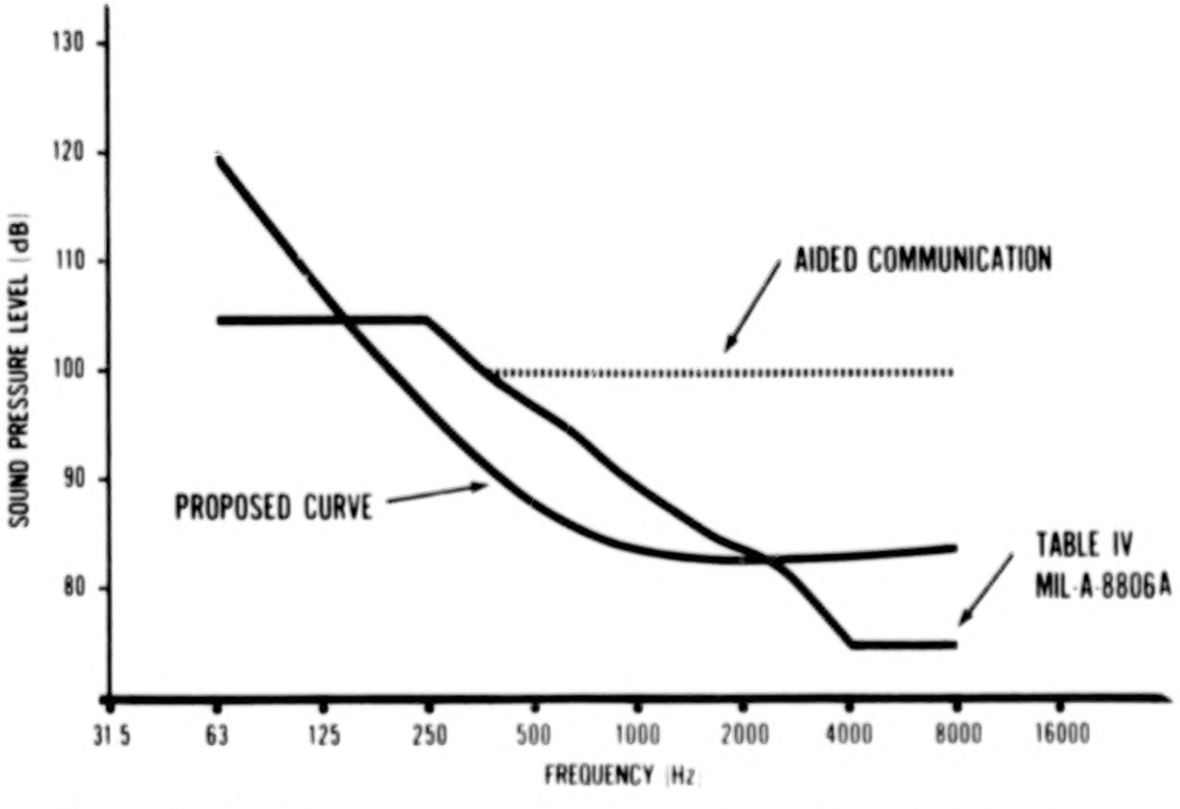

Figure 7.- Working group proposed design curve for noise levels.

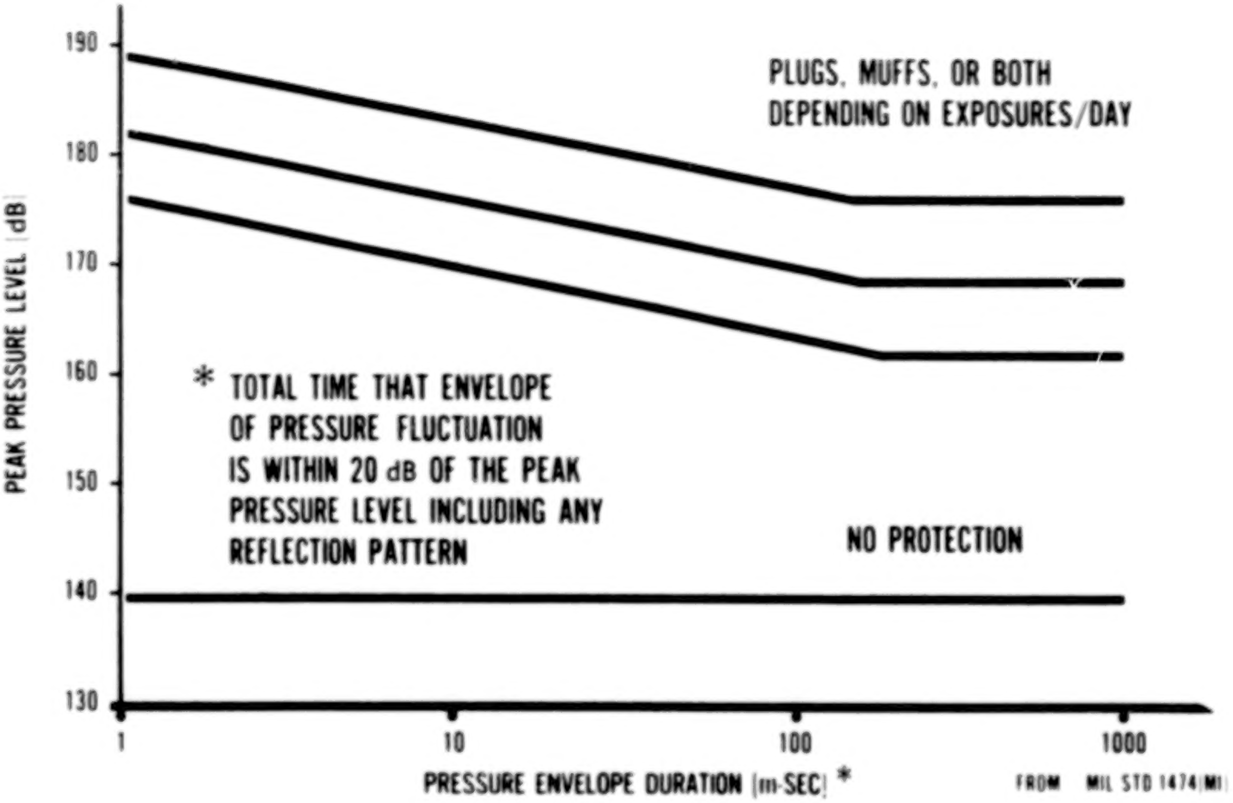

Figure 8.- Peak pressure level and B-duration limits for impulse noise.

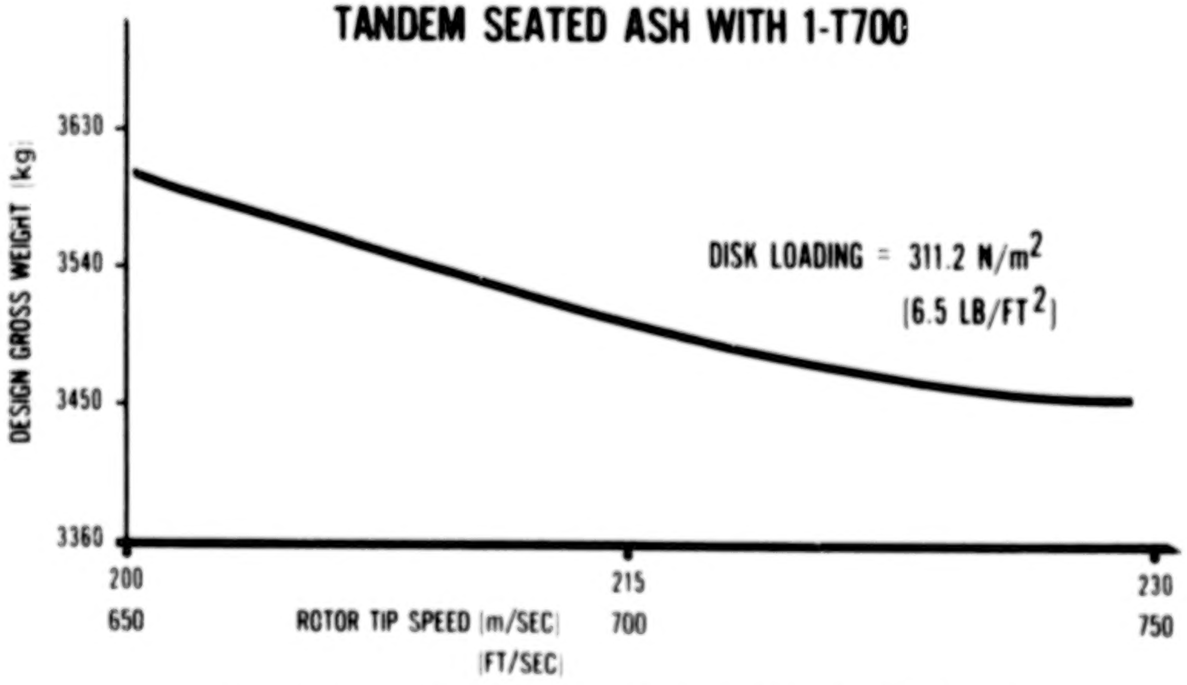

Figure 9.- Design gross weight impact of tip speed.

THE IMPACT OF URBAN OPERATIONS ON HELICOPTER NOISE REQUIREMENTS

Stanley R. Spector
Hughes Helicopters

SUMMARY

The national state of urban transportation, vis-a-vis traffic congestion and extended travel time, has generated a need for solutions to improved urban mobility. The helicopter is one of the solutions for alleviating this problem, lending itself naturally to the urban setting through its vertical lift operation. The helicopter is a necessary urban transport by virtue of its ability to perform unique public safety missions as well as its potential contribution to the economic well-being of the city. The helicopter will be to the city's economic development what the fixed-wing aircraft is to the nation's economic development. The helicopter will do the same job as the fixed-wing aircraft, only over shorter distances.

However, the role of the helicopter in the city has been severely limited by the public resistance to helicopter noise and concern for operating safety. This has resulted in the adoption of noise regulations which can severely restrict helicopter operations near residential areas, even in the middle of urban commercial and industrial zones. The consequence has been a lack of public heliport development necessary for the expansion of urban helicopter operations.

These factors dictate the need for adoption of quiet helicopter operating techniques and the industry-wide development of helicopter quieting improvements. Unless and until this is achieved, industry growth will not reach its full potential.

INTRODUCTION

While the helicopter industry has enjoyed considerable growth in the last 10 years, the executive transport segment of the market has had a limited growth due to restricted operations in major metropolitan centers of the world. This is the result of public resistance to urban helicopter operations because of the concern for safety and noise over the city. It has had a negative impact on the establishment of public-use heliports within the city. These factors along with helicopter productivity and operating cost are the primary factors affecting the helicopter industry growth, specifically in expansion of the executive market in urban operations.

This paper focuses on the interrelationship of urban helicopter operations, helicopter noise, and the establishment of urban public-use heliports. The impact of these factors on industry growth dictates the need for government and industry effort to reduce helicopter noise.

URBAN HELICOPTER TRANSPORTATION REQUIREMENTS

The most recognized importance of helicopters today by the general public is in public safety applications such as law enforcement patrol, fire fighting, and emergency rescue. Most citizens are aware of the role the helicopter plays in emergency situations and have come to rely on it for this purpose, particularly in the city. Many surveys by city law enforcement agencies have shown that over 90 percent of the public support the continuation of urban law enforcement patrol, for example. However, such acceptance has been accompanied by many noise complaints during orbiting operations at 153 meters (500 feet), prompting law enforcement agencies' interest in quieter helicopters.

A less understood but equally vital role of the helicopter is in providing transportation for urban business and industry who support the local economies through employment and taxes. The continuation and growth of helicopter operations in the city will assure a city's economic viability and growth. This will be achieved through the future development of intercity helicopter transport such as helicabs, helibuses and helitrucks as a means of offsetting the declining mobility in megalopolitan areas. However, this growth in urban helicopter transportation and the future economy of the cities can take place only if there are public heliports which can be used economically. Support for these relationships can be found by examining the impact of air transportation on national economic development. Previous studies (ref. 1) have shown that there is a correlation between air travel and business development nationally. This correlation can be related to the city because the population and employment continue to increase in the city's metropolitan rings resulting in increased travel distances and travel times. As in the national case, more rapid and convenient mobility is needed to facilitate commerce.

Specifically, the population growth in 24 of the largest cities' metropolitan rings is expected to increase at the rate of 6 million people per year between now and 1985 (ref. 2) as shown in figure 1. Conversely, central cities' population will remain relatively constant.

The same pattern is reflected in employment growth where there is a significantly greater rise in total employment in the city metropolitan rings as compared with that in the central cities, as shown in figure 2. These patterns reflect a clear decentralization of business and population around metropolitan areas. Furthermore, it is found (ref. 3) that transit usage does not stem the tide of decentralization of population and employment from the central city. In fact, central cities with the highest transit usage consistently exhibit the smallest increases or the largest declines in employment and population in both their central cities and metropolitan rings. In addition, the latest census shows that commuters in 21 of the largest metropolitan areas are abandoning public transit at the average rate of 0.7 percent per year in favor of their cars, which means more traffic congestion. Yet, massive emphasis is being put on rapid transit servicing central cities to the exclusion of alternate modes of transportation that could provide rapid service between business enterprises in the metropolitan rings.

Decentralization results in an increase in distance between companies doing business with each other in the city's metropolitan rings and the central city. This requires a transportation system to service the business, industry, and others who have the need to travel around the city in a fast, safe, convenient, low-cost transportation system not impeded by surface congestion. The helicopter fills these requirements and in addition requires a relatively small investment and a minimum of premium land. Helicopter transportation will help prevent the erosion of central city business and help assure a sound growth of business and industry in the city's metropolitan rings.

Four- to five-place light helicopters now provide business transportation within the city. This application will grow in the coming years with the achievement of competitive operating cost compared to taxis in the 1980's and up to two times faster helicopter delivery for 32-kilometer (20-mile) trips. The light helicopter is also capable of providing 454-kilogram (1/2-ton) freight transport now. This application will also grow in the coming years with the achievement of competitive operating costs compared to 454-kilogram (half-ton) trucks in the 1980's and up to 3 to 12 times faster helicopter delivery for 320-kilometer (200-mile) trips.

An analysis of the growth in the U.S. helicopter fleet and expected flying hours shown in figure 3, indicates a potential threefold growth in urban operations by 1985, contingent upon acceptance of helicopters in the city. This will depend on helicopter quieting and heliport availability. The continued economical operation and growth of helicopter utilization in the city will encourage the economic growth that is under way in the urban area outside 24 of the largest central cities. The availability of fast helicopter transportation will contribute to the establishment of new industries. The 250,000 new jobs per year previously cited in manufacturing, trade, and selected services represent an increase in local income for the cities of $100 billion over a 20-year period.

Noise Constraints

With the emphasis throughout the United States on noise suppression and control, by law, the U.S. Environmental Protection Agency has imposed requirements on all levels of government to improve the quality of the environment. This has resulted in some aggressive and imaginatively new noise standards. One standard of noise that has been considered by some governments is a calculated value. It is an integration of the measured sound level and exposure time that results in a maximum day-night noise level requirement (Ldn) at property lines of residential areas. The sound level is measured in decibels on an "A" weighted scale (dBA) which reflects the way the human ear responds to sound frequencies. Exposure time is a function of the number of flights, duration, and the hour of day that the sound occurs. The result of this new measurement standard is an average hourly noise level which permits a tradeoff of time integrated sound levels with the number of flights in a 24-hour period to achieve a balance with the noise level requirements. In the state of California, the maximum average hourly noise level is 65 dB Ldn for new heliports.

The equation for this noise standard is as follows:

$$\boxed{\mathrm{Ldn} = 10\ \mathrm{LOG}\left[\frac{15}{24}\ \Sigma\,\mathrm{ANTILOG}\ \frac{\left(\begin{smallmatrix}\mathrm{HNL}\\ \mathrm{DAY}\end{smallmatrix}\right)}{10} + 10\left(\frac{9}{24}\right)\Sigma\,\mathrm{ANTILOG}\ \frac{\left(\begin{smallmatrix}\mathrm{HNL}\\ \mathrm{NIGHT}\end{smallmatrix}\right)}{10}\right]}$$

$$\boxed{\mathrm{HNL} = 10\ \mathrm{LOG}\left\{\overset{\mathrm{TAKEOFF}}{\Sigma\left[\left(\mathrm{ANTILOG}\ \frac{\mathrm{dBA}}{10}\right)\times\Delta t\right]} + \overset{\mathrm{LANDING}}{\Sigma\left[\left(\mathrm{ANTILOG}\ \frac{\mathrm{dBA}}{10}\right)\times\Delta t\right]}\right\} - 35.6}$$

The basic equation averages the hourly noise level for a 24-hour period. Night operations from 2200 hours to 0700 hours are penalized by a factor of 10 times compared to those flights between 0700 and 2200 hours. The noise event or the hourly noise level (HNL) is measured on the A-weighted scale and is integrated over the period of duration and the number of events. This computation is made for both landings and takeoffs and applies to noise above some ambient threshold level.

A similar measurement is the community noise equivalent level (CNEL). This breaks the evening into two intervals with two different weightings for a total of three intervals in a 24-hour period. CNEL measurements are within 1/2 dB of the Ldn measurements.

Operational Impact

The foregoing noise constraints limit the number of flight operations at a heliport depending on its location relative to an impacted residential area. In many cities, residential areas can be found in the middle of industrial and commercial zones. Notwithstanding the zoning use, residents are still protected under the law as is the case in the State of California. To understand the significance of this, an evaluation was made of the noise impact on urban helicopter operations from heliports in close proximity to residential areas.

A [illegible] single-engine turbine helicopter takeoff, observing conventional height/velocity constraints would have a flight profile as shown in figure 4. A typical condition in a city like Los Angeles might find a residence within 244 meters (800 feet) of the takeoff and landing position. During takeoff, for the example shown, the helicopter might be required to fly over a residence where the helicopter would be 31 meters (100 feet) above the observer at the closest distance. With representative sound levels shown in figure 5, a light turbine helicopter would have as high as a 92 dBA sound level at the observer. The sound level time history of this takeoff and landing is shown in figure 6, where the daytime ambient is 65 dBA and the nighttime ambient is 50 dBA. These ambient conditions are typical for large cities.

Applying these results to the Ldn equation produces day-night average noise levels as shown in figure 7 for a range of light turbine helicopter operations. At the 65 dB Ldn regulation level, flights are restricted to approximately 1 per hour under the foregoing operating conditions. If heavy turbine helicopters are included in the operation as shown in figure 8, the combined operating limit is still approximately 1 flight per hour at 65 dB Ldn, but a little more restrictive at higher noise levels. These operations are severely limiting for a commercial downtown, public-use heliport while they are probably compatible with privately operated heliports in the same location.

If the observer's distance from the landing and takeoff point is doubled to 488 meters (1600 feet), then there is a fivefold improvement in the number of flights at 65 dB Ldn. On the other hand, if a vertical takeoff is executed with a light turbine helicopter, the permissible flight operations are doubled.

The impact of noise requirements on helicopter operations can also be seen by examining the noise footprints. Using 65 dB Ldn with a shallower 1:6 flight slope during daytime operations only, the resulting footprint is shown in figure 9. With the impact zone at 488 meters (1600 feet) from the takeoff point approximately 120 flights per day can be achieved. By increasing the maximum allowable noise level to 70 dB Ldn, the footprint shown in figure 10 is approximately one-half the size for the same number of flights.

Therefore, 65 dB Ldn is a restrictive requirement in terms of locating heliports in central cities or metropolitan rings where residential areas are within 305 meters (1000 feet) of the heliport under the flight path. As seen above, 70 dB Ldn gives the heliport planner less restriction in finding suitable locations.

However, there are alternatives for increasing helicopter operations rather than raising the regulated maximum noise level which regulatory groups are reluctant to do. The alternatives consist of noise reduction techniques which will be applied in the establishment of the first public-use heliport in the City of Los Angeles. The site selected is the top level of a parking structure adjacent to the Los Angeles Convention Center in the downtown area, shown in figure 11. Not far from the facility are residential buildings, potentially impacted; but the site was chosen because of its proximity to a major freeway with a daytime ambient of 66 dBA at the residence adjacent to the freeway, to the right of the picture. Freeways in Los Angeles are prescribed routes for helicopter operation at the option of the pilot. By observing several flight operation techniques shown in figure 12, noise impact is reduced. Approaches and takeoff/departures are executed over the freeway away from the residential area. Final approach and takeoff can be as steep as safely possible, with a high rate of climb during takeoff.

By following these procedures, approach sound levels for light turbine helicopters were reduced by 13 dBA and departures reduced by 19 dBA. However, even at the highest sound levels in this particular case, the light turbine helicopters could execute 10 flights per hour while flying over the residence using a steep slope path. The noise reduction techniques increased the number of permissible takeoffs and landings fivefold, to 50 per hour, far in excess of the flight operations actually expected at the heliport.

NOISE REDUCTION PROGRAMS

While the results in the Los Angeles public-use heliport case are favorable, the site location and operating techniques made the difference. Experiences in other cities are not always as favorable, nor is it favorable for many other desirable locations in Los Angeles. With regulatory control becoming ever tighter, there's a need for a concerted effort by Government and industry to develop and implement a noise reduction program for helicopters. The Federal Government and the helicopter industry have been working on noise reduction for the last 9 years on an irregular basis. Some of the technology for quieting helicopters became known in the Quiet Helicopter Program conducted by Hughes Helicopters in 1971 for the U.S. Advanced Research Projects Agency and the Eustis Directorate, U.S. Army Mobility Research and Development Laboratory. The product of that program was the Quiet One shown in figure 13. Up to a 90-percent reduction in sound level was achieved in an effort to find the limits of quieting. The program demonstrated that the helicopter can be the quietest of all aircraft when they are compared on the same basis. The economic reasonableness of all the quieting techniques was not determined, but the FAA is now investigating this. Some of the techniques used consist of muffling engine inlet and exhaust ports, reducing rotor speed, rotor blade aerodynamic redesign, and piloting procedures.

Approximately $5 million has been spent by the Federal Government and industry over the 9-year period to reduce helicopter noise. However, many times that amount has been spent to reduce engine noise for fixed-wing aircraft. It appears as if the time has come to put some increased effort on quieting helicopters. The FAA noise certification standards for helicopters, now being developed, will dictate this. Hughes, for example, is now in the process of implementing a four-bladed tail rotor with reduced tip speed in the 500D light turbine helicopter (fig. 14) which is expected to provide a substantial subjective noise reduction. Hughes already offers a quiet helicopter, its model 300CQ (fig. 15), which is an extension of its model 300C light piston helicopter. Both model 300's are used extensively in law enforcement patrol. The 300CQ has a dual muffler kit and is certificated to operate in a quiet mode at 93 percent of full engine RPM. At 80 km/hr (50 mph) patrol speed and 873 kilograms (1925 pounds) gross weight (921 kilograms (2030 pounds) is normal maximum with the quieting kit) the 300CQ provides a 12 dBA sound reduction and a 65 dBA overall sound pressure level at ground level during a 152-meter (500-foot) altitude flyover.

SUMMARY

Helicopter noise has brought government regulation. This has restricted heliport locations and operations in urban areas, specifically where residential areas are impacted. The importance of the helicopter in the city is increasing as alternate modes of transportation are required to offset the growing surface traffic congestion. Traffic congestion is a deterrent to future rejuvenation of the central city and the needed industrial expansion of cities' metropolitan rings. Helicopter noise must be reduced in order to encourage its increased use in the city. Until this is done, the growth of an important segment of future helicopter application is impaired.

In order to achieve the national goals for urban redevelopment and related transportation improvement, the government needs to include helicopter improvement and heliport design and construction in its national transportation plan. Specifically, a government/industry quieting development program is needed for all classes of helicopters, including the application of available engine quieting technology. The application of present and evolving technology will assure that helicopters will become an important adjunct to urban transportation and a good neighbor.

REFERENCES

1. Stuelpnagel, Thomas R., "The Helicopter is a Necessary Urban Transport for the 1980s," Verti-Flite, vol. 19, no. 2, Mar/Apr 1973, pp. 18-19, 22-23.

2. Ganz, Alexander, "Emerging Patterns of Urban Growth and Travel," Project Transportation, Massachusetts Institute of Technology (Cambridge, Mass. 1968). (Updated by S. R. Spector in 1976 from Department of Commerce data.)

3. Meyer, J. R.; Kain, J. F.; Wohl, M., "The Urban Transportation Problem," (Cambridge, Mass., Harvard University Press, 1971).

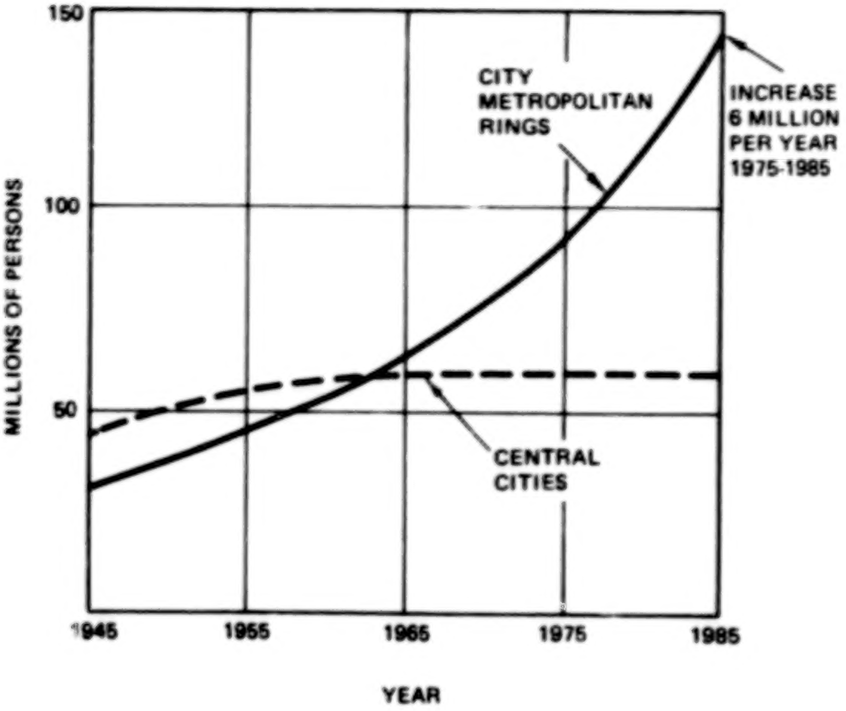

Figure 1.- Urban population growth. (From ref. 2.)

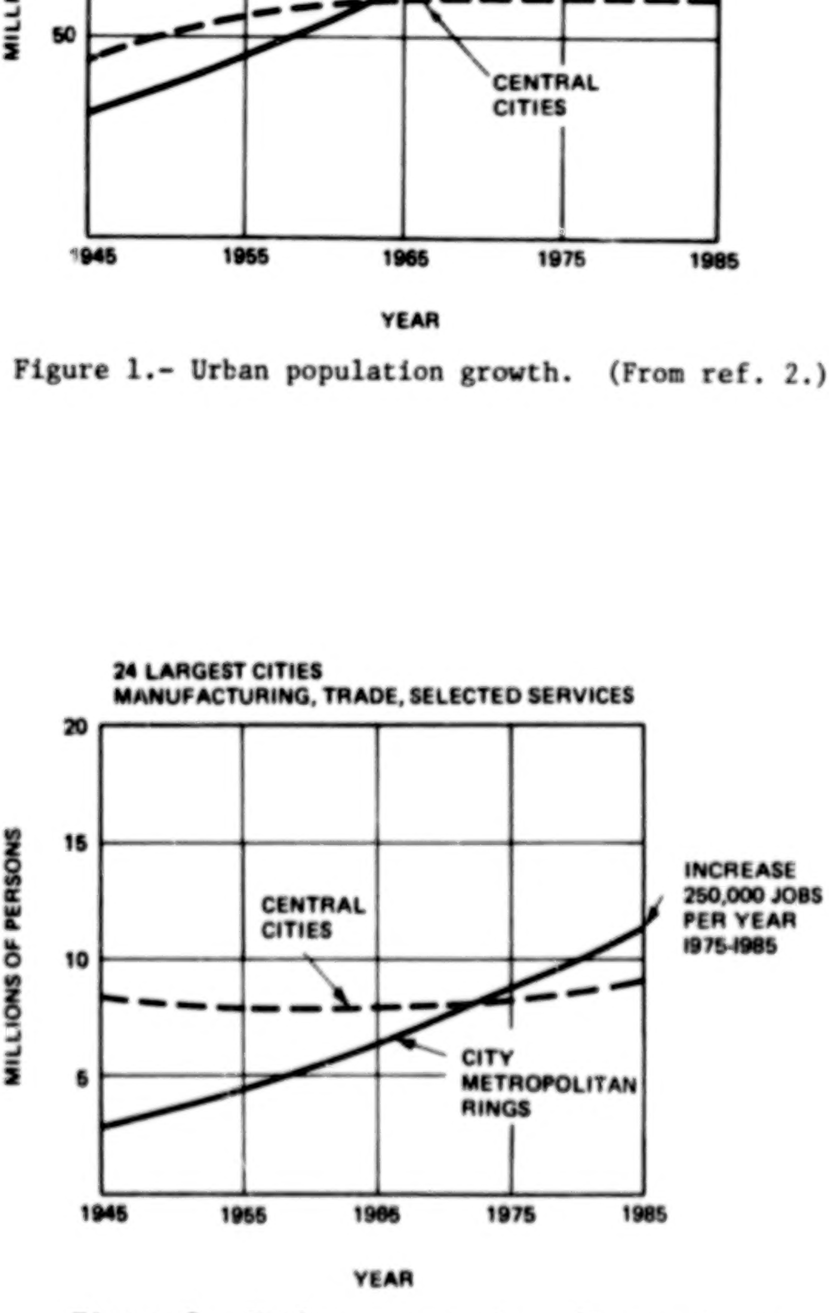

Figure 2.- Employment growth. (From ref. 2.)

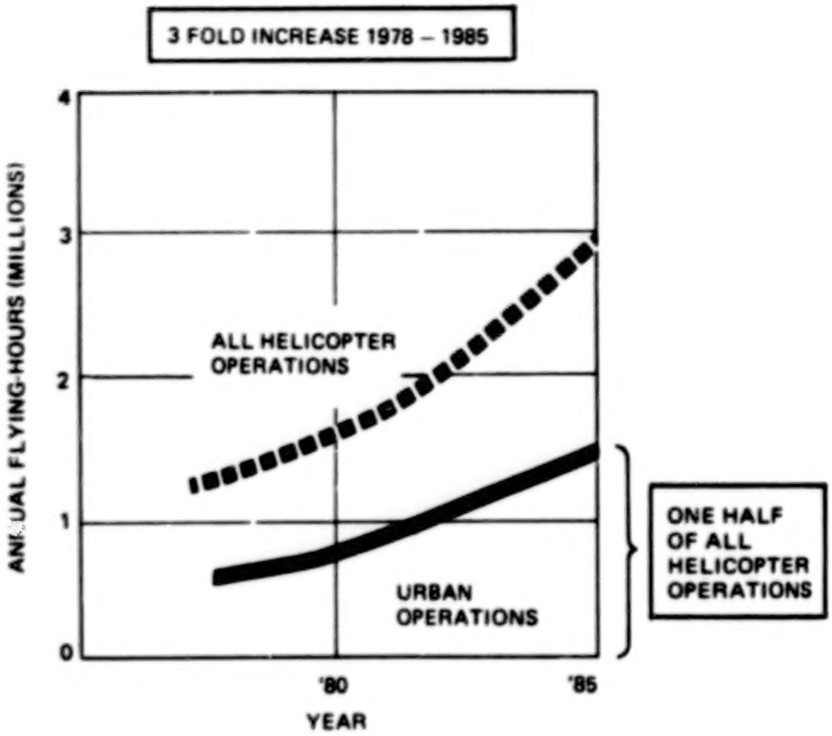

Figure 3.- Growth in U.S. urban operations.

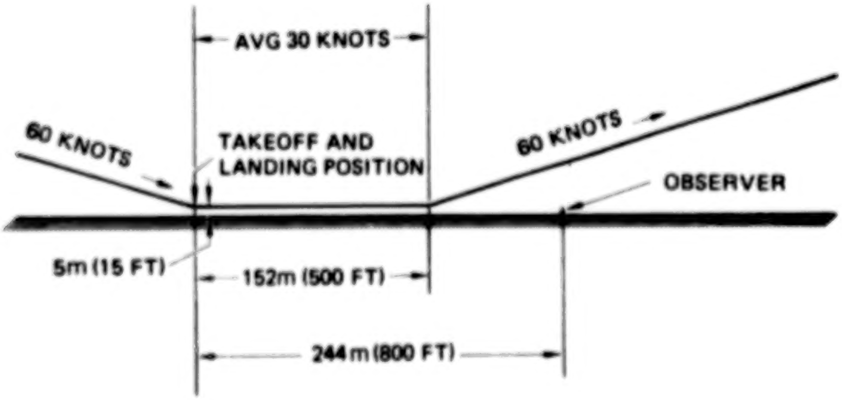

AVG 30 KNOTS
60 KNOTS
TAKEOFF AND LANDING POSITION
60 KNOTS
OBSERVER
5m (15 FT)
152m (500 FT)
244m (800 FT)

Figure 4.- Light turbine flight path - 1:3.5 slope.

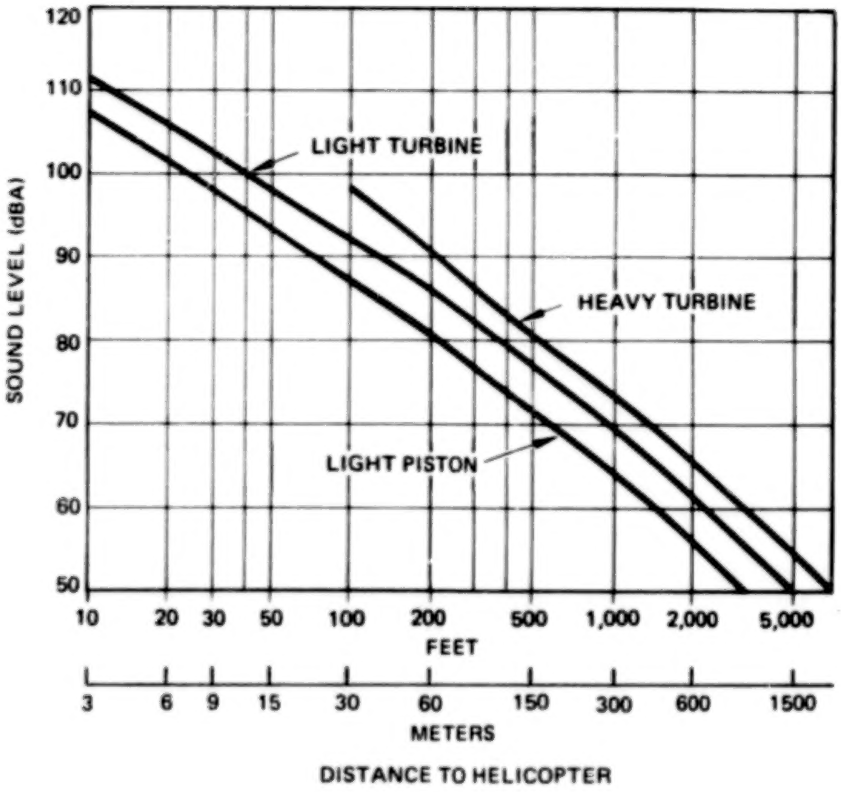

Figure 5.- Helicopter sound level.

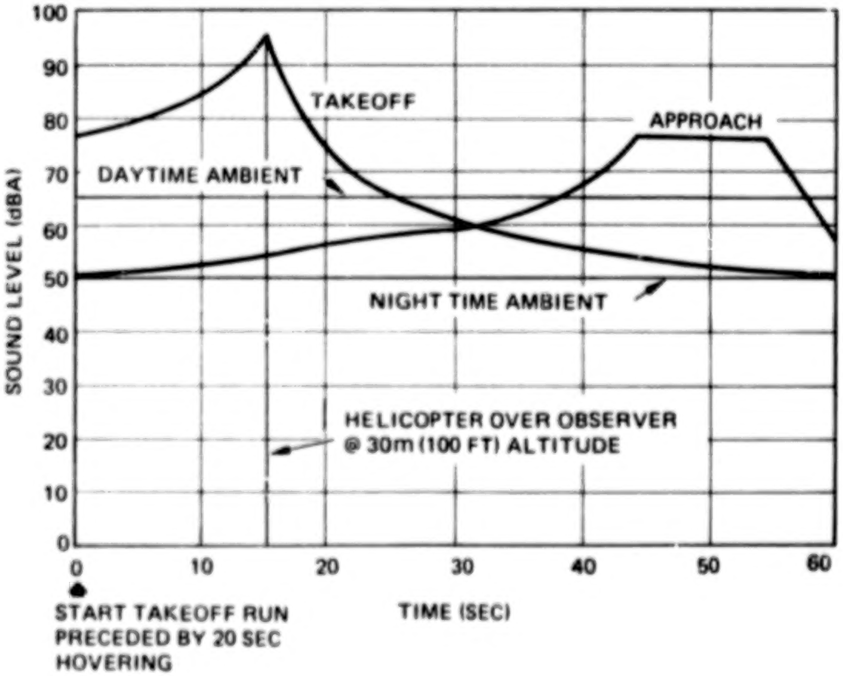

Figure 6.- Light turbine sound history.

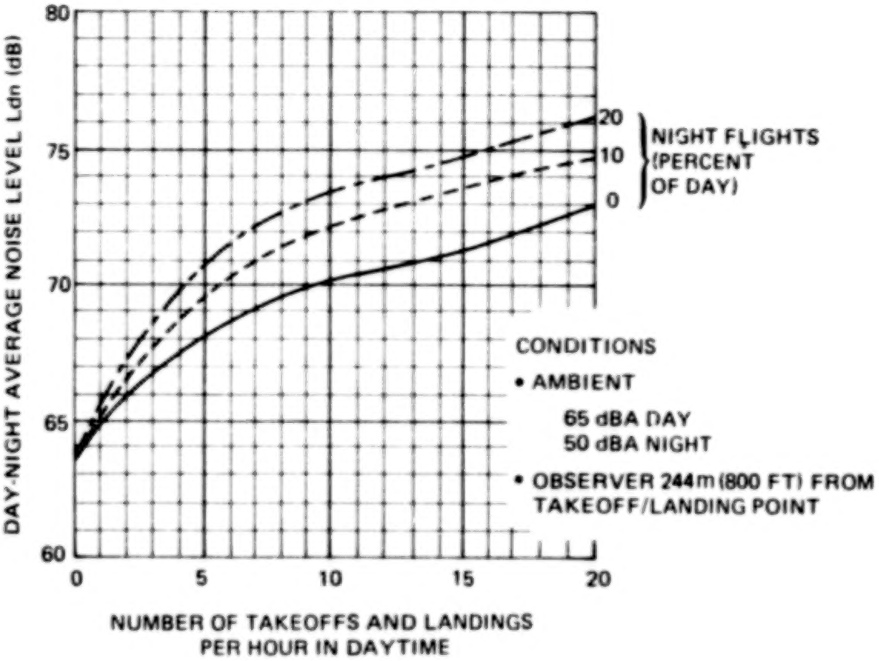

Figure 7.- Light turbine operating noise level.

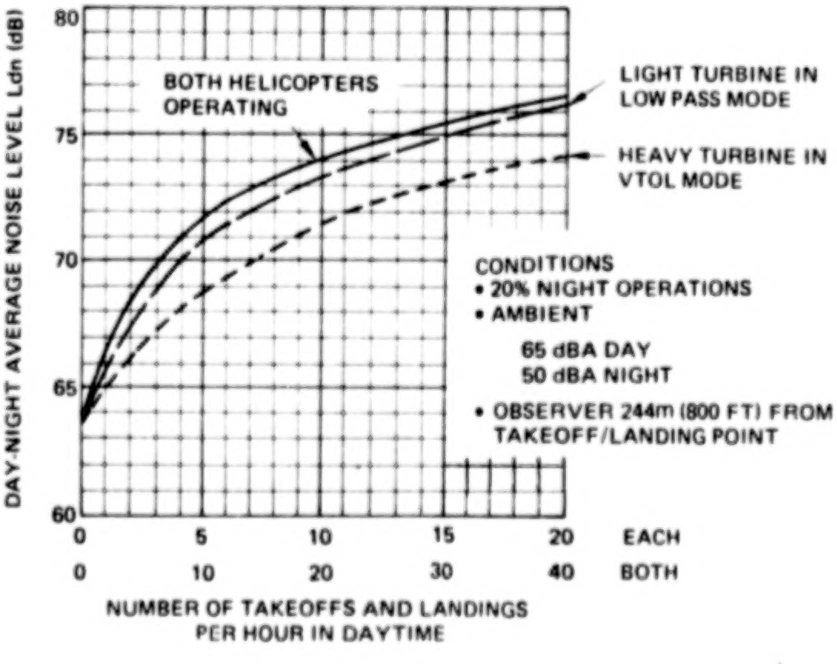

Figure 8.- Light and heavy turbine helicopters operating noise levels.

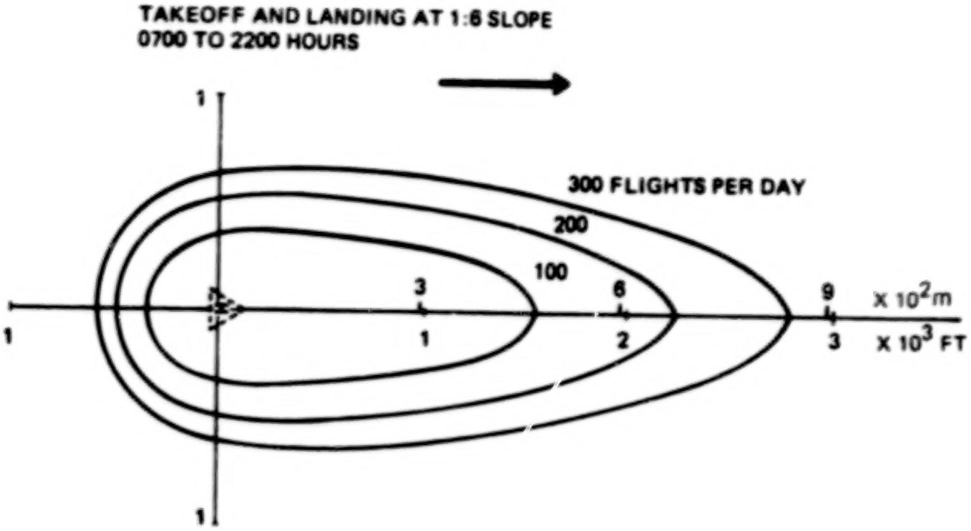

Figure 9.- Noise footprint for a light turbine helicopter.
Ldn = 65 dBA.

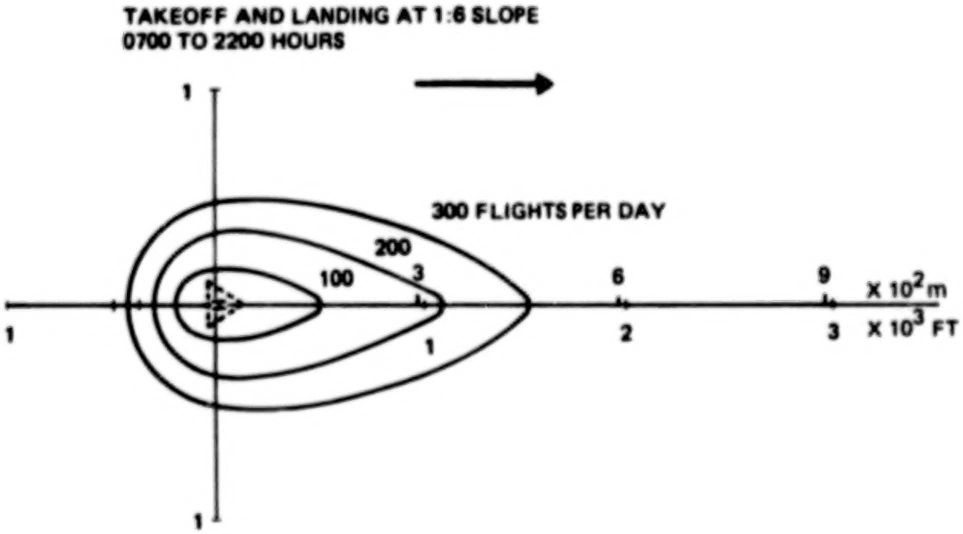

Figure 10.- Noise footprint for a light turbine helicopter.
Ldn = 70 dBA.

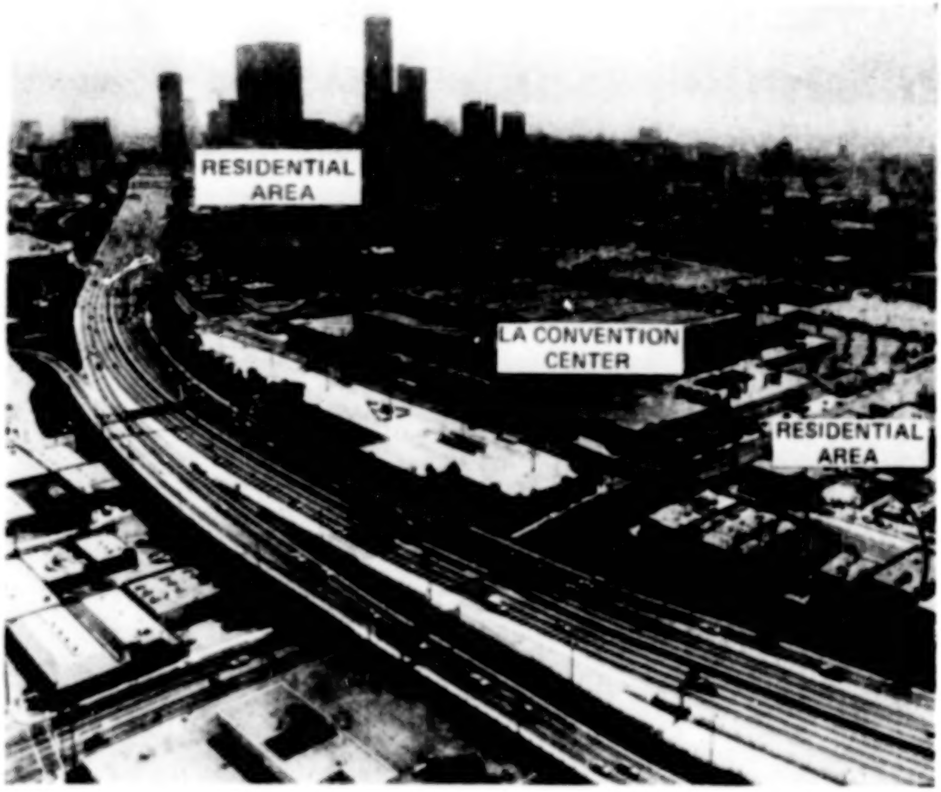
RESIDENTIAL AREA
LA CONVENTION CENTER
RESIDENTIAL AREA

Figure 11.- Proposed Los Angeles public-use heliport.

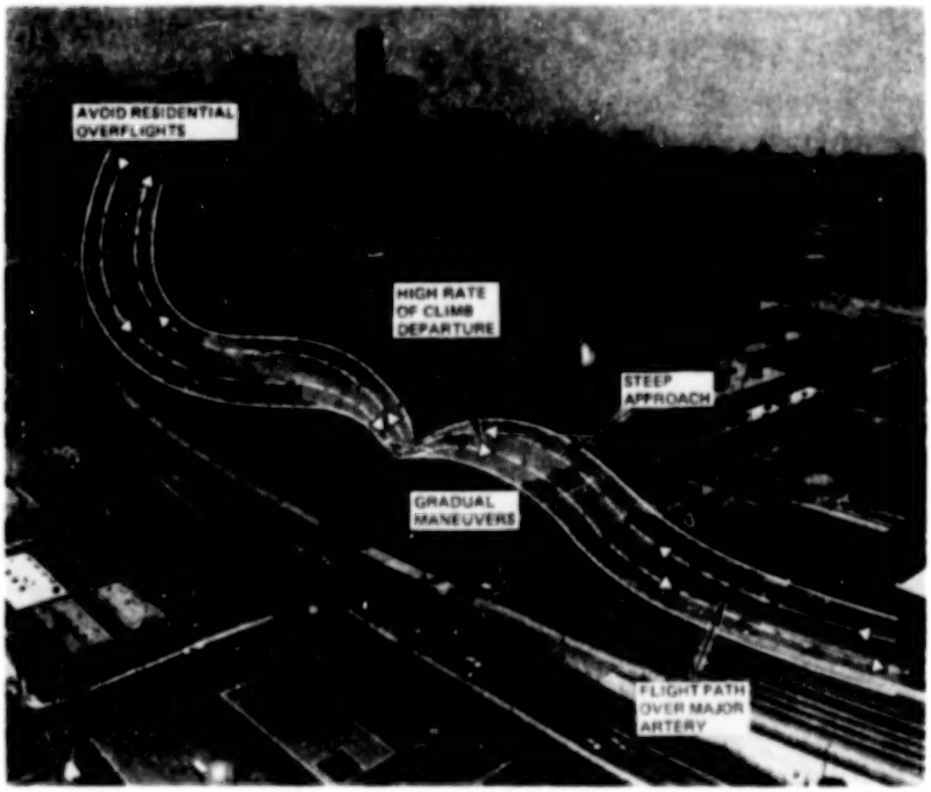
AVOID RESIDENTIAL OVERFLIGHTS
HIGH RATE OF CLIMB DEPARTURE
STEEP APPROACH
GRADUAL MANEUVERS
FLIGHT PATH OVER MAJOR ARTERY

Figure 12.- Noise reduction techniques.

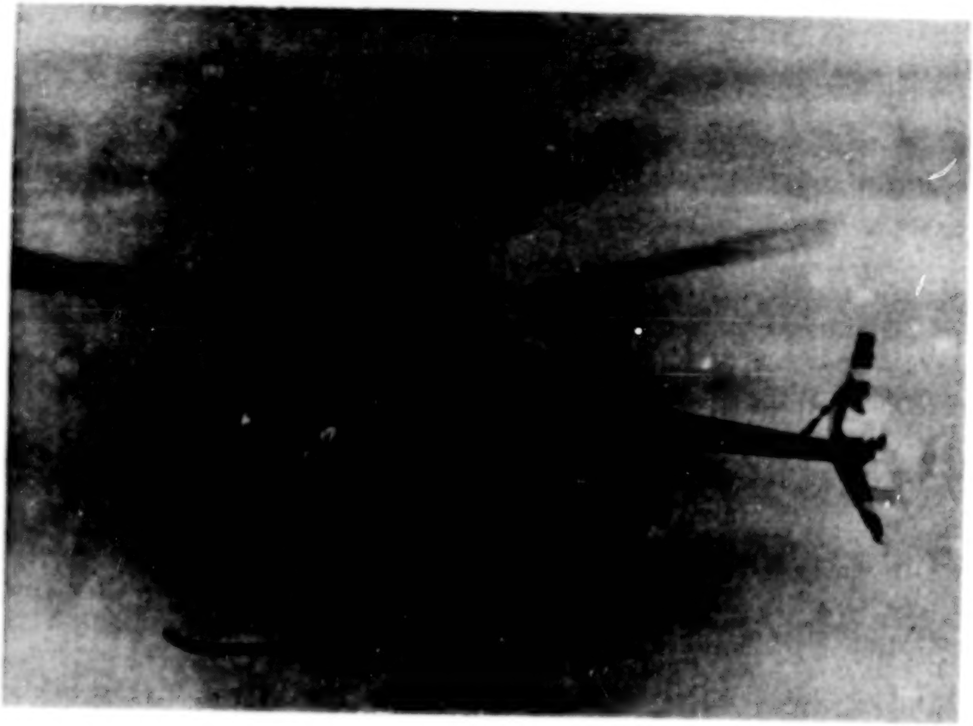

Figure 13.- The quiet one.

Figure 14.- 500D.

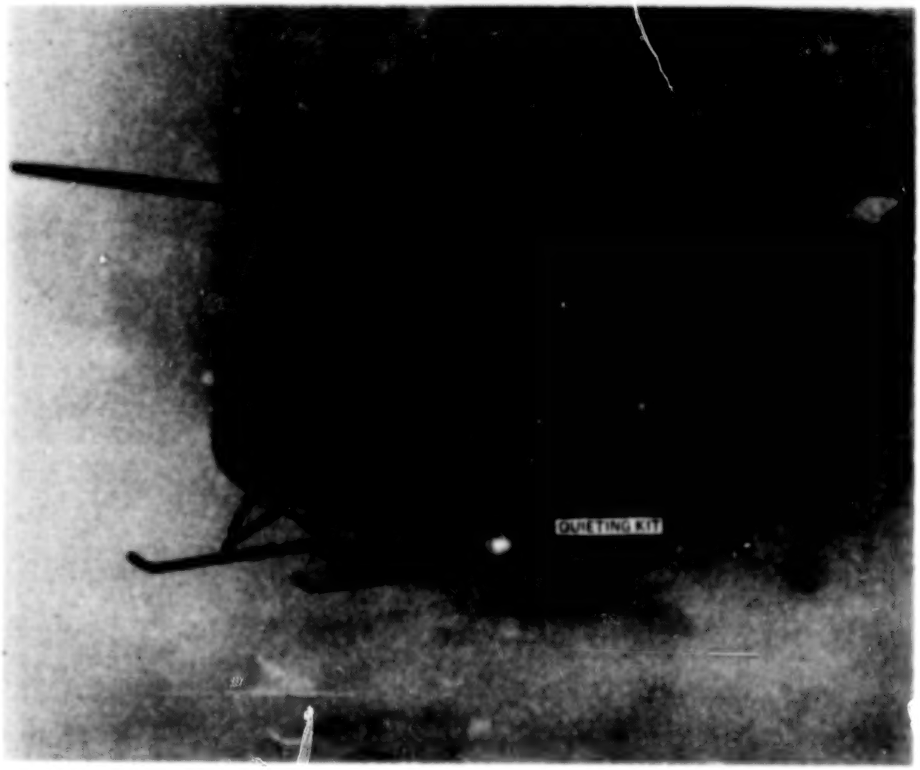
QUIETING KIT

Figure 15.- 300CQ.

Blank Page

60

5

PREDICTION AND REDUCTION OF ROTOR BROADBAND NOISE

Richard E. Hayden and Krishna S. Aravamudan
Bolt Beranek and Newman Inc.

INTRODUCTION

For helicopter rotors not undergoing bladeslap or other impulsive noise generation, broadband radiated noise is a dominant contributor to subjective weightings used to assess aircraft noise. Since the predominant trend in current and advanced helicopter designs is toward low speed rotors - i.e., those which avoid transonic relative tip Mach numbers at maximum cruise speeds, the relative need to control broadband noise will increase. There is a substantial body of research which has been performed on stationary and rotating airfoils, both for helicopter and non-helicopter applications, which can provide guidance in prediction and reduction of broadband rotor noise. This paper summarizes prediction techniques which can be or have been applied to subsonic rotors, and methods for designing helicopter rotors for reduced broadband noise generation. It is the primary purpose of this paper to show how detailed physical models of the noise source can be used to identify approaches to noise control.

SYMBOLS

B	number of rotor blades
c_0	speed of sound
C	numerical coefficient
$\tilde{C}_F$	force coefficient
D_r	dipole strength
f_k	frequency
F	force
G	Green's function
I	intensity
J_n	Bessel function

k	wavenumber variable
L	wetted length of trailing edge
ℓ_j (j=1,2,3)	turbulence correlation scale in the j-direction
M_o	characteristic flow Mach number U/c_o
M_{OR}	component of Mean M in the observer direction
M_v	V/c_o
M_0	U_0/c_o; also rotational Mach No.
p_I	pressure fluctuation without Kutta condition applied
q_0	mean dynamic pressure
r, R	distance from source to observer
t	thickness of wake
U	characteristic flow velocity
U_0	mean stream/flight speed
$\underset{\sim}{v}$	velocity
$\underset{\sim}{\bar{V}}$ or V_c	mean eddy convection velocity
υ	root mean square turbulence velocity
x_j (j=1,2,3)	rectangular coordinates
β	angle between V and x_1 -axis
Γ	vortex strength; also angle of gust with respect to the edge of airfoil
ρ, ρ_0	density
υ	numerical constant
Φ	spectrum function

ϕ	observer orientation with respect to plane of rotation
ω, Ω	radian frequency

MODELING CONSIDERATIONS

There are a variety of approaches to modeling aeroacoustic sources, ranging from exact mathematical descriptions typically involving solutions of Lighthill's acoustic analogy (1952), to semi-empirical descriptions of postulated sources using parametric data to arrive at prediction methods, to simple "data base" descriptions of special situations. Over the past 10 - 15 years, the state of rotor noise prediction capability has progressed from the "data base" stage to the exact solution stage, although many "exact solutions" require detailed physical measurements of flow field parameters which are beyond the current capabilities.

The modeling of broadband sources presented below will include representative available inputs from all levels of the above hierarchy. However, since our goal is to demonstrate that accurate source models, when stated in terms of measurable flow and geometric parameters, provide valuable insight into source reduction, we prefer to treat the broadband noise problem as a linear system analogy separating input and response functions.

To obtain a relationship between flow field characteristics and the sound radiated by lifting rotors, it is necessary to determine which mechanism is primarily responsible for the radiation. Each postulated mechanism leads to a particular characterization of the sound field and of its relationship to the flow field characteristics. Measurements and similarity arguments can then be used to establish *a posteriori* verification of the choice of the mechanism.

To form a clear physical view of the processes of interest in noise generation by rotating airfoils, it is desirable to analyze the various ways in which airfoils can interact with the surrounding viscous media to generate noise. The actual sources of sound generation by flow/surface interaction are fluid dynamic disturbances, which for the case of interest here may be separated into three categories, which may be separated as shown in Figure 1 (from Hayden, 1972, 1973).

Inflow turbulence, such as that arising from the atmosphere, previous blades, or the wake shear layer of an upstream disturbance, may produce lift and drag fluctuations of the whole surface.

A second category of fluid dynamic sources is the *turbulent boundary layer* which may radiate sound directly or, more importantly, creates a spanwise array of uncorrelated dipoles when it passes over the trailing edge. The characteristic dimensions of the boundary layer turbulence are small compared to the scale of the airfoil; therefore high frequencies are generally associated with turbulent boundary layer interaction with the trailing edge.

The third category of fluid dynamic sources is the *wake* of the airfoil, which may produce large scale "whole body" lift and drag fluctuations associated with large scale eddies in the wake, and "trailing-edge noise" at higher frequencies due to interaction (hydrodynamically) of small scale wake turbulence immediately downstream of the trailing edge with the edge. In the case of helicopter blades which follow each other in the same plane or in intersecting planes (e.g., tail rotors operating in main rotor downwash), the wake has further significance in that it becomes a source of inflow turbulence to downstream airfoils. The hydrodynamic wake and related acoustic spectra may be either very narrowband or broadband. Narrowband wakes are usually associated with laminar flow instabilities on an airfoil (or cylinder), whereas broadband wakes are usually associated with high Reynolds numbers wherein the upstream boundary layer is turbulent on both upper and lower surfaces.

Thus, the principal noise prediction problem becomes one of identifying and quantifying flow field parameters which "drive" the noise generation process.

The prediction of rotor broadband noise will now be addressed from the point of view of the source of excitation - environmental turbulence, versus self-generated boundary layer and wake turbulence.

It should be noted that much of the treatment of the broadband noise problem has been derived from work on stationary (non-rotating) airfoils, half planes, and the like. The utilization of the stationary surface information on rotating systems involves accounting for radial variation of mean and unsteady flow parameters, departures from quasi-two-dimensional flow situations at the tip of a rotating blade, and rotating acoustic source effects.

PREDICTION OF BLADE/TURBULENCE INTERACTION NOISE

Helicopter main rotors experience random fluctuations in the amplitude and direction of inflow due to atmospheric turbulence and, under some flight conditions, by turbulence from preceding rotor blades. Tail rotors operate in the main rotor downwash, atmospheric turbulences and, occasionally, in the wake of the fuselage and tail boom. A lifting rotor produces a mean downward velocity field which draws environmental eddies through the rotor plane with a convection velocity V_c. This random variation in "upwash" induces a random variation in the angle of incidence and hence a fluctuating blade load. Regardless of the source of inflow disturbance, the turbulence contains a spectrum of wave number components, resulting in a blade loading spectrum which produces acoustic energy over a wide range of frequencies.

Many of the possible mechanisms for broadband noise generation by a single stationary airfoil in a moving stream have been the subject of various investigations. The non-uniform velocity field associated with turbulence leads to an unsteady blade load that is dipole in nature. Recent thorough models of the problem include that of Amiet (1975), Homicz (1974), Amiet (1976), and Aravamudan and Harris (1978).

Formulation

Homicz and George (1974) gave an expression for the frequency f_0 beyond which the spectrum of the broadband noise is smooth as follows:

$$\frac{f_0}{\Omega} = \frac{B\left(1 + \frac{M_0}{M_c}\right)}{2(1 - M_0 \cos\phi)} \tag{1}$$

where B is number of blades, M_0 and M_c are rotational and convection Mach numbers and ϕ is the observer orientation with respect to plane of rotation. This implies that at frequencies above f_0, the consecutive blade passage time is much greater than the eddy convection time and hence there is no significant blade-to-blade correlation. Under such circumstances, the total radiation may be obtained by summing the uncorrelated sound power spectral densities of each of the blades. The radiation of a single blade approximated by a rotating point dipole has been given by Ffowcs Williams and Hawkings (1969) as

$$\langle S_{pp}(r,f)\rangle = \frac{f^2}{4\rho_0 c_0^3 r^2} \sum_{n=-\infty}^{\infty} D_r(\phi, f - n\Omega) J_n^2\left(\frac{fR\cos\phi}{c_0}\right) \tag{2}$$

where $D_r(\phi,f)$ is the power spectral density of the dipole strength in the direction of radiation. Since the dipole strength is a direct consequence of the unsteady lift acting on the airfoil, it may be readily expressed in terms of the power spectral density of the unsteady lift

$$D_r(\phi,f) = \Phi_{LL}(f)\sin^2\phi \qquad (3)$$

Under the assumptions of stationary and homogeneous random processes, the unsteady lift response function is related to excitation spectral density (turbulent upwash) and the aerodynamic transfer function in the following manner:

$$\Phi_{LL}(f) = \iiiint_{-\infty}^{\infty} d^3k\,d\tau\,\Phi_{ww}(\vec{k})\ |K(k_c,k_s)|\ \exp[i2\pi(k_xQ - f)\tau] \qquad (4)$$

which may be simplified to

$$\Phi_{LL}(f) = \frac{2}{Q}\iint_{-\infty}^{\infty} dk_y dk_z\ \Phi_{ww}(f/Q,k_y,k_z)\ |K(f/Q,k_y)|^2 \qquad (5)$$

where Φ_{ww} is the spectrum of turbulence upwash and K is the aerodynamic transfer function. Equation (5) is general in the sense that any known turbulence upwash spectrum and/or an aerodynamic transfer function may be used to yield appropriate lift power spectral densities.

Effects of Aerodynamic Transfer Function

If we assume that at every instant the rotor blade behaves like a two-dimensional airfoil in a three-dimensional sinusoidal upwash pattern, the three governing parameters for the aerodynamic transfer function are k_t, Γ and M_0. Here

$$\Gamma = \tan^{-1}\left(\frac{k_s}{k_c}\right) \text{ and } k_t = (k_c{}^2 + k_s{}^2)^{\frac{1}{2}}$$

where k_c and k_s are components of the gust wave vector parallel to the chord and span of the blade, respectively, and are normalized with respect to blade semi-chord. During each revolution, a blade will encounter some regions in which Γ approaches a right angle, implying nearly steady but definitely three-dimensional flow. In some other region, Γ may be very small, so that the flow is nearly two-dimensional, but definitely unsteady. In either case, the loading is less than that predicted by quasi-steady two-dimensional theory.

To check this quantitatively, Homicz and George (1974) computed the load response to a convected sinusoidal upwash pattern of amplitude w_0 and wave number k_t for the two extreme cases of $\Gamma = 0$ and $\Gamma = \pi/2$ and various Mach numbers. The results for $M_0 = 0.4$ are presented in Figure 2. The curve for $\Gamma = 0$ was obtained from Osborne's (1973) asymptotic expression for the compressible extension of the two-dimensional Sears function (1941):

$$|S_{eff}| = \left[J_0^2 \left(\frac{M_0^2 k_t}{\beta^2}\right) + J_1^2 \left(\frac{M_0^2 k_t}{\beta^2}\right) \right]^{\frac{1}{2}} \left| H\left(\frac{k_t}{\beta^2}\right) \right| \qquad (6)$$

where $\beta^2 = (1 - M_0^2)$ and $H(k)$ is the magnitude of the original incompressible Sears function which, to a very good approximation, is given by

$$H(k) \simeq (1 + 2\pi k)^{-\frac{1}{2}}$$

The $\Gamma = \pi/2$ curve in Figure 2 was obtained from Filotas' (1969) work on the $(k_t, \Gamma, 0)$ solution in conjunction with a similarity rule derived by Graham (1970). From Figure 2, it is evident that the two curves are rather close at low frequencies, tend to diverge as frequency increases, and approach the same slope at high frequencies. This result is of significance in discussing the effect of swept blades on noise reduction, where the value of Γ is ranging from 0 to approximately $\pi/2$ along the span of the blade, thus reducing the unsteady lift fluctuations.

Effect of Free Stream Turbulence

For a given unsteady aerodynamic transfer function, the unsteady lift response function is dependent only on the spectrum of turbulent upwash. While considering the response of main rotors to atmospheric turbulence, Homicz and George (1974) used the Dryden form of the spectrum for turbulence input:

$$\Phi_{ww}(k) = 64\pi^3 \bar{\omega}^2 \Lambda_f^5 \frac{k_x^2 + k_y^2}{[1+4\pi^2 \Lambda_f^2 k^2]^3} \qquad (7)$$

where $k^2 = k_x^2 + k_y^2 + k_z^2$ and Λ_f is the integral scale of turbulence. Their predicted sound pressure levels were lower than the measured full scale rotor spectra of Leverton (1973). Aravamudan and Harris (1978) used a von Karman spectrum of turbulence and compared the computed results with the measured sound pressure levels of a model rotor operating in an open jet anechoic wind tunnel facility. Figure 3 shows a comparison of their measured and computed results for two Mach numbers and integral scales of turbulence. The details of these measurements and predictions are presented in another paper by Aravamudan, Lee and Harris (1978) in this conference.

The resulting scaling law to scale blade/turbulence interaction noise from model tests is:

$$
\begin{aligned}
SPL_p = SPL_m &+ 20 \log \frac{b_p c_p}{b_m c_m} + 10 \log \frac{\bar{\omega}_p^2}{\bar{\omega}_m^2} \\
&+ 40 \log \frac{M_{tp}}{M_{tm}} + 20 \log \left[\frac{(1+\mu_p)^2 + \left(\frac{M_{cp}}{M_{tp}}\right)^2}{(1+\mu_m)^2 + \left(\frac{M_{cm}}{M_{tm}}\right)^2} \right] \\
&- 3.3 \log \frac{\Lambda_{fp}}{\Lambda_{fm}} - 20 \log \frac{r_p}{r_m} + 10 \log \frac{\sin^2 \phi_p}{\sin^2 \phi_m} \qquad (8)
\end{aligned}
$$

where subscripts p and m stand for prototype and model rotors, b is the blade span, c is blade chord, μ is advance ratio, M_c is convection Mach number through rotor disc, and M_t is tip Mach number.

To facilitate comparison with the full scale rotor data of Leverton, we used the prediction procedure developed in Aravamudan et al. (1978) with the estimated turbulence properties of $\Lambda_f = 0.57$m, $(\bar{\omega})^{\frac{1}{2}} = 1$ m/sec (George and Kim (1976)). The resulting sound pressure spectrum is compared with the measured spectrum of Leverton (1973) in Figure 4. Similar analyses can be used for the prediction of broadband noise radiation from tail rotors operating in the downwash of main rotors; however, the appropriate aerodynamic inputs have not been measured in detail.

TRAILING EDGE NOISE

When turbulent boundary layers or other surface-attached air flows pass over a discontinuity in the surface such as a trailing edge, substantial sound may be radiated. In the last ten years, there has been a proliferation of theoretical and experimental work aimed at describing the sound generation by this fluid dynamic source for a semi-infinite half plane. Following on the suggestions of Powell (1959), Hayden (1969) and Chanaud (1970) attempted to model the trailing edge sound generation process as a distribution of point dipoles, and developed some semi-empirical correlations with data from a wall jet over a rigid plate. At the same time, Ffowcs Williams and Hall (1970) were solving Lighthill's acoustic analogy for a semi-infinite half-plane with a generalized turbulent flow past the edge. Since that time, several models have been advanced by numerous authors. Unfortunately, many of these models have been based on different flow field approximations and different surface/observer geometries. Therefore a direct comparison of the models was difficult. Recently, Howe (1977) undertook a comparison of various half-plane models for a situation of consistent flow field conditions. He found that the predominant source mechanism is dipole in nature and that, when cast in terms of a common system of flow parameters for a semi-infinite plane, most of the theories predicted the same result for low Mach number conditions: (Ffowcs Williams and Hall (1970); Crighton (1972); Chandiramani (1974); Chase (1972, 1975); Hayden et al. (1976); and Howe (1977)). Howe developed a unified model which also took into account moving medium and moving source effects. The details of this model are contained in Howe (1977). For the half-plane geometry shown in Figure 5 , Howe's model predicts the following relationship between flow parameters and radiated sound for "blade-fixed" coordinates:

$$\langle p_I^2 \rangle = \frac{C\rho^2 \upsilon^2 V^2 M_V}{2\pi} \left(\frac{L\ell^3}{R^2}\right) \frac{\sin\alpha \sin^2\left(\frac{\bar{\theta}}{2}\right)\cos^3\beta}{(1+M_{OR})^2(1-M_{VR})^2(1-M_{V1}\sin\alpha)} \qquad (9)$$

Howe's work concluded that the question of application of the Kutta condition at the trailing edge is unresolved with substantial differences occurring in predicted levels depending upon the presence or absence of this condition. Furthermore, for finite chord surfaces, the relationship is expected to become more complicated; indeed, the trailing edge noise problem has not been fully described analytically for finite surface geometries. Several parameters in Howe's equation are of interest from the point of view of reduction of broadband noise. These are turbulence velocity υ, mean and eddy convection velocities, spanwise length scale, and the angle β, which is the angle between the trailing edge and the direction of the turbulent flow. From the point of view of reduction of trailing edge noise, one might seek to modify these parameters by either selecting a location for the rotor where the turbulence parameters are minimized, or by modifying the geometry of the rotor to take advantage of the sweep effects (e.g., $\cos^3\beta$). Furthermore, surface modifications (e.g., leading edge serrations or vortex generators) could, in principle, be used to modify the turbulence intensity and length scale parameters. Application of these concepts will be discussed in subsequent sections.

"VORTEX SHEDDING" NOISE FROM ROTATING AIRFOILS

It has been known since the early 1900's that the shedding of a vortex wake produces sound, and there is a rather large literature on this subject. Much of this literature is concerned with the frequency of vortex shedding and of the attendant sound, for a variety of two-dimensional shapes. More recently Hanson (1970), Hersh and Hayden (1971), and Patterson *et al.* (1973) made studies of vortex shedding noise from isolated stationary and rotating airfoils and arrived at different expressions to predict the frequency of discrete tones. Hanson used a wake momentum thickness, Hersh and Hayden used a wake thickness, and Patterson *et al.* found good correlation by using a laminar boundary layer thickness on the pressure side of the airfoil. Aravamudan, Lee and Harris (1978) performed a series of experiments with a model rotor and found that a Strouhal scaling with respect to thickness of the airfoil yielded favorable comparisons with measurement. However, since all of the shear layer thicknesses are interrelated for unstalled airfoils, the frequency prediction issue has become a second-order affair.

For cases when the frequency of unsteady vorticity "shedding" is such that the resultant acoustic wavelength is much greater than the chord of the airfoil, the unsteady force can be represented as an acoustic dipole, as first noted by Yudin (1947). Later, Phillips (1956) showed by starting with Curle's equation that, for low Mach numbers, and for the case of an acoustically-compact rigid body experiencing a harmonic force, the radiated acoustic intensity at distance r is:

$$I = \frac{9f^2 |F_0|^2 \cos^2\theta}{8\rho c_0^3 r^2} \tag{10}$$

Nondimensionalizing F with a force coefficient leads to

$$F = \frac{1}{\sqrt{2}} \rho U_0^2 \quad t\ell_3 \ \tilde{C}_F \tag{11}$$

where $\tilde{C}_F$ is the rms oscillating lift coefficient, t is the thickness, and ℓ_3 is a spanwise length over which the shed vortices are correlated, which may be small compared to the total span of a blade. Integrating the resulting expression for the intensity of sound over the span of a rotating blade leads to the total acoustic intensity which may be scaled as follows:

$$I \approx \left(\frac{ft}{U_0}\right)^2 \tilde{C}_F^{\,2} \; M_0^3 \, U_0^3 \, b\ell_3 \; \cos^2\theta \qquad (12)$$

where b is the span of the rotating blade and θ is the angle between the fluctuating force axis and the observer. Since rms fluctuating lift is, in general, a function of strength of shed vortices and the separation of vortex sheets, it can also be represented in terms of the steady state drag coefficient C_D. Noting that a Strouhal number can be defined by:

$$S = \frac{ft}{U_0} \qquad (13)$$

this leads to an expression for the total acoustic intensity as follows:

$$I \approx S^2 C_D^2 \left(\frac{\tilde{C}_F}{C_D}\right)^2 \; M_0^3 \, U_0^2 \, b\ell_3 \; \cos^2\theta \qquad (14)$$

Ross (1964; see also Ungar *et al.*,(1972)) showed that expressions for the dimensionless drag coefficient and Strouhal number have reciprocal dependencies on the ratio of wake separation h, to the body thickness t. As a result, the product is independent of the relative wake width. The resultant expression is dependent only on the relative induced velocity u/U_0. The relative induced velocity is a function of the shape of the body shedding vorticity, and tends to be constant for a given shape over a wide range of Reynolds number. As discussed in detail in the literature survey by Ross (1964), experiments show a clear trend for the oscillating lift to be a constant fraction of the drag coefficient over a wide range of Reynolds numbers. For cylinders, this fraction is about one-third and there are no data available for other shapes. As we are dealing with the drag associated with the shed vortices, it would follow that for other shapes the rms oscillating lift will also be approximately one-third of the steady-state profile drag. The unknown function ℓ_3, the spanwise coherence length, is the only expression that is strongly dependent on the Reynolds number which is essential in explaining some of the observed phenomena.

Thus the key issue in predicting "vortex noise" is estimating wake intensities and spanwise correlation lengths. Aravamudan, Lee and Harris (1978) present further discussion on this matter.

It should also be noted that there are several empirical methods available to predict the high frequency broadband noise radiation from helicopters rotors and propellers. Ungar *et al.* (1972) reviewed the existing literature and obtained the following expressions for the overall sound pressure levels (SPL) due to vortex shedding from airfoils:

$$\mathrm{SPL} = -48 + 10 \log A_b + 60 \log U_{0.7} + 10 \log\left(\frac{C_D}{0.01}\right)$$

$$+ 10 \log \{\tfrac{1}{2}[1-J_0(2\beta)\cos 2\theta]\} - 20 \log \frac{r}{3} \quad (15)$$

where A_b is the disc area, $U_{0.7}$ is the rotational velocity at 70% of blade span and β is pitch angle. The spectrum was calculated using the Strouhal frequency relation

$$f_p = 0.28 \frac{U_{0.7}}{d_p} \quad (16)$$

where $d_p = t \cos \alpha + c \sin \alpha$ and is the wake-projected airfoil thickness. In Figure 6 is shown the comparison between predicted and measured vortex noise spectra for the H-D 1 hovercraft using equations (15) and (16).

NOISE REDUCTION AT THE SOURCE

The preceding formulations for the various flow/surface interaction noise mechanisms can be examined to identify physical parameters which could, in principle, be altered to reduce the strength of the noise source, or change its characteristic frequency. In general, the approaches can be roughly reduced to two classes of options:

- reduce the aerodynamic excitation, or
- reduce the response to the excitation.

Below we examine such approaches to reducing the broadband noise generation for the blade/turbulence interaction source and the trailing edge sources, including "vortex shedding". Since it has long been obvious that all rotor sources can be reduced by reducing the rotation speed, the following discussion presupposes that designers would take advantage of lower rotor speeds to the maximum extent allowed by performance requirements, Thus the approaches presented could be viewed as a means for additional noise reduction, or alternatives to further lowering of rotor speed.

Blade/Turbulence Interaction Noise

The best approach to reduction of blade/turbulence interaction noise is to try to locate the rotor blades where inflow turbulence will be minimized. On single rotor helicopters, the primary source of inflow turbulence to the main rotor is the atmosphere, except in certain flight modes where turbulence from preceding blades may be encountered. Fortunately, the most intense atmospheric turbulence occurs at such low frequencies that its farfield acoustic consequences are negligible.

Tail rotors often experience a mean inflow distortion and turbulence which are created by the downwash from the main rotor, in conditions of forward flight. Both of these conditions can be mitigated in the initial design stages of the helicopter by locating the tail rotor outside the envelope of main rotor downwash trajectories expected throughout the flight regime. Pegg and Shidler (1978) discuss the results of an extensive experimental program which demonstrated this most powerful approach for reducing tail rotor noise.

If one is unable to avoid inflow turbulence to a particular rotor, then the only available approach to reducing the noise is to reduce the fluctuating loads experienced by the blades operating in the turbulent flow. If the predominant reduced frequency is high enough, increasing the blade chord could reduce the response; however, substantial increases are required to achieve much benefit from this effect, and other aerodynamic design tradeoffs would be required. An interesting and promising technique has been advanced by Brown *et al.* (1977), which is based upon the premise that the component of inflow velocity (both mean and turbulent) which causes the blade response is that normal to the leading edge. Using a dipole model for the noise generation process, they determined that the radiated intensity is related to the flow velocity by $\cos^3\beta$ where β is the angle between the flow and the vector normal to the leading edge. (Note that Howe (1978) also finds the same result for turbulent boundary layer/trailing edge interaction noise (Eq. 9)). Furthermore, the frequency of the noise generation will vary with the cosine of β. Thus, the hypothesis is made that propellers with their leading edges swept forward or backward will generate less blade/turbulence interaction noise than a blade with radial leading edge. Brown tested two 40 cm dia. propellers in the BBN acoustic wind tunnel to verify this hypothesis - one with a symmetrical chord distribution about a radial line, and the other with 51° of midchord sweep. The chord lengths at corresponding radii were identical. A consistent source of broadband turbulence was introduced upstream of the propellers, and a range of advance ratios was explored. The results shown in Figure 7 are quite dramatic and agree well with what would be predicted by the $\cos^3\beta$ intensity model, and frequency shifting by $\cos\beta$.

We note at this time that swept blades have been successfully used to reduce noise due to steady loads and thickness effects on a high speed turbofan (Hayden *et al.*, 1977) and that Farassat (1978) has recently predicted the same trends for high speed free rotors (see paper by Farassat, Nystrom, and Brown in this conference). Thus, the swept blade concept for reducing broadband noise is compatible with a demonstrated concept for reducing discrete frequency noise.

Trailing Edge and "Vortex Shedding" Noise Reduction

Trailing edge sources can also be reduced by modifying turbulence parameters (intensity and length scales), or by sweeping the trailing edge relative to the mean flow direction. In helicopter rotors, excessive local load levels often occur, leading to intense local blade-generated turbulence, and consequently high broadband noise levels. Thus, a high priority is to attempt to design rotors to avoid excessive local loading. Given the overall complexity of the helicopter's aerodynamics and the general lack of available data on full-scale helicopters, the ability of designers to avoid local blade stall in all flight regimes may be limited for some time.

Modification of Turbulent Structure

In unstalled portions of a rotor, the turbulence structure can, in principle, be modified to reduce trailing edge sources, by the use of vortex generators or leading edge serrations. The latter technique has been studied as a means for reducing the so-called high frequency broadband noise peak in propellers and rotor noise spectra (see, for example, Hersh and Hayden (1971), Hersh *et al.*, (1974)). Figure 8 shows the noise reduction achieved on a model rotor for varying spanwise amounts of leading edge treatments. Although the high frequency peak is generally thought to be associated with pressure-surface laminar flow instability, and therefore possibly limited to small low speed rotors, George (1977) and Aravamudan *et al.* (1978) point out the existence of this peak in full scale rotor data. Thus, the serration concept could be useful in reducing this source.

Sweep

Arguments similar to those made above regarding the importance of the normal velocity component in noise generation can be advanced for trailing edge mechanisms. Howe's formulation for semi-infinite surfaces predicts a $\cos^3\beta$ dependence on overall radiated intensity. A dipole model for wake vortex shedding noise such as discussed earlier would predict a $\cos^5\beta$ intensity dependence (e.g., see Brown, 1977). Both models predict characteristic frequency variation with $\cos\beta$. The results of an experiment conceived to demonstrate this effect are shown in Figure 9. One propeller had a radial trailing edge while the other had a smoothly curved trailing edge which always produced a normal velocity vector about 45° from radial. The results seem to indicate that the $\cos^5\beta$ law is closely followed.

Porous Trailing Edge

The final concept to be discussed for reduction of broadband noise is the porous or variable impedance trailing edge concept, which involves replacing the solid surface of the blade with a surface(s) which is (are) porous, thus allowing a more gradual acceleration of the medium around the edge than occurs when boundary layer turbulence encounters a sharp surface discontinuity. Further, the porous surfaces near the edge reduce the intensity of various band wakes, since the strong pressure gradients involved in the formation of such wakes cannot exist. Further background on the concept is given in Hayden and Chanaud (1973 a,b) and in Hayden (1976). Figure 10a illustrates the notion that there exists a variety of impedance-change contours which can serve to reduce the noise generation. Figure 10b indicates that there are at least four general structural arrangements possible to implement the concept, all of which have been investigated on stationary surfaces. There is presently analytical work under way at BBN to develop methods for optimizing the reduction of a single wavenumber component, or the entire spectrum, based upon surface porosity, edge length/wavelength, etc.

Some results pertinent to helicopter rotors are given in Figures 11a and 11b, in which the nearly total elimination of the wake-related peak and 5 - 10 dB reduction of the broadband peak may be seen. Similar results have been measured on powered lift flaps and simple rotating blades (Hayden 1976;1977). We believe that the potential for 10 dB of broadband noise reduction exists for practical rotor systems. However, work on materials characterization and verification of analytical predictions is needed, as well as on the aerodynamics of airfoils with porous surfaces, with or without cavities behind them.

CONCLUSIONS

This paper has provided some evidence that accurate detailed source models cast in terms of physically measurable or controllable parameters can point the way to noise reduction approaches. Rotor broadband mechansisms are quite well understood for Mach numbers below the transonic regime; at higher speeds, additional mechanisms such as randomly-modulated thickness noise, shock/turbulence interaction, and shock instability may become important. These additional mechanisms are not presently well understood and deserve attention. *However, for all mechanisms, a critical deficiency exists in the specification of both mean and unsteady flow field components needed to estimate the strength, spectral characteristics, and spatial location of the noise mechanisms.* The effective selection and application of rotor noise reduction measures depends upon the ability to predict or measure the location of the source to be reduced. Further improvements in the rotor noise prediction area will come about only after development of a data base and prediction capability for details of steady and unsteady flows around rotors.

We have shown several promising noise reduction concepts that have been developed from, or can be explained by, accurate source models. The concepts have been verified on simplified systems for which important flow field information could be developed. The applicability to helicopters is clear, but the success in optimally implementing the concepts will depend upon the ability to develop the relevant design information, especially flow field conditions.

BIBLIOGRAPHY

Aravamudan, K.S., Lee, A., and Harris, W.L., "Wind Tunnel Investigations of Model Rotor Noise at Low Tip Speeds". Helicopter Acoustics, NASA CP-2052, Pt. I, 1978. (Paper no. 12 of this compilation.)

Aravamudan, K.S. and Harris, W.L., "Effects of Free Stream Turbulence on Low Frequency Broadband Noise Generated by a Model Rotor", to be published in Journal of Fluid Mechanics, 1978.

Amiet, R.K., "Acoustic Radiation from an Airfoil in a Turbulent Stream", Journal of Sound and Vibration, 41, pp. 407 - 420, 1975.

Amiet, R.K., "Noise Produced by Turbulent Flow into a Propeller or Helicopter Rotor", AIAA Paper 75-560, 3rd AIAA Aeroacoustic Conference, Palo Alto, CA, July 20-23, 1976.

Bohn, A.J., "Edge Noise Attenuation by Porous Edge Extensions", AIAA Paper 76-80, 1976.

Brown, N.A., "Noise and Fluids Engineering", ASME, 1977 Winter Annual Meeting, Atlanta, GA.

Chandiramani, K.L., "Diffraction of evanescent waves with Applications to Aerodynamically Scattered Sound and Radiation from Unbaffled Plates," J. Acoust. Soc. Am. 55, pp. 19-29, 1974.

Chanaud, R.C. and Hayden, R.E., "Edge Sound Produced by Two Turbulent Wall Jets", Paper FF-11, Spring Meeting of Acoustical Society of America, Atlantic City, New Jersey, 1970.

Chase, D. M., "Sound Radiated by Turbulent Flow off a Rigid Half-Plane as Obtained from a Wavevector Spectrum of Hydrodynamic Pressure," J. Acoust. Soc. Am. 52, pp. 1011-1023, 1972.

Chase, D.M., "Noise Radiated from an Edge in Turbulent Flow", AIAA J. 13, pp. 1041-1047, 1975.

Crighton, D.G., "Radiation from Vortex Filament Motion near a Half-Plane," J. Fluid Mech. 51, pp. 357-362, 1972.

Curle, N., "The Influence of Solid Boundaries upon Aerodynamic Sound", Proc. Roy. Soc. Lond. A231, pp. 505-514, 1955.

Farassat, F., Nystrom, P.A., and Brown, T.J., "Bounds on Thickness and Loading Noise of Rotating Blades and the Favorable Effect of Blade Sweep on Noise Reduction". Helicopter Acoustics, NASA CP-2052, Pt. I, 1978. (Paper no. 18 of this compilation.)

Ffowcs Williams, J.E. and Hawkings, D.L., "Theory Relating to the Noise of Rotating Machinery", Journal of Sound and Vibration, 10, PP. 10-21, 1969.

Ffowcs Williams, J.E. and Hall, L. H., "Aerodynamic Sound Generation by Turbulent Flow in the Vicinity of a Scattering Half-Plane," J. Fluid Mech. 40, 657-670, 1970.

Filotas, L.T., "Theory of Airfoil Response in a Gusty Atmosphere, Part I: Aerodynamic Transfer Function," UTIAS-139, Toronto University, 1969.

George, A.R. and Kim, Y.K., "High Frequency Broadband Rotor Noise", AIAA Paper 76-561, 3rd AIAA Aeroacoustic Conference, Palo Alto, CA, July 20-23, 1976.

George, A.R., "Helicopter Noise - State of the Art", AIAA Paper 77-1337, 4th Aeroacoustics Conference, Atlanta, GA, October 3-5, 1977.

Graham, J.M.R., "Lifting Surface Theory for the Problem of an Arbitrarily Yawed Sinusoidal Gust Incident on a Thin Aerofoil in Incompressible Flow," Aeron. Quart., vol. 21, pp. 182-198, 1970.

Hanson, C.E., "An Investigation of the Near Wake Properties Associated with Periodic Vortex Shedding from Airfoils", MIT Acoustics and Vibration Laboratory, TR76234-5, 1970.

Hayden, R.E., "Sound Generation by Turbulent Wall Jet Flow over a Trailing Edge," M.S. Thesis, Purdue University, 1969.

Hayden, R.E., "Noise from Interaction of Flow with Rigid Surfaces: A Review of Current Status of Prediction Techniques," BBN Report No. 2276; also NASA CR-2126, 1972.

Hayden, R.E., "Fundamental Aspects of Noise Reduction from Powered Lift Devices," SAE Paper 730376, SAE Transactions, 1973.

Hayden, R.E., and Chanaud, R.C., "Method of Reducing Sound Generation in Fluid Flow Systems Embodying Foil Structures and the Like", U.S. Patent 3,779,338, 1973a.

Hayden, R.E., and Chanaud, R.C., "Foil Structure with Reduced Sound Generation", U.S. Patent 3,853,428, 1973b.

Hayden, R.E., Fox, H.L., and Chanaud, R.C., "Some Factors Influencing Radiation of Sound from Flow Interaction with Edges of Finite Surfaces," NASA CR-145073, 1976.

Hayden, R.E., "Reduction of Noise from Airfoils and Propulsive Lift Systems Using Variable Impedance Surfaces," AIAA Paper 76-500, Palo Alto, CA, 1976.

Hayden, R.E., "Some Advances in Design Techniques for Low Noise Operation of Propellers and Fans", NOISE-CON 77 Proceedings, Hampton, VA, August, 1977.

Hayden, R.E., Bliss, D.B., *et al.*, "Analysis and Design of a High Speed, Low Noise Aircraft Fan Incorporating Swept Leading Edge Rotor and Stator Blades", BBN Report 3332; NASA CR-135092, December, 1977.

Hersh, A.S., and Hayden, R.E., "Noise Generation by Airfoils with and without Leading Edge Serrations," BBN Report 2095, NASA CR-114370, 1971.

Hersh, A.S., Soderman, P.T., and Hayden, R.E., "Investigation of Acoustic Effects of Leading Edge Serrations on Airfoils," J. of Aircraft, 11, No. 4, 1974.

Homicz, G. F., and George, A.R., "Broadband and Discrete Frequency Radiation from Subsonic Rotors", Journal of Sound and Vibration, 36, pp. 151-177, 1974.

Howe, M.S., "A Review of the Theory of Trailing Edge Noise", BBN Report 3679; NASA CR-3021, 1978 (to be published in Journal of Sound and Vibration, 1978).

Leverton, J.W., "The Noise Characteristics of a Large 'Clean' Rotor," Sound and Vibration, 27,3, pp. 357-376, 1973.

Lighthill, M.J. "On Sound Generated Aerodynamically. I. General Theory," Proc. Roy. Soc. Lond. A211, pp. 564-587, 1952.

Osborne, C., "Unsteady Thin Airfoil Theory",AIAA Journal, 11, pp. 205-209, 1973.

Paterson, R.W., Vogt, P.G., Fink, M.R., and Munch, C.L., "Vortex Shedding Noise from Isolated Airfoils", U.S. Army Research Office, Report K910867-6, 1971; also appeared in J. of Aircraft, 10, 1973.

Pegg, R.J., and Shidler, P.A., "Exploratory Wind-Tunnel Investigation of the Effect of the Main Rotor Wake on Tail Rotor Noise". Helicopter Acoustics, NASA CP-2052, Pt. I, 1978. (Paper no. 11 of this compilation.)

Phillips, O.M., "The Intensity of Aeolian Tones", J. Fluid Mechanics, 1, 1956.

Powell, A.O., "On the Aerodynamic Noise of a Rigid Flat Plate Moving at Zero Incidence," J. Acoust. Soc. Am. 31(12), pp. 1649-1653, 1959.

Ross, D., "Vortex Shedding Sound of Propellers", BBN Report 1115, 1964 (see synopsis in Ungar *et al.*, 1972).

Scheiman, J., Hilton, D.A., and Shivers, J.P., "Acoustical Measurements of the Vortex Noise for a Rotating Blade Operating With and Without its Shed Wake Blown Downstream", NASA TND-6364, 1971.

Sears, W.R., "Some Aspects of Non-Stationary Airfoil Theory and Its Applications", Journal of Aeronautical Sciences, 8, pp. 104-108, 1941.

Ungar, E.E., *et al.*, "A Guide For Predicting the Aural Detectability of Aircraft", AFFDL-TR-71-22, 1972.

Yudin, E.Y., "On the Vortex Sound from Rotating Rods," Zhurnal Technicheskoi Fiziki, 14, NACA Tech Memo 1136, 1947.

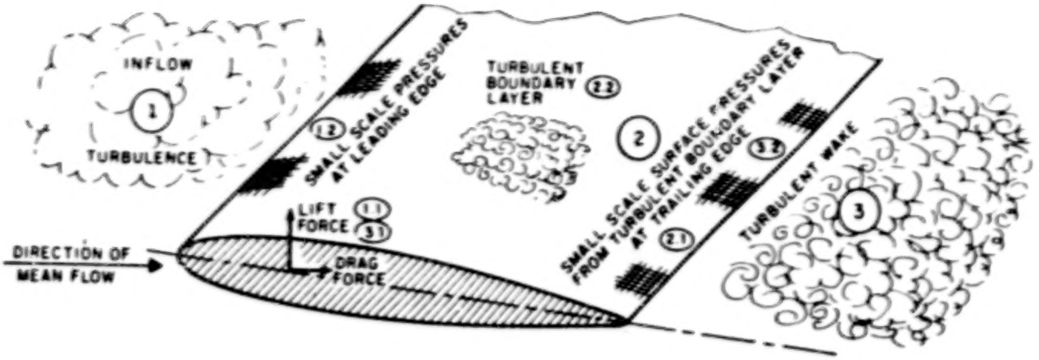
INFLOW
1
TURBULENCE
SMALL SCALE PRESSURES AT LEADING EDGE
1.2
TURBULENT BOUNDARY LAYER
2.2
2
SMALL SCALE SURFACE PRESSURES FROM TURBULENT BOUNDARY LAYER AT TRAILING EDGE
3.2
2.1
TURBULENT WAKE
3
LIFT
1.1
FORCE
3.1
DRAG FORCE
DIRECTION OF MEAN FLOW

FLUID SOURCE	MAJOR ACOUSTIC SIGNIFICANCE
① INFLOW TURBULENCE	(1.1) LIFT AND DRAG FLUCTUATIONS OF WHOLE SURFACE (1.2) SMALL SCALE PRESSURE FLUCTUATIONS AT LEADING EDGE
② TURBULENT BOUNDARY LAYER	(2.1) SMALL SCALE PRESSURE FLUCTUATIONS AT TRAILING EDGE (2.2) ACOUSTICALLY "FAST" PRESSURES THAT RADIATE DIRECTLY
③ TURBULENT WAKE	(3.1) LIFT AND DRAG FLUCTUATIONS ON WHOLE SURFACE (3.2) SMALL SCALE PRESSURE FLUCTUATIONS AT TRAILING EDGE

Figure 1.- Fluid dynamic sources of broadband noise.

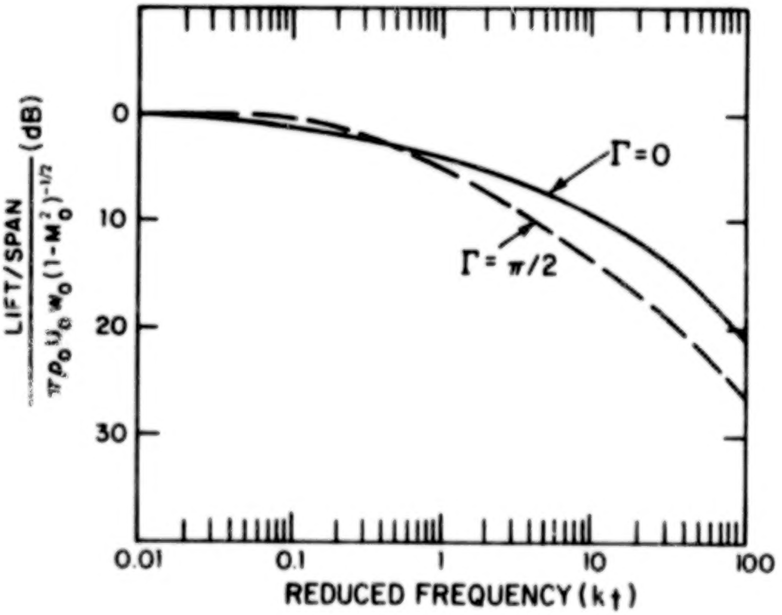

Figure 2.- Effect of spanwise component of gust velocity on lift response function.

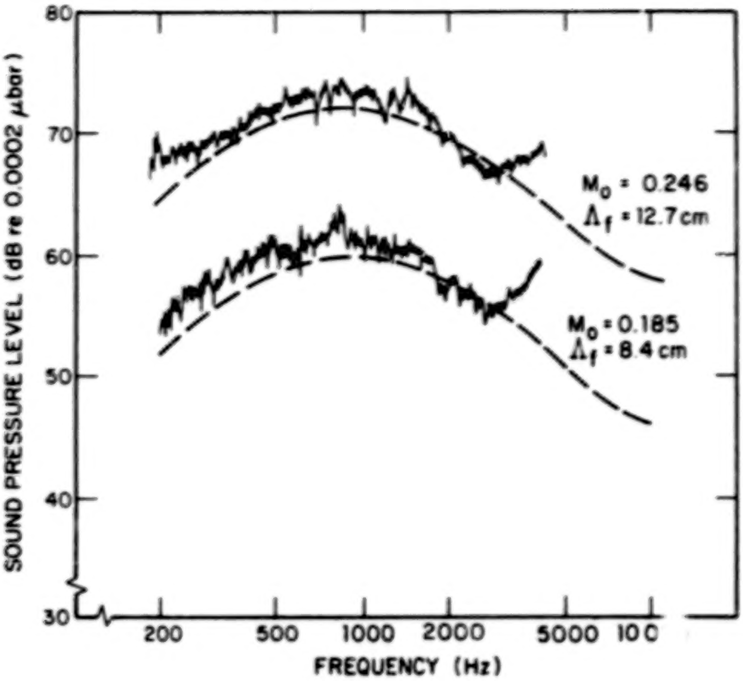

Figure 3.- Computed and measured spectra from model rotor in wind tunnel with simulated turbulence.

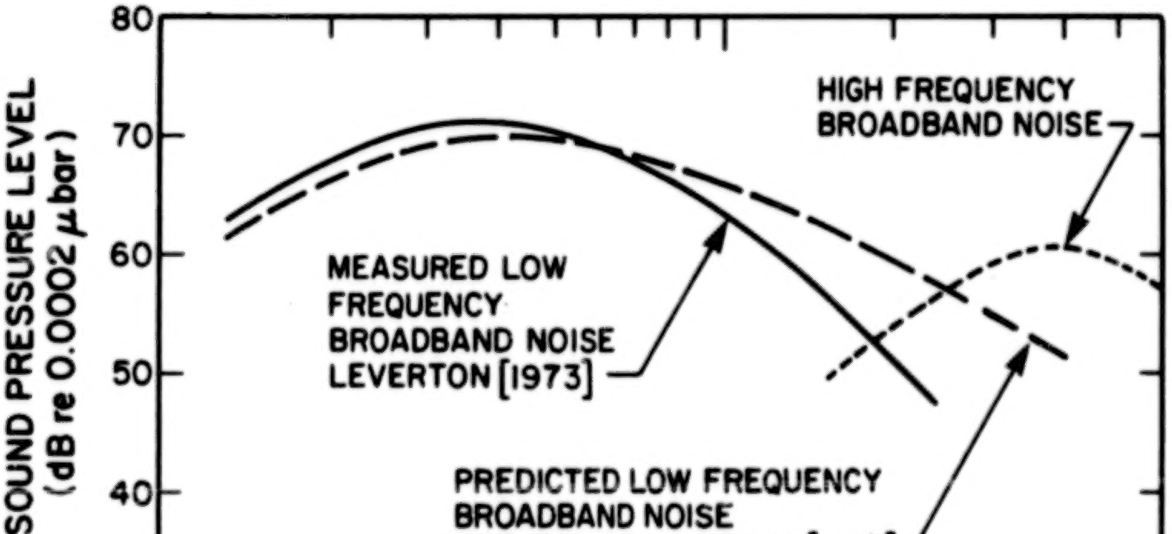

Figure 4.- Prediction of full-scale rotor broadband noise from model data.

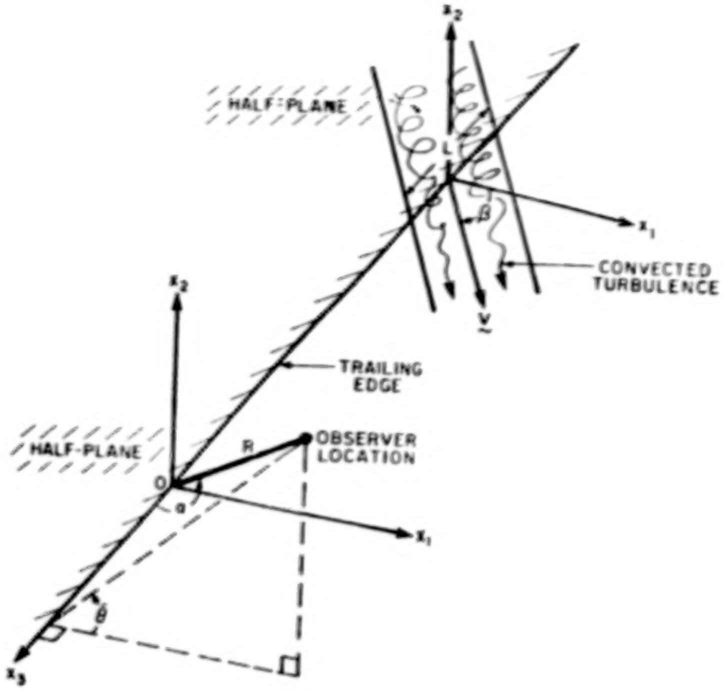
x_2
HALF-PLANE
L
β
x_1
CONVECTED TURBULENCE
$\underset{\sim}{V}$
x_2
TRAILING EDGE
HALF-PLANE
R
OBSERVER LOCATION
O
α
x_1
θ
x_3

Figure 5.- Coordinate and flow field definitions for trailing edge noise calculations.

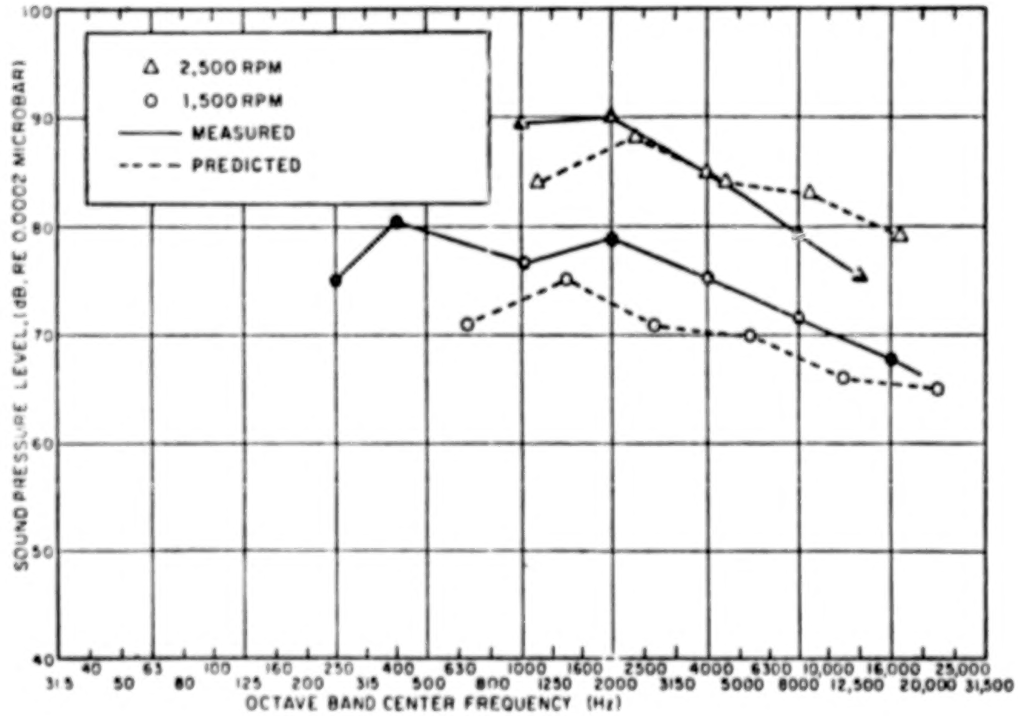

Figure 6.- Comparison of measured and predicted vortex noise for H.D. 1 Hovercraft at 15° out of propeller plane, 30 m from hub.

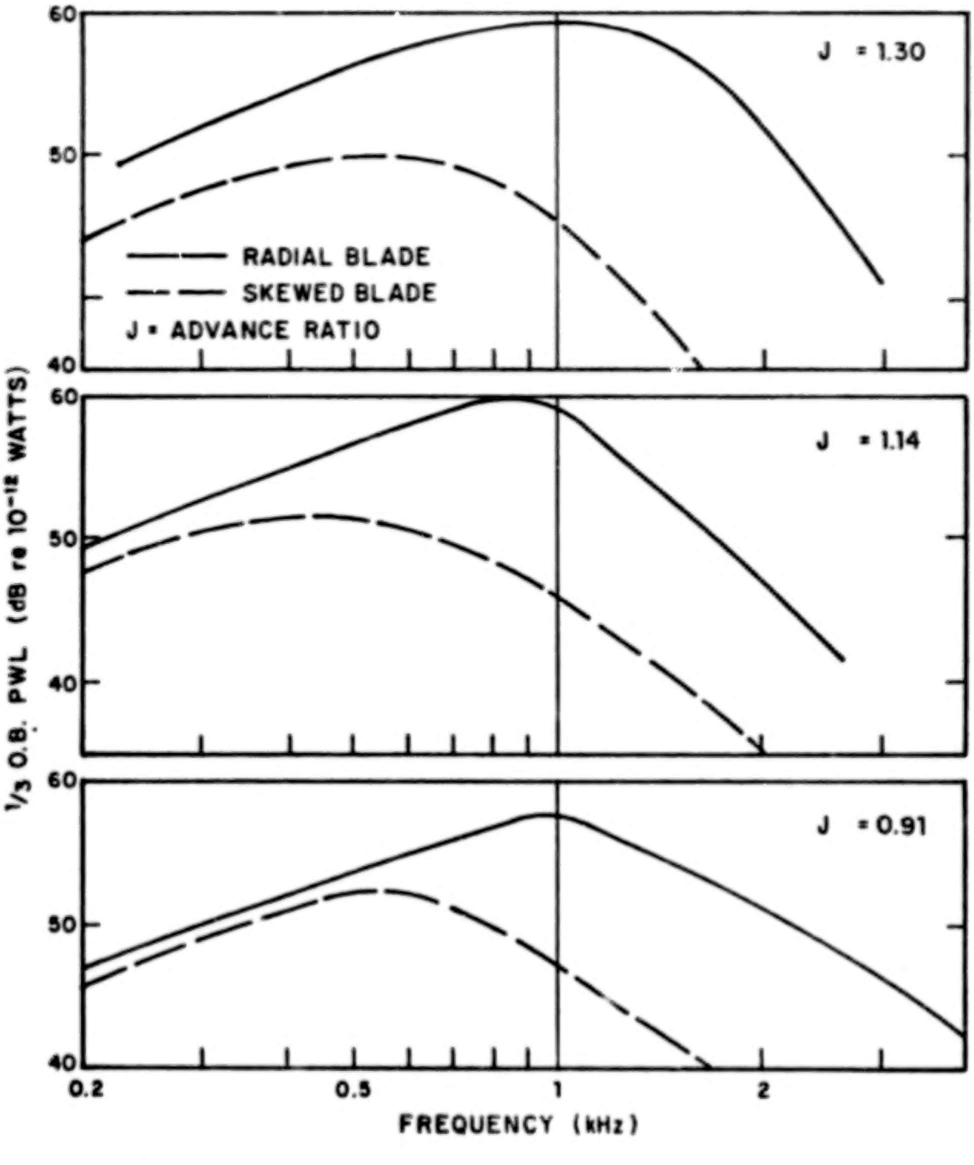

Figure 7.- Effect of 50° sweep on rotor/turbulence interaction noise spectra.

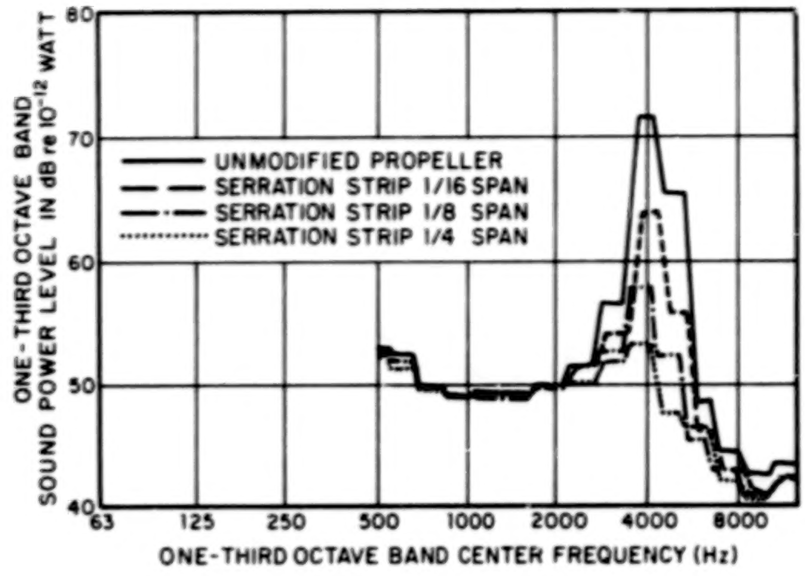

Figure 8.- Effect of properly located leading edge serrations.

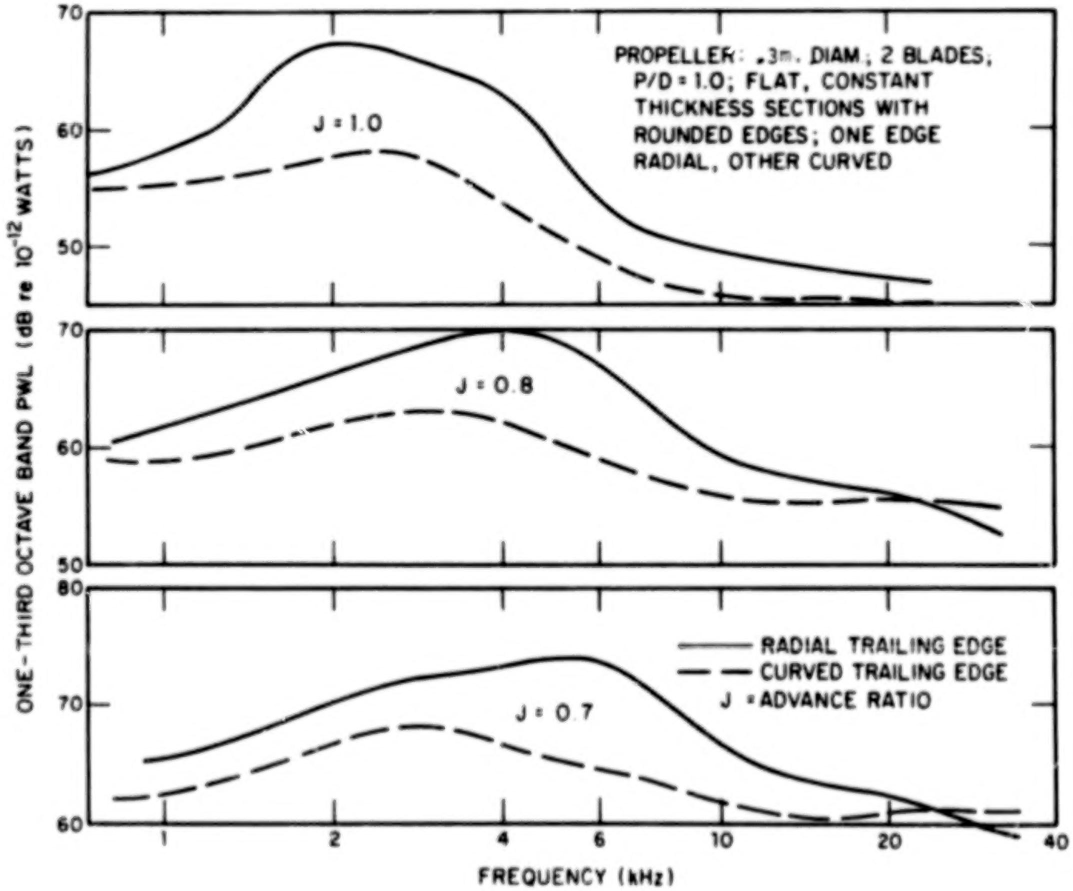

Figure 9.- Effect of sweep on trailing edge noise of rotor.

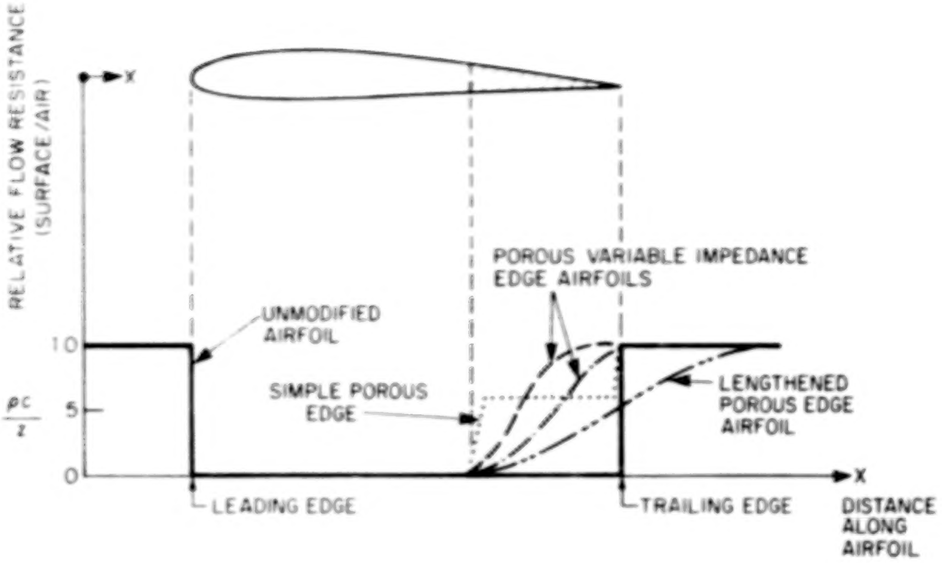
RELATIVE FLOW RESISTANCE (SURFACE/AIR)
x
$\frac{\rho c}{z}$
10
5
0
UNMODIFIED AIRFOIL
SIMPLE POROUS EDGE
POROUS VARIABLE IMPEDANCE EDGE AIRFOILS
LENGTHENED POROUS EDGE AIRFOIL
LEADING EDGE
TRAILING EDGE
x
DISTANCE ALONG AIRFOIL

(a) Schematic of porous edge concept and families of impedance changes.

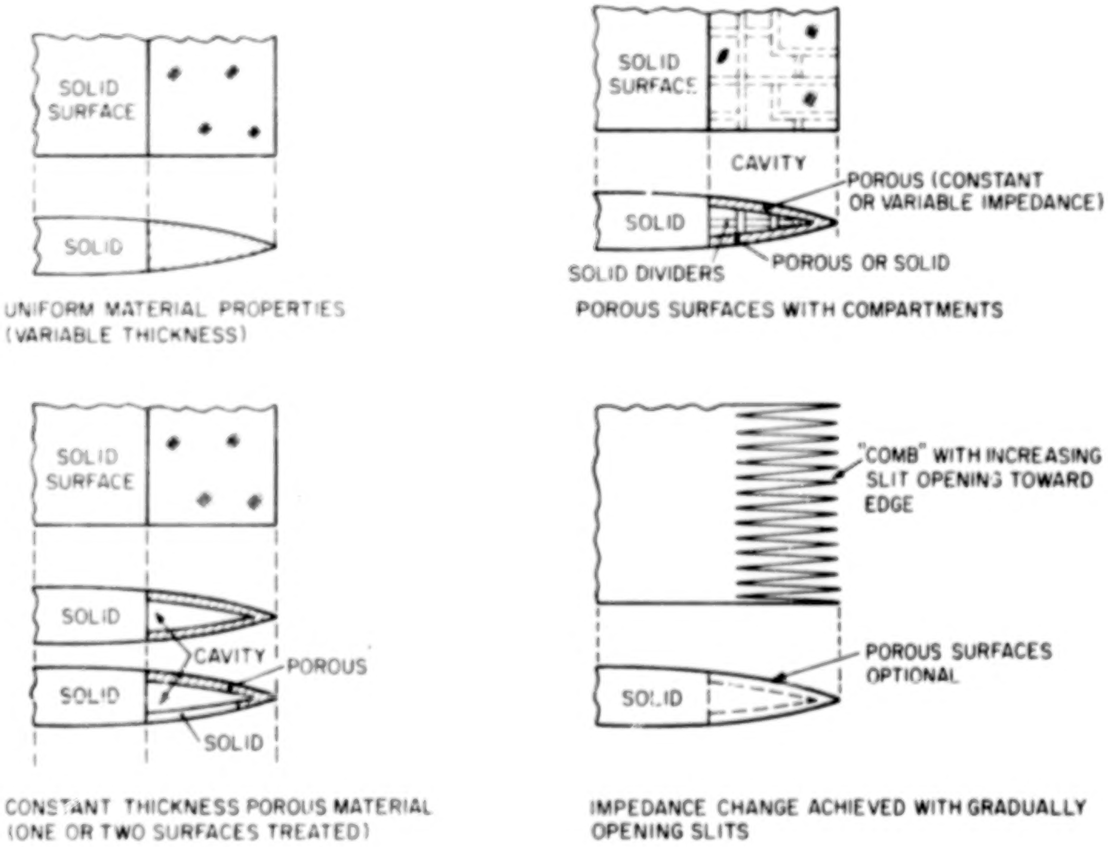
SOLID SURFACE
SOLID
UNIFORM MATERIAL PROPERTIES (VARIABLE THICKNESS)
SOLID SURFACE
CAVITY
SOLID
POROUS (CONSTANT OR VARIABLE IMPEDANCE)
SOLID DIVIDERS
POROUS OR SOLID
POROUS SURFACES WITH COMPARTMENTS
SOLID SURFACE
SOLID
CAVITY
POROUS
SOLID
SOLID
CONSTANT THICKNESS POROUS MATERIAL (ONE OR TWO SURFACES TREATED)
"COMB" WITH INCREASING SLIT OPENING TOWARD EDGE
POROUS SURFACES OPTIONAL
SOLID
IMPEDANCE CHANGE ACHIEVED WITH GRADUALLY OPENING SLITS

(b) Classes of variable impedance edge structures.

Figure 10.- Porous, or variable impedance, trailing edge concept.

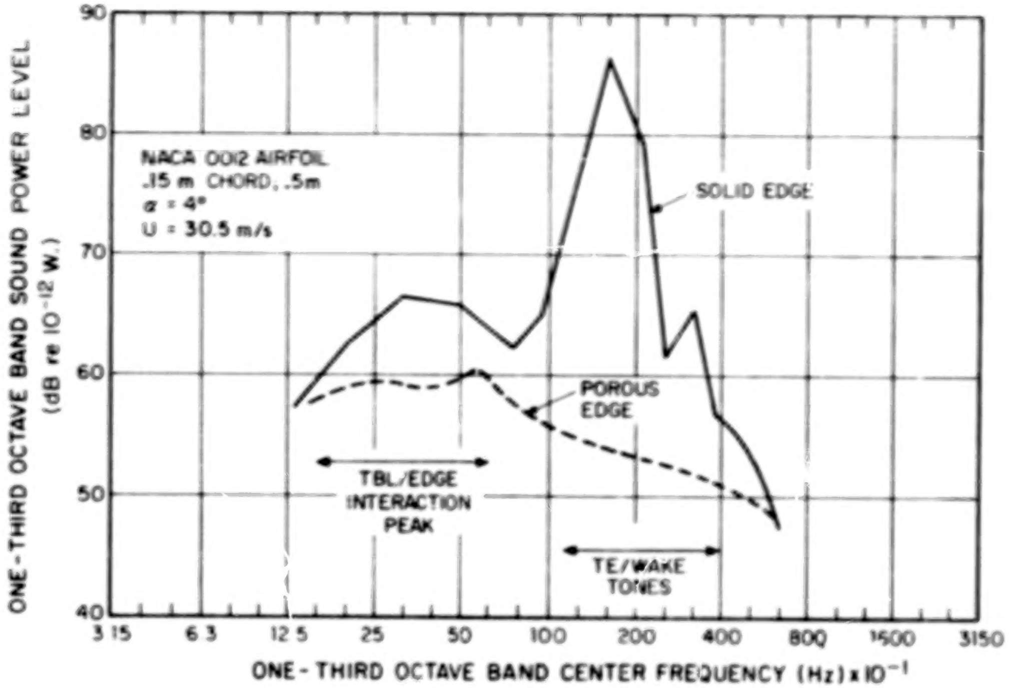

(a) NACA 0012 Airfoil (0.15 m chord; 0.45 m span). $U_o = 30$ m/s; $\alpha = 4^o$.

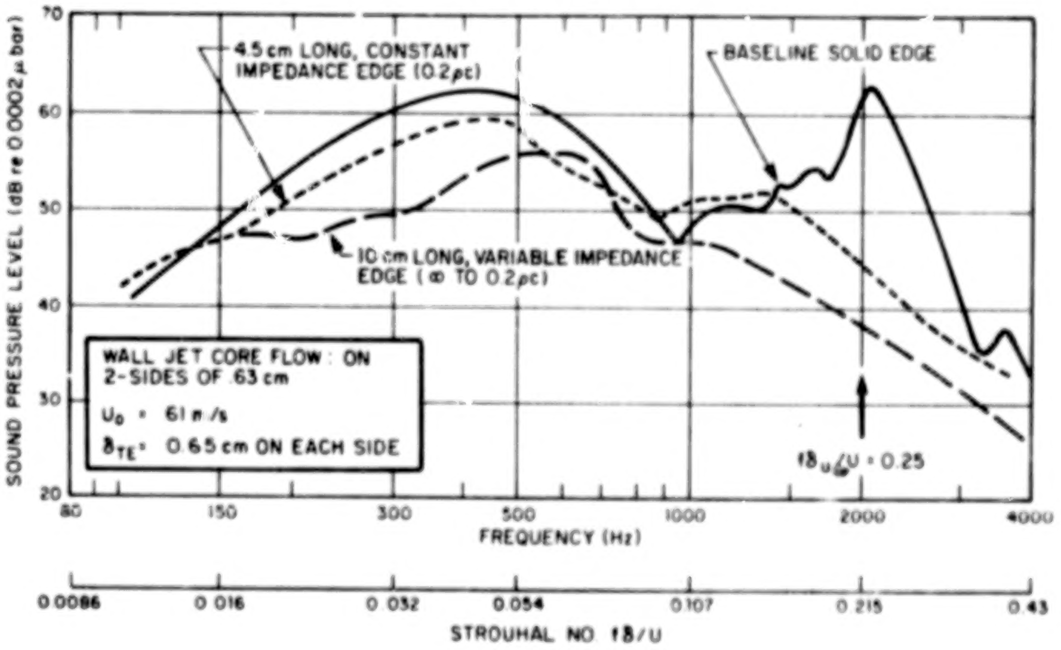

(b) Wall jet/trailing edge noise reduction with two types of porous edges. $U_o = 60$ m/s.

Figure 11.- Noise reduction of fixed airfoil and plate with variable impedance edges.

Blank Page

6

THEORETICAL MODELS OF HELICOPTER ROTOR NOISE

D. L. Hawkings
Westland Helicopters Limited

SUMMARY

This paper examines some of the traditional theoretical models of helicopter noise. For low speed rotors, it is shown that unsteady load models are only partially successful in predicting experimental levels. A new theoretical model is presented which leads to the concept of "unsteady thickness noise." This gives better agreement with test results. For high speed rotors, it is argued that present models are incomplete and that other mechanisms are at work. Some possibilities are briefly discussed.

INTRODUCTION

The considerable theoretical effort expended on rotor noise in recent years has, as yet, had little impact on helicopter design practice. However, the impending era of helicopter noise legislation presents new challenges and opportunities for the researcher since designers will increasingly demand methods for reducing noise levels.

The objectives of this paper are to show that there are several areas of rotor noise where traditional theoretical ideas and mechanisms need revision and to suggest some ways forward. It is not intended to present a balanced state-of-the-art assessment of theoretical models to achieve this end, but rather to discuss a few selected topics which will illustrate the main points. (See ref. 1 for a recent review.) It is important to recognise that each topic has a strong practical motive behind it. The topics arise from a need to predict real helicopter noise in realistic situations. If these areas were more fully understood it would go a long way towards helping the designer reduce helicopter external noise.

SYMBOLS

Measurements and calculations were made in British Imperial Units. They are presented herein in the International System of Units (SI) with the equivalent values given parenthetically in the British Imperial Units.

a_o	speed of sound
BW	analysis band width

c	blade chord
D	in-plane drag force
div	divergence
e	exponential function
f	frequency factor
H	non-dimensional blade thickness distribution
h	physical blade thickness
i,j,β	indices
k	harmonic number
J_n	Bessel function
L	local unsteady lift
l	wave number
M	source Mach number
m	wave number
mB	harmonic number
M_t	tip Mach number
$\underline{n}$	surface normal
P	acoustic power spectrum
p	pressure
R	blade radius
r	distance between source and observer
S	true blade surface
SPL	sound-pressure level
T	thrust
t	time
T_{ij}	quadrupole source strength

T_{ref}	reference thrust
U	typical blade speed
u	velocity
V_c	convection velocity
$\underline{v}$	response velocity
W	power spectrum of input gust
w	gust velocity
$\underline{x}$	vector position
x_1,x_2,x_3	axes
x,y,z	axes
α	frequency
δ	small parameter
θ	angle between observation direction and rotor axis
Λ	integral scale length
λ	negative constant
ρ	density
Σ	mean blade planform
Ω	angular velocity of rotor

A bar over a symbol denotes a non-dimensional value; a bar below a symbol indicates a vector quantity.

UNSTEADY BLADE LOAD MODELS

The problem of main rotor hover noise has been central to rotor noise research over the past decade. The corresponding foundation stone for theoretical models was the realisation that small, oscillatory blade loads can result in a significant noise output far in excess of that resulting from the steady aerodynamic loads. These unsteady loads are assumed to result from disturbed inflow (such as atmospheric turbulence or blade wakes) entering the rotor and are accepted as the physical mechanism responsible for hover noise.

CONTENTS

Part I

PREFACE . . . . iii 1/A6

REGULATIONS

1. HELICOPTER EXTERNAL NOISE REQUIREMENTS - FAA PERSPECTIVE 1 1/A8
Charles R. Foster

2. HELICOPTER NOISE REGULATIONS: AN INDUSTRY PERSPECTIVE 17 1/B10
R. A. Wagner

3. NOISE REQUIREMENTS FROM A MILITARY POINT OF VIEW 33 1/C12
Charles C. Crawford, Jr.

4. THE IMPACT OF URBAN OPERATIONS ON HELICOPTER NOISE REQUIREMENTS . . . 45 1/D10
Stanley R. Spector

ROTOR NOISE

5. PREDICTION AND REDUCTION OF ROTOR BROADBAND NOISE 61 1/E12
Richard E. Hayden and Krishna S. Aravamudan

6. THEORETICAL MODELS OF HELICOPTER ROTOR NOISE 89 1/G12
D. L. Hawkings

7. NOISE DUE TO ROTOR-TURBULENCE INTERACTION 109 2/B6
R. K. Amiet

8. THEORY ON ACOUSTIC SOURCES 127 2/C10
S. E. Wright

9. POTENTIAL ACOUSTIC BENEFITS OF CIRCULATION CONTROL ROTOR 149 2/E5
Robert M. Williams and Ian C. Cheeseman

10. HELICOPTER NOISE RESEARCH AT THE LANGLEY V/STOL TUNNEL 181 2/G9
Danny R. Hoad and George C. Greene

11. EXPLORATORY WIND-TUNNEL INVESTIGATION OF THE EFFECT OF THE MAIN ROTOR WAKE ON TAIL ROTOR NOISE 205 3/B7
Robert J. Pegg and Phillip A. Shidler

12. WIND TUNNEL INVESTIGATIONS OF MODEL ROTOR NOISE AT LOW TIP SPEEDS . . . 221 3/C9
K. S. Aravamudan, A. Lee, and W. L. Harris

13. HELICOPTER EXTERNAL NOISE PREDICTION AND CORRELATION WITH FLIGHT TEST 263 3/F11
Bharat P. Gupta

14. FULL-SCALE TESTING OF AN OGEE TIP ROTOR 277 3/G11
Wayne R. Mantay, Richard L. Campbell, and Phillip A. Shidler

15. HOVERING IMPULSIVE NOISE - SOME MEASURED AND CALCULATED RESULTS 309 4/C4
D. A. Boxwell, Y. H. Yu, and F. H. Schmitz

16. IMPROVED METHODS FOR CALCULATING THE THICKNESS NOISE 323 4/D4
Yoshiya Nakamura and Akira Azuma

17. THE IMPORTANCE OF QUADRUPOLE SOURCES IN PREDICTION OF TRANSONIC TIP SPEED PROPELLER NOISE 339 4/E6
Donald B. Hanson and Martin R. Fink

18. BOUNDS ON THICKNESS AND LOADING NOISE OF ROTATING BLADES AND THE FAVORABLE EFFECTS OF BLADE SWEEP ON NOISE REDUCTION 373 4/G12
F. Farassat, Paul A. Nystrom, and Thomas J. Brown

19. A STUDY OF THE NOISE RADIATION FROM FOUR HELICOPTER ROTOR BLADES . . . 387 5/A14
Albert Lee and Marianne Masher

Mathematical models of this mechanism were first confined to the discrete tone generation (refs. 2, 3), but subsequent refinement (refs. 4, 5, 6) has extended it to broad band noise so that a unified treatment of the whole spectrum is now possible.

This concept, that noise arises from blade loads caused by disturbed inflow entering the rotor, has dominated thinking in the subject to the virtual exclusion of other ideas. However, for various reasons, it has not proved possible to convert this idea into a convincing prediction method. The most obvious difficulty is knowing details of the unsteady blade loads. These cannot be measured, and the inference from acoustic results is that they are extremely sensitive to extraneous influences such as wind or atmospheric turbulence, at least for the subjectively important higher frequencies. Thus the theories usually resort to "guestimating" average levels and trends, either of the loads directly (ref. 2) or of an input distortion spectrum which, combined with a simple blade response model, can give the loads indirectly (refs. 5, 6).

An additional difficulty arises when the observer lies in or near the rotor plane, which is often the case of practical interest. Here the noise field is dominated by the in-plane "drag" forces; but, the origins and characteristics of these unsteady drag forces are obscure, especially for inviscid flow at high reduced frequencies. Consequently, the acoustic studies have of necessity avoided this issue either by taking the drag forces to be zero or by simply relating them to the unsteady lifting forces.

Some of these difficulties are illustrated in figures 1-4 which show some comparisons between theory and fullscale test results for rotor discrete tones. The experiments were conducted on a whirl tower several years ago, and the test series and equipment are fully reported in references 7 and 8 (although some of the results used here do not appear in those references). The experiments have been compared with the theoretical predictions of reference 2, modified to permit alternative loading laws to be used. (These loading laws assume that the harmonics of the unsteady blade loading decay as n^{λ}, where n is the harmonic number and λ is an empirically chosen negative constant.)

Figure 1 illustrates both the variability of discrete tone test data and the wide range of prediction levels. The two test spectra were taken under nominally identical conditions, but in different seasons. The theoretical results are based on reference 2 for the different loading laws indicated. The main points to note are the possible scatter on test results - up to 10 dB - and the even wider range of theoretical results which can be obtained by adjusting the loading law. It should be remembered that for main rotors it is the higher rotational harmonics ($n > 40$) which are subjectively important, and these are the least accurately predicted.

Figures 2, 3, and 4 illustrate several points. The experimental data have been collapsed on a T^2 basis (to a reference thrust of 4 kN (1000 lb)), and this yields a good reduction of the data. This result is commonly found but is puzzling nonetheless; since, apart from general scale ideas, there is no direct reason to expect the unsteady blade loads to vary linearly with total rotor thrust.

Comparisons between the predictions of equations (13) and (14) and the experimental results are shown in Figures 3, 4, 6, and 7. The length scale Λ has been taken equal to the blade chord, and the mean square intensity $\overline{w^2}$ equal to $10^{-5}\, U_{tip}^2\, (T/T_{ref})^2$. Again, a T^2 dependence has been enforced upon the gust intensity, but there is no direct reason why this should be true. These levels of disturbance appear realistic; they vary from 1 m/s to 4 m/s for the test series quoted.

Figures 3 and 4 show the comparison of discrete tone levels for the in- and near-plane microphones. The agreement is very good, both in spectral shape and level, for the important higher rotational harmonics. The present theory clearly performs better than the previous model near the rotor plane.

Figures 6 and 7 show the corresponding broad band levels in a stylised form; and again, reasonable agreement is found near the rotor plane. Exactly the same input spectrum has been used for both the discrete and broad band noise; the difference is a matter of coherence scales. The input is insufficiently coherent at the higher frequencies to generate discrete tones. This transition from discrete tone to broad band noise is a natural feature of the model.

The main objective of this section has now been achieved. It has been shown that an alternative formulation of the rotor-gust interaction problem appears possible; this could lead to a better understanding of experimental results. The theory has the right trends for spectral shape, directionality, and speed dependence. Obviously some empiricism has been incorporated, but no more than in the loads model; and, this is outweighed by the more direct representation of the acoustic field. This is clearly a new avenue for research in the classic area of rotor-inflow distortion noise.

HIGH SPEED FLIGHT NOISE

Another area where the traditional unsteady loads model has not found favour is in rotor noise generation at high advance ratios. In this flight regime, a periodic impulsive noise signature is produced which increases significantly with flight speed. Containment of this increase is essential if future high speed helicopters are to meet certification levels. The cause of this noise has been considered in several theoretical papers (refs. 10, 11, 12), and these conclude that it is dominated by thickness noise. This is the noise caused by the direct volume displacement of the air by the blades as distinct from the forces they exert. The experimental work of reference 13 is usually cited to support this proposition; it shows negative pressure acoustic pulses of precisely the form predicted by the theory. The pulses vary in level very much as expected.

However, it is the contention of this section that thickness noise is not the sole cause of high speed flight noise since there are significant anomalies between test data and theory. Although the data of reference 13 tally with many aspects of the theory, the absolute levels do not. The experimental levels are roughly double those predicted theoretically. This is illustrated in figure

However, in practice these surface sources are moved to the mean blade planform Σ (which lies in the rotor disc plane, fig. 5); the upper and lower surface sources are combined. The resultant source strength can be identified with minus local unsteady lift L and in-plane drag force D. Hence equation (1) becomes

$$4\pi p(\underline{x},t) = \frac{\partial}{\partial x_3}\int \left[\frac{L}{r(1-M_r)}\right] d\Sigma + \frac{\partial}{\partial x_\beta}\int \left[\frac{D_\beta}{r(1-M_r)}\right] d\Sigma \qquad (2)$$

where x_3 is the direction normal to Σ and $\beta = 1,2$ are the two in-plane directions. This equation forms the mathematical foundation of the unsteady loads model.

Unfortunately, this last step is questionable. Acoustic sources cannot be moved around with impunity (without incurring additional multipoles), and, if the true integral equation status of the solution is to be retained, what boundary condition applies? Is it to be enforced at the true blade surface S or at the mean planform?

More important, it is very difficult to obtain the correct distribution for the high frequency drag component, even if viscous effects are omitted. This component depends directly on the full pressure distribution over the blade surface, and finite thickness and three dimensional effects must be retained in calculating that pressure distribution. Consequently, simple aerodynamic response theory will not yield it.

These difficulties can be overcome if the sources are placed on the mean planform at the outset of the acoustic analysis rather than afterwards. Source strengths are sought whose associated fields satisfy the equations of motion and the correct boundary conditions. This, of course, is just the classic method of singularities, but its application in the present context appears novel. The key to the analysis is the proper treatment of the boundary condition.

For simplicity, consider a thin symmetrical blade at zero incidence passing through a region of disturbed flow, figure 5. (Camber and incidence effects can easily be included in the analysis but make little difference to the final results). Let x, y, z be a stationary coordinate system, with x, y lying in the rotor plane and z normal to it. Let the upper blade surface be given by the equation $z = \delta H(x,y,t)$, where δ is a small parameter. If the gust velocity is denoted by $\underline{w}$ and the corresponding response velocity by $\underline{v}$, then the unsteady boundary condition on S is $(\underline{v} + \underline{w}).\underline{n} = 0$, where $\underline{n}$ is the surface normal. Hence at each instant

$$(w_z + v_z) = \delta \left\{(w_x + v_x)\frac{\partial H}{\partial x} + (w_y + v_y)\frac{\partial H}{\partial y}\right\} \text{ , on S} \qquad (3)$$

Since this is to be satisfied at $z = \delta H(x,y,t)$, expand each side of equation (3) in a series about $z = 0$,

$$v_z^{(2)} = \left\{ v_x^{(1)} \frac{\partial H}{\partial x} + v_y^{(1)} \frac{\partial H}{\partial y} - H \frac{\partial v_z^{(1)}}{\partial z} \right\} \pm \left\{ \frac{\partial H}{\partial x} (H\bar{w}_x) + \frac{\partial}{\partial y} (H\bar{w}_y) \right\} \text{ on } z = \pm 0 \qquad (10)$$

The first part of this expression, being symmetric about $z = 0$, can be satisfied by another dipole distribution similar to equation (9). This exhibits no novel features since it represents a small second order modification to the lift distribution arising from the displacement of the boundary condition. It will not be considered further. However, the second half of equation (10), being anti-symmetric about $z = 0$, requires a monopole type of source distribution to satisfy it. The appropriate form is

$$4\pi p^{(2)}(\underline{x},t) = 2\rho_0 \frac{\partial}{\partial t} \int \left[\frac{\frac{\partial}{\partial x}(H\bar{w}_x) + \frac{\partial}{\partial y}(H\bar{w}_y)}{r(1-M_r)} \right] d\Sigma \qquad (11)$$

This equation is now multiplied by δ^2 and returned to dimensional form; $2\delta H$ is written as h, the physical blade thickness. Finally, since the source strength contains space derivations, these may be taken outside the integral. Hence equation (11) becomes

$$4\pi p(\underline{x},t) = \frac{\partial^2}{\partial t \partial x_\beta} \int \left[\frac{\rho_o h w_\beta}{r(1-M_r)} \right] d\Sigma \qquad (12)$$

where β is again confined to the two in-plane directions. This expression is taken as the definition of "unsteady thickness noise." It is the direct analogue of the conventional thickness noise equation (ref. 10) with the blade speed $\underline{V}$ here replaced by the unsteady gust velocity $\underline{w}$.

Equations (9) and (12) are the central result of this section. They imply that the noise field can be represented by two distributions spread over Σ. Equation (9) is an unsteady lift dipole distribution and is equivalent to its counterpart in equation (2). However, equation (12) represents a hybrid source whose strength is related to the product of the blade thickness and gust velocity clearly differing from the drag dipole term of equation (2). This does not mean that equation (2) is incorrect. In the present simplified situation the drag dipoles must possess considerably more structure than hitherto suspected, and consequently the acoustic field can be expressed in an alternative simpler form, equation (12). It is emphasised that equation (1) is an exact result, whereas equation (2) is an approximation to it; equations (9) and (12) are an alternative approximate solution to the same problem. However, since equation (12) relates the field directly to known quantities, many of the difficulties associated with equation (2) are avoided.

The main feature of equation (12), however, is that essentially it represents an in-plane quadrupole field (because of the double derivative outside the integral); and, this is of major acoustic significance. A simple order of magnitude comparison shows that this unsteady thickness noise can be significantly higher than the

Next, the theory of reference 2 has been used incorporating a total loading law of $\lambda = -2$ (not $\lambda = -2.5$) for comparison purposes. It is seen that a fair agreement with the data is obtained, at least for the lower speed, near axis combinations. From an empirical viewpoint, this agreement is encouraging and could form the basis for prediction in this regime. It should be remembered that the use of a simple loading law is an empirical convenience; the precise value of λ is not determined by the theory.

However, it is equally clear that nearer the rotor plane (where the drag forces are important), the theory significantly underestimates the levels of the higher harmonics. Furthermore, it is not capable of giving the observed humped spectral shape, no matter what value of λ is chosen. Thus, although the theory can be adjusted to fit in some directions, it fails elsewhere and does not provide a self-consistent description of the full discrete tone noise field.

The purpose of the above discussion is to demonstrate one area where present theoretical models are unsatisfactory. The model can be manipulated to match part of the test data set but does not match all of it; the model fails completely to explain some important features. Thus, although the idea that noise results from unsteady blade loads is an important physical notion, present models based on that idea do not appear to tell the whole story. This provides the motivation for a re-examination of the theory to see if any important aspects have been overlooked.

UNSTEADY THICKNESS NOISE

The unsteady blade loads model arises from one particular solution of the governing wave equation. However, there are many other possible solutions to this equation, and the art of aeroacoustics is choosing the form of solution most appropriate to the task in hand. In this section it is shown that a slightly different formulation of the problem, which leads to some different conclusions concerning certain aspects of the noise field, appears possible.

Consider a rotor running through a region of disturbed inflow. The mathematical basis of the unsteady loads model lies in the FW-H equation (ref. 9). If viscosity and T_{ij} quadrupoles are neglected and only the additional sound induced by the inflow distortion is considered, it follows from that equation that the sound field is given by the integral

$$4\pi p(\underline{x},t) = -\frac{\partial}{\partial x_j}\iint\left[\frac{pn_j}{r(1-M_r)}\right] dS \qquad (1)$$

Here the notation is standard; but, it is emphasized that pn_j is the local unsteady force per unit area exerted on the air; S is the true blade surface. Thus the field is represented by a surface distribution of dipoles, but strictly speaking their strengths are unknown and have to be determined from the zero normal velocity condition. Equation (1) is a well posed integral equation.

$$(w_z + v_z)\big|_{z=0} + \delta H \frac{d}{dz}(w_z + v_z)\big|_{z=0} + \cdot \cdot \cdot \cdot = \delta A\big|_{z=0} + \delta^2 H \frac{dA}{dz}\big|_{z=0} + \cdot \cdot \cdot \qquad (4)$$

where δA temporarily denotes the right side of equation (3). In practice, the gust velocity is small compared with the blade speed; typically $w/U \sim \delta$. The response velocity $\underline{v}$ is also of this order. Thus write $\underline{w}$ as $\delta\underline{\bar{w}}$ and expand $\underline{v}$ in a series

$$\underline{v} = \delta \underline{v}^{(1)} + \delta^2 \underline{v}^{(2)} + \cdot \cdot \cdot \qquad (5)$$

This expansion is inserted in equation (4) and like powers of δ equated. Hence

$$\text{order} \quad (\delta : v_z^{(1)} + \bar{w}_z = 0) \qquad \text{on } z = +0 \qquad (6)$$

$$\text{order} \quad \delta^2 : v_z^{(2)} + H \frac{\partial}{\partial z}(\bar{w}_z + v_z^{(1)}) = \left\{ (\bar{w}_x + v_x^{(1)}) \frac{\partial H}{\partial x} + (\bar{w}_y + v_y^{(1)}) \frac{\partial H}{\partial y} \right\} \text{on } z = +0 \qquad (7)$$

If the input gust is assumed to be incompressible, div $\underline{\bar{w}} = 0$, and equation (7) can be re-written

$$v_z^{(2)} = \frac{\partial}{\partial x}(H\bar{w}_x) + \frac{\partial}{\partial y}(H\bar{w}_y) + v_x^{(1)}\frac{\partial H}{\partial x} + v_y^{(1)}\frac{\partial H}{\partial y} - H\frac{\partial v_z^{(1)}}{\partial z} \qquad \text{on } z = +0 \qquad (8)$$

This analysis applies to the upper blade surface; similar results apply to the lower surface.

The acoustic problem is solved by finding appropriate source distributions to satisfy these boundary conditions. It is assumed that linearised acoustic equations hold. The first order boundary condition demands that $v_z^{(1)}$ equals $-\bar{w}_z$ on $z = \pm 0$, and this can be accomplished formally by a dipole distribution similar to the first part of (2),

$$4\pi p^{(1)}(\underline{x},t) = \frac{\partial}{\partial x_3}\iint \left[\frac{L}{r(1-M_r)} \right] d\Sigma \qquad (9)$$

Of course, the appropriate lift distribution L is still to be found in terms of $\bar{w}_z$, but equation (9) is now a well posed integral equation and a formal solution to the first order problem.

Now consider the second order problem. Considerations of symmetry about $z = 0$ show that the boundary condition equation (8) can be written drag noise for the acoustically important higher frequencies. A drag dipole typically has a local source strength of order $0{\cdot}1\rho Uw$ (U= typical blade speed), whereas the quadrupole source is of order $0{\cdot}1cw\rho$(c= blade chord). However, this has to be multiplied by an extra acoustic frequency factor f because of the additional time derivative outside the integral. Hence, the ratio of the thickness noise to drag noise is typically fc/U, and this exceeds unity if the frequency exceeds about the 20th harmonic of the rotational frequency. For main rotors, this is the whole of the subjectively important range. Essentially the increased acoustic efficiency of the quadrupoles rapidly overcomes their weaker source strength. Thus the in-plane noise is considerably larger than unwitting use of the drag formula would suggest.

In order to illustrate the application of equation (12), some comparisons have been made with the test data cited earlier. To achieve this, the analysis of equation (12) has been taken considerably further, although only the outline is presented here. The gust velocity $w_\beta(x, y, t)$ is expressed in terms of its frequency and spatial wave number spectrum. Then, by following the ideas of references 5 and 6, it is possible to obtain the following expression for the acoustic power spectrum $P(\underline{x},f)$:

$$P(\underline{x},f)=\left\{\frac{\rho_0 f^2 R\sin\theta}{4\pi a_0 r}\right\}^2 \sum_{n=-\infty}^{+\infty} |h_n|^2 \int_{-\infty}^{\infty}\int_{-\infty}^{\infty} W(l,\ m,\ \alpha_n)F_n^2\ (R[(l+f\sin\theta)^2+m^2]^{1/2})\,dl\,dm \quad (13)$$

(See Appendix.) Here $W(l, m, \alpha)$ is the power spectrum of the input gust, as a function of frequency α and spatial wave numbers l, m. No point source approximation is made in this analysis; the full blade source distribution is retained.

To use this result, it is necessary to assume a form for the gust spectrum W. Here a "frozen turbulence" model which is convected through the rotor with velocity V_c with integral length scale Λ, is adopted. The form used in the present calculations is

$$\left(W(l,\ m,\ \alpha) = \frac{3\bar{w}^2}{4\pi}\ \frac{\Lambda^3}{V_c}\left\{1+\Lambda^2[l^2+m^2+(\alpha/V_c)^2]\right\}^{-5/2}\right) \quad (14)$$

This form has been chosen both for its relative simplicity and its ability to yield good agreement with the experimental results. The justification for this is that the present objective is to show that unsteady thickness noise is possibly a significant noise source, not that it is definitely so. Consequently, it is permissible to show that plausible assumptions concerning spectral levels and shapes can lead to experimentally observed levels. It should be remembered that at present there are no experimental facts on the nature and level of the gusts entering a helicopter rotor; models of laboratory or atmospheric turbulence may not apply. The spectrum in equation (14) is similar to the Dryden spectrum used in references 5 and 6 but decays more rapidly at high frequencies.

8, which shows that although the data collapse reasonably well on the theoretically indicated parameter (ref. 10) there is a 6 dB gap between them. This is probably due to quadrupole sources (see below).

More important, many other aircraft do not show this type of acoustic signature. The literature contains several different examples of helicopter high speed approach signatures, (refs. 10, 14, 15), and it is clear from these that many aircraft exhibit signatures with both negative and positive going pressure spikes of more or less equal magnitude. It is usually argued that the negative spike is thickness noise and the positive one a "compressibility effect." This argument is given credence by the BO105 data (ref. 15), which show that thinner blades remove both the shock waves and the positive acoustic pulse. However, if this is so, why does the UH-1H aircraft (ref. 13) exhibit only an archetypal thickness noise pulse when running furthest into the compressibility regime?

Thus, experimental evidence appears to show that thickness noise is not the complete explanation of this phenomenon. What are the other possibilities? The next most obvious choice is the cyclic blade forces associated with the nominal rotor aerodynamics. The lift force suffers from the disadvantage that its field is zero in the rotor plane where the observed field is apparently a maximum. The cyclic drag, on the other hand, gives insignificant acoustic levels (ref. 16). From a theoretical viewpoint this is not surprising; simple cyclic load models do not contain any of the higher harmonics essential to noise generation by a force mechanism.

The last observation points to another possible explanation for high speed flight noise. It may be that unsteady blade loads associated with rapid and local transient effects, rather than slowly varying cyclic effects, are responsible for the noise. A blade bypassing a vortex is an obvious example, and in a stable flight regime this would be a repetitive event. It would be rich in the higher blade load harmonics and might explain the variability between aircraft types. This idea does not appear to have been sufficiently explored in this flight regime and merits attention. The unsteady thickness formulation described in the previous section may prove useful in this context, since it is capable of predicting the in-plane noise solely from a model of the flow disturbance.

There remains the important question of whether quadrupoles are a possible source of high speed flight noise. There have been several unsuccessful attempts at proving this, but a breakthrough appears to have been made in a very recent paper (ref. 17). Briefly, that paper shows that for a transonic propeller, the ρu^2 quadropole makes a significant contribution to the noise only for those blade sections operating above their critical Mach number and below unit Mach number. In this regime, the quadrupole noise is approximately equal to the thickness noise.

It remains to be seen to what extent this mechanism applies to helicopter rotors. At present the model takes no account of tip relief effects, cyclic velocity variations, or possible hysteresis effects in the transonic blade flow. All of these details may be important in a helicopter application. Nonetheless, at first sight it does appear that this mechanism applies to helicopter rotors and consequently could offer an explanation for the anomaly between theory and the data of reference 13 noted earlier. However, it is not immediately apparent whether it could also explain the negative-positive pulse shapes exhibited by most aircraft. This is a promising area which needs to be explored.

It is worthwhile to conclude this discussion of quadrupole effects on a cautionary note. There is a great temptation in performing quadrupole studies to base the source strength on any model which can be readily calculated. However, since the FW-H equation is exact (applying to all fluid flows), only the full solution to the problem will strictly provide the correct quadrupole source strength for use in that equation. This, of course, is never known. Thus the quadrupole integral only becomes useful if some local approximation to T_{ij} can be employed, but as yet the existence and nature of this approximation is not established. It can only be revealed by alternative analysis, involving carefully considered physical arguments and mathematical modelling. The resultant quadrupole source strength may then turn out to be very different from that indicated by the superficial form of T_{ij}. The quadrupole integral is not just another source to be added on; it plays a more subtle role, and its relevance to the high speed noise problem remains an open question.

It is clear from this that the high speed noise question is not fully answered. There is sufficient experimental evidence to show that it is not all thickness noise, although this undoubtedly plays a prominent role and provides a reasonable basis for 'first-cut' predictions. However, there still appear to be some unexplored mechanisms which could considerably improve our understanding in this area.

CONCLUSIONS

The purpose of this paper has been to highlight some deficiencies in traditional ideas about rotor noise and to suggest some possible improvements. Section 2 was concerned with the conventional unsteady loads model. It was concluded that although this model could provide a reasonable basis for prediction at the lower speed near axis configurations, it fared badly for the higher frequencies near the rotor plane. This regime is subjectively important and the theory significantly underpredicts the noise in this situation.

In section 3, a new approach to this problem was described. It was shown that the rotor-gust interaction problem could be reformulated, and this led to a description of the in-plane noise in terms of a set of unsteady thickness quadrupole sources. These replace the traditional drag dipoles and overcome many of their practical difficulties. Better agreement with the experimental levels in and near the rotor plane was obtained from this model, for both discrete tone and broad band noise.

In the final section, the problem of high speed flight noise was discussed. Although no new mathematical models were proposed, it was argued that this noise could not be due entirely to blade thickness sources. It was suggested that repetitive transient effects may be important for some aircraft in this flight regime. However, since it now appears proven that quadrupole sources do become important at transonic blade speeds, several new mechanisms may soon emerge relevant to this problem. This appears to offer a very promising direction for further research.

APPENDIX

In equation (13), R denotes the rotor tip radius, and θ the angle between the observation direction and the rotor axis. If the angular velocity of the rotor is Ω rads/sec, then $\alpha_n = f+n\Omega$. F_n and h_n are defined as follows:

$$F_n\,(X) = \frac{1}{X}\int_0^X J_n(x)\,dx$$

which is the average value of Bessel function, and

$$h_n = \int_{-c/2}^{+c/2} h(\xi)\,e^{-in\xi/R}\,d\xi$$

which is the Fourier component of chordwise distribution of blade thickness, assumed independent of spanwise station. If there are B blades, n must be restricted to multiples of B and value of integral multiplied by B.

REFERENCES

1. George, A.R.: Helicopter Noise - state of the art. AIAA paper 77-1337, 4th AIAA Aeroacoustic Conference 1977.

2. Lowson, M.V.; Ollerhead, J.B.: A theoretical study of helicopter rotor noise. J. Sound Vib (1969) 9 pp. 197-222.

3. Wright, S.E.: Sound radiation from a lifting rotor generated by asymmetric disk loading. J. Sound Vib (1969) 9 pp. 223-240.

4. Ffowcs Williams, J.E.; Hawkings, D.L.: Theory relating to the noise of rotating machinery. J. Sound Vib (1969) 10 pp. 10-21.

5. Homicz, G.F.; George, A.R.: Broadband and discrete frequency radiation from subsonic rotors. J. Sound Vib (1974) 36 pp. 151-157.

6. George, A.R.; Kim, Y.N.: High frequency broadband rotor noise. AIAA Journal (1977) 15 pp. 538-545.

7. Leverton, J.W.: The noise characteristics of a large 'clean' rotor. J. Sound Vib (1973) 27 pp. 357-376.

8. Leverton, J. W.: Discrete frequency rotor noise. AIAA paper 75-451 2nd AIAA Aeroacoustics conference 1975.

9. Ffowcs Williams, J.E.; Hawkings, D.L.: Sound generation by turbulence and surfaces in arbitrary motion. Phil. Trans. Roy. Soc. (1969) 264 pp.321-342.

10. Hawkings, D.L.; Lowson, M.V.: Noise of high speed rotors. AIAA paper 75-450, 2nd AIAA Aeroacoustics Conference 1975.

11. Farassat, F.; Pegg, R.J.; Hilton, D.A.: Thickness noise of helicopter rotors at high tip speed. AIAA paper 75-453, 2nd AIAA Aeroacoustic Conference 1975.

12. Hanson, D.B.: Near field noise of high tip speed propellers in forward flight. AIAA paper 76-565, 3rd AIAA Aeroacoustics Conference 1976.

13. Schmitz, F.H.; Boxwell, D.A.: In-flight far-field measurement of helicopter impulsive noise. Paper 1062, 32nd Annual Forum of AHS 1976.

14. Wright, S.E.: The relative importance of acoustic sources generated by helicopter rotors in high speed flight. Paper 16, 2nd European Rotorcraft and Powered Lift Aircraft Forum 1976.

15. Laudien, E.; Huber, H.: Impulsive helicopter rotor noise. Paper 2.4 GARTEur-5 Specialist Meeting on propeller and helicopter noise 1977.

16. Schmitz, F.H.; Yu, Y.H.: Theoretical modeling of high speed helicopter impulsive noise. Paper 54, 3rd European Rotorcraft and Powered Lift Aircraft Forum 1977.

17. Hanson, D.B.; Fink, M.R.: The importance of quadrupole sources in prediction of transonic tip speed propeller noise. Paper presented to Spring Meeting of Institute of Acoustics, Cambridge, England.

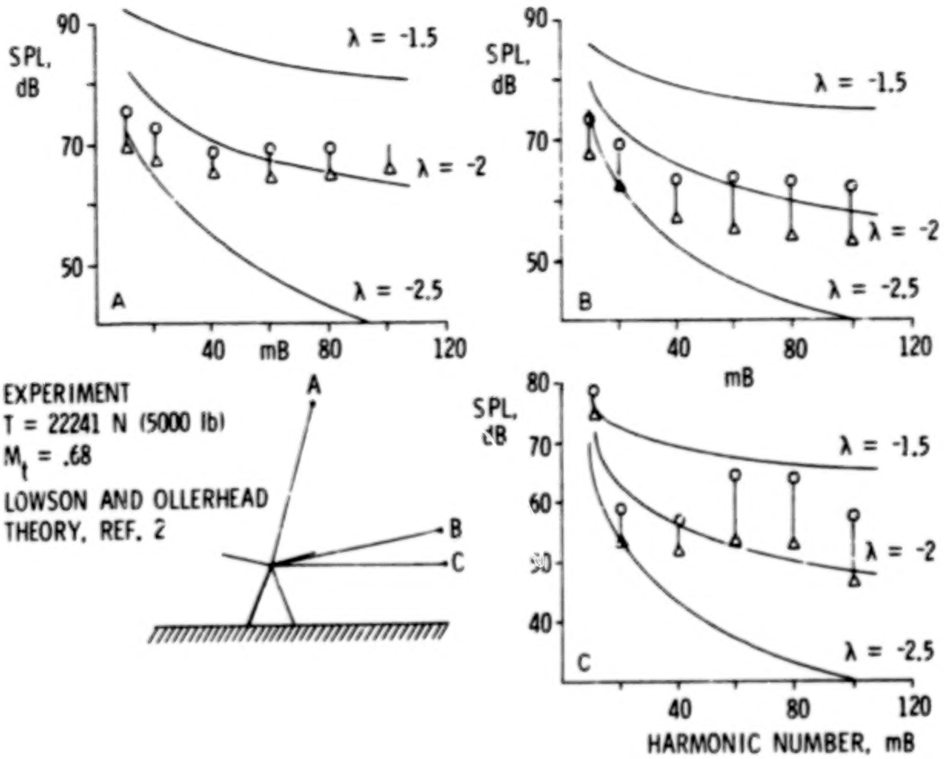

Figure 1.- Variability of rotor discrete tone noise.

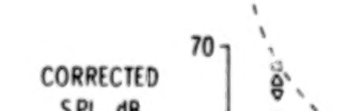

Figure 2.- Rotor discrete tone noise, microphone A (75° from rotor plane).

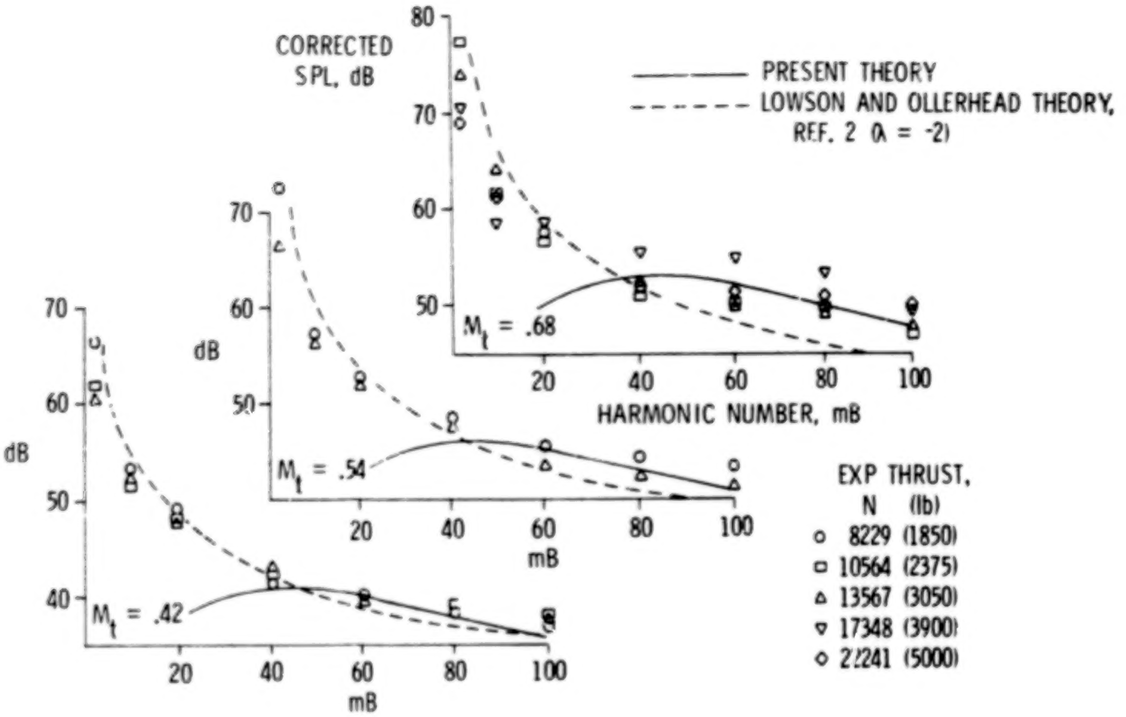

Figure 3.- Rotor discrete tone noise, microphone B (11.5° from rotor plane).

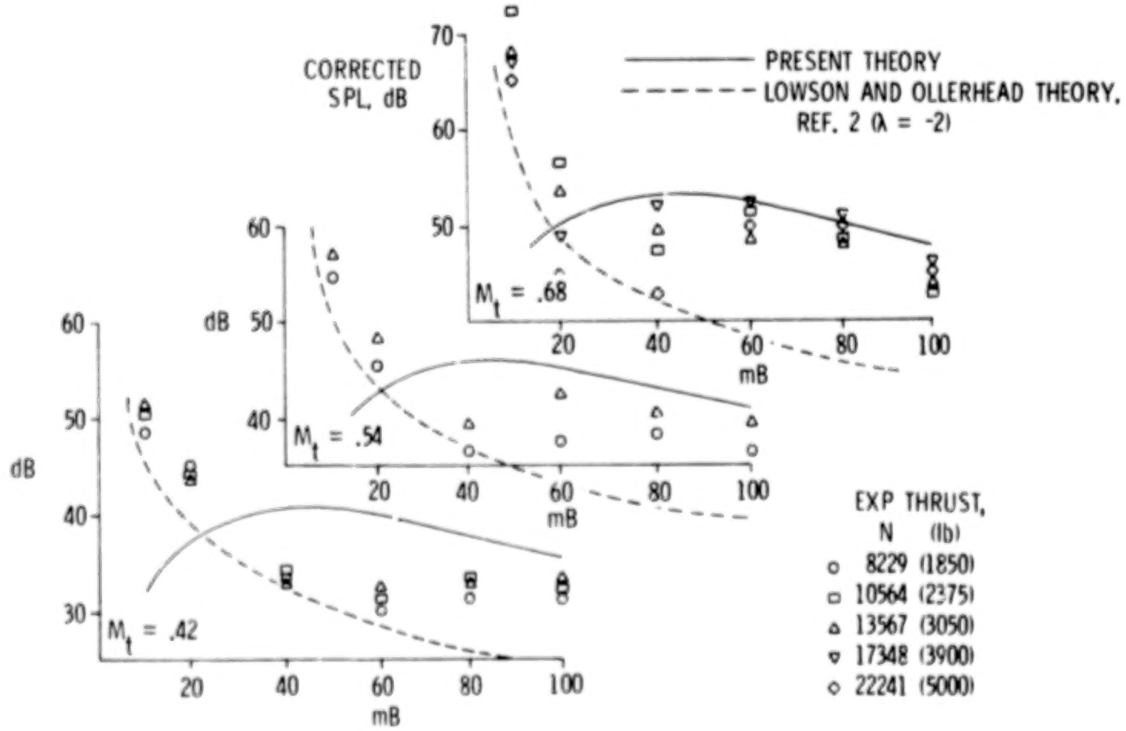

Figure 4.- Rotor discrete tone noise, microphone C (in rotor plane).

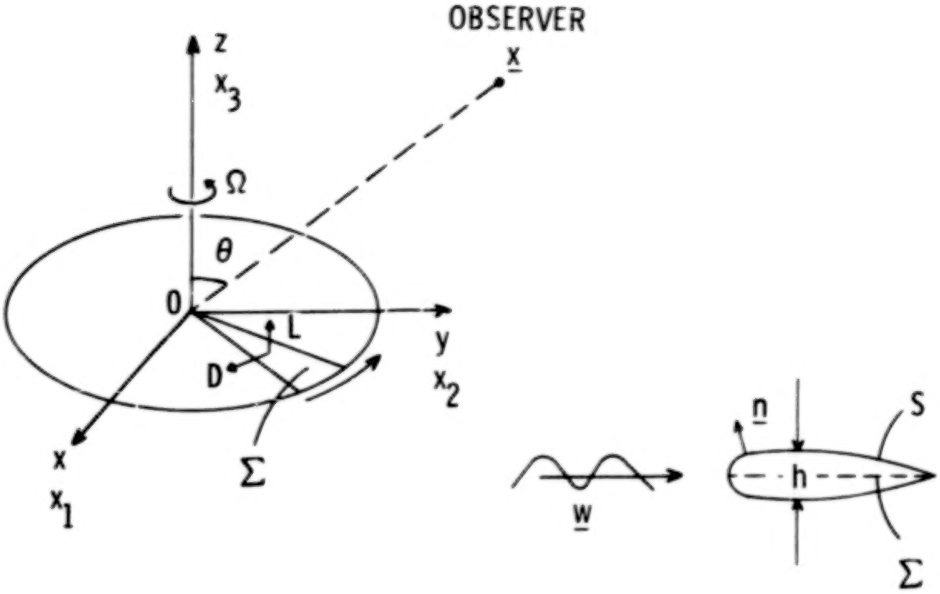
OBSERVER
x
z
x_3
Ω
θ
0
L
D
y
x_2
x
x_1
Σ
w
n
h
S
Σ

Figure 5.- Rotor geometry and coordinate system.

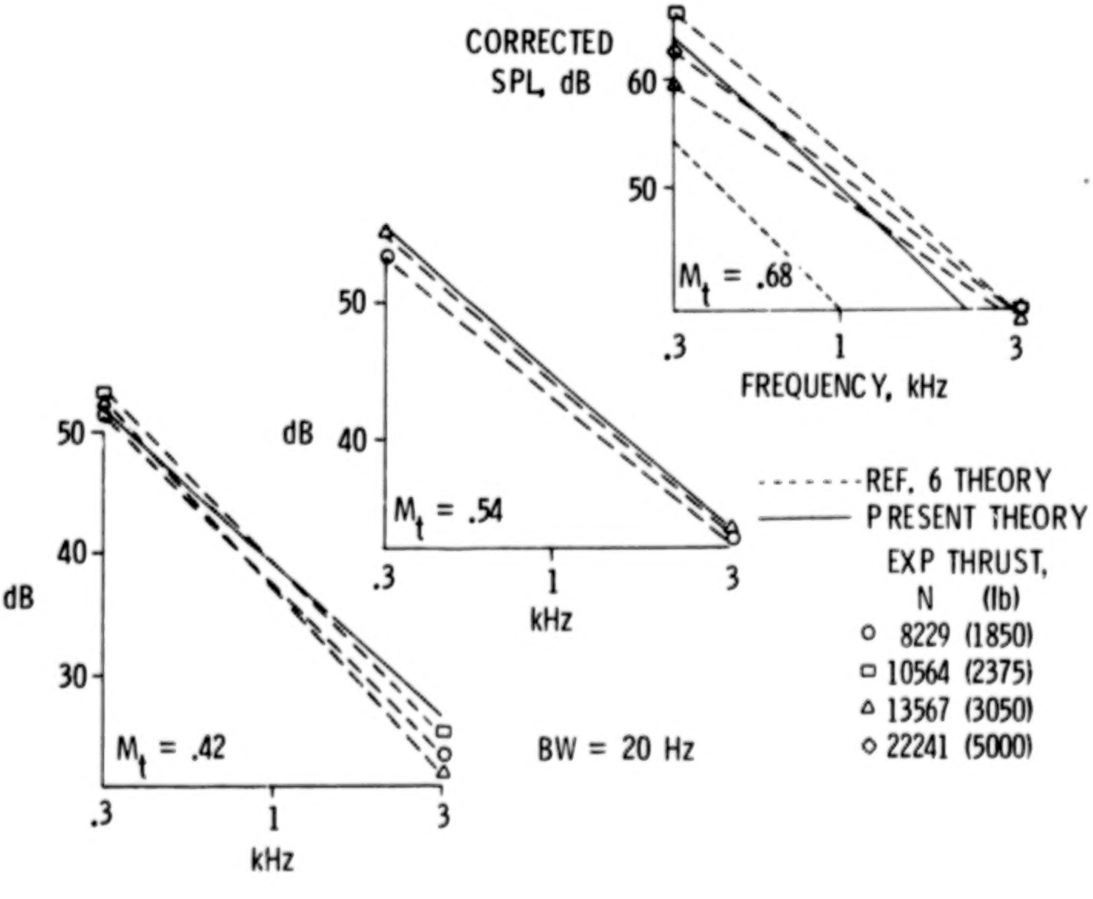

Figure 6.- Rotor broad band noise, microphone B.

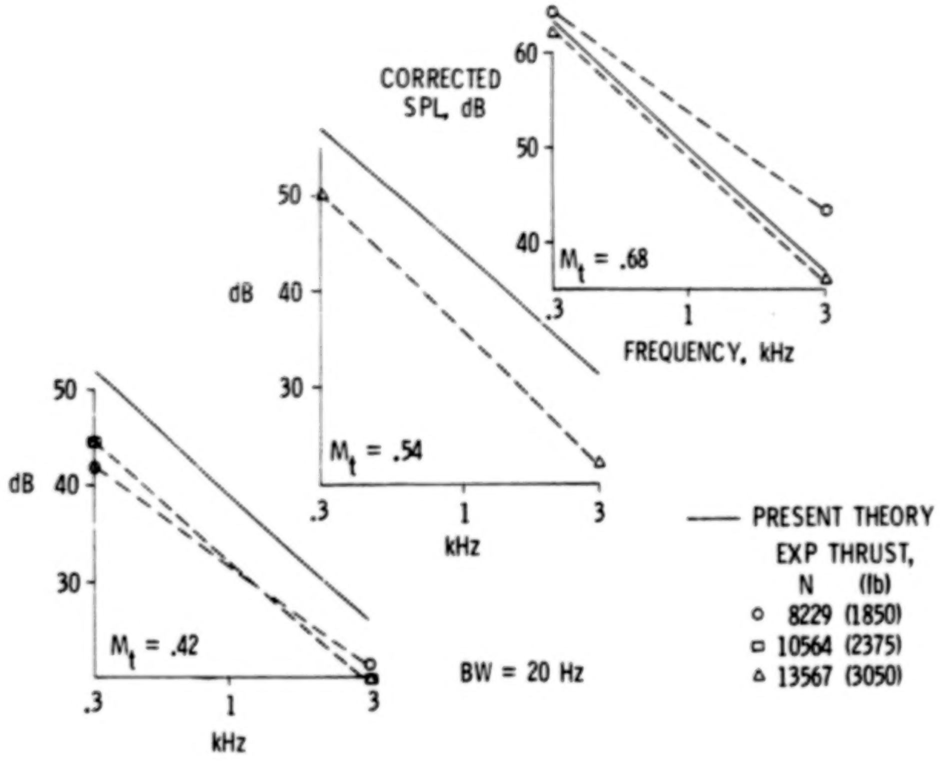

Figure 7.- Rotor broad band noise, microphone C.

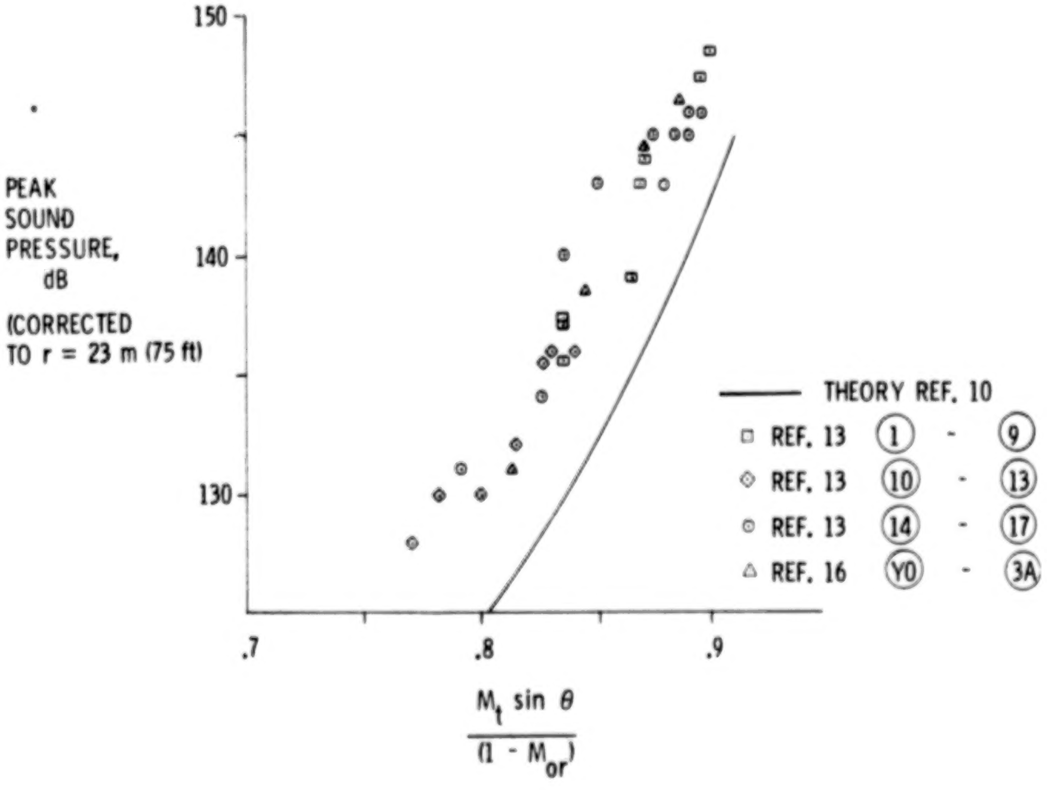

Figure 8.- UH-1H impulsive noise.

NOISE DUE TO ROTOR-TURBULENCE INTERACTION

R. K. Amiet
United Technologies Research Center

SUMMARY

A procedure for calculating the noise due to turbulent inflow to a propeller or helicopter rotor in hover is summarized. The method is based on a calculation of noise produced by an airfoil moving in rectilinear motion through turbulence. At high frequency the predicted spectrum is broadband, while at low frequency the spectrum is peaked around multiples of blade passage frequency. This paper provides the results of a parametric study of the variation of the noise with rotor tip speed, blade number, chord, turbulence scale and directivity angle. A comparison of the theory with preliminary experimental measurements shows good agreement.

INTRODUCTION

One of the potential sources of both rotor harmonic noise and broadband noise is that due to inflow turbulence. The turbulent velocity field produces a fluctuating angle of attack of the rotor blade leading to unsteady blade loading and the production of noise. If the axial length scale of the turbulence is such that a given eddy is chopped by more than one blade, the noise will tend to concentrate around multiples of blade passage frequency, while if a given eddy is chopped only once, there is no blade-to-blade correlation and the noise is broadband.

The most rigorous method of treating this problem is to combine a model of the turbulence spectrum with airfoil response functions to determine the airfoil loading and an acoustical theory to determine the subsequent noise field. This is the approach used in references 1-3; the present study gives extensions and further results of the analysis presented in reference 1. This analysis is in turn an extension of the analysis given in reference 4 for an airfoil in rectilinear motion through turbulence which has been verified by extensive comparison with experiment in reference 5.

The basis for the extension of the rectilinear motion theory to rotational motion is that so long as the acoustic frequency is somewhat greater than the rotational frequency of the rotor, the effects of rotation can be ignored and the blade treated as being in rectilinear motion at each instant of time. The sound can then be calculated by averaging the calculated instantaneous spectrum for one revolution of the rotor. This is described more completely in reference 1. The present analysis treats the case of helicopter hover, vertical ascent or propeller forward flight with an axial velocity. An extension to the case of helicopter forward flight is expected to be completed in the near future.

A preliminary comparison of experiment and theory shows excellent agreement between the two for the case of a model rotor with nonzero axial flow. Further comparisons between theory and experiment are presently being made.

A recent review of this and other helicopter noise sources is given in the paper by George (ref. 6).

SYMBOLS

B	Blade number
b	Blade semichord
c	Blade chord
c_o	Sound speed
d	Blade semispan
E	Acoustic energy in a harmonic peak
E(k)	Energy spectrum of turbulence
f	Acoustic frequency
g	Airfoil response function
G	Integrated airfoil response
K_x, K_y	Chordwise turbulence wavenumber and spanwise turbulence wavenumber
$\bar{k}$	$\omega b/V_\gamma$
k_e	Wavenumber range of energy-containing eddies
$\bar{k}_o$	Value of $\bar{k}$ for f = 1 Hz and $M_\gamma = 0.628$

L	Turbulence integral scale
ℓ	Effective lift
M_γ, M_z, M_r	Azimuthal, axial and relative blade Mach numbers
ΔP	Pressure jump on airfoil
R	Effective radius of rotor
r	Distance to observer
RPS	Revolutions per second
S_{pp}	Acoustic spectrum
$S_{pp_{max}}$	Maximum spectrum level of a harmonic peak
s	Rotor span
T	Blade passage time
t	Time
$\overline{u^2}$	Mean square turbulence velocity
V_γ, V_z, V_r	Azimuthal, axial and relative rotor velocities
w_o	Unsteady velocity normal to rotor blade
$\underline{X}$	Vector position of observer
x,y,z	Cartesian coordinate system fixed to rotor hub; nonrotating
x',y',z'	Cartesian coordinate system; y' along rotor span; x' along chord
γ	Azimuthal angle
Γ	Gamma function
θ	Angle of observer from rotor axis
λ	Acoustic wavelength
ρ_o	Density

Φ_{ww}	Turbulence spectrum
ω	Radian frequency of blade forces
ω_o	Doppler shifted frequency heard by observer

THEORETICAL FORMULATION

Notation and Summary of Analytical Method

The geometry for the problem is given in figure 1 and is the same as that of reference 1. The rotor blade is divided into segments and the noise contribution of each segment is calculated. The relative velocity V_r of a blade segment is related to the azimuthal velocity V_γ and the axial velocity V_z by

$$V_r{}^2 = V_\gamma{}^2 + V_z{}^2 \tag{1}$$

The basis for the analytical method is to utilize a noise calculation procedure for an airfoil in rectilinear motion through turbulence (see refs. 4-5). This calculation is applied to calculate the noise produced in the far-field by a segment of the rotor span as if that segment were in rectilinear motion. This is repeated for different azimuthal rotor positions, and an average spectrum is then obtained by integrating over the azimuth, remembering to account for the differing amounts of retarded time spent by the rotor in each azimuthal location.

The final result for the far-field spectrum given in reference 1 is (note that the expression in reference 1 is for a single blade and is here multiplied by the number B of blades)

$$S_{pp}(\omega_o,\underline{x}) = \frac{V_r B}{T V_\gamma V_z} \int_0^{2\pi} \frac{\omega}{\omega_o}\, G \sum_{n=-\infty}^{\infty} \Phi'_{ww}\left(K_x, K_y, \frac{V_r}{V_\gamma V_z}\left(\omega_o + 2\pi n/T\right)\right) d\gamma \tag{2}$$

The function G represents the integrated airfoil response function and is given by

$$G \equiv \left[\frac{\omega \rho_o b z}{C_o (r + M_r x')^2}\right]^2 \quad \pi V_r\, d \left|\mathcal{L}\right|^2 \frac{\omega}{\omega_o} \tag{3}$$

with

$$\mathcal{L} \equiv \int_{-1}^{1} g(\xi)\, e^{i\xi K_y x'/y'}\, d\xi \tag{4}$$

Without the exponential factor in equation (5), $\mathcal{L}$ would be just the airfoil lift per unit span. The exponential factor accounts for differences in propagation time to the observer from different points on the airfoil surface. Thus, $\mathcal{L}$ could be called an effective lift and it depends on observer location. A skewed gust of the form

$$w_g = w_0\, e^{i(\omega t - K_x x' - K_y y')} \tag{5}$$

produces a pressure jump distribution ΔP on the airfoil. The airfoil response function g is then defined by the normalization

$$g \equiv \Delta P\, e^{-(i\omega t - K_y y')} / (2\pi \rho_0 V_r w_0) \tag{6}$$

Analytical expressions for g can be found in references 7-8 and the evaluation $\mathcal{L}$ is discussed further in reference 1.

In equation (2), T is the blade passage time, Φ'_{ww} is the turbulence spectrum for the velocity component normal to the airfoil as written in the primed coordinate system, and K_x and K_y are the chordwise and spanwise turbulence wavenumbers. The radian sound frequency ω in an airfoil fixed frame is related to K_x by

$$K_x = \omega / V_r \tag{7}$$

The relevant K_y turbulence wavenumber is determined by the observer location; i.e.,

$$K_y = K_x M_r y'/(r + M_r x') \tag{8}$$

The radian frequency ω_0 is the sound frequency measured in a nonrotating frame fixed to the rotor hub and so is related to ω by a Doppler factor, i.e.,

$$\frac{\omega}{\omega_0} = \frac{1 - M_z \cos\theta}{1 + M_r x'/r} \tag{9}$$

The airfoil semichord is b, d and s are the semispan and span, respectively, and R is the distance of the airfoil segment from the rotor axis.

Energy in an Isolated Harmonic Peak

When the harmonic narrow-band-random peaks in the spectrum are separated by deep troughs it is possible to derive a simple expression for the overall energy contained in each peak. To determine the energy in a peak, equation (2) must be integrated over ω_o between the troughs bordering the peak of interest. The peaks will be isolated (i.e., there will be a rapid drop off with ω_o on each side of a peak) if the k_z or third argument of Φ_{ww} varies rapidly enough with ω_o; more explicitly, the peaks will be isolated if

$$V_r L >> V_z V_\gamma T \tag{10}$$

where L is the turbulence integral scale. If this is the case, then the variation of K_x and K_y with ω_o can be neglected in the ω_o integral. The troughs in the sound spectrum are separated by $2\pi/T$. Thus the range of integration is ω_1 to $\omega_1 + 2\pi/T$ where ω_1 represents the trough to the left of the peak. Then noting that for any functions f(x)

$$\sum_{n=-\infty}^{\infty} \int_{x_1}^{x_1+2\pi/T} f(x+2\pi n/T)\,dx = \int_{-\infty}^{\infty} f(x)\,dx \tag{11}$$

the energy contained in a peak is found by integration of equation (2) to be

$$E(\omega_o, \underline{X}) = \int_{\omega_1}^{\omega_1+2\pi/T} S_{pp}(\omega_o, \underline{X})\,d\omega_o \tag{12}$$

$$= \frac{B}{T} \int_0^{2\pi} \frac{\omega}{\omega_o} G(\omega) \int_{-\infty}^{\infty} \Phi'_{ww}(K_x, K_y, \xi)\,d\xi\,d\gamma$$

It will be noted that this is the same energy which would be calculated to be in the band $\omega_1 < \omega_o < \omega_1 + 2\pi/T$ if there were no blade-to-blade correlation. Thus, blade-to-blade correlation acts to concentrate the acoustic energy around multiples of blade passage frequency, but it is not basically a method of increasing the total acoustic energy radiated (unless one considers large correlation lengths and low frequencies such that blades are simultaneously correlated so that in the far field one adds pressures rather than intensities).

For an observer on the centerline, a simple result can be obtained for the ratio of the sound energy in a discrete harmonic peak to the maximum peak level. For an observer on the propeller axis the γ integration in equation (2) simply introduces the factor 2π. At a blade passing harmonic, ω_0 will be some multiple of $2\pi/T$. Since the harmonic peaks are widely separated, then using equation (10) it can be seen that only the first term in the sum is needed. The maximum at a peak is then

$$S_{PP_{max}}(\omega_0, z) = \frac{2\pi B G V_r}{T V_\gamma V_z} \Phi'_{ww}(K_x, 0, 0) \tag{13}$$

In this equation, the parameter ω to be used in G, K_x and K_y is equal to ω_0 as expected since there is no Doppler shift for an observer on the centerline. This can be seen also from equation (9) by noting that

$$x' = \frac{1}{V_r}\left[V_\gamma(x \sin\gamma - y \cos\gamma) - V_z z\right]$$

which becomes $x' = -V_z z/V_r$ for an observer on the z axis. Likewise, for an observer on the z axis, equation (12) for the energy in a peak becomes

$$E(\omega_0, z) = 2\pi \frac{B}{T} G \int_{-\infty}^{\infty} \Phi'_{ww}(K_x, 0, k_z)\, dk_z \tag{14}$$

Taking the ratio of equations (13) and (14) gives

$$\frac{E}{S_{PP_{max}}} = \frac{V_\gamma V_z}{V_r} \int_{-\infty}^{\infty} \frac{\Phi'_{ww}(K_x, 0, k_z)}{\Phi'_{ww}(K_x, 0, 0)}\, dk_z \tag{15}$$

Introducing the Kármán spectrum function

$$\Phi_{ww}(k_x,k_y,k_z) = \frac{E(k)}{4\pi k^2}\left(1-k_z^2/k^2\right)$$

$$E(k) = \frac{Ik^4}{\left[1+(k/k_e)^2\right]^{17/6}}$$

$$k^2 = k_x^{\ 2} + k_y^{\ 2} + k_z^{\ 2}$$

$$I = \frac{55}{9\sqrt{\pi}}\ \frac{\Gamma(5/6)}{\Gamma(1/3)}\ \frac{\overline{u^2}}{k_e^5} \tag{16}$$

$$k_e = \frac{\sqrt{\pi}}{L}\ \frac{\Gamma(5/6)}{\Gamma(1/3)}$$

allows the integral in equation (15) to be calculated giving

$$\frac{E}{S_{PP_{max}}} = \frac{16\pi}{55}\ \frac{V_y V_z}{V_r L}\ \sqrt{1+K_x^{\ 2}/k_e^{\ 2}} \tag{17}$$

This should be a useful result for calculating the overall intensity at a given directivity location. Strictly speaking it is only valid for an observer on the rotor axis, but it should provide meaningful estimates for other observer positions.

CALCULATED RESULTS

Several calculated spectra will be presented here for the purpose of illustrating the type of results expected, and for determining the dependence on the various parameters of the problem. In reference 1 it was shown that the results obtained by placing the entire span at an effective radius, R, equal to 0.8 of the tip radius were not significantly different from the results obtained by integration over the blade span. Thus, the present calculations will use the effective radius approach. For the calculations presented here, unless specified otherwise, the following input parameters to the calculation will be assumed.

$R/c = 10$ $\qquad M_z = 0.1$

$s/c = 10$ $\qquad B = 2$

$r/c = 100$ $\qquad (\overline{u^2}/V_z^{\ 2})^{1/2} = 0.01$

$c_o/c = 1000$ $\qquad RPS = 10$

$L/c = 100$ $\qquad \theta = 0$

Figure 2 shows the effect of tip Mach number on the noise. At low frequencies, harmonics of blade passage frequency begin to stand out as shown by the dashed lines. In subsequent figures only the envelope of the peaks and troughs will be shown. The abscissa is a reduced frequency, $\bar{k} = \omega b/V_\gamma$, normalized by a reference value $\bar{k}_0$ which is the value of $\bar{k}$ for $f = 1$ Hz and $M_\gamma = 0.628$. Thus, since the smaller of the two tip velocity cases is half of the higher one, a given value of frequency for the smaller V_γ case occurs at an abscissa which is twice the value for the large V_γ case. The reason for normalizing the frequency abscissa in this manner is so that for a given abscissa value, both cases will show the results of an interaction with the same turbulence wavenumber component. In other words, for a given turbulence component, as the blade velocity is increased, the frequency of the sound produced will increase.

Dipole noise is commonly associated with a V^6 velocity dependence. However, this is based on certain assumptions which do not hold for the present problem, e.g., the turbulence intensity is here assumed to remain fixed as the rotor velocity increases, rather than increasing proportional to the rotor speed. In discussing the velocity dependence of the spectrum, the high frequency and the low frequency portion of the curve will be discussed separately.

For high frequency and for V_r not too near 1, $|\mathcal{L}|^2$ behaves as $1/V_r$ for fixed $\bar{k}$. Thus, for large ω and fixed $\bar{k}$, G varies approximately as V_r^2 for an on-axis observer. For large ω the summation in equation (2) can be replaced by an integral over k_z, bringing the factor $V_z V_\gamma T/(2\pi V_r)$ out front of the integral. The final result is that the high frequency portion of the spectrum increases as V_r^2 at a given fixed $\bar{k}$. The overall energy contained in the spectrum in the range from a given $\bar{k}$ value to infinity will increase as V_r^3, however, since the plotted spectra represent the energy per unit Hertz rather than per unit $\bar{k}$ and there is a factor of 2 in the frequency ranges of the two curves. (Added note: equation (2) represents the energy per unit ω_0, and a factor of 2π must be introduced to convert it to a per Hertz basis. The plotted spectra are on a per Hertz basis.)

At low frequency $|\mathcal{L}|$ is independent of V_r. Thus, for an on-axis observer G varies as V_r^3 for fixed $\bar{k}$. The summation in equation (2) reduces to the single term $\Phi'_{ww}(K_x, 0)$ at a peak of a blade passing harmonic. For $V_z \ll V_\gamma$, $V_r \sim V_\gamma$ and the spectrum then is proportional to V_r^3/T. The variation of V_γ in figure 2 was obtained by varying the rotor rotational frequency, while that of figure 3 was obtained by varying the rotor effective radius at constant rotational frequency. Thus, T varies with V_γ in figure 2 but not in figure 3; in figure 2 the amplitude of a harmonic peak varies as V_r^4 and in figure 3 it varies as V_r^3. In calculating the overall energy, it will be noted that halving V_γ cuts the number of harmonic peaks in half. This together with the approximately 9 dB drop in the peaks gives approximately a 12 dB effect, the same as for figure 2. Using equation (17) for the ratio of energy to harmonic peak amplitude shows that there is no additional V_r dependence so that the final velocity dependence of the energy at low frequency is V_r^4.

These results are in accord with the results for an airfoil in rectilinear motion given by equation (17) of reference 9. If the turbulence intensity had been allowed to vary with rotor velocity, the velocity dependence of the acoustic energy would have been the more familiar results V^5 and V^6 at high and low frequency, respectively.

Figures 4 and 5 show the effect of changing the number of rotor blades. At high frequency there is no blade-to-blade correlation and each rotor blade acts independently of the others. Thus, doubling B increases the noise by 3 dB. This is illustrated in figure 4 where 3 dB has been subtracted from the curve for B = 4 to illustrate that for high frequencies it then becomes coincident with the B = 2 curve. Figure 5 shows the effect on the envelope of the harmonics at low frequency. Note that the abscissa has a factor of B in it. Thus, for a given value of the abscissa, the two curves which have values of B differing by a factor of 2 will differ in frequency also by a factor of 2. Then every harmonic peak in one of the two plots will have a corresponding peak in the other plot. For this problem the first and subsequent blade passing harmonics are in the range $k >> k_e$. Equations (16) then show that $\Phi_{ww} \sim \omega^{-11/3}$. Since the reduced frequency $\overline{k}$ is small, ℓ is not a strong function of ω and equation (3) shows that $G \sim \omega^2$. The frequency of any given harmonic varies as $\omega^2 \sim B/T$. Thus, from equation (13) $S_{pp_{max}} \sim \omega^{1/3}$ which is a weak dependence, and the levels of corresponding harmonics in figure 5 would be expected to be about the same. This is seen to be the case. Equation (17) then shows that the energy contained in each of the harmonics for B = 4 will be twice that for B = 2. Thus, both the low and high frequency regimes give a 3 dB effect; that is, an overall doubling of the noise for a doubling of the blade number. It should be remembered, however, that the present calculation does not include any steady loading effects on the noise. If this were important, then decreasing the steady loading by increasing the blade number could have a significantly different effect.

Figure 6 shows the effect of changes in blade chord on the noise. In equation (2) the chord appears explicitly only in the airfoil response function. When the sound wavelength becomes smaller than about 4 chords, the airfoil begins to act like an airfoil of infinite chord. Thus, changes in chord have little effect at high frequency as is noted in figure 6. For a given frequency, as the chord decreases the reduced frequency decreases to the point where eventually the airfoil is responding in a quasi-steady manner. In this regime the airfoil response is proportional to the chord, and the sound is proportional to the square of the chord. This can be seen by comparing the first harmonic of the C/10 curve (54 dB) with that of the C curve (72 dB, shown in figures 2-5);

i.e., a tenfold change in chord gives a 20 dB change in the noise at low frequency. Again it should be remembered that this ignores the effects on the other noise sources that changing the chord might have.

Figure 7 shows the effect that variation in the turbulent length scale has. From equations (16) it will be noted that for an on-axis observer when $k >> k_e$ $(10\ f\ L >> V_r)$ Φ_{ww} behaves as $L^{-2/3}$. This gives a 6.67 dB decrease for each tenfold increase in L, a relation which is seen to hold in figure 7 over most of the frequency range for all three curves. In fact, it is only below 100 Hz for the curve representing the smallest turbulence scale (L = C) that this relation does not hold.

Figure 8 shows the effect of finite Mach number on directivity. The small Mach number case given has a directivity which is nearly that of a compact dipole. The directivity is not exactly that of a dipole since the rotor blades are aligned with the relative flow, rather than lying in the plane of rotation. All the curves are normalized to 0 dB at $\theta = 0$; i.e., on the upstream axis. The directivity plots for the higher Mach number cases tend to be pushed outward toward the rotor axis for most angles when compared with the low Mach number case.

Figure 9 presents a comparison of theory with preliminary experimental results. The experiment was performed in the UTRC open-jet Acoustic Research Tunnel. The turbulence was generated by an upstream grid as in reference 5, and measurements verified that the turbulence was essentially isotropic. The experimental results are presented "as measured," while the theoretical results include a correction to account for the presence of the tunnel open-jet shear layer through which the sound must pass before reaching the observer. It should be emphasized that there were no adjustable parameters in the theory which could be used to improve agreement between theory and experiment. The turbulence length scale and intensity were measured independently of the acoustic test. The large peak at blade-passage-frequency is due to the steady blade loading. Other than this steady loading effect which is not included in the present formulation, the agreement between theory and experiment appears accurate to within a few dB. Additional experiments are presently in progress to give further assessment of the theory.

CONCLUDING REMARKS

The change in the noise produced by a variation of the parameters affecting turbulence ingestion noise can be summarized as follows for an observer on the axis of the rotor:

(1) The acoustic energy has a V_γ^4 dependence at low frequency and a V_γ^3 dependence at high frequency.

(2) The acoustic energy increases linearly with blade number at high frequency and nearly linearly at low frequency.

(3) The effect of blade chord on noise is small for wavelengths greater than about 4 chords. For chords small compared to the wavelength, the noise is proportional to the square of the chord.

(4) The noise spectrum varies with the -2/3 power of the turbulence integral scale except when L is comparable to or less than the chord and the frequency is low.

(5) The directivity plots tend to be flattened toward the rotor plane when the Mach number is significant.

The most effective method of reducing the noise appears to be through reduction of blade tip speed because of the rather strong velocity dependence of the noise, although not as strong as V^6 which one often expects for dipole noise. In lowering the tip velocity, other parameters would also have to be changed to maintain rotor thrust, and this could offset somewhat the beneficial effect of a decrease in tip speed.

A comparison with preliminary experimental results gives strong support to the theory. A more comprehensive experimental assessment of theory is currently in progress. These experiments include the case of simulated forward flight in which the ambient flow is not axial. The present theory is being extended to treat this case. Also, although the calculations performed here were for the case of isotropic turbulence, the case of anisotropic turbulence can be treated if a satisfactory model of the turbulence spectrum is available.

REFERENCES

1. Amiet, R. K.: Noise Produced by Turbulent Flow into a Propeller or Helicopter Rotor. AIAA Paper no. 76-560, July 1976. Also AIAA Journal, vol. 15, no. 3, March 1977, pp. 307-308.

2. Homicz, G. F. and George, A. R.: Broadband and Discrete Frequency Radiation from Subsonic Rotors. J. Sound and Vib., vol. 36, 1974, pp. 151-177.

3. George, A. R. and Kim, Y. N.: High Frequency Broadband Rotor Noise. AIAA Journal, vol. 15, no. 4, April 1977, pp. 538-545.

4. Amiet, R. K.: Acoustic Radiation from an Airfoil in a Turbulent Stream. J. Sound and Vib., vol. 41, 1975, pp. 407-420.

5. Paterson, R. W. and Amiet, R. K.: Noise and Surface Pressure Response of an Airfoil to Incident Turbulence. J. Aircraft, vol. 14, no. 8, August 1977, pp. 729-736.

6. George, A. R.: Helicopter Noise-State of the Art. AIAA Paper no. 77-1337, October 1977.

7. Amiet, R. K.: Compressibility Effects in Unsteady Thin-Airfoil Theory. AIAA Journal, vol. 12, February 1974, pp. 252-255.

8. Amiet, R. K.: High Frequency Thin Airfoil Theory for Subsonic Flow. AIAA Journal, vol. 14, August 1976, pp. 1076-1082.

9. Paterson, R. W. and Amiet, R. K.: Acoustic Radiation and Surface Pressure Characteristics of an Airfoil Due to Incident Turbulence. NASA CR-2733, 1976.

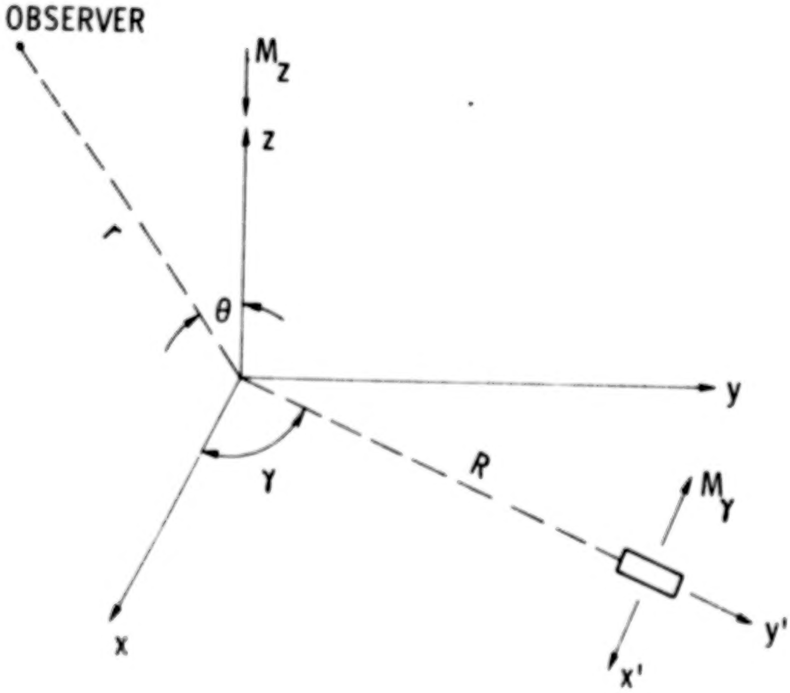
OBSERVER
M_Z
z
r
θ
y
γ
R
$M_γ$
x
y'
x'

Figure 1.- Geometry for rotating blade segment.

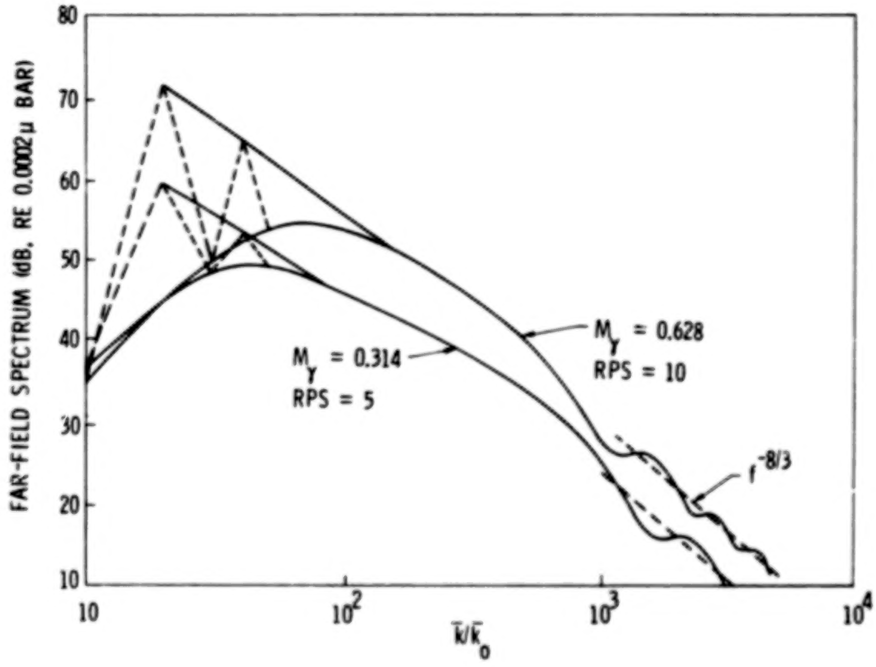

Figure 2.- Effect of tip Mach number on spectrum; variation of rotational frequency.

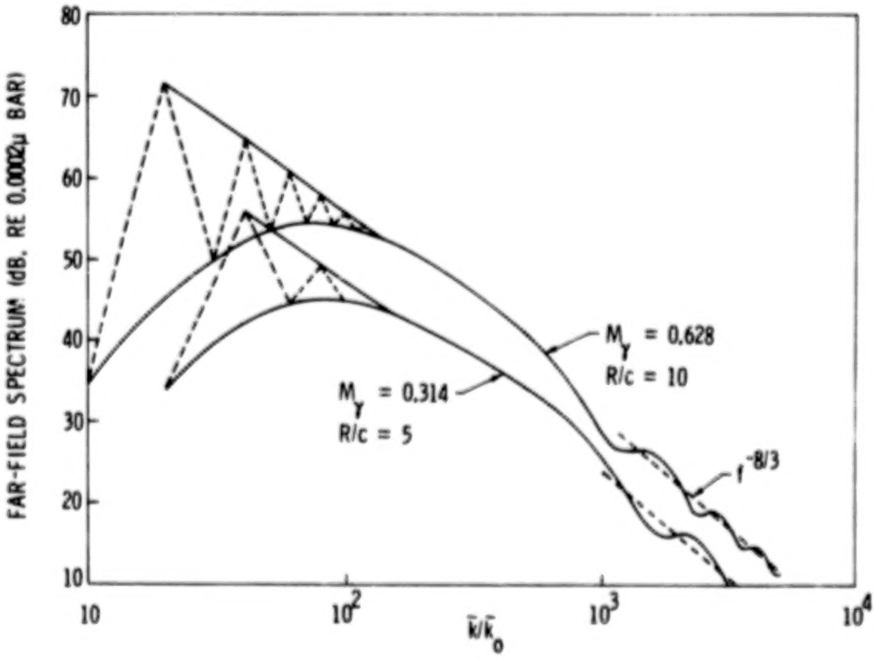

Figure 3.- Effect of tip Mach number on spectrum; variation of effective blade radius.

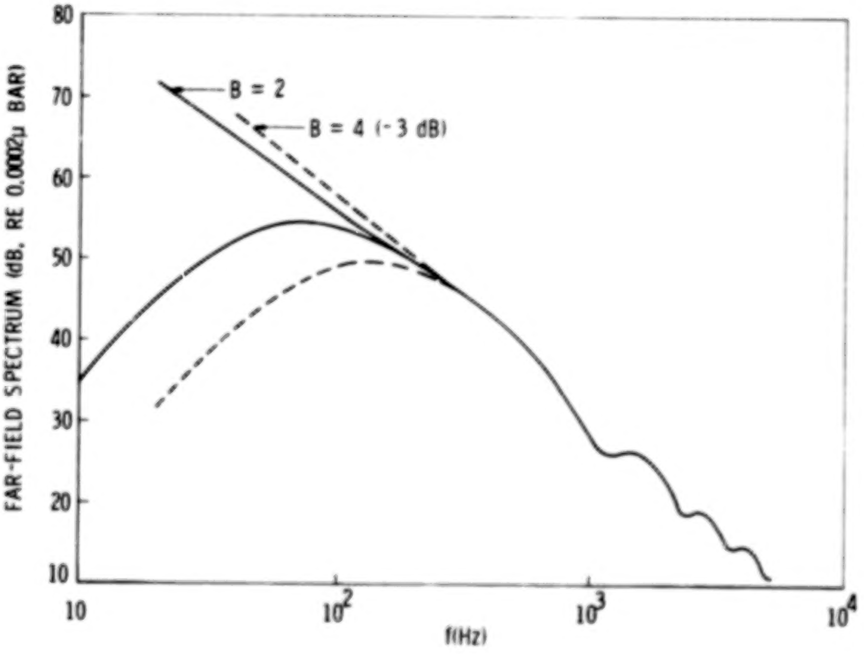

Figure 4.- Effect of blade number on spectrum.

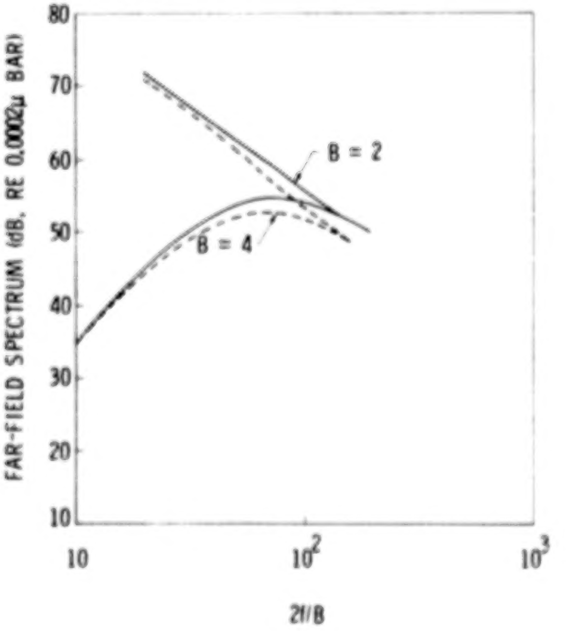

Figure 5.- Effect of blade number on low frequency spectrum.

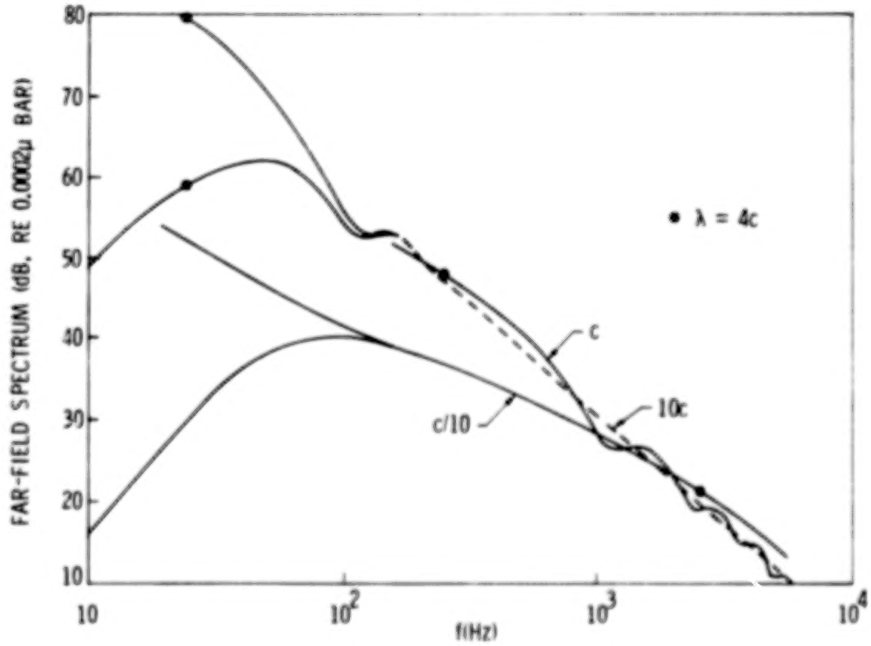

Figure 6.- Effect of blade chord on spectrum.

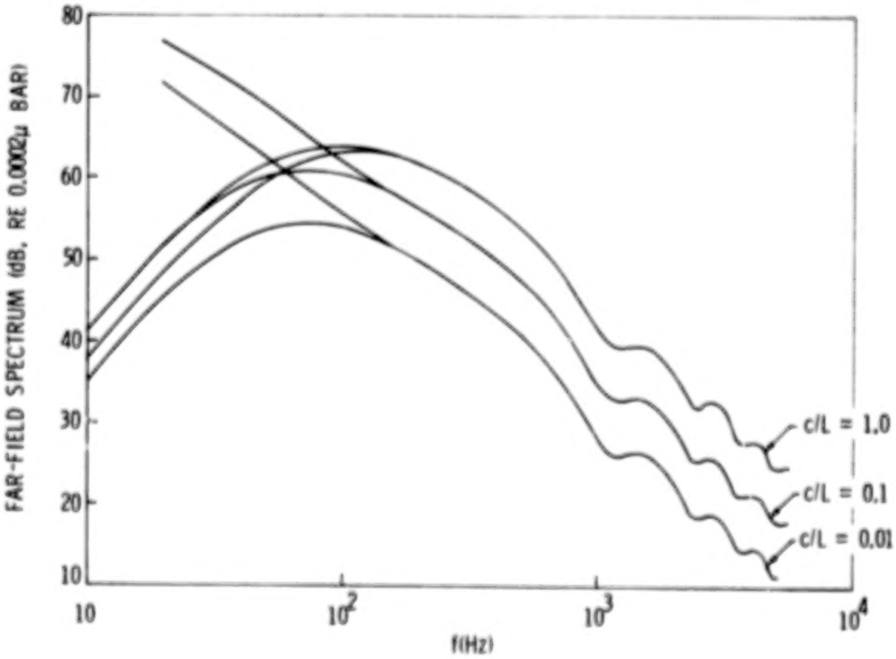

Figure 7.- Effect of turbulence length scale on spectrum.

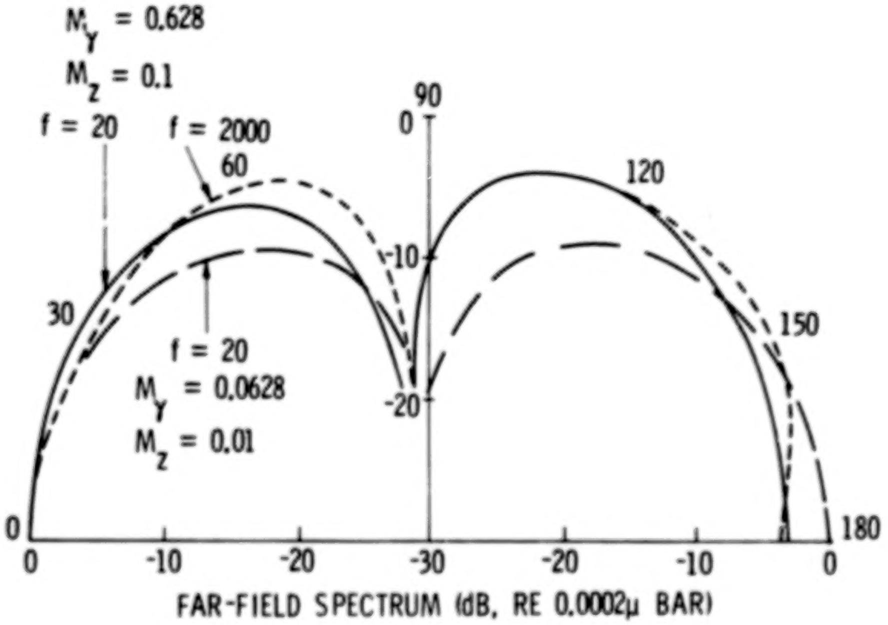

Figure 8.- Effect of tip Mach number on directivity.

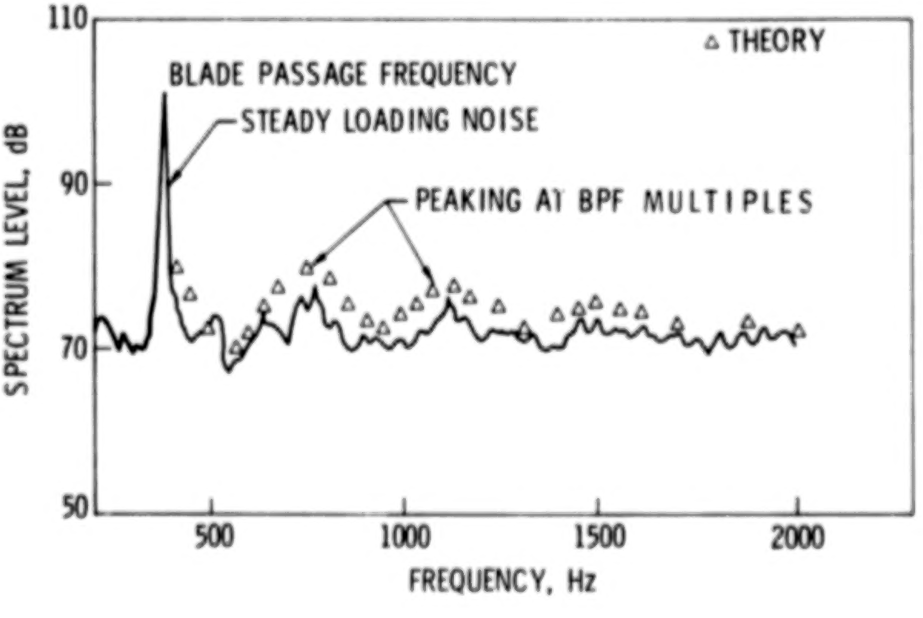

Figure 9.- Comparison of theory and experiment. $M_z = 0.097$; $M_Y = 0.418$; $c/L = 1.1842$; $B = 4$, $c_0/c = 6022.5$; $(\overline{u^2}/V_z^2)^{1/2} = 0.067$; $R/c = 4.3$; $r/c = 4.3$; $r/c = 53.3$; $s/c = 5.33$; RPS = 94.0; $\theta = 124.85$.

THEORY ON ACOUSTIC SOURCES*

S. E. Wright
Joint Institute for Aeronautics and Acoustics
Department of Aeronautics and Astronautics
Stanford University

SUMMARY

A theory is described for the radiation emission from acoustic multipole sources. The sources can be stationary or moving at speeds including supersonic and experience stationary or moving disturbances. The effect of finite source distributions and disturbances is investigated as well as the manner in which they interact. Distinction is made between source distributions that respond as a function of time and those that respond as a function of space.

It is found that motional amplification, for a point source, is given by $|1 - M \cos\sigma|^{-(N+2)}$, where N is the multipole order. Also, that motional attenuation from finite source distributions can be as high as $|1 - M \cos\sigma|^{3z}$, where z depends on the shape of the source distribution (typically between 1 and 2).

INTRODUCTION

In the last few years, there has been much interest in the noise from high speed sources. Particularly in the new generation of jet engines and in helicopter rotors in high speed flight. One knows from experience that moving sources produce a change of pitch as they pass, that whips crack, and that supersonic sources go bang. What we do not know in detail is how these sources radiate.

One of the first published works on isolated sources in motion was that by Oestreicher (ref. 1) in 1951. Using physical arguments involving the time it takes for an emitted sound to travel along a moving source, Oestreicher deduced that the effective source length in the direction of motion should change by (ε^{-1}).† By assuming, without justification, that the effective source density (strength per unit effective length of the source) was unchanged, he concluded that the total source strength and, therefore, the radiation would change by ε^{-1}. Although this model now appears inaccurate, it was useful at the time in that it predicted some kind of an acoustic beaming effect, when $M \cos\sigma = 1$.

---

*This work was supported by ONERA Châtillion-sous-Bagneux (Paris). Service Technique Aéronautique, Paris. Aerospatiale SNIAS Marignane (Marseille).

†$\varepsilon = |1 - M \cos\sigma|$, where M is the source Mach number and σ is the observation angle made with the direction of motion. ε is referred to as a zero and ε^{-1} as a pole, infinity, or singularity. ε^{-1} is the inverse of ε.

Soon after Oestreicher, Lighthill (ref. 2), using formal methods, again interpreted that the effective source dimension should change by ε^{-1}. He also found that each space derivative for the higher order sources produced a further ε^{-1}. However, Lighthill, like Oestreicher, assumed that the effective source strength density (not the actual source strength) was unchanged by motion and that the radiation magnitude change was affected by the effective source volume change. Lighthill, therefore, applied the ε^{-1} singularity in blanket fashion to all types of sources. This made the total singularity power for a multipole of order N, where N is the number of space derivatives equal to N + 1, i.e., $(\varepsilon^{-1})^{N+1}$.

Unlike Lighthill's approach, which uses a moving-stationary coordinate transform (Jacobian) to obtain the radiation from moving sources, the following theory simulates source motion by using a stationary source region of appropriately phased elements.

The main difference between this and Lighthill's theory is that the actual source strength in this theory is assumed to be unchanged by motion and that motional amplification is affected entirely by temporal transform changes between moving and stationary sources; this is contrary to the assumption that motional amplification is caused by an apparent source volume change and, therefore, total source strength change as in references 1 and 2. There is, of course, an effective source volume change through motion; but, according to the following theory, this produces motional attenuation only, the converse to what Oestreicher and Lighthill had originally thought.

In this present theory, it is first found necessary to distinguish clearly between multipole sources (sources constructed from an array of discrete mass displacement sources), aerodynamic sources (sources with source strengths in terms of physical quantities such as fluid mass flow and forces applied to the propagating fluid), and finite sources (sources whose acoustic wavelength is small compared to the source distribution size). When this is done, motional amplification in terms of the multipole source is found to be $(\varepsilon^{-1})^{N+2}$ where N is the number of dipoles forming the source, i.e., the result is one degree higher than Lighthill's series $(\varepsilon^{-1})^{N+1}$. For an aerodynamic source, the theory gives $(\varepsilon^{-1})^{p}$, where $p = 2, 1, 1, 2$, for a mass displacement (fundamental source), mass injection (simple source), force, and stress source, respectively.

It can be seen that both theories are in agreement as far as the simple source is concerned. (Lighthill makes no comment regarding the fundamental source.) However the higher order aerodynamic sources appear to have a singularity less than those predicted by Lighthill. Note that a multipole source and an aerodynamic source in this theory can have the same multipole order but a different singularity power.

Finally, motional attenuation for finite sources is found to be $(\varepsilon)^{z_a + z_b + z_c}$, where the z's are the shape orders of the source distributions in the three coordinate directions. Typically, the z values are between 1 and 2 once the acoustic wavelength is less than the distribution size. Thus motional amplification is only possible if the singularity power $p > z_a + z_b + z_c$.

THEORY DESCRIPTION

The theory is described in detail in reference 3; only a brief description of the main points of the theory is given below.

The radiation equations are first written in terms of multipole analysis, except that the mass displacement source is used as the fundamental acoustic source. For stationary sources, it is not important whether the fundamental source or the time derivative of the fundamental source (simple source) is used. However, for motional effects, it is important to make the distinction. To reduce the complexity of the radiation equations, far field approximations are applied. This enables the directivity effects between acoustic poles and source distributions to be effectively separated.

Source motion is then taken into account by using the concept of a source region. Here, a stationary region is defined with respect to the stationary propagating fluid. Source motion is simulated within the region by allowing the phase of the source region density function to vary with space in such a way as to produce waves of finite phase velocity to pass across the region. Using this model, individual source distributions and disturbances can be accommodated with relative velocities between each other and the stationary coordinate system. At all times the analysis remains in the far field with respect to the stationary coordinate system thus avoiding the use of stationary to moving coordinate transforms such as Jacobian and Lorentz.

To evaluate the radiation from the source region, the source distribution and disturbance functions are Fourier analyzed into spatial harmonics (modes). The resulting double Fourier summation is then simplified into sum and difference mode pairs. The radiation from a single mode is then evaluated, and the radiation from all the modes of the source region summed. In this way, the radiation from any complex source region structure can be evaluated.

It is found that each mode has a characteristic radiation pattern. The directivity has a dominant lobe corresponding to when the mode phase speed, resolved in the direction of the observer, equals the speed of sound, plus finer radiation details at least 14 dB lower than the dominant lobe. Beautiful and complex radiation patterns can result, therefore, depending on the modal content and thus the source region structure.

Fortunately, for most source situations of interest, the finer radiation details cancel and only the dominant mode radiation need be considered. This reduces the complexity of the problem considerably. In fact, in the dominant mode solution, the source region can be considered simply as a "black box" frequency changer. Source frequencies f_s go in, and radiation frequencies f_r come out, with the simple relationship between the two of ε^{-1}.

This simple frequency changing action, however, has a more profound effect. It results in the source radiation emission, for the fundamental source, being increased in the direction of motion by ε^{-2}. The effective multipole leverage (distance between poles) is increased by ε^{-1} and therefore the acoustic interference between poles is reduced giving a further amplification factor of ε^{-N}. Thus the total multipole motional emission is changed by $(\varepsilon^{-N})^{N+2}$.

To convert a multipole source (constant fundamental source strength) into an aerodynamic source (constant aerodynamic source strength), it is found that the transform $(\epsilon^{-1})^n$ is valid, where n = 0, 1, 2, 2 for the mass displacement, mass flow, applied force, and stress source, respectively. Therefore the motional amplification for an aerodynamic source becomes $(\epsilon^{-1})^p$ where $p = N + 2 - n$, thus p = 2, 1, 1, 2 for sources of the type m, q, f_i, and t_{ij}, respectively.

For finite source distributions, the effective source size in the direction of motion is also increased by ϵ^{-1}; however, this results in an increased acoustic interference across the source distributions and, therefore, an attenuation effect of ϵ. For radiation wave lengths smaller than the source distribution size, the attenuation can be as great as ϵ^{3z}, where 3 is for the three source dimensions, if all spatially modulated, and z depends on the source distribution shape (z is typically between 1 and 2).

The degree of motional amplification, therefore, depends on the multipole or aerodynamic order (number of mathematical poles) and the shape and nature of the source distribution (number of zeros z and whether the distributions are time or spatially modulated). Thus it appears that source motion alters the multipole and distribution size, but not the order.

Consider now the disturbance function which generates the source frequencies. Its radiated scale is decreased in the direction of motion by ϵ, the converse to the distribution size. For a given radiated frequency, the disturbance gives an acoustic beam, the longer the disturbance the sharper the beam. The radiation can be greater for a disturbance of longer duration although the rise and fall time is less. Also, sources experiencing finite steady disturbances in motion radiate finite radiation, including an infinite steady disturbance duration.

Distinction is also made between source distributions that respond as a whole to the disturbance as a function of time, similar to a loudspeaker (time modulated), and distributions whose elements respond individually as a function of space, similar to aerodynamic sources (spatially modulated). At subsonic source speeds, spatially modulated sources are effectively less compact than time modulated sources by a factor of $M \cos\theta$. That is, the onset of distributed interference across the source distributions can take place at a much lower frequency than time modulated sources for the same source dimensions. The effect is also experienced normal to the direction of motion in the case of a spatially modulated source.

Further, the fascinating situation is considered where the source is stationary and the disturbance is in motion, such as in an open wind tunnel (ignoring flow effects). Although there is no Doppler effect (stationary source), an acoustic beam is again generated at high flow speeds. Compared with a moving source, the logic here appears to be in reverse. For example, the effective source distribution size now decreases in the direction of motion by ϵ, and the distribution interference now effectively generates the acoustic beam, not attenuates it.

In general, it is found that there is nothing extraordinary regarding accelerating or nonrectilinear source motion. The radiation level at any instant is proportional to the instantaneous velocity and is not dependent on the acceleration of previous or subsequent flight paths.

For example, the notion that steady sources rotating in a circle radiate through centripetal acceleration is, according to this theory, fallacious. The same sources travelling in a straight line will radiate similarly.

It should be pointed out that the theory derived in this paper is based on the observed fact that acoustic propagation is simple, i.e., its propagation is at all times relative to the propagating fluid and not with respect to some coordinate system, moving or otherwise, as in the propagation of electromagnetic waves (relativity theory). Thus, there are no relativistic time or space changes; all space changes in this theory are related to the radiated scale (wavelength).

ILLUSTRATIONS

Figure 1 shows the relationship between an observer and the source region. X_i is the observation point and Y_i is a source point within the source distribution. For far field radiation conditions, i.e., observation distances large compared with the source distribution size, $X_i \gg Y_i$, $|X_i| \approx R$ and R becomes the representative distance of all the source elements in the distribution.

Figure 2 illustrates how the radiation at the observer, for far field radiation conditions, can be represented by the product of two interference effects. K_w represents the interference between monopoles, $\tilde{H}$ represents the acoustic interference across the source distribution and $K_w\tilde{H}$ represents the total interference effect. This is a particularly useful concept as we can treat the multipole and distributive acoustic properties separately.

Figure 3 gives some examples of the multipole directivity function K_w. $\frac{X_i}{R}$ are the direction cosines made with the observer and the multipole directional vectors. This multipole interference effect between poles is well known, and nothing further need be said except to emphasize that these properties are independent of source motion. We now need to concentrate on the H function, which is not so simple, particularly for sources in motion.

Figure 4 illustrates how the source and disturbance motion is accommodated within a stationary source region. Motion is accomplished by allowing the phase of the acoustic density function h_r to vary across the source region. In this manner, h_r can be made to contain information regarding the number, shape, and speed of the source distributions and disturbances. $\tilde{H}$ is then the summation of h_r across the source region (total radiation activity).

Figure 5 shows how the h_r function is represented by two functions, a disturbance function h_w and a source distribution function h_a. The h_w function is the instantaneous value of the summation of h_r across the source distribution at each source position x. The h_a function describes how this summation value is distributed across each source.

In Figure 6, the h_w and h_a functions are Fourier analyzed into spatial harmonics. The resulting double Fourier summation generates a modulated mode system shown in the center figure. This system is then simplified further into simple mode pairs as indicated on the right. Thus any complicated source region structure can be represented by the summation of simple modes, the radiation from which depends on the mode amplitude and radiation efficiency of each mode.

Figure 7 illustrates how simple spatial functions can be converted into spectrum functions, χ, where χ is a nondimensional Fourier coefficient whose maximum value is unity. Each of the disturbance and distribution shape functions is converted into a disturbance and distribution spectrum function χ_s and χ_{mB}, respectively. The mode amplitude then depends on the product spectrum function $\chi_s \chi_{mB}$. Thus, a knowledge of the amplitude, duration, and shape of the spatial functions will give an idea of the mode spectrum amplitude.

Figure 8 concerns the other controlling factor which determines the radiation, i.e., the mode radiation efficiency. Here the radiation is summed for each mode travelling across the source region of dimension d. The radiation depends on the radiation frequency η/d, the number of mode wavelengths ξ across d, and the mode speed η/ξ.

Figure 9 shows the typical radiation directivity for each mode. The mode interference function χ_ξ has a maximum value of unity (dominant lobe); this corresponds to when the mode speed, resolved in the direction of the observer, equals the speed of sound plus finer radiation details at least 14 dB lower. Thus the total radiation from a source region is composed of many such mode radiation directivities, one for each mode generated.

Figure 10 illustrates three specifying characteristics of a radiating source. Figure 10(a) shows the directivity for a single source frequency, f_s, which gives rise to whole family of modes, each mode giving a directivity similar to that in figure 9. Here it can be seen that the directivity envelope containing the dominant lobe is controlled by the distribution spectrum function χ_{mB} only. Figure 10(b) shows the directivity for a given radiation frequency f_r from a complete disturbance. Here the directivity envelope is given by both the disturbance and distribution spectrum functions χ_s, χ_{mB}. Figure 10(c) shows the radiated spectrum at a given observation angle σ. In this case each source frequency generates a passband of discrete frequencies with a dominant center frequency given by χ_ξ. The spectrum envelope (dominant frequencies) is given by $\chi_s \chi_{mB}$. Thus it can be seen that the disturbance and distribution spectrum functions, for a given source speed, control the major acoustic properties of a radiating source.

Figure 11 summarizes the radiation properties for three different source situations. The first column depicts the properties of a moving inphase source experiencing a stationary disturbance (time modulated). Column 2 is for a moving source whose elements respond individually to the disturbance as a function of space (spatially modulated). The last column shows the properties of a stationary modulated source experiencing a moving disturbance. The disturbance can be a simple sinusoidal disturbance, in which case the radiation directivity is given in row a . Or the disturbance can be some arbitrary periodic disturbance. In this case, the directivity for a single radiation frequency is given in row b, and the resulting spectrum at a given observation angle is shown in row c. These directivity and spectrum envelopes indicate the dominant lobe and radiation frequencies only; the finer radiation details given in figures 9 and 10 are not shown.

Concentrating for a moment on the top left hand square, block 1a represents the directivity for a point source experiencing a single source frequency. This directivity is given by $(\varepsilon^{-1})^p$ where $\varepsilon = 1 - M\cos\sigma$ and p is the aerodynamic order. Thus at the Mach angle $\cos\sigma = 1/M, \varepsilon = 0, \varepsilon^{-1} = \infty$, the directivity has a series of poles or infinities of order p giving infinite radiation. Block 2a represents the acoustic interference effect across finite source distributions given by χ_{mB}. This function contains zeros, ε, of order z_a, the power of which depends on the shape of the source distributions. This function, of course, gives zero radiation at the Mach angle. Thus, motional amplification or attenuation can occur depending on the balance of the poles p (aerodynamic order) and on the number of zeros z_a (source distribution shape).

Continuing along the top row of Figure 11, the main difference between a time-modulated source, 1a, and a spatially modulated source, 2a, is that the distribution spectrum function, in 2a, is also operative at right angles to the source motion. Whereas in 1a, at 90^0 to the source motion, χ_{mB} is unity, i.e., there is no distributive source interference effect. In the case of the stationary spatially modulated source experiencing a moving disturbance, 3a, there are no poles in the point source term as the source is stationary. Here the directivity is given by the distributive interference effect χ_{mB} only. At the Mach angle, χ_{mB} has unities of order z_a giving the acoustic beam. Thus the sharpness of the beam is given solely by the shape of the source distributions.

Moving along the second row of Figure 11, the radiation directivity at a given radiation frequency from a periodic disturbance is considered. For a time-modulated source, 1b, the directivity is given by both χ_s and χ_{mB}, where disturbance spectrum function χ_s is responsible for generating the acoustic beam. This function has unities of order z_w where z_w depends on the shape of the disturbance function. Thus the disturbance shape determines the shape (sharpness) of the acoustic beam. The main effect of the disturbance spectrum function χ_{mB} is to attenuate the acoustic beam in the direction of source motion. In the case of the moving spatially modulated source, 2b, the χ_{mB} function is omnidirectional, thus giving no attenuation of the acoustic beaming effect given by χ_s. In the last situation, 3b, χ_s is now nondirectional and the acoustic beaming is given by χ_{mB}. Note that situations 3a and 3b are the same, as the source is stationary making both the source and radiation frequencies identical.

Finally the radiation spectrum characteristics arising from a periodic disturbance are given along the bottom row of Figure 11. The spectrum is the product of the three functions χ_s, χ_{mB} and $(f_r)^p$. The disturbance and distribution spectrum function depress the acoustic spectrum after the "start" of the decay of these functions, given by $(f_r)_w$ and $(f_r)_a$, have been exceeded. The decay rate then depends on the order z_w and z_a of the disturbance and distribution functions, respectively. Thus the acoustic spectrum rises at low frequencies according to the frequency multiplier $(f_r)^p$, where p depends on the aerodynamic order, and finally decays according to $(f_r)^{p-z_w-z_a}$. It can be seen that the spectra can be quite different for each source situation depending on the individual break frequencies $(f_r)_w$ and $(f_r)_a$. Here v is the disturbance speed with respect to the source, u is the source speed and a_o is the speed of sound. Note that in situations 1c and 2c, the radiated disturbance scale w_r in comparison to the actual disturbance scale w, in the direction of motion, is reduced by ε_u and the radiated source distribution size a_r in comparison to the actual size a, is increased in the direction of motion by ε_u^{-1}. In the last situation, 3c, the radiated and actual disturbance scales are the same, and the radiated distribution size is now decreased in the direction of motion by ε_v.

THEORETICAL BASIS

To help indicate the differences between this and other theories, the essential principles on which the theory is based are summarized below. The detailed analysis of the following statements can be found in reference 3.

(a) Fundamental source.

The mass displacement source m is considered as the fundamental or basic acoustic source. The simple source q, usually taken to be the simplest acoustic source, is, in fact, the time derivative of the fundamental source.

$$m = \rho_o v_o \qquad\qquad q = \frac{\partial m}{\partial t} \tag{1}$$

m and q are the mass displacement and mass flow source strengths, respectively; ρ_o is the density of the displaced propagating fluid and v_o is the displaced volume. For a stationary harmonic source of the form

$$m_s = \hat{m} \cos \omega_s t \qquad\qquad \omega_s = 2\pi f_s \tag{2}$$

where $\hat{m}$ is the amplitude and ω_s is the source frequency. The acoustic strength h_s is then

$$h_s = \left(\frac{\partial}{\partial t}\right)^2 m_s = \omega_s^2 m_s \tag{3}$$

(b) Moving fundamental source.

The only basic effect of source motion is to change the radiation frequency, $f_s \rightarrow f_r$. The source strength $\hat{m}$ remains unchanged by motion

$$m_r = \hat{m} \cos \omega_r t \qquad\qquad \omega_r = \varepsilon^{-1} \omega_s \tag{4}$$

The acoustic source strength then becomes

$$h_r = \left(\frac{\partial}{\partial t}\right)^2 m_r = \omega_r^2\, m_r = \left(\varepsilon^{-1}\right)^2 \omega_s^2\, m_r \quad . \tag{5}$$

i.e., the radiation amplitude between a stationary and moving fundamental source, all other things being equal, is

$$\hat{h}_r = \left(\varepsilon^{-1}\right)^2 \hat{h}_s \tag{6}$$

(c) Multipole source.

A multipole source is defined as an array of 2^N discrete equispaced fundamental sources where N is the multipole order (number of dipoles). The acoustic strength is given by

$$h_s = d_i^N \left(\frac{\partial}{\partial t}\right)^{N+2} m_s \tag{7}$$

where d_i is separation distance between monopole sources. The acoustic strength of a moving multipole source is then

$$h_r = d_i^N \left(\frac{\partial}{\partial t}\right)^{N+2} m_r = d_i^N\, \omega_r^{N+2}\, m_r = \left(\varepsilon^{-1}\right)^{N+2} d_i^N\, \omega_s^{N+2}\, m_r \tag{8}$$

i.e., $$\hat{h}_r = \left(\varepsilon^{-1}\right)^{N+2} \hat{h}_s \quad (\hat{m}\ \text{constant}) \tag{9}$$

(d) Aerodynamic source.

If g represents the source strength of an aerodynamic source, such as mass flow q, applied force f_i, and stress t_{ij}, then the acoustic relation between these sources is

$$g_r = d_i^N \left(\frac{\partial}{\partial t}\right)^{n} m_r \tag{10}$$

N	0	0	1	2
g	m	q	f_i	t_{ij}
n	0	1	2	2

and the acoustic strength in terms of g becomes

$$h_r = d_i^N \left(\frac{\partial}{\partial t}\right)^{N+2} m_r = \left(\frac{\partial}{\partial t}\right)^{p} g_r \quad , \qquad p = N + 2 - n \tag{11}$$

$$= \omega_r^p\, g_r = \left(\varepsilon^{-1}\right)^p \omega_s^p\, g_r \tag{12}$$

i.e., $$\hat{h}_r = \left(\varepsilon^{-1}\right)^p \hat{h}_s \quad (\hat{g}\ \text{constant}) \tag{13}$$

(e) Sound pressure.

The sound pressure for an aerodynamic source, is then given by

$$SP = \frac{1}{4\pi R} K_N \left[h_r\right] \quad , \qquad K_N = \left(\frac{X_i}{R} \; \frac{1}{a_o}\right)^N \tag{14}$$

$$= \frac{1}{4\pi R} K_N \left(\frac{\partial}{\partial t}\right)^P \left[g_r\right] \quad , \qquad \left[g_r\right] = \hat{g} \cos \omega_r \left[t\right] \tag{15}$$

$$\left[t\right] = t - \frac{R}{a_o} \; , \quad \omega_r = \varepsilon^{-1} \, \omega_s \tag{16}$$

$$= \frac{1}{4\pi R} K_N \left(\varepsilon^{-1}\right)^P \; \omega_s^P \left[g_r\right] \tag{17}$$

The $\frac{1}{4\pi R}$ term gives the spherical spreading effect; K_N gives the interference effect between poles; and, $\frac{X_i}{R}$ are the direction cosines made with the source directional vectors and the observer.

Or in a more familiar form:

(1) Wave equation.

$$WE = \frac{\partial^2 m}{\partial t^2} + \frac{\partial q}{\partial t} - \frac{\partial f_i}{\partial x_i} + \frac{\partial^2 t_{ij}}{\partial x_i \, \partial x_j} \tag{18}$$

$$SP = \frac{1}{4\pi R} \left\{ \frac{\partial^2 [m]}{\partial t^2} + \frac{\partial [q]}{\partial t} - \frac{\partial [f_i]}{\partial x_i} + \frac{\partial^2 [t_{ij}]}{\partial x_i \, \partial x_j} \right\} \tag{19}$$

Far field solution (20)

$$\frac{\partial^N [g]}{\left(\partial x_i\right)^N} = \left(- \frac{X_i}{R} \, \frac{1}{a_o}\right)^N \left(\frac{\partial}{\partial t}\right)^N [g]$$

$$SP = \frac{1}{4\pi R} \left\{ \frac{\partial^2 [m]}{\partial t^2} + \frac{\partial [q]}{\partial t} + \left(\frac{X_i}{R} \, \frac{1}{a_o}\right) \frac{\partial [f_i]}{\partial t} + \left(\frac{X_i}{R} \, \frac{1}{a_o}\right)^2 \frac{\partial^2 [t_{ij}]}{\partial t^2} \right\} \tag{21}$$

$$= \frac{1}{4\pi R} K_N \left(\frac{\partial}{\partial t}\right)^P [g] \tag{22}$$

Equations (19) and (22) are valid only for a stationary source.

(2) Moving harmonic source.

By using a stationary source region of elements with varying phase, the effect of source motion can be simulated. In this case, the solution (22) above is valid provided

$$\begin{tikzcd} & g_s = \hat{g}\cos\omega_s t \quad (23) \\ g \arrow[ur, "\text{sta.}"] \arrow[dr, "\text{mov.}"'] & \\ & g_r = \hat{g}\cos\omega_r t \qquad \omega_r = \left(\varepsilon^{-1}\right)\omega_s \quad (24) \end{tikzcd}$$

where sta. and mov. are for stationary and moving sources. This gives

$$SP = \frac{1}{4\pi R} K_N \left(\frac{\partial}{\partial t}\right)^p [g_r] \tag{25}$$

$$= \frac{1}{4\pi R} K_N \left(\varepsilon^{-1}\right)^p \omega_s^p [g_r] \tag{26}$$

(3) Stationary source equivalence for a point source.

$$|h_r| = \left|\left(\frac{\partial}{\partial t}\right)^p g_r\right| = \left|\left(\varepsilon^{-1}\right)^p \left(\frac{\partial}{\partial t}\right)^p g_s\right| \tag{27}$$

$$\hat{SP}_{\text{mov.}} = \left(\varepsilon^{-1}\right)^p \hat{SP}_{\text{sta.}} \tag{28}$$

$$\hat{SP}_{\text{mov.}} = \frac{1}{4\pi R} K_N \left\{\left(\varepsilon^{-1}\right)^2 \frac{\partial^2[m]}{\partial t^2} + \left(\varepsilon^{-1}\right) \frac{\partial[q]}{\partial t} + \left(\varepsilon^{-1}\right) \frac{\partial[f_i]}{\partial t} + \left(\varepsilon^{-1}\right)^2 \frac{\partial^2[t_{ij}]}{\partial t^2}\right\}_{\text{sta.}} \tag{29}$$

The main difference between equation (29) and other general results is that it makes a clear distinction between the mass displacement source (m) and the mass flow source (q) indicated by the first two terms and that the last two source terms, f_i and t_{ij} in equation (29), have a singularity (ε^{-1}) less than other general results.

PRINCIPLE CONCEPTS

In summary, the main concepts used in the finite source theory are listed below.

(1) Radiation equation.

$$SP = \frac{1}{4\pi R} \cdot K_N \cdot \tilde{H}_r \tag{30}$$

$$K_N = \left(\frac{X_i}{R}\frac{1}{a_o}\right)^N \qquad \tilde{H}_r = \int [h_r] d_x \tag{31}$$

i.e., the radiation equation can be represented by two separate interference effects: (i) the interference between poles, represented by K_N, which is independent of motion; (ii) the interference effect, represented by H_r, across finite source distributions.

(2) Relation between h_r, m_r, and g_r.

$$h_r = d_i^N \left(\frac{\partial}{\partial t}\right)^{N+2} m_r \qquad (32)$$

$$g_r = d_i^N \left(\frac{\partial}{\partial t}\right)^{n} m_r \qquad (33)$$

$$h_r = \left(\frac{\partial}{\partial t}\right)^{p} g_r \qquad (34)$$

g	N	n	p
m	0	0	2
q	0	1	1
f_i	1	2	1
t_{ij}	2	2	2

$$p + n = N + 2 \qquad (35)$$

h_r = acoustic strength, m_r = fundamental source strength, g_r = aerodynamic source strength.

(3) Disturbance and distribution function.

$$h_r = h_w \cdot h_a \qquad (36)$$

For a source region of finite source distributions and periodic disturbances, the acoustic activity (h_r) can be represented by the product of a disturbance function (h_w) and a distribution function (h_a).

(4) Modal analysis.

$$h_r = h_w h_a = \sum_s h_s \sum_{mB} h_{mB} = \sum_s \sum_{mB} h_\xi \quad , \quad h_\xi = h_s h_{mB} \qquad (37)$$

The disturbance and distribution functions are Fourier-analyzed into a double summation of simple modes (spatial harmonics).

(5) Radiation integral.

$$\tilde{H}_r = \int_d [h_r]\, dx = \sum_s \sum_{mB} \chi_s\, \chi_{mB}\, \chi_\xi\, [H_r] \qquad (38)$$

$$[H_r] = H \cos\left(2\pi f_r [t] + \theta_r + \phi\right), \; H = \left(\frac{\partial}{\partial t}\right)^{P} G \qquad (39)$$

$$G = \frac{2BE}{d} \int_w |g_w|\, dx \qquad\qquad g_w = \int_a |g_r|\, dx \qquad (40)$$

The radiation integral (total acoustic activity) $\tilde{H}_r$ is the summation of the acoustic radiation from all the modes of the source region. χ_s and χ_{mB} are the disturbance and distribution spectrum functions which give the mode amplitude. χ_ξ is the mode acoustic interference function which gives the mode radiation efficiency.

(6) Dominant mode solution.

$$\chi_\xi = 1 \qquad \theta_r = 0 \qquad mB = \mp s \left(\frac{\Delta - M_r \cos \sigma}{\delta - M_r \cos \sigma} \right) \tag{41}$$

$$\tilde{H}_r = \chi_s \chi_{mB} \left[H_r \right] \qquad f_r = \epsilon_u^{-1} f_s \tag{42}$$

In the dominant mode solution, the mode interference function χ_ξ becomes unity, and the radiation phase angle θ_r becomes zero. Thus, the complexity of the radiation integral $\tilde{H}_r$ is reduced considerably.

(7) Sound pressure.

$$SP = \frac{1}{4\pi R} K_N \chi_s \chi_{mB} \left[H_r \right] \tag{43}$$

$$\left[H_r \right] = \left(\frac{\partial}{\partial t} \right)^P G \cos \left(2\pi f_r [t] + \phi \right) \tag{44}$$

$$= \frac{1}{4\pi R} K_N \left(2\pi f_r \right)^P \chi_s \chi_{mB} \left[G_r \right] \qquad \text{single } f_r \tag{45}$$

$$= \frac{1}{4\pi R} K_N \left(\epsilon_u^{-1} \right)^P \left(2\pi f_s \right)^P \chi_s \chi_{mB} \left[G_r \right] \qquad \text{single } f_s \tag{46}$$

The sound pressure (dominant mode solution) for a given radiation frequency is given by equation (45) and for a given source frequency by equation (46). The total radiation for a complete disturbance is given by $\sum_s (f_r)$ or $\sum_s (f_s)$.

(8) Motional amplification.

$$\hat{SP}_{mov.} = \left(\epsilon_u^{-1} \right)^P \hat{SP}_{sta.} \quad \text{(point source)} \tag{47}$$

$$\hat{SP}_{mov.} = \left(\epsilon_u^{-1} \right)^P \left(\epsilon_u \right)^z \hat{SP}_{sta.} \quad \text{(finite source)} \tag{48}$$

$$\left(f_s \right)_{a,b,c} < f_s < \left(f_s \right)_{d_i} \tag{49}$$

$$p > z \qquad z = z_a + z_b + z_c \tag{50}$$

A finite source is considered to be one whose source frequencies are greater than the source distribution cut off frequencies $(f_s)_{a,b,c}$ and less than the multipole leverage cut off frequencies $(f_s)_{d_i}$. Motional amplification, for a finite time-modulated source, occurs only if the aerodynamic order p is greater than the sum of the source distribution order z in the three coordinate directions.

REFERENCES

1. Oestreicher, H. L. The effect of motion on the acoustic radiation of a sound source. Tech. Data Digest 16, no. 9, Centr. Air. Docum. Off. (Washington) 1951, pp. 16-19.

2. Lighthill, M. J. On sound generated aerodynamically. I. General Theory. A 211, Proc. Roy. Soc., 1952, pp. 564-587.

3. Wright, S. E. Theorie sur les source acoustiques. H/DE-ER 351-91. Bureau D'etudes Aerospatiale Marignane, 1978.

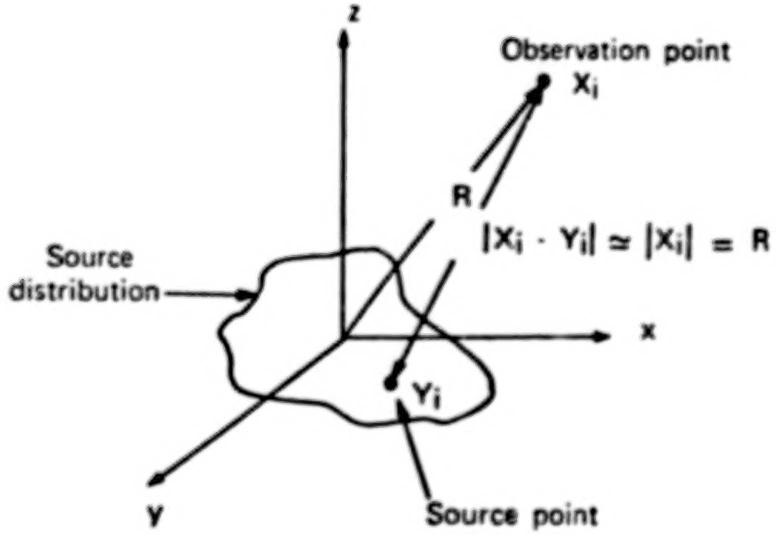
z
Observation point
X_i
R
$|X_i - Y_i| \simeq |X_i| = R$
Source
distribution
x
Y_i
y
Source point

Figure 1.- Source-observer definition.

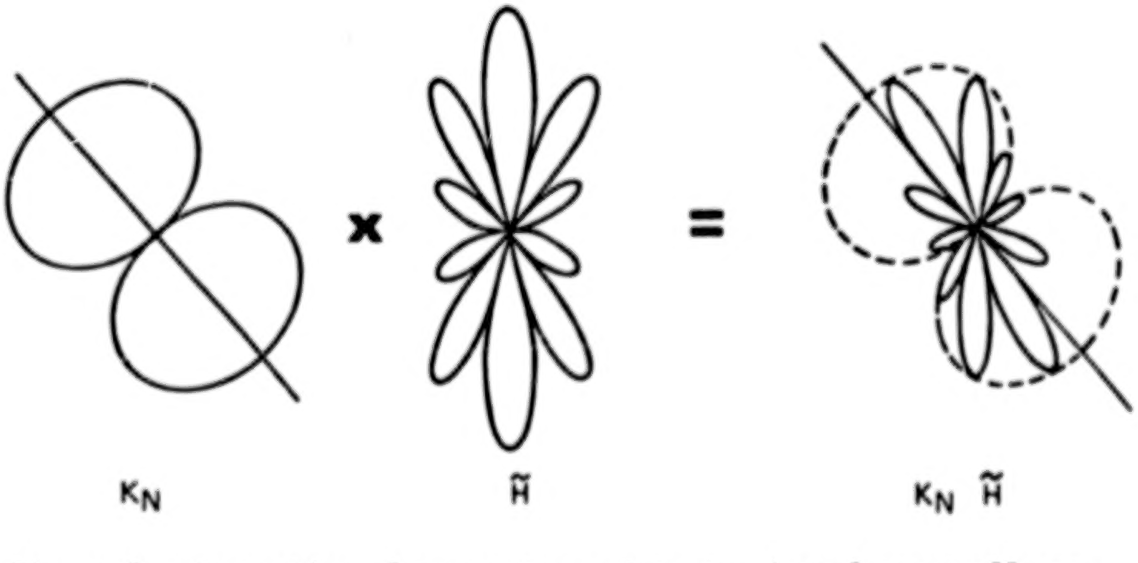
x
=
K_N
$\tilde{H}$
$K_N \tilde{H}$

Figure 2.- Separation of source terms into two interference effects.

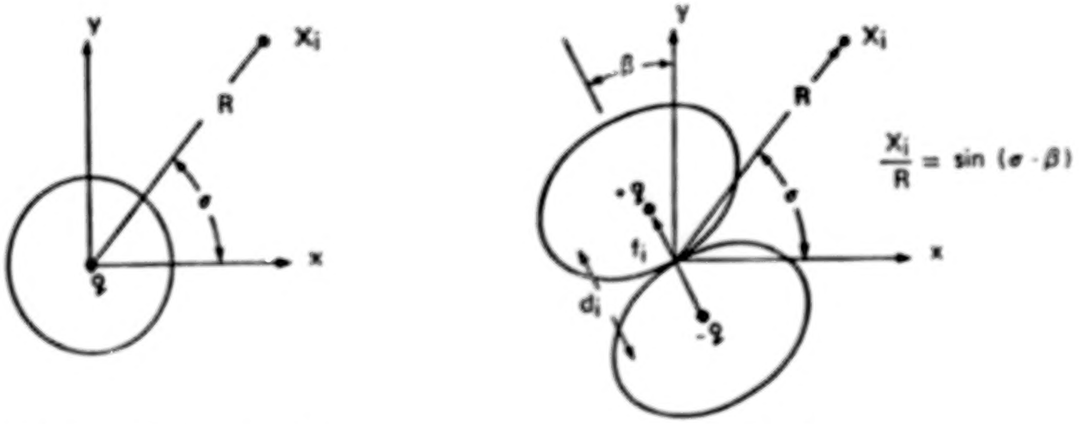
y
X_i
R
σ
x
q
y
β
X_i
R
$\frac{X_i}{R} = \sin(\sigma - \beta)$
σ
-q
f_i
x
d_i
-q

(a) K_0 simple source. (b) K_1 dipole.

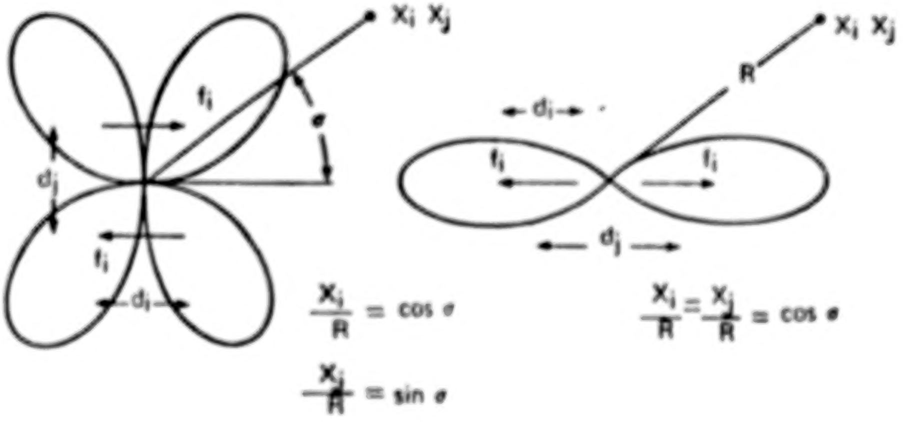
X_i X_j
f_i
σ
d_j
f_i
d_i
$\frac{X_i}{R} = \cos\sigma$
$\frac{X_j}{R} = \sin\sigma$
X_i X_j
R
d_i
f_i
f_i
d_j
$\frac{X_i}{R} = \frac{X_j}{R} = \cos\sigma$

(c) K_2 lateral and longitudinal quadrupole.

Figure 3.- Equivalence of aerodynamic sources in terms of simple sources.

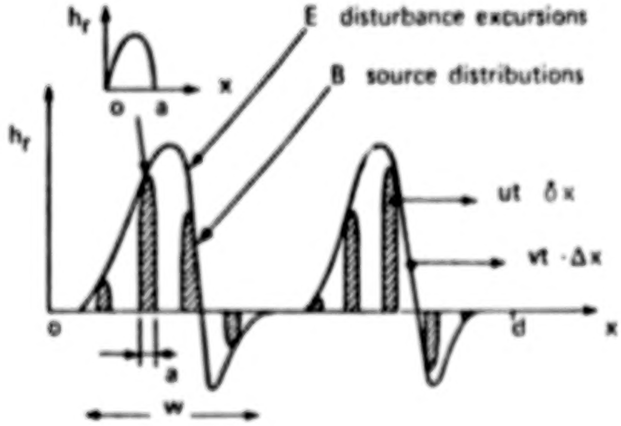
h_r
x
o
a
E disturbance excursions
B source distributions
h_r
ut δx
vt · Δx
o
d
x
a
w

Figure 4.- Source region description.

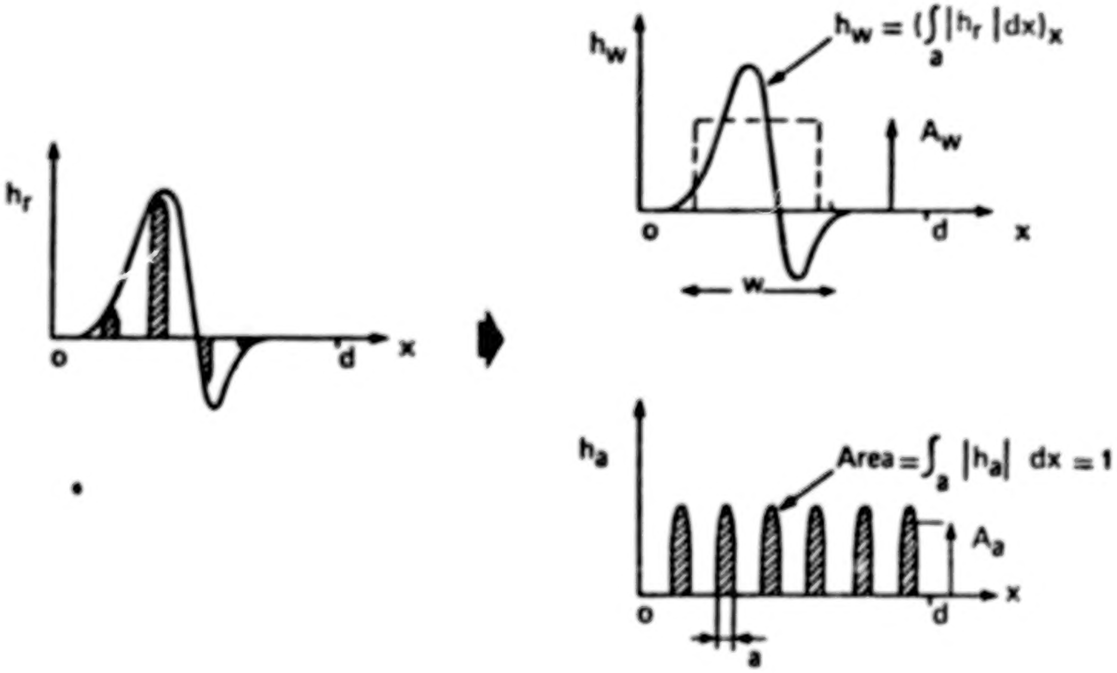
h_r
o
d
x
h_w = (∫_a |h_r| dx)_x
h_w
A_w
o
d
x
w
h_a
Area = ∫_a |h_a| dx = 1
A_a
o
d
x
a

Figure 5.- Representation of density function by a disturbance and distribution function.

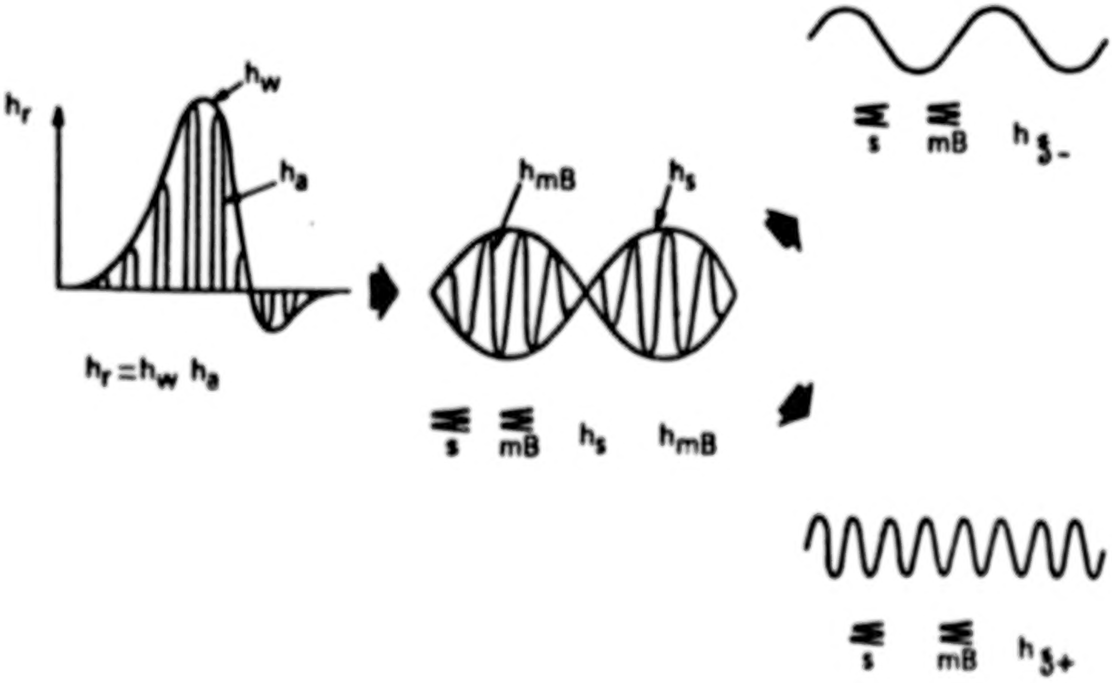
h_w
h_r
h_a
h_r = h_w h_a
h_mB
h_s
M_s M_mB h_s h_mB
M_s M_mB h_§-
M_s M_mB h_§+

Figure 6.- Decomposition of density function into simple mode pairs.

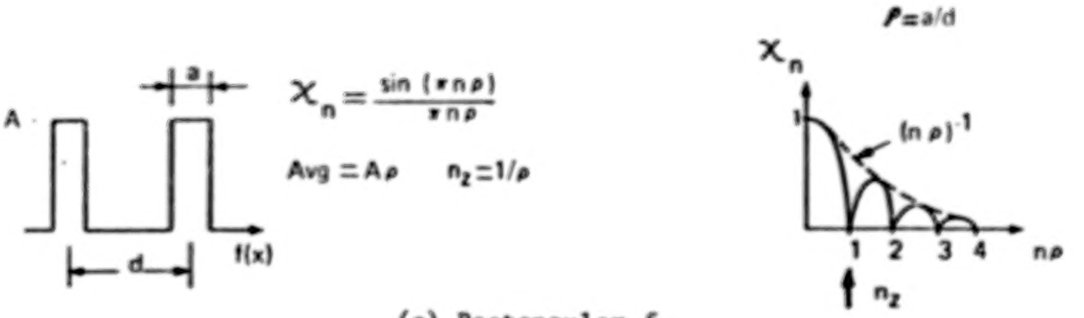

$$\chi_n = \frac{\sin(\pi n\rho)}{\pi n\rho}$$

Avg $= A\rho$ $\quad n_z = 1/\rho$

(a) Rectangular f_n.

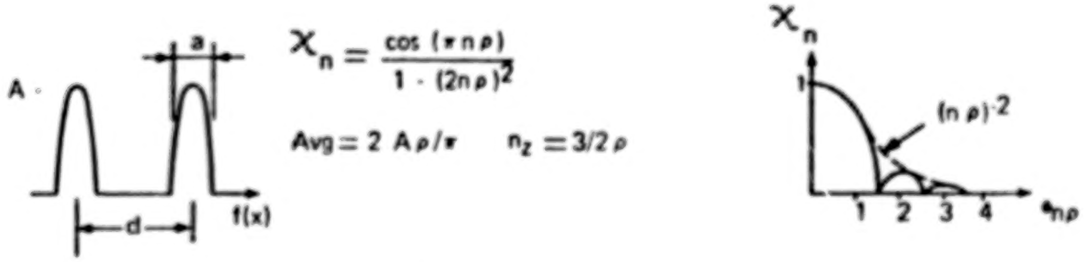

$$\chi_n = \frac{\cos(\pi n\rho)}{1-(2n\rho)^2}$$

Avg $= 2A\rho/\pi$ $\quad n_z = 3/2\rho$

(b) Half cosine f_n.

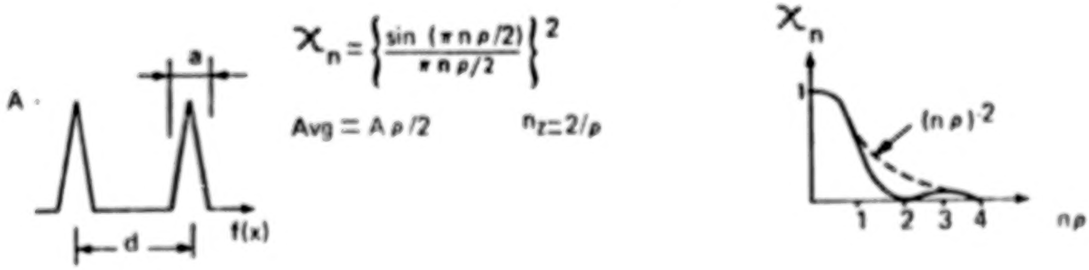

$$\chi_n = \left\{\frac{\sin(\pi n\rho/2)}{\pi n\rho/2}\right\}^2$$

Avg $= A\rho/2$ $\quad n_z = 2/\rho$

(c) Triangular f_n.

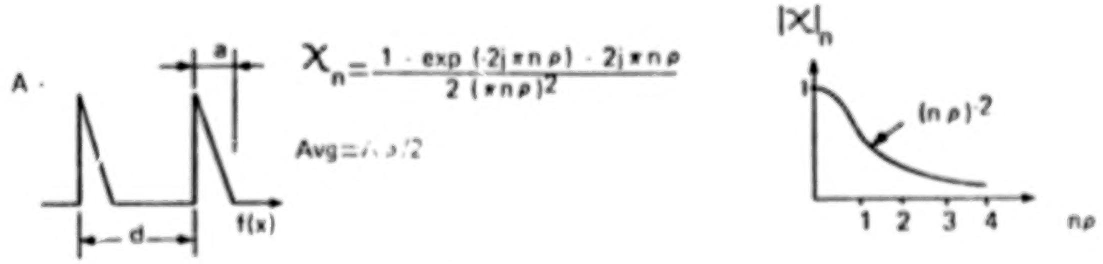

$$\chi_n = \frac{1-\exp(-2j\pi n\rho)-2j\pi n\rho}{2(\pi n\rho)^2}$$

Avg $= A\rho/2$

(d) Sawtooth f_n.

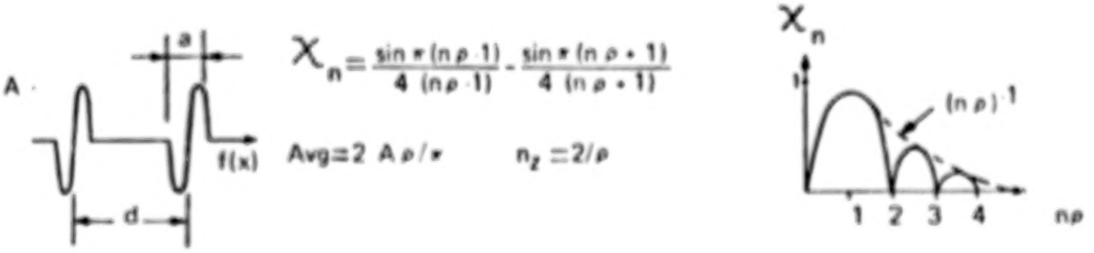

$$\chi_n = \frac{\sin\pi(n\rho-1)}{4(n\rho-1)} - \frac{\sin\pi(n\rho+1)}{4(n\rho+1)}$$

Avg $= 2A\rho/\pi$ $\quad n_z = 2/\rho$

(e) Full sine f_n.

Figure 7.- Spectrum function χ_n for some simple shape functions.

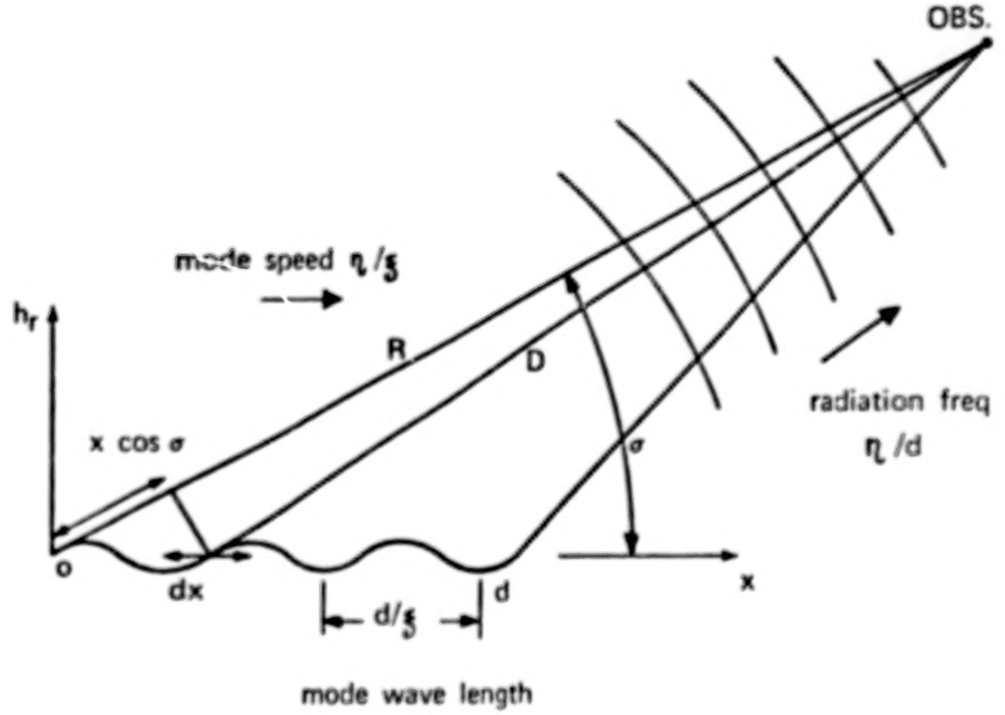
OBS.
mode speed η/ξ
h_r
R
D
radiation freq
η/d
x cos σ
σ
o
dx
d
x
d/ξ
mode wave length

Figure 8.- Mode radiation details.

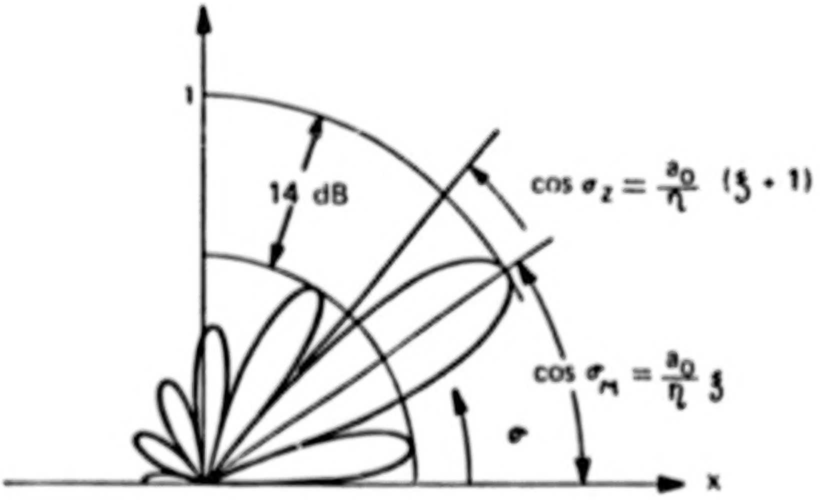
1
14 dB
cos σ_z = a_0/η (ξ + 1)
cos σ_M = a_0/η ξ
σ
x

Figure 9.- Directivity properties of the mode interference function χ_ξ.

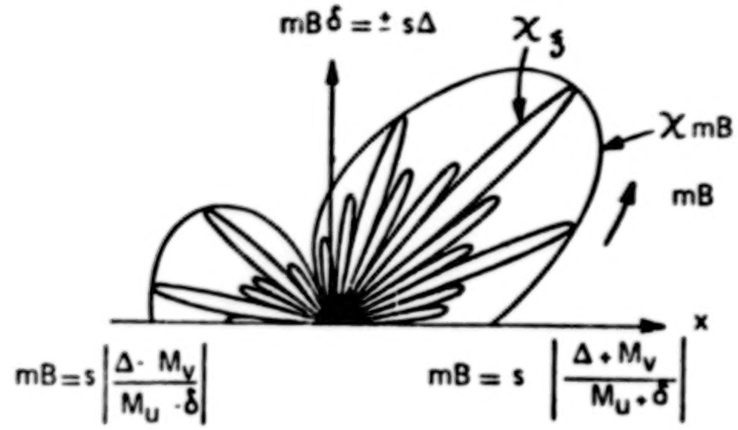
$mB\delta = \pm s\Delta$
χ_ξ
χ_{mB}
mB
x
$mB = s\left|\frac{\Delta - M_v}{M_u - \delta}\right|$
$mB = s\left|\frac{\Delta + M_v}{M_u + \delta}\right|$

(a) Directivity for given f_s.

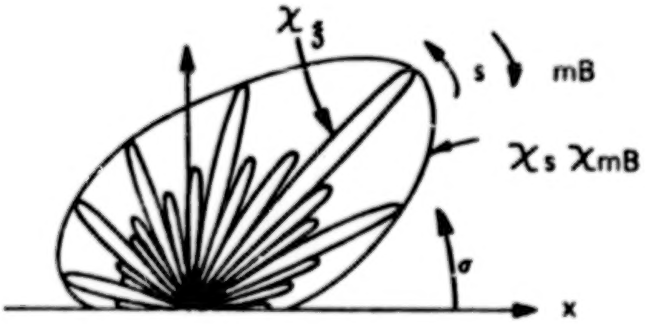
χ_ξ
s
mB
$\chi_s\,\chi_{mB}$
σ
x

(b) Directivity for given f_r.

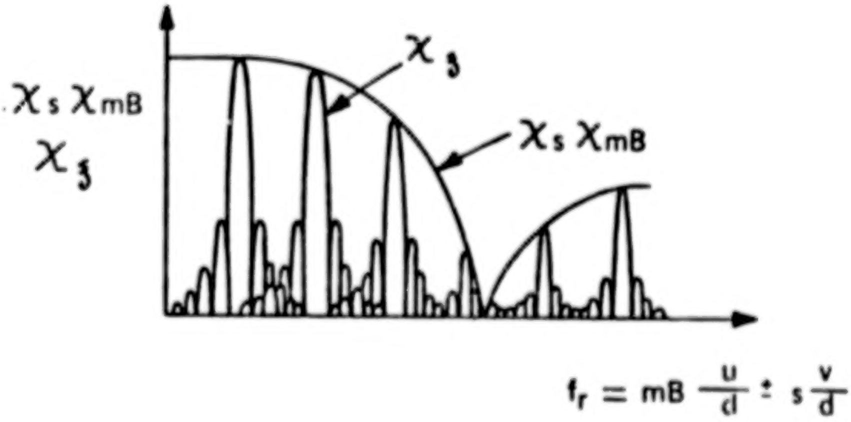

(c) Spectrum for given σ.

Figure 10.- Three specifying characteristics of a radiating source.

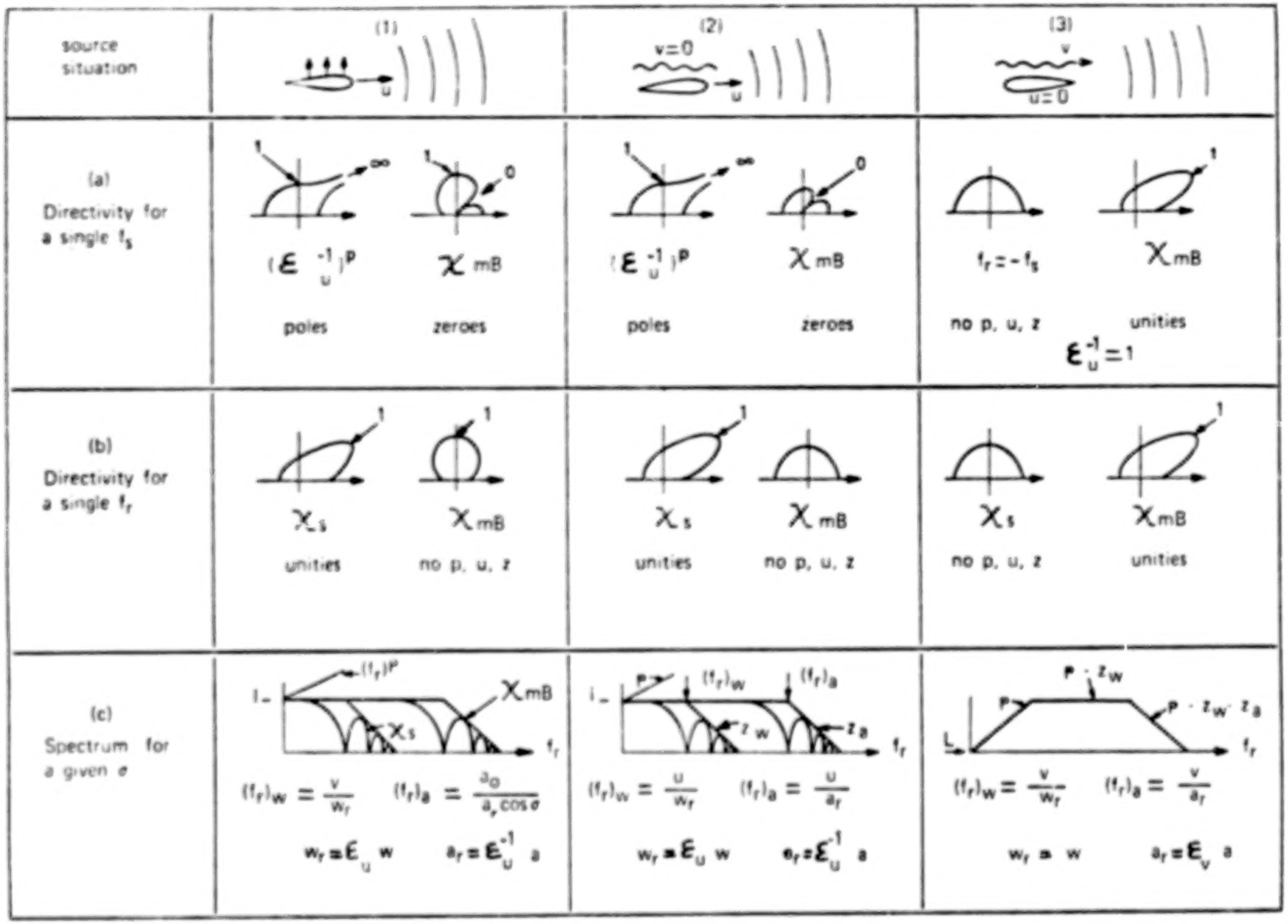
source situation
(1)
u
(2)
v=0
u
(3)
v
u=0
(a) Directivity for a single f_s
1
∞
0
$(\varepsilon_u^{-1})^p$
χ_{mB}
poles
zeroes
$f_r = -f_s$
no p, u, z
unities
$\varepsilon_u^{-1} = 1$
(b) Directivity for a single f_r
1
χ_s
χ_{mB}
unities
no p, u, z
(c) Spectrum for a given σ
L
$(f_r)^p$
χ_{mB}
χ_s
f_r
$(f_r)_w = \frac{v}{w_r}$
$(f_r)_a = \frac{a_0}{a_r \cos\sigma}$
$w_r = \varepsilon_u w$
$a_r = \varepsilon_u^{-1} a$
p
$(f_r)_w$
$(f_r)_a$
z_w
z_a
$(f_r)_w = \frac{u}{w_r}$
$(f_r)_a = \frac{u}{a_r}$
$a_r = \varepsilon_u^{-1} a$
$p \cdot z_w$
$p \cdot z_w \cdot z_a$
$(f_r)_w = \frac{v}{w_r}$
$(f_r)_a = \frac{v}{a_r}$
$w_r = w$
$a_r = \varepsilon_v a$

Figure 11.- Summary of time and spatially modulated source radiation characteristics.

Blank Page

POTENTIAL ACOUSTIC BENEFITS OF CIRCULATION CONTROL ROTORS

Robert M. Williams
David W. Taylor Naval Ship Research and Development Center

Ian C. Cheeseman
University of Southampton

SUMMARY

The Circulation Control Rotor (CCR) possesses certain unique aerodynamic characteristics which may alter the fundamental aeroacoustic mechanisms responsible for noise generation on a rotating blade. The purpose of this research, in the absence of directly applicable experimental data for the CCR, is to theoretically examine the various potential source mechanisms and attempt to predict their contribution to the overall rotor sound pressure level. Results from a new theory for airfoil trailing edge noise are presented. Modifications and extensions to other source theories are described where it is necessary to account for unique aspects of CC aerodynamics. The CCR, as embodied on an X-Wing vertical take off and landing (VTOL) aircraft, is used as an example for computational purposes, although many of the theoretical results presented are generally applicable to other CC applications (such as low speed rotors, propellers, compressors, and fixed wing aircraft). Using the analytical models, it is shown that the utilization of CC aerodynamics theoretically makes possible unprecedented advances in rotor noise reduction. For the X-Wing VTOL these reductions appear to be feasible without incurring significant attendant performance and weight penalties.

INTRODUCTION

Circulation Control Rotors (CCR) have been undergoing more or less continuous research since the early 1960's (refs. 1 to 4). This technology has now matured to the point where two U.S. Navy advanced development rotor programs are reaching the full scale wind tunnel evaluation stage. The first of these developments is a relatively low speed CCR intended to demonstrate a remarkable simplification of the helicopter rotor hub. A 13.4 m (44 ft) diameter, 4 bladed rotor is currently undergoing whirl testing by Kaman Aerospace preparatory to entry in the NASA Ames 12 x 24 m (40 x 80 ft) tunnel and eventual flight testing on the UH-2 airframe. A secondary objective of the program will be to investigate the potential of the CCR to reduce vibratory airloads both by active means (higher harmonic blowing) and by using the inherent passive characteristics of CC airfoils wherein the lift is substantially independent of velocity. The basic CCR concept employed in the Kaman program is illustrated schematically in figure 1. Briefly, a thin jet sheet of air is ejected tangentially over the rounded trailing edge of a quasi-elliptical airfoil, suppressing boundary layer separation and moving the rear stagnation streamline toward the lower surface, thereby increasing lift in proportion to the duct pressure. The azimuthal variation of lift is controlled by a simple nondynamic pneumatic valve in the hub.

For higher speeds and advance ratios, a second duct and leading edge slot are used (fig. 2) so that the rotor can develop significant lift in the region of reverse flow. Two-dimensional airfoil experiments showed that it is possible to develop large lift coefficients by blowing from either slot individually *or from both simultaneously*. The latter technique is used for advance ratios greater than 0.5 where the retreating blade experiences "mixed flow" (i.e., locally reversed flow on the inboard sections and forward flow on the outer sections). This is the CCR implementation used in the X-Wing, a unique stoppable rotor VTOL concept. A 7.62 m (25 ft) diameter X-Wing rotor is currently being fabricated by the Lockheed California Company for testing late in 1978.

The X-Wing potentially represents a major breakthrough in subsonic VTOL design and has eventual applicability to a wide range of military and civil missions. Although the focus of current interest is on resolution of certain critical proof-of-concept technologies, it is, nevertheless, of interest to explore the design aspects of a civil version (which might look similar to the artist's conception in fig. 3). It was previously known that the X-Wing should possess several outstanding civil VTOL design features such as excellent range/payload, high 'block speed' and relative insensitivity to gusts. The effect of noise constraints on the design, however, were totally unknown - hence the reason for the present study. That acoustic design requirements can be extremely important in rotary VTOL design is evidenced by several civil application studies. For example, reference 5 indicates an increment in gross weight of approximately 25 percent to achieve a noise reduction of 10 PNdB on a tilt rotor VTOL design. It is reasonable to suspect therefore that in the highly competitive civil transport market the margin for economic viability may well hinge on the impact of noise requirements on the aircraft design.

In the absence of any applicable measurements, the acoustic characteristics of the CCR (and in particular an X-Wing CCR) are essentially unknown at present. The only acoustic test ever performed on a CCR was conducted at the National Gas Turbine Establishment (NGTE), U.K. on a very different design to that of the X-Wing. The rotor, an early prototype of I.C. Cheeseman's original CCR, was 3.7 m (12 ft) in diameter and utilized a circular airfoil section. Despite its relative crude design this rotor was found to produce virtually no rotational noise and approximately 5 dB reduction of broadband noise relative to a conventional rotor.

A direct application of current semiempirical theories indicates that the CCR should readily achieve large noise reductions by simply reducing tip speed. In the case of the X-Wing this is an attractive possibility because the rotor is *designed* for operation at all rpm's (resonances excluded). Furthermore, the blowing system and blade planform are designed by the high speed 'conversion' maneuver from rotary to fixed wing flight. This latter characteristic suggests that it may be possible to utilize the excess blowing power available in hover and at low speed to enable the rotor to operate at reduced tip speeds. These low tip speed possibilities appeared sufficiently promising that it was decided to investigate the acoustics of the CCR in greater detail. In particular, the need to either revise conventional theories or to develop new ones to account for the unique aerodynamic mechanisms of a CCR was quite apparent. As the research progressed, a very intriguing possibility appeared: due to the unique fluid mechanics of a low velocity boundary layer control wall jet operating over the curved Coanda surface and controlling the circulation, the aeroacoustic mechanisms were themselves unique. In fact, according to theory, a properly designed CCR will possess *major noise reductions relative to conventional rotors at identical operating conditions.* No less than *five* of the ten separate source mechanisms identified were found (theoretically) to be substantially reduced by the aeroacoustic characteristics of the CCR.

SYMBOLS

AR	aspect ratio
B	number of rotor blades
b/c	wake width-to-chord ratio
C_{d_p}	profile drag coefficient
C_{d_w}	'wake drag' coefficient

C_ℓ	lift coefficient
C_p	pressure coefficient
C_T	thrust coefficient
C_μ	jet momentum coefficient
c	chord length, m (ft)
D	rotor diameter (slot span), m
D/t	slot span-to-height ratio
f_p	peak SPL frequency
$f_{p\ell}$	'5 dB down' lower frequency
f_{pu}	'5 dB down' upper frequency
h	height, m
L/D_e	lift to equivalent drag ratio
M	Mach number
R	distance to microphone from source, m
R_N	Reynolds number
S	wing area (or rotor disk area), m^2
T/S	disk loading
t/c	slot height-to-chord ratio
V	velocity, m/s
X	dimensionless rotor radius
Z/c	downstream distance from trailing edge-to-chord ratio
α	angle of attack, deg.
γ	turbulence intensity
δ_w/c	wake vertical deflection-to-chord ratio
θ	microphone elevation with respect to rotor plane, positive downward, deg.
λ	planform taper ratio C_{tip}/C_{root} (or turbulence wave length)
σ	solidity ratio

Abbreviation

rpm	revolutions per minute

POTENTIAL BROADBAND NOISE SOURCES

The possible significant sources of so-called 'broadband' noise radiation from a CCR may be categorized as follows (refer to fig. 4):

(1) Classical 'trailing edge noise' (sometimes called 'vortex noise') associated with the turbulent interaction of the viscous shed wake (made up of the jet and boundary layers) and the rigid airfoil trailing edge.

(2) 'Laminar boundary layer instability noise' produced by an aeroacoustic feedback between viscous trailing wake pressure disturbances (apparently due to wake transition) and the instability point of the lower surface laminar boundary layer.

(3) 'Jet noise,' actually comprising several separate mechanisms: (a) free jet 'mixing noise' (in the case of a wake velocity excess); (b) free jet 'excess noise' produced by the interaction of the free jet turbulence with the rigid airfoil trailing edge; and (c) 'wall jet noise' produced by turbulent mixing and surface pressure fluctuations on the curved Coanda surface itself.

(4) 'Incident turbulence noise' produced primarily by the airfoil unsteady response to the normal component of the inflow turbulence (this source may also exhibit discrete noise spectra).

(5) Direct radiation from the separating surface boundary layer.

These source mechanisms are associated with the two-dimensional airfoil section. In addition, there is a potentially important three-dimensional 'tip radiation noise' which is:

(6) Produced by separated flow and high turbulence in the boundary layer region of the rotor tip.

POTENTIAL DISCRETE FREQUENCY NOISE SOURCES

The potential sources of 'discrete' or 'rotational' noise for the CCR appear to be essentially identical to conventional rotors as follows:

(7) 'Gutin' type noise due to the rotation of the blade steady forces.

(8) Noise associated with periodic variation of the blade forces due to variations of inflow angle and blade cyclic lift control.

(9) Under certain conditions where close vortex-blade interactions occur (such as steep descent and low shaft angles) additional impulsive blade pressure fluctuations are produced due to sudden changes of inflow angle, giving rise to blade 'bang.'

(10) As advancing tip Mach number increases the blade profile geometry (thickness distribution and chord) gives rise to combined monopole-dipole-quadrupole contributions which produce impulsive 'slap' noise.

BROADBAND NOISE REDUCTION WITH CC

(1) Trailing edge noise - A new theory of trailing edge noise has been developed which allows the calculation of both conventional rotors and circulation control rotors.* The theory indicates that the maximum sound intensity varies directly with the product of drag coefficient squared, velocity to the fifth power, and wake-based Strouhal number; and varies inversely with the dimensionless wake width. Figure 5 presents a comparison of this new theory for aircraft power-off fly over data from reference 6. Figure 6 presents a comparison of 'peak broadband excrescence noise' data as defined by Wright (ref. 7) and the trailing edge theory modified to include the effect of a source near the rotating rotor tip. It can be surmised that the theory is accurate, devoid of empiricism, and applicable to arbitrary airfoil, wing, or rotor configurations. To apply the theory to the CCR it is necessary to utilize two-dimensional airfoil data from tests of the applicable CC airfoil. Figure 7 shows measured variations of the trailing wake width and wake drag coefficients for the X-Wing tip section (as required by the theory). Figure 8 presents the calculated noise reduction boundaries based on this two-dimensional data (relative to the noise of a 'baseline' conventional NACA 0012 airfoil of equal chord at zero angle of attack). It can be noted that a relatively wide design corridor of lift coefficient and angle of attack is predicted wherein the *inherent* X-Wing trailing edge noise will be significantly lower than for a conventional rotor. (These curves are based only on the drag coefficient and wake width and do not reflect the additional reductions which accrue due to reduced tip speed and tip chord.) A measure of caution is needed when applying these two-dimensional test results to an actual rotor blade such as the X-Wing. The existence of obstructions upstream of the slot (such as air holes in the main spar) will produce some spanwise variation of the Coanda sheets. These 'shadows' induce three-dimensional effects which may modify the two-dimensional mechanism described.

---

*Presentation of the trailing edge noise theory will be made in a future paper due to space limitations.

(2) Laminar boundary layer instability noise - The presence of discrete acoustic tones has been detected in airfoil tests and glider fly over data. Tam (ref. 8) and Wright (ref. 7) have apparently separately identified the source of these tones as a result of a lower surface laminar boundary layer instability participating in an aeroacoustic feedback loop with the airfoil wake. Using the stability theory, the presence of this acoustic source has been identified on a CC lifting cylinder operating at very high lift coefficients. These calculations are directly applicable to the experimental data on the 3.7 m (12 ft) CC rotor tested by the NGTE (which employed circular sections). Figure 9 presents the calculated instability center frequencies for the experimental rotor hover data. These results suggest that the instability mechanism was, in fact, the *dominant* noise source for this (very quiet) low tip speed circular section CCR. Using a similar approach, the boundary layer stability of the X-Wing root and tip sections was calculated for a high-lift hover condition. Figure 10 presents calculations for several different rotor sizes and indicates that *the X-Wing should be entirely free* of this acoustic source. It should be noted, however, that these results are calculated for a small positive blade pitch setting such that the tip section is operating at zero angle of attack. At higher angles of attack or much lower tip speeds the lower surface boundary layer will tend toward full laminar flow.

(3) Jet Noise - The phenomena of CC jet noise was analyzed using a semi-empirical method developed from turbulent wall jet acoustic theory and limited experimental data from the NGTE (circular section) 3.7 m (12 ft) CCR measured with the rotor stopped. This data represents an extreme case because the Coanda wall jet actually curves 180 degrees around the airfoil section and then separates into quiescent surroundings, thus introducing wall jet, free jet mixing, and some trailing edge or slot edge noise as well as any 'upstream' noise due to turbulence from the internal air valving in the rotor head. Figure 11 presents the measured rotor jet noise in terms of the wall jet theory parameters. Two different observation angles, measured with respect to the rotor tip path plane, are included. The variation with jet Mach number can be seen to be quite different from conventional free jet theory at the low jet Mach numbers and varies not unlike the 'excess noise' of subsonic jet engines in this regime. Using the power law exponent variations derived from these data, the predicted jet noise and peak SPL frequency for the X-Wing are shown in figure 12. In view of the fact that relative velocity effects are known to have a significant noise reduction effect, it is concluded that the jet noise should be quite low over the high subsonic slot exit velocity range of the X-Wing. This conclusion is also in agreement with subjective assessments made during the NGTE tests, DTNSRDC CCR model rotor tests and tests of the Tip Air Mass

Injection System (TAMI) at NASA Langley. A note of caution is needed here, however. The large variation of the velocity exponent at low jet velocities suggests that there are at least two distinct phenomena which dominate the 'jet noise.' At high jet velocities the V^8_{jet} follows the expected trend and indeed appears to be jet mixing noise. At lower velocities the data suggests another source mechanism, quite possibly due to separated flow upstream of the jet exit. In this circumstance the 'jet noise' at low jet velocities would be strongly design dependent and would be sensitive to the details of the valving system and, in particular, to any separated flow close to the jet exit itself. The latter case is potentially of concern for the X-Wing flight demonstrator design where significant turbulence is introduced by air holes cut in the main spar.

(4) Incident Turbulence Noise - The most difficult noise source to calculate on the CCR is that due to variations of the inflow velocity over the disk. The resultant noise may contain both broadband and (if blade-to-blade correlation exists) also discrete components. The origins of the inflow variation on a rotor have been attributed to a variety of factors including blade twist, atmospheric turbulence, recirculation, tip vortex oscillations, etc. However, in a close examination of the rotor broadband mechanisms of a large variety of rotors, propellers, and fans under widely varying conditions, Wright (ref. 7) has reached the rather startling finding that these explanations do not adequately or consistently account for the arbitrary variations found in practice. Wright concluded that the incident turbulence (or 'excess broadband') noise mechanism is more likely "...intrinsically connected with the rotor, (and) appears to be supercritical on the slightest flow asymmetry."

One rather compelling argument in support of Wright's conclusion can be based on the unique experimental data of Schieman (ref. 9). Schieman's measurements of the noise of an untwisted rotor in hover and of a nonlifting, twisted rotor in axial flow strongly suggest that the viscous wake has a very marked effect. Figure 13 shows typical data from these tests. Reductions of as much as 15 dB in the comparative spectra were demonstrated when the (viscous) wake was 'blown' downstream by axial tunnel flow. The incident turbulence theory of Fink (ref. 10) has been modified to produce the correlation with Schieman's data shown in figure 14 (for a rotor operating in its own wake) where the independent parameters are the inflow turbulence intensity and turbulence wave length. A maximum turbulence intensity value of 16 percent was found to predict the maximum SPL. In view of the fact that typical normal turbulence levels in the free shear layer behind an airfoil can be on the order of 15 to 20 percent it seems quite plausible that the 'intrinsic' mechanism alluded to by Wright is actually a blade interaction with the viscous shed wake behind a preceding blade. It is possible that these wakes 'stack up' on each other, layer upon layer, with a separation dependent on the downwash velocity through the disk. Any slight perturbation of the layer would then result in a small change of circulation on the following blade due to the redistribution of the inplane velocity normal to a given span station (the blade element is essentially experiencing stratified flow). A change of circulation produces a shed wake which further perturbs the viscous layer (and so forth) until a system of 'standing waves' is set up around the azimuth.

Based on the preceding theoretical correlation, a calculation of the incident turbulence noise can be attempted for the CCR. Using measured airfoil data and corrections for three-dimensional effects, the wake deflection and turbulence intensity encountered by the following blade was estimated as shown in figure 15. The turbulence encountered by the following blade is assumed to vary directly with the drag coefficient (from mixing length theory for a free wake) and inversely with the wake deflection (lift). It can be noted from these calculations that for values of section lift coefficient greater than 0.5 the incident turbulence noise due to self-induced wake phenomena would be negligible.

The validity of the preceding explanation of incident turbulence noise has yet to be fully confirmed despite the encouraging correlation of figure 14. Certainly the apparent absence of incident turbulence noise from the high lift NGTE CCR data is encouraging. However, the basic incident turbulence acoustic mechanism is heavily dependent on the rate of change of surface pressure with incidence, particularly close to the leading edge. The circular sections of this rotor exhibit very low gradients ($dC_p/d\alpha$), hence the final conclusion is not obvious. In any event, the possibility of other incident turbulence sources cannot yet be discounted for the CCR as embodied on the X-Wing. In the absence of other solutions, the use of reduced tip speeds may be required to finally suppress this noise.

(5-6) Direct boundary layer noise and 'tip radiation noise' - Direct radiation from the attached turbulent boundary layers has been shown by several investigators to be about two orders of magnitude below other broadband sources. However, if separated flow exists, the levels of fluctuating surface pressure may be as much as 30 dB higher than for the attached case. The regions where separation may occur on a CCR are (a) just beneath the separating wall jet and (b) at the rotor tip. The former case is apparently the same phenomena as the trailing edge noise discussed previously. This can be deduced from cross correlations on conventional airfoils of the normal component of turbulence and the pressure in the separated zone at the trailing edge. (The physical problem is actually one of sound refraction about the edge from the turbulent quadrupole source.) The situation at the rotor tip is rather unclear at present. However, there is sufficient experimental information available to definitely relate tip drag to noise level. The emerging picture of the phenomena is quite complex. The high velocity air sweeping up around the rotor tip entrains the lower surface boundary layer and encounters a retarding pressure gradient along the highly curved tip surface. The (entrained) boundary layer separates under these conditions giving rise to a separation locus in the streamwise direction, on the rotor tip proper. The separated flow then sweeps up and over and forms a reattachment line inboard of the tip (similar to a delta wing vortex). The separating viscous fluid forms the well known 'vortex core' with a considerably higher velocity defect and turbulence level than the inboard airfoils. It is quite possible that this turbulence interaction with the blade tip and trailing edge is the dominant broadband noise mechanism of the tip - not unlike the trailing edge noise mechanism discussed previously. (Other source mechanisms may also be present; for example, Cheeseman has noted that the vortex location fluctuates more with 'noiser' tips, apparently giving rise to increased rotational noise.)

The approach taken to reduce this noise mechanism for the X-Wing tip was to develop a design which, in concept, essentially eliminated it. Such a design (shown in fig. 16) is a simple rotation of the Coanda surface about the tip airfoil midchord. The Coanda jet then extends around the tip, blowing in the spanwise direction. Tuft and oil measurements of this design (tested as a wing tip) indicate that: (a) the tip region with tip blowing 'off' was partially separated, but with blowing 'on' was observed to be fully attached; (b) the tip vortex actually formed off of the tip, approximately in the plane of the blade (as shown in fig. 17); and (c) that the measured drag was significantly reduced at high lift (fig. 18). The overall aerodynamic efficientcy (measured as a fixed wing equivalent lift to drag ratio, L/D_e) did not increase however, due to the additional blowing power required. The conclusion drawn from this work is that the potential high frequency broadband source of the rotor tip should be essentially eliminated by the Coanda tip design.

DISCRETE FREQUENCY (ROTATIONAL) NOISE REDUCTION WITH CC

(7-8) 'Gutin' noise and blade load variation - The Lowson-Ollerhead theory (ref. 11) for predicting the noise due to both steady and unsteady blade loads is directly applicable to the CCR. The primary uncertainty in this theory is the determination of the proper harmonic order and magnitude for the blade lift force. Several studies have indicated the need for inclusion of additional loading harmonics - depending on the blade twist. (In general, an increase in blade twist produces a more uniform downwash distribution with fewer wake distortions.) For the X-Wing, the hover downwash distribution can be 'designed' to be very close to ideal by choice of either collective pitch setting, and/or slot height distribution. Figure 19 illustrates this point by showing the predicted downwash variation for the X-Wing at various collective pitch settings with a simple linear slot height distribution. This design feature, in conjunction with the 'velocity independence' aspect of a CC airfoil and a more uniform chordwise loading profile, should permit the X-Wing to enjoy the more rapid fall-off in loading harmonics given by the unmodified theory. Figure 20 presents the predicted rotational noise for the X-Wing in hover at various tip speeds (a case applicable to low speed forward flight is also shown).

(9) Vortex-blade interaction noise - The potential of the CCR for reducing impulsive 'bang' noise is largely unknown at present; however, the application of available theory suggests that the rotor may not produce this source at all. According to Leverton's theoretical and experimental analysis of blade 'bang' (ref. 12), the sound pressure level is given by

$$\mathrm{SPL}_n = 10 \log_{10} [V^4 A_n^2 (r_o - r_1)^2] + \text{constant}$$

where, V is the velocity of the blade passing through the vortex, A_n is the amplitude of the nth harmonic of the blade upwash velocity, and $(r_o - r_1)$ is the span width over which the gust acts. One major noise reduction effect with the CCR is the intersection velocity produced by operation at lower tip speeds (higher C_T/σ). In the case of the X-Wing with Coanda tip blowing, the peak vortex core tangential velocities are expected to be reduced due to the increased mixing produced by the jet. Wake vorticity measurements by Rochester Applied Science (ref. 13) on a similar normal blowing tip design (fig. 21) indicated a reduction of the peak core velocities of more than 50 percent, a doubling of the core radius and an outboard shift of the vortex position. The latter effect (shown in fig. 17) was measured with the Coanda tip installed on a fixed X-Wing blade. Furthermore, model rotor acoustic testing of the tip air mass axial injection system (ref. 14) showed marked reductions of blade 'bang' intensity (fig. 22). The axial system is believed to produce less efficient mixing and peak velocity reductions than the present Coanda design. Application of the Leverton equation using the measured velocity profiles and a rotor tip speed of 167 m/s (550 ft/sec) indicates that the X-Wing blade vortex noise will be below the subjectively significant level.

(10) Blade Slap - Operations in a flight condition where blade slap may be produced is not anticipated for X-Wing (except possibly for a short duration near conversion speeds). The various source mechanisms associated with high speed impulsive noise, or blade slap, are currently undergoing intensive study. Research by Schmitz (ref. 15) and others indicated the primary factors to be: (a) advancing tip Mach number; (b) blade thickness, thickness distribution, and chord near the rotor tip (chord appears to be the dominant term); (c) blade drag; and (d) the existence of shock waves. In the case of the X-Wing with generally low tip speeds, the primary effect of advancing tip Mach number will be reduced (except close to the speed for conversion to a stopped mode). Furthermore, although the section thickness ratio is high at the tip (15 percent for an X-Wing CCR relative to 6-10 percent for a conventional rotor), the blades incorporate a 2:1 planform taper so that the *dimensional* thickness and chord are actually somewhat reduced. For example, assuming an X-Wing CCR and a conventional rotor of the same diameter, number of blades, and solidity (but with much lower tip speeds, for example 152 m/s (500 ft/sec) for CCR and 213 m/s (700 ft/sec) for the 10 percent thick conventional rotor), the CCR would have equal thickness but only 2/3 the chord dimension.

In the case of the blade drag (c) the lower chord and generally lower advancing tip speeds appear to more than offset the somewhat higher drag coefficients found on the advancing side of the X-Wing. The transonic behavior of a CC airfoil operating near zero angle of attack and zero lift is determined by the off-setting effects of high thickness ratio and the near optimum elliptical thickness distribution. As a consequence the 15 percent ellipse has a critical Mach number of 0.75 compared with approximately 0.78 for a 10 percent symmetrical airfoil. It can therefore be seen that even the shock phenomena would appear to be reduced when accounting for the smaller blade chord.

PERFORMANCE AND WEIGHT PENALTIES

The X-Wing is a unique VTOL concept which can potentially extend the application of rotorcraft into several different areas where noise is an important factor. The apparent favorable modification of fundamental acoustic mechanisms may actually produce a quieter rotor at the nominal 204 m/s (670 ft/sec) 'baseline' X-Wing CCR design tip speed. It may also be desirable, however, to fully exploit the variable rpm capability and excess hover 'blowing' capacity of this rotor. It is useful, therefore, to perform a preliminary assessment of the design penalties which are incurred by operation at reduced tip speeds and higher blowing levels.

Figures 23 and 24 present the calculated variations of hover power components of a 15.2 m (50 ft) diameter X-Wing. Constant rotor thrust is prescribed so that, with the rotor geometry specified, only the collective pitch and blowing level are varied with tip speed to tradeoff shaft 'torque' power and blowing power. An antitorque fan was designed for the 'baseline' configuration of the study and perturbed slightly for other designs. It can be noted from the trends that total power is relatively insensitive to a large range of tip speeds – a sharp contrast with conventional rotors. Another interesting aspect is the variation of rotor shaft torque. As tip speed is reduced the increased blowing allows the 'torque' power (profile, pumping and induced power) to also reduce so that the torque itself vaires only weakly with rpm.

A general conclusion which may be deduced from the preceding example is that a CC rotor of X-Wing planform can perform efficiently at low tip speeds without the necessity to increase blade chord. For tip speeds in the range of 167 m/s (550 ft/sec) essentially *no power penalty* is incurred relative to the 204 m/s (670 ft/sec) 'baseline' design tip speed. The actual shaft power is reduced so that in a propulsion system design which provides the blowing air from an independent source (such as fan bypass air) the engine shaft power and size would actually be slightly *reduced* by about 5 percent. The increased blowing power requirement of almost 50 percent is the price paid for reduced tip speed with no rotor geometry change and only a small (6 percent) increase of torque. However, for the X-Wing the blowing power is inconsequential in view of the excess installed to perform the conversion maneuver.

The design weight penalty to operate at lower rotor tip speed is not amenable to simple treatment for the X-Wing. The rotor geometry and blowing power are actually designed by forward flight (conversion) requirements so that it is necessary to conduct a complete design study to assess the overall impact. The propulsion system selection is also inextricably involved in such a study because of the sharing of torque power and blowing power. Figure 25 illustrates one of several possible schemes for providing rotor torque, blowing air, and propulsive power. The figure depicts variable pitch fans providing power at high rpm directly to a centrifugal compressor and then into a main gear box. This arrangement permits extraction of the blowing power on the high rpm side of the transmission thus significantly reducing the maximum transmission torque requirement. A further advantage of this propulsion system is the quietness potential of the variable pitch propulsion fan which may either be operated at low pitch settings or decoupled entirely.

An indication of the weight trend associated with reducing tip speed for this particular propulsion system is shown in figure 26. For the present example no additional rotor system weight or compressor weight is introduced by low rpm operations as these components are both designed by the conversion flight condition. In effect, only the drive system and tail fan weights are impacted by the low rpm requirements.

These results are very encouraging in that they imply a net weight penalty of only about 0.5 percent to drop tip speed from the baseline 204 m/s (670 ft/sec) to 167 m/s (550 ft/sec) for low rotor noise. However, they do not encompass the additional weight penalties which would be incurred in *quieting the tail fan*. The 'baseline' tail fan is unacceptably noisy and would require a 30-40 percent reduction in tip speed and a large increase in diameter to achieve compatible PNdB levels with the main rotor. The proper calculation of this penalty is complex and beyond the scope of this paper. It is worthwhile mentioning, however, that a large diameter antitorque tail fan is not the only means possible to produce large moments, low weight, and low noise. An interesting alternate approach is to incorporate circulation control on the aft fuselage itself as sketched in figure 27. The fuselage would operate in downwash velocities on the order of 18 m/s (60 ft/sec) and with a thick elliptical cross section it could easily generate lift coefficients of 5.0 or more in an extremely efficient manner. A rough calculation for the civil X-Wing design indicates that a very efficient antitorque system would be possible. The CC fuselage blowing will not be a replacement for a tail fan (or internal fan), which is required for certain flight conditions where the main rotor wake is skewed off of the fuselage. However, during hover and low speed flight it should significantly unload the primary controller thus producing a lower weight, lower power solution to the antitorque noise problem. It is significant to note that first mention of this concept was made in one of the earliest landmark analyses of helicopter noise by Davidson and Hargest in 1965 (ref. 1). More recently (1978) Logan (ref. 16) has actually implemented the concept with considerable success in the OH-6A light helicopter.

CONCLUSIONS AND RECOMMENDATIONS

The present theoretical study focused on the fundamental aeroacoustic mechanisms of the Circulation Control Rotor. There appears to be an excellent inherent potential with the CCR for making major advances in the reduction of rotorcraft noise without incurring significant performance and weight penalties. The single outstanding source requiring further definition is the incident turbulence noise. If, as suggested herein, the dominant contributor to incidence fluctuations is the wake of the preceding blade, then the problem is amenable to direct control by CC. In this case the entire noise spectrum would be suppressed down to the (very low) trailing edge and jet noise levels without recourse to reduced tip speeds. If however, there are other more significant causes (for example, atmospheric turbulence) then it will be necessary to reduce tip speed. Quite apparently, the next logical step is to conduct a careful acoustic experiment to both resolve this key issue and also to explore the other theoretical claims.

With regard to the overall X-Wing civil concept, the antitorque system requires further definition. In particular, fuselage-mounted Coanda blowing, the fan-in-fuselage, and circulation control incorporated on the antitorque fan itself all appear worthy of further consideration.

REFERENCES

1. Davidson, J. M.; and Hargest, T. G.: Helicopter Noise, Jol. of the Royal Aeronautical Society, vol. 69, May 1965, pp. 325-336.

2. Cheeseman, I. C.: The Application of Circulation Control by Blowing to Helicopter Rotors, Jol. of the Royal Aeronautical Society, vol. 71, no. 679, July 1967.

3. Williams, R. M.: The Application of Circulation Control to a Stopped Rotor Aircraft, vol. 1, no. 1, VERTICA, Pergammon Press, 1976.

4. Stone, M. B.; and Englar, R. J.: Circulation Control - A Bibliography of NSRDC Research and Selected Outside References, Naval Ship Research and Development Center Report 4108, Jan. 1974.

5. Gibs, J.; Stepniewski, W. Z.; and Spencer, R.: Effects of Noise Reduction on Characteristics of a Tilt-Rotor Aircraft, Jol. of Aircraft, vol. 13, no. 11, Nov. 1976, pp. 919-925.

6. Fink, M. R.: Approximate Prediction of Airframe Noise, Jol. of Aircraft, vol. 13, no. 11, Nov. 1976, pp. 833-834.

7. Wright, S. E.: The Acoustic Spectrum of Axial Flow Machines, Institute of Sound and Vibration Research, University of Southampton, Rep. 69, Apr. 1975.

8. Tam, C. K. W.: Discrete Tones of Isolated Airfoils, Jol. of the Acoustical Society of America, vol. 55, no. 6, June 1974, pp. 1173-1177.

9. Schieman, J.; et al: Rotating-Blade Vortex Noise, Mideast Region Symposium on Status of Testing and Modeling Techniques for V/STOL Aircraft, Essengton, Pa., Oct. 1972.

10. Fink, M. R.; Schlinker, R. H.; and Amiet, R. K.: Prediction of Rotating-Blade Vortex Noise from Noise of Nonrotating Blades, NASA CR-2611, Mar. 1976.

11. Lowson, M. V.; and Ollerhead, J. B.: A Theoretical Study of Helicopter Rotor Noise, Jol. of Sound and Vibration, vol. 9, Mar. 1969, pp. 197-222.

12. Leverton, J. W.: Helicopter Noise - Blade Slap, (Part 1: Review and Theoretical Study), NASA CR-1221, Oct. 1968.

13. Shipman, K. W.; White, R. P.; and Balcerak, J. C.: Drag Reduction of a Lifting Surface by Alteration of the Forming Tip Vortex, Rochester Applied Science Associates, Rep. 74-06, May 1974.

14. White, R. P.: Wind Tunnel Tests of a Two Bladed Model Rotor to Evaluate the TAMI System in Descending Forward Flight, Systems Research Laboratories, Inc., SRL Rep. 14-76-2, 1976.

15. Schmitz, F. H.; and Yung, H. Yu: Theoretical Modeling of High-Speed Helicopter Impulsive Noise, Third European Rotorcraft and Powered Lift Aircraft Forum, Aix-En-Provence, France, Sept. 1977.

16. Logan, A. H.: Evaluation of a Circulation Control Tail Boom for Yaw Control, USARTL-TR-78-10, Mar. 1978.

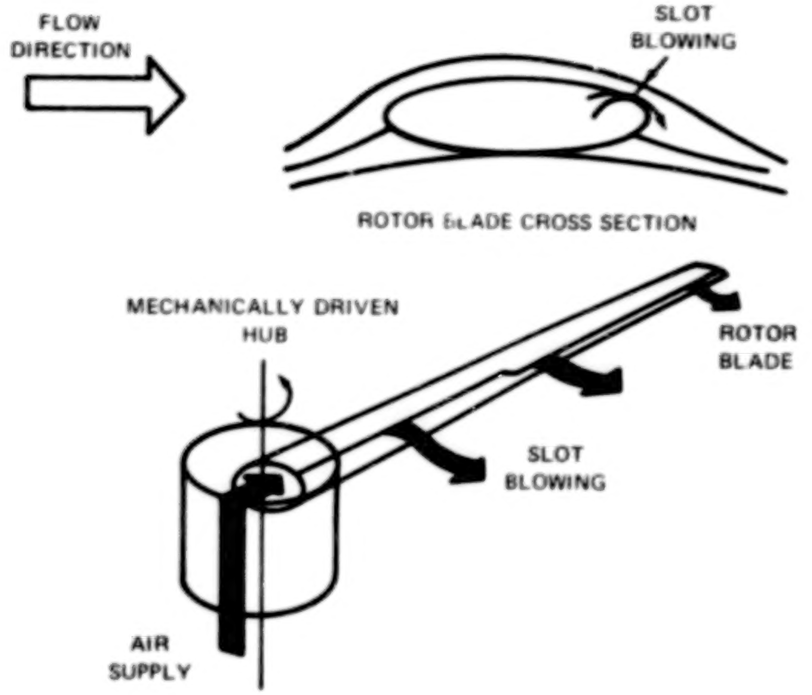
FLOW DIRECTION
SLOT BLOWING
ROTOR BLADE CROSS SECTION
MECHANICALLY DRIVEN HUB
ROTOR BLADE
SLOT BLOWING
AIR SUPPLY

Figure 1.- Circulation Control Rotor — basic concept.

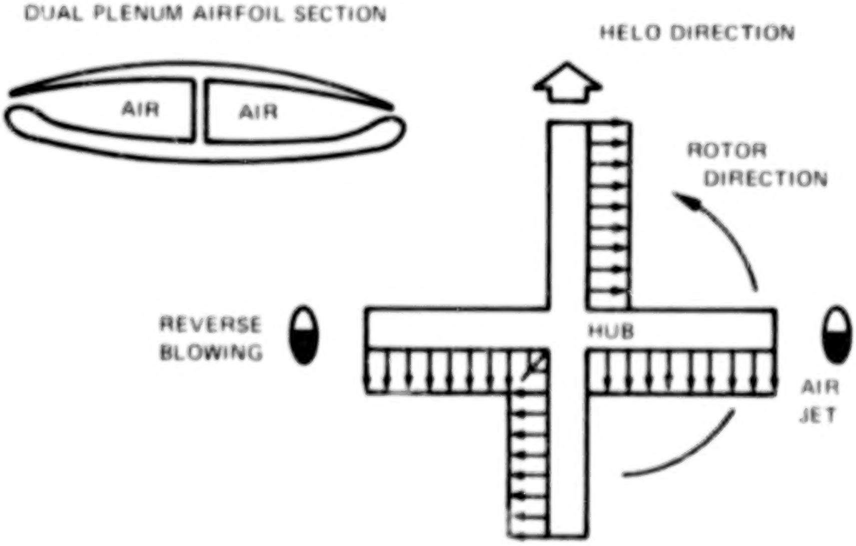
DUAL PLENUM AIRFOIL SECTION
AIR
AIR
HELO DIRECTION
ROTOR DIRECTION
REVERSE BLOWING
HUB
AIR JET

Figure 2.- Dual blowing concept for operation at high advance ratios and during conversion of the X-Wing.

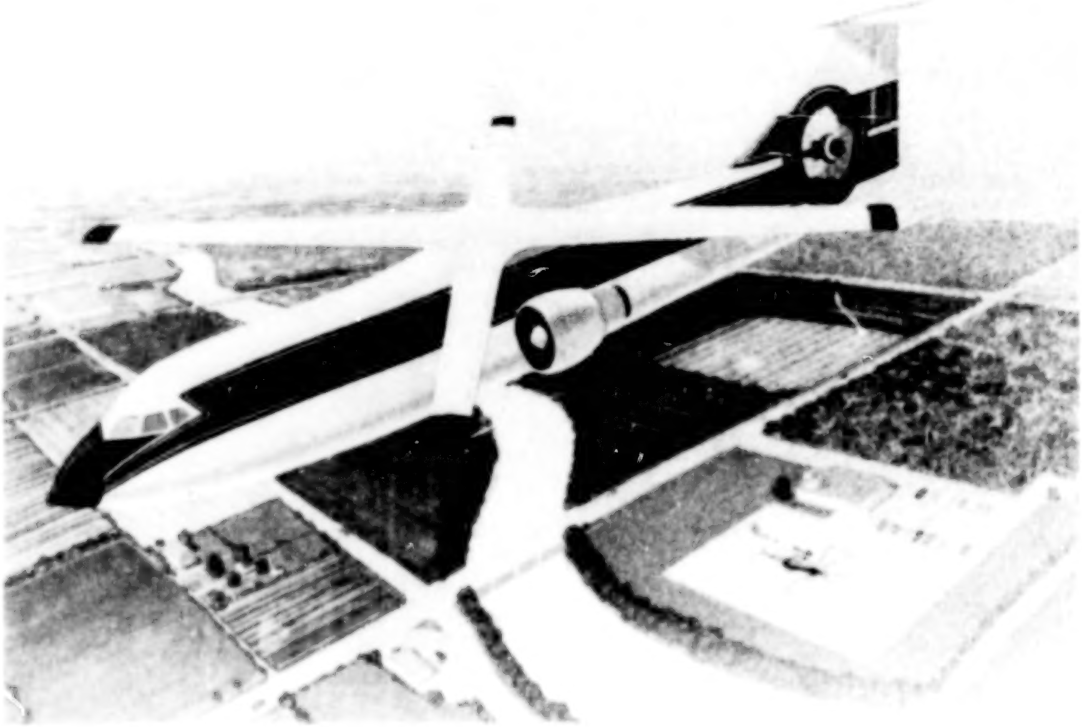

Figure 3.- Conceptual X-Wing civil transport.

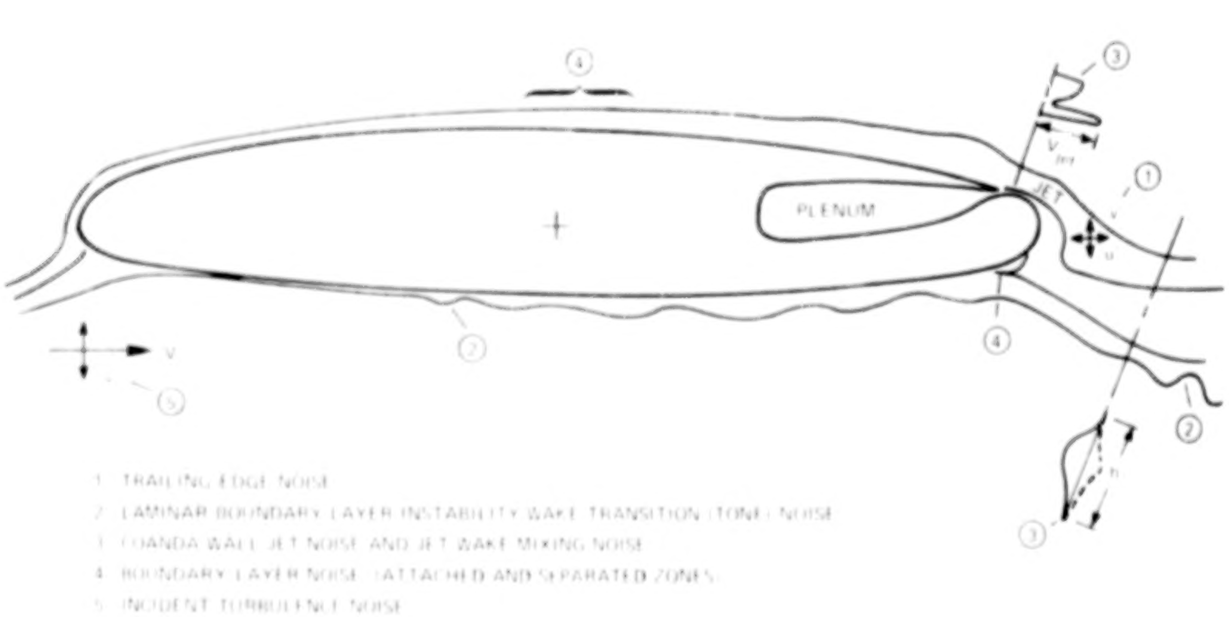
④
③
V_{jet}
JET
①
PLENUM
u
v
V
②
④
⑤
②
h
③
1 TRAILING EDGE NOISE
2 LAMINAR BOUNDARY LAYER INSTABILITY WAKE TRANSITION (TONE) NOISE
3 COANDA WALL JET NOISE AND JET WAKE MIXING NOISE
4 BOUNDARY LAYER NOISE (ATTACHED AND SEPARATED ZONES)
5 INCIDENT TURBULENCE NOISE

Figure 4.- Potential broadband noise mechanisms of a Circulation Control airfoil.

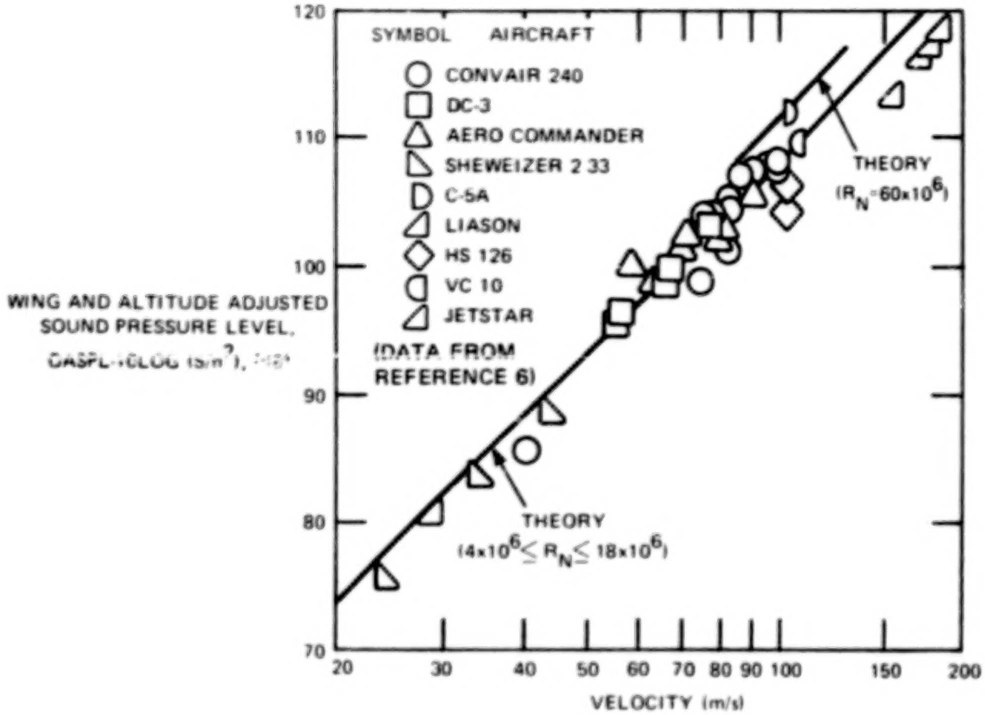

(a) Measured and calculated OASPL for conventional airframes with retracted gear and flaps.

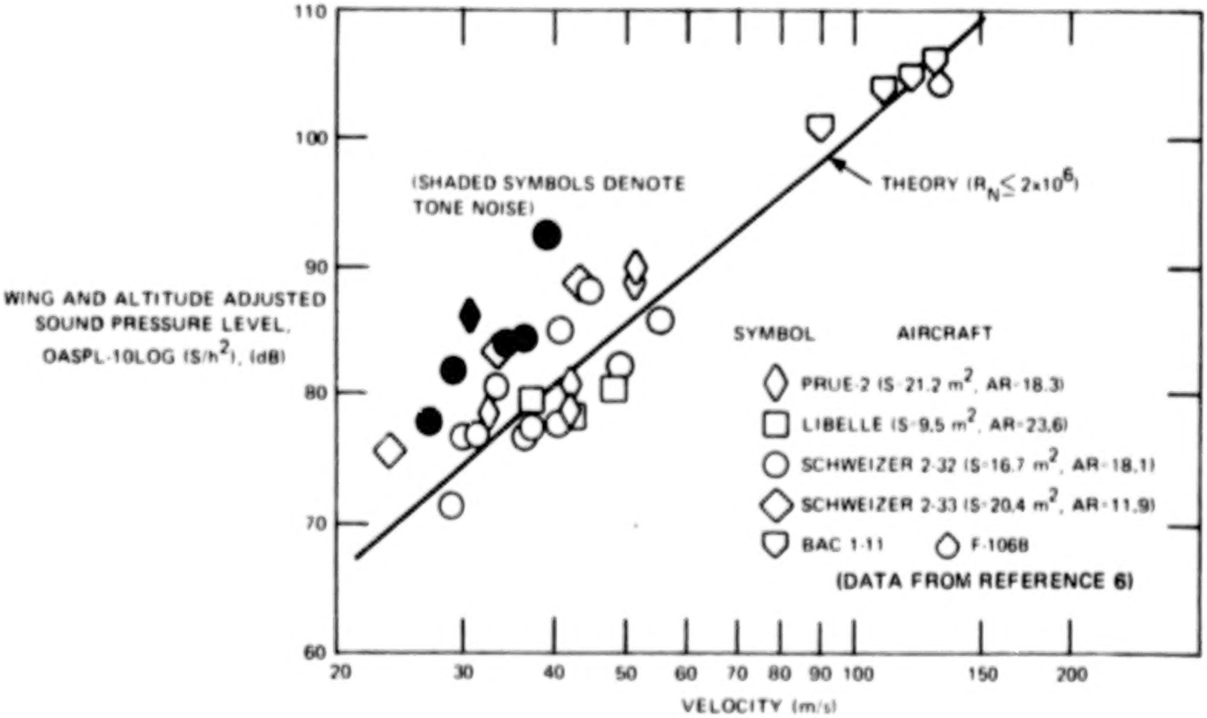

(b) Measured and calculated OASPL for low drag aircraft (primarily gliders).

Figure 5.- Comparison of new trailing edge noise theory with fly-over data.

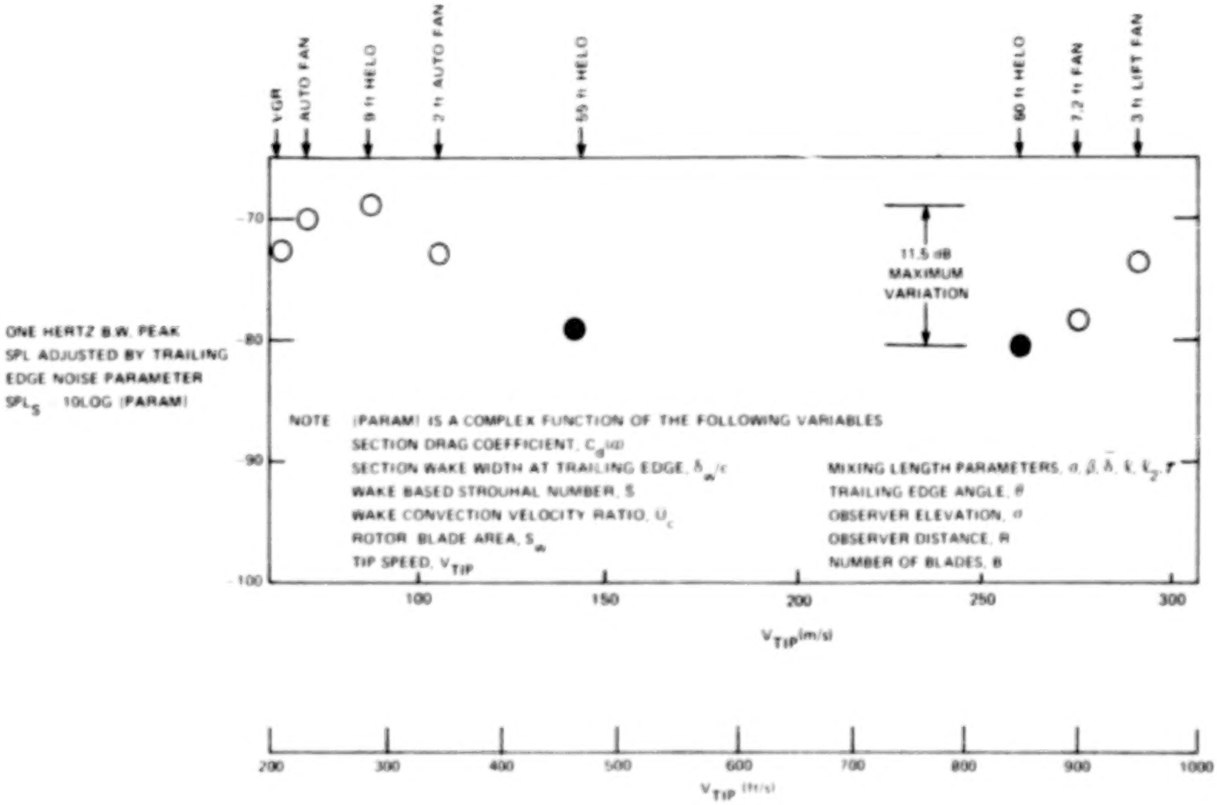

Figure 6.- Evaluation of new trailing edge noise theory using the peak broadband excrescence data of Wright (ref. 7). (1 ft = 0.3048 m.)

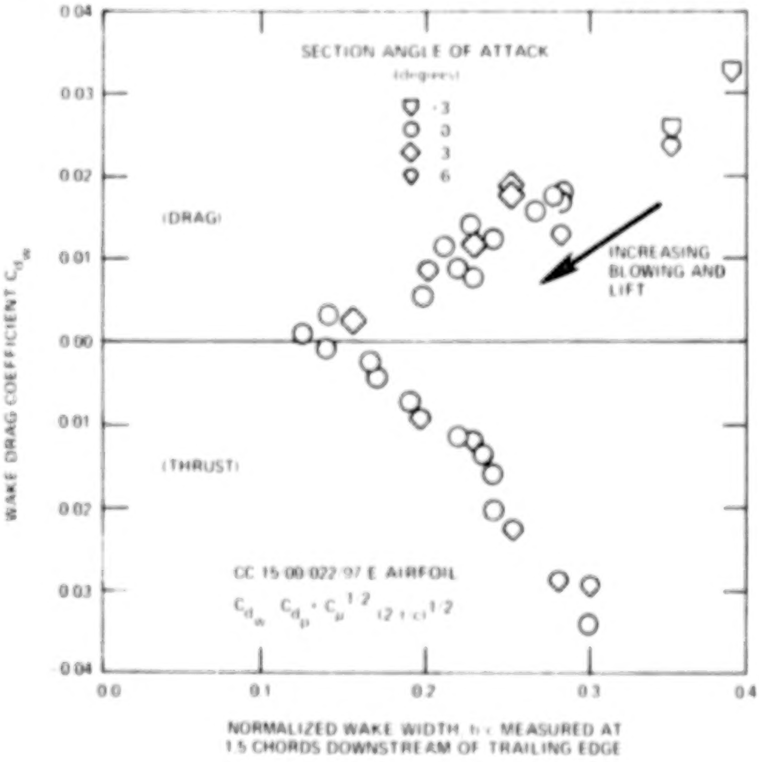

Figure 7.- Measured variation of the viscous wake width of the X-Wing tip section with wake drag coefficient.

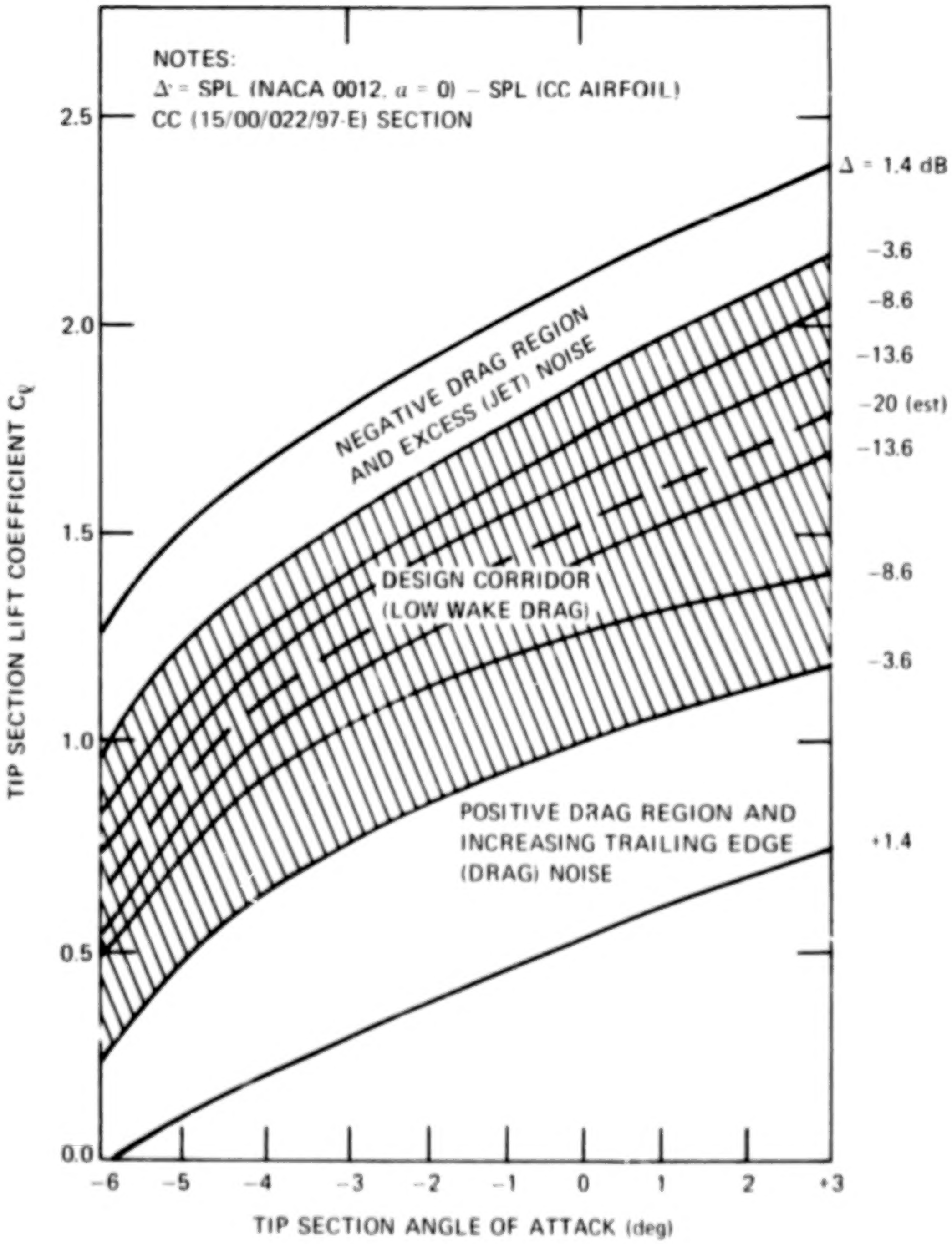

Figure 8.- Predicted trailing edge noise reduction of the X-Wing tip section relative to a NACA 0012. (Reference airfoil at zero angle of attack and lift.)

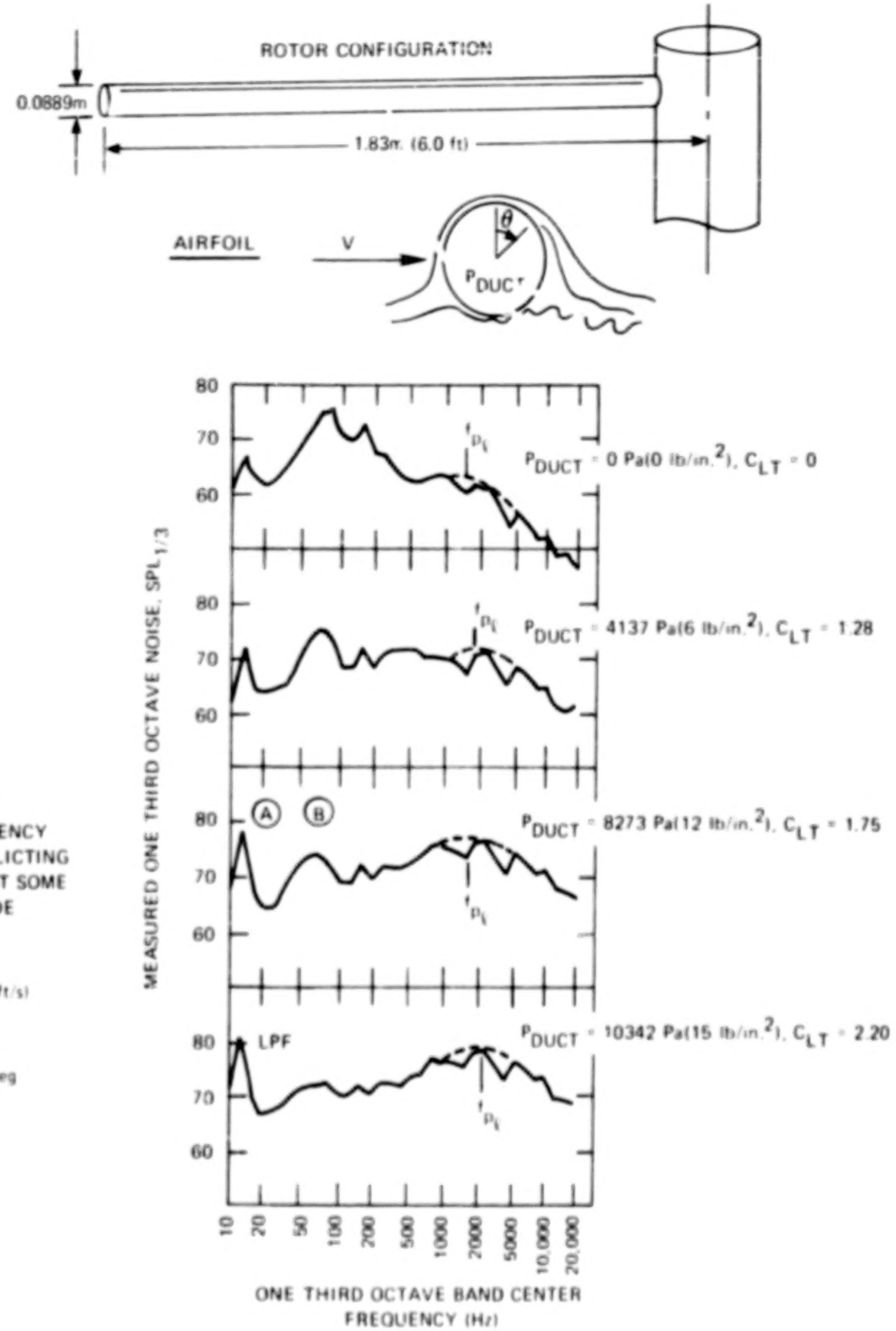

NOTES:

f_{p_ℓ} IS THE MINIMUM ALLOWABLE FREQUENCY FOR TOLLMEIN-SCHLICTING WAVES TO OCCUR AT SOME POINT ON THE BLADE

2 BLADES
V_{TIP} = 78.3 m/s (257 ft/s)
C_{LT} = $2(C_T/\sigma)$
RADIUS/DIA = 3.0
ELEVATION, θ = 45 deg

Figure 9.- Comparison of experimental data with stability theory for the 3.66 m (12 foot) NGTE CCR.

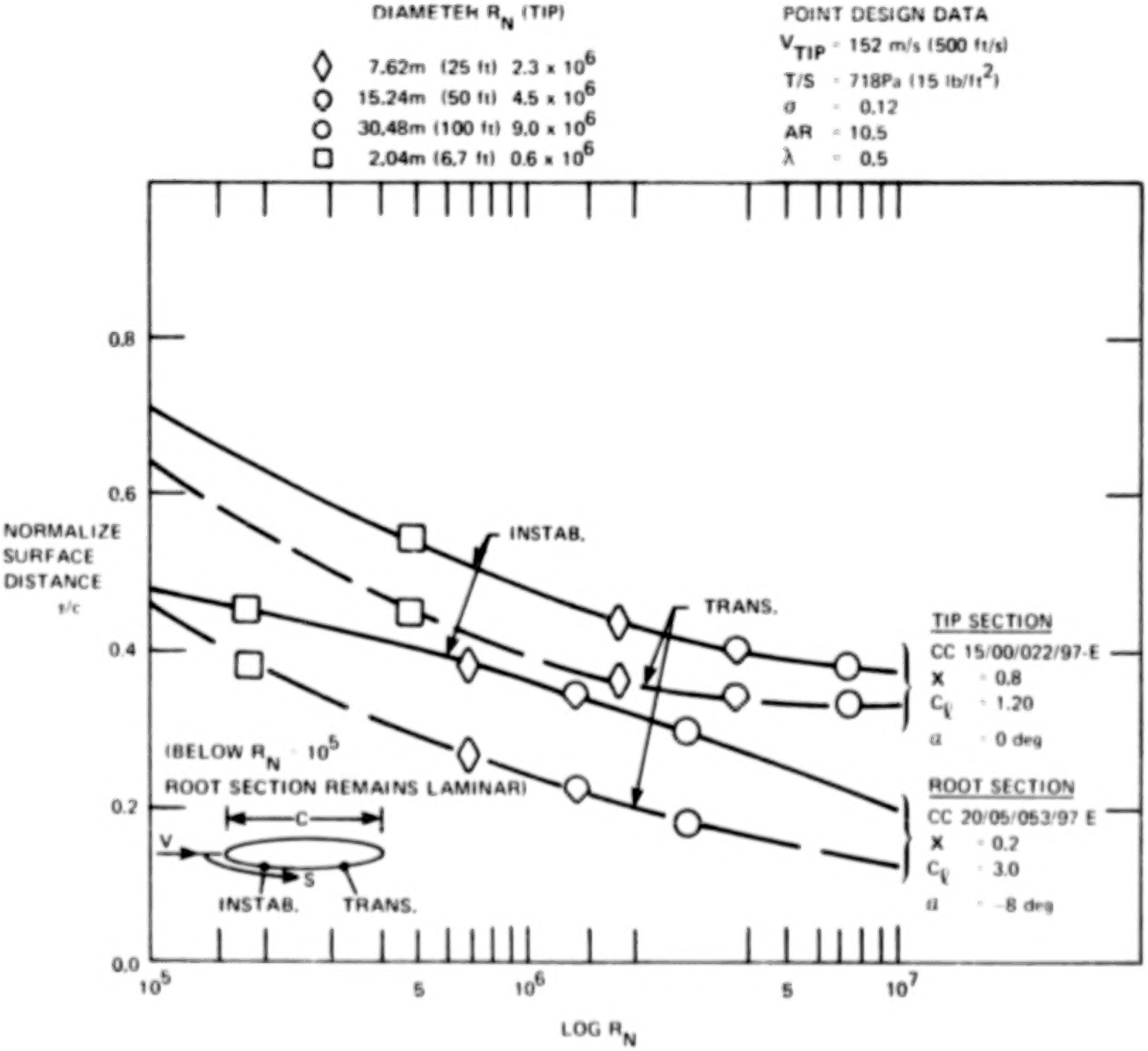

Figure 10.- Calculated instability and transition points for the X-Wing root and tip sections (demonstrating transition and hence avoidance of instability tone noise mechanism).

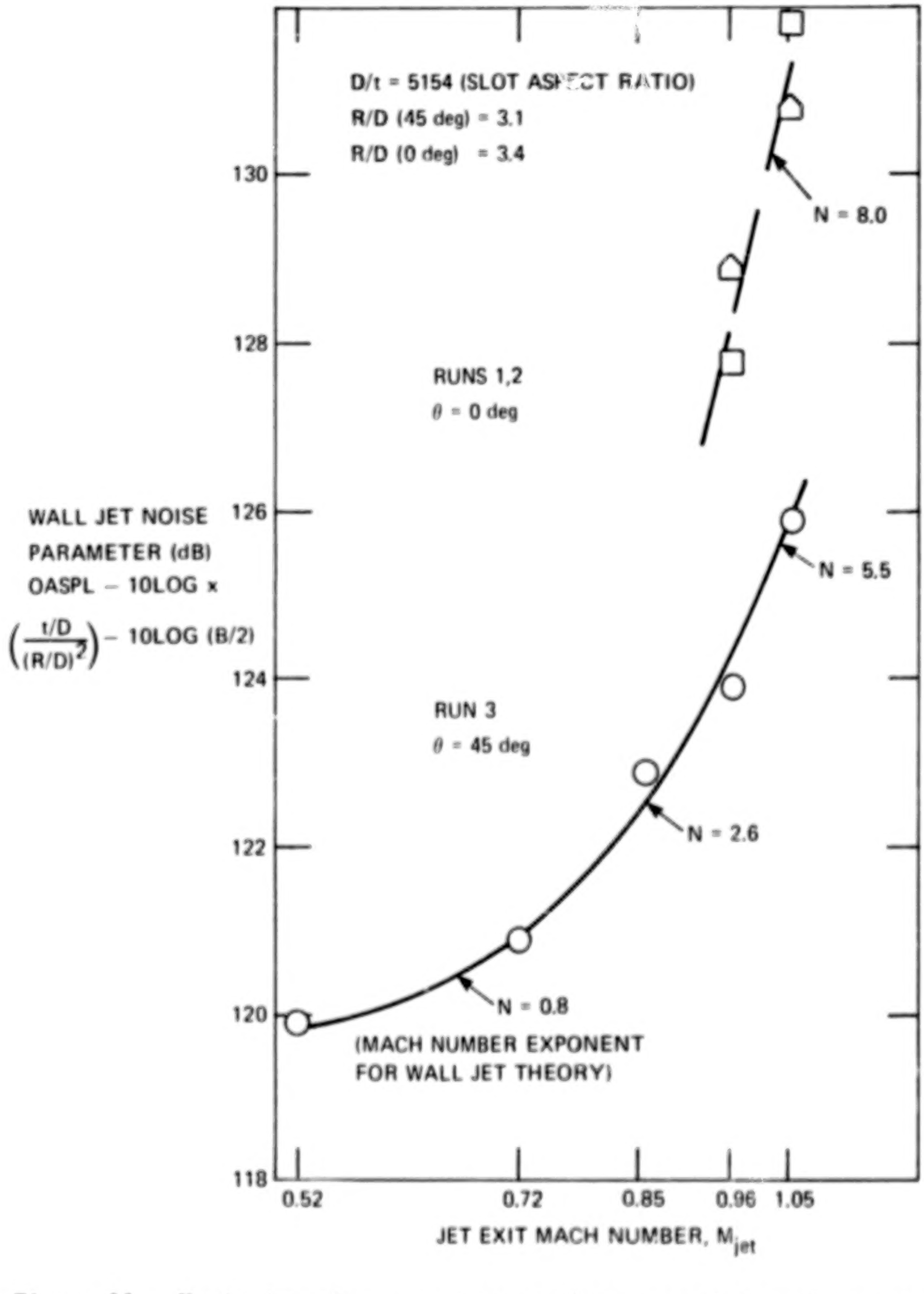

Figure 11.- Variation of measured Coanda 'jet noise' from NGTE 3.66 m (12 foot) CCR tests.

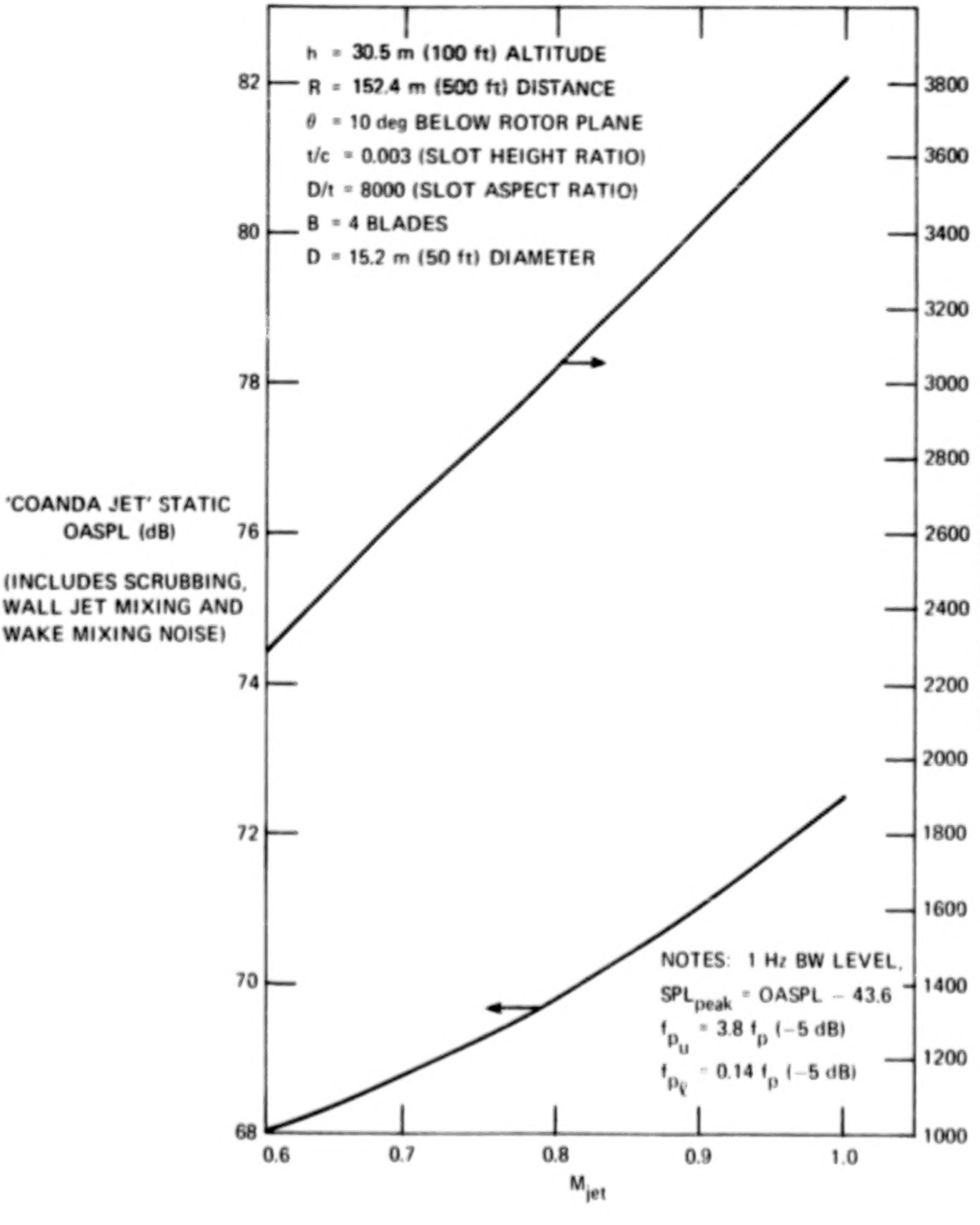

Figure 12.- Calculated 'Coanda jet' OASPL and frequency for a 15.2 m (50 foot) diameter (static rotor-worst case).

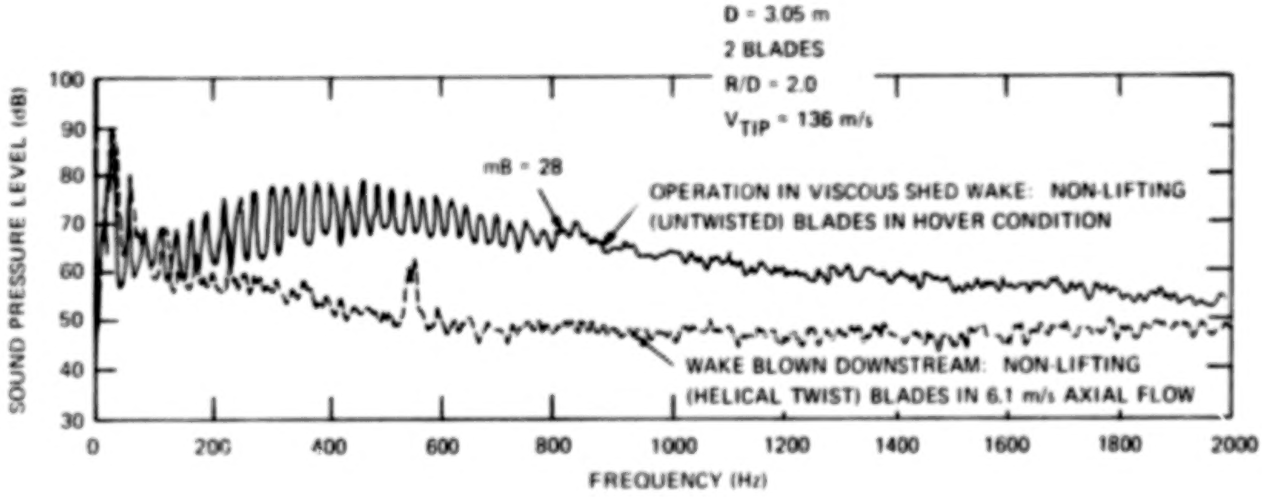

Figure 13.- Incident turbulence noise produced by two nonlifting NACA 0012 rotors (from ref. 9).

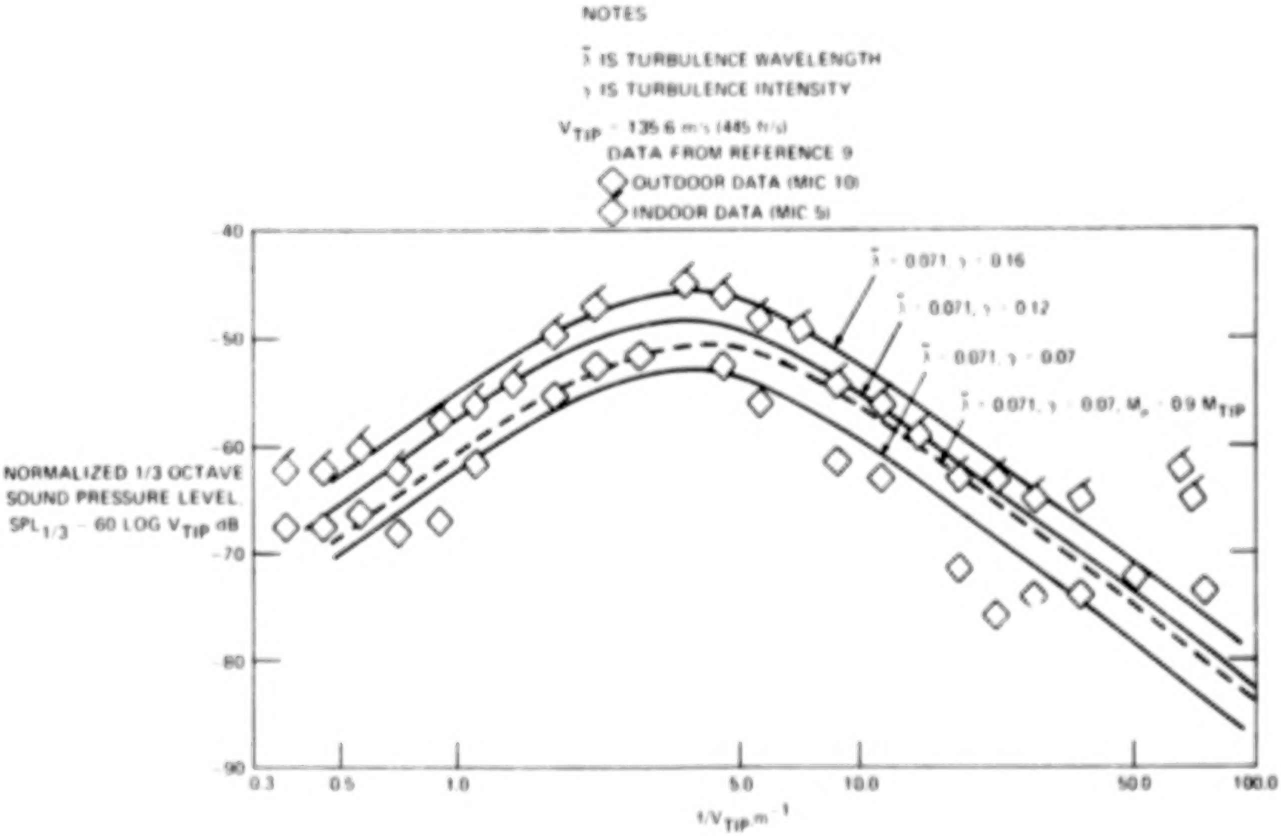

Figure 14.- Comparison of experimental incident turbulence data for an untwisted NACA 0012 rotor operating in its own viscous wake (zero lift) and incident turbulence theory modified from reference 10.

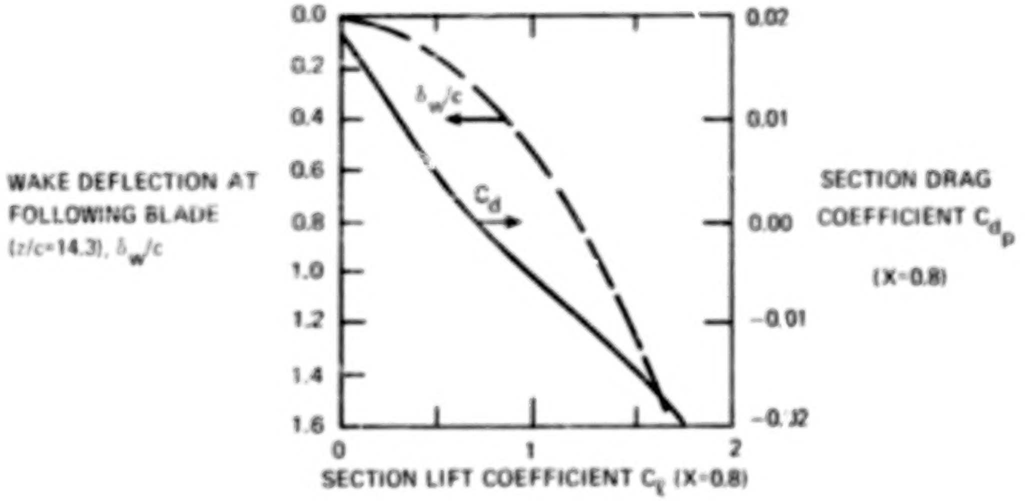

(a) Estimated wake deflection with lift variation.

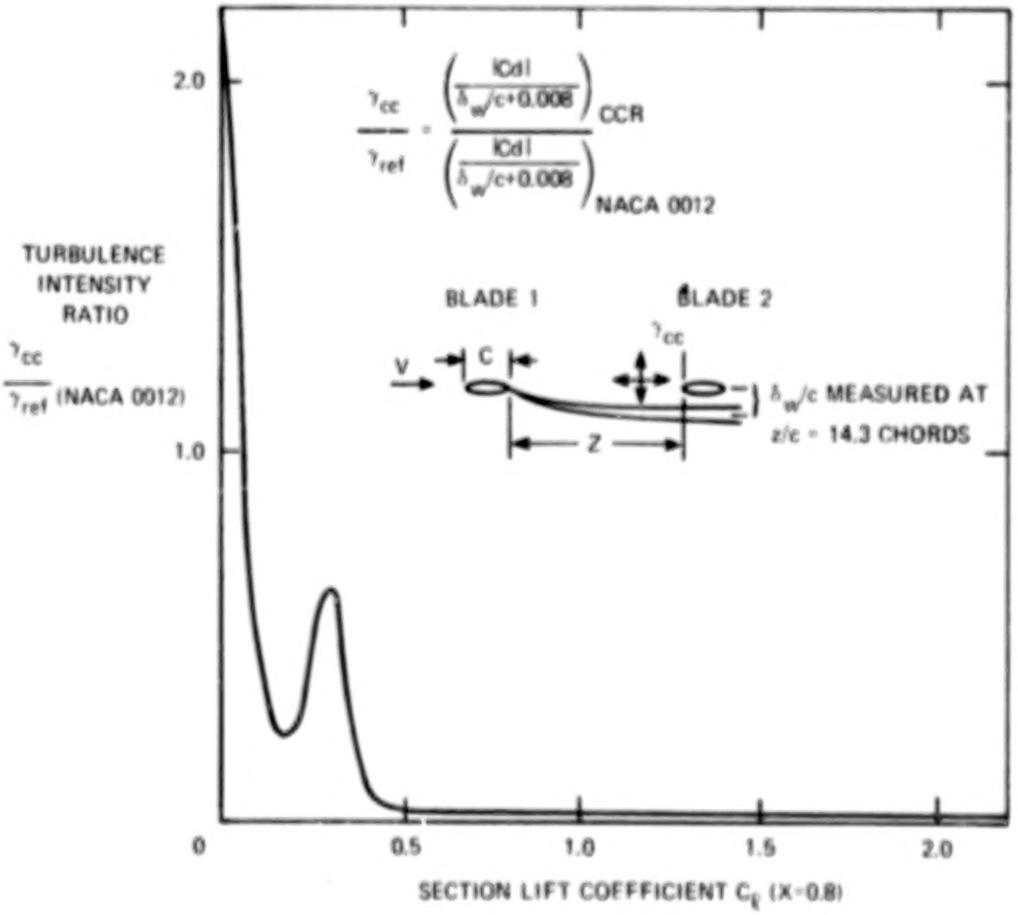

(b) Variation of turbulence intensity ratio with lift.

Figure 15.- Estimated viscous wake deflection and turbulence intensity of X-Wing tip section (relative to an untwisted NACA 0012 rotor operating in its own wake).

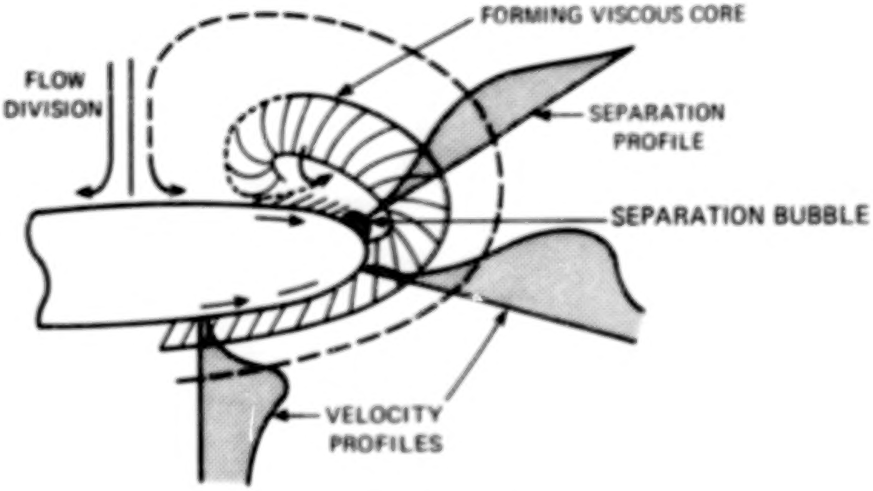
FORMING VISCOUS CORE
FLOW DIVISION
SEPARATION PROFILE
SEPARATION BUBBLE
VELOCITY PROFILES

(a) No blowing – vortex core inboard.

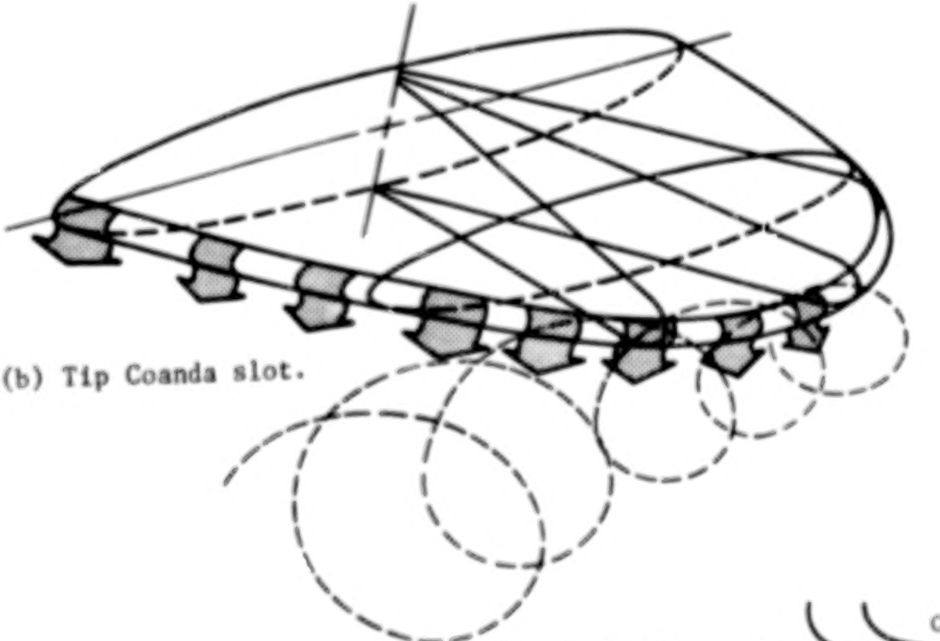

(b) Tip Coanda slot.

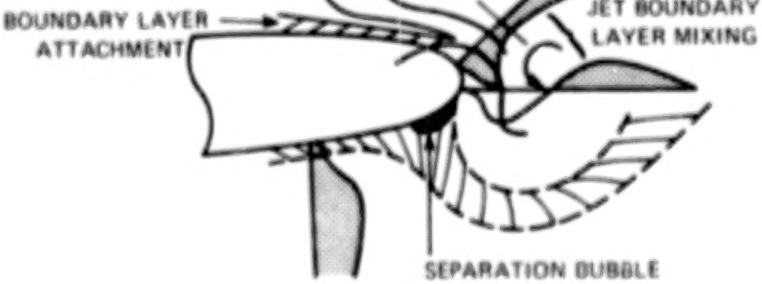
CORE
BOUNDARY LAYER ATTACHMENT
JET BOUNDARY LAYER MIXING
SEPARATION BUBBLE

(c) Vortex core outboard.

Figure 16.- Conceptual function of Coanda tip blowing design.

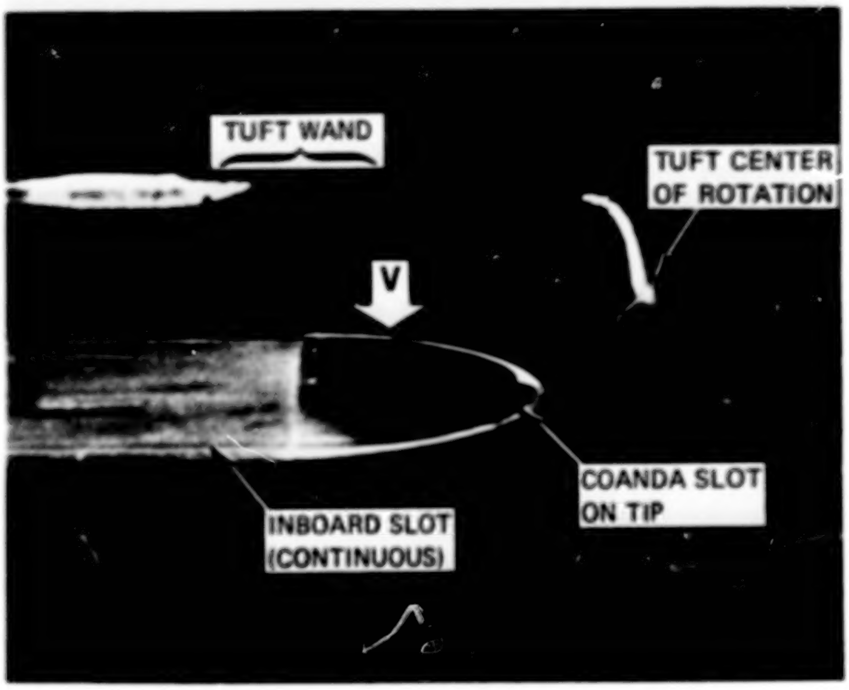
TUFT WAND
TUFT CENTER OF ROTATION
V
COANDA SLOT ON TIP
INBOARD SLOT (CONTINUOUS)

(a) View from top and rear.

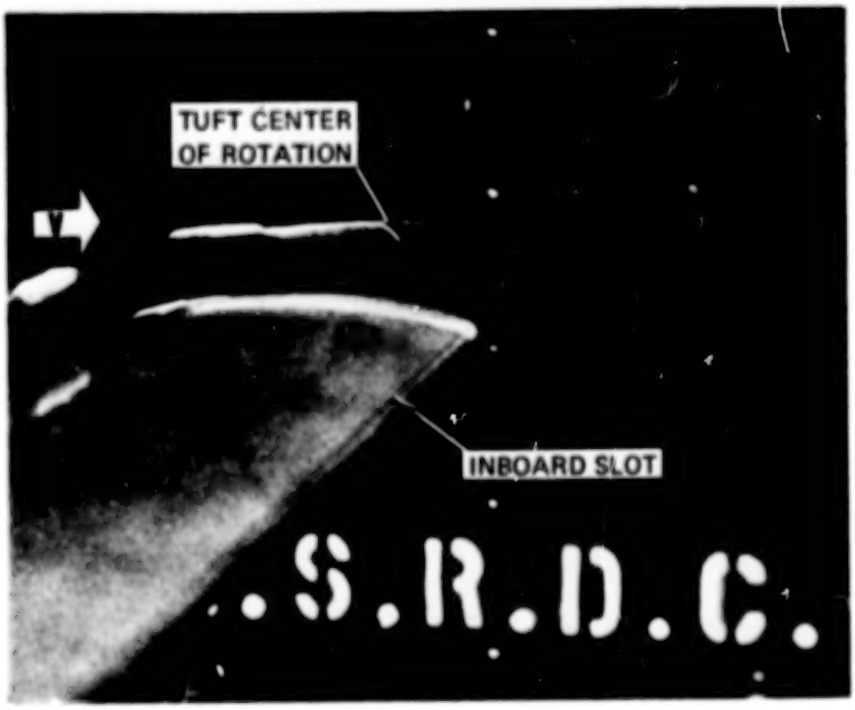
TUFT CENTER OF ROTATION
V
INBOARD SLOT
.S.R.D.C.

(b) View along span.

Figure 17.- Tuft wand flow studies of the effect of Coanda tip blowing on the formation of the vortex off the tip.

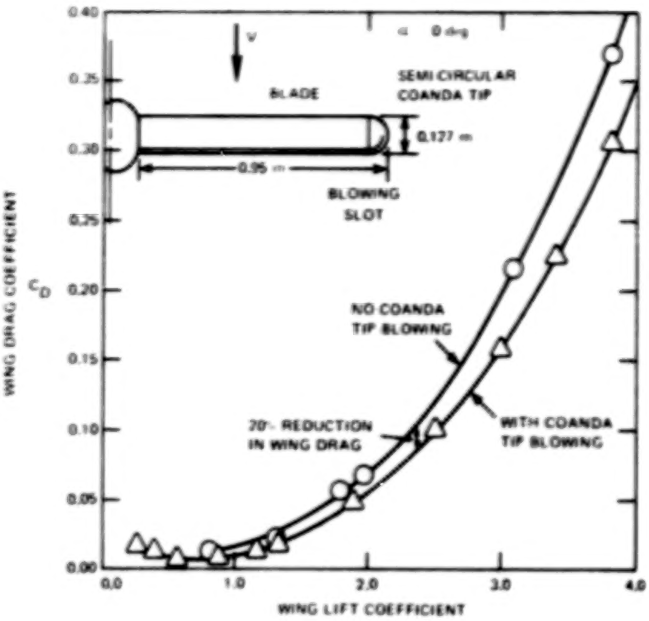

Figure 18.- Effect of Coanda tip blowing on drag of a single circulation control blade tested as a fixed wing.

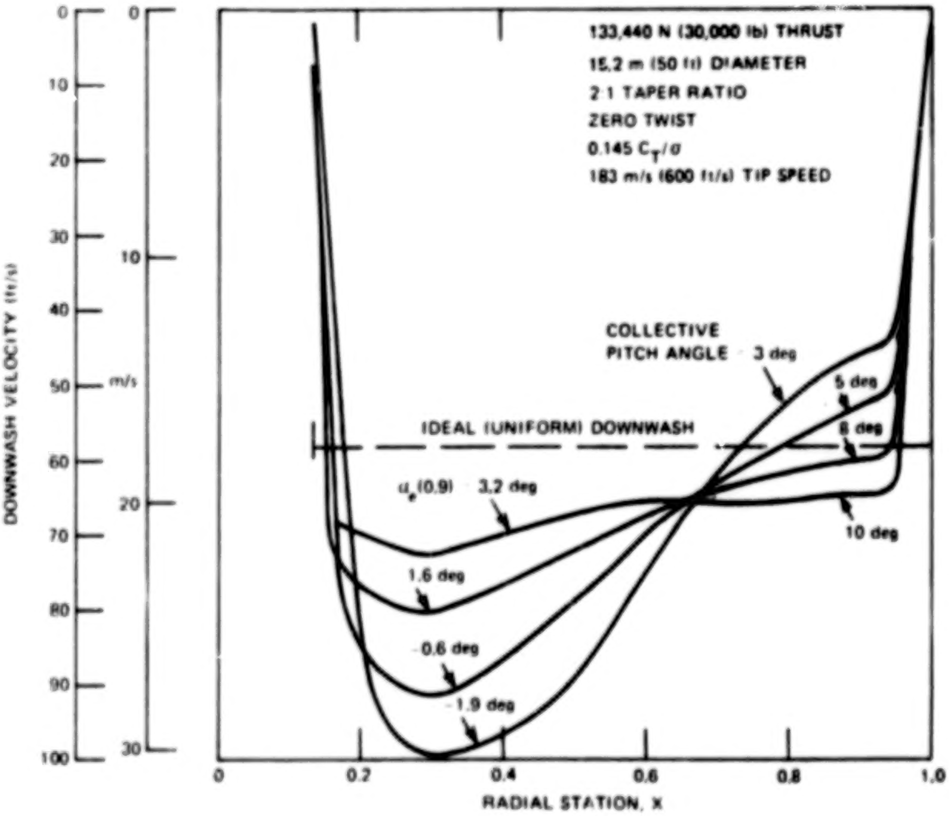

Figure 19.- Approximate induced velocity distribution of an X-Wing CCR in hover.

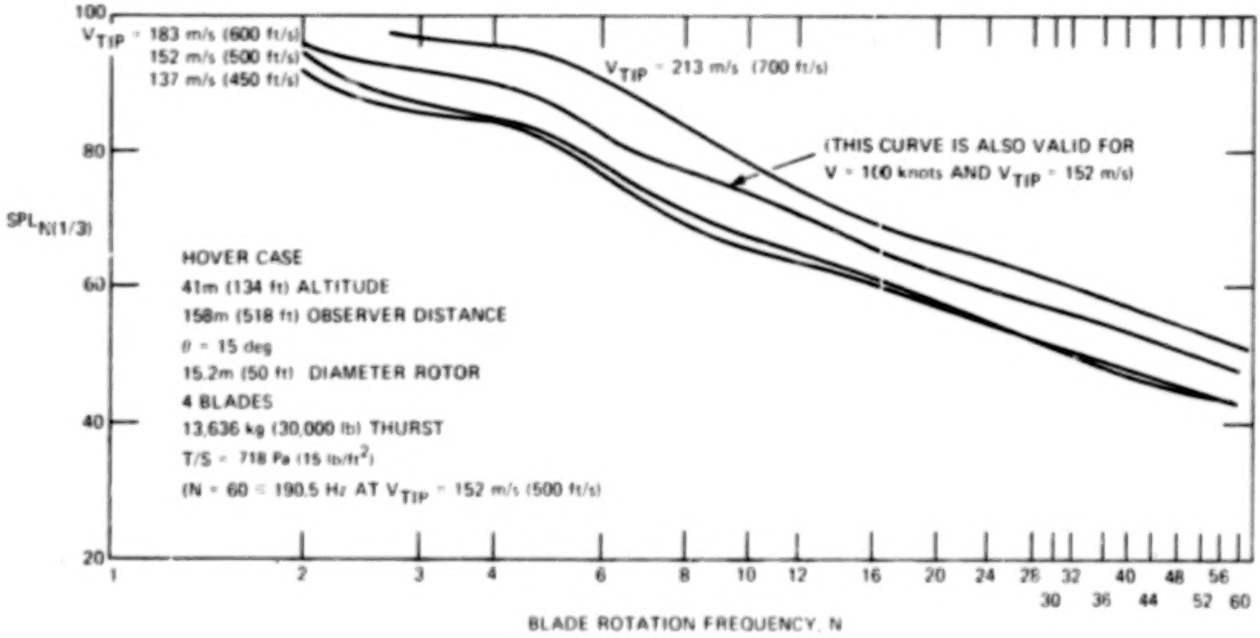

Figure 20.- Calculated effect of tip speed on rotational noise spectrum of 15.2 m (50 foot) diameter X-Wing.

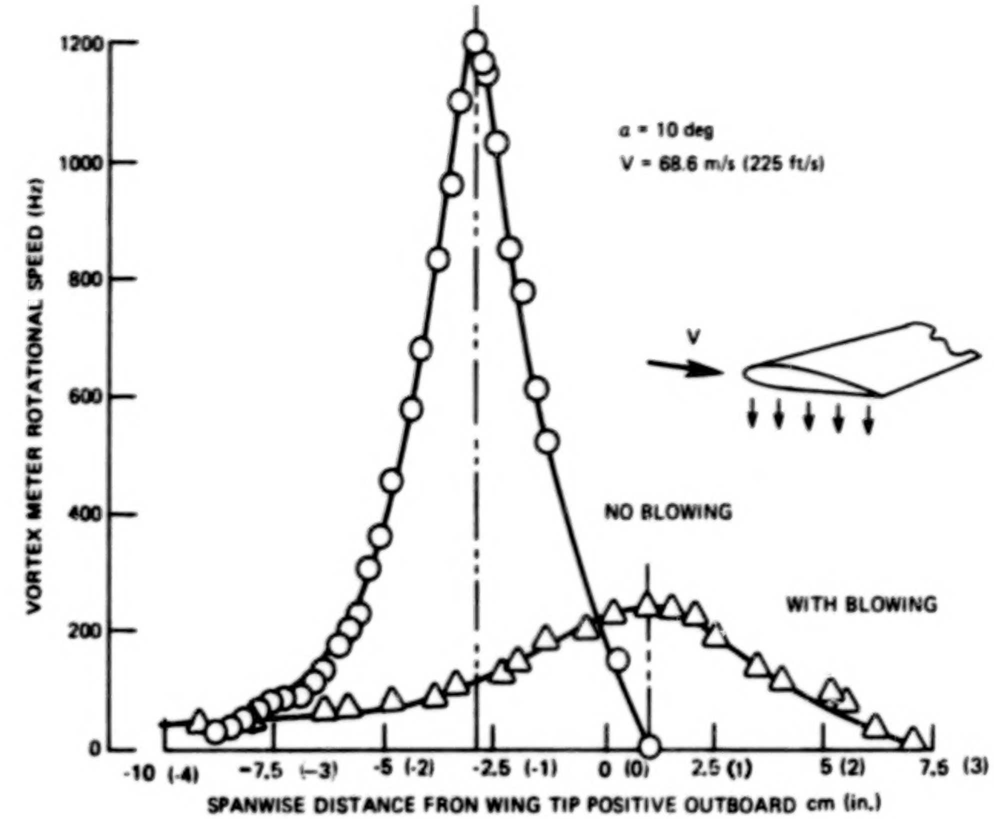

Figure 21.- Effect of normal chordwise blowing from reference 13 showing spanwise vorticity surveys with and without mass injection from nozzle #lv.

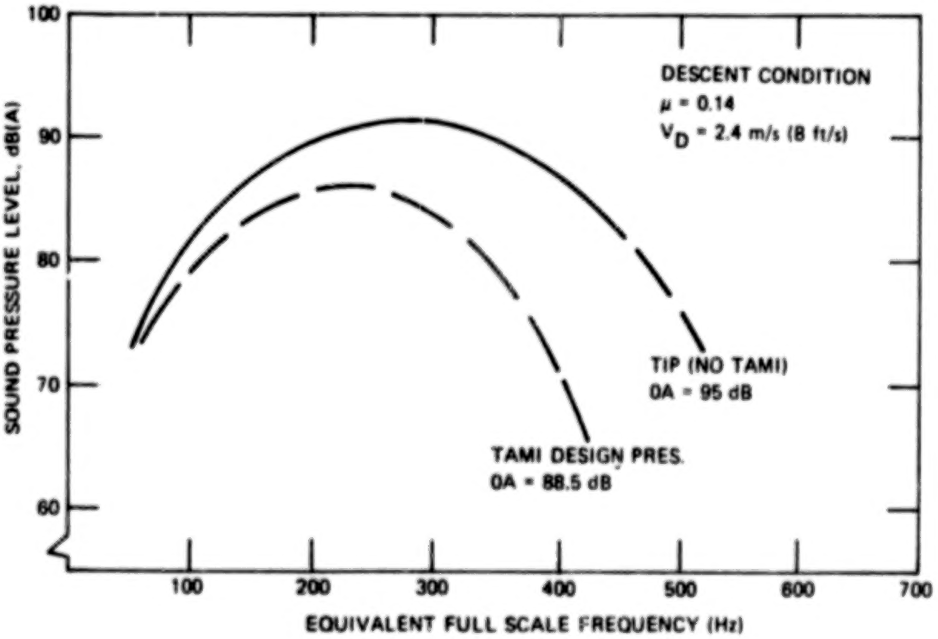

Figure 22.- Sound pressure level dB (A) with and without axial Tip Air Mass Injection (TAMI) into forming vortex core (from ref. 14).

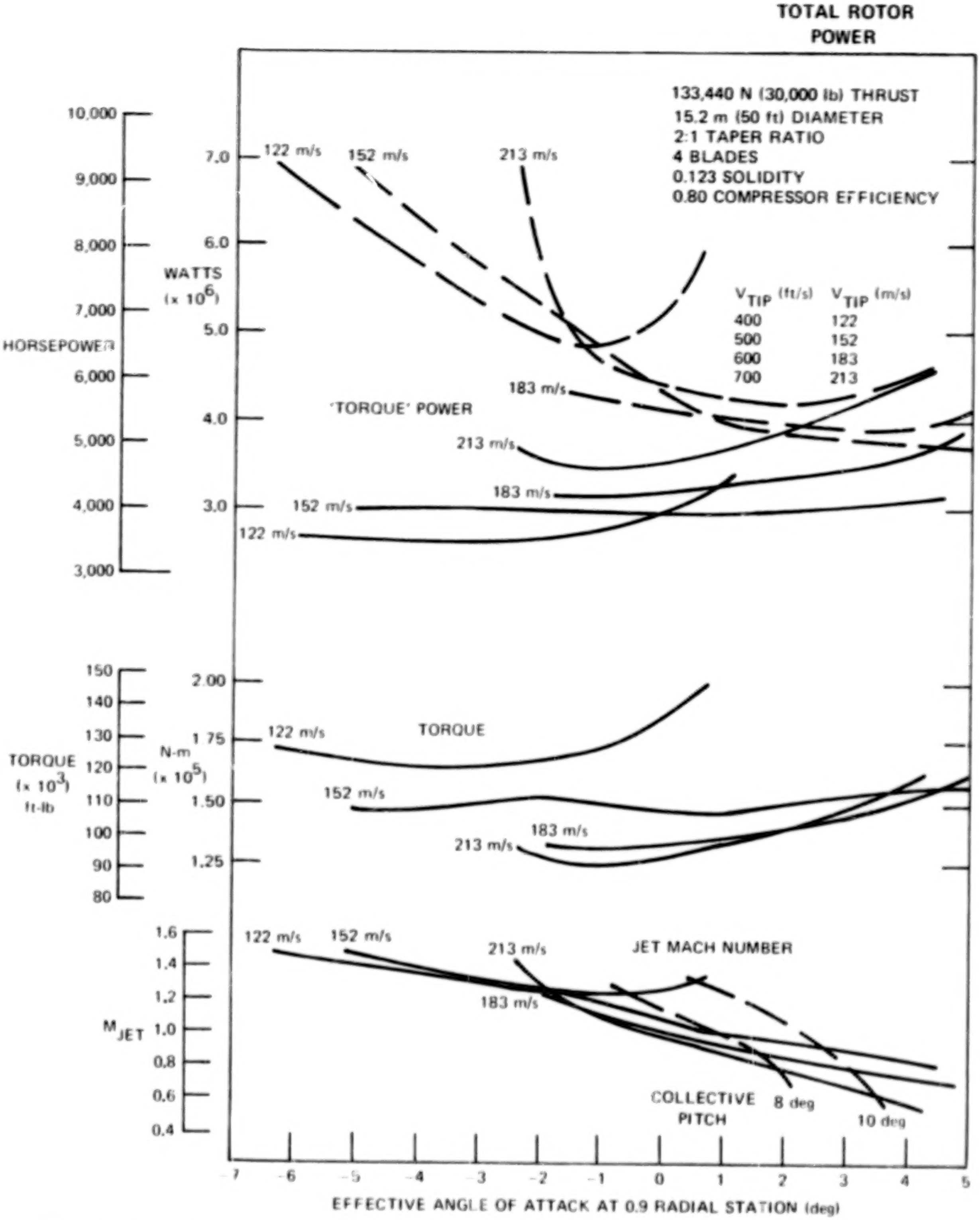

Figure 23.- Variation of X-Wing rotor hover performance parameters with angle of attack and tip speed.

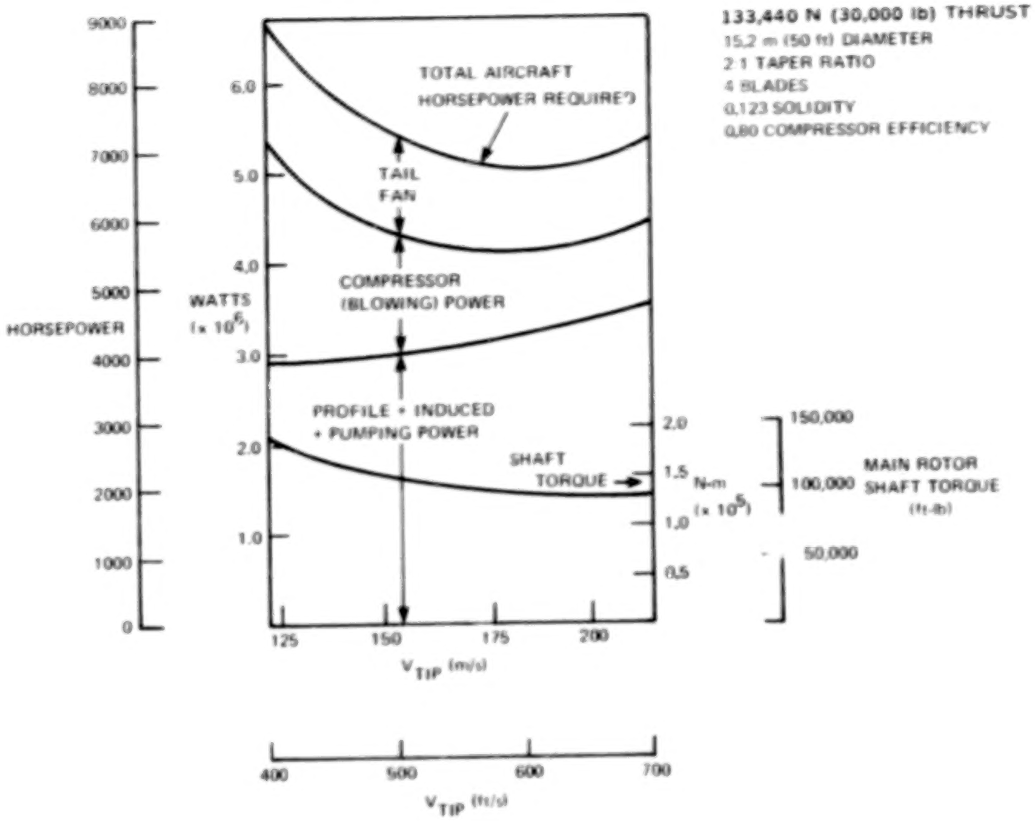

Figure 24.- Variation of power requirements in hover for an X-Wing VTOL (comparison performed for constant (zero) angle of attack at 0.90 radial station).

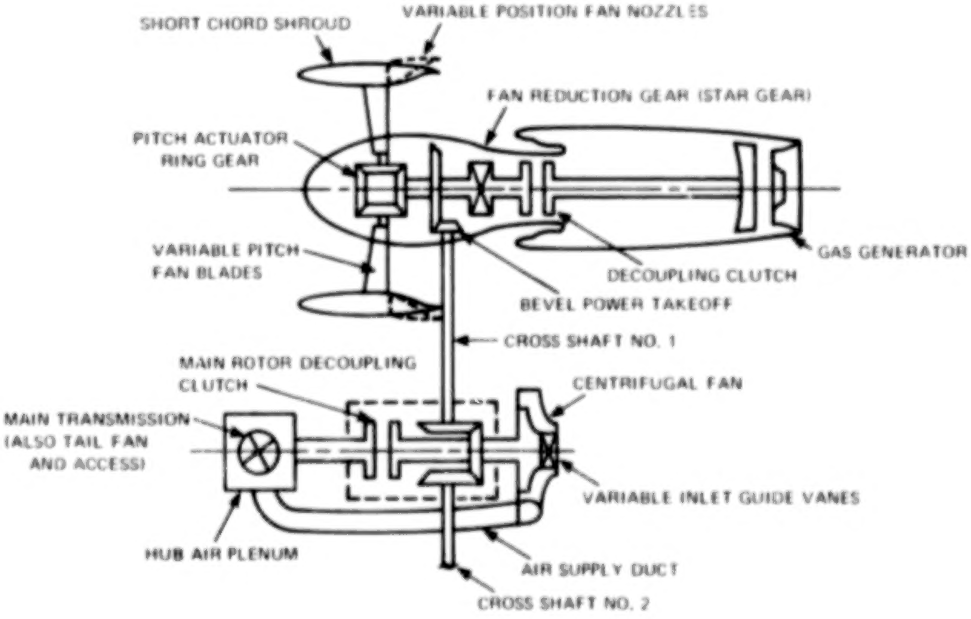
SHORT CHORD SHROUD
VARIABLE POSITION FAN NOZZLES
FAN REDUCTION GEAR (STAR GEAR)
PITCH ACTUATOR RING GEAR
GAS GENERATOR
VARIABLE PITCH FAN BLADES
DECOUPLING CLUTCH
BEVEL POWER TAKEOFF
CROSS SHAFT NO. 1
MAIN ROTOR DECOUPLING CLUTCH
CENTRIFUGAL FAN
MAIN TRANSMISSION (ALSO TAIL FAN AND ACCESS)
VARIABLE INLET GUIDE VANES
HUB AIR PLENUM
AIR SUPPLY DUCT
CROSS SHAFT NO. 2

Figure 25.- One possible propulsion system arrangement for the X-Wing (twin, convertible, low noise, compound fan-shaft engines and centrifugal compressor).

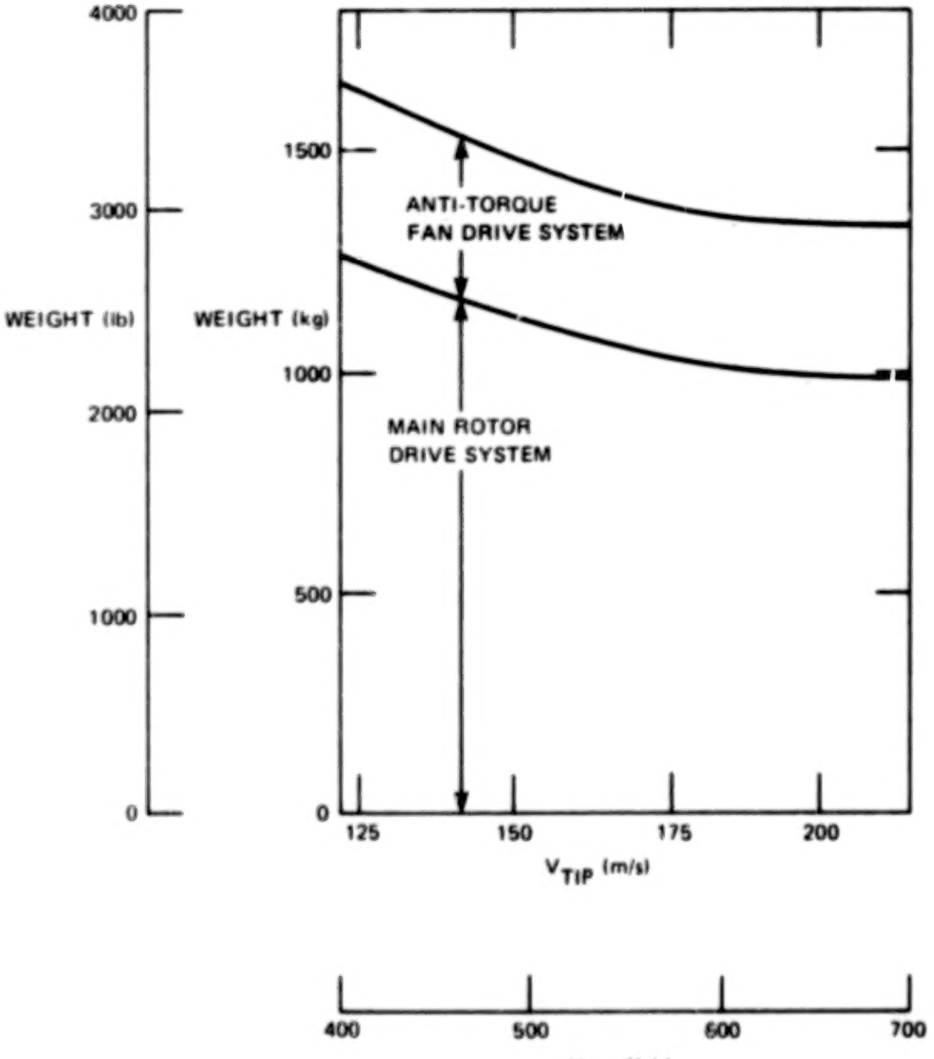

133,440 N
(30,000 lb) THRUST
15.2 m
(50 ft) DIAMETER
718 Pa
(15 lb/ft^2) DISK LOADING
4 BLADES
2:1 TAPER RATIO
$\sigma = 0.123$
$\eta_c = 0.80$

V_{TIP} (ft/s)	V_{TIP} (m/s)
400	122
500	152
600	183
700	213

Figure 26.- Drive system and antitorque tail fan weight trends with tip speed.

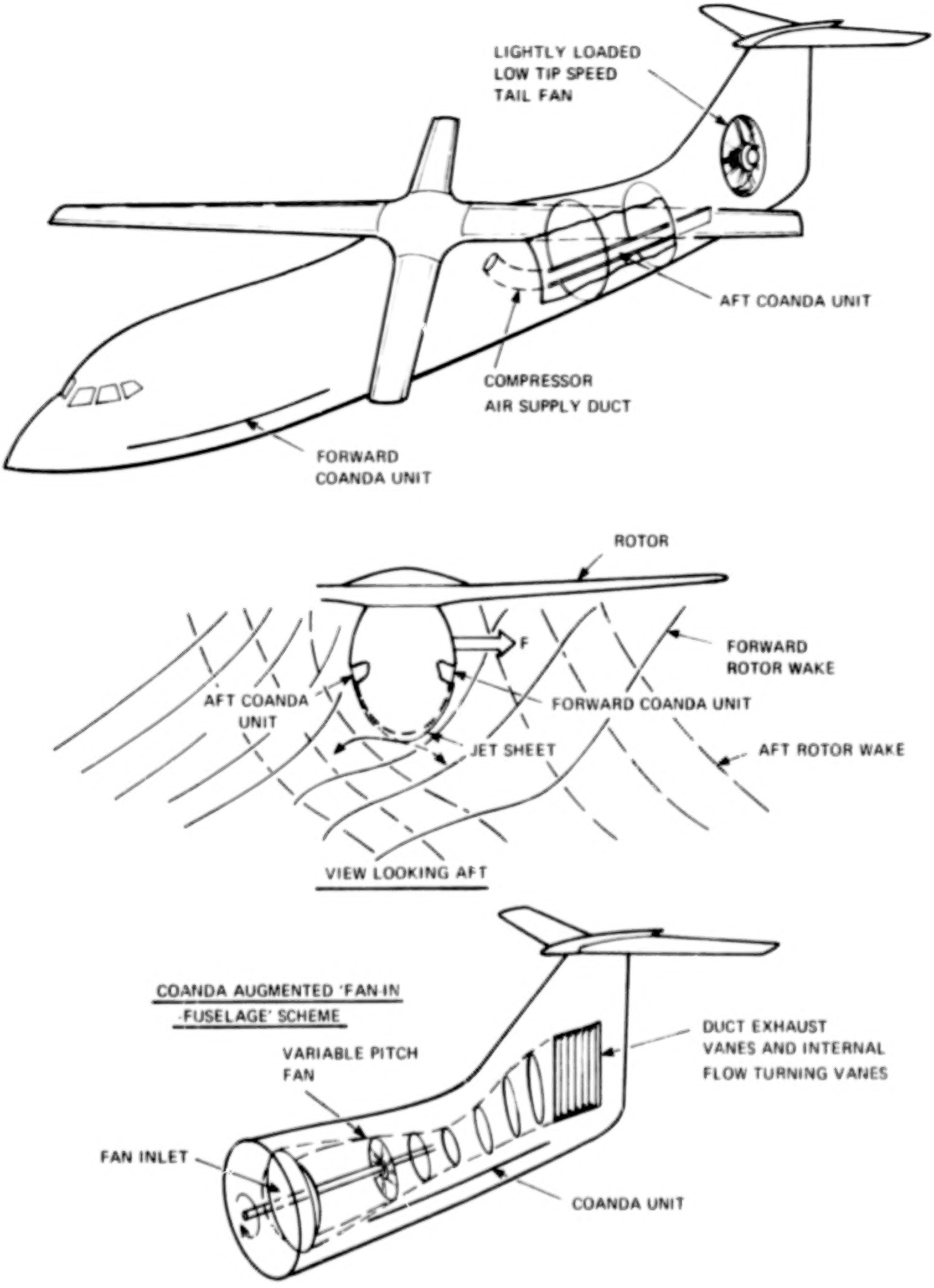
LIGHTLY LOADED
LOW TIP SPEED
TAIL FAN
AFT COANDA UNIT
COMPRESSOR
AIR SUPPLY DUCT
FORWARD
COANDA UNIT
ROTOR
F
FORWARD
ROTOR WAKE
AFT COANDA
UNIT
FORWARD COANDA UNIT
JET SHEET
AFT ROTOR WAKE
VIEW LOOKING AFT
COANDA AUGMENTED 'FAN-IN-FUSELAGE' SCHEME
VARIABLE PITCH
FAN
DUCT EXHAUST
VANES AND INTERNAL
FLOW TURNING VANES
FAN INLET
COANDA UNIT

Figure 27.- Coanda blowing units to produce antitorque moments and low noise in hover and low speeds.

Blank Page

HELICOPTER NOISE RESEARCH AT THE LANGLEY V/STOL TUNNEL

Danny R. Hoad
Structures Laboratory, U.S. Army R&T Laboratories (AVRADCOM)

George C. Greene
NASA Langley Research Center

SUMMARY

An investigation of the noise generated from a 1/4-scale AH-1G helicopter configuration was conducted in the Langley V/STOL tunnel. Microphones were installed in positions scaled to those for which flight-test data were available. Model and tunnel conditions were carefully set to properly scaled flight conditions. Data presented in this paper indicate a high degree of similarity between model and flight-test results. It was found that the pressure time history waveforms are very much alike in shape and amplitude. Blade slap when it occurred seemed to be generated in about the same location in the rotor disk as on the flight vehicle. If model and tunnel conditions were properly matched, including inflow turbulence characteristics, the intensity of the blade-slap impulse seemed to correlate well with flight.

INTRODUCTION

Helicopter rotor noise is typically separated into categories, such as rotational noise, broadband turbulent interaction noise, and impulsive noise (see ref. 1). When present, impulsive noise is usually the most objectionable for the community and represents a significant problem for reducing ground detectability of military helicopters. It can occur during high-speed flight as a result of the relatively high advancing blade tip Mach numbers or during partial power descent as a result of the interaction of a blade with a vortex generated by a prior blade passage.

One of the most definitive papers on source identification of the blade-vortex interaction (blade slap) type of impulsive noise was published by Tangler (ref. 2). He has demonstrated that blade-vortex interaction can induce local supersonic flow about the blade's lower surface and linked this observed flow condition with measured blade slap.

Rotor noise research at the Langley V/STOL tunnel has focused on the blade-slap impulsive noise source. A completely instrumented model rotor system is available for testing various rotor systems of interest (ref. 3). On-line computing capability and off-line data reduction required for efficient and safe operation of rotor systems are very similar in concept to those used by other facilities involved in rotor sytem research (ref. 4). The unique capability of the V/STOL tunnel to quickly convert to an open throat test chamber and its low background noise level provided an extension of its usefulness as an aero-acoustic facility. Initial tests of the rotor system model in the V/STOL tunnel were designed to demonstrate the feasibility of conducting rotor noise research in the facility (ref. 5).

The investigation described in this paper was conducted using a model of a helicopter known to generate intense blade slap and for which an extensive flight data base exists (ref. 6). The characteristics of the blade-slap signature are discussed as it affects the spectral content of the overall noise signature measured during the model tests. The primary objective of this paper is to present a comparison of model and flight recorded pressure time histories at properly scaled flight conditions and to discuss the acceptability of using model data to study the noise characteristics of the AH-1G helicopter.

SYMBOLS

The units used for physical quantities defined in this paper are given in both the U.S. Customary Units and the International System of Units. Most quantities were obtained using the U.S. Customary Units. Conversion factors used between these systems are provided in reference 7.

b	number of blades
c	rotor blade chord, m (ft)
C_T	rotor thrust coefficient, $\frac{\text{Thrust}}{\rho\sigma\pi R^2(\Omega R)^2}$
R	rotor disk radius, m (ft)
OASPL	overall sound pressure level, dB (re 2×10^{-5} Pa)
p	acoustic pressure, Pa (lb/ft^2)
SPL	sound pressure level, dB (re 2×10^{-5} Pa)
V_f	tunnel velocity corrected, or true airspeed, knots
V_∞	tunnel velocity, knots
V	rotor tip speed, m/sec (ft/sec)
Ω	rotor rotational speed, rpm
ρ	free-stream density, kg/m^3 (slugs/ft^3)
σ	rotor solidity, $bc/\pi R$

APPARATUS AND TEST TECHNIQUE

The model to flight comparison described in this test used the General Rotor Model System (GRMS) at the Langley V/STOL tunnel configured as an AH-1G helicopter without tail rotor. An aerodynamic investigation of this model without main rotor is described in reference 8. The fuselage had to be enlarged from a 1/4-scale version laterally only to accomodate the GRMS motor and transmission assembly. The model had a 3.35-m (11.00-ft) diameter teetering rotor system scaled from the AH-1G flight vehicle. (See ref. 9.) The blades used a modified NACA 0012 airfoil section and had 10° of washout. A photograph of the model installed in the Langley V/STOL tunnel is presented in figure 1(a), and a photograph of the flight vehicle used in reference 6 is presented in figure 1(b). Microphones were installed on the nose, wings, and tail surfaces of this vehicle for inflight noise measurements. A complete description of the flight test can be obtained from reference 6.

The Langley V/STOL tunnel has a test section that is 4.42 m (14.50 ft) high and 6.63 m (21.75 ft) wide. The semi-anechoic characteristics of the test section are provided by raising the test-section walls and ceiling and are enhanced by treating the floor and ceiling from 5.41 m (17.75 ft) ahead of the model to 2.51 m (8.25 ft) behind the model with 10.16 cm (4.00 in.) thick open-cell polyurethane foam. (See fig. 1(a).) The ceiling surface in the raised position was about 4.7 m (15.4 ft) above the rotor system.

INSTRUMENTATION

The acoustic sensors used for these tests were 1.27-cm (0.50-in.) diameter condensor microphones fitted with standard nose cones. Five microphones were positioned in the flow around the model as presented in figure 2. Three microphones were mounted to the fuselage in locations scaled from positions used on the flight-test vehicle (ref. 6). These microphones can be seen in figure 1(a). The acoustic recording system was consistent with that described in reference 5. All five microphone signals were recorded with a rotor-blade azimuth indicator and time code on a 14-channel frequency-modulated (FM) tape recorder.

The basic frame of the rotor model is completely instrumented for measurement of rotor loads (six-component strain-gage balance) and complete model loads. This plus complete rotor collective and cyclic remote controls (ref. 3) provides complete, precise knowledge of the rotor performance characteristics during the acoustic investigation.

Both flight test and model test provided a blade azimuth position indicator in the form of an electronic blip generated at the vehicle and recorded on the acoustic FM recorder when the instrumented blade passed over the tail cone of the vehicle. This 1/rev blip is indicated in all pressure time histories presented herein.

MODEL-FLIGHT SCALING

To properly match flight-test operating conditions, the tunnel model must be operated with certain parameters matched. Full-scale Reynolds number matching is always desirable, but impossible in this type of model test. Other items suggested in reference 10 as being important to proper performance modeling of rotor systems are blade elasticity and rotor solidity. Unfortunately, these blades were not elastically scaled. The rotor tip speed (V_T), advance ratio, and thrust coefficient are parameters which must be maintained to provide scaled wake effects on the rotor system or the fuselage. Due to structural limitations in the rotor blades and hub, the full-scale tip speed (227.5 m/sec (746.4 ft/sec)) could not be exactly matched. The required rotor speed Ω (1296 rpm) for this tip speed could not be tested but was set at 1200 rpm. This resulted in a tip speed reduction to 210.7 m/sec (691.2 ft/sec). The advance ratio (V_∞/V_T), however, was carefully matched to the quoted flight-test advance ratio. In this case, the tunnel free-stream velocity was reduced from the flight velocity by:

$$V = V_f \frac{V_{T(\text{model})}}{V_{T(\text{flight})}} = V_f \; 0.925$$

The forward speed values quoted for model data in this paper are corrected by this factor. The flight-test data presented in reference 6 are at various indicated airspeeds at various altitudes. Flight records provided Langley concerning these data provide some information about the pressure altitude. The forward speed values quoted for flight data in this paper are corrected for this pressure altitude. In some cases, gustiness (especially at low altitude) resulted in an uncertainty in flight speed by as much as ±5 knots.

Rotor lift was carefully maintained at a scaled value based on matching rotor thrust coefficient

$$C_T = \frac{\text{Thrust}}{\rho\sigma\pi R^2(\Omega R)^2}$$

For a quoted nominal 37.36 kN (8400 lb) weight flight-test vehicle, the scaled model weight (lift) was kept at 2.00 kN (450 lb). The flight records indicated that the estimated gross weight at the beginning of each series of runs was consistently 37.54 kN (8440 lb), but the fuel consumption during each series of runs was not recorded in every case. One series recorded indicated fuel usage of 1.27 kN (285 lb), which results in a scaled weight uncertainty of 68 N (15 lb). This uncertainty in flight vehicle gross weight will affect primarily the rotational noise amplitude and is not considered significant.

Typically, the occurance of blade slap has been found to be a function of flight speed and descent velocity. An assessment of the strength of the intensity of the blade slap is usually obtained by an observer in the cabin of the helicopter. This was performed for the investigation reported in reference 6 and is shown in figure 3. It has been found by many researchers that this observation does not always provide a real assessment of the propagation, or occurrence of blade slap, even if compared with measurements just outside the cabin. It does, however, provide a gross indication of the flight conditions required to bracket the envelope of blade-slap intensity.

The procedure used to establish each flight condition simulation was to set a constant tunnel velocity which would provide the correct matched advance ratio. At this velocity, the tip-path plane angle of attack was varied until desired descent velocity was obtained as computed from the ratio of overall drag to lift

$$\text{Descent velocity} = V_f \sin\left\{\tan^{-1}\left(\frac{\text{Drag}}{\text{Lift}}\right)\right\}$$

At each of these descent velocities, the model collective and cyclics were varied to trim the model in lift, pitching moment, and rolling moment. When all variables described above were set properly then approximately 30 seconds of information from the microphones was recorded on the FM tape recorder. Corresponding model and tunnel information was recorded on the tunnel computer data acquisition system coincidentally. The information presented in this paper is only a small portion of the data collected as described. At each tunnel velocity tested, background noise measurements were made wtih blades off and rotor hub turning at the test speed (1200 rpm).

NOISE DATA REDUCTION AND PRESENTATION

Only data from the nose and right-wing microphones are presented in this paper. One-third octave analyses were performed on model data over a 16-second averaging time and are presented in figure 4. Narrow band analyses were performed for selected portions of the model data presented. It was performed digitally for 20 revolutions of the rotor at a digitizing rate of 20 000 samples per second, resulting in a constant band width of 20 Hz with a resolution of 10 000 Hz. These are presented in figure 5. Detailed comparisons of pressure time-history between model and flight are provided in figures 6, 7, 8, and 9.

DISCUSSION

Acoustic data recorded during the model test at a flight-speed simulation of about 50 knots is presented in figures 5(a) and 5(b). Pressure time histories are presented on the right side of the figure as a function of descent velocity. These correspond to the information analyzed in one-third octave format as presented in the left side of the figure.

The strong impulse signature indicative of blade slap is present in the pressure time histories, and it is evident that the magnitude of the impulse is a direct function of the descent velocity. The position of the impulse on the trace relative to the 1/rev blip is a function of the location of the source mechanism in the rotor disk. Although difficult to locate accurately, it is obvious that the positon of the source did not vary with descent velocity, indicating that the range in descent velocity caused a vertical displacement in the blade-to-vortex spacing only.

Data recorded from the nose microphone at 50.7 knots simulated flight speed (fig. 4(a)) indicates a suprisingly clean signal at nearly zero descent velocity.

One-third octave analysis of these data shows the obvious high amplitude blade-passage frequency fundamental (40 Hz) with associated harmonics. The broadband high frequency noise, which can be associated with turbulence interaction, in this case is of much lower amplitude (about 35 dB less than the fundamental). The background noise in this case is well under the clean rotor signal except in the 200-800 Hz one-third octave band range. The effect of the blade slap impulse can be seen as an increased amplitude above the third harmonic of the blade-passage frequency. This change in the one-third octave spectrum from a descent velocity of 1.067 m/sec (210 ft/min) to 3.302 m/sec (650 ft/min) was primarily associated with the impulse as generated by the blade vortex interaction. Since the rotor thrust was maintained at about 4.413 kN (450 lb) throughout, the amplitudes of blade passage and the first few harmonic frequencies were unaffected by the blade slap. This indicates that, although the impulse noise was repetitive with blade passage, the energy associated with it is well below the low frequency noise (fundamental blade-passage frequency and its first few harmonics) generated by blade loading.

The data recorded from the right wing microphone at these simulated flight conditions (fig. 4(b)) show the same trends. The pressure time histories are not as clean, but the blade passage is evident. Note the change in amplitude scale of the pressure time histories in figures 4(b) and 4(d). The broadband turbulence interaction noise for near level flight is about 25 dB less than the blade passage frequency amplitude. Background noise in this case is well below the rotor noise throughout the spectrum. The impulsive signature energy again reflects itself in the high frequency range beginning at the fourth harmonic of the blade-passage frequency.

The noise characteristics from the nose microphone and right wing microphone at a simulated flight speed of 71.1 knots (figs. 4(c) and 4(d)) were similar to those at 50.7 knots, except some of the data were contaminated by background noise (200-1250 one-third octave band center frequencies). Bulging of the spectral characteristics is evident to some extent above about 200 Hz due to the blade-slap impulse. In this case, the range of descent velocities encompassed the entire region of the intense blade slap, indicating that the vortex was below the rotor disk at low descent velocities, passed through the disk at moderate descent velocities, and was above the disk at high descent velocities.

It is well known that this blade vortex interaction noise when Fourier-analyzed presents itself as harmonics of the blade-passage frequency, just as the Fourier analysis of a pure repetitive impulsive function. Narrow-band analysis was performed on these data, and four samples are presented in figure 5. At 50.7 knots simulated airspeed and 3.302 m/sec (650 ft/min) descent velocity (fig. 6(a)), the harmonics are evident to above 4000 Hz (over 100 harmonics of blade passage). At 71.1 knots, the impulsive harmonics are evident up to at least 8000 Hz (over 200 harmonics of blade passage). Noise generated by blade loading can also be seen in these figures below about 200 Hz, where it is not affected by descent velocity. Above 200 Hz, that noise which can be associated with blade slap is up to 15 dB higher in magnitude than without blade slap. A subjective response to the two signals in figure 6(a), as demonstrated in figure 4, would probably result in the blade slap case being rated as much more objectionable. It is interesting to note the overall sound pressure level of

CONTENTS

Part I

PREFACE . . . . iii 17A6

REGULATIONS

1. HELICOPTER EXTERNAL NOISE REQUIREMENTS - FAA PERSPECTIVE 1 1/A8
Charles R. Foster

2. HELICOPTER NOISE REGULATIONS: AN INDUSTRY PERSPECTIVE 17 1/B10
R. A. Wagner

3. NOISE REQUIREMENTS FROM A MILITARY POINT OF VIEW 33 1/C12
Charles C. Crawford, Jr.

4. THE IMPACT OF URBAN OPERATIONS ON HELICOPTER NOISE REQUIREMENTS . . . 45 1/D10
Stanley R. Spector

ROTOR NOISE

5. PREDICTION AND REDUCTION OF ROTOR BROADBAND NOISE 61 1/E12
Richard E. Hayden and Krishna S. Aravamudan

6. THEORETICAL MODELS OF HELICOPTER ROTOR NOISE 89 1/G12
D. L. Hawkings

7. NOISE DUE TO ROTOR-TURBULENCE INTERACTION 109 2/B6
R. K. Amiet

8. THEORY ON ACOUSTIC SOURCES 127 2/C10
S. E. Wright

9. POTENTIAL ACOUSTIC BENEFITS OF CIRCULATION CONTROL ROTOR 149 2/E5
Robert M. Williams and Ian C. Cheeseman

10. HELICOPTER NOISE RESEARCH AT THE LANGLEY V/STOL TUNNEL 181 2/G9
Danny R. Hoad and George C. Greene

11. EXPLORATORY WIND-TUNNEL INVESTIGATION OF THE EFFECT OF THE MAIN ROTOR WAKE ON TAIL ROTOR NOISE 205 3/B7
Robert J. Pegg and Phillip A. Shidler

12. WIND TUNNEL INVESTIGATIONS OF MODEL ROTOR NOISE AT LOW TIP SPEEDS . . . 221 3/C9
K. S. Aravamudan, A. Lee, and W. L. Harris

13. HELICOPTER EXTERNAL NOISE PREDICTION AND CORRELATION WITH FLIGHT TEST 263 3/F11
Bharat P. Gupta

14. FULL-SCALE TESTING OF AN OGEE TIP ROTOR 277 3/G11
Wayne R. Mantay, Richard L. Campbell, and Phillip A. Shidler

15. HOVERING IMPULSIVE NOISE - SOME MEASURED AND CALCULATED RESULTS 309 4/C4
D. A. Boxwell, Y. H. Yu, and F. H. Schmitz

16. IMPROVED METHODS FOR CALCULATING THE THICKNESS NOISE 323 4/D4
Yoshiya Nakamura and Akira Azuma

17. THE IMPORTANCE OF QUADRUPOLE SOURCES IN PREDICTION OF TRANSONIC TIP SPEED PROPELLER NOISE 339 4/E6
Donald B. Hanson and Martin R. Fink

18. BOUNDS ON THICKNESS AND LOADING NOISE OF ROTATING BLADES AND THE FAVORABLE EFFECTS OF BLADE SWEEP ON NOISE REDUCTION 373 4/G12
F. Farassat, Paul A. Nystrom, and Thomas J. Brown

19. A STUDY OF THE NOISE RADIATION FROM FOUR HELICOPTER ROTOR BLADES . . . 387 5/A14
Albert Lee and Marianne Mosher

these two signals are both 129.5 dB. It is obvious that the low frequency rotational noise is dominating these values, and to provide any comparison with human response to this type of noise, weighting factors must be applied. Langley Research Center is involved in this area (ref. 11).

Model-Flight Test Comparison

Comparison between model and flight test data are presented in figures 6, 7, 8, and 9 for the nose and right wing microphones. Recorded pressure time histories from one revolution of the rotor from each test are presented for comparable flight conditions. The frequency content of the model data spectral analysis must be scaled by rotor speed; however, presenting the pressure time history as a function of rotor revolutions, instead of time, effectively scales this factor. Since the rotor tip speed could not be matched to flight and the thrust was scaled by matching thrust coefficient, the thrust was slightly less than disk loading scaling required. The pressure amplitudes of the model data were corrected by this factor for these comparisons.

It is important to note at this point, again, that the flight velocity presented for the flight-test data are corrected values from quoted indicated airspeed based on limited information about pressure altitude. Flight data include effects of tail rotor operation which was not on the model.

Noise signatures from model and flight at a free-stream velocity of about 50 knots are presented in figure 6 for several descent velocities. At a low descent velocity (figs. 6(a) and 6(b)), blade slap, if present, is difficult to identify. Model and flight comparison for the nose microphone indicate the suprisingly clean signal recorded. The waveform is different for the model, probably caused by blade loading variations from Reynolds number or blade elasticity effects. Comparisons for the right wing microphone show very similar waveforms if the tail-rotor blade-passage spikes were removed from the flight data. In fact, an approximate calculation of the difference in pressure amplitude indicates that the properly scaled model blade-passage frequency amplitude was about 1 dB higher than flight. This difference for the nose microphone was about 5 dB. These characteristics are typical of all the comparisons presented herein.

At a high descent velocity (figs. 6(c) and 6(d)), the impulsive signature from blade-vortex interaction is evident in both tests. Even though the waveform recorded on the model nose microphone is different from flight, the impulse is in about the same location in the signature as in flight-test data relative to the 1/rev blip. This indicates that the source mechanism of blade slap occurred in about the same location on the model as flight. The shape and size of the model impulse is remarkably similar to that from flight test. The high descent rate condition probably would be considered to be objectionable in a subjective analysis; however, figure 3 indicates that blade-slap intensity was rated as very light for this flight condition. This is one flight condition where the slap intensity was not detected by cabin observers.

Similar comparisons between model and flight are presented in figures 7, 8, and 9 for a flight velocity of approximately 70 knots. At a low descent velocity (figs. 7(a) and 7(b)), the flight recorded pressure time history shows a definite blade-vortex interaction which is not present in model data. At a moderate descent velocity (figs. 8(a), 8(b), and 8(c)), model data indicated a weak blade-vortex interaction at nearly the same position as at 50 knots. Flight-test data at nearly the same descent velocity shows a very intense blade slap. These data were recorded at a relatively high altitude in "smooth" air. These tests were also conducted at a lower pressure altitude, 396.2 m (1300 ft), in "bumpy" air. Flight records indicated that measurement of indicated airspeed was uncertain (±5 knots) due to this turbulence. The relative position of the impulse on the pressure time history did not change, but the amplitude did. Reference 6 suggests that this variation was caused by turbulence interaction with the tip vortex. This condition seems to compare more favorably with model tests. The V/STOL tunnel experiences a relatively larger turbulence factor at this speed than at lower speeds. At the high descent velocity (fig. 9), model data (fig. 9(a)) indicate a maximum for blade slap as does flight data at the low, bumpy air pressure altitude (fig. 9(c)). Flight data at the high, smooth air, pressure altitude (fig. 9(b)) indicate a lower blade slap intensity than at the lower descent velocity (fig. 8(b)). These data indicate that turbulence characteristics inflow to the rotor system can cause considerable variance in the degree of blade-slap intensity in flight and in model testing.

CONCLUDING REMARKS

An investigation of the noise generated from a 1/4-scale AH-1G helicopter configuration was conducted in the Langley V/STOL tunnel. Microphones were installed about the model in positions scaled to those locations for which flight-test data were available. Model and tunnel conditions were carefully set to properly scaled flight conditions. Acoustic data recorded during the model tests indicated that:

1. As expected, blade-slap intensity is a direct function of descent velocity, probably caused by only vertical displacement in the blade-vortex interaction.

2. Spectral analysis of a signal with blade slap shows energy concentration above about the third harmonic of the blade-passage frequency.

3. Narrow-band analysis indicated that the blade-slap impulsive signature showed up as harmonics of the blade-passage frequency up to at least 200 harmonics.

Comparisons between model and flight data have been presented in pressure time history form, properly scaled in amplitude and time. The comparison between model and flight-test noise data indicated considerable similarity in waveform, especially that for the right wing microphone. Difference in amplitude was estimated to be about 5 dB for the nose microphone and about 1 dB for the right wing microphone at the blade-passage frequency. At different flight speeds and descent velocities, the comparisons indicated that:

1. Model scale blade-slap occurrence and location on time history relative to 1/rev blip were similar to those recorded in flight at two descent speeds and at 50 knots flight velocity.

2. Intense blade slap recorded on the microphones at 3.302 m/sec (650 ft/min) descent velocity and 50 knots flight speed was not noted during subjective tests in the flight vehicle cabin.

3. With an approximate flight speed of 70 knots, model scale blade slap was not generated as intensely as in flight at high "smooth air" pressure altitudes.

4. At low, "bumpy air" pressure altitudes, flight test and model test blade-slap intensity and its relationship with descent velocity compared very well.

5. A higher turbulence factor in the V/STOL tunnel at 70 knots than at lower speeds and the comparability of model and flight data at the lower turbulent pressure altitude suggest that turbulence inflow into the rotor system can alter the intensity and the occurrence of blade slap.

REFERENCES

1. Langenbucher, V.: Noise Phenomena With Helicopter Rotors and Possibilities of Noise Reduction. European Space Agency Rep. No. ESA-TT-244, Feb. 1976

2. Tangler, James L. L.: Schlieren and Noise Studies of Rotors in Forward Flight. Am. Hel. Soc. Paper 77-33-05, May 1977

3. Wilson, John C.: A General Rotor Model System for Wind-Tunnel Investigations. J. Aircraft, vol. 14, no. 7, July 1977, pp. 639-643

4. Hardy, William G. S.; and Pyne, Edward J.: The Use of Computers in Rotary Wing Testing. AGARD CP-210, Numerical Methods and Wind Tunnel Testing, pp. 4-1-4-12

5. Scheiman, James; and Hoad, Danny R.: Investigation of Blade Impulsive Noise on a Scaled Fully Articulated Rotor System. NASA TM X-3528, 1977

6. Sakowski, P. C., Jr.; Charles, B. D.; Cox, C. R.; and Shockey, G. A.: Noise Measurement Test Results for AH-1G Operational Loads Survey. Bell Hel. Co. Rep. 299-099-831, vols. I and II, Feb. 1976

7. Mechtly, E. A.: The International System of Units - Physical Constants and Conversion Factors (Second Revision). NASA SP-7012, 1973

8. Freeman, Carl E.; and Yeager, William T., Jr.: A Wind-Tunnel Investigation of an Unpowered Helicopter Fuselage Model With a V-Type Empennage. NASA TM X-3476, 1977

9. Finnestead, Rodger L.; Laing, Emmett; Connor, William J.; and Buss, Marvin W.: Engineering Flight Test AH-1G Helicopter (Hueycobra). U.S. Army Aviation Systems Test Activity Rep. No. USAASTA 66-06, April 1970

10. Yeager, William T., Jr.; and Mantay, Wayne R.: Correlation of Full-Scale Helicopter Rotor Performance in Air With Model-Scale Freon Data. NASA TN D-8328, 1976

11. Powell, Clemans A.: Annoyance Due to Simulated Blade-Slap Noise. Helicopter Acoustics, NASA CP-2052, Pt. II, 1978. (Paper no. 23 of this compilation.)

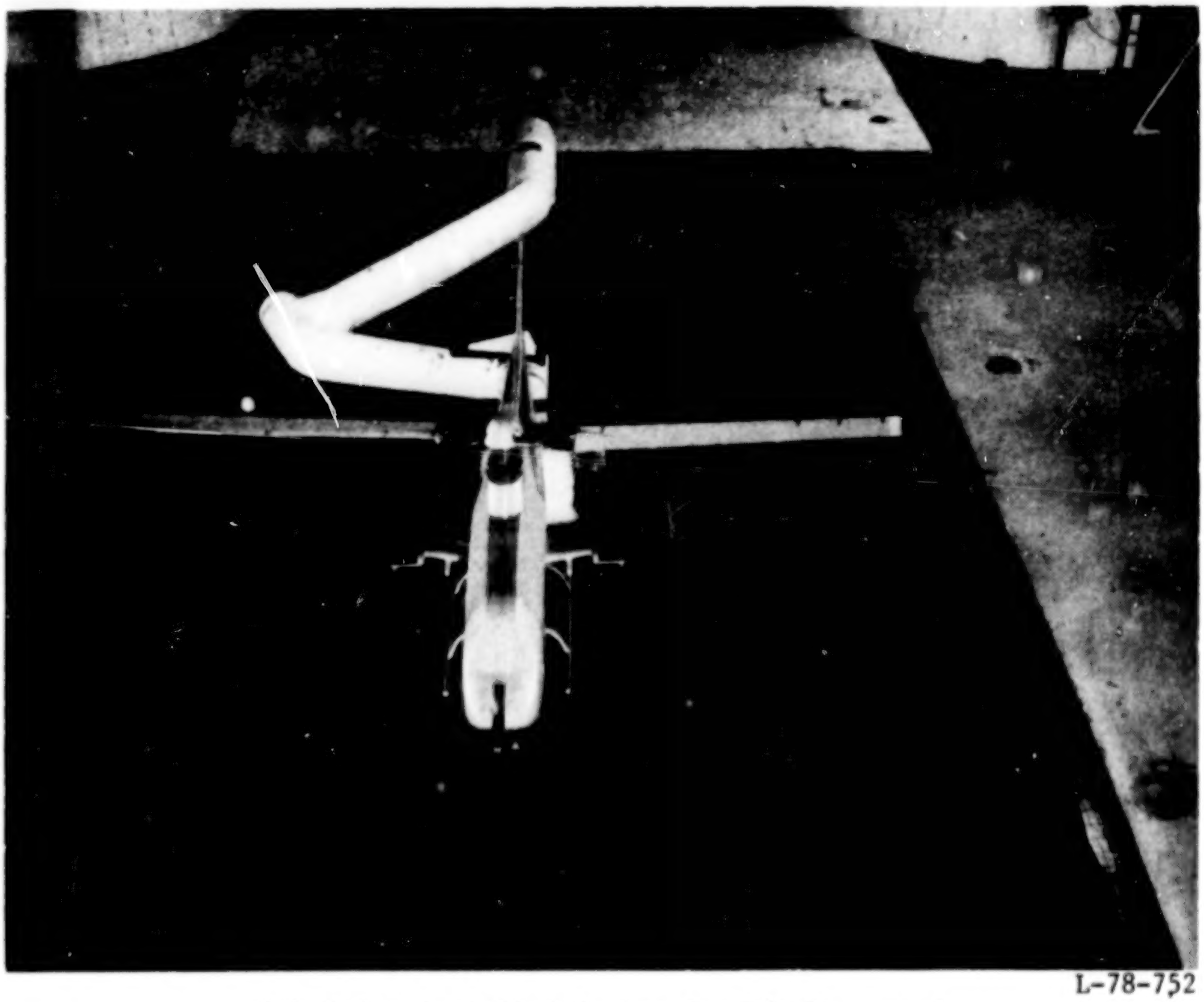

L-78-752

(a) Model installed in Langley V/STOL tunnel.

Figure 1.- AH-1G helicopter.

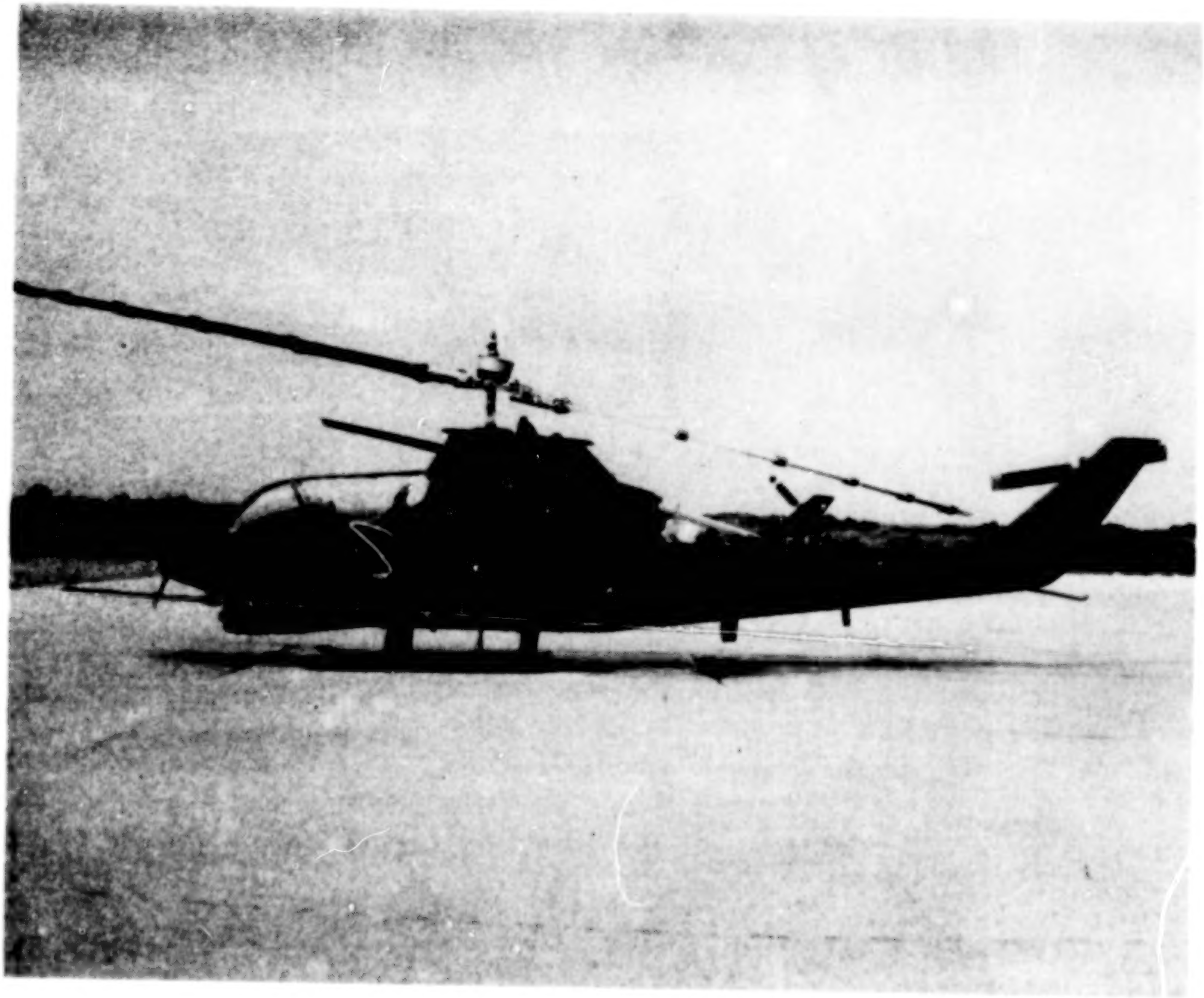

(b) Flight-test vehicle.

Figure 1.- Concluded.

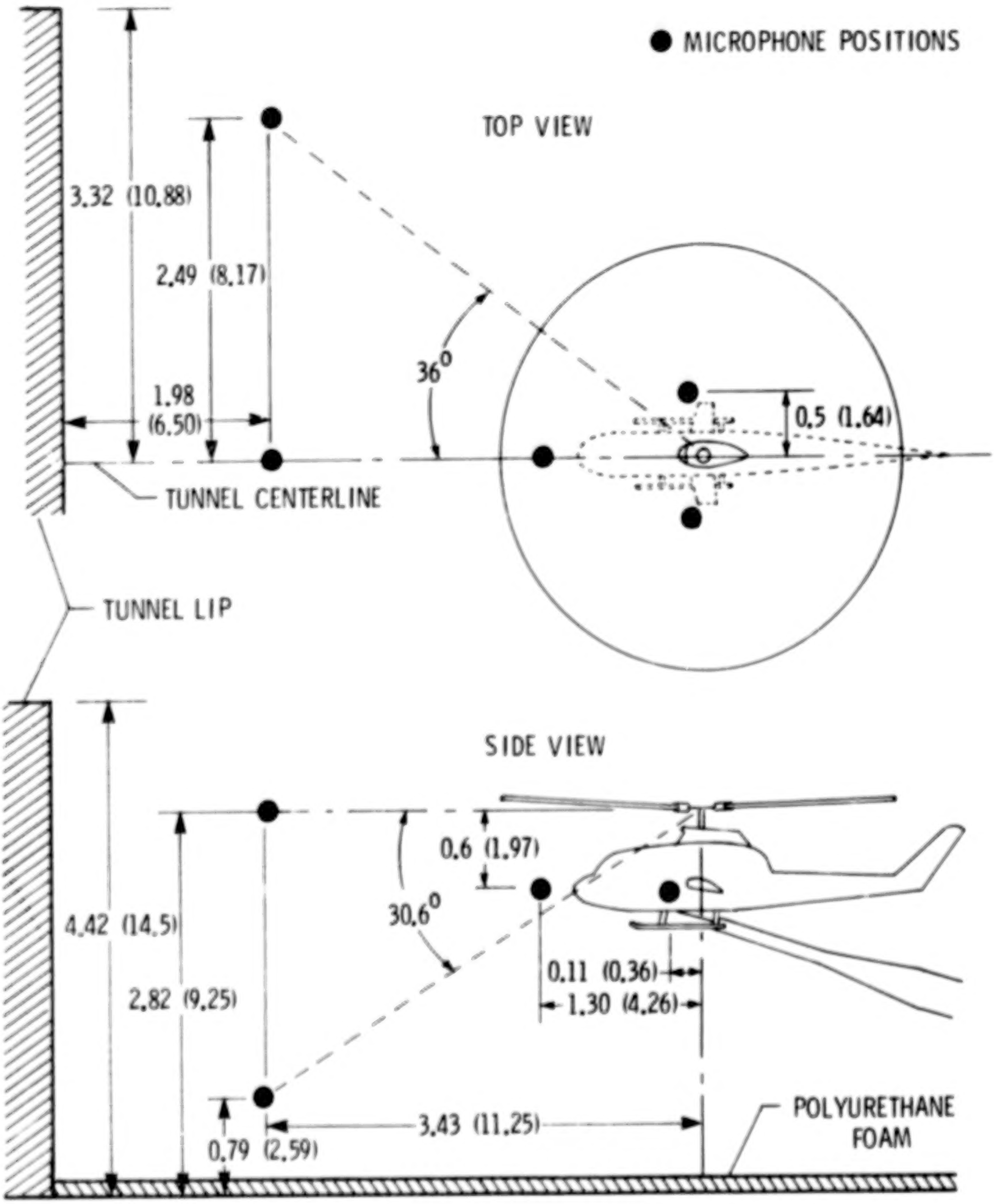
● MICROPHONE POSITIONS
TOP VIEW
3.32 (10.88)
2.49 (8.17)
36°
1.98
(6.50)
0.5 (1.64)
TUNNEL CENTERLINE
TUNNEL LIP
SIDE VIEW
0.6 (1.97)
30.6°
4.42 (14.5)
2.82 (9.25)
0.11 (0.36)
1.30 (4.26)
3.43 (11.25)
0.79 (2.59)
POLYURETHANE FOAM

Figure 2.- Model and microphone position in tunnel. Dimensions in m (ft).

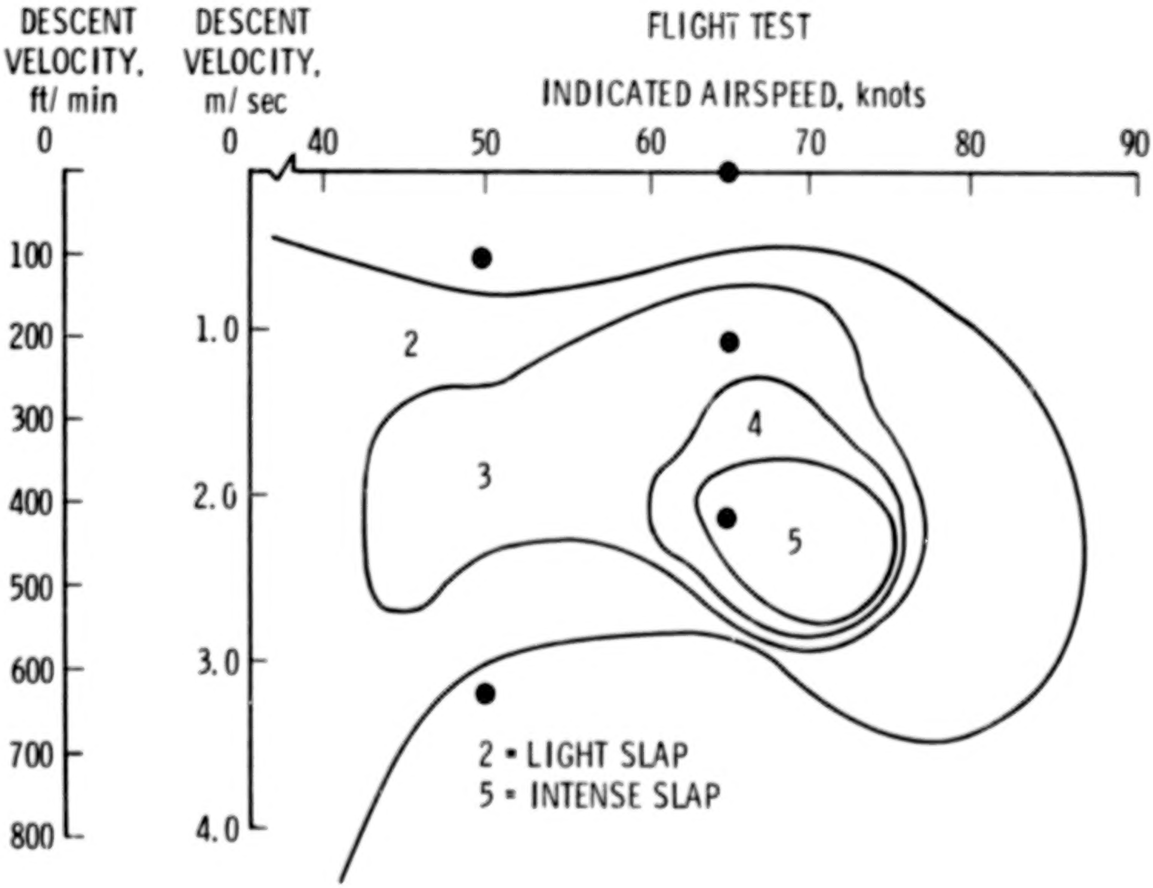

Figure 3.- Internal noise, observer objective response, AH-1G flight test.

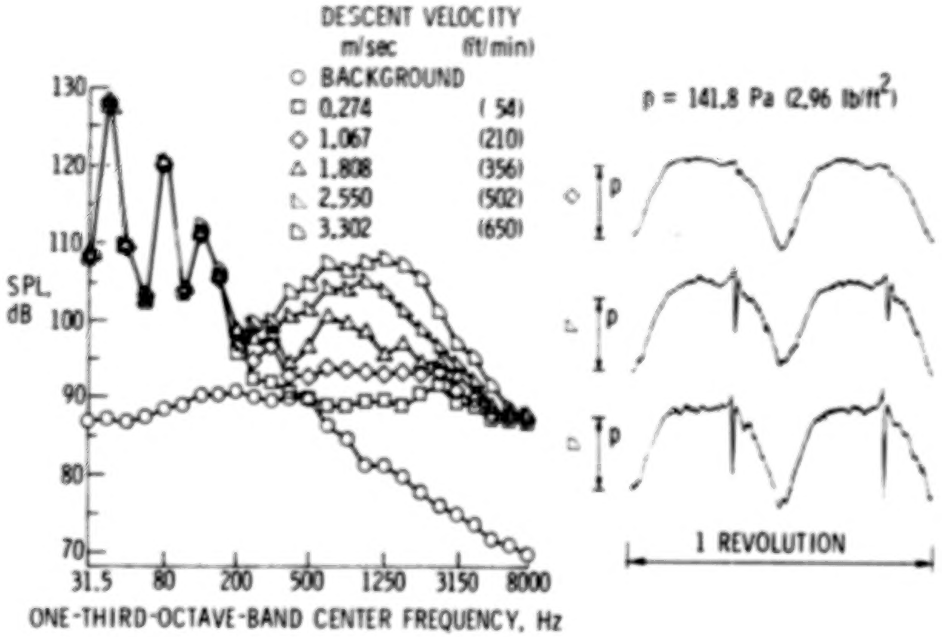

(a) Nose microphone, V_f = 50.7 knots.

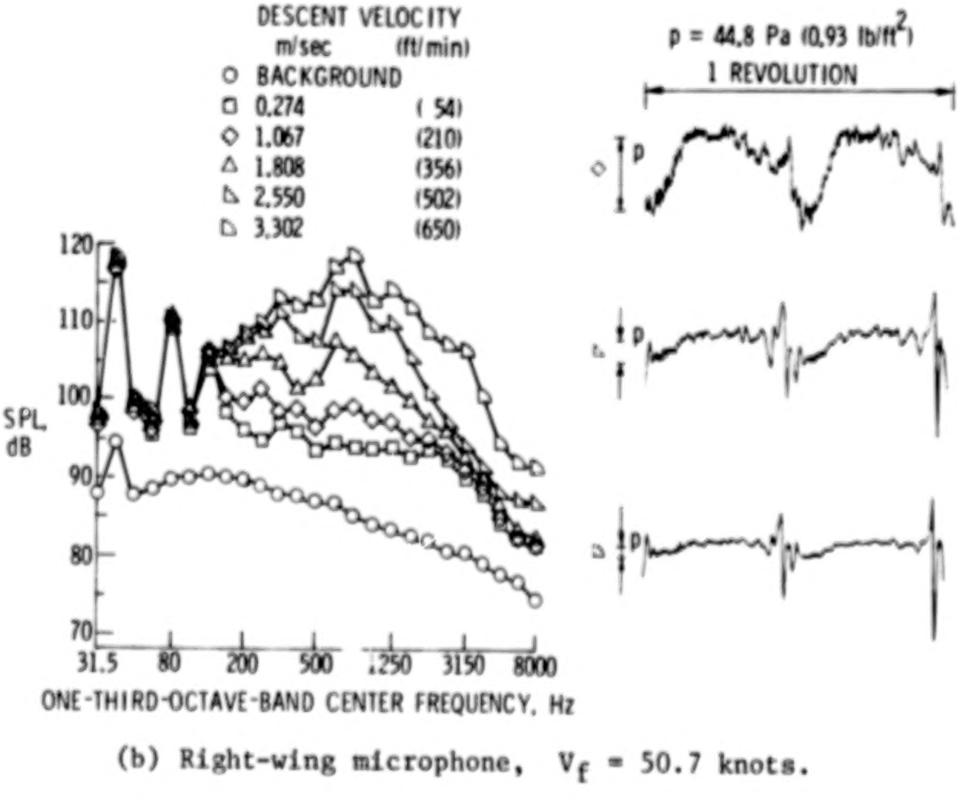

(b) Right-wing microphone, V_f = 50.7 knots.

Figure 4.- Effect of descent velocity on one-third-octave spectrum and time history for model test.

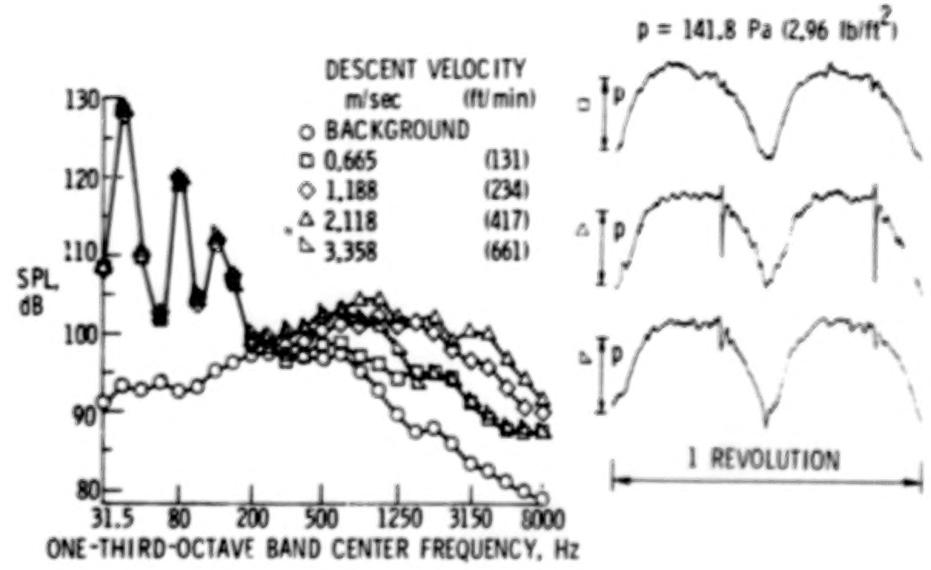

(c) Nose microphone, V_f = 71.1 knots.

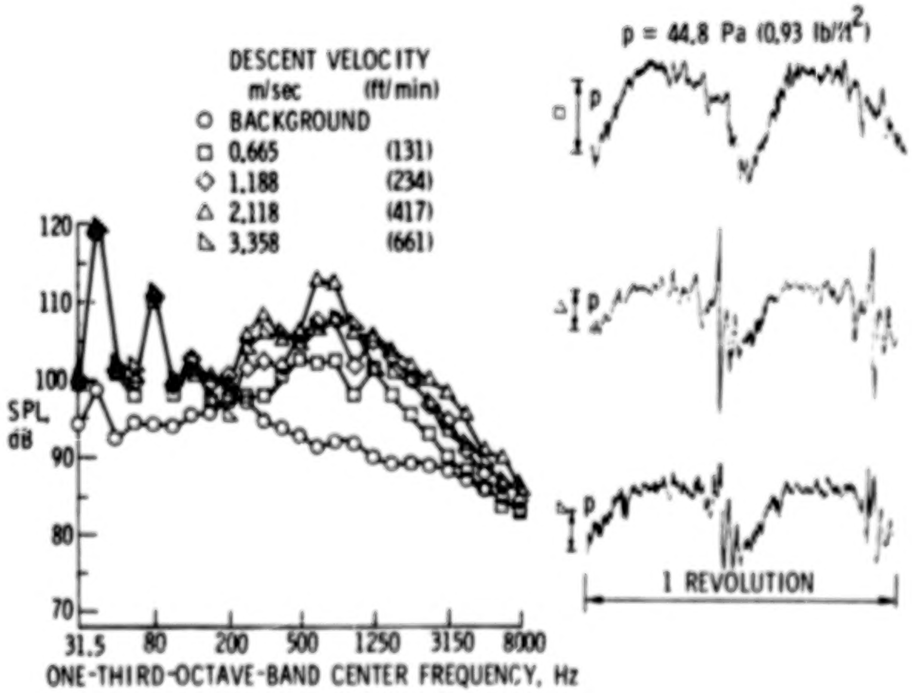

(d) Right-wing microphone, V_f = 71.1 knots.

Figure 4.- Concluded.

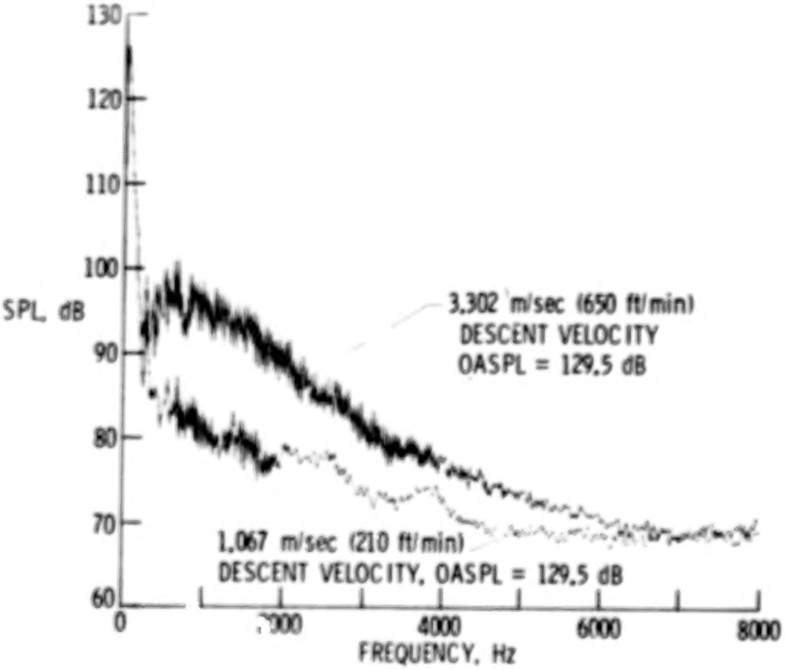

(a) V_f = 50.7 knots.

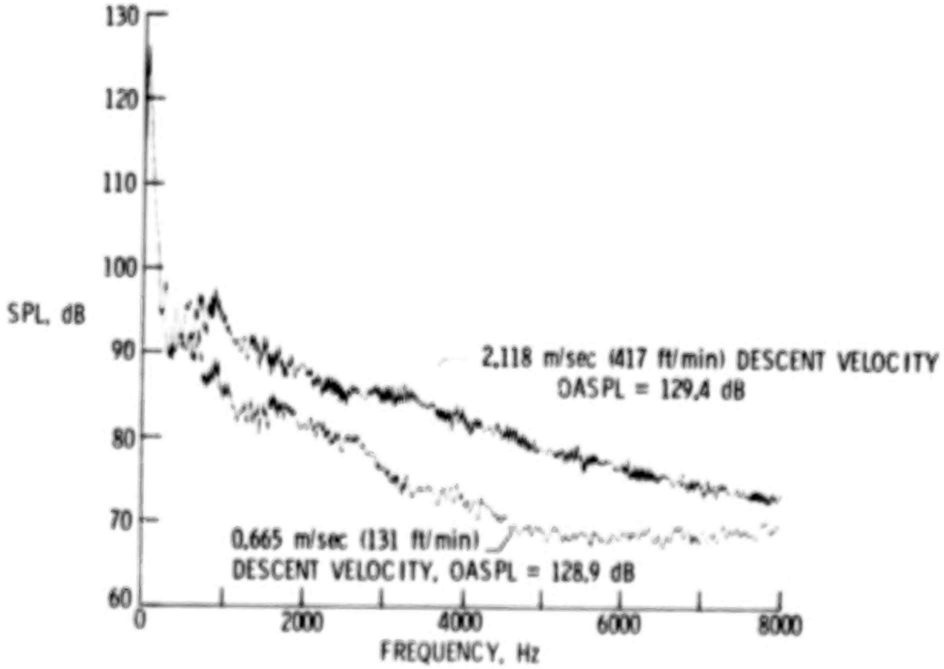

(b) V_f = 71.1 knots.

Figure 5.- Comparison of narrow band analysis of two descent velocities for model tests, nose microphone.

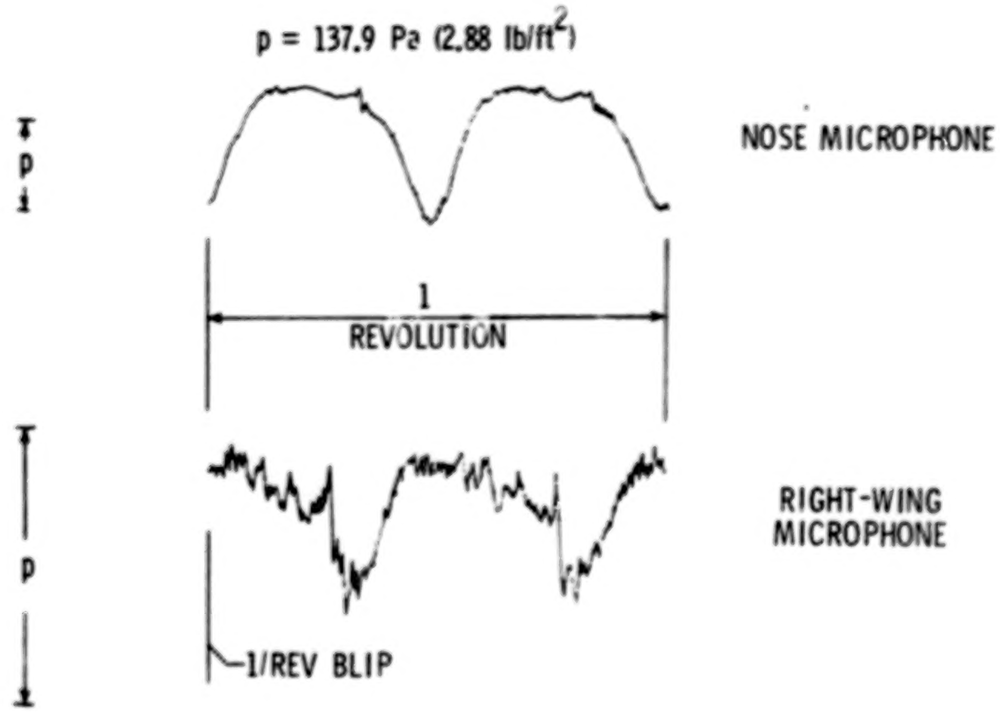

(a) Model data; Descent velocity = 1.067 m/sec (210 ft/min); V_f = 50.7 knots.

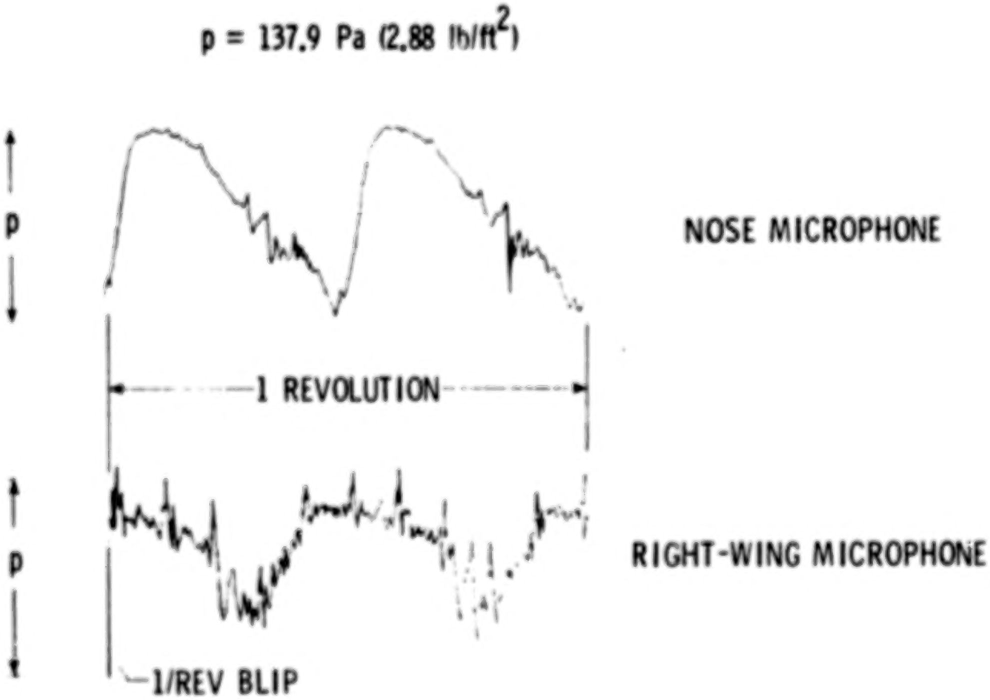

(b) Flight-test data; Descent velocity = 0.508 m/sec (100 ft/min); $V_f \approx 53$ knots.

Figure 6.- Comparison of model and flight recorded acoustic time history for two microphone positions.

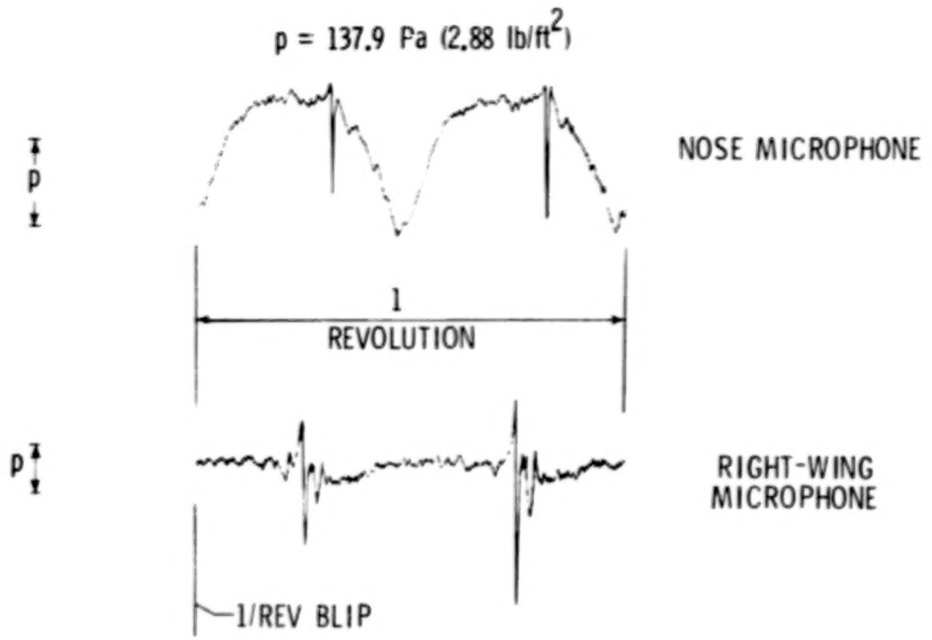

(c) Model data; Descent velocity = 3.302 m/sec (650 ft/min); V_f = 50.7 knots.

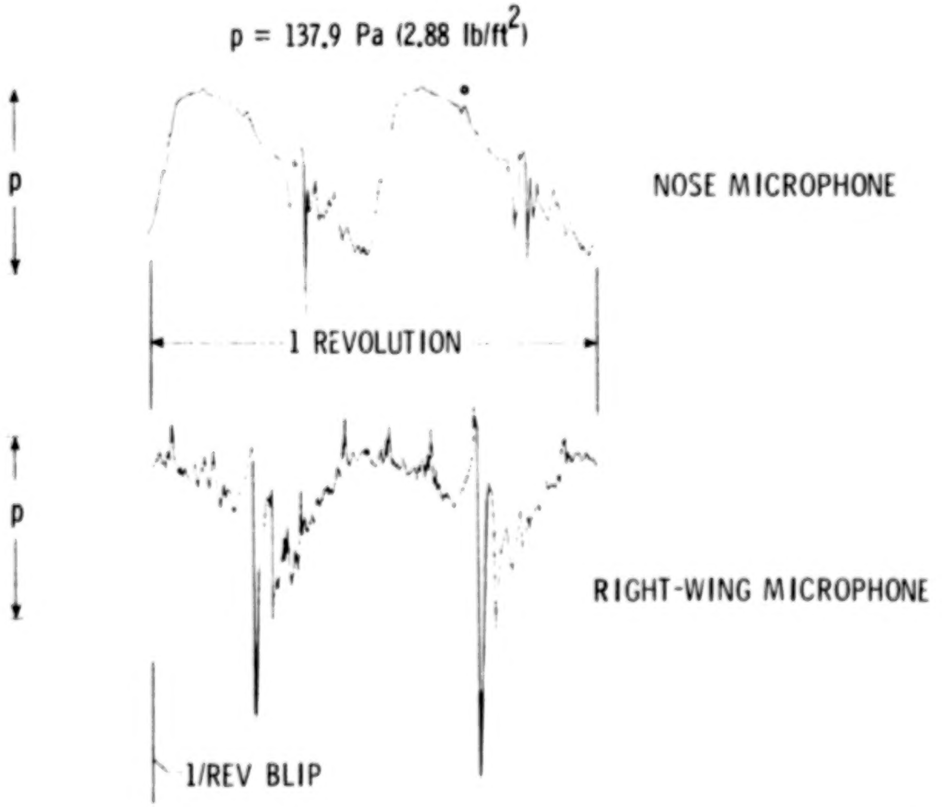

(d) Flight-test data; Descent velocity = 3.048 m/sec (600 ft/min); $V_f \approx 53$ knots.

Figure 6.- Concluded.

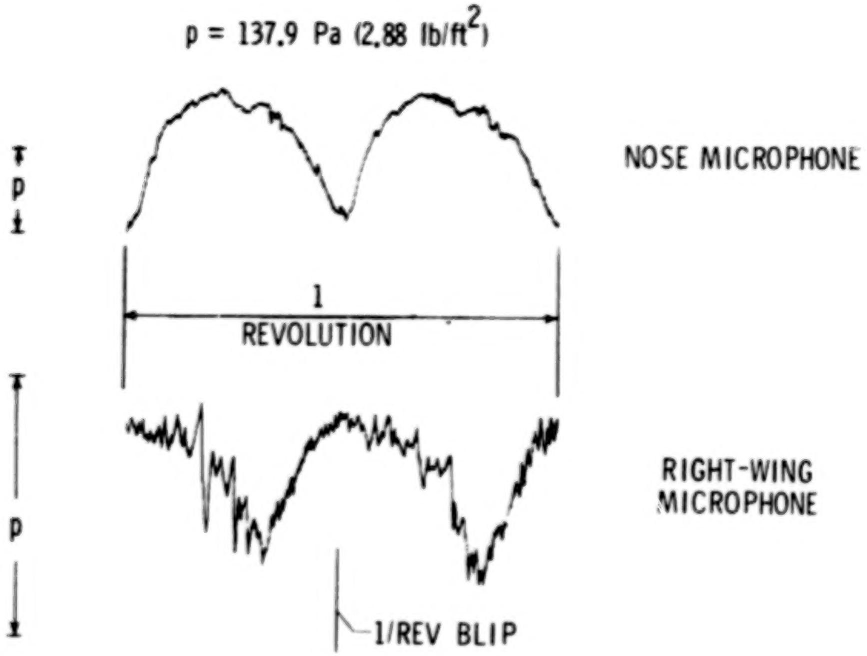

(a) Model data; Descent velocity = 0.665 m/sec (131 ft/min); V_f = 71.1 knots.

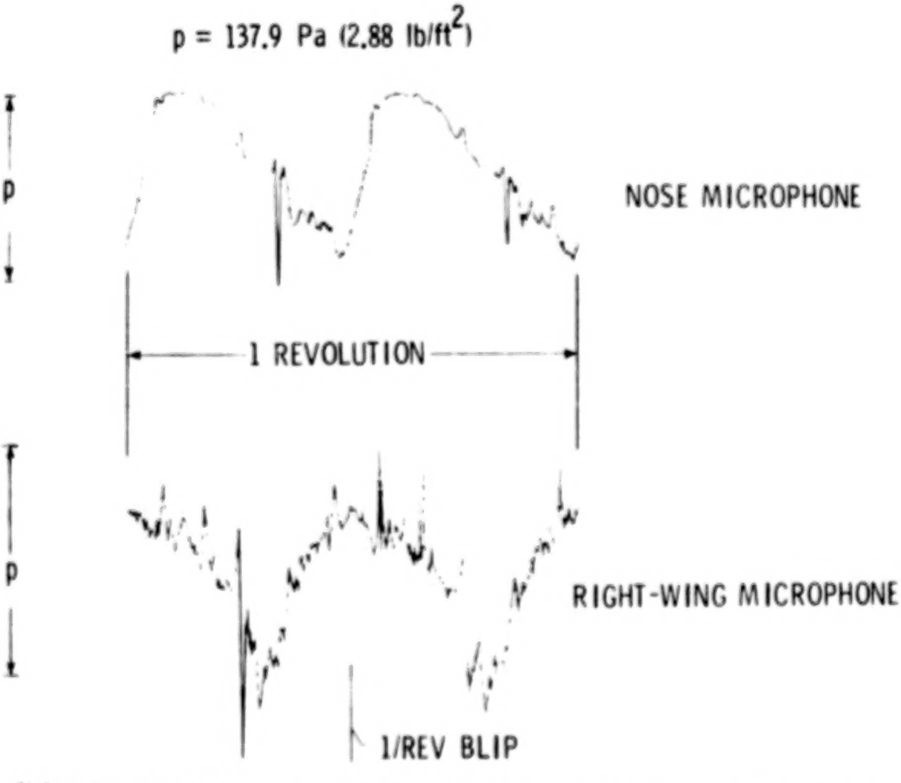

(b) Flight data; Descent velocity = 0 m/sec (0 ft/min); $V_f \approx$ 68 knots; ≈914.4 m (≈3000 ft) pressure altitude.

Figure 7.- Comparison of model and flight recorded acoustic time history for two microphone positions. Low descent velocities.

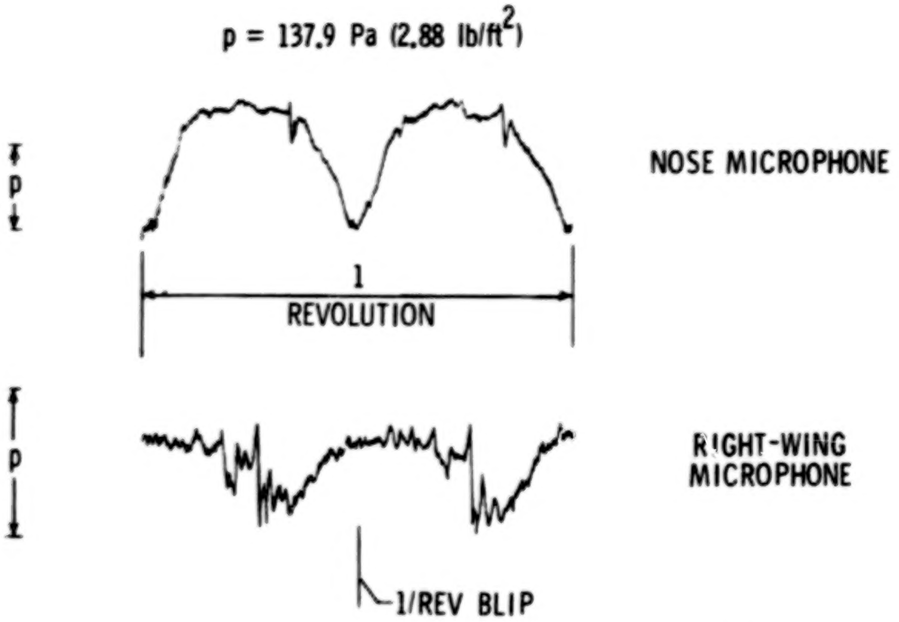

(a) Model data; Descent velocity = 1.188 m/sec (234 ft/min); V_f = 71.1 knots.

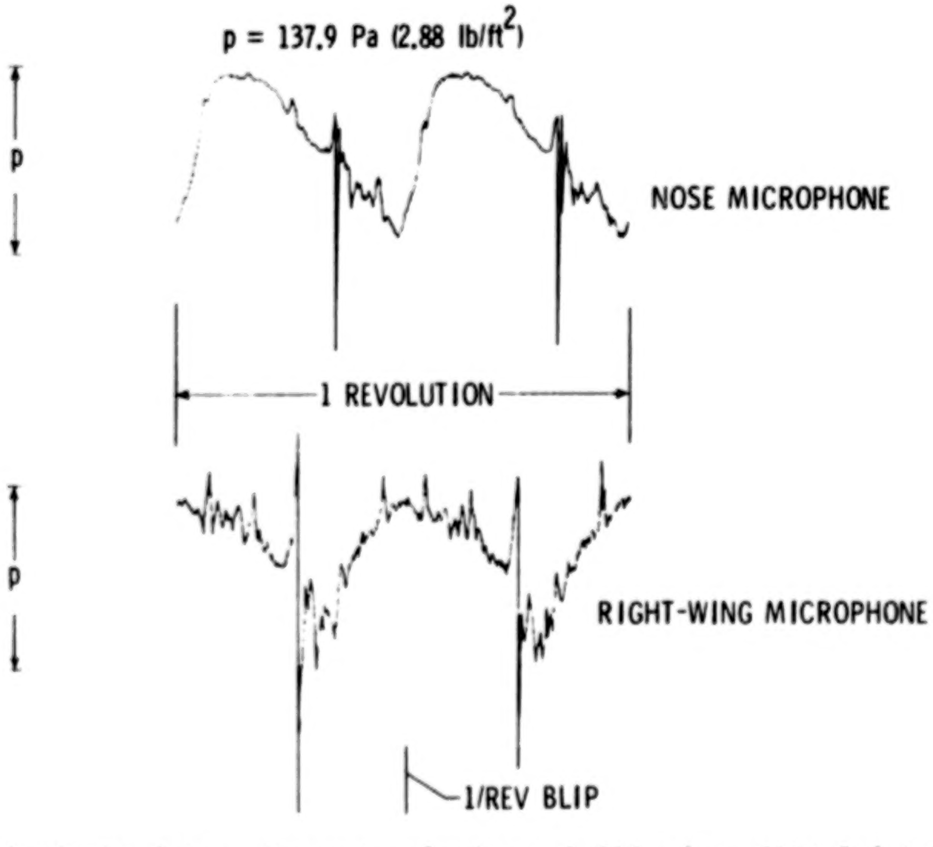

(b) Flight data; Descent velocity = 1.016 m/sec (200 ft/min); V_f = 68 knots; ≈914.4 m (≈3000 ft) pressure altitude.

Figure 8.- Comparison of model and flight recorded acoustic time history for two microphone positions. Moderate descent velocities.

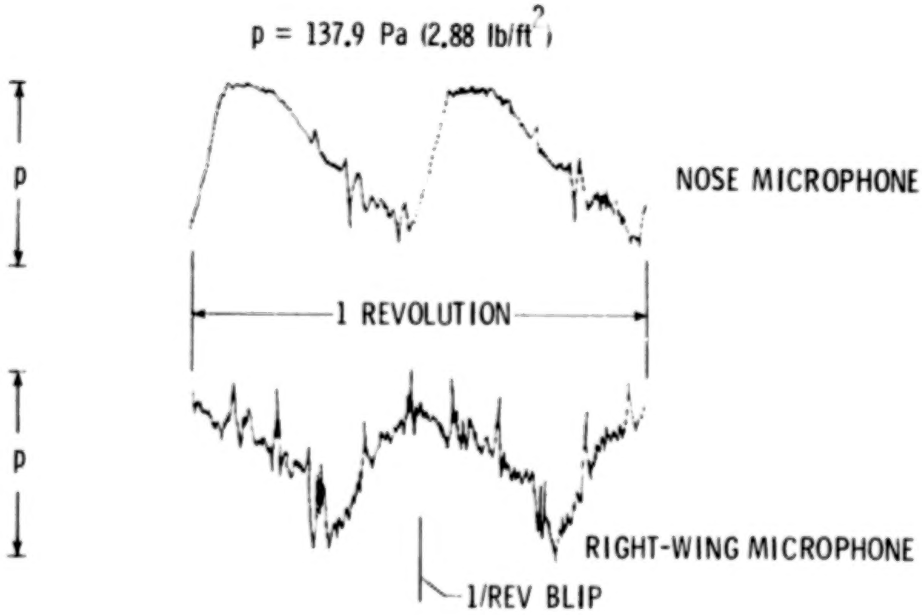

(c) Flight data; Descent velocity = 1.016 m/sec (200 ft/min); $V_f \approx$ 66 knots; ≈396.2 m (≈1300 ft) pressure altitude.

Figure 8.- Concluded.

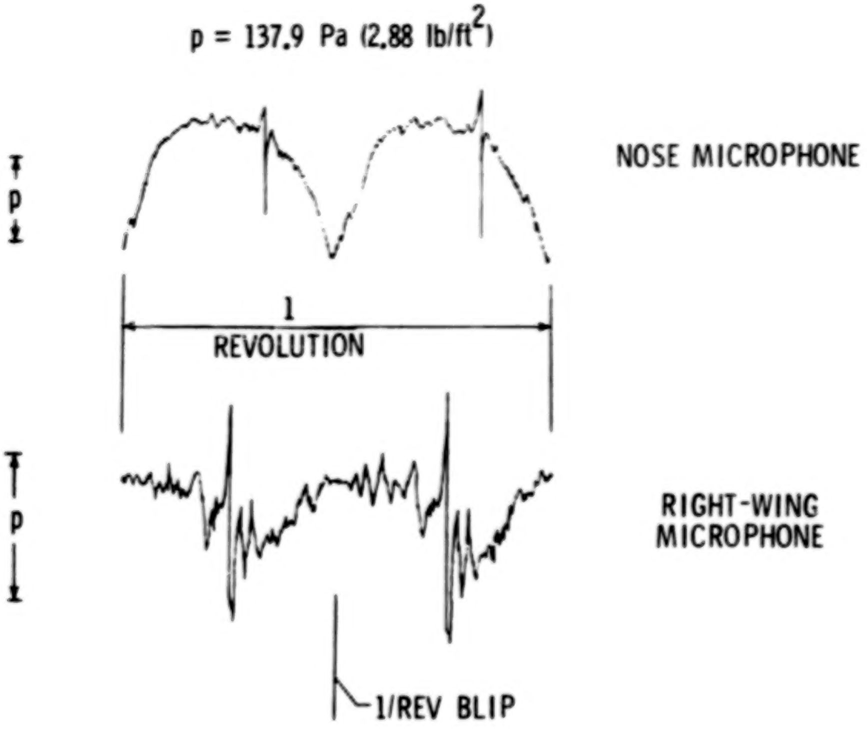

(a) Model data; Descent velocity = 2.118 m/sec (417 ft/min); V_f = 71.1 knots.

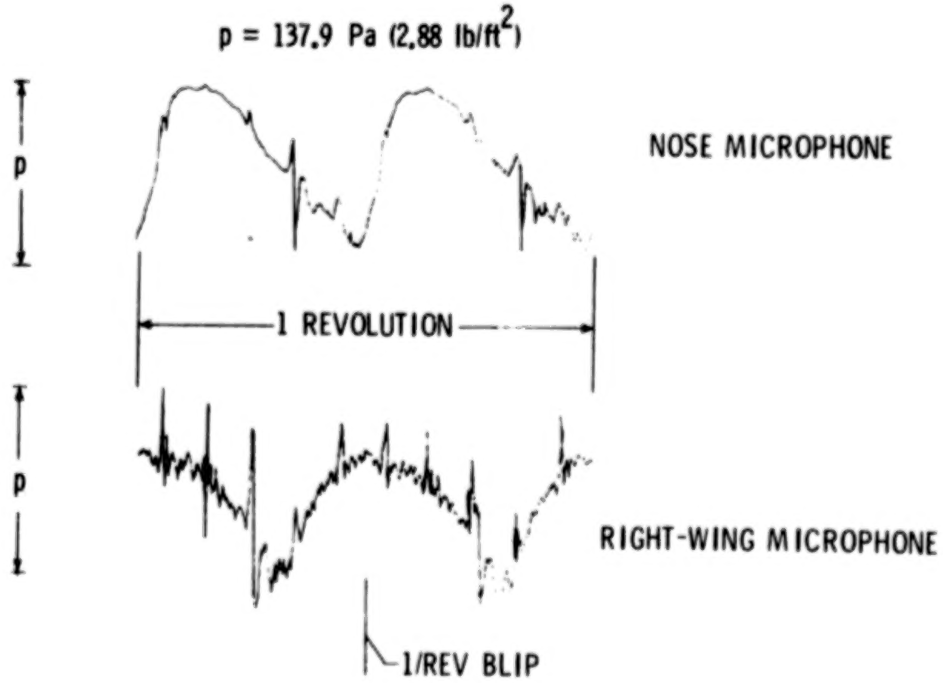

(b) Flight data; Descent velocity = 2.032 m/sec (400 ft/min); V_f ≈ 68 knots; ≈914.4 m (≈3000 ft) pressure altitude.

Figure 9.- Comparison of model and flight recorded time history for two microphone positions. High descent velocities.

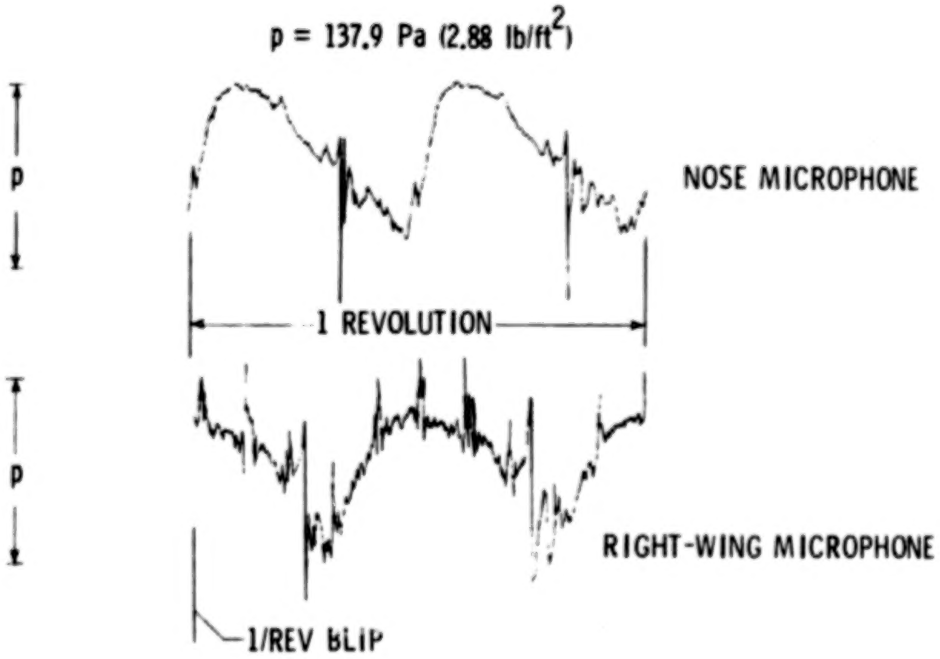

(c) Flight data; Descent velocity = 2.032 m/sec (400 ft/min); $V_f \approx 66$ knots; ≈396.2 m (≈1300 ft) pressure altitude.

Figure 9.- Concluded.

EXPLORATORY WIND-TUNNEL INVESTIGATION OF THE EFFECT OF THE MAIN ROTOR WAKE ON TAIL ROTOR NOISE

Robert J. Pegg and Phillip A. Shidler
NASA Langley Research Center

SUMMARY

One of the primary sources of noise from a helicopter is the noise of the tail rotor. To a large extent, the intensity of this noise is affected by the interaction of the tail rotor blades with the wake of the main rotor. Under most flight conditions the flow from the main rotor is very turbulent and unsteady and results in higher levels of tail rotor noise than that which would normally occur from the tail rotor operating in an undisturbed flow. This increase in tail rotor noise apparently arises from ingestion of the main rotor non-uniform wake into the tail rotor and the interactions of the main rotor tip vortices with the tail rotor blades.

Approaches to minimizing this interaction noise have included repositioning of the tail rotor with respect to the main rotor, changes in the rotational direction of the tail rotor, and modification of the main rotor tip vortex. No straight-forward solution, however, exists for all situations.

In view of the complexity of the problem of main rotor/tail rotor interactions and lack of suitable analytical techniques to study the problem in detail, an experimental program was conducted in order to further the understanding of this noise phenomenon.

A variable geometry model was built which had the capability of varying tail rotor position relative to the main rotor as well as direction of tail rotor rotation. Acoustic data taken from the model in the Langley anechoic noise facility indicates interaction effects due to both the main rotor shed vortex and the main rotor turbulence.

INTRODUCTION

For the vast majority of helicopters flying today torque compensation and directional control is accomplished by means of a tail rotor. Although the tail rotor produces less thrust and consumes less power than the main rotor, it can be a serious source of noise since its harmonics usually predominate in the frequency range from 200 Hz to 3000 Hz.

References 1, 2, and 3 detail some operational problems and design considerations which are involved in current tail rotor design procedures. In addition to these requirements, constraints are being considered to have helicopters conform to governmental noise regulations.

The intensity of the tail rotor noise is affected by the interaction of the tail rotor blades with the wake of the main rotor. Under most flight conditions the ingested flow from the main rotor is very turbulent and unsteady and results in higher levels of tail rotor noise than would occur normally if the tail rotor were operating in undistrubed flow. Reference 4 discusses the results of a test program with a production helicopter in which significant noise reduction was achieved by reversing the direction of the tail rotor rotation. Because of the numerous other constraints (refs. 1, 2, and 3) placed on the tail rotor design, no straight-forward solution to the noise problem exists for all operational situations. Tail rotor noise problems, however, were treated analytically by Levine in reference 5 for a large helicopter. A wind-tunnel model was built and a preliminary experimental program was conducted in order to further the understanding of this noise phenomenon. The intial effort is reported in reference 6. The focus of the present investigation is to extend the work of reference 6 and to provide an insight into the flow mechanism causing the interaction noise.

INTERACTION NOISE MECHANISM

The tail rotor on most conventional helicopters is subjected to a highly turbulent and unsteady flow environment which has the potential to produce noise levels that would not be present in a quiescent flow. This excess noise is in addition to rotational and broadband noise gathered by a free rotor. Specifically, the tail rotor disk is immersed totally or partially in the main rotor wake during most flight conditions and is influenced by whatever installation effects are found for a particular design (i.e., effect of tail rotor fin on tail rotor inflow). The water tunnel flow studies of reference 7 provide an indication of the flow environment at the tail rotor. This wake disturbance is comprised of two principal ingredients: the shed vortices from the main rotor and the random turbulent wake lying between the upper and lower vortex boundaries. Figure 1 illustrates a cross-section of the complex flow field in which the tail rotor operates. As outlined in reference 8, the effect of the random, non-uniform part of the inflow on the tail rotor noise is to increase the level of the discrete tones at blade passage frequency as a result of non-uniform blade loading. Both reference 4 and reference 6 indicate that discrete frequencies which are not multiples of the tail rotor rotational speed are also produced.

The noise resulting from the interaction of the blades with the shed tip vortices of the main rotor is characterized by discrete tones occurring at combination frequencies which are nTR ± mMR. MR and TR are blade passage frequencies of the main and tail rotors and n and m are harmonic integers. Depending on the number of tail rotor blades and the flight condition, a blade may intersect a vortex several times before it passes through the tail rotor disk.

In order to examine the interaction noise in detail, it is necessary to determine how the main rotor wake intersects the tail rotor. This can be done by using a free-wake analysis to predict accurate vortex trajectories. This technique, however, requires considerable computer time to obtain a satisfactory answer (ref. 9.) A simplified approach to the tip vortex trajectory problem can be obtained from the modified momentum analysis of Coleman in reference 10. This simplified approach does not account for wake instabilities or rotor disk leading edge lap-over that has been observed on helicopters under actual flight conditions. It is assumed, however, that the wake distortion in forward flight at the tail rotor position is of second order importance because of the close proximity of the tail rotor to the main rotor. The following equations have been used to determine the fore and aft wake trajectory boundaries adjacent to the main rotor:

wake trajectory at center of rotor:

$$\text{Tan}\ \chi_o = -\frac{\mu}{\lambda_0} \qquad (1)$$

where:

χ_o is the wake angle at the center of the rotor; μ is the advance ratio and λ_0 is the inflow ratio at the rotor center.

Induced velocities at the leading and trailing edge of the rotor disk:

$$w = w_o(\pm\tan\chi_o/2) \qquad (2)$$

where:

w_o is the induced velocity at the center of the rotor disk. The positive sign indicates the induced velocity from the aft portion of the disk.

The fore and aft wake angles are:

$$\tan\chi_F = -\frac{V_F\cos\alpha}{V_F\sin\alpha - w_F} \qquad (3a)$$

$$\tan\chi_R = -\frac{V_F\cos\alpha}{V_F\sin\alpha - w_R} \qquad (3b)$$

where:

V_F and α are the forward velocity and rotor angle of attack, respectively.

Figure 2 shows the calculated wake trajectories for the six different forward flight operating conditions used in this program.

MODEL TEST PROGRAM

The tests were conducted in the Langley anechoic noise facility and were planned as the initial phase of a detailed program to reduce tail rotor noise. This section of the paper describes the helicopter model, the test setup, and the data acquisition and reduction procedures.

Helicopter Model

A photograph of the model used for this investigation is shown in figure 3. The model uses a two-bladed rotor system with offset flapping hinges. The two main rotor blades have a radius of 59.06 cm (18.0 in.), a 4.45 cm (1.36 in.) chord, and a -8° linear twist from blade root to blade tip. The blades have an NACA 0015 airfoil section. Flapping hinge offset from the center of rotation is 1.92 cm (0.756 in.) or 4.2 percent of the radius. The two-bladed tail rotor is 19.1 cm (7.5 in.) in diameter and has a chord of 1.14 cm (0.45 in.). The untwisted tail rotor blade has an NACA 0015 airfoil section and is cantilevered to the hub. The spacing between the fin and the tail rotor is approximately 1.3 cm (0.5 in.) Both the main and tail rotors have square blade tips.

The helicopter model was designed in such a manner as to provide the capability for variations in the main rotor wake/tail rotor operating parameters (fig. 3). The design features of the model which provided this flexibility are: (a) adjustable tail boom length, (b) adjustable tail boom angle, (c) variable tail rotor rotational speed, (d) direction of the tail rotor rotation, (e) direction of tail rotor thrust, (f) variation of main rotor thrust and rotational speed, and (g) variation in model angle of attack. Table I lists the range over which these parameters could be varied. The model was operated such that the tail rotor downwash was against the fin and that the advancing blade was in the upper portion of the disk.

The helicopter model is provided with two electric motors. A 2.2-kw (3 hp), 220-V, 60-Hz motor powers the main rotor. A 0.003 kw (0.004 hp) motor drives the tail rotor. Rotational speed on both motors can be varied from 0 to a maximum of 4400 rpm on the main rotor drive and 13,000 rpm on the tail rotor. Load measuring devices around the main rotor shaft and at the base of the tail boom are used to measure the main and tail thrust.

Wind-Tunnel Tests

The wind-tunnel tests were conducted in the Langley anechoic noise facility. Figure 4 is a schematic diagram of the microphone positions with respect to the model. Tunnel speeds for the tests were 0.0, 10.0, 20.1, and 29.8 m/sec resulting in advance ratios of 0, 0.10, 0.20, and 0.29, respectively, at a nominal main rotor rotational speed of 2120 rpm. A summary of the test conditions and model configurations are presented in Table I. Tests were conducted with the model both in and out of trim, these conditions are shown in figure 5 as a function of main rotor blade setting and tunnel velocity. Also given are the vortex circulation values, Γ, for each operating point.

Typical background noise levels are shown in a narrow band presentation to 5000 Hz for the four test velocities in figure 6. These spectra were obtained with the model in place and with the rotors stopped. These background noise levels are shown below the measured data. The tones which appear in the spectra are apparently due to vortex shedding from the model.

Data Acquisition and Reduction

The noise measurement equipment used for these tests was a commercially available system. Four free-field microphones were used in the test program. These microphones are condenser types having a 1.27 cm (0.5 in.) diameter active diaphram and a frequency response that was flat to within ± 1½ dB over the frequency range from 5 to approximately 15 000 Hz. An FM magnetic tape recorder was used to record the microphone output for these tests. The response was flat within ±3 dB from 0 to 10 000 Hz at 38 cm/sec (15 ips) tape speed with wide band recording. All acoustic measurements were made in accordance with the recommendation of reference 11. The entire sound measurement system was calibrated immediately before and after the tests by means of a discrete-frequency calibrator. A 100 Hz high-pass filter was used to obtain greater dynamic range. The data of interest in this investigation is all well above the 100 Hz cutoff frequency.

The data obtained from these tests were reduced by analog methods. Narrow band analyses were made using a spectrum analyzer. The resultant spectra cover a range from 0 to 2000 Hz with a 12 Hz resolution and from 0 to 5000 Hz with a 30 Hz resolution.

TEST RESULTS

The test program discussed in this paper is the first phase of a more extensive investigation into tail rotor noise due to interaction effects. The results will be presented to illustrate the acoustic characteristics of the basic helicopter model and the effects of the interaction. The data will be in the form of sound pressure time histories and acoustic spectra. figure 7 illustrates a typical acoustic time history of the complete model and a corresponding spectrum. The tail rotor harmonics and tail rotor/fin tones are identifiable. This is an installation effect and is due to the momentary disturbance of the uniform loading of the tail rotor by the presence of the fin.

No-flow Interaction Effects

A typical acoustic spectrum of the main and tail rotors alone and also together are shown in figure 8. The tunnel velocity for this condition is zero and for this particular case data were taken from microphone 2. There was no ground plane used during these hover tests. The main rotor was lightly loaded as is indicated by the circulation value in figure 5. The discrete tones of the tail rotor have been identified and are the maximum levels as marked by the circles. The broadband noise floor level is below the dynamic range of the recording system. The acoustic spectrum for the main rotor alone is given with the solid lines. Harmonics are discernable to the 21st blade passage frequency. The broadband noise floor for the main rotor varies from approximately 50 dB to 55 dB.

For the hover flight condition, the interaction appears to affect the noise of the main rotor. Although the fundamental and first few harmonics do not change when the main and tail rotors are operated together, there is a definite increase in the higher order main rotor harmonics. No appreciable changes are noted in the tail rotor harmonics. This phenomenon is probably due to the local velocity field around a small portion of the main rotor induced by the tail rotor.

Interaction Effects With Tunnel Flow

The effect of forward speed on the source of the interaction noise, namely the main rotor wake, is to skew the wake into the tail rotor beginning at very low speeds. The calculated wakes are shown schematically in figure 2. The effect of increased forward speed at different tail positions is shown in figures 9 and 10 for 10 and 20 m/sec. From the data of these figures it can be seen that combination tones are present that have frequencies nTR ± mTR. These tones are generated by the intersection of shed main rotor vortices and the tail rotor blades. As a vortex passes through the tail rotor disk, it may intersect each blade at different radial stations depending on the blade azimuth. An intersection on an advancing blade tip will produce a stronger impulsive type loading than one farther down the blade because of the relative velocities of the blade and vortex and the short duration of the encounter. Numerous intersections can be made as the vortex passes through the tail rotor disk.

A comparison of the acoustic pressure time histories in Figure 11 indicates a progression of events. The sound pressure time history at 10 m/sec and low tail rotor position clearly shows the passage of the tail rotor blade; however, as the tunnel velocity is increased to 29.8 m/sec, the tail rotor modulated pressure signal is overshadowed by the individual blade-vortex intersections. At the higher tail rotor position the impulsive character of these intersections are somewhat reduced but are still the prevalent noise source.

The effect of inflow turbulence on the acoustic spectra to 5,000 Hz is shown in figure 12. For the tail rotor in the raised position and 29.8 m/sec tunnel velocity, significant tones at tail rotor blade passage frequency occur between 2000 Hz and 5000 Hz. This phenomenon was noted only in this operating condition.

CONCLUDING REMARKS

A research program has been initiated to investigate the aero/acoustic mechanisms relating to the increased tail rotor noise from the influence of the main rotor. This paper discusses the results of the first phase of this program. The helicopter model with a 118 cm (3 ft) diameter main rotor was used in the investigation. This model can vary tail rotor position with respect to the main rotor, tail rotor speed and thrust direction and overall model and wake orientation. In general, it was shown that a model of this size had the capability of providing information relative to the mechanisms involved in interaction noise and thus is a tool to explore techniques for reducing this noise source.

During the investigation it was found that certain characteristics of tail rotor noise were attributable to the interaction effects of the main rotor wake turbulence and shed vortices and certain installation effects. Interaction effects are hypothesized to originate from the intersection of the tail rotor baldes with the shed main rotor vortices and turbulent main rotor wake. These sources create additional tones which are combinations of the main and tail rotor frequencies as well as increasing the level of existing tail rotor harmonics. The primary installation effect is due to the asymmetric loading on the tail rotor disk due to a tail rotor blade passing over the tail fin. This effect produces acoustic harmonics which, under uniform loading conditions would cancel completely in the disk.

During hover conditions, the main rotor noise reflected an interaction effect on the tail rotor on the main rotor flow field. Although the first several main rotor acoustic harmonics did not change in amplitude, the higher main rotor harmonics were increased as well as the level of the broadband noise floor.

REFERENCES

1. Lynn, R. R.; Robinson, F. D.; Batra, N. N.; and Duhon, J. M.: Tail Rotor Design. Part I: Aerodynamics. J. American Helicopter Soc., Vol. 15, no. 4, Oct. 1970, pp. 2-15.

2. Sheridan, Philip F.; and Wiesner, Wayne: Aerodynamics of Helicopter Flight Near the Ground. Preprint No. 77.33-04. Presented at 33rd Annual Nat. Forum of the American Helicopter Soc., May 1977.

3. Wiesner, Wayne; and Kohler, Gary: Tail Rotor Performance in Presence of Main Rotor, Ground, and Wings. J. American Helicopter Soc., Vol. 19, No. 3, July 1974, pp. 2-9.

4. Leverton, John W.; Pollard, John S.; and Willis, Christopher R.: Main Rotor Wake/Tail Rotor Intersection. Vertica, Vol. 1, 1977, pp. 213-221.

5. Levine, Larry S.: An Analytic Investigation of Techniques to Reduce Tail Rotor Noise. NASA CR-145014, 1976.

6. White, Richard P.; Balcerak, John C.; and Pegg, Robert J.: A Parametric Model Study of the Noise Generated by the Aerodynamic Interaction of the Tail Rotor with the Wake of the Main Rotor. American Helicopter Soc. Mid-East Region Symposium on Rotor Technology. Essington, Pa., Aug. 1976.

7. Lehman, August F.: Model Studies of Helicopter Tail Rotor Flow Patterns In and Out of Ground Effect. USAAVLABS TR 71-12, April 1971.

8. Hayden, Richard R.: Some Advance in Design Techniques for Low Noise Operation of Propellers and Fans. Presented at Noise-Con 77 (Hampton, Va.), Oct. 1977.

9. Sadler, S. Gene: Development and Application of a Method for Predicting Rotor Free Wake Positions and Resulting Rotor Blade Air Loads. NASA CR-1911, Dec. 1971.

10. Coleman, Robert P.; Feingold, Arnold M.; and Stempin, Carl W.: Evaluation of the Induced-Velocity Field of an Idealized Helicopter Rotor. NACA WR L-126, 1945. (Formerly NACA ARR L5E10.)

11. Measurements of Aircraft Exterior Noise in the Field. ARP796, Soc. Automotive Eng., Inc., June 15, 1965.

TABLE I.- SUMMARY OF NOMINAL OPERATING CONDITIONS

[θ_m, main rotor blade pitch; θ_T, tail rotor blade pitch; α_e, model angle of attack; ℓ_t, boom extension; α_B, boom angle]

Run	Rotor speed, rpm		Tunnel conditions		Model configuration				
	Main	Tail	Speed, m/sec	Temp., °C	θ_m, deg	θ_T, deg	α_e, deg	$\Delta\ell_t$, cm	α_B, deg
Untrimmed conditions									
1	0	0	10	26.7	----	---	-----	-----	-----
2	0	0	20	26.7	----	---	-----	-----	-----
3	0	0	29.8	26.7	----	---	-----	-----	-----
4	2120	0	10	27.2	11.5	5	-8	10.67	-19.3
5	2120	0	20	27.2	11.5	5	-8	10.67	-19.3
6	2120	0	29.8	27.8	11.5	5	-8	10.67	-19.3
7	0	10 800	10	29.4	11.5	5	-8	10.67	-19.3
8	0	10 800	20	29.4	11.5	5	-8	10.67	-19.3
9	0	10 800	29.8	30.6	11.5	5	-8	10.67	-19.3
10	2120	10 800	10	30.0	11.5	5	-8	10.67	-19.3
11	2120	10 800	20	30.0	11.5	5	-8	10.67	-19.3
12	2120	10 800	29.8	30.0	11.5	5	-8	10.67	-19.3
13	2120	10 800	10	30.0	11.5	5	-8	10.67	+4
14	2120	10 800	20	30.0	11.5	5	-8	10.67	+4
15	2120	10 800	29.8	30.6	11.5	5	-8	10.67	+4
16	2120	10 800	10	29.4	11.5	5	-8	23.37	+4
17	2120	10 800	20	30.0	11.5	5	-8	23.37	+4
18	2120	10 800	29.8	30.6	11.5	5	-8	23.37	+4
19	2120	10 800	10	30.6	11.5	5	-8	17.02	+4
20	2120	10 800	20	30.6	11.5	5	-8	17.02	+4
21	2120	10 800	29.8	30.6	11.5	5	-8	17.02	+4
22	2120	10 800	10	27.8	11.5	5	-8	10.67	-.2
23	2120	10 800	20	27.8	11.5	5	-8	10.67	-.2
24	2120	10 800	29.8	28.3	11.5	5	-8	10.67	-.2
25	2120	10 800	10	28.3	11.5	5	-8	17.02	-.2
26	2120	10 800	20	28.3	11.5	5	-8	17.02	-.2
27	2120	10 800	29.8	28.3	11.5	5	-8	17.02	-.2
28	2120	10 800	10	28.9	11.5	5	-8	17.02	-.2
29	2120	10 800	20	28.3	11.5	5	-8	23.37	-.2
30	2120	10 800	29.8	28.3	11.5	5	-8	23.37	-.2
31	2120	10 800	10	28.9	11.5	5	-8	23.37	-19.3
32	2120	10 800	20	28.9	11.5	5	-8	23.37	-19.3
33	2120	10 800	29.8	28.9	11.5	5	-8	23.37	-19.3
34	2120	10 800	10	28.9	11.5	5	-8	23.37	-19.3
35	2120	10 800	20	28.9	11.5	5	-8	23.37	-19.3
36	2120	10 800	29.8	28.9	11.5	5	-8	23.37	-19.3
Trim conditions									
1	2120	0	0	26.1	11.5	5	-8	14.48	-19.3
2	0	10 800	0	26.1	11.5	5	-8	14.48	-19.3
3	2120	10 800	0	26.1	11.5	5	-8	14.48	-19.3
4	2120	10 800	10	26.7	14.5	4.1	-2.3	14.48	.2
5	2120	10 800	10	27.2	14.5	4.1	-2.3	14.48	3.8
6	2120	10 800	10	27.2	14.5	4.1	-2.3	14.48	-19.3
7	2120	10 800	20	27.2	14.3	2.7	-5.6	14.48	-19.3
8	2120	10 800	20	28.3	14.3	2.7	-5.6	14.48	.2
9	2120	10 800	20	28.9	14.3	2.7	-5.6	14.48	3.8
10	2120	10 800	29.8	30.0	15.9	3.2	-10.0	14.48	3.8
11	2120	10 800	29.8	30.0	15.9	3.2	-10.0	14.48	.2
12	2120	10 800	29.8	30.6	15.9	3.2	-10.0	14.48	-19.3

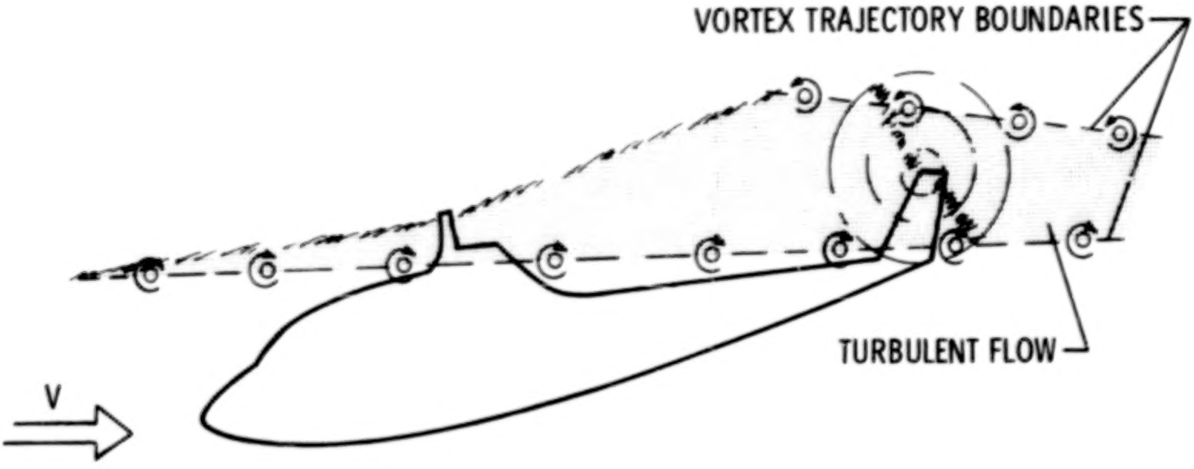
VORTEX TRAJECTORY BOUNDARIES
TURBULENT FLOW
V

Figure 1.- Cross-section of main rotor wake disturbances on tail rotor.

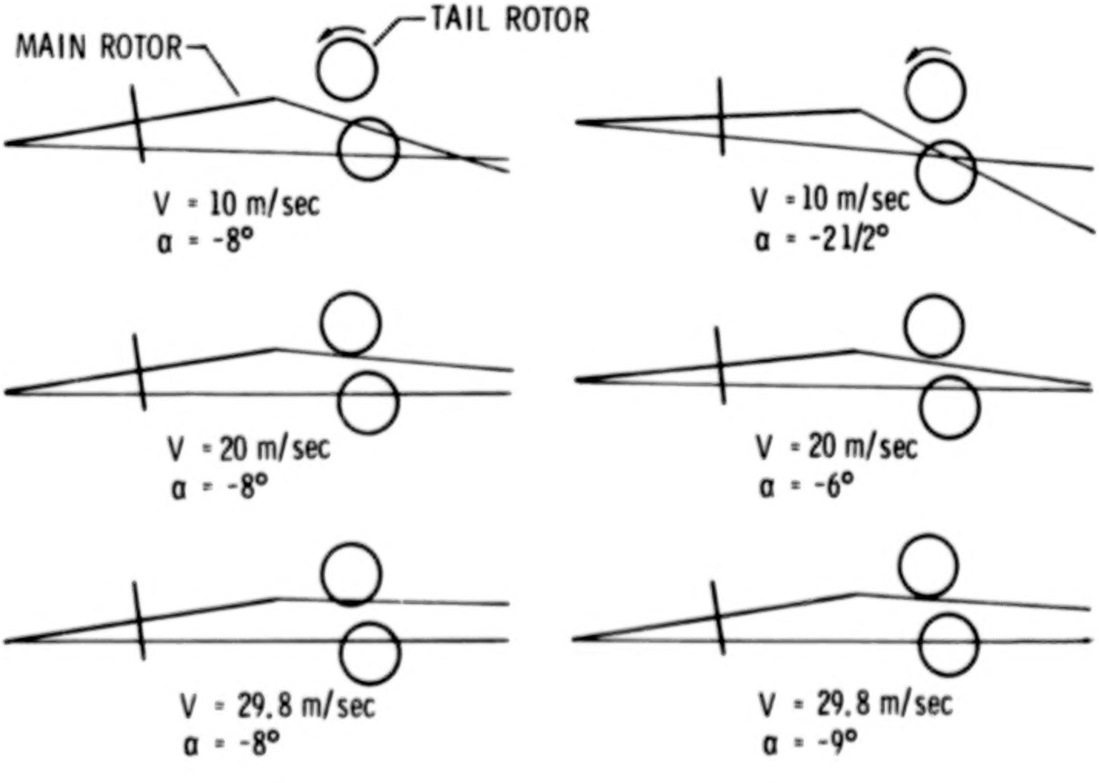
MAIN ROTOR
TAIL ROTOR
V = 10 m/sec
α = -8°
V = 10 m/sec
α = -21/2°
V = 20 m/sec
α = -8°
V = 20 m/sec
α = -6°
V = 29.8 m/sec
α = -8°
V = 29.8 m/sec
α = -9°

Figure 2.- Calculated wake trajectories.

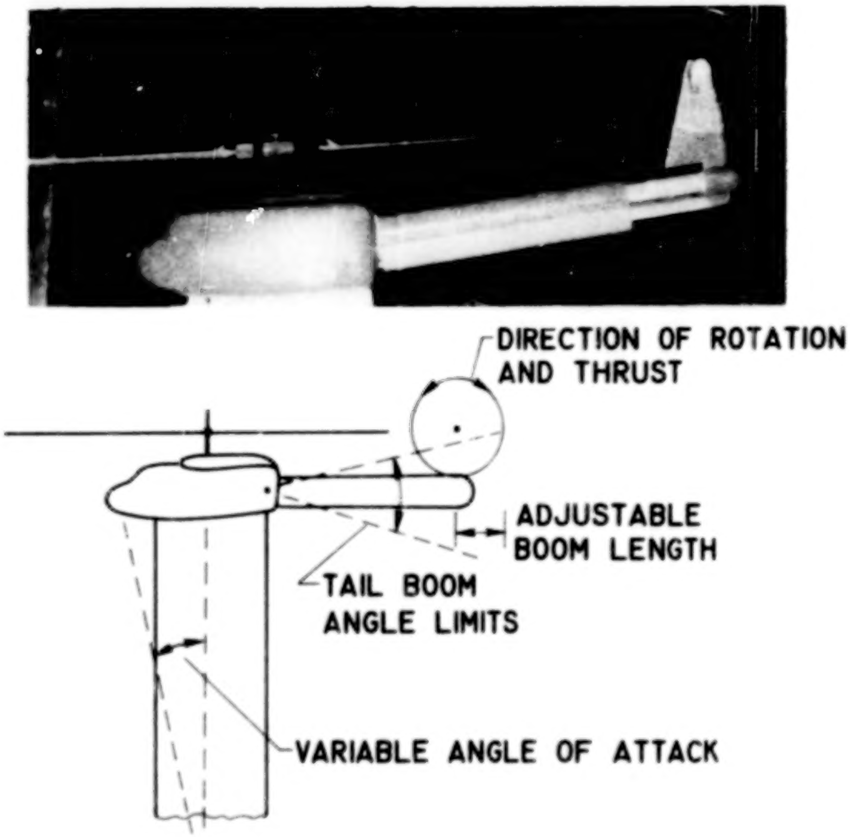
DIRECTION OF ROTATION AND THRUST
ADJUSTABLE BOOM LENGTH
TAIL BOOM ANGLE LIMITS
VARIABLE ANGLE OF ATTACK

Figure 3.- Wind-tunnel model showing configuration variables.

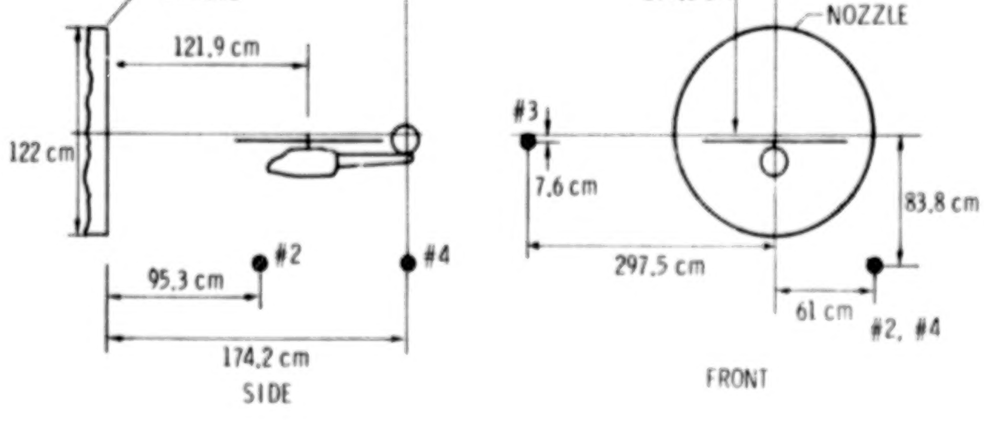
MICROPHONE
#1
NOZZLE
121.9 cm
122 cm
95.3 cm
#2
#4
174.2 cm
SIDE
#1
289.6 cm
NOZZLE
#3
7.6 cm
83.8 cm
297.5 cm
61 cm
#2, #4
FRONT

Figure 4.- Microphone locations.

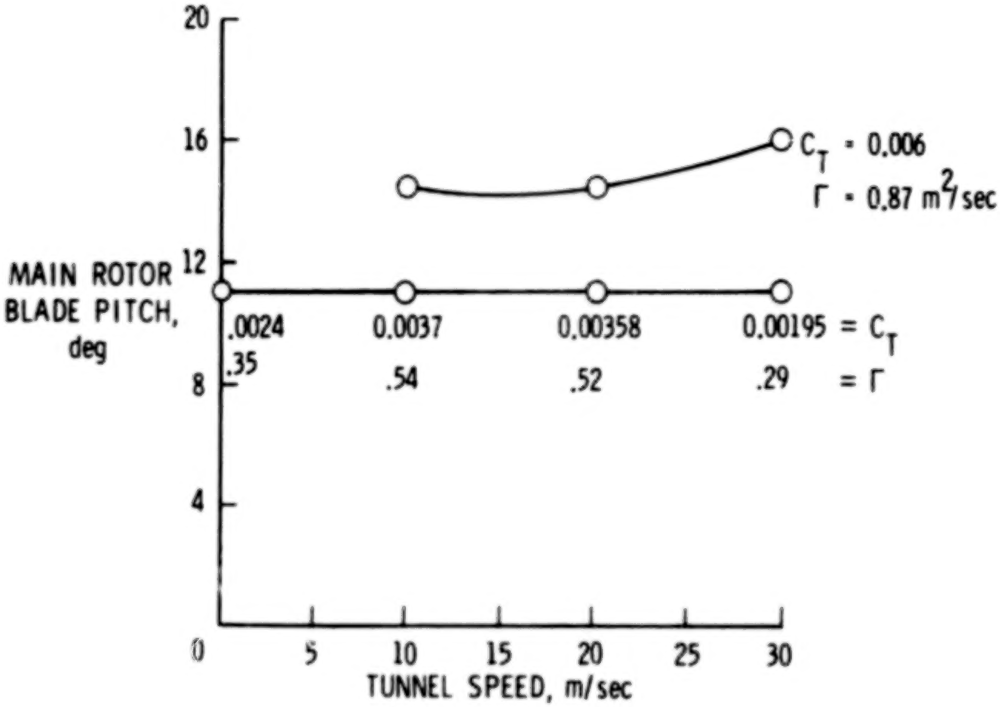

Figure 5.- Model operating conditions.

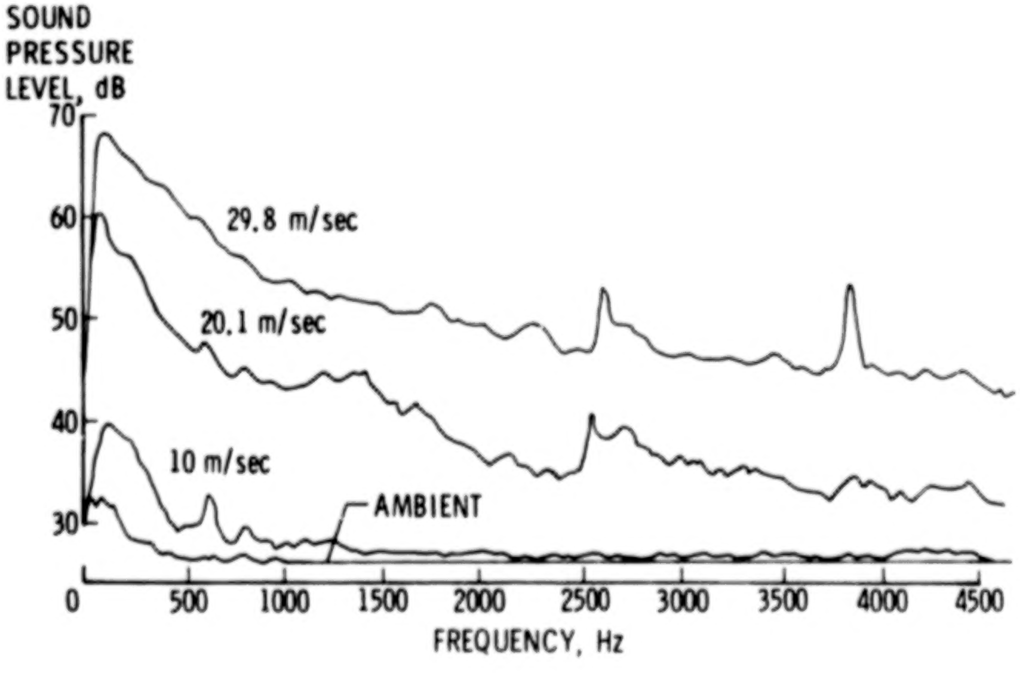

Figure 6.- Anechoic flow facility background noise levels with model installed.

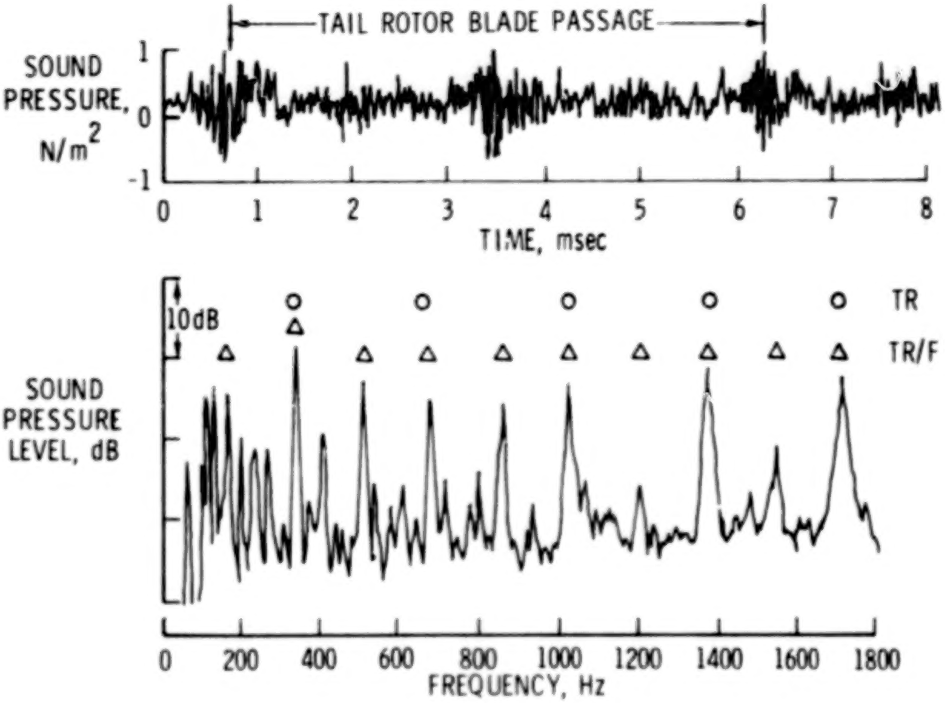

Figure 7.- Typical time history and spectra.

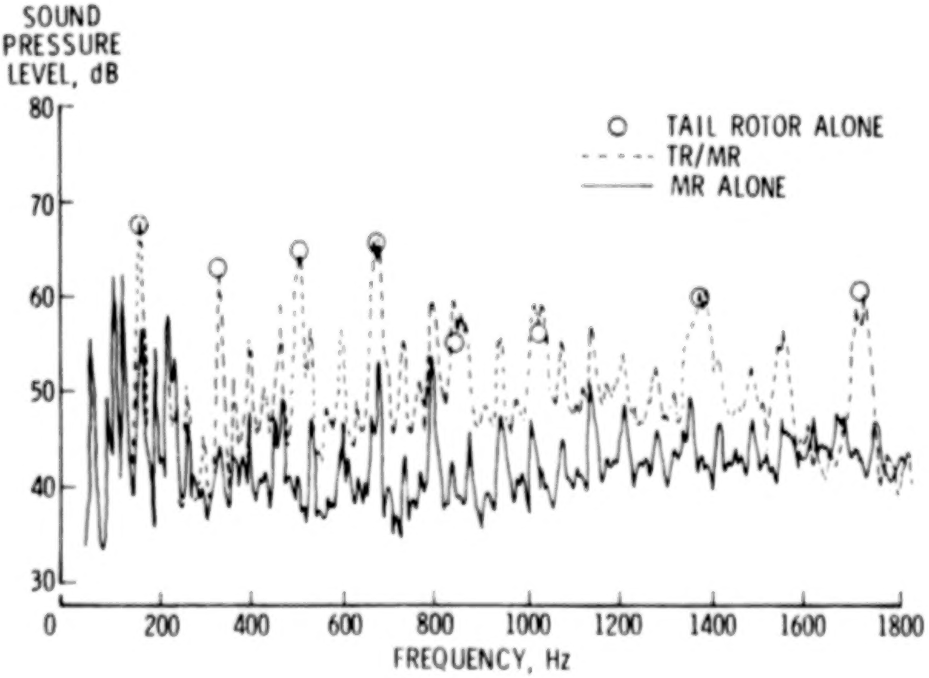

Figure 8.- Hover interaction noise.

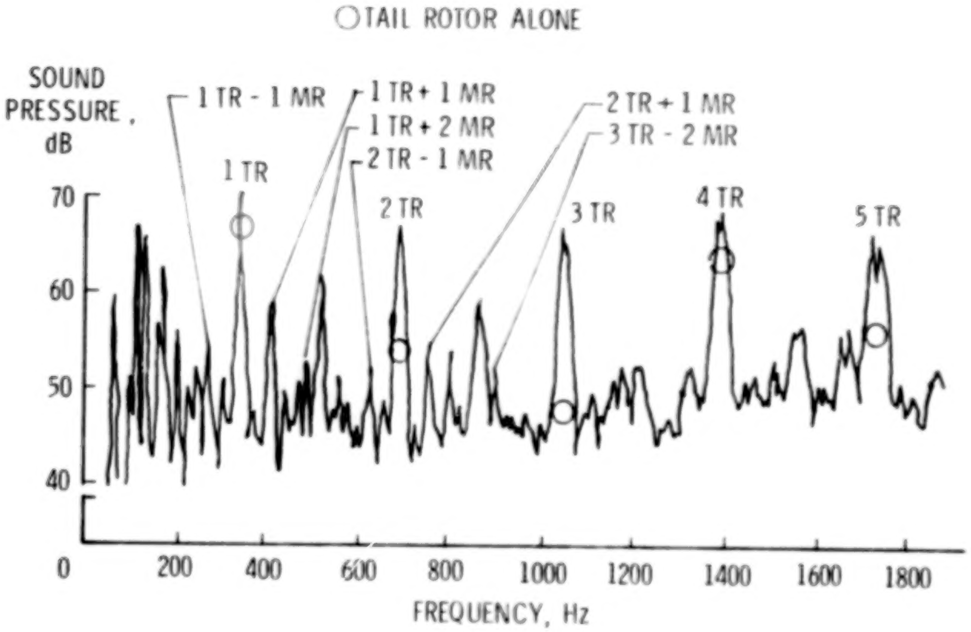

Figure 9.- Tail rotor noise due to main rotr wake interaction. V_{tun} = 10 m/sec.

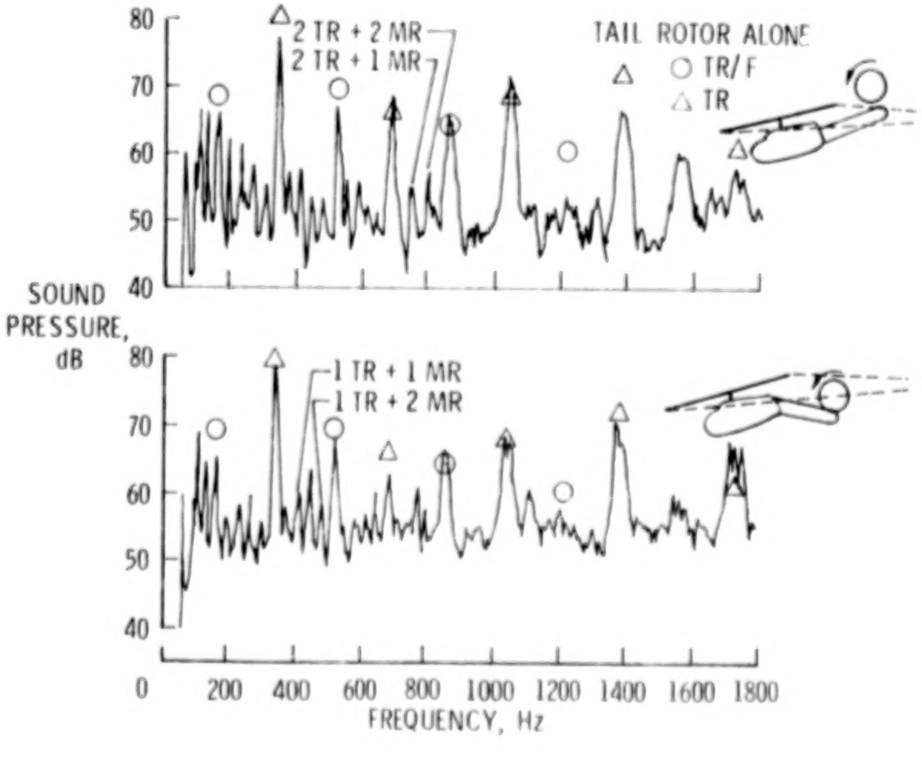

Figure 10.- Tail rotor noise due to main rotor wake interaction. V_{tun} = 20 m/sec.

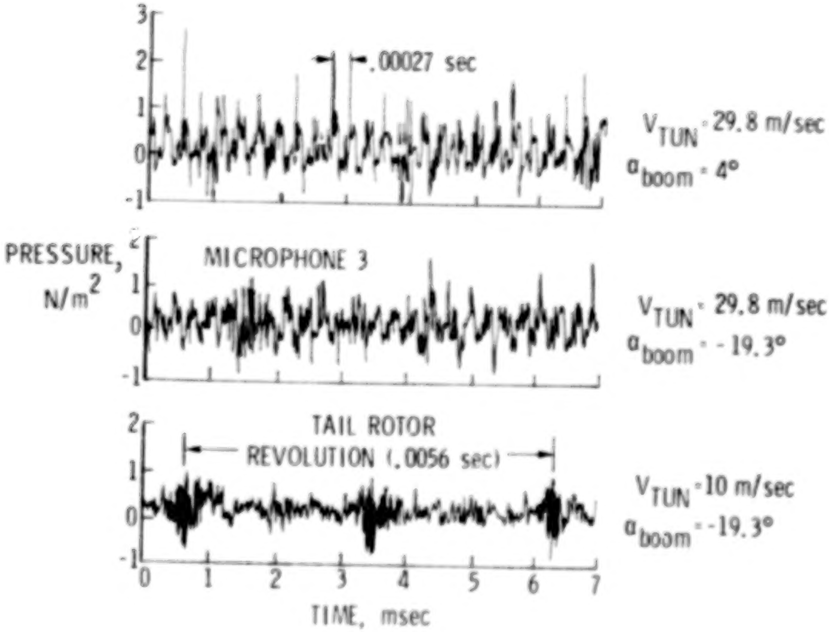

Figure 11.- Acoustic pressure time histories showing vortex intersects.

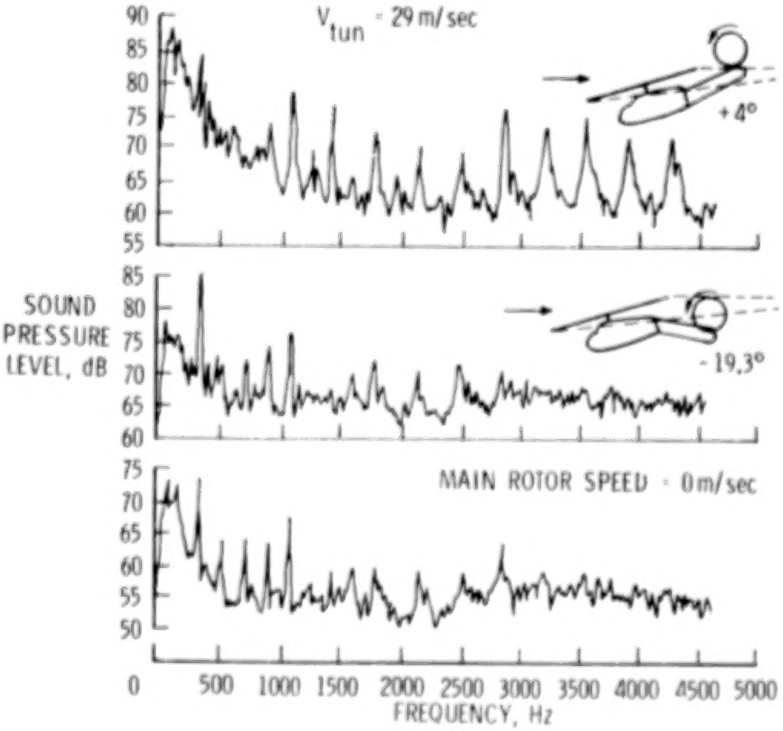

Figure 12.- Effect of tail rotor position on noise.

Blank Page

WIND TUNNEL INVESTIGATIONS OF MODEL ROTOR NOISE AT LOW TIP SPEEDS*

K. S. Aravamudan, A. Lee, and W. L. Harris
Massachusetts Institute of Technology

SUMMARY

This paper summarizes the experimental and related analytical results on model rotor rotational and broadband noise obtained at M.I.T. since 1975. The objectives of this research program have been to define the various noise sources, to determine the effects of helicopter performance parameters on the noise generated by a model main rotor, and to derive appropriate scaling laws for the various types of main rotor noise.

A description of the M.I.T. anechoic wind tunnel and rotor facility and some of the findings of this research group have been reported previously. The parameters under study were the variation of helicopter performance parameters such as number of blades, blade pitch (thrust), and advance ratio. In addition, the research program has consisted of an examination of the effects of intensity and size scales of injected turbulence on the intensity and spectra of broadband noise.

INTRODUCTION

Helicopter rotors generate complex acoustic signatures. A variety of mechanisms are responsible for the radiated acoustic energy and only a few of these mechanisms are understood.

The sound radiated by a lifting rotor at low to moderate tip speeds is essentially due to the time varying pressure distributions on the blade. This, often termed as "rotational noise", was originally studied by Gutin [1]†, where only steady, azimuthally constant blade loads were considered. These discrete frequency components occur at multiples of blade passage frequency and the unsteady nature of the blade forces prevents the harmonics from decaying, as originally predicted by Gutin. Random noise formerly was called "vortex noise," but investigators now prefer "broadband noise" since vortex shedding itself is not believed to be the principal mechanism.

At higher tip speeds and/or high flight speed, the flow over the blade section may exceed sonic velocity and result in generation of a local shock. These are termed as "shock noise" and are characterized by sharp peaks in the acoustic pressure time history, resulting in highly annoying banging noise.

---

*This research program has been supported by the U.S. Army, Army Research Office, under contract DAAG29-76-C-0027.

†Numbers in brackets indicate reference numbers.

Another dominant noise source is due to "blade-vortex interaction." A blade that passes close to a wake vortex filament experiences [2,3] a rapid change in the aerodynamic loading. This, often termed as "blade slap," is dependent on the geometry of the wake. Both these noise sources are impulsive in nature and occur only at certain flight conditions of a helicopter. In the absence of these mechanisms, the discrete and broadband noise dominate the rotor noise spectra.

Whereas the rotational or discrete noise from the rotors is fairly well understood, the situation for broadband noise is most unsatisfactory. Almost nothing can be said unequivocally about the broadband noise and this is simply because of the difficulty in pinpointing the noise sources experimentally. Opinions regarding the origins and behavior of broadband noise vary somewhat among investigators, but there is general agreement that turbulence in the flow seen by rotor blades is the basic physical mechanism responsible for broadband noise. Recent experimental data for a full scale helicopter rotor obtained by Leverton [4] and Leverton and Pollard [5] seem to suggest that the broadband noise is dependent only on the nature of turbulence. Thus, the turbulence may be due to inflow, the boundary layer of the blades, or the wake itself and may generate an unsteady lift on the airfoil and hence the noise. Principal areas of uncertainty include the effects of velocity and the size scale of turbulence on the intensity and spectra of the broadband noise. The work of Leverton [4] fails to show any kind of Strouhal frequency scaling with velocity for full scale rotors.

Much of the recent impetus to study the rotational and broadband noise comes from improved data processing technique and equipment. Narrowband analysis of rotor noise data has shown discrete frequency components extending well beyond 150 Hz, which historically was believed to be the transition region between rotational noise and broadband noise for typical helicopter rotors. Work by Lowson, Whatmore, and Whitfield [6] and by Leverton [4] emphasizes that low frequency broadband noise could have different causative physical mechanisms and acoustic behavior than high frequency broadband noise. It is generally believed that the inflow turbulence interaction with the rotor blades is responsible for the low frequency broadband noise. The high frequency component is attributed to the vortex shedding by the airfoils. In Figure 1 is shown a typical 6% bandwidth acoustic spectrum of a model rotor. Identified in this figure are the regions of rotational noise, low frequency broadband noise, and high frequency broadband noise.

To obtain the relationship between flow field characteristics and the sound radiated by lifting rotors, it is necessary to determine which mechanism is primarily responsible for the radiation. Each postulated mechanism leads to a particular characterization of the sound field and of its relationship to the flow field characteristics. Empirical measurements and similarity arguments can then be used to establish a posteriori verification of the choice of the mechanism. To this end, we assume that (i) the steady and unsteady loading harmonics are responsible for radiation of rotational noise, (ii) the intensity and size scale of turbulence are the governing factors for low frequency broadband noise radiation, and (iii) the periodic vortex shedding is the dominant mechanism responsible for radiation of high frequency broadband noise. The major contribution of the research effort described in this report is the development of appropriate Mach number scaling laws for model helicopter rotor noise and experimental verification of these laws. Equally important has been the obtainment of a definition of the effects of helicopter performance parameters on model helicopter rotor noise. These latter effects have been reported previously by references 7, 8, and 9.

Here, an attempt has been made to study the influence of free stream disturbances on the acoustic signatures generated by a model helicopter rotor. Appropriate theoretical modelling for rotational noise, low frequency broadband noise, and high frequency broadband noise are made by exploiting the existing knowledge of acoustic radiation from a rotating dipole source and unsteady aerodynamics associated with rotating blades. Details of the experimental facility and the theoretical analysis may be found in a recent report by Aravamudan and Harris [7] and several other archival publications of the members of the Fluid Dynamics Research Laboratory of M.I.T. [8 and 9].

In the section entitled "Description of Experiments," a brief description of the M.I.T. anechoic wind tunnel and model rotor facility is presented, along with the instrumentation used for acquisition and processing of various rotor noise components. Here we have discussed the nature of the artificially generated tunnel turbulence and the appropriate theoretical modelling of its spectrum.

In the section entitled "Mach Number Scaling of Model Rotor Noise," a simple Mach number scaling procedure is derived to predict the intensity and spectra of various components of model rotor noise, and the computed and the measured results are compared and described. The conclusions of our efforts are discussed in the Conclusion section.

DESCRIPTION OF EXPERIMENTS

The M.I.T. anechoic wind tunnel facility was used to study the rotational and broadband noise components of a model rotor. Controlled turbulence of varying intensity and scale was generated at the inlet of the tunnel test section by inserting biplanar grids of different sizes in the tunnel contraction section. In this section, the experimental apparatus used in obtaining and analyzing both turbulence and acoustic data is described.

The M.I.T. Anechoic Tunnel and Rotor Facility

The wind tunnel has a 1.52 x 2.29 meter inlet open jet test section which is enclosed in a 3.65 x 3.65 x 7.3 meter anechoic chamber. The sides of the chamber were covered with Cremer Blocks and the floor of the chamber was covered with 15-cm thick polyurethene foam. The anechoic properties of the tunnel were measured and the acoustic cut-off frequency above which free field conditions prevail was found to be 160 Hz. The effects of the shear layer of the open jet on refraction and scattering of acoustic waves were studied by using aeolian tones as a sound source and were found to be insignificant under the present test conditions.

The model helicopter rotor system consists of a 1.27 meter diameter rotor and has blades made of fiberglass. The rotor hub is designed to take up to 8 blades and is connected to a thrust measuring dynamometer. The dynamometer consists of four sets of BLH SPB 3-20-35 semiconductor strain gages mounted on two sets of flexures. Lebow slip ring was used to transmit the signals from the rotating dynamometer. The details of the model rotor system are summarized in Table 1.

Instrumentation

Data flow for all the experiments performed for this study was from microphones and hot wire sensors to a magnetic tape and later from the magnetic tape to appropriate spectrum analyzers.

The acoustic measurements were made along a circular arc at a radius of 1.32 meters from the rotor disc plane, perpendicular to the direction of the wind, and passing through the axis of the rotor. Acoustic signals were measured using a 1/2 inch B & K microphone type 4133 with a cathode follower type 2614 (1/2 in. = 1.27 cm). The signals were amplified by a B & K microphone amplifier and were recorded on magnetic tape using a P.I. 4 channel tape recorder model 6204 in direct mode. The microphones were calibrated using a B & K piston phone type 4220. In addition to the acoustic signal, a timing pulse at a period of $1/B\Omega$ was also recorded on one of the channels of the tape recorder. The steady thrust measurements were made simultaneously with the aid of a digital volt meter.

The fluctuating velocity signals were measured with an X-type hot wire sensor type DISA 55P51. The probe was placed 19 cm directly above the rotor plane, 10 cm aft the axis of the rotor. Flow Corporation constant temperature anemometer type 900-1 was used in conjunction with Flow Corporation linearizers type 900-4 and type 4835-C. An attenuator was used with the latter linearizer in order to adjust the sensitivity of both the wires to be same. The probe was calibrated over anticipated test velocities and the responses of both wires were found linear. The linearized signals were processed through a Flow Corporation sum and difference unit to yield the longitudinal and vertical components of velocities. These signals were further passed through a Flow Corporation suppressor filter unit type 900-3 to yield only the fluctuating quantities of the signal. All the signals were constantly monitored with the aid of a Flow Corporation digital volt meter type 900-2D. The fluctuating signals were then recorded on two F.M. channels of a P.I. 4 channel tape recorder type 6204. The r.m.s. values of the signals were measured by using HP 3400A RMS volt meters. In Figure 2 a schematic of instrumentation used in acquisition of turbulence and acoustic data is shown. The acoustic, thrust, and turbulence measurements were made simultaneously.

The measured acoustic signals were processed with the aid of a B & K audio frequency analyzer type 2107 and a B & K graphic level recorder. The turbulence data were analysed with the aid of a Federal Scientific UA-15A Spectrum analyzer together with a 1015 averager.

The grids employed in this study were designed based on the data of Baines and Peterson [10]. The grids were biplanar consisting of bars of 1.91 cm with a mesh size of 15 cm and bars of 8.9 cm with a mesh size of 50.8 cm. The grid solidities were 0.23 and 0.32, respectively. The grid Reynolds numbers based on the lowest tunnel velocity were 9×10^4 and 3×10^5, respectively. The longitudinal and vertical integral scales Λ_f and Λ_g of the grid generated turbulence were determined near the axis of rotor. For convenience, we estimated Λ_f from the Eulerian integral time scale τ_e. The values of τ_e were determined from the extrapolated zero intercept of the power spectra of longitudinal and vertical velocities. The length scales, then, are given by

$$\Lambda_f = U_0 \tau_{ef} \ ; \quad \Lambda_g = U_0 \tau_{eg} \tag{1}$$

The measured longitudinal and vertical integral scales of grid generated turbulence were observed to be independent of free stream velocity. In absence of grids, the Eulerian time scales were very large and fluctuating. This resulted in large length scales that vary considerably with free stream velocity, but do not follow any definite pattern. Details of these measurements are presented by Aravamudan and Harris [7]. Table 2 summarized the measured characteristics of turbulence with and without the grids.

In Figures 3 and 4 are the measured power spectral densities of the longitudinal and vertical components of turbulence, respectively, as a function of wave number. In plotting these figures, Taylor's hypothesis of frozen turbulence has been applied to convert the turbulence spectrum from an experimentally obtained temporal frame to a spatial frame. The axial wave number is related to frequency by $k_x = 2\pi f/U_0$ and this is nondimensionalized with respect to k_e as $3k_x/8\pi k_e$. Here k_e is the wave number range of energy containing eddies and is related to the longitudinal integral scale Λ_f by $k_e = 0.75/\Lambda_f$. Also shown in the figures is the empirical isotropic turbulence spectrum derived from von Karman's interpolation formula. The nondimensionalized power spectral densities for longitudinal and vertical components of turbulence are given as follows

$$\Phi_{uu}(k_x) = \Phi_{uu}(o)/[1 + k_x^2/k_e^2]^{5/6} \tag{2}$$

$$\Phi_{ww}(k_x) = \frac{\Phi_{ww}(o)[1 + 8/3\ k_x^2/k_e^2]}{[1 + k_x^2/k_e^2]^{11/6}} \tag{3}$$

The measured data show good agreement with the von Karman spectrum, including a -5/3 power decrease at high frequencies. However, in the absence of grids, the tunnel turbulence seems to deviate slightly from the predicted von Karman power spectrum.

Extensive measurements of the background noise for the M.I.T. anechoic wind tunnel facility have been made by Harris and Lee [11]. However, it is very likely that an upstream turbulence generator would alter the background noise spectra of the tunnel. To ensure that the acoustic measurements were not affected by such noise, a survey of the tunnel background noise was made at various tunnel speeds with and without the turbulence generating grids in place.

To isolate the low frequency rotational noise components of the rotor from the relatively high intensity tunnel background noise, a periodic sampling technique was used. This technique involves the use of a PAR wave-form eductor, Model TDH-9. The waveform eductor samples the repetitive input and stores them in a 100 channel capacitance memory. After a sufficient number of sweeps have occurred, the noise from nonrepetitive sources (background noise in the present case) will be suppressed since their average value will approach zero. The processed rotor data will contain only the rotational noise. The timing pulse of $1/B\Omega$ was used to average the waveform of the signal. The spectrum was obtained by using a Federal Scientific UA-15A Spectrum Analyzer with a 1015 averager.

Since the present study also involves the influence of free stream disturbances on the low frequency broadband noise sources, it was necessary to ensure that (i) the rotational harmonics do not contribute significantly to the broadband noise generated by the rotor and (ii) the background noise level in the tunnel is low enough to yield the necessary signal to noise ratio. The first task was accomplished with the use of the above mentioned periodic sampling technique.

In Figure 5 are plotted the 6% bandwidth spectra for a two-bladed rotor operating at 672 rpm and an advance ratio of 0.3. The 1.91 cm x 15 cm turbulence generating grid was located upstream and the Figure compares the spectra obtained with and without periodic sampling technique. The rotational harmonics obtained from the periodic sampling technique are very distinct and they decay very rapidly. As can be seen from Figure 5, above 200 Hz, which we assume as the transition from rotational noise to broadband noise, the levels of broadband noise are significantly higher than those of rotational harmonics.

The second task was accomplished by measuring the acoustic signals at a given observer location with and without the rotor system operating. Figures 6 and 7 show the measured 6% bandwidth sound pressure levels for 1.91 cm x 15 cm grid and 8.9 cm x 50.8 cm grid, respectively. Also drawn in these figures are the typical noise spectra with the model rotor operating in the tunnel. From Figures 6 and 7, it is evident that the background noise in the wind tunnel does not affect the rotor generated broadband noise. In the absence of turbulence generating grids, the background noise of the wind tunnel seems comparable to the intensity of low frequency broadband noise. Hence, we have not used this experimentally obtained low frequency broadband noise data in our prediction techniques.

MACH NUMBER SCALING OF MODEL ROTOR NOISE

As mentioned above, the acoustic spectra generated by a typical rotor may be decomposed into rotational noise, low frequency broadband noise, and high frequency broadband noise components. The intensity and spectral content of each of these components are strongly dependent on the blade tip Mach number. Most model rotor systems can not simulate the high tip Mach numbers of real helicopters and hence there is a need for a simple prediction procedure based on the blade tip Mach number and other performance parameters. In this section, we have attempted to use the existing theories of radiation from subsonic rotors to yield a simplified Mach number scaling formula for the intensity and spectra of various components of model rotor noise. Due to nature of this article, we have deliberately abstained from presenting the complex mathematical development of the scaling procedures but confine ourselves to discussions of relevant assumptions and the final scaling formulae. Similarly, our findings on the effects of helicopter performance parameters on model helicopter rotor noise will not be presented in this paper.

Mach Number Scaling of Rotational Noise Component

The rotational noise of subsonic rotors is mainly attributed to force and thickness effects. The relative importance of force and thickness effects depends strongly on the blade Mach number. The source strength of the force term is larger than that of the thickness term. However, the acoustic efficiency of the thickness source radiation is far greater than that due to the force. Thus, which mechanism dominates the acoustic field is essentially a question of whether the added acoustic efficiency of the thickness source can overcome its inherently weak strength. Since the acoustic efficiency decays rapidly with decreasing Mach number, there is a rapid fall-off in acoustic effectiveness for blade stations inboard of the tip. Hence, in the following order-of-magnitude considerations on the force and thickness effects, only tip regions need to be considered.

For each source, its effective Mach number $M_e = M_t \sin \alpha/(1-M_{or})$ is maximum in a direction straight ahead of the rotor. The factor $(1-M_{or})$ is minimum for the advancing blade and hence the sources in the vicinity of the advancing blade contribute more. The front rotor disc plane is chosen as the observer location since the thickness noise is most intense in this location. We further assume that the tip Mach numbers are below the critical Mach numbers and hence compressibility corrections are omitted. Hawkings and Lowson [12] found the acoustic source strength of thickness, direct force, and force derivative terms to be of the order of $\rho_0\Omega^2 t$, $\Omega F_r/c_0$, and $1/c_0(\partial F_r/\partial\tau)$. The thickness source term $\rho_0\Omega^2 t$ may be rewritten as $(\rho_0 c_0 \Omega)(M_t\, c/b)(t/c)$. Ignoring the directional properties of F_r, one can rewrite the second term as $1/2\, C_f M_S^2(\rho_0 c_0 \Omega)$ where $M_S = (1+\mu)M_t$ for the advancing blade. Based on quasi-steady approximations, Hawkings and Lowson [12] suggested an order of $0.1\, \rho_0 c_0 \Omega$ for force derivative term. For typical helicopter rotors, $b/c \approx 12$, $t/c \approx 0.12$, $C_f \approx 0.06$, and the order of magnitude of these sources is $0.01\, M_t \rho_0 c_0 \Omega$, $0.03\, M_S^2 \rho_0 c_0 \Omega$, and $0.1 \rho_0 c_0 \Omega$, respectively. Based on calculations of Hawkings and Lowson, the approximate expressions for the acoustic efficiency of each of these sources are given by $2.6 \times 10^4 M_e^{11.4}/(1-M_1)^3$, $2.2 \times 10^2 M_e^{8.4}/(1-M_1)^2$ and $1.8 \times 10^2 M_e^{6.3}/(1-M_1)^2$, respectively. Combining the source strength and its acoustic efficiency, the ratio of acoustic pressure due to thickness, force, and force derivative is given as follows:

$$260\, M_e^{6.1} : 6.6\, M_s^2\, M_e^{2.1} : 18$$

For a typical helicopter with an advance ratio of 0.3, $M_e = 0.6$, $M_s = 0.65$, and the second term is of the order of unity. The thickness and force derivative terms are equally important at a value of $M_e = 0.65$ where both the terms are of same order. However, as the Mach number is decreased to about 0.60, the thickness term is about 4 dB less than the corresponding force derivative term and at $M_e = 0.5$, it is about 14 dB less. Hence, in our Mach number scaling formulation, we need consider only force derivative terms and the formulation would still be valid for relatively high up Mach numbers; the tip Mach number is limited by 0.65.

Lowson and Ollerhead [13] derived the expressions for the farfield acoustic radiation due to a rotating fluctuating point source in terms of an infinite sum of loading harmonics due to thrust, drag, and centrifugal forces. For a typical helicopter rotor, the proportions of thrust, drag, and radial forces are of the order of 10:1:1. Further, the complex Fourier coefficient consisting of two Bessels functions of order $(n + \lambda)$ and $(n - \lambda)$ may readily be interpreted as representing rotational modes of $n\Omega/(n + \lambda)$ and $n\Omega/(n - \lambda)$, respectively. Since faster modes have higher efficiency, the contributions of slower modes may be ignored. Under such assumptions, the complex Fourier coefficient for sound radiation from a source at a distance R from axis of rotation will be simplified to the following expression:

$$C_n = \sum_{\lambda=0}^{\infty} \frac{(i)^{-(n-\lambda)}}{4\pi} \frac{n\Omega x}{c_0 r_1^2} [i\, a_{\lambda T} - b_{\lambda T}] J_{n-\lambda}(nMy/r_1) \tag{4}$$

For the case of a helicopter rotor, the observed sound is the result of the continuous distributed loading along the span of the blade. Therefore the power spectral density of radiated sound is given by

$$P(\vec{x},n) = \lim_{T\to\infty} \frac{1}{T} \int_0^T dt \int_\eta \int_{\eta'} C_n(\vec{x},\eta)\, C_n^*(\vec{x},\eta')\, d\eta\, d\eta' \tag{5}$$

where C_n^* is the complex conjugate of C_n. Substituting for C_n from equation (4) and noting that the summation and the integral remains unchanged, provided the argument of the Bessels functions $M_t y/r_1$ is constant, result in the following Mach number scaling law to predict the rotational noise of n^{th} harmonics

$$P(\vec{n}_2,\, n,\, M_t) \;=\; P(\vec{x}_1,\, n,\, M_{t_1}) \left\{\frac{M_{t_2}}{M_{t_1}}\right\}^6 \left\{\frac{c_2}{c_1}\right\}^2 \left\{\frac{r_1}{r_2}\right\}^2 \left\{\frac{\sin\alpha_2}{\sin\alpha_1}\right\}^2 \tag{6}$$

where $\sin\alpha = x/r_1$.

In case of forward flight, r_1 should be replaced by $r_1(1-M_{Or})$ where M_{Or} is the component of forward flight Mach number in the direction of observer. Following similar procedure cited above, we obtain

$$P(\vec{x}_2,n,M_{t2}) \;=\; P(\vec{x}_1,n,M_{t_1}) \left\{\frac{M_{t_2}}{M_{t_1}}\right\}^6 \left\{\frac{c_2}{c_1}\right\}^2 \left\{\frac{r_1}{r_2}\right\}^2 \left\{\frac{\sin\alpha_2}{\sin\alpha_1}\right\}^2$$

$$\left\{\frac{1 + \mu_1 M_{t_1}\cos\alpha_1,\ \cos\phi_1}{1 + \mu_2 M_{t_2}\cos\alpha_2\ \cos\phi_2}\right\}^4 \tag{7}$$

A special case arises when the observer is directly above the axis of the rotor. For this case, $y/r_1 = b$, and the entire sound field will be due to only one loading harmonic $n = \lambda$. Hence both equations (6) and (7) reduce to

$$P(\vec{x}_2,\, n,\, M_{t2}) \;=\; P(\vec{x}_1,\, n,\, M_{t_1}) \left\{\frac{M_{t_2}}{M_{t_1}}\right\}^6 \left\{\frac{c_2}{c_1}\right\}^2 \left\{\frac{r_1}{r_2}\right\}^2 \tag{8}$$

which is the conventional sixth power Mach number scaling law.

To verify the validity of the Mach number scaling formula, a detailed experimental program was completed in the M.I.T. anechoic wind tunnel facility. A periodic sampling technique which is described above was used in determining the intensity of rotational harmonics.

In Figures 8 and 9 are shown the results of the Mach number scaling formula for lower and higher rotational harmonics of a two-bladed rotor on axis. The experimental results at a tip Mach number of 0.15 were used to predict the sound pressure levels at other Mach numbers. As can be seen from Figures 8 and 9, the theoretical Mach number scaling formula given by equation (8) yields better comparison with the experimentally obtained data for higher rotational harmonics. The discrepancy of the scaling formula for lower rotational harmonics is attributed to the fact that the measurements were made in the acoustic near field because of the physical limitations of the wind tunnel facility. In Figures 10 and 11 are shown the scaling results for the lower and higher harmonics of a two-bladed rotor off axis. Here the experimental results of the rotor operating at a tip Mach number of 0.15 and at an angle of 59° were used to predict the sound pressure levels at other Mach numbers.

Figure 12 depicts the directivity of rotational harmonics of a two-bladed rotor. The directivity data were obtained by positioning the microphones at 10° intervals and using the periodic sampling technique. As can be seen from Figure 12, the directivity is dependent on the harmonic number and becomes all the more important for the off axis Mach number scaling law.

Mach Number Scaling of Low Frequency Broadband Noise

Since the broadband noise from rotors and propellers often appears to follow roughly a M_0^6 dependence, it is natural to postulate that unsteady, but random, forces on blades are responsible for its generation. Lowson and Ollerhead [13], Ffowcs Williams and Hawkings [14], and Morfey and Tanna [15] have theoretically related the radiated broadband acoustic spectrum from a single blade to the blade load spectrum without specifying how the loads are generated. Their results take no account of blade-to-blade correlations which might exist in practical applications. Lowson [16] proposed to account for this by postulating a frequency independent spatial correlation scale. Rotational harmonics are generated by the passage of blades through steady asymmetric velocity variations in the plane of the rotor. The low frequency broadband noise, on the other hand, is generated by passage of blades through a turbulent or a randomly varying velocity field. One essential difference between the harmonic loading and random loading is the bandwidth of excitation. The origin of turbulence, as related to its effects on broadband noise, in most cases seems rather inconsequential. It is mainly due to atmospheric inhomogeneities, but upstream obstructions such as fuselage and/or the wakes shed by the moving wing or blade might very well be the source of turbulence. A lifting rotor produces a mean downward velocity field which draws the atmospheric eddies through the rotor plane with a convecting velocity V_C. This random variation in "upwash" induces a random variation in the angle of incidence and hence a fluctuating blade load. As atmospheric turbulence contains a spectrum of wave number components, the resulting loading spectrum may affect the acoustic spectrum over the entire range of frequencies.

Many of the possible mechanisms for broadband noise generation by a single stationary airfoil in a moving stream have been the subject of various investigators. The nonuniform velocity field associated with turbulence leads to an unsteady blade load that is dipole in nature. Amiet [17] studied the resulting noise pattern by using the nonstationary airfoil theory of Sears [18]. However, in the case of rotating blades, the problem becomes more complex. The very fact that the blades are rotating can be looked at in terms of Doppler shifts in frequency. The presence or absence of a blade at various spatial locations may in fact be interpreted as temporal variations seen in the observer coordinates. Thus, a wide range of frequencies is generated at a single blade passage harmonic $mB\Omega$.

A hovering or low forward speed rotor may modify any ingested turbulence due to distortion of fluid elements drawn into the rotor plane. The turbulent eddies, in general, are elongated in the direction of convection velocity and often are chopped several times as they pass through the plane of the rotor. Figure 13 depicts the rotor geometry showing the definitions of symbols and convection velocity of a turbulent eddy. The time interval Δt for equally spaced blades to pass a fixed point on the rotor plane is given by:

$$\Delta t = \frac{2\pi R_0/B}{2\pi\Omega R_0} = \frac{1}{\Omega B} \tag{9}$$

On the other hand, the time scale for an eddy of wavelength λ_ξ to be convected past a given point in the rotor plane is given by

$$t_\xi = \frac{\lambda_\xi}{V_c} \tag{10}$$

Here the eddy wavelength λ_ξ is given by $2\pi\Lambda/\xi$. Thus the ratio of blade passage time to eddy convection time is

$$\frac{\Delta t}{t_\xi} = \frac{1}{2\pi}\,\frac{\xi V_c}{B\Lambda\Omega} \tag{11}$$

Homicz and George [19] gave an expression for the far field radiated sound resulting from loading due to a turbulent upwash and predicted a smooth spectrum at frequencies beyond f_0 which is

$$\frac{f_0}{\Omega} = \frac{B(1 + M_0/M_C)}{2(1 - M_0\cos\phi)} \tag{12}$$

Also, the values of turbulent wave numbers ξ which make significant contributions to the acoustic spectrum at a given frequency f are given by

$$\frac{(f/\Omega)(1 - M_0\cos\phi)}{(V_c/\Lambda\Omega)(1 + M_0/M_c)} < \xi < \frac{(f/\Omega)(1 + M_0\cos\phi)}{(V_c/\Lambda\Omega)} \tag{13}$$

Combining equations (7) and (8), the lower limit for ξ which makes significant contributions for frequencies $f >> f_0$ is obtained as

$$\xi_f > \frac{B\Lambda\Omega}{2V_c} \tag{14}$$

Using equation (6), this result may be interpreted as follows

$$\frac{\Delta t}{t_\xi} >> 1 \qquad \text{when } f >> f_0 \tag{15}$$

Thus, a turbulent eddy of length scale of about 1 meter will take the order of one second to be drawn through a rotor plane with a convection velocity of about 1 m/sec. Hence, for a two-bladed rotor at 10 Hz, about 10 blade passages will encounter parts of the same eddy. This results in a pronounced blade-to-blade correlation effect and leads to positive and negative interference between acoustic waves generated by blades. On the other hand, a turbulent eddy of length scale of about 10 cm or less will completely pass through the plane of the rotor between consecutive blade passage. The resulting rapid modulation of high frequency blade loading implies wider side bands and hence the radiated sound spreads over a large part of the acoustic spectrum.

When there is no significant blade-to-blade correlation, the total radiation is given by simply adding the uncorrelated sound power spectral densities of each of the blades. The radiation of a single blade, approximated by a rotating point dipole, has been given by Ffowcs Williams and Hawkings [14] as

$$<S_{pp}(\vec{x},f)> = \frac{f^2}{4\rho_0 C_0^3 r^2} \sum_{n=-\infty}^{\infty} D_r(\phi,\ f-n\Omega)\ J_n^2\left(\frac{fR_0 \cos\phi}{c_0}\right) \tag{16}$$

where $D_r(\phi,f)$ is the power spectral density of the dipole strength in the direction of radiation. The dipole source field is a direct consequence of the unsteady forces acting on the airfoil surface and is related to the power spectral density of the unsteady lift as follows

$$D_r(\phi,f) = \Phi_{LL}(f) \sin^2\phi \tag{17}$$

Under the assumptions of stationary isotropic turbulence, the unsteady lift spectrum is directly related to the turbulence upwash spectrum and the aerodynamic transfer function. For frequencies f >>0, the one sided power spectral density is given by

$$\Phi_{LL}(f) = \frac{2}{Q} \int_{-\infty}^{\infty}\int_{-\infty}^{\infty} dk_y dk_z \Phi_{ww}(f/Q,\ k_y,\ k_z)\ |K(f/Q,\ k_y)|^2 \tag{18}$$

Since the measured spectrum of turbulence was close to the one predicted by von Karman's interpolation formula, the corresponding two dimensional spectrum of the vertical component is given by

$$\Phi_{ww}(k_x,\ k_y) = 0.4548\ \bar{w}^2 \Lambda_f^4 \frac{k_x^2 + k_y^2}{[1 + 1.793\Lambda_f^2\ (k_x^2 + k_y^2)]^{7/3}} \tag{19}$$

The aerodynamic transfer function used in equation (18) was given by Osborne [20] as follows

$$|K(k_x,\ k_y)| = \frac{1}{2}\rho_0 Qbc \frac{\frac{2\pi}{\beta}\left[J_0^2\left(\frac{M_0^2 \pi c}{\beta^2} k_T\right) + J_1^2\left(\frac{M_0^2 \pi c}{\beta^2} k_T\right)\right]^{1/2}}{\left[1 + \frac{2\pi^2 c}{\beta^2} k_T\right]^{1/2}} \tag{20}$$

where $k_T = (k_x^2 + k_y^2)^{1/2}$

Substitution of equations (20) and (19) in (18) and then in equation (16) yields the expression for the intensity and spectrum of low frequency broadband noise as follows

$$<S_{pp}(\vec{x},f)> \;=\; \frac{f^2 \sin^2\phi}{2Qc_0^3 r^2 \rho_0(1 + bf/Q)} \sum_{n=-\infty}^{\infty} D_r(f-n\Omega) J_n^2\left(\frac{fR_0 \sin\phi}{c_0}\right) \qquad (21)$$

where

$$D_r(f) \;=\; \frac{\pi^2\rho^2 Q^2 b^2 c^2 (0.4548)}{\beta^2}\, \bar{w}^2\, \Lambda_f^4$$

$$\frac{\int_0^\infty dk_y[(f/Q)^2 + k_y^2][J_0^2(\frac{M_0^2\pi c}{\beta^2}\sqrt{(f/Q)^2+k_y^2}) + J_1^2(\frac{M_0^2\pi c}{\beta^2}\sqrt{(f/Q)^2+k_y^2})]}{[1 + \frac{2\pi^2 c}{\beta^2}\sqrt{(f/Q)^2 + k_y^2}][1 + 1.793\Lambda_f^2\{(f/Q)^2 + k_y^2\}]^{7/3}} \qquad (22)$$

Numerical calculations were performed for the measured values of turbulence intensities and integral scales for various advance ratios and tip Mach numbers. The note that the above analysis of low frequency broad band noise follows closely that of Homicz and George [19] and George and Kim [21].

Figure 14 and Figure 15 compare the predicted and the measured narrow band spectra for the large and the small turbulence generating grids, respectively. The acoustic spectra obtained are corrected for the experimentally obtained two-bladed rotor results with a 6% bandwidth analysis by adding 3 dB to the entire spectrum. The experimental plot is deliberately terminated around 3000 Hz, beyond which is assumed to be the region of high frequency broadband noise. As can be seen from Figures 14 and 15, the agreement between measured and the predicted spectra is better for the larger grid with an integral scale of 8.5 cm. The results of the rotor operating with no upstream turbulence generator are not plotted because at these frequencies the background noise was comparable to the intensity of the low frequency broadband noise. In Figure 16 is plotted the effect of advance ratio on the predicted peak intensity of the low frequency broadband noise. As can be seen from the figure, a doubling of advance ratio results in an increase of peak sound pressure level of about 8 dB. This result is not surprising because of the increased r.m.s. value of turbulence in the tunnel with increasing forward speed. Since the theory predicts a 6 dB increase in doubling the turbulence velocity, only the remainder must be thought of as the true influence of advance ratio. Caution must be exercised in comparing these results with those of full scale rotors since increase in advance ratio does not significantly change the turbulence encounter.

In Figure 17 is plotted the peak intensity of the low frequency broadband noise as a function of the relative tip velocity. In plotting this figure, the effect of the increase in the r.m.s. turbulence levels is removed by taking out 20 log $\bar{w}_2/\bar{w}_1$ from the predicted sound pressure levels. The levels are normalized with respect to the predicted sound pressure level at a velocity of 34.8 m/sec. Also plotted in the figure are measured sound pressure levels for a two-bladed rotor. As can be seen from the figure, a 12 dB increase per doubling velocity seems to fit the predicted and the measured data very well. Including the effect of increase in r.m.s. turbulence levels would result in the conventional V_t^6 power law. The location of the peak intensity in the frequency domain increases with increase in tip velocities.

In Figure 18 are plotted the predicted sound pressure levels as a function of the turbulence integral scale for a fixed value of the tip velocity of 80.8 m/sec. Once again, we observe that the location of the peak intensity in the frequency domain decreases with an increase in the integral scale of turbulence. In Figure 19 is plotted the peak intensity of LFBN as a function of the longitudinal integral scale Λ_f of turbulence. Here, the effect of the rotational velocity and the increase in turbulence intensity are removed. As can be seen from the figure, the peak intensity is a very weak function of Λ_f. This weak dependence can be readily explained by an examination of equation (22) For relatively large values of frequency, we may approximate the denominator of equation (22) as

$$[1 + \frac{2\pi^2 c}{\beta^2} \sqrt{(f/Q)^2 + k_y^2}\,][1.793\ \Lambda_f^2\ \{(f/Q)^2 + k_y^2\}]^{7/3}$$

Since the integral is independent of Λ_f, we readily obtain a scaling factor based on Λ_f as

$$D_r(f) \sim \Lambda_f^{-2/3}$$

which would result in a reduction of approximately 2 dB per doubling the integral scale.

An examination of Figures 14 through 19 suggests that the location of the peak intensity of low frequency broadband noise in the frequency domain can be scaled with reference to a Strouhal number defined as follows

$$S = \frac{f_p \Lambda_f}{V_t} \tag{23}$$

In Figure 20 are plotted the spectra of sound pressure levels for various Mach numbers and size scales of turbulence. It is interesting to see how the entire data collapse to a single curve defining a normalized acoustic spectra for the model rotor turbulence interaction noise as a function of the non-dimensionalized Strouhal frequency. The peak intensity appears at a frequency corresponding to a Strouhal number of about 1.5.

Mach Number Scaling of High Frequency Broadband Noise

In the preceeding section we discussed the possible mechanisms of low frequency broadband noise radiation from rotating airfoils and arrived at an acceptable Strouhal frequency scaling to predict intensity and spectrum of such a radiation. It was observed that at high enough frequencies, this radiation decays approximately like f^{-2}. Therefore, in absence of any other mechanism of radiation, the intensity of rotor generated noise would be insignificant at frequencies well beyond the peak of low frequency broadband noise radiation. But, our experimentally obtained model data as well as the full scale rotor data of Leverton [4] do not exhibit such a decrease in the measured acoustic spectra. In fact, the evidence of existence of another mechanism which radiates efficiently over the frequency range well beyond low frequency broadband noise peak is overwhelming. In this section we shall discuss the possible mechanisms appropriate for such high frequency radiation.

As mentioned before, the broadband part of the rotor noise spectrum is attributed to the nonperiodic time dependent loads. These fluctuations in force may arise as a result of (i) free stream disturbances generating a fluctuating angle of incidence, (ii) a turbulent boundary layer on the surface of the airfoil, and (iii) a spanwise vorticity in the wake of the airfoil. These mechanisms, in general, interact through nonlinear fluid mechanical processes. However, under certain conditions, it is possible to consider them as being mutually independent.

The interaction of the turbulent boundary layer with the trailing edge of an airfoil imparts momentum fluctuations to the surrounding media and the total radiated spectrum may be divided into turbulent boundary layer dominated components and wake dominated components. Chanaud and Hayden [22] have shown that when the dimensions of the radiating surface are small compared to the acoustic wave length, the contributions of the turbulent boundary layer to the total acoustic intensity are usually negligible relative to the contributions from the inflow turbulence or wake. In the absence of significant inflow turbulence, the wake generated noise would dominate the high frequency regime of the acoustic spectra.

Several independent experiments by Hersh and Hayden [23], Paterson, Vogt, Fink, and Munch [24], and Clark [25] revealed that discrete tones are emitted from isolated airfoils under certain operating conditions. Over a wide range of Reynolds number based on the chord of the airfoil, the total radiated sound could be dominated by these discrete tones. Further, the frequencies of these tones appear to be a well defined function of free stream velocity and form an organized pattern. There is a considerable amount of difference of opinion regarding the Strouhal frequency scaling of these discrete tones. Hersh and Hayden [23] and Paterson, Vogt, Fink, and Munch [24] have all attributed the generation of these tones to the classical vortex shedding along the span of the airfoil. The shed vortices generate a periodic pressure fluctuation over the airfoil at that particular Strouhal frequency, resulting in a edge dipole radiation.

Lee [26] made measurements of the peak frequency location of the high frequency broadband noise of the present model rotor system operating at various tip speeds. Based on his measurements, he defined a Strouhal number

$$S = \frac{ft}{V_e}$$

where V_e was the rotational velocity measured at 75% of the blade span. His experimental results lead to a Strouhal number of about 1. Following Lee's [26] argument that there is a need for a frequency scaling based more on geometrical parameters of the system than on the fluid dynamical characteristics, we define a priori a frequency scaling law as follows

$$f = \frac{SV_t}{t} \tag{24}$$

Based on our experimental results, the validity of such a relationship will be demonstrated below.

If we assume the compactness of the source and that the shed vortices are correlated over a distance ΔL of the blade span, the instantaneous pressure fluctuation at the observer location is readily given by

$$\Delta p = -\frac{1}{4\pi c_0} \frac{\cos\theta}{r_1} \frac{\partial}{\partial\tau} p_i(\tau)\,(c\Delta L)$$

where p_i is the instantaneous pressure fluctuation on the airfoil surface due to shed vortices. Normalizing the pressure with respect to the blade sectional velocity and integrating the mean square of the pressure over the span of the blade lead to the amplitude scaling of the high frequency broadband noise.

$$S_{pp}(f) \simeq \frac{S^2 c^2 \rho_0^2 b\, V_t^6 \Delta L}{c_0^2 t^2 r_1^2} \left[1 + \frac{14}{3}\mu + \frac{42}{5}\mu^2\right] \tag{25}$$

where the frequency f is given by the equation (24). The effect of number of blades may be included by multiplying equation (25) by blade number, B.

Mugridge [27] and Clark [28] demonstrated experimentally that the correlation lengths over a stationary airfoil are directly proportional to the displacement thickness of the turbulent boundary layer. In the case of a rotating airfoil, the thickness of the boundary layer is influenced by the local Reynolds number as well as by the spanwise flow. Realistic estimates of correlation lengths for rotating airfoils are not presently available. However, since the mechanism is similar to that of a stationary airfoil, we assume for scaling purposes that the correlation length behaves in a manner similar to the boundary layer displacement thickness at a representative spanwise location. Since the displacement thickness for the turbulent boundary layer varies like $c/(R_e)^{0.2}$, the high frequency broadband noise levels vary like $V_t^{5.8}$.

To verify the validity of the Mach number scaling procedure developed in this section, a series of experiments were performed under various operating conditions of the model rotor. The experimental results indicated that the mean thrust generated by the rotor had little effect on the intensity and spectrum of high frequency broadband noise. The increase in number of blades increased the intensity of high frequency broadband noise in addition to broadening of the high frequency broadband noise'hump.' A 3 dB per doubling of blade number fitted the measured data very well. The advance ratio had a significant effect on the intensity of high frequency broadband noise without affecting its spectrum. A 8 dB per doubling the advance ratio showed good agreement with the experimental data.

In Figure 21 are plotted typical high frequency broadband noise spectra for various rotational speeds at constant advance ratio for a two-bladed rotor. As noted above, the advance ratio had no significant effect on the peak frequency location, and this justifies use of rotational tip velocity in equation (24) for Strouhal scaling of shed vortices. Figure 22 shows a plot of peak frequency as a function of the blade tip velocity. As can be seen from Figure 22, the peak frequency is directly proportional to the blade tip velocity with a proportionality constant of 16.5. At higher tip speeds, the high frequency broadband noise is spread over a narrow range of frequencies and hence there is some scatter in the measured data. Using maximum blade thickness in equation (24), the resulting Strouhal frequency is 1.08. Although a wake characteristic length such as displacement of momentum thickness should be the appropriate length scale to be used, a simple relationship based on the geometrical parameter may be very useful in practical applications.

In Figure 23, an estimate of the peak sound pressure levels calculated using the measured values of a two-bladed rotor operating at 550 rpm as a base is plotted. The three-bladed rotor data are normalized with respect to the two-bladed rotor data by taking out 10 log B_2/B_1 from measured sound pressure levels. As can be seen from Figure 22, the prediction scheme presented herein gives good correlations with the measured two-blade and three-blade data except at very low rotational velocities. It was observed that at these low velocities, corresponding to a rotational speed of 300 and 400 rpm, the measured high frequency broadband noise spectra showed intense peaks. This probably is due to a fairly laminar flow on both sides of the airfoil resulting in more intense shedding of vortices. The peak intensity decreased slightly as we increased the rotational velocity to about 500 rpm, and then started increasing according to the postulated power law.

The effect of free stream turbulence, in general, is to decrease the intensity of high frequency broadband noise. In Figure 24 is shown the effect of turbulence on the 6% bandwidth spectrum of a two-bladed rotor operating at 672 rpm. One obvious reason for the reduction in the intensity of high frequency broadband noise is the premature transition of the laminar boundary layer on the blade surface. Evans and Horlock [29] studied the effect of free stream turbulence on a developing boundary layer and concluded that the displacement thickness of the boundary layer decreased with increasing free stream turbulence intensity. In Figure 25 are depicted the computed and measured intensities of high frequency broadband noise as a function of turbulence in the free stream. From Figure 25 it is evident that the influence of turbulence on the intensity of high frequency broadband noise is indeed significant.

CONCLUSIONS

The objective of this study has been to arrive at suitable velocity dependent factors to predict the various noise components of a model helicopter rotor. To this end, we have performed a series of experiments at the M.I.T. anechoic wind tunnel facility. The rotational and the broadband noise components were isolated and studied independently. An analysis based on existing theoretical modelling of unsteady aerodynamics has been presented and the computed results have been compared with the measured data. In this section, based on our analysis and measured data, we have proposed the appropriate scaling laws governing the radiation of various components of model rotor noise.

It is postulated that the rotational noise from model rotors is a direct consequence of steady and unsteady loading harmonics and the broadband noise may further be classified into low frequency and high frequency components because of the inherent differences in their causative mechanisms. The low frequency broadband noise is attributed to the interaction of ingested turbulence with the rotor blades. The high frequency broadband noise is associated with the periodic vortex shedding from the rotating airfoils.

Analytical expressions were developed to determine the spectral content of the rotational noise components using existing theories of radiation from rotating dipole sources. An order of magnitude study indicated that the contribution of force derivative terms outweighs the contributions of force and thickness terms for tip Mach numbers of 0.6 or less. Such an approximation yielded simpler expressions for the complex Fourier coefficients of sound radiation from a rotating point source. The resulting Mach number scaling formula for rotational noise is as follows

$$\begin{aligned} SPL_2 = SPL_1 &+ 60 \log \frac{M_{t_2}}{M_{t_1}} + 20 \log \frac{c_2}{c_1} \\ &- 20 \log \frac{r_2}{r_1} + 20 \log \frac{\sin\alpha_2}{\sin\alpha_1} \\ &- 40 \log \left[\frac{1 + \mu_2 M_{t_2} \cos\alpha_2 \cos\phi_2}{1 + \mu_1 M_{t_1} \cos\alpha_1 \cos\phi_1} \right] \end{aligned} \tag{26}$$

The location in the frequency domain is simply given by the blade passage harmonic, nBΩ.

Theoretical analysis of the low frequency broadband noise was made exploiting the existing knowledge of unsteady thin airfoil theory and the characteristics of the inflow turbulence. Assumptions of isotropy and homogeneity of turbulence were made to make the analysis feasible. The measured spectrum of turbulence justified the validity of such assumptions. Further, it was observed that the measured turbulence spectra could easily be interpreted in terms of von Karman's interpolation formula. With the aid of this and the two dimensional Sears function, the unsteady lift acting on the airfoil was computed. The resulting acoustic intensity and spectra were dependent on the flow and rotational Mach numbers, intensity, and size scale of turbulence. The peak intensity of low frequency broadband noise was found to be varying with the Mach number according to a M_t^4 power law, and with r.m.s. values of turbulence velocity according to a $\bar{w}^2$ power law. The influence of size scale of turbulence on the peak intensity was found to be insignificant, approximately $\Lambda_f^{-0.33}$. However, the location of peak intensity in the frequency domain was found to be strongly dependent on the Mach number and the longitudinal scale of turbulence. To this end, we plotted the normalized acoustic intensity as a function of Strouhal frequency $f\Lambda_f/V$. It was observed that the peak intensity of LFBN occurred at a Strouhal number of about 1.5. With this, a scaling law can readily be proposed to evaluate the peak intensity of low frequency broadband noise. Under similar flow environ, the sound pressure level of a rotor system 2 in terms of a rotor system 1 will then be given as follows

$$\begin{aligned} SPL_2 = SPL_1 &+ 20 \log \frac{b_2 c_2}{b_1 c_1} + 10 \log \frac{\bar{w}_2^2}{\bar{w}_1^2} \\ &+ 40 \log \frac{M_{t_2}}{M_{t_1}} + 20 \log \frac{\left|(1 + \mu_2)^2 + (M_{c_2}/M_{t_2})^2\right|}{\left|(1 + \mu_1)^2 + (M_{c_1}/M_{t_1})^2\right|} \\ &- 3.3 \log \frac{\Lambda_{f_2}}{\Lambda_{f_1}} - 20 \log \frac{r_2}{r_1} \end{aligned} \tag{27}$$

The location of the peak intensity in the frequency domain is given by

$$f_{p_{1,2}} = \frac{1.5\, V_{1,2}}{\Lambda_{f_{1,2}}} \tag{28}$$

for respective rotor system.

To obtain a similar scaling procedure for high frequency broadband noise generated by a model rotor, we assumed that noise sources were acoustically compact and computed the instantaneous pressure due to an element of an airfoil where vortices are being shed. Extending experimentally obtained results for the spanwise correlation lengths for stationary airfoils to rotating airfoils and assuming that the correlation lengths vary like the displacement thickness of the boundary layer, it was observed that the peak intensity of high frequency broadband noise has a $V_t^{5.8}$ factor. An expression which scales the location of peak intensity in the frequency domain was obtained based on the rotor blade geometric parameters. The resulting scaling laws for peak intensity was found to be

$$\begin{aligned} SPL_2 = SPL_1 &+ 60 \log \frac{M_{t_2}}{M_{t_1}} + 20 \log \frac{c_2 t_1}{c_1 t_2} \\ &+ 10 \log \frac{b_2}{b_1} - 20 \log \frac{r_2}{r_1} + 10 \log \frac{(\Delta L)_2}{(\Delta L)_1} \\ &+ 10 \log \{[1 + \frac{14}{3} \mu_2 + \frac{42}{5} \mu_2^2] \Big/ [1 + \frac{14}{3} \mu_1 + \frac{42}{5} \mu_1]\} \end{aligned} \tag{29}$$

and the peak frequency was found to be given by

$$f_{p_{1,2}} = 1.08\, V_{t_{1,2}} \Big/ t_{1,2} \tag{30}$$

for the respective rotor systems. The effects of intensity and size scale of turbulence were less obvious in the study of high frequency broadband noise. One of the effects of free stream turbulence is to alter the correlation lengths of shed vortices. To this end, we used an existing integral boundary layer calculation to predict the turbulent boundary layers developing in a turbulent free stream. The results indicated that increase in the intensity of free stream turbulence in general would tend to decrease the correlation length, thus resulting in reducing the intensity of high frequency broadband noise.

The scaling laws obtained for the intensities of rotational noise components were experimentally verified over a range of operating conditions. The measured data showed general agreement with the scaling procedure except at low rotational harmonies. It is believed that the geometric and acoustic near field effects might have caused some ambiguity in the measured rotor noise spectra at very low frequencies. The low frequency broadband noise prediction procedures were experimentally verified under various operating conditions of the rotor and varying intensity and size scale of turbulence. A comparison of predicted peak frequency and sound pressure levels with experimental data showed good agreement except for the case of effect of turbulence on the intensity of high frequency broadband noise. In this case, the data showed general agreement with the prediction technique, but the measured intensity levels were higher than the predicted levels. We further add that improvements in modelling more of the fluid mechanical aspects of the flow field are desired to place this scaling procedure on a firmer basis.

Our efforts in modelling the rotational noise components of the model rotor and understanding the effects of free stream turbulence on the nature of high frequency and low frequency broadband noise components have been greatly benefited from the detailed experimental task performed by Lee [26]. The utility of our results for scaling of low frequency and high frequency broadband noise remains as demonstrated in the above comparison of predictions and data. The scaling procedures developed in this study may be considered as a first order attempt in responding to the challenge of Mach number and Reynolds number scaling of full scale rotors.

REFERENCES

1. Gutin, L., "On the Sound Field of a Rotating Propeller," NACA TM 1195, 1948.

2. Cox, C.R., "Aerodynamic Sources of Rotor Noise," Journal of American Helicopter Society, 18, pp. 3-9, 1973.

3. Morfey, C.L., "Rotating Blades and Aerodynamic Sound," Journal of Sound and Vibration, 28, pp. 587-617, 1973.

4. Leverton, J.W., "The Noise Characteristics of a Large Clean Rotor," Journal of Sound and Vibration, 27, pp. 357-376, 1973.

5. Leverton, J.W. and Pollard, J.S., "A Comparison of Overall and Broadband Noise Characteristics of Full Scale and Model Helicopter Rotors," Journal of Sound and Vibration, 30, pp. 135-152, 1973.

6. Lowson, M.V., Whatmore, A.R., and Whitfield, C.E., "Source Mechanisms for Rotor Noise Radiation," NASA CR-2077, 1973.

7. Aravamudan, K.S. and Harris, W.L., "Experimental and Theoretical Studies on Model Helicopter Rotor Noise," M.I.T. Fluid Dynamics Research Laboratory Report 78-1, January 1978.

8. Lee, A., Harris, W.L. and Widnall, S.E., "A Study of Helicopter Rotor Rotational Noise," Journal of Aircraft, 14, 11, 1977, pp. 1126-1132.

9. Aravamudan, K.S., Lee, A., and Harris, W.L., "A Simplified Mach Number Scaling Formula for Helicopter Rotor Noise," Journal of Sound and Vibration, 57, 3, 1978.

10. Baines, W.D. and Peterson, E.G., "An Investigation of Flow Through Screens," Transactions of ASME, 73, pp. 467-480, 1951.

11. Harris, W.L. and Lee, A., "The Development of Experimental Techniques for the Study of Helicopter Rotor Noise," AIAA paper 75-455, AIAA 2nd Aeroacoustics Conference, Hampton, Virginia, March 24-26, 1975.

12. Hawkings, D.L. and Lowson, M.V., "Noise of High Speed Rotors," AIAA paper 75-450, AIAA 2nd Aeroacoustics Conference, Hampton, Virginia March 24-26, 1975.

13. Lowson, M.V. and Ollerhead, J.B., "A Theoretical Study of Helicopter Rotor Noise," Journal of Sound and Vibration, 9, pp. 197-222, 1969 (also Wyle Research Staff Report WR 68-9, 1968).

14. Ffowcs Williams, J.E. and Hawkings, D.L., "Theory Relating to the Noise of Rotating Machinery," Journal of Sound and Vibration, 10, pp. 10-21, 1969.

15. Morfey, C.L. and Tanna, H.K., "Sound Radiation from a Point Source in Circular Motion," Journal of Sound and Vibration, 15, pp. 325-351, 1971.

16. Lowson, M.V., "Rotor Noise Radiation in Non-Uniform Flow," Proceedings of the Symposium on Aerodynamic Noise, Loughborough University, Paper D2, 1970.

17. Amiet, R.K., "Acoustic Radiation from an Airfoil in a Turbulent Stream," Journal of Sound and Vibration, 41, pp. 407-420, 1975.

18. Sears, W.R., "Some Aspects of Non-Stationary Airfoil Theory and Its Applications," Journal of Aeronautical Sciences, 8, pp.104-108,1941.

19. Homicz, G.F. and George, A.R., "Broadband and Discrete Frequency Radiation from Subsonic Rotors," Journal of Sound and Vibration, 36, pp. 151-177, 1974.

20. Osborne, C., "Unsteady Thin Airfoil Theory," AIAA Journal, 11, pp. 205-209, 1973.

21. George, A.R. and Kim, Y.N., "High Frequency Broadband Rotor Noise," AIAA Journal, 15, 4, pp. 538-546, 1977.

22. Chanaud, R.C. and Hayden, R.E., "Edge Sound Produced by Two Turbulent Wall Jets," Paper FF-11, Spring Meeting of Acoustical Society of America, Atlantic City, New Jersey, 1970.

23. Hersh, S. and Hayden, R.E., "Aerodynamic Sound Radiation from Lifting Surfaces with or without Leading Edge Serrations," NASA CR-114370, 1971.

24. Paterson, R.W., Vogt, P.G., Fink, M.R., and Munch, C.L., "Vortex shedding Noise from Isolated Airfoils," Journal of Aircraft, 10, pp.296-302, 1973.

25. Clark, L.T., "The Radiation of Sound from an Airfoil Immersed in Laminar Flow," Journal of Engineering for Power, 13, Ser. A, pp.366-376, 1971.

26. Lee, A., "Theoretical and Experimental Study of Helicopter Rotor Noise," PhD. Thesis, Dept. of Aeronautics and Astronautics, M.I.T., 1975.

27. Mugridge, B.D., "Turbulent Boundary Layers and Surface Pressure Fluctuations on Two Dimensional Aerofoils," Journal of Sound and Vibration, 18, pp. 475-486, 1971.

28. Clark, L.T., "A Prediction Model for Wake Related Sound Generation," Ph.D. Thesis, University of Washington, 1973.

29. Evans, R.I. and Horlock, J.H., "Calculation of the Development of Turbulent Boundary Layers with a Turbulent Free Stream," ASME Paper 74-FE-24, 1974.

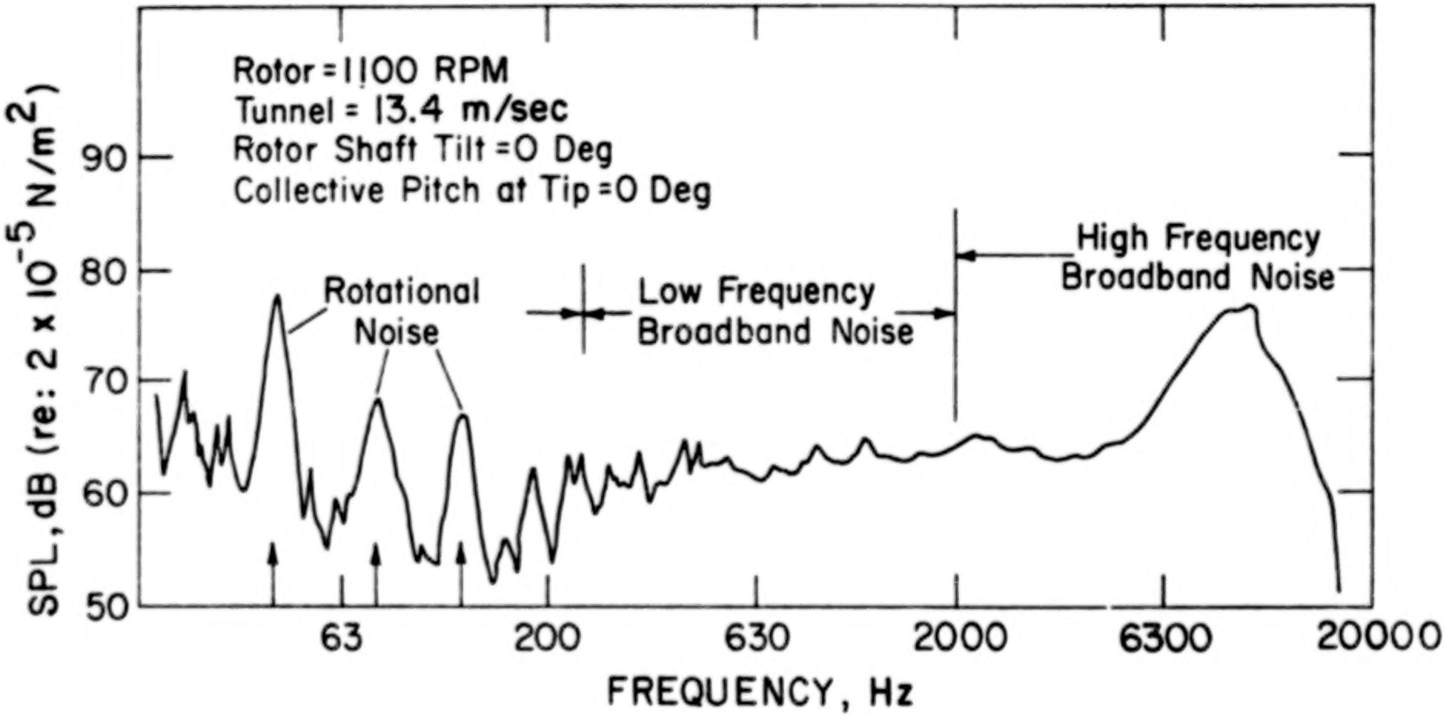

Figure 1.- 6% bandwidth spectrum of model rotor noise.

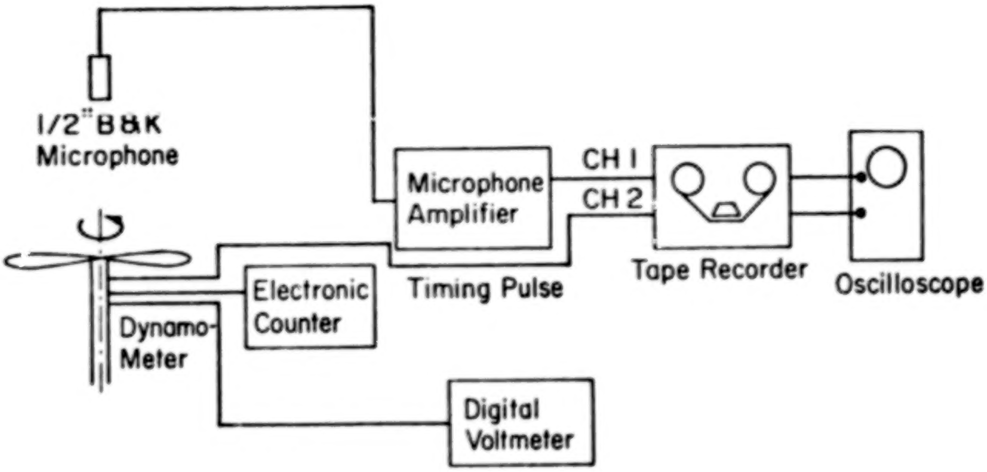
1/2" B&K
Microphone
Microphone
Amplifier
CH 1
CH 2
Tape Recorder
Oscilloscope
Timing Pulse
Electronic
Counter
Dynamo-
Meter
Digital
Voltmeter

SCHEMATIC OF INSTRUMENTATION FOR ACQUISITION OF ACOUSTIC DATA

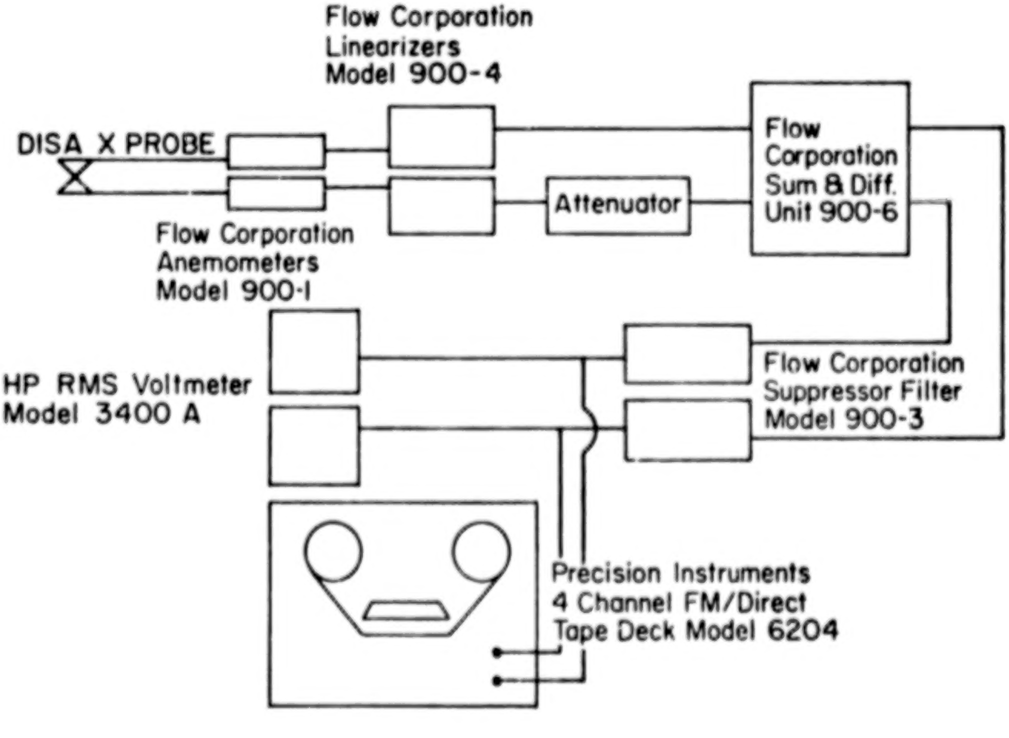
Flow Corporation
Linearizers
Model 900-4
DISA X PROBE
Flow
Corporation
Sum & Diff.
Unit 900-6
Attenuator
Flow Corporation
Anemometers
Model 900-1
HP RMS Voltmeter
Model 3400 A
Flow Corporation
Suppressor Filter
Model 900-3
Precision Instruments
4 Channel FM/Direct
Tape Deck Model 6204

SCHEMATIC OF INSTRUMENTATION FOR ACQUIRING TURBULENCE DATA

Figure 2.- Schematic of instrumentation for acquiring turbulence data. (1/2 in. = 1.27 cm.)

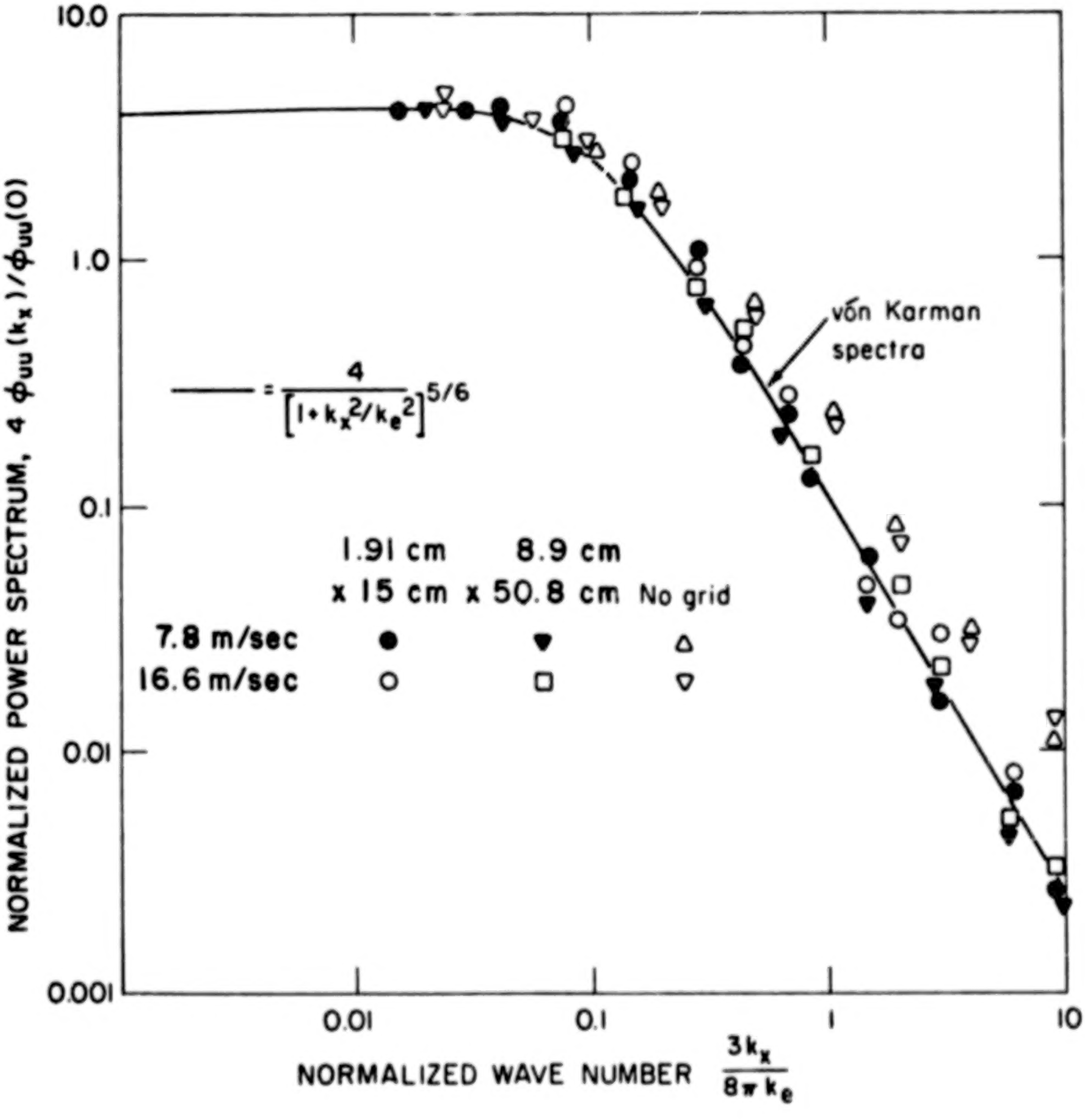

Figure 3.- One dimensional spectrum of axial component of grid turbulence.

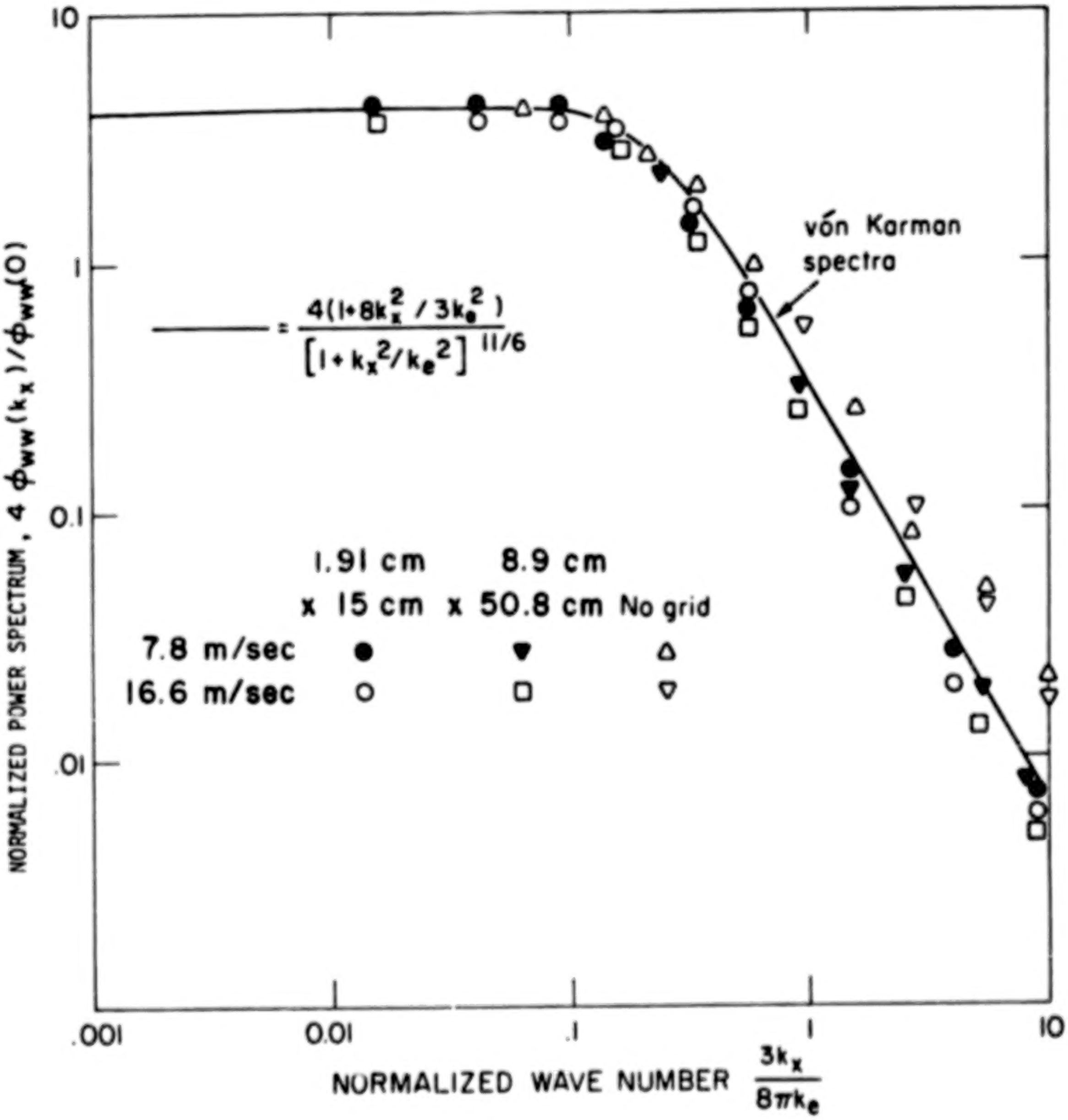

Figure 4.- One dimensional spectrum of vertical component of grid turbulence.

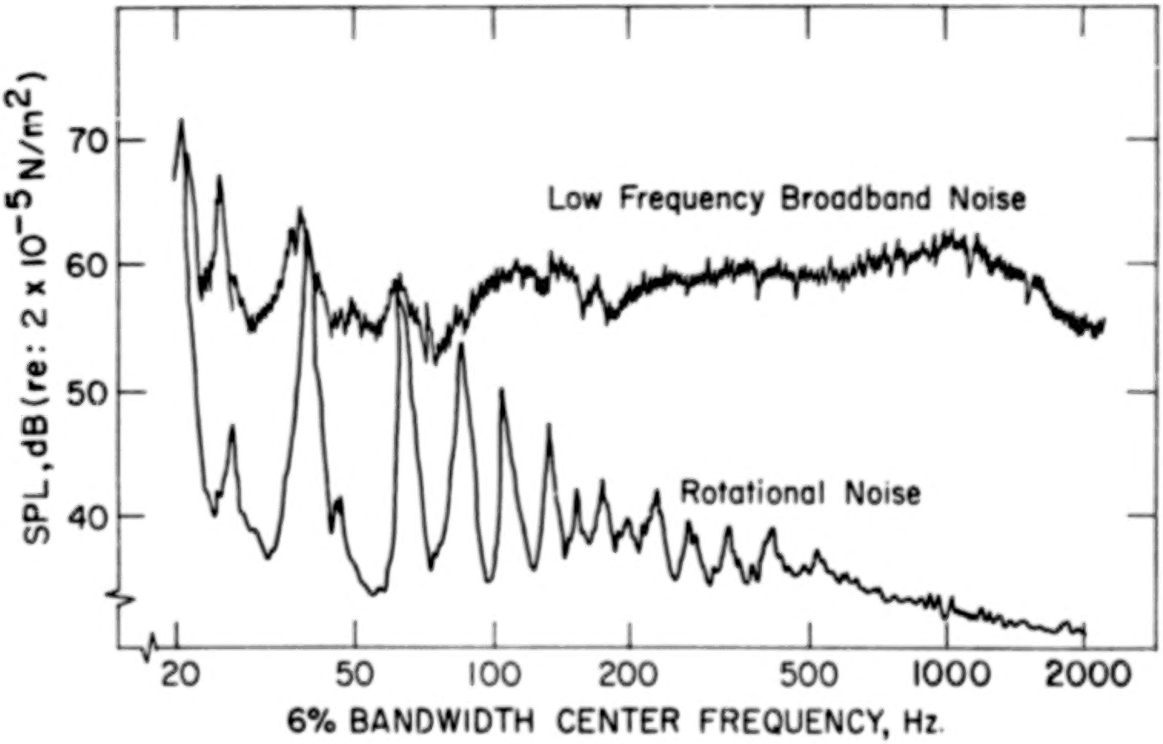

Figure 5.- Comparison of rotational noise and low frequency broadband noise at high frequencies for 1.91 cm × 15 cm turbulence grid; $B = 2$; $\Omega = 672$ rpm; $U_o = 13.4$ m/sec.

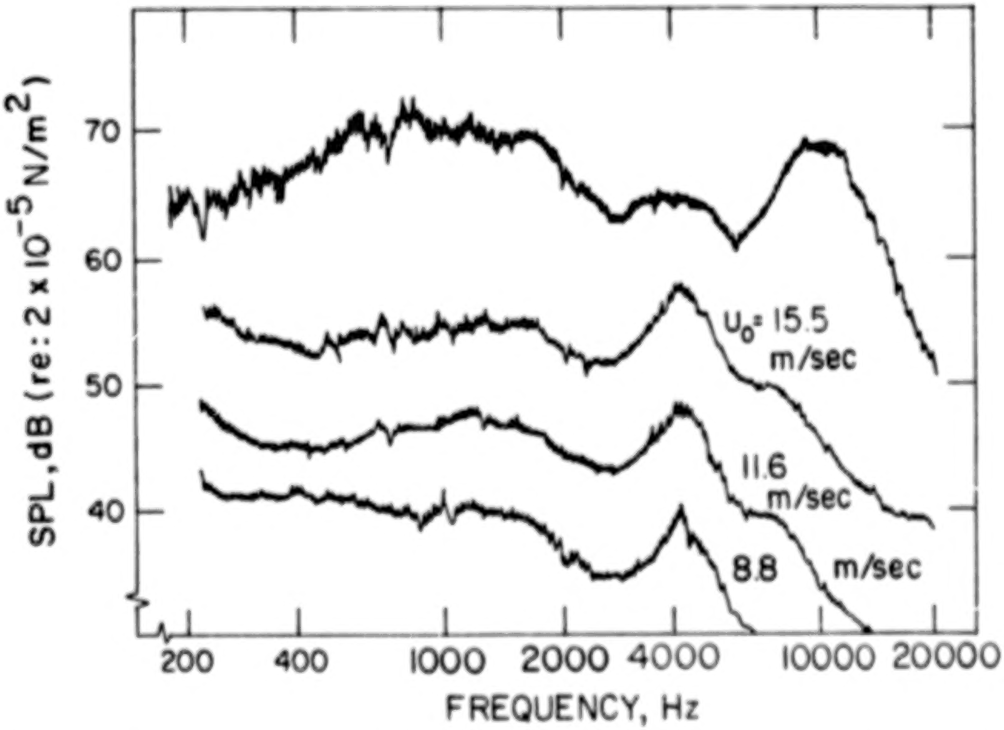

Figure 6.- 6% bandwidth background spectra at various tunnel speeds for 1.91 cm × 15 cm turbulence grid. Top curve: Rotor generated noise for $B = 3$; $\Omega = 1000$ rpm; and $U_o = 15.5$ m/sec.

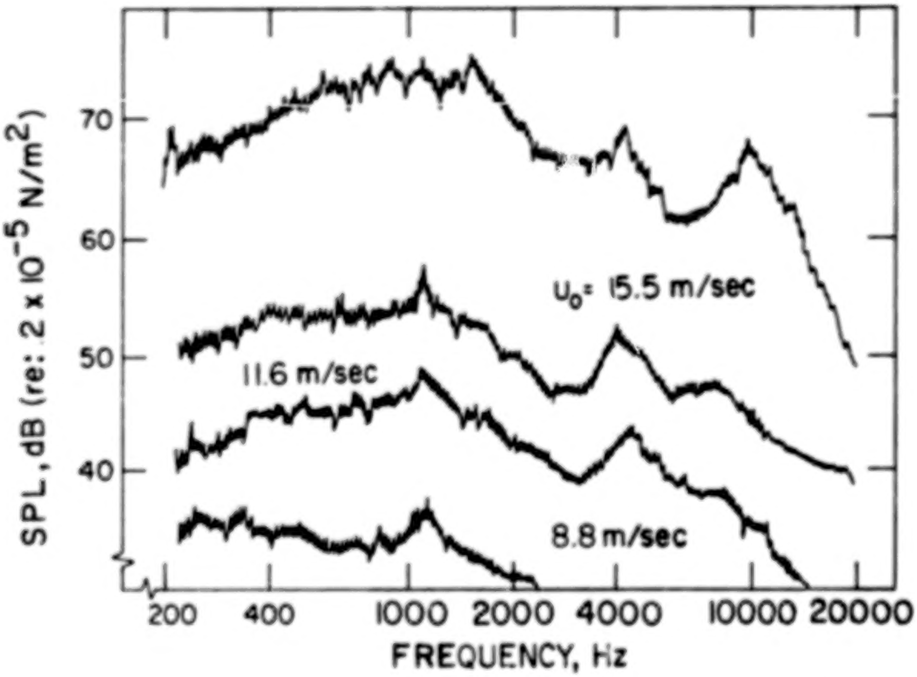

Figure 7.- 6% bandwidth background spectra at various tunnel speeds for 8.9 cm × 50.8 cm turbulence grid. Top curve: Rotor generated noise for $B = 3$; $\Omega = 1000$ rpm; and $U_o = 15.5$ m/sec.

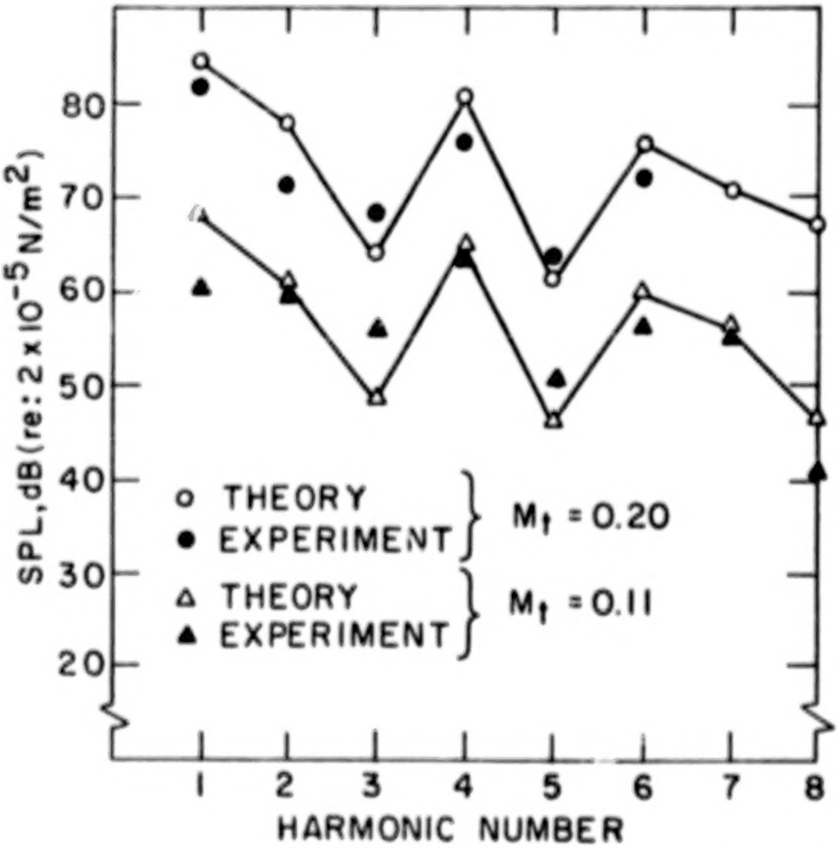

Figure 8.- Mach number scaling for lower harmonics of a two-bladed rotor on axis.

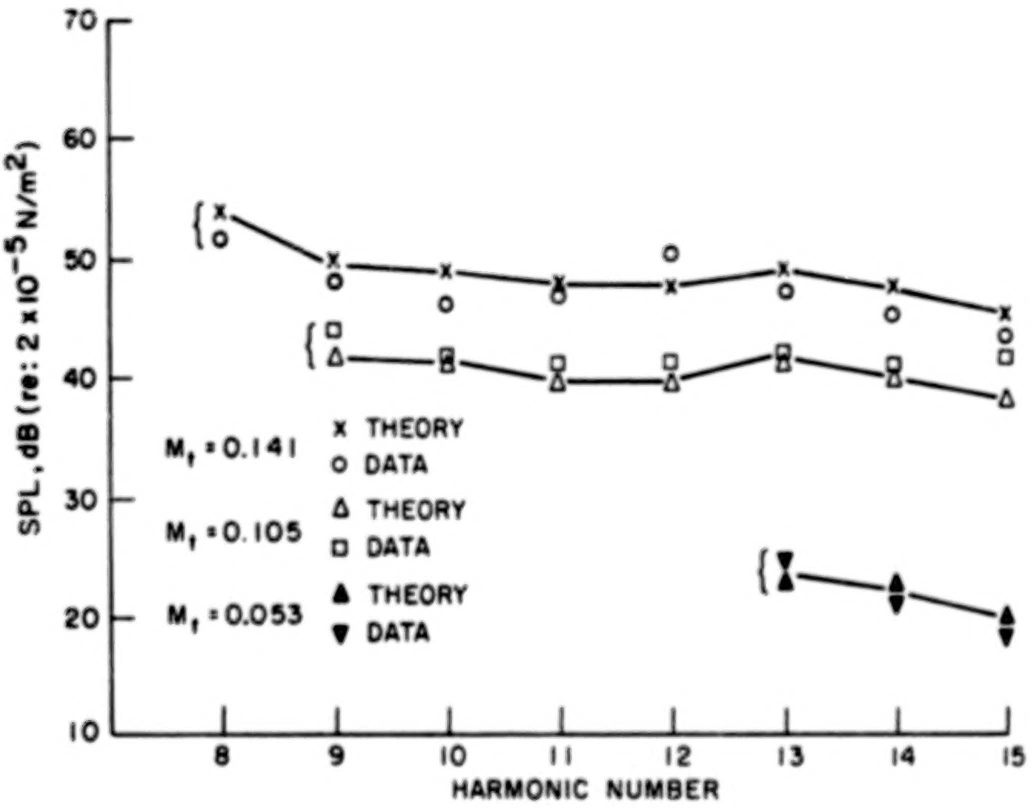

Figure 9.- Mach number scaling for higher harmonics of a two-bladed rotor on axis.

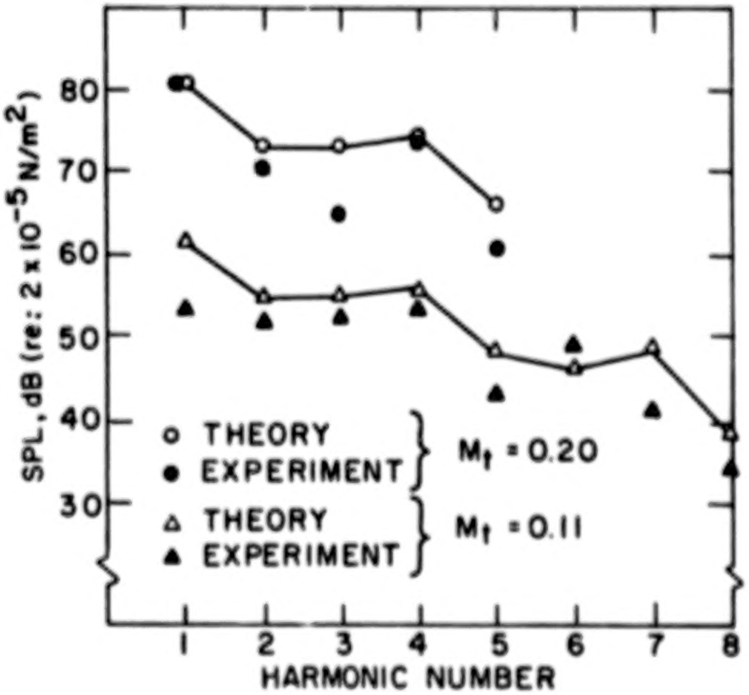

Figure 10.- Mach number scaling for lower harmonics of a two-bladed rotor off axis.

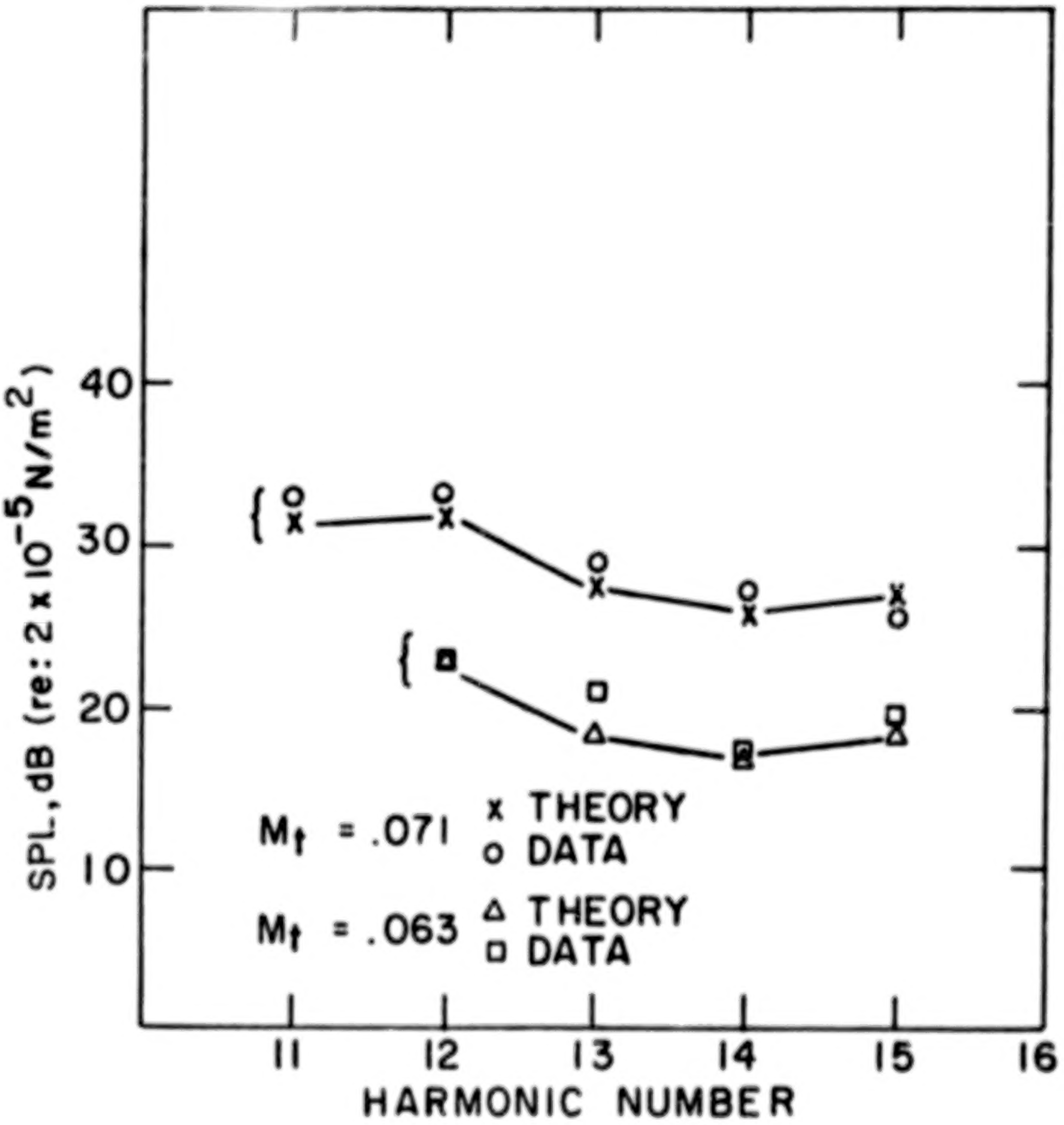

Figure 11.- Mach number scaling for higher harmonics of a two-bladed rotor off axis.

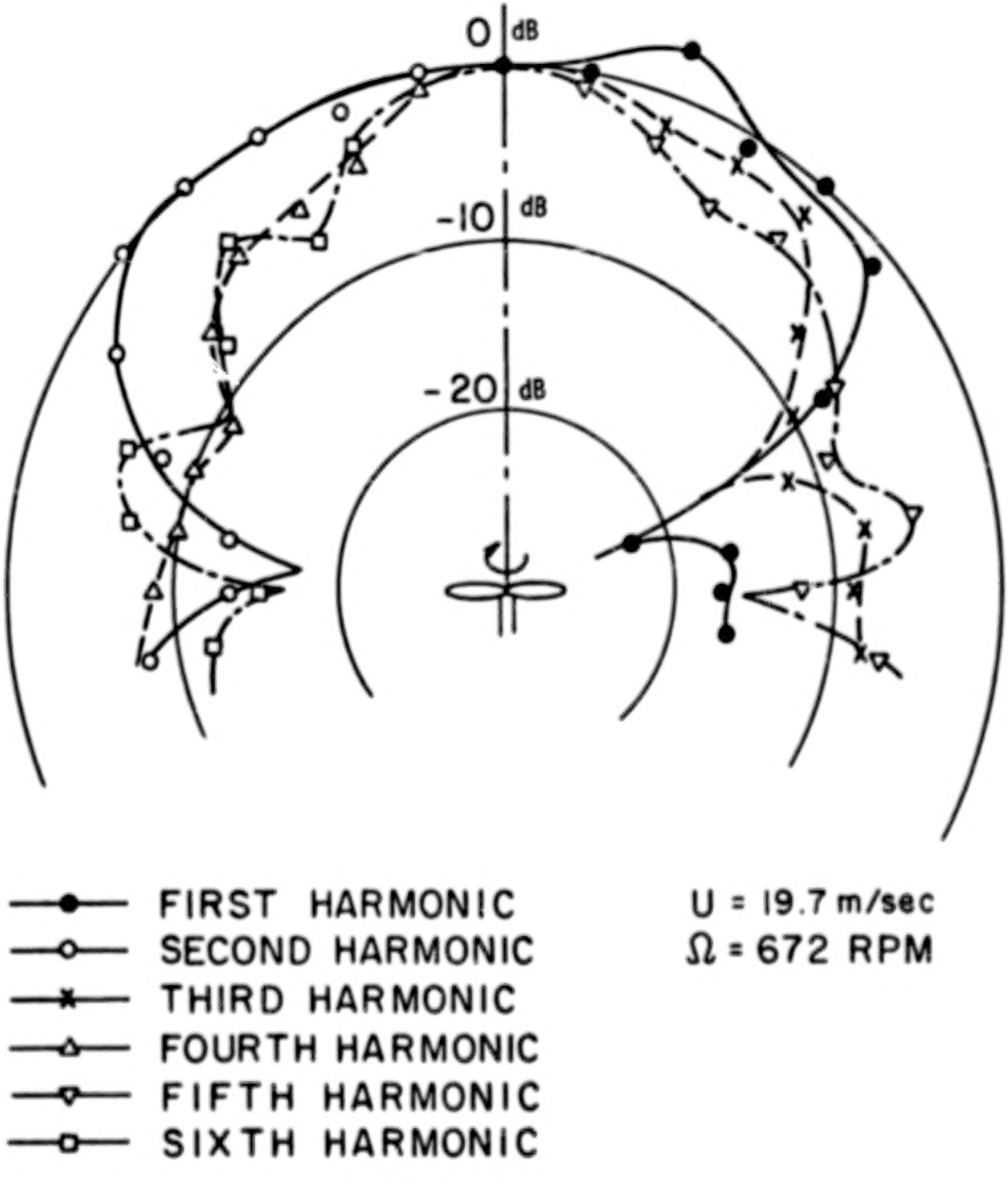

Figure 12.- Directivity of rotational harmonics of a two-bladed rotor.

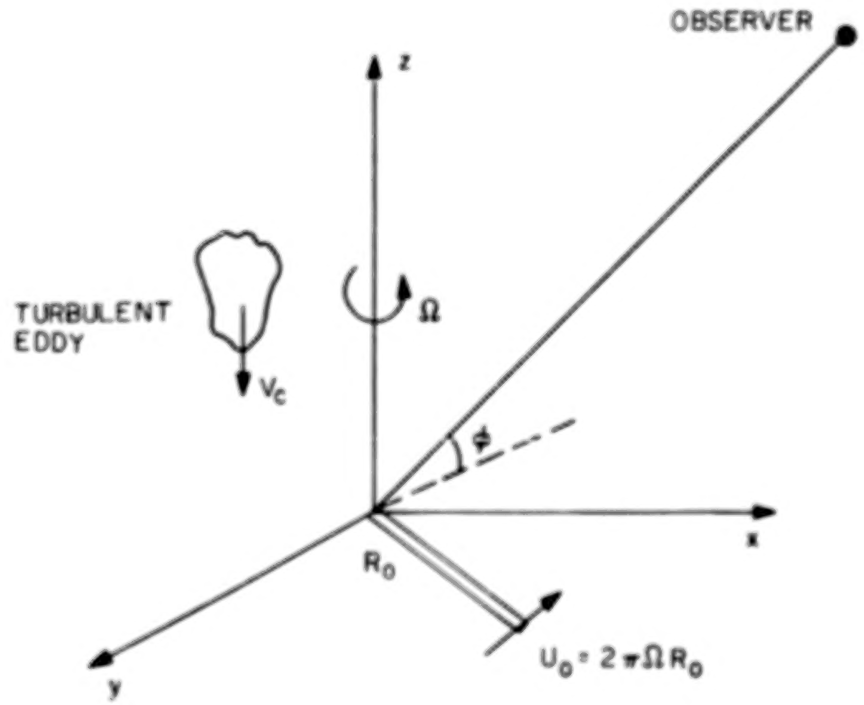
OBSERVER
z
TURBULENT
EDDY
V_c
Ω
ϕ
x
R_0
y
$U_0 = 2\pi\Omega R_0$

Figure 13.- Rotor geometry and coordinate system used.

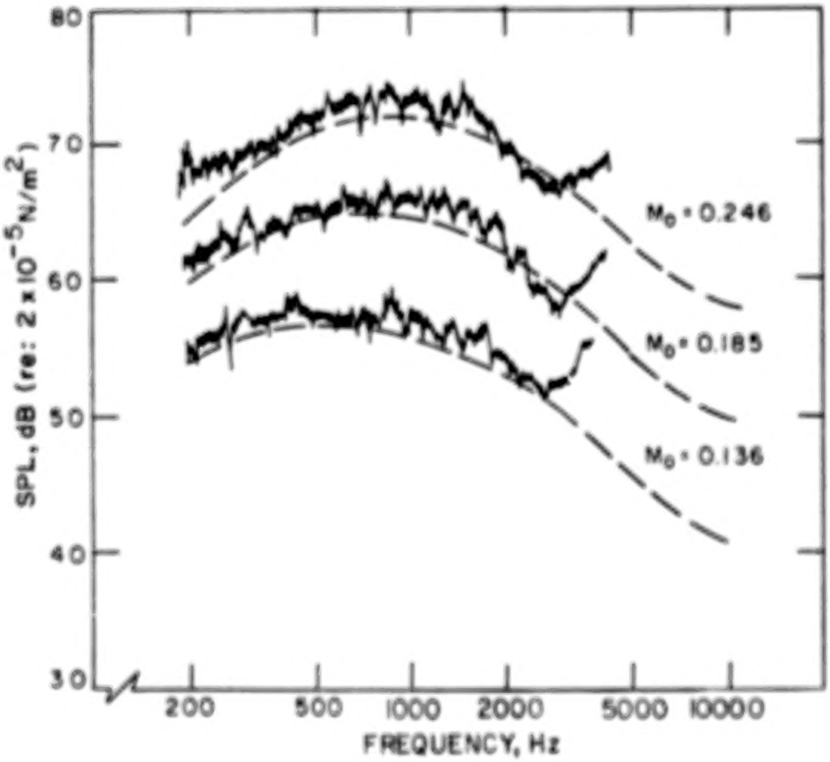

Figure 14.- Effect of Mach number on predicted and measured low frequency broadband noise for the larger grid with a Λ_f = 12.82 cm.

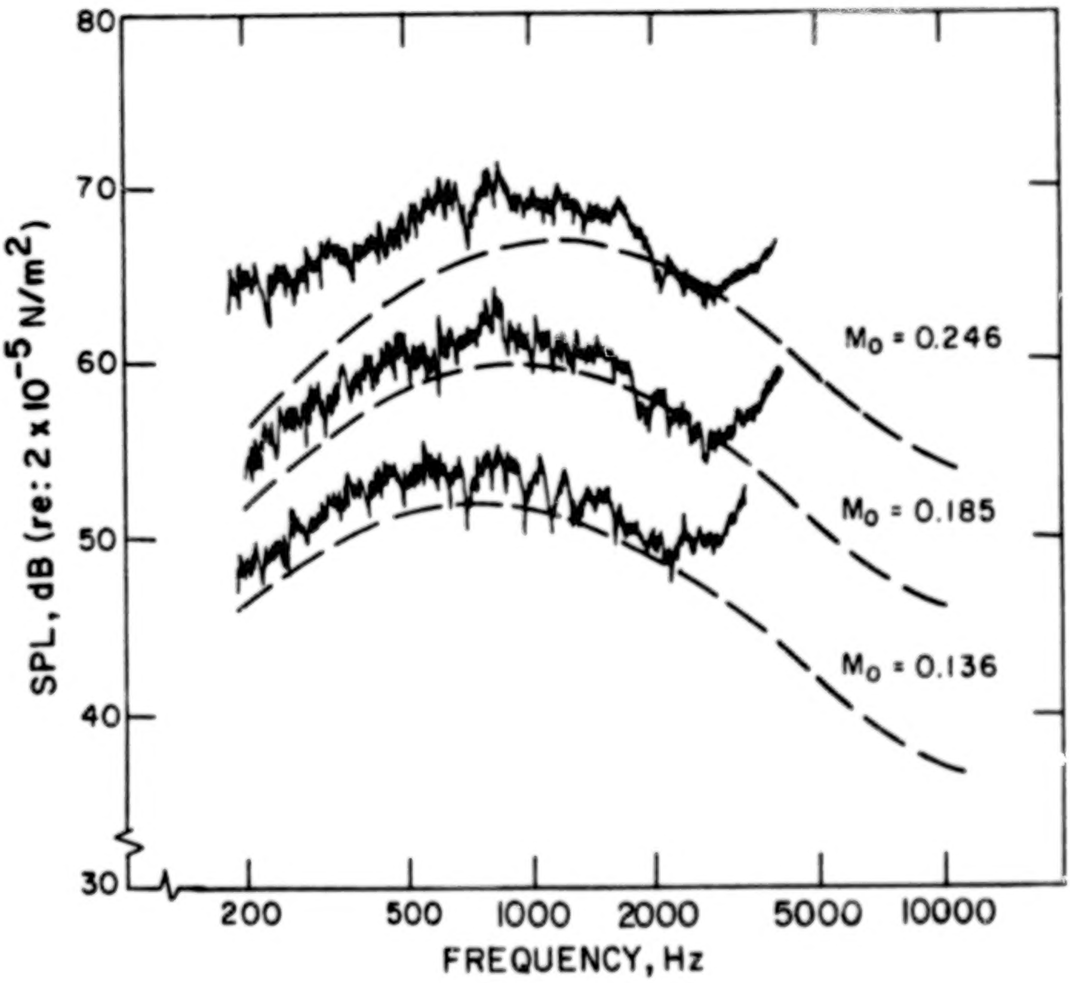

Figure 15.- Effect of Mach number on predicted and measured low frequency broadband noise for the smaller grid with a Λ_f = 8.46 cm.

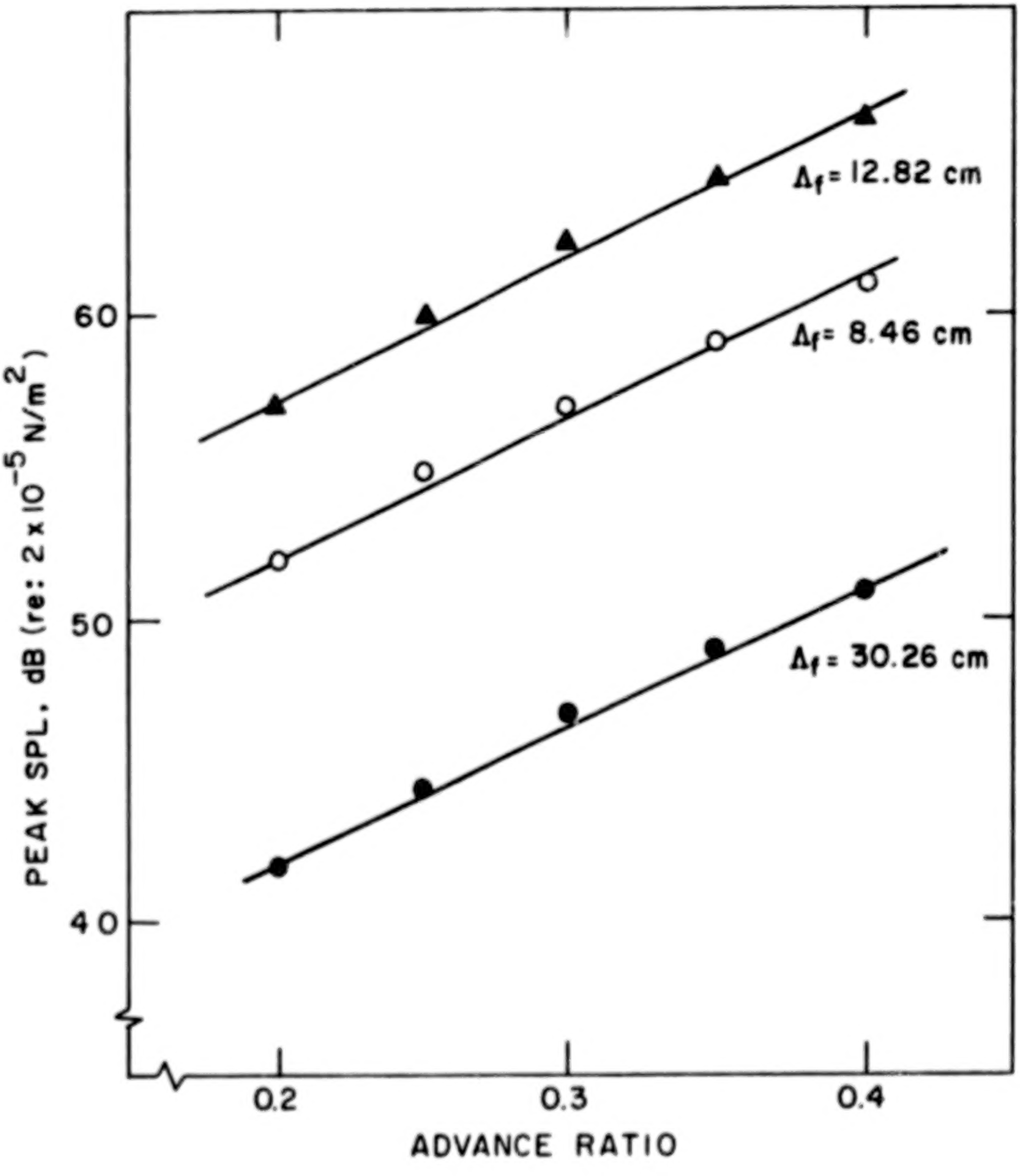

Figure 16.- Effect of advance ratio on the peak intensity of low frequency broadband noise.

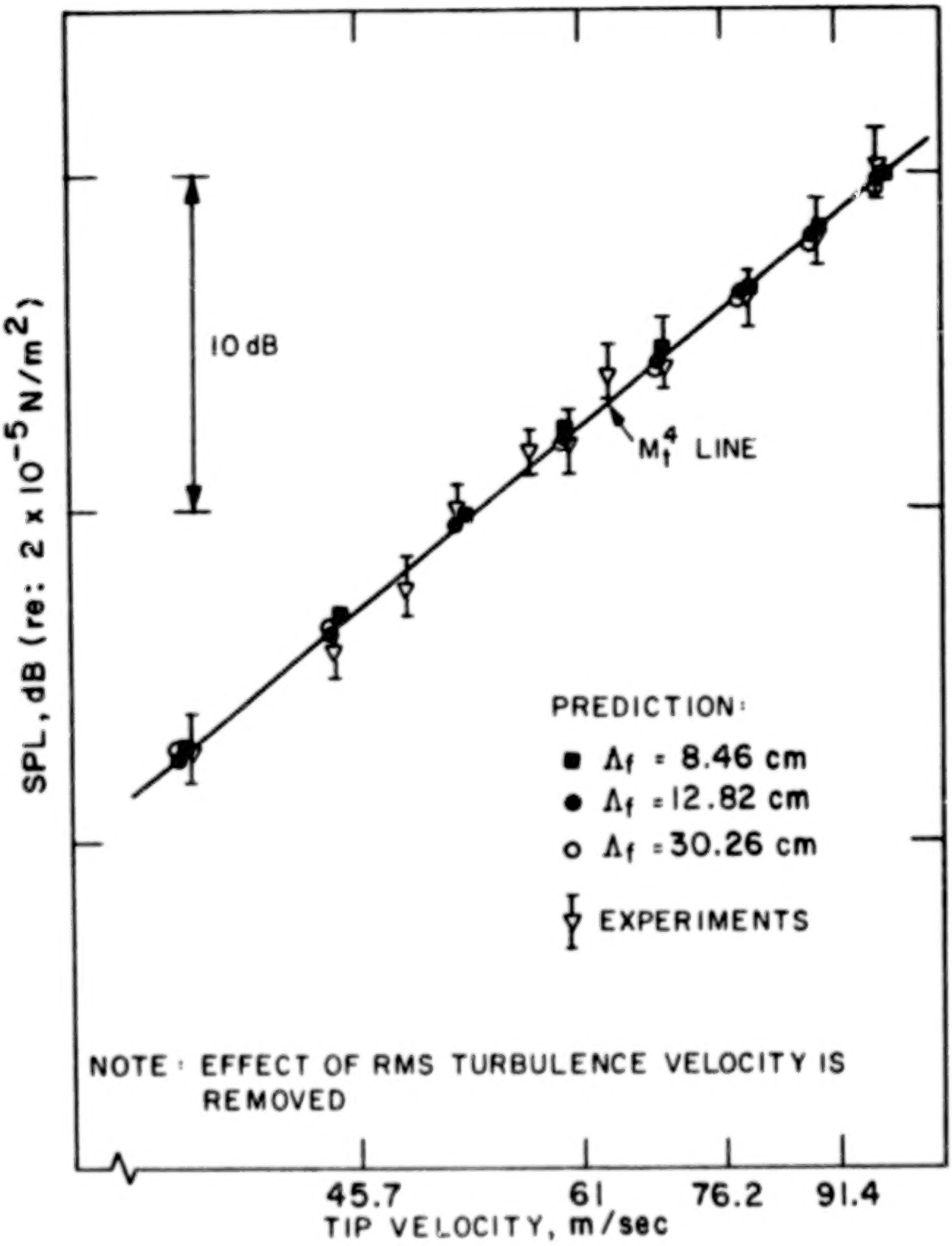

Figure 17.- Effect of tip velocity on predicted and measured peak low frequency broadband noise intensity.

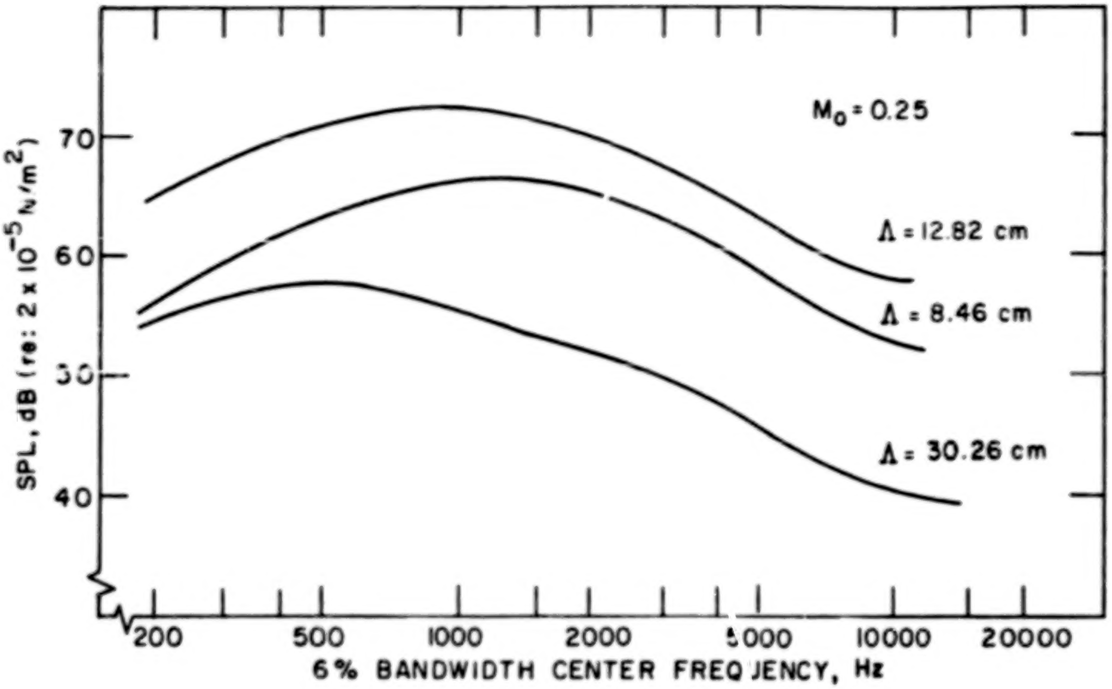

Figure 18.- Effect of integral scale on predicted low frequency broadband noise spectra for $M_o = 0.25$.

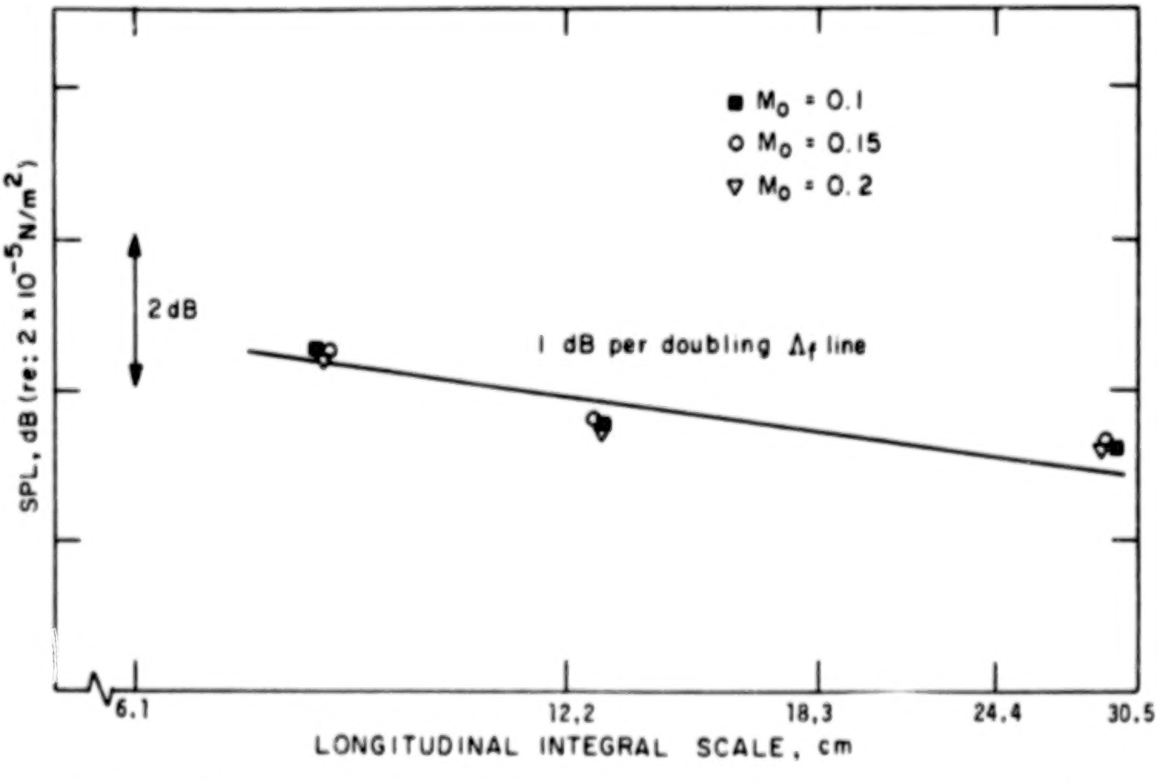

Figure 19.- Effect of turbulence scale on the peak intensity of low frequency broadband noise.

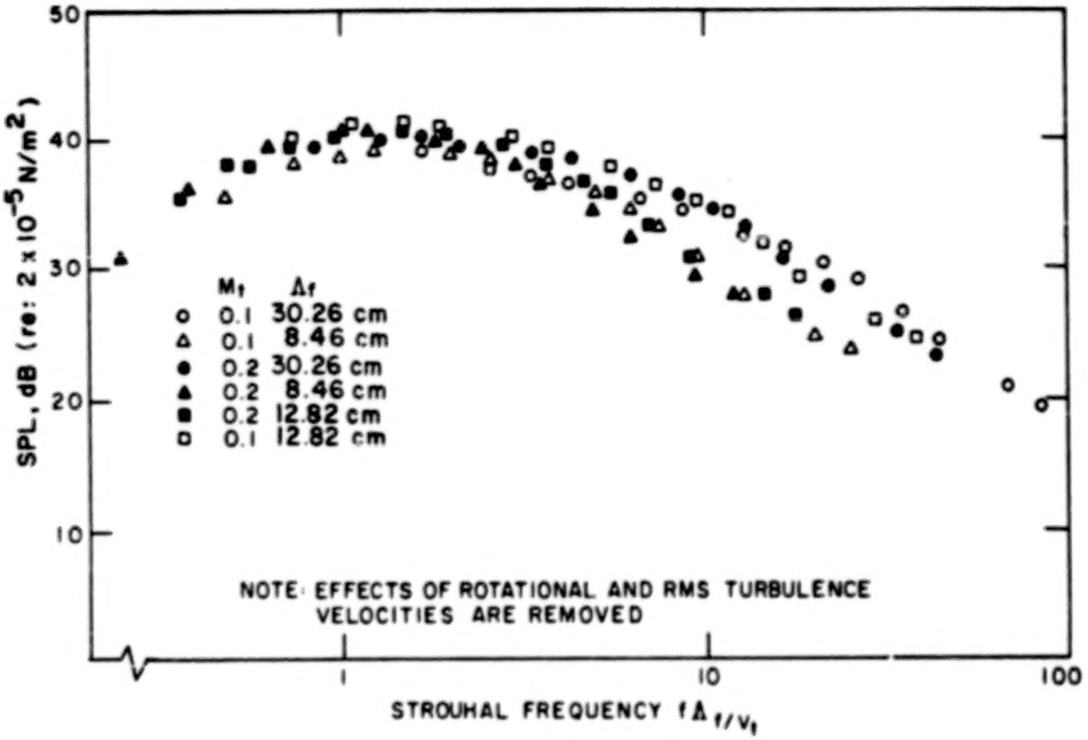

Figure 20.- Spectrum of low frequency broadband noise as a function of nondimensional frequency.

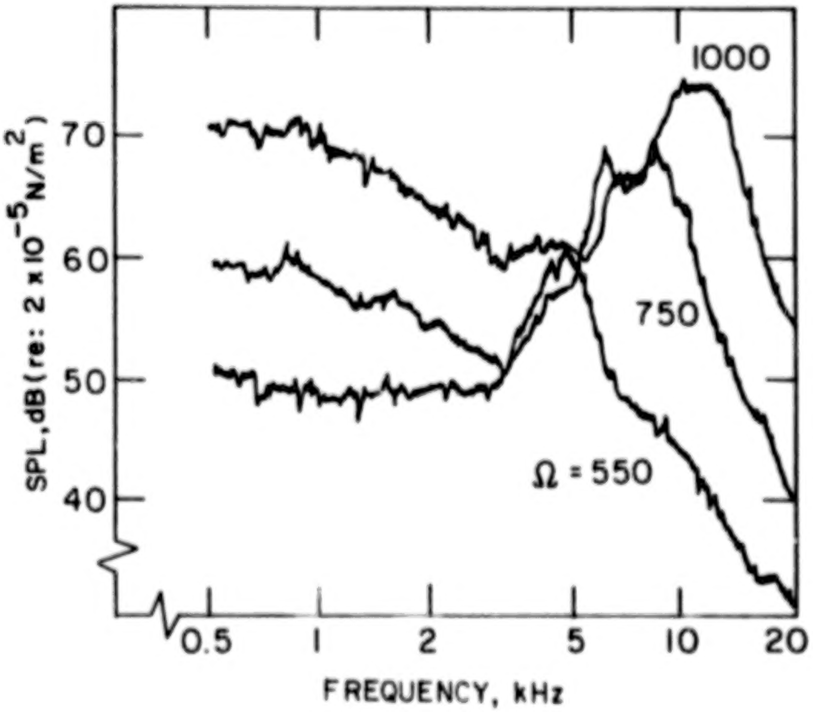

Figure 21.- Typical spectra of high frequency broadband noise at various rotational speeds.

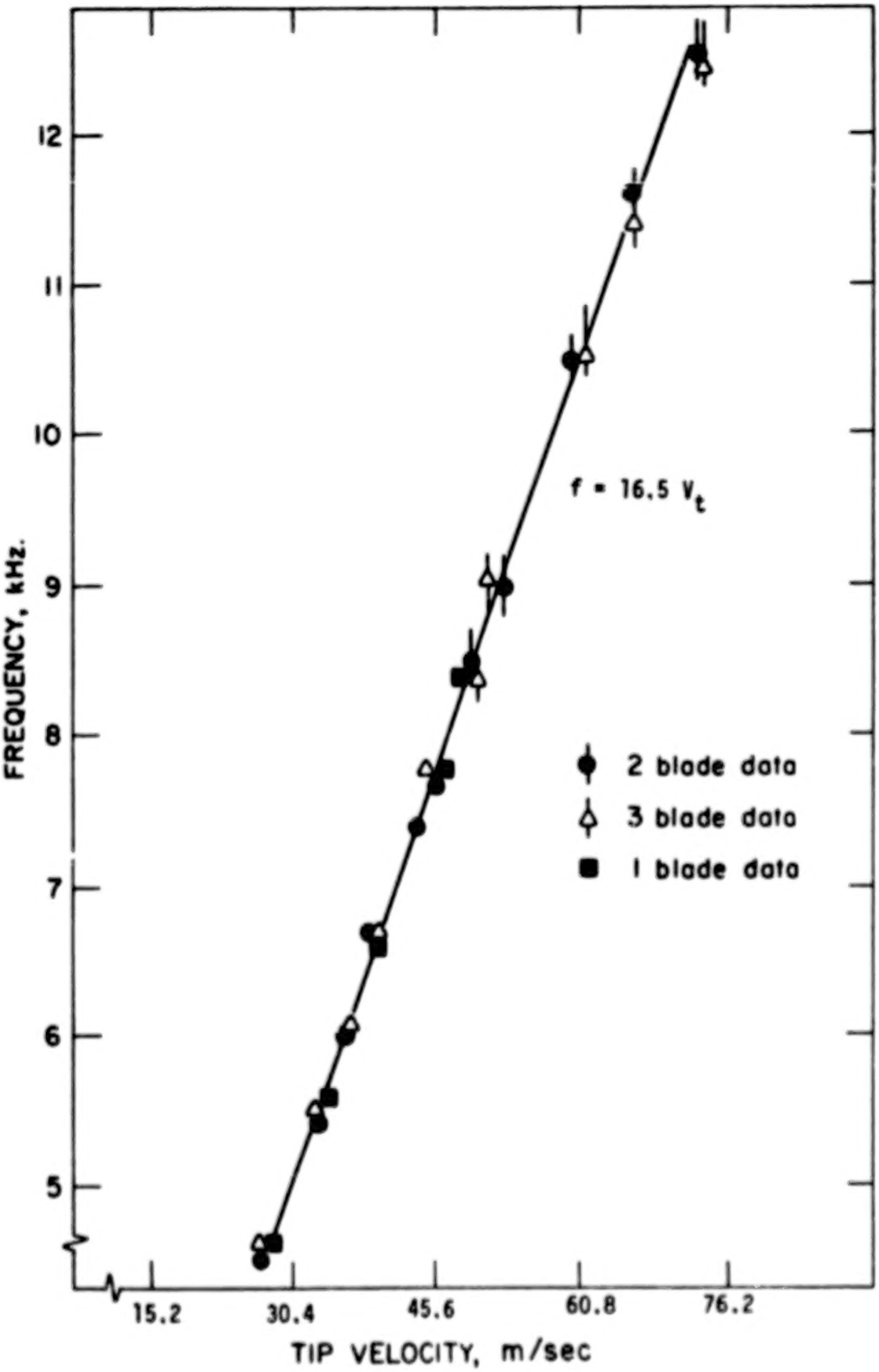

Figure 22.- Peak frequency location as a function of blade tip speed.

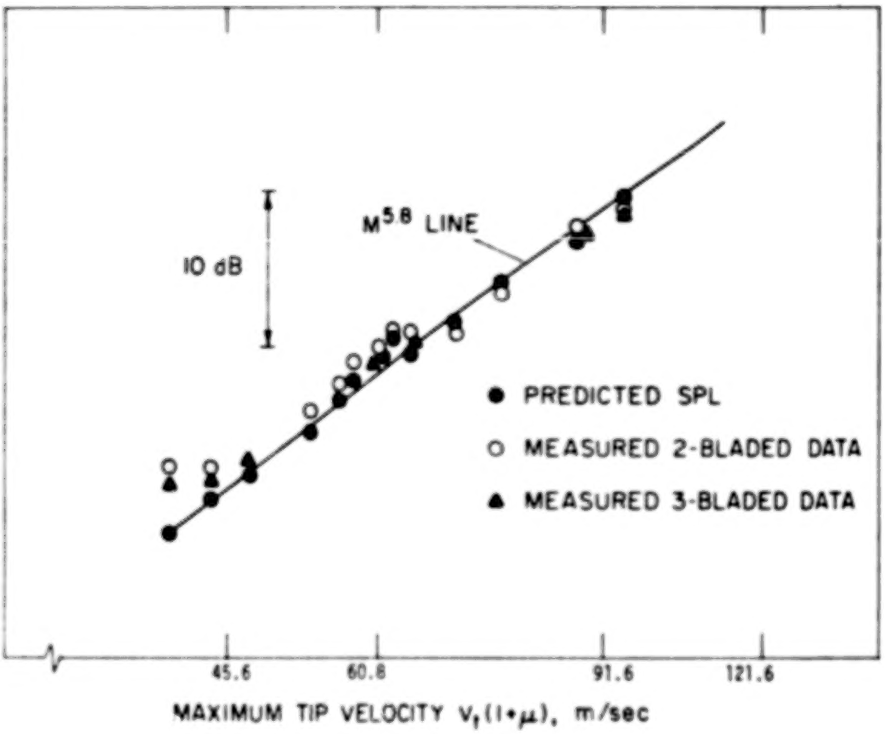

Figure 23.- Velocity scaling of high frequency broadband noise.

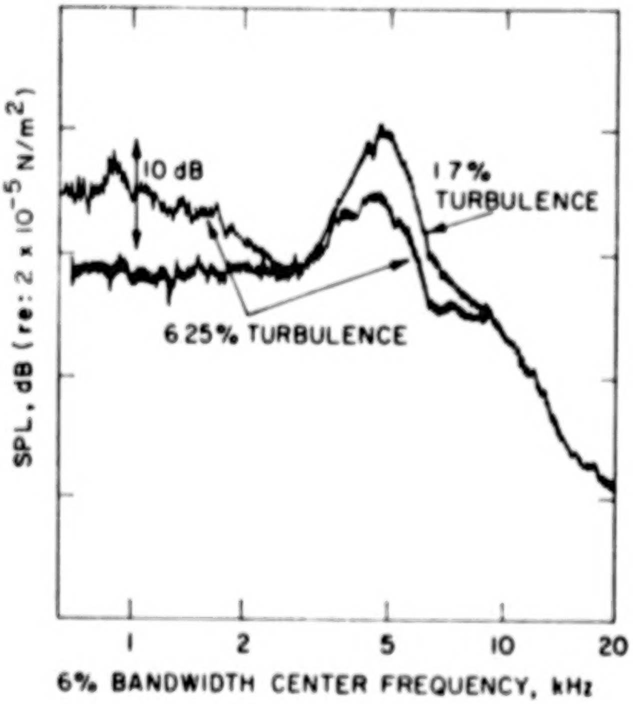

Figure 24.- Effect of free stream turbulence on spectra of high frequency broadband noise.

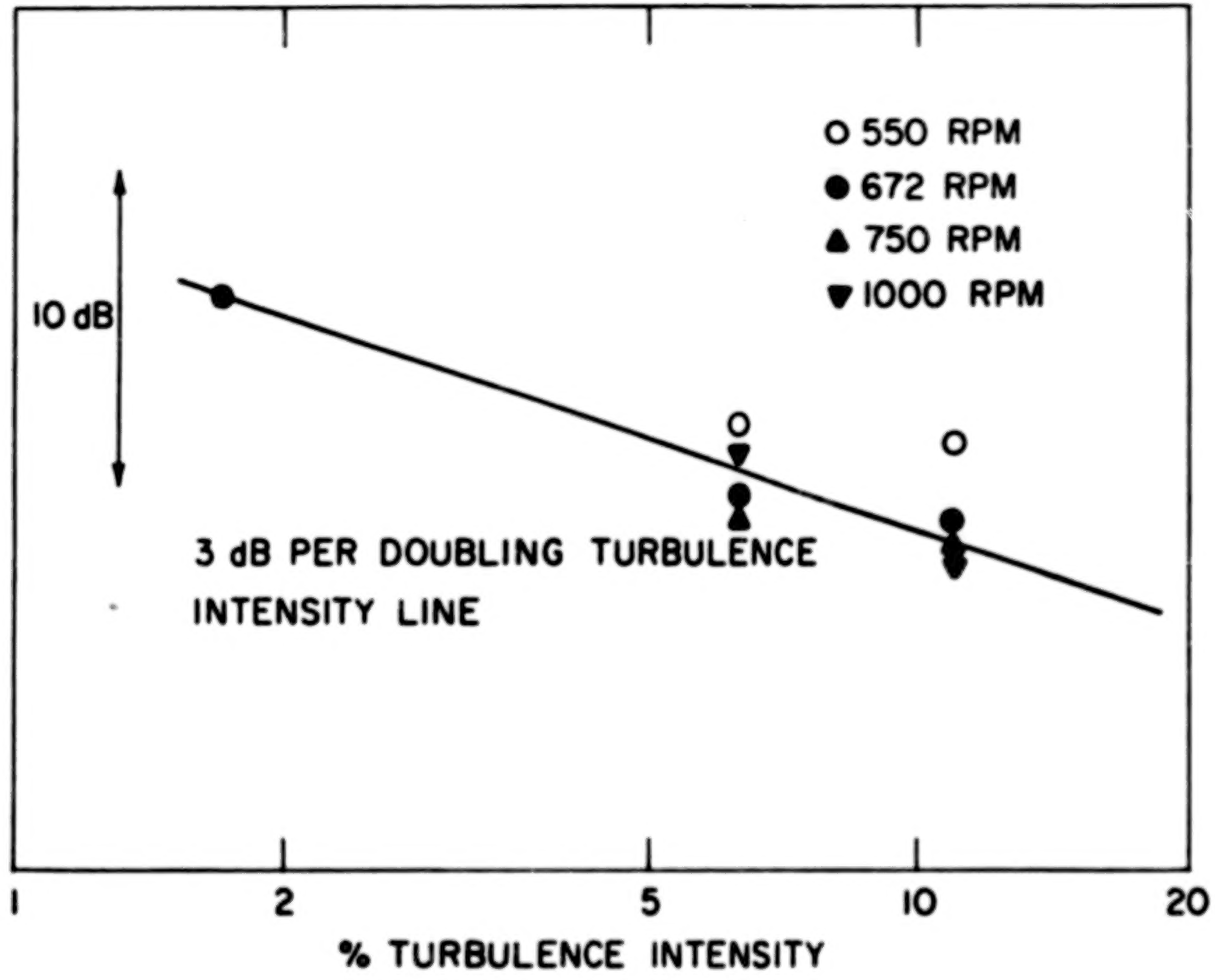

Figure 25.- Effect of free stream turbulence on peak intensity of high frequency broadband noise.

Blank Page

HELICOPTER EXTERNAL NOISE PREDICTION AND CORRELATION WITH FLIGHT TEST

Bharat P. Gupta
Bell Helicopter Textron

SUMMARY

The helicopter external noise prediction requires consideration of many aerodynamic sources. Mathematical analysis procedures for predicting the main and tail rotor rotational and broadband noise have been presented. The blade slap and thickness noise contributions, which normally become important in extreme flight conditions, have not been analyzed during this investigation.

The aerodynamic and acoustical data from Operational Loads Survey (OLS) flight program have been used for validating the analysis and noise prediction methodology. For the long method of rotational noise prediction, the spanwise, chordwise, and azimuthwise airloading is used. In the short method, the airloads are assumed to be concentrated at a single spanwise station and for higher harmonics an airloading harmonic exponent of 2.0 is assumed. For the same flight condition, the predictions from long and short methods of rotational noise prediction are compared with the flight test results. The short method correlates as well or better than the long method.

The correlations at low-speed cruise and hover are fair. The correlations at high-speed and low-speed partial power descent conditions are poor. At high speed and partial power descent flight conditions, the blade slap contributions should be added to the external noise spectrum to improve correlations. Additional sources (i.e. main rotor wake tail rotor interaction and thickness noise) which will improve the correlation further should also be analyzed.

Further recommendations deal with the subject of extensive validation of the prediction procedures. Since the total helicopter noise is composed of contributions from several sources, errors made in calculating one source component might be offset by opposite errors in other source component calculations. Prediction procedures, therefore, should be correlated for several helicopter types and several flight conditions.

INTRODUCTION

The need for accurate helicopter external noise prediction is urgent. In the very near future, the external noise of the helicopters will be regulated. When the noise regulations are in effect, the success of a new helicopter design might well depend upon how accurately the external noise of the helicopter can be predicted. An inaccurate prediction procedure will require the external noise design goal for a new helicopter to be much below the required regulation limit, thereby unduly penalizing the design.

In the present state-of-the-art, the external noise of the helicopters cannot be predicted accurately for most flight conditions. For other flight conditions, such as low-speed cruise, external noise can be predicted only with moderate accuracy. The reason for this state of affairs is that typical helicopter external noise is composed of several components such as main rotor noise, tail rotor noise, broadband noise, blade slap at low-flight speed, blade slap at high speeds, interaction noise, etc. The aerodynamic sources of these noise components are different and sometimes unrelated. In order to predict the total external noise, therefore, separate analytical procedures for these sources need to be developed. The problem is further complicated by the fact that proper aeroacoustics analysis procedures for calculating the external noise from many of these sources are presently not available; hence, the external noise for some flight conditions cannot be accurately predicted.

A typical helicopter noise is produced by lift and drag forces at rotors, rotor interactions with turbulence, pressure discontinuity sources (i.e. those due to local shocks) and mass displacement monopole sources termed thickness noise. The noise component due to harmonic airloads on the blades is referred to as rotational noise. Rotor interactions with turbulence is nonharmonic source and is referred to as broadband noise. The term blade slap is used to describe the rotor thumping noise and is commonly attributed to both pressure discontinuities produced at high tip Mach numbers and occasionally due to blade vortex interactions.

Several rotor noise prediction methods are available for predicting the rotational noise, thickness noise, and blade slap noise (ref. 1 thru ref. 3). Recently, methods for predicting the broadband noise of helicopters have become available (ref. 4). While these methods address the prediction of individual noise components, the problem of predicting the total helicopter noise for specified flight conditions (for example, proposed noise regulation flight conditions) has not been resolved. In this paper, methods for predicting rotational and broadband noise components are presented. Two independent methods for predicting the rotational noise components have been developed. The short method uses the rotor airloads concentrated at a single span station and an airloading harmonic exponent. The long method utilizes spanwise, chordwise, and azimuthwise airload distribution for calculating the rotor external noise. An attempt has been made to predict the total external noise spectrum of the helicopter by combining the rotational and broadband noise component for both main and tail rotors. The correlations for several flight conditions are presented which indicate the accuracy of the noise prediction procedure for a given flight condition.

New concepts for predicting the rotor rotational and broadband noise components are not being proposed in this paper. The primary objective is, however, to address the prediction of the total helicopter noise spectrum. In this process, the simultaneous aerodynamic and acoustical helicopter flight test data have been used. The correlations carried out for several flight conditions point out the need for improving the correlation through additional analyses.

NOISE GENERATING MECHANISMS

Lighthill has proposed aerodynamic mechanisms for the generation of sound (ref. 5). These mechanisms relate to fluctuations of mass, momentum, and momentum flux rates which can be related to the mathematical concepts of source, dipole, and quadrupole, respectively.

The rotational noise component from main and tail rotors is harmonic in nature and important in the low- to mid-frequency range. However, the broadband noise of main and tail rotors is nonharmonic and is due to external or rotor-generated turbulence at the rotor blades.

Blade slap, the most characteristic helicopter noise component, is produced during certain flight conditions and is a rotor thumping sound which is impulsive in nature and important in the mid- to high-frequency range. The operating conditions where blade slap is dominant are partial power descent and high-speed flight. Considerable research has been conducted in identifying the noise-generating mechanism of blade slap. Tangler (ref. 6) has shown a shocklike pressure discontinuity generated during blade vortex interactions and also during high transonic Mach number at the tip. Farassat (ref. 2) has shown the blade slap to be generated by a thickness source, and Schmitz and Boxwell (ref. 7) have found both the thickness- and shock-related peaks in their in-flight measurements of helicopter noise at high speeds.

THEORETICAL FORMULATION

In the present paper, the methodology for predicting the rotational and broadband noise components of the helicopter is presented. The calculation of blade slap or thickness noise contributions has not been attempted.

Long Method of Rotational Noise Prediction

The propogation of sound in a uniform medium is governed by the equation,

$$\frac{\partial^2 \rho}{\partial t^2} - c^2 \nabla^2 \rho = \frac{\partial Q}{\partial t} - \frac{\partial F_i}{\partial x_i} + \frac{\partial^2 T_{ij}}{\partial x_i \, x_j}$$

where,

ρ = perturbation density
c = velocity of sound in the medium
Q = mass per unit volume, per unit time introduced at $\vec{x}$ at time t,
F_i = the fluctuating external force field per unit volume of the medium
T_{ij} = the applied fluctuating stress tensor
x_i = position vector components

For rotational noise calculation, only the $\frac{\partial F_i}{\partial x_i}$ terms on the right-hand side need be considered. In the long method, the spanwise, chordwise, and azimuthwise airload distribution is considered. The rotor disc is divided into radial and azimuthal segments. Each segment is treated as a rotating source, and the doppler correction factors are introduced to account for any translational source motions.

Short Method of Rotational Noise Prediction

Again, the $\partial F_i/\partial x_i$ terms of the acoustical equations are considered. In the short method, the airloads are assumed concentrated at a single spanwise location and an air-loading harmonic exponent is used. This prediction procedure is valid only in far field (observer-to-hub location greater than 5-6 rotor diameters). The theoretical formulation is similar to the procedure in section 11.3 of Morse and Ingard (ref. 8).

Referring to figure 1 consider the coordinate system based on the helicopter. The origin of the coordinate frame coincides with hub center. The axis vertically downward is Z, X is the axis in longitudinal direction and perpendicular to the Z axis, and the Y axis is perpendicular to both X and Z. Let the location of the source (thrust) be a distance r_1 from the hub center. If the reference point is at azimuth Ψ_1, as measured from negative X axis, the source coordinates are $(-r_1\cos\Psi_1, r_1\sin\Psi_1, 0)$. The observer is at a distance r from the hub, and the observer coordinates are $(-r\sin\sigma\cos\Psi, r\sin\sigma\sin\Psi, r\cos\sigma)$.

The expression for the total sound pressure field can be written down as

$$\rho = \frac{1}{4\pi r} \sum_{n=1}^{\infty} (2nk_1\alpha_n) \left\{ \sum_{\ell=0}^{\infty} \left(\beta_\ell F_t \cos\sigma + \delta_\ell \frac{nB-\ell}{nBM} F_d\right) \right.$$

$$\times J_{nB-\ell}(nBM\sin\sigma) \sin\left[nk_1(r-ct)+(nB-\ell)(\Psi+\pi/2)\right]$$

$$+ \sum_{\ell=0}^{\infty} \left(\beta_\ell F_t \cos\sigma + \delta_\ell \frac{nB+\ell}{nBM} F_d\right) \times J_{nB+\ell}(nBM\sin\sigma)$$

$$\left. \times \sin\left[nk_1(r-ct) + (nB+\ell)(\Psi+\pi/2)\right] \right\}$$

where,

n = n^{th} acoustical harmonic

k_1 = wave number = $\frac{\omega_1}{c} = \frac{B\Omega}{c}$

c = speed of sound

B = number of blades

F_t = thrust force

F_d = drag force

β_ℓ = ℓ^{th} harmonic of thrust force for nonuniform flow

δ_ℓ = ℓ^{th} harmonic of drag force for nonuniform flow

α_n = n^{th} harmonic coefficient for fourier expansion of the forces

$J_n(\ )$ = the Bessel Functions

M = rotational Mach number defined at the effective radius where the thrust and drag force is located

If a helicopter carrying such a rotor moves through the air with velocity components (V_1, V_2, V_3), the following Doppler corrections can be made.

Let $s = \vec{r}-\vec{r}_1$

where,

$\vec{r}$ = observer position vector

$\vec{r}_1$ = source position vector

then

$$M_r = \sum_{i=1}^{3} \frac{V_i(\vec{r}-\vec{r}_1)_i}{cs}$$

and

$$C_1 = \sqrt{M_r^{\,2} + (1-M^2)}$$

$$C_2 = \frac{M_r + \sqrt{M_r^2 + (1-M^2)}}{(1-M^2)}$$

The distance r in the acoustical equation is modified to C_1r, and the argument of the Bessel function, nBMsinσ, is modified to C_2nBMsinσ.

Broadband Noise Prediction Using Similarity Scaling

For prediction of broadband noise, an empirical technique using similarity scaling of measured data has been developed. The data base is obtained from model outdoor stand tests by Scheiman et al. (ref. 9) of NASA-Langley Research Center (LRC). These tests were conducted at zero lift conditions at hover mode. The model was a two-bladed rotor, 3.05 m (10 ft) in diameter, and the blade section was NACA 0012 of 0.424 m (16.7 in.) chord. The similarity laws derived include observer distance, rotor size, Mach number, and sound directivity parameter.

AH-1G FLIGHT TESTS

To gain experimental insight into helicopter rotor aerodynamic, dynamic, and acoustic environments, the Operational Loads Survey (OLS) flight test program was conducted on a Model AH-1G Cobra helicopter. The flight test was conducted in 1975 at Bell Helicopter Textron under U.S. Army sponsorship (ref. 10).

For the purpose of the OLS flight test, two AH-1G main rotor blades were modified and instrumented with surface-flow sensors, absolute pressure transducers, hot-wire sensors, semiconductor accelerometers, and strain gauges. The test helicopter with the instrumented rotor installed is shown in figure 2.

The aerodynamic instrumentation consisted of absolute pressure transducers and surface-flow and hot-wire sensors. These measurements were taken at five spanwise stations. The absolute pressure transducers measure static pressures and are located on upper and lower airfoil surfaces from leading to trailing edge. The surface-flow sensors consist of differential pressure transducers. Wire sensors are also located at five radial stations to measure leading-edge stagnation.

Acoustical instrumentation consisted of five microphones mounted on the helicopter and a ground-based microphone system to record flyover and flyby noise.

The flight program was made up of both low and high gross weight airspeed sweeps, high 'g' maneuvers, descents, and nap-of-the-earth (NOE) maneuvers.

NOISE PREDICTION CORRELATIONS

For the purpose of noise prediction correlation, the OLS flight program provides both the acoustical and aerodynamic data. The acoustical data for several critical conditions have been used for correlations. In addition, the chordwise, spanwise, and azimuthwise static pressure distributions for high-speed flight conditions have been used to provide the aerodynamic inputs to the long method for the rotational noise prediction program.

The correlations have been attempted for three important flight conditions, i.e. low-speed flight, high-speed level flight, and low-speed partial power descent conditions for Bell Model AH-1G. Additional correlations have been conducted for tie-down hover in ground effect for a Bell-manufactured medium helicopter.

The correlations are shown in figures 3 through 7. Figure 3 is the correlation for the long method of rotational noise prediction. The spanwise and azimuthwise airloads from the Operational Loads Survey flight program were used to calculate main rotor noise at the ground microphone. Since tail rotor airloads information was unavailable, tail rotor noise was calculated using the short method and was added to the predicted main rotor noise. The overall spectrum compares favorably with the flight test noise spectrum. There is as much as 13 to 15 decibels deviation at moderate frequencies. This deviation could be explained by the fact that this condition corresponds to high-speed level flight (84.9 m/s or 165 knots) where blade slap contributes to the total helicopter noise, and also by the fact that a mechanism for blade slap is not included in the prediction procedure.

Figure 4 depicts the same flight condition, although the short method of rotational noise prediction has been used. An air-loading harmonic exponent of 2.0 was also used.

Low-speed cruise flight condition is shown in figure 5. The flight corresponds to 30.9 m/s (60 knots) level flight. Deviations in the mid-frequency range cannot be explained logically.

Figure 6 is the correlation for the 33.4 m/s (65 knots), 2.03 m/s (400 ft/min) partial power descent flight condition. Deviations in the mid-frequency region appear; however, there are more significant deviations in the high-frequency region. The high-frequency deviations could be explained in terms of blade slap being produced due to blade vortex interactions in a partial power descent flight condition.

Correlations for tie-down hover conditions shown in figure 7 have been carried out in terms of dBA.

CONCLUSIONS

The correlations are carried out for four important flight conditions - low-speed cruise, high-speed cruise, low-speed partial power descent, and hover. For the same flight condition, the short method correlates as well as or better than the long method. This could be explained by numerical errors associated with approximating the rotor disc into discrete segments, and also by the fact that high-frequency airloads are hard to define and extract from the flight data.

The correlations at high-speed and low-speed partial power descent conditions are poor. Under these conditions, high-speed blade slap and low-speed blade vortex interactions are present. Adding the blade slap contributions to the predicted noise should improve the correlation.

The correlations at low-speed cruise and hover is fair, which might indicate that the noise sources have been correctly identified and correctly analyzed.

RECOMMENDATIONS

The present state-of-the-art of the noise prediction technology is poor. For the correlations attempted, deviations as much as 12 dBA were present. Some of the deviations could be reduced by adding the blade slap and main rotor wake tail rotor interaction noise components to the predicted noise. The noise sources for high-speed and low-speed blade slap are presently being researched amd analysis procedures will soon be available. It is recommended that workable analysis procedures for calculating the blade slap and main rotor wake tail rotor interaction noise components be developed.

The next recommendation deals with the subject of extensive validation of the external noise prediction procedures. The total noise of helicopters is composed of several components. When comparing predicted and flight-measured noise spectrums, it is possible to draw wrong conclusions regarding the degree of correlation. The errors in predicting a one source noise component might be compensated by errors in predicting some other source. It is therefore recommended that noise prediction procedures be extensively correlated for several conditions and for several helicopter types before being used in a design iteration cycle.

REFERENCES

1. Lowson, M. V.; and Ollerhead, J. B.: Studies of Helicopter Noise, USAAVLABS TR 68-60, 1969.

2. Farassat, F.; Pegg, R. J.; and Hilton, D. A.: Thickness Noise of Helicopter Rotors at High Tip Speeds, AIAA 2nd Aero-Acoustics Conference, Hampton, Virginia, March 1975.

3. Schmitz, F. H.; and Yu, Y. H.: Theoretical Modeling of High-Speed Helicopter Impulsive Noise. Paper No. 54, Third European Rotorcraft and Powered Lift Aircraft, France, Sept. 1977.

4. George, A. R.; and Kim, Y. N.: High-Frequency Broadband Rotor Noise, AIAA Journal, Vol. 15, No. 4, pp. 538-545, April 1977.

5. Lighthill, M. J.: On Sound Generated Aerodynamically I, General Theory, Proc. Roy. Soc., A211, 1952, pp. 564-587.

6. Tangler, J. L.: Schlieren and Noise Studies of Rotors in Forward Flight, Preprint No. 77.33-05, 33rd Annual National Forum of the American Helicopter Society, May 1977.

7. Schmitz, F. H.; and Boxwell, D. A.: In-Flight Far Field Measurement of Helicopter Impulsive Noise, Journal of the American Helicopter Society, Vol. 21, No. 4, October 1976.

8. Morse, P. M.; and Ingard, K.V.: Theoretical Acoustics, McGraw Hill, New York, 1968.

9. Scheiman, J.; Hilton, D. A.; and Shivers, J. P.: Acoustical Measurements of the Vortex Noise for a Rotating Blade Operating With and Without Its Shed Wake Blown Downstream, NASA TN D-6364, August 1971.

10. Shockey, G. A.; Williamson, J. W.; and Cox, C. R.: AH-1G Helicopter Aerodynamic and Strctural Load Survey, USAAMRDL-TR-76-39, Bell Helicopter Textron, February 1977.

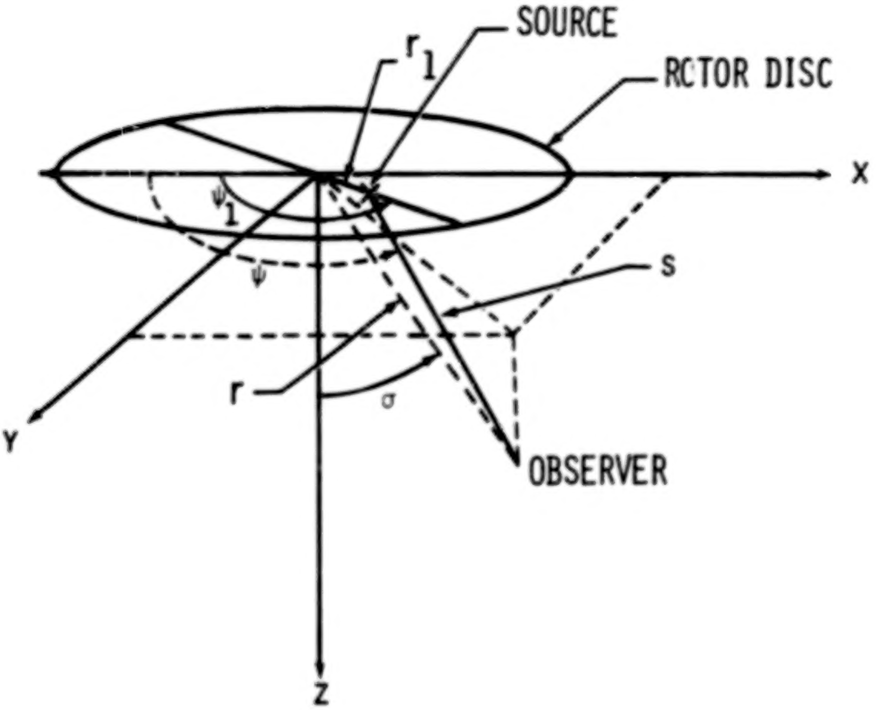
SOURCE
r_1
RCTOR DISC
X
ψ_1
ψ
S
r
σ
Y
OBSERVER
Z

Figure 1.- Theoretical formulation.

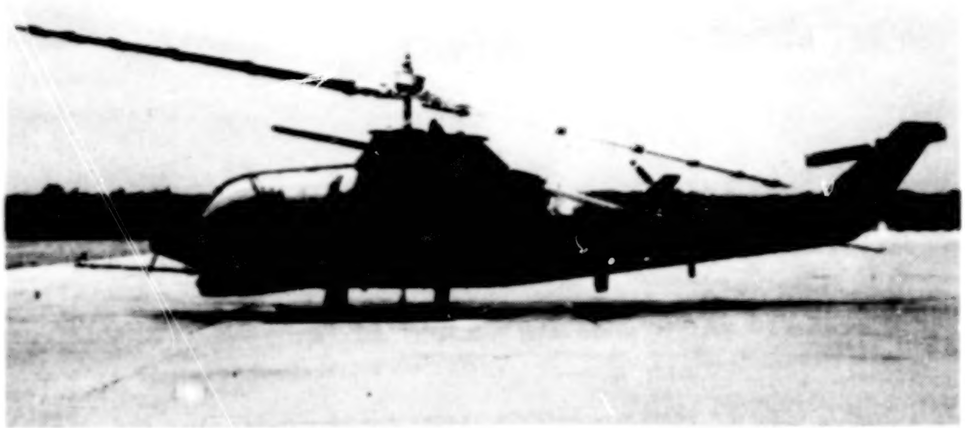

Figure 2.- AH-1G for Operational Loads Survey (OLS) flight test.

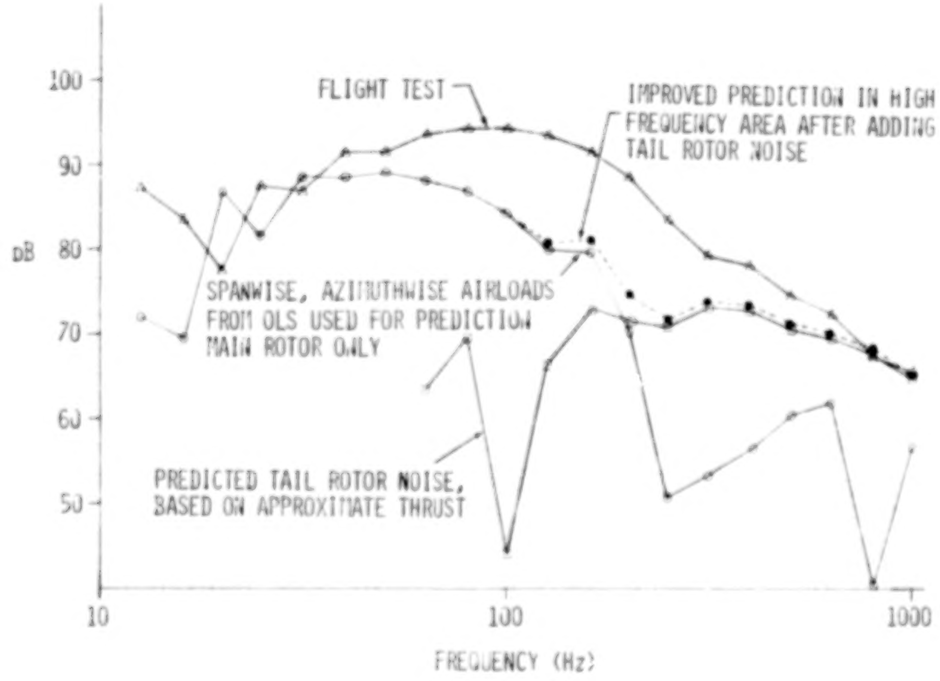

Figure 3.- Third octave sound pressure level. Correlation of long rotational noise prediction method. AH-1G flight at 84.9 m/s (165 knots).

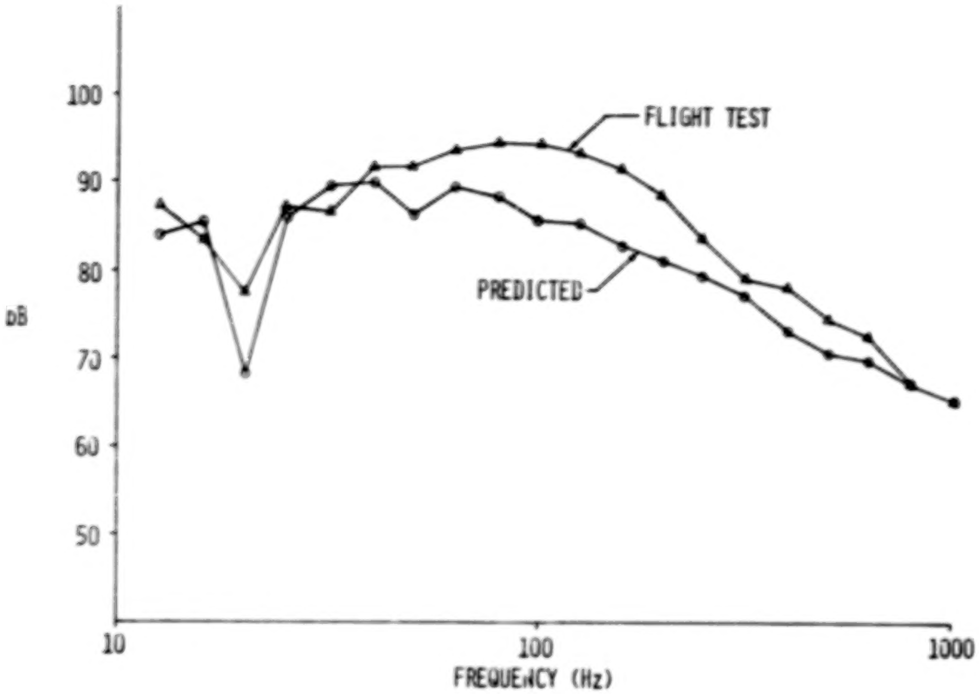

Figure 4.- Third octave sound pressure level. Correlation of short rotational noise predictions method. AH-1G flight at 84.9 m/s (165 knots).

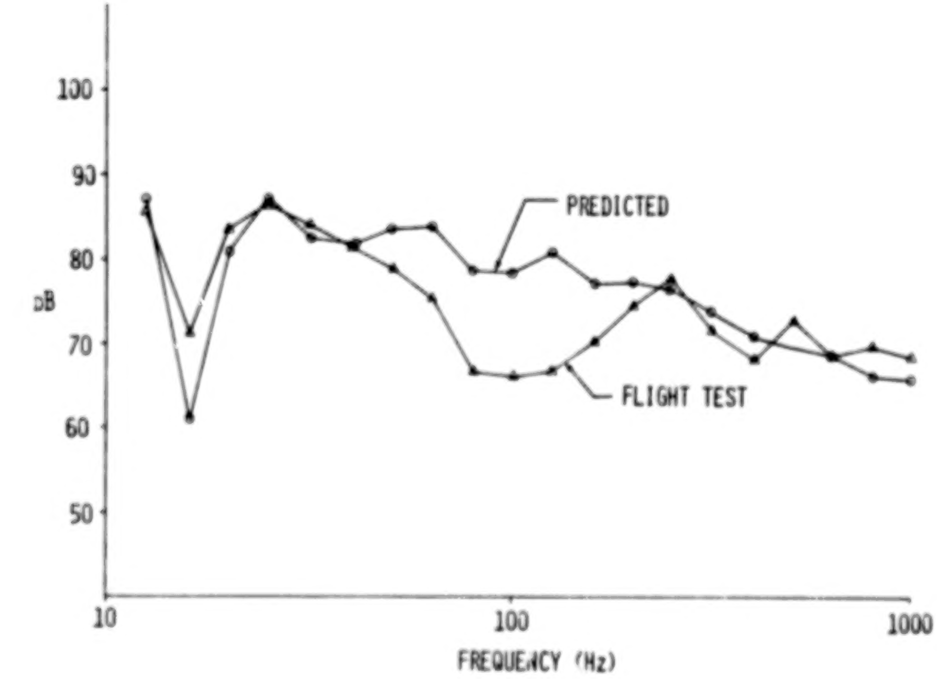

Figure 5.- Third octave sound pressure level. AH-1G flight at 30.9 m/s (60 knots).

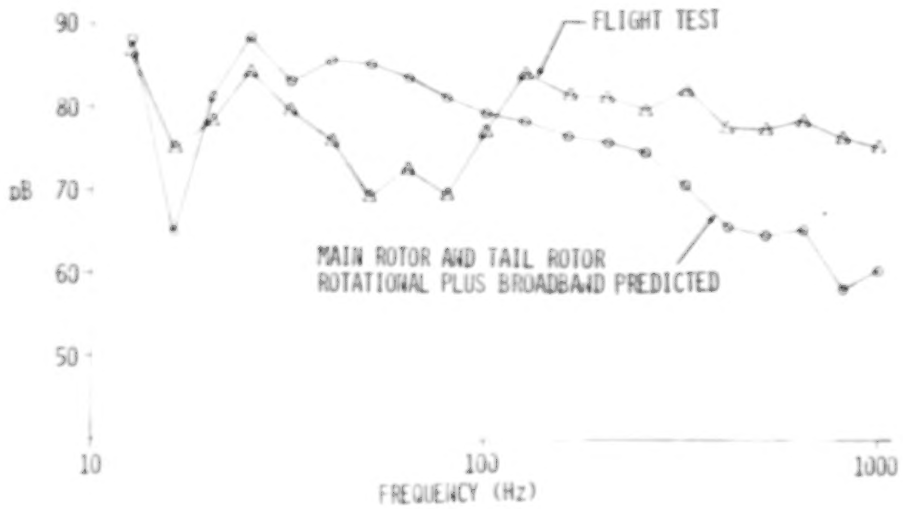

Figure 6.- Third octave sound pressure level. AH-1G at 33.4 m/s (65 knots). Partial power descent at 2.03 m/s (400 ft/min).

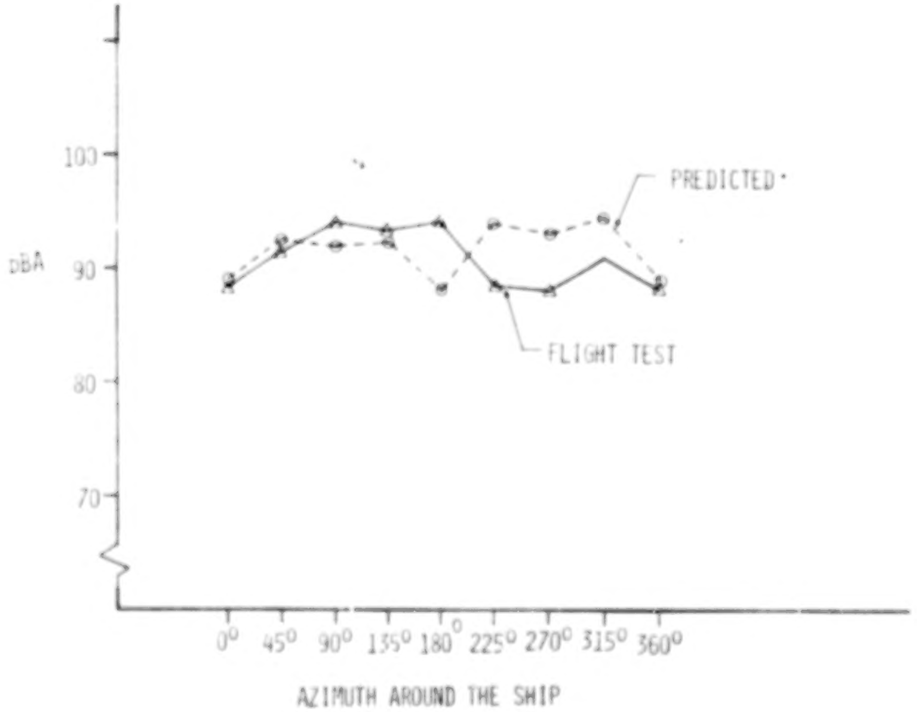

Figure 7.- Correlation of dBA for Bell medium helicopter in tie-down hover. Microphone at 61 m (200 ft) skid height 6.1 m (20 ft).

Blank Page

14

FULL-SCALE TESTING OF AN OGEE TIP ROTOR

Wayne R. Mantay
Structures Laboratory, U.S. Army R&T Laboratories (AVRADCOM)

Richard L. Campbell and Phillip A. Shidler
NASA Langley Research Center

SUMMARY

Full-scale tests were utilized to investigate the effect of the Ogee tip on helicopter rotor acoustics, performance, and loads. Two facilities were used for this study: the Langley whirl tower and a UH-1H helicopter. The test matrix for hover on the whirl tower involved thrust values from 0 to 44 480 N (10 000 lb) at several tip Mach numbers for both standard and Ogee rotors. The full-scale testing on the UH-1H encompassed the major portion of the flight envelope for that aircraft. Both near-field acoustic measurements and far-field flyover data were obtained for both the Ogee and standard rotors. Data analysis of the whirl-tower test shows that the Ogee tip does significantly diffuse the tip vortex while providing some improvement in hover performance at low and moderate thrust coefficients. Flight testing of both rotors indicates that the strong impulsive noise signature of the standard rotor can be reduced with the Ogee rotor. Analysis of the spectra indicates a reduction in energy in the 250 Hz and 1000 Hz range for the Ogee rotor. Forward-flight performance was significantly improved with the Ogee configuration for a large number of flight conditions. Further, rotor control loads were reduced through use of this advanced-tip rotor.

INTRODUCTION

The present day helicopter's usefulness and effectiveness is reduced by the high noise and vibration levels it generates. The increasing use of helicopters for military and commercial purposes necessitates a reduction in vibration as well as internal and external noise levels for reduced detection and community and passenger acceptance.

The interaction of a rotor blade tip vortex with the following blades is a major cause of increased helicopter acoustic signature, vibration, and loads (ref. 1). Numerous methods of reducing this vortex-blade interaction have been investigated in the past. One method, tip-shape modification, has shown some promise in reducing the severity of this phenomenon. One of the more promising tip configurations is the Ogee planform (fig. 1). Previous small-scale smoke studies indicated that this shape would diffuse the rotor blade tip vortex, and following blades might thus encounter a weaker vortex field with accompanying benefits. The Ogee tip shape (ref. 1) was evaluated by a series of analytical and experimental programs (refs. 2-5). Based on the encouraging results of the vortex flow data, pressure data, and performance information from these preliminary studies, full-scale testing of this tip shape was initiated.

Tests were conducted to investigate the effect of the Ogee tip on full-scale rotor acoustics, performance, and loads. The Langley whirl tower was utilized for hover flight measurements, and an extensively instrumented UH-1H provided forward-flight data.

SYMBOLS

Values are given in both S.I. and U.S. Customary Units. The measurements and calculations were made in U.S. Customary Units.

a	local speed of sound, m/sec
C_L	rotor lift coefficient, $\frac{GW}{\rho\pi R^2(\Omega R)^2}$
C_P	engine power coefficient, $\frac{P}{\rho\pi R^2(\Omega R)^3}$
C_Q	rotor torque coefficient, $\frac{Q}{\rho\pi R^3(\Omega R)^2}$
C_T	rotor thrust coefficient, $\frac{T}{\rho\pi R^2(\Omega R)^2}$
GW	helicopter gross weight, N (lb)
M_{TIP}	rotor tip Mach number, $\frac{\Omega R}{a}$
n	rotor load factor, g
OASPL	overall sound pressure level, dB
P	engine power, N-m/sec
Q	rotor torque, N-m
R	rotor radius, m (ft)
R/D	rate of descent, m/sec (ft/min)
T	rotor thrust, N
V_t	true airspeed, knots
z	height of aircraft above array center microphone, m

ρ local air mass density, kg/m^3

Ω rotor rotational speed, rad/sec

Superscript

$\overline{}$ mean value

Subscript

o standard sea level condition

METHOD OF APPROACH

A systematic and controlled investigation of the effect of an advanced tip shape on rotor acoustics, loads, and performance was conducted on an Ogee tip rotor and a standard UH-1H square-tip rotor. Test facilities used for this study included the NASA-Langley whirl tower, an instrumented UH-1H helicopter, and the acoustic range at NASA Wallops Flight Center. Both near- and far-field acoustic data were obtained, as well as rotor performance, loads data, and wake flow visualization.

Description of Test Facilities and Hardware

Whirl tower.- The Langley helicopter rotor test facility (hereinafter referred to as the Langley whirl tower) has the capability of testing rotors through a complete hover envelope of thrust and rotational speed. The characteristics of this facility are shown in figure 2 and table I. The tower was used to verify the structural integrity of the Ogee design as well as provide performance, acoustics, and flow visualization.

Test helicopter.- The test vehicle for this investigation was a UH-1H helicopter. As shown in figure 3, the vehicle was equipped with electronic data systems, including an in-flight acoustic measurement system. Nominal test weights for the UH-1H were 33 805 N (7600 lb) and 38 253 N (8600 lb). The aircraft was flown with a crew of four, resulting in a nominal longitudinal center of gravity location 17.8 cm (7 in.) aft of the main rotor hub.

Rotor systems.- The geometric characteristics of both standard and Ogee rotors used in the tests are given in table II. Two sets of each rotor were used, one set of each for the tower investigation and one set of each for flight testing on the same test helicopter. Figure 4 shows the planform of both the standard rotor and Ogee tip rotor blades.

NASA Wallops Flight Center acoustic range.- An acoustic array was used to measure far-field noise from the helicopter. This array was located at the approach end of runway 10. Radar was used to track the vehicle over the approach to the array.

Description of Instrumentation

Whirl-tower data acquisition.- The parameters directly measured by the whirl-tower data system are listed in table III. Performance data as well as blade structural data were monitored in real time and recorded on FM tape. Acoustic data were obtained through an electronic system identical to that used in the Wallops Flight Center acoustic instrumentation, to be discussed later in this paper, with one microphone placed 76.2 m (250 ft) from the center of the tower on a ground board.

Helicopter instrumentation.- The UH-1H helicopter utilized three unique data systems. One onboard data package recorded and telemetered select helicopter parameters which included vehicle aerodynamic state, attitudes, powertrain data, rotor structural information, and vibratory loads. Table IV lists these parameters and the measurement techniques used. A second onboard data system digitally sampled tip pressures, strain-gage information, and rotor azimuth on the Ogee rotor. The electronics of this system were imbedded in the Ogee tip and enabled sampling rates as high as 2000 Hz to be obtained.

The in-flight acoustic measurement system (IFAMS) measured and recorded the near-field pressure signature of the test helicopter in various flight conditions. The system consists of two externally mounted microphones. The location of these is shown on figure 3. The condenser microphones, fitted with a streamlined nose section, could be adjusted ±10 degrees from centerline into the resultant local airflow. The microphone diaphragms were located 190 cm forward of the main rotor teeter axis and 304 cm beneath it. The microphone booms extended 2.7 m from the centerline of the aircraft. The acoustic data from the IFAMS were recorded by two independent systems with a common 1 KHz time code.

Acoustic array instrumentation.- A schematic diagram of the noise data-acquisition system for the flyover tests is shown in figure 5. During the test program, the microphones were fitted with wind screens and positioned 1.2 m above ground surface, oriented for grazing incidence. The condenser microphones in this array had a frequency response flat to within ±3 dB over the frequency range 10 Hz to 20 000 Hz. The signal outputs from all microphones were recorded at each of the mobile data-acquisition stations on FM tape at 76.2 cm/sec using a center frequency of 54 KHz. All recorded acoustic array data contained the same time code as the onboard data systems. The frequency of the complete acoustic system was flat to ±3 dB from 10 Hz to 10 000 Hz.

TEST PROCEDURE

Evaluation of the Ogee tip shape required a systematic and controlled test environment for the measurement of acoustic signature, rotor loads, and performance. The goal of the whirl-tower tests was to explore the hover envelope of both standard and Ogee rotors. The helicopter flight tests explored those conditions which created impulsive noise through blade-vortex interactions or compressibility. In both types of testing, simultaneous measurements of rotor loads and performance were made along with acoustic data acquisition.

CONTENTS

Part I

PREFACE . . . . iii 1/A6

REGULATIONS

1. HELICOPTER EXTERNAL NOISE REQUIREMENTS - FAA PERSPECTIVE 1 1/A8
Charles R. Foster

2. HELICOPTER NOISE REGULATIONS: AN INDUSTRY PERSPECTIVE 17 1/B10
R. A. Wagner

3. NOISE REQUIREMENTS FROM A MILITARY POINT OF VIEW 33 1/C12
Charles C. Crawford, Jr.

4. THE IMPACT OF URBAN OPERATIONS ON HELICOPTER NOISE REQUIREMENTS . . . 45 1/D10
Stanley R. Spector

ROTOR NOISE

5. PREDICTION AND REDUCTION OF ROTOR BROADBAND NOISE 61 1/E12
Richard E. Hayden and Krishna S. Aravamudan

6. THEORETICAL MODELS OF HELICOPTER ROTOR NOISE 89 1/G12
D. L. Hawkings

7. NOISE DUE TO ROTOR-TURBULENCE INTERACTION 109 2/B6
R. K. Amiet

8. THEORY ON ACOUSTIC SOURCES 127 2/C10
S. E. Wright

9. POTENTIAL ACOUSTIC BENEFITS OF CIRCULATION CONTROL ROTOR 149 2/E5
Robert M. Williams and Ian C. Cheeseman

10. HELICOPTER NOISE RESEARCH AT THE LANGLEY V/STOL TUNNEL 181 2/G9
Danny R. Hoad and George C. Greene

11. EXPLORATORY WIND-TUNNEL INVESTIGATION OF THE EFFECT OF THE MAIN ROTOR WAKE ON TAIL ROTOR NOISE 205 3/B7
Robert J. Pegg and Phillip A. Shidler

12. WIND TUNNEL INVESTIGATIONS OF MODEL ROTOR NOISE AT LOW TIP SPEEDS . . . 221 3/C9
K. S. Aravamudan, A. Lee, and W. L. Harris

13. HELICOPTER EXTERNAL NOISE PREDICTION AND CORRELATION WITH FLIGHT TEST 263 3/F11
Bharat P. Gupta

14. FULL-SCALE TESTING OF AN OGEE TIP ROTOR 277 3/G11
Wayne R. Mantay, Richard L. Campbell, and Phillip A. Shidler

15. HOVERING IMPULSIVE NOISE - SOME MEASURED AND CALCULATED RESULTS 309 4/C4
D. A. Boxwell, Y. H. Yu, and F. H. Schmitz

16. IMPROVED METHODS FOR CALCULATING THE THICKNESS NOISE 323 4/B4
Yoshiya Nakamura and Akira Azuma

17. THE IMPORTANCE OF QUADRUPOLE SOURCES IN PREDICTION OF TRANSONIC TIP SPEED PROPELLER NOISE 339 4/E6
Donald B. Hanson and Martin R. Fink

18. BOUNDS ON THICKNESS AND LOADING NOISE OF ROTATING BLADES AND THE FAVORABLE EFFECTS OF BLADE SWEEP ON NOISE REDUCTION 373 4/G12
F. Farassat, Paul A. Nystrom, and Thomas J. Brown

19. A STUDY OF THE NOISE RADIATION FROM FOUR HELICOPTER ROTOR BLADES . . . 387 5/A14
Albert Lee and Marianne Masher

Whirl-tower test procedure.- The test matrix for hover on the whirl tower involved thrust values from 0 to 44 480 N (10,000 lb) at several tip Mach numbers. Table V shows the test conditions for both rotors on the whirl tower. For each rotor tested, the blades were tracked throughout the rpm range to be tested using a strobe-television system. The tracked and balanced blades were then subjected to the nominal conditions cited in table V. Performance and acoustic data were taken at each test point after the rotor environment became stable. The points were repeated several times. Wake flow visualization was achieved through the smoke rake shown in figure 2. High-speed movies were taken of the smoke flow entrained by the rotor wake. In hover performance cases, the average ambient wind was less than 2 knots and the tip Mach number was achieved within 1 percent.

Flight-test procedure.- The flight testing of both standard and Ogee rotors on the UH-1H helicopter encompassed the major portions of the flight envelope for that aircraft. Those flight conditions which generated significant impulsive noise were of prime interest, but numerous other flight conditions were also explored. Table VI shows the flight conditions for both rotors where all onboard data systems were acquiring data. Table VII indicates the flight conditions over the acoustic array at Wallops Flight Center. During the acoustic-array data acquisition, the aircraft was flown only at its lower nominal gross weight of 33 805 N (7600 lb). The flight-test conditions outlined in table VI contained at least 30 seconds of time-correlated data from all data systems. The conditions in table VII for the acoustic array flyovers involved positioning the aircraft over the array and tracking the position with radar. The majority of the level flights over the acoustic array were done at 30 and 61 m altitude. Descending flights were commenced approximately 2100 m from the threshold of the runway and continued approximately 300 m past the threshold with a flight path to put the helicopter at a nominal altitude of 122 m over the center of the microphone array. In general, at least two runs at each airspeed and rate of descent were flown during these flyover tests. Acoustic-array data were acquired during the entire approach and flyover for each run. Onboard data were taken during a 30-second period which included the time interval when the aircraft was directly over the array.

DISCUSSION OF RESULTS

The results of the full-scale rotor tests described above are presented in three segments. Acoustic data are shown in figures 6 to 12. Loads measurements are presented in figure 13, while performance information in hover and forward flight is contained in figures 14 and 15.

Acoustic Data

Hover acoustic data.- The overall sound pressure levels from the whirl-tower hover tests are shown in figure 6. Since blade-vortex interaction is not achieved in hover, these overall sound pressure levels represent rotational and broadband noise. The rotational noise from these rotors in hover has the expected trends with thrust and tip Mach number. It should be noted that the lower tip loading of the Ogee rotor results in a reduction of rotational noise level, as does the thin profile at the Ogee rotor's tip. Figure 6 also indicates a greater sensitivity of Ogee rotational noise to thrust coefficient. This may result in a merging or crossover of OASPL for the two rotors at very high thrust coefficients although this point was not reached in the present test matrix. Figure 7 shows a segment from high-speed smoke movies of both rotors' wake. The operating conditions on the whirl tower are nominal, and, as shown, develop tip vortices which exhibit characteristics similar to those seen from small-scale studies (ref. 3). Specifically, the Ogee tip vortex has a larger core and is less well defined in the lower wake. This vortex diffusion will be shown to affect the impulsive noise.

Near-field rotor noise.- The noise perceived in a helicopter cabin and measured by external microphones is generated by several sources. Rotational noise and tail-rotor noise are certainly contributors to the overall acoustic energy; however, impulsive noise in the near field below the rotor is dominated by blade-vortex interaction. The directivity of this type of impulsive noise, as well as an explanation of its aerodynamic causes, is given in several references (refs. 6 and 7).

The test matrix for quantification of impulsive noise has already been described. From the onboard microphone data, peak levels of near-field impulsive noise below each rotor were found at conditions indicated in figure 8 for the moderate gross weight cases. The blade-vortex interaction impulsive-noise conditions for the standard rotor were moved to higher rates of descent for a given airspeed through the use of the Ogee rotor. This phenomenon may be due to the diffuse Ogee tip vortex requiring a closer proximity to the succeeding blades to generate impulsive noise. It should be noted that the maximum intensity of the Ogee impulsive noise below the rotor is significantly lower than the maximum noise of the standard rotor for the nominal 33 805 N case. At higher gross weights (38 253 N) the maximum near-field levels are similar for the two rotors although the contour for the Ogee continues to occur at higher rates of descent than the standard. The near-field acoustic data discussed in this section will be taken from these areas of maximum impulsive noise for both rotors at both ranges of gross weight.

Time histories of data from the advancing-blade microphone are shown in figure 9 for both rotors during rates of descent at moderate gross weights. The conditions chosen are those which were observed to bracket the strongest impulsive noise for both rotors. The strongest vortex-blade interaction occurs on the advancing side of the disk (ref. 7) and hence the advancing-side microphone data best illustrate the changes in such phenomena. The Ogee rotor significantly reduces this type of near-field impulsive noise as well as the rotational and tail-rotor noise in some rates of descent. (See fig. 9(a).) The rotational noise difference has been addressed in the last section. The tail-rotor noise is a function of power required and, as will be shown, significant reductions in tail-rotor power for the Ogee main rotor may be realized for some gross weights and flight conditions. Tail-rotor interactions with the main-rotor wake also cause changes in the acoustic signature of the tail rotor which are dependent on the wake's strength and trajectory.

For the higher gross-weight conditions, figures 10(a) and 10(b) bracket the strongest impulsive noise for both rotors. Figure 10(a) shows the loudest near-field impulsive level for the standard rotor while figure 10(b) indicates the Ogee trend through its loudest near-field condition. For both airspeeds shown, the Ogee peak impulsive noise occurs at a significantly higher rate of descent than the standard rotor. It should be noted that all near-field data in this study are uncorrected for atmospheric density effects. A relation which normalizes acoustic pressure to a given atmospheric density (ref. 6, eq. B-1) can be applied to the near-field data. The difference between the acoustic pressure observed at altitude and that normalized to sea level standard conditions never exceeded 2 dB for each rotor. Most data points never varied more than 0.5 dB from the normalized value. Since both rotors were flown at the same nominal range of density altitudes for this study, differences between standard and Ogee impulsive-noise levels due to variations in density are not significant.

Near-field impulsive noise for both standard and Ogee rotors contain energy souces at many harmonics. Spectrum plots of the near-field data were made using a digital analyzer operating on 2048 points from 0 to 1000 Hz. Figure 11(a) contains the spectra corresponding to the flight conditions and data of figure 9(a). The most noted changes between rotors in harmonic content occur at 250 and 1000 Hz. The absence of Ogee acoustic energy at these frequencies is due to the reduction afforded in impulsive noise by the Ogee rotor at this flight condition.

The flight condition and acoustic time histories of figure 9(b) indicated a 5.1 dB reduction in near-field impulsive noise with the Ogee tip. The corresponding spectra, figure 11(b), show that this reduction occurs mainly at 250 Hz and 1000 Hz. When the near-field impulsive noise of the two rotors are within 1 dB, such as shown in figure 9(c), the corresponding spectra (fig. 11(c)) indicate that any acoustic differences between rotors occur in the high harmonics.

Blade-to-blade acoustic variability, shown by the standard-rotor pressure time histories, has been observed in previous research efforts such as reference 6. The spectra just discussed show this variability in the frequency domain. Specifically, the standard-rotor 1-per-rev predominant-impulsive spike contrasts with the Ogee 2-per-rev trace. The width of the individual spectrum pulses shows this phenomenon.

Far-field rotor noise.- Flight tests over an acoustic array result in data as shown in figures 12(a) to 12(e). These time histories show not only the acoustic phenomena illustrated in the near-field data, but also a significant addition to the acoustic energy, impulsive noise generated by compressibility. This very directional (ref. 6) noise is shown by area A in figures 12(a) and 12(b) for level flight. The aerodynamic cause of these negative pressure pulses is discussed in references 6, 7, and 8. The compressibility noise spikes (area A) for each rotor show differences which are magnified as aircraft speed increases. Figure 12(a) shows this for level flight where compressibility on the advancing blade is maximized. The thin profile of the Ogee rotor seems to decrease the magnitude of the compressibility impulsive noise. For a low-speed, nominally level flight condition, the difference in far-field noise between rotors is not as dramatic (fig. 12(b)) but is still significant.

During rates of descent, the blade-vortex interactions generate the signature in area B of figure 12(c) as well as the compressibility spikes (area A). The trend of the vortex-blade interaction far-field noise with rates of descent and rotor tip shape is similar to near-field trends discussed earlier. Specifically, figure 12(c) shows a case where near-field data (fig. 9(d)) indicated high standard-rotor impulsive noise whereas Ogee near-field impulsive noise at this condition was significantly less. The acoustic difference is also shown by the far-field data. Figure 12(d) presents a case where Ogee and standard near-field impulsive noise (fig. 9(c)) was shown to be nearly equal. However, this flight condition produced a measurable difference in far-field acoustic energy between the rotors with the Ogee rotor noise being less impulsive. At certain portions of the flight regime, notably, high rates of descent, the Ogee rotor can produce far-field blade-vortex impulsive noise that is comparable to the standard, although both levels are fairly low. Figure 12(e) shows the far-field noise for the two tip shapes during such a flight condition.

Rotor Loads

The character of a rotor's structural loads is very dependent on the local aerodynamic environment. The rotating pitch-link loads of both Ogee and standard rotors are shown in figures 13(a) to 13(d) for level flight. The rotors are matched in $\bar{C}_L$ within 3 percent. It may be noted in figure 13 that the trend of pitch-link load/density ratio with V_t for each rotor is similar. The significant control load differences between rotors at the low values of $\bar{C}_L$ are not as pronounced at higher $\bar{C}_L$ magnitudes (figs. 13(a) and 13(d), respectively). The reduction in peak-to-peak pitch-link loads for the Ogee rotor in level flight is probably due to a reduction in local tip chord.

Rotor Performance

Hover performance.- Hover-test data from the Langley whirl tower are shown in figures 14(a) to 14(c) for three tip Mach numbers. At low and moderate values of thrust coefficient, the performance of the Ogee rotor exceeds that of the standard. This is probably due to a substantial decrease in torque-weighted solidity for the Ogee tip while thrust-weighted solidity is only moderately decreased. At high thrust coefficient values, the performance of the two rotors merges. The value of thrust coefficient at which this occurs increases with decreasing tip Mach number. Specifically, the standard sea-level thrust values below which the Ogee is more efficient are 35 744 N (8036 lb) for 0.714 tip Mach number and 40 588 N (9125 lb) for a tip Mach number of 0.657. When both rotors were stalled in hover at low rpm (M_{TIP} = 0.535), the Ogee tip rotor performance line diverged from that of the standard rotor. The probable cause of this is the absence of sufficient thrust-weighted solidity needed at high thrust coefficients.

Forward flight.- Level-flight performance for standard and Ogee rotors as measured on the UH-1H test helicopter is indicated in figures 15(a) to 15(d). Thrust coefficients and tip Mach numbers were matched between rotors at a given airspeed with no greater than 3 percent difference in $\bar{C}_L$ between rotors in any figure. The trends of power coefficient with V_t for each rotor are similar at low and moderate speeds. At high speeds, the Ogee rotor C_p is more dependent on $\bar{C}_L$ than is the standard rotor.

The performance data for moderate thrust coefficients (figs. 15(a) and 15(b)), show a significant improvement in performance with the Ogee rotor throughout the speed range. This is probably due to profile power differences between the two rotors. At a $\bar{C}_L$ of 0.00361 (fig. 15(c)), the Ogee is more efficient at high speed, nearly coincident in C_p at cruise, and less efficient than the standard at low speeds. This low-speed trend continues at higher $\bar{C}_L$ (fig. 15(d)) and is probably due to the reduced thrust-weighted solidity of the Ogee rotor. The improvement in forward-flight performance, when it occurs, is due to a substantial decrease in torque-weighted solidity for the Ogee tip, while thrust-weighted solidity is only moderately decreased.

CONCLUDING REMARKS

Full-scale tests were utilized to investigate the effects of the Ogee tip on helicopter rotor acoustics, loads, and performance. A whirl tower and an instrumented UH-1H were used for this study. From the data analyzed to date, the Ogee tip changed the characteristics of the standard UH-1H rotor as follows:

1. The impulsive noise caused by vortex-blade interaction and compressibility was reduced for many flight conditions tested. Blade-vortex interaction noise was reduced by as much as 15 dB.

2. Rotational noise in hover was reduced throughout the thrust range tested on the whirl tower.

3. Oscillatory control loads were reduced by as much as 50 percent.

4. Forward-flight performance was significantly increased through use of the Ogee tip for some flight conditions.

5. Whirl-tower hover performance of the standard rotor was improved by the Ogee tip for low and moderate thrust coefficients. The performance advantage was dependent on tip Mach number and was eliminated at high values of thrust coefficient.

6. The tail-rotor noise was lower for many flight conditions with the Ogee tip main rotor.

REFERENCES

1. Ward, John F.; and Young, Warren H., Jr.: A Summary of Current Research in Rotor Unsteady Aerodynamics with Emphasis on Work at Langley Research Center. AGARD Conference Proceedings No. 111 on Aerodynamics of Rotary Wings, Fluid Dynamics Panel Specialists' Meeting (Marseilles, France), Sept. 13-15, 1972. pp. 10.1-10.20.

2. Balcerak, John C.; and Feller, Raymond F.: Vortex Modification by Mass Injection and by Tip Geometry Variation. USAAMRDL Tech. Rept. 73.45, 1973.

3. Landgrebe, Anton J.; and Bellinger, E. Dean: Experimental Investigation of Model Variable-Geometry and Ogee Tip Rotors. NASA CR-2275, 1974.

4. Balcerak, John C.; and Feller, Raymond F.: Effect of Sweep Angle on the Pressure Distributions and Effectiveness of the Ogee Tip in Diffusing a Line Vortex. NASA CR-132355, 1973.

5. Rorke, James B.; and Moffitt, Robert E.: Wind Tunnel Simulation of Full Scale Vortices. NASA CR-2180, 1973.

6. Schmitz, F. H.; and Boxwell, D. A.: In-Flight Far-Field Measurement of Helicopter Impulsive Noise. J. of Am. Helic. Soc., vol. 21, no. 4, Oct. 1976, pp. 2-16.

7. Tangler, James L.: Schlieren and Noise Studies of Rotor in Forward Flight. Preprint 77.33-05, 33rd Ann. Nat. Forum of the Am. Helic. Soc., (Washington, DC), May 1977.

8. Farassat, F.: Theory of Noise Generation from Moving Bodies with an Application to Helicopter Rotors. NASA TR R-451, 1975.

TABLE I.- WHIRL-TOWER CHARACTERISTICS

Rotor height from ground	12.8 m (42 ft)
Available power	1.119 MW (1500 hp)
Type of rotor drive	Electric motor

TABLE II.- TEST ROTOR CHARACTERISTICS

	STANDARD	OGEE
Type of hub	Teetering	Teetering
Rotor radius	7.315 m (24 ft)	7.315 m (24 ft)
Blade chord	53.34 cm (21 in.) Constant	53.34 cm (21 in.) Varying
Blade airfoil	0012	0012
Blade twist (root to tip)	-10.9^{0} Linear	-10^{0}
Precone angle	2.375^{0}	2.375^{0}
Number of blades	2	2
Rotor nominal rotational speed	324 rpm	324 rpm
Rotor solidity	0.04655	0.04412

TABLE III.- WHIRL-TOWER INSTRUMENTATION AND ACCURACIES

INSTRUMENTATION

Parameter	Sensor
Thrust	Load cells
Torque	Strain-gage bridge
Angular velocity	Photo counter
Thrust correction	Strain-gage bridge
Collective pitch angle	Potentiometer
Ambient temperature	Thermocouple
Static pressure	Barometer
Blade loads	Strain-gage bridges

ACCURACIES

Rotational speed, rpm	± Thrust coefficient accuracy	± Torque coefficient accuracy
324	3.5×10^{-5}	1.12×10^{-6}
291	4.35×10^{-5}	1.39×10^{-6}
240	6.39×10^{-5}	2.05×10^{-6}

TABLE IV.- FLIGHT DATA PARAMETERS

PARAMETER	SENSOR	DATA TYPE	ACCURACY*
● Three vehicle attitudes	Gyro	PCM	1.0%
● Three angular rates	Gyro	PCM	1.0%
● Three linear accelerations	Accelerometer	PCM	1.0%
● Four control inputs	Transducer	PCM	1.0%
● Angle of attack	Vane/potentiometer	PCM	1.0%
● Angle of sideslip	Vane/potentiometer	PCM	1.0%
● Main rotor blade angle	Control position transducer	PCM	1.0%
● Main rotor azimuth	Shaft encoder	PCM	1.0%
● Total temperature	Hot wire	PCM	1.0%
● Static/differential pressure	Pressure transducer	PCM	1.0%
● Main rotor speed	Magnetic counter	PCM	1.0%
● Engine torque pressure	Pressure transducer	PCM	1.0%
● Rate of climb	Inertial vertical speed indicator	PCM	1.0%
● Chordwise bending moment at stations 84 and 192 on main rotor blade	Strain gage	FM	2.5%
● Flapwise bending moment at stations 84 and 192 on main rotor blade	Strain gage	FM	2.5%
● Rotating pitch link load	Strain gage	FM	2.5%
● Time code	36-bit time code generator		
● Ogee tip joint bending moments	Strain gage	High-speed PCM	1.0%
● Ogee tip pressures	Flush-mounted pressure transducers	High-speed PCM	1.0%

*Full scale

TABLE V.- WHIRL-TOWER HOVER TEST MATRIX

		RPM			
Thrust, N	(lb)	240	291	324*	356**
0	0	↓	↓	↓	↓
8 896	(2 000)				
17 792	(4 000)				
26 688	(6 000)				
35 684	(8 000)				
44 480	(10 000)				

*Nominal aircraft operating rpm.
**Ogee rotor only.

TABLE VI.- FLIGHT-TEST ENVELOPE FOR NEAR-FIELD ACOUSTIC AND SYSTEMS DATA

INDICATED AIRSPEED, KNOTS	RATE OF DESCENT, FT/MIN*	FLIGHT CONDITION
30, 40	-25 to -200	Climb
20-120	0	Level flight
55-115	100 to 1500	Descent
50, 60, 80, 90	0 (1.5 g, 2.0 g turns)	Maneuver
0	0 (In ground effect; out of ground effect)	Hover

*1 ft/min = 0.0051 m/sec.

TABLE VII.- FLIGHT CONDITIONS OVER ACOUSTIC ARRAY

INDICATED AIRSPEED, KNOTS	RATE OF DESCENT, FT/MIN*
55, 80, 115	0
55, 70, 80, 90	100, 250, 350, 600, 1000

*1 ft/min = 0.0051 m/sec.

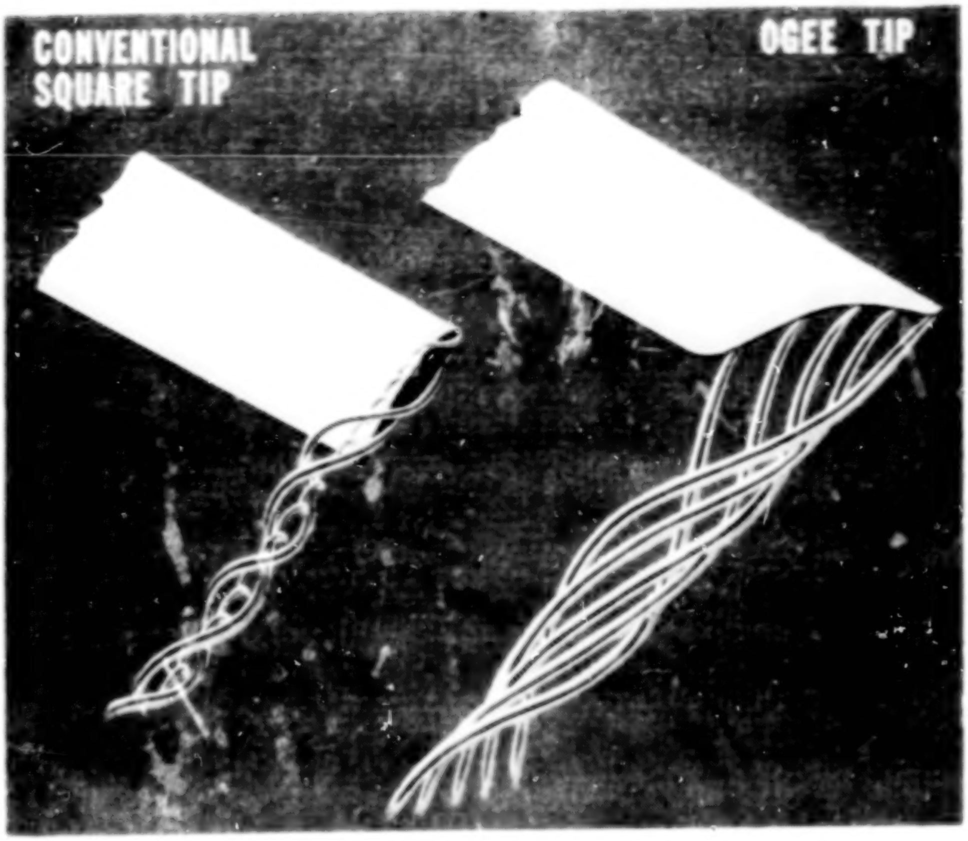
CONVENTIONAL SQUARE TIP
OGEE TIP

Figure 1.- Ogee planform and vortex diffusion concept.

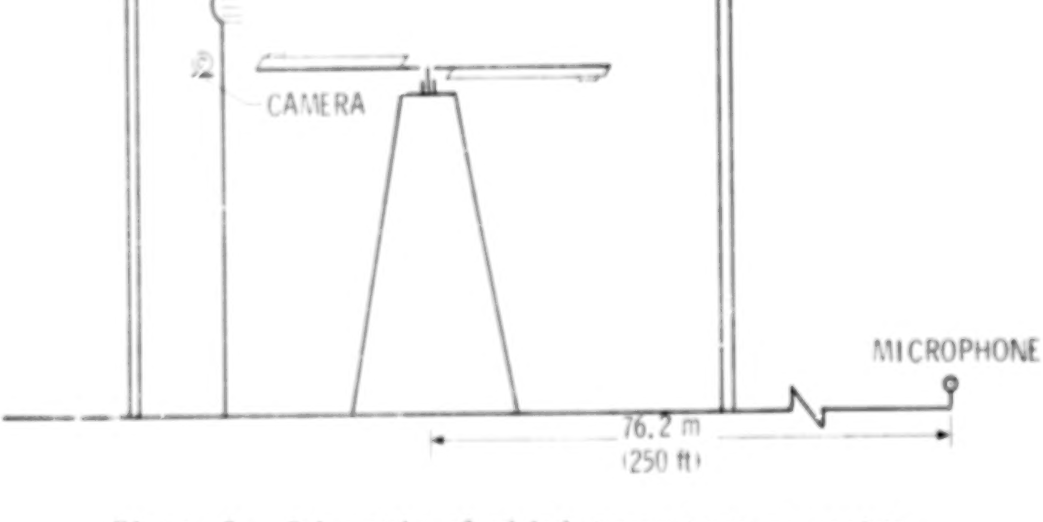
24.4 m (80 ft) DIAMETER CIRCULAR SCREEN
SMOKE RAKE
CAMERA
MICROPHONE
76.2 m (250 ft)

Figure 2.- Schematic of whirl-tower test apparatus.

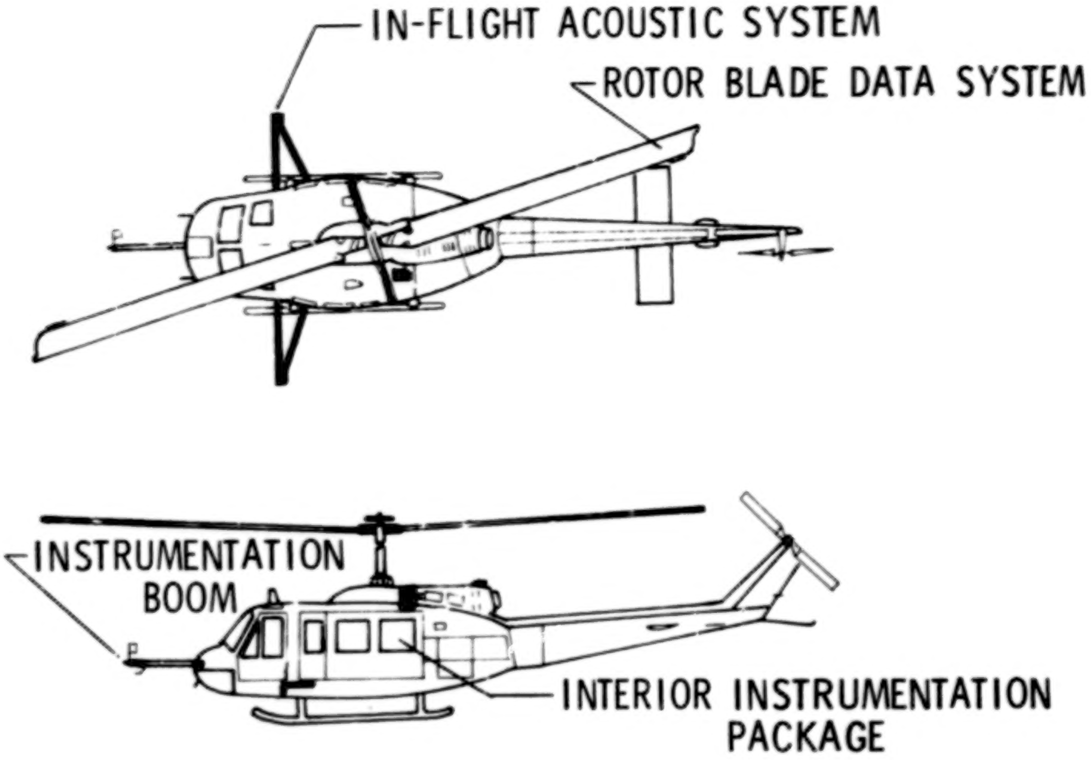
IN-FLIGHT ACOUSTIC SYSTEM
ROTOR BLADE DATA SYSTEM
INSTRUMENTATION BOOM
INTERIOR INSTRUMENTATION PACKAGE

Figure 3.- UH-1H test helicopter.

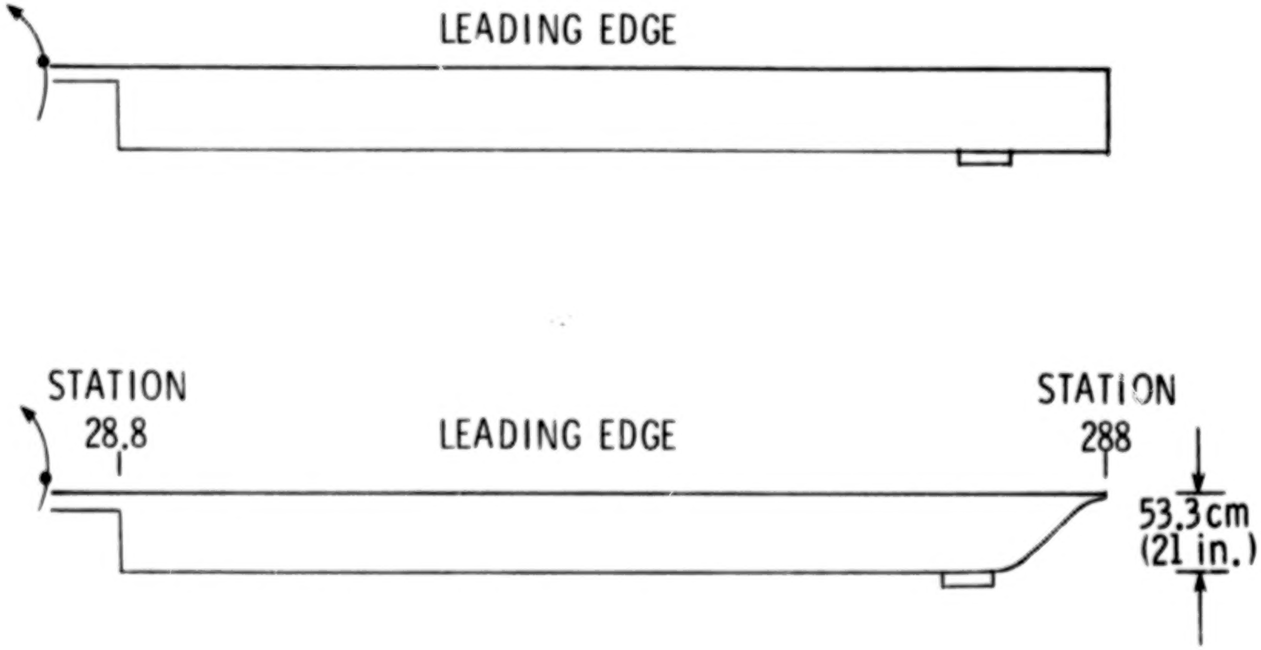
LEADING EDGE
STATION 28.8
LEADING EDGE
STATION 288
53.3 cm (21 in.)

Figure 4.- Test rotor planforms.

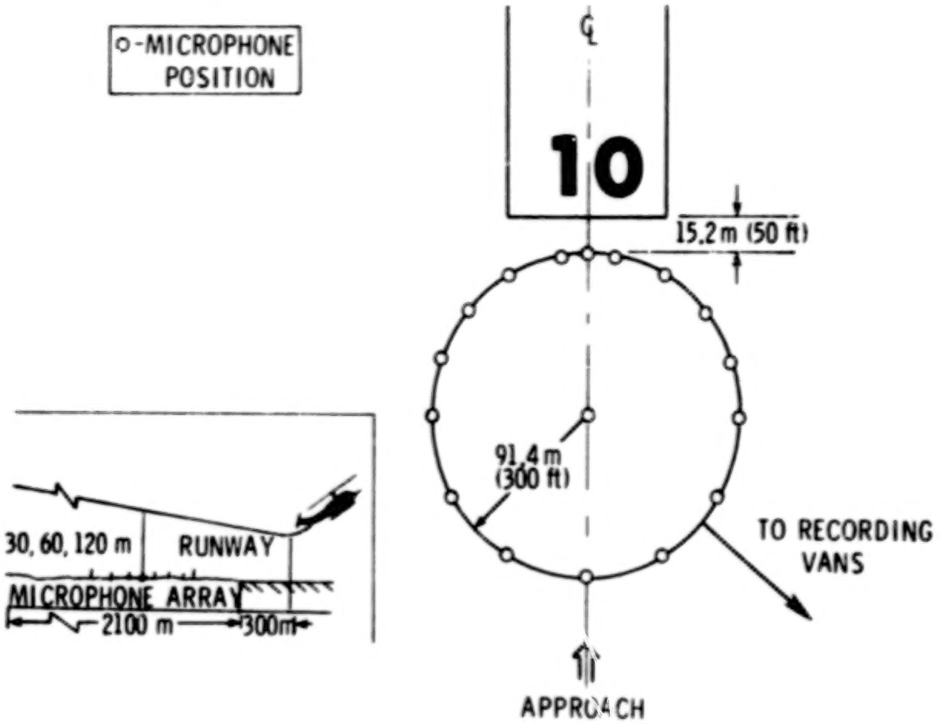
○-MICROPHONE POSITION
℄
10
15.2 m (50 ft)
91.4 m (300 ft)
TO RECORDING VANS
APPROACH
30, 60, 120 m
RUNWAY
MICROPHONE ARRAY
2100 m
300 m

Figure 5.- Acoustic array schematic.

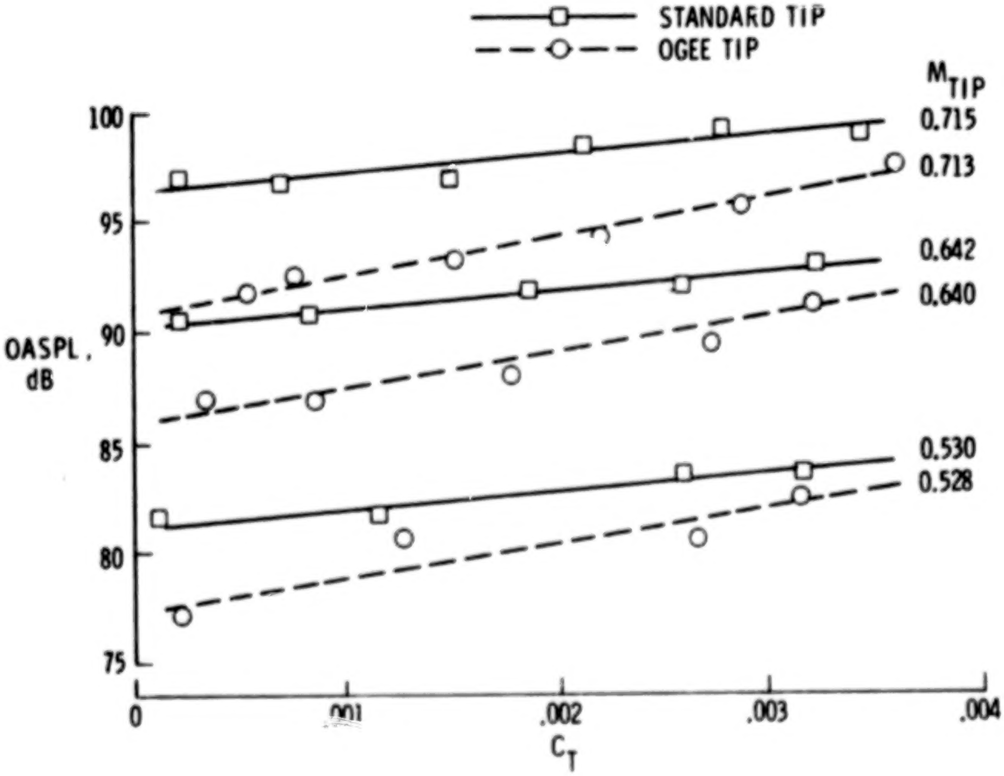

Figure 6.- Overall sound pressure levels for Ogee and standard rotors in hover.

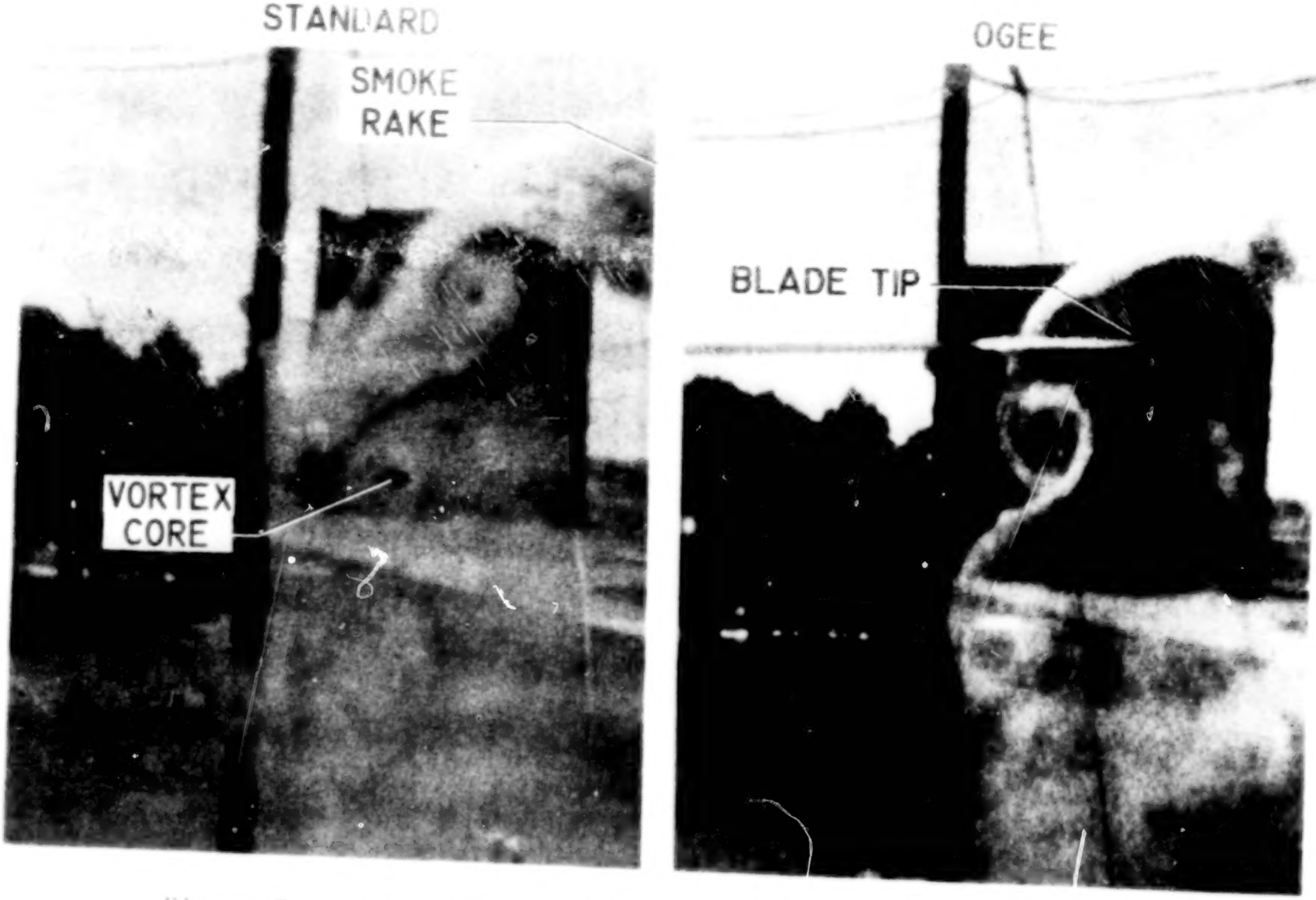
STANDARD
SMOKE RAKE
VORTEX CORE
OGEE
BLADE TIP

Figure 7.- Smoke flow visualization of vortex wake in hover for 35 584 N (8 000 lb) thrust at 324 rpm.

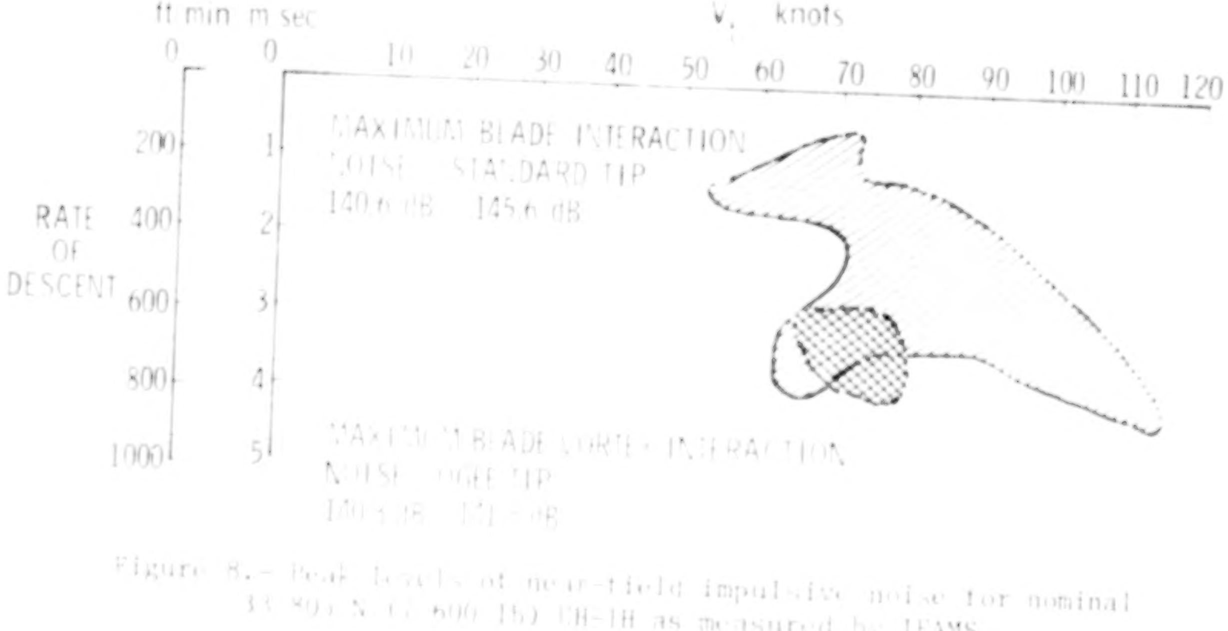

Figure 8.- Peak levels of near-field impulsive noise for nominal 33 805 N (7 600 lb) UH-1H as measured by IFAMS.

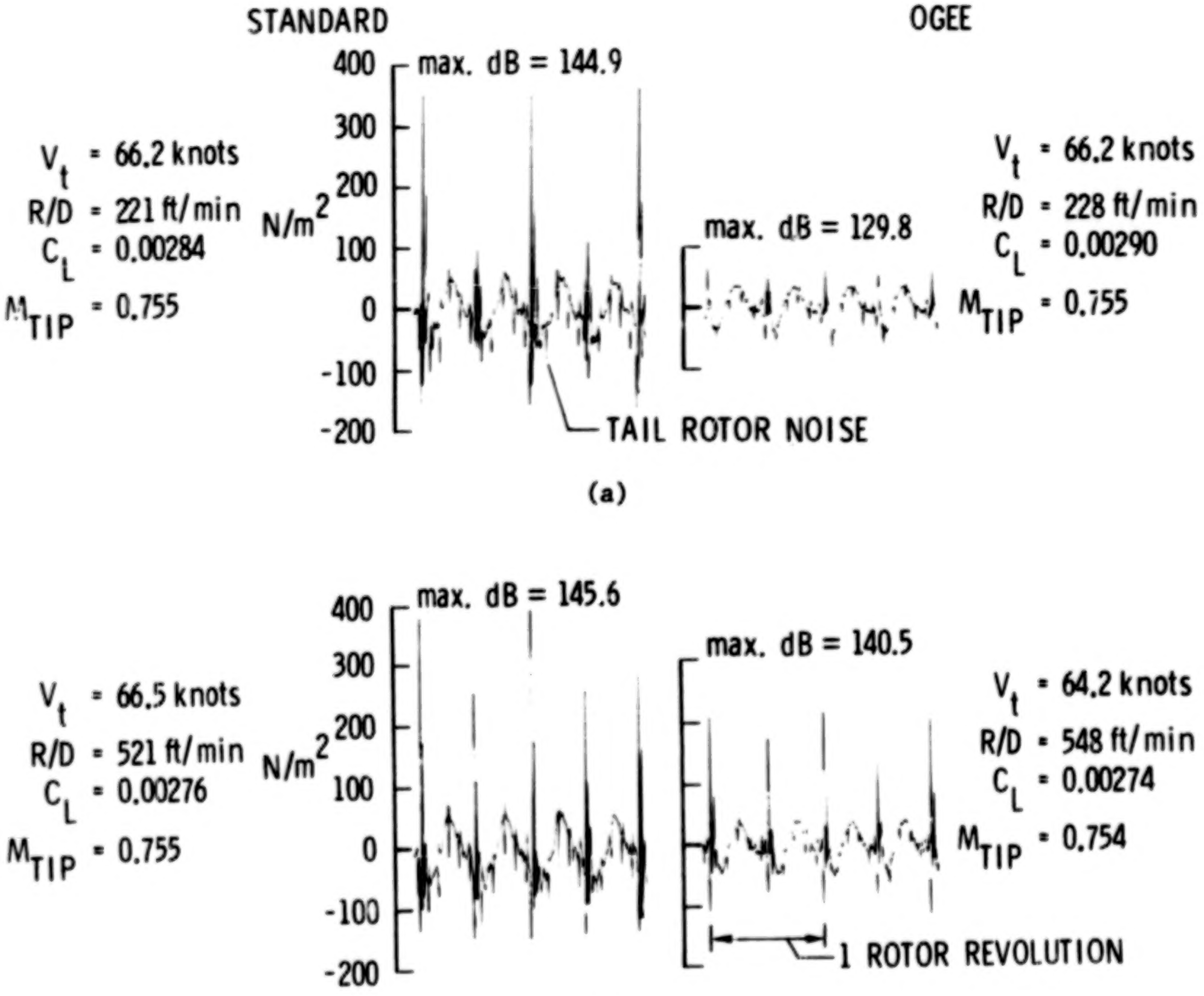

(a)

(b)

Figure 9.- Advancing-side microphone pressure time histories.

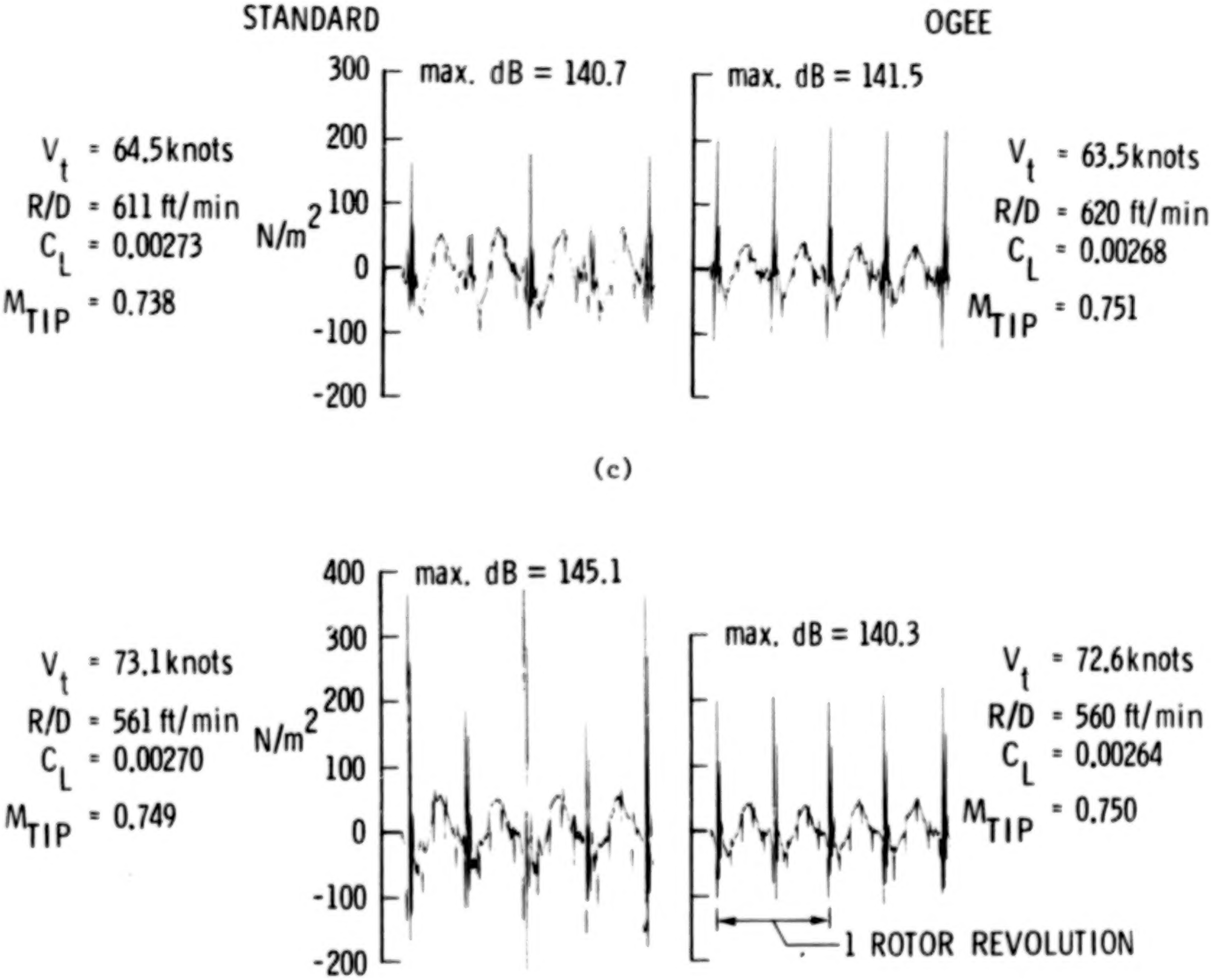

(c)

(d)

Figure 9.- Concluded.

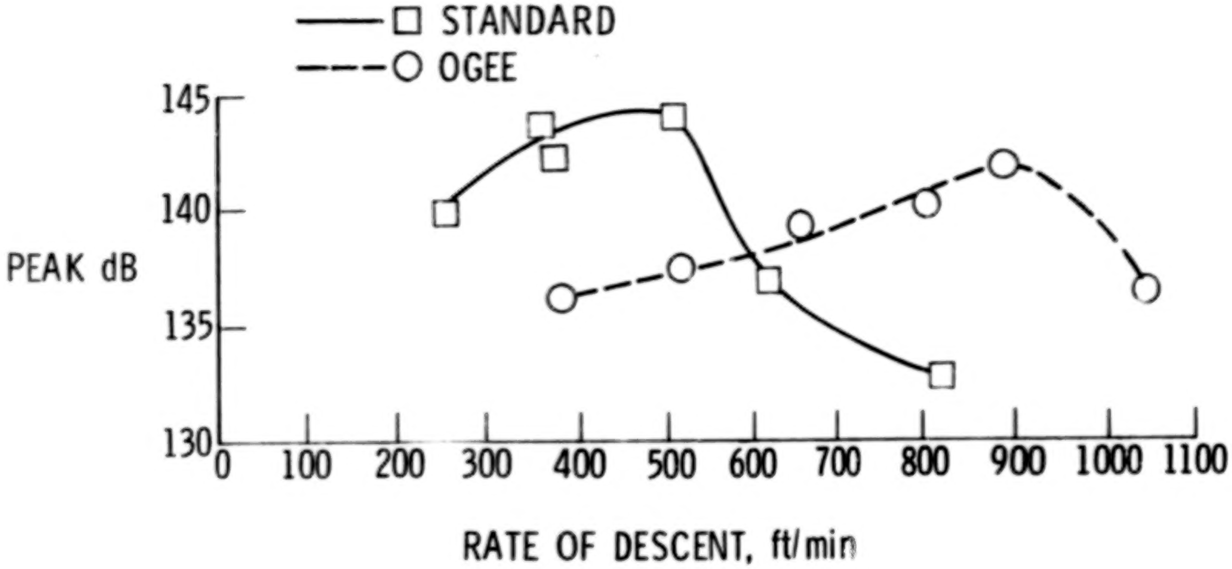

(a) $\bar{V}_t = 72.7$ knots; $\bar{C}_L = 0.00309$.

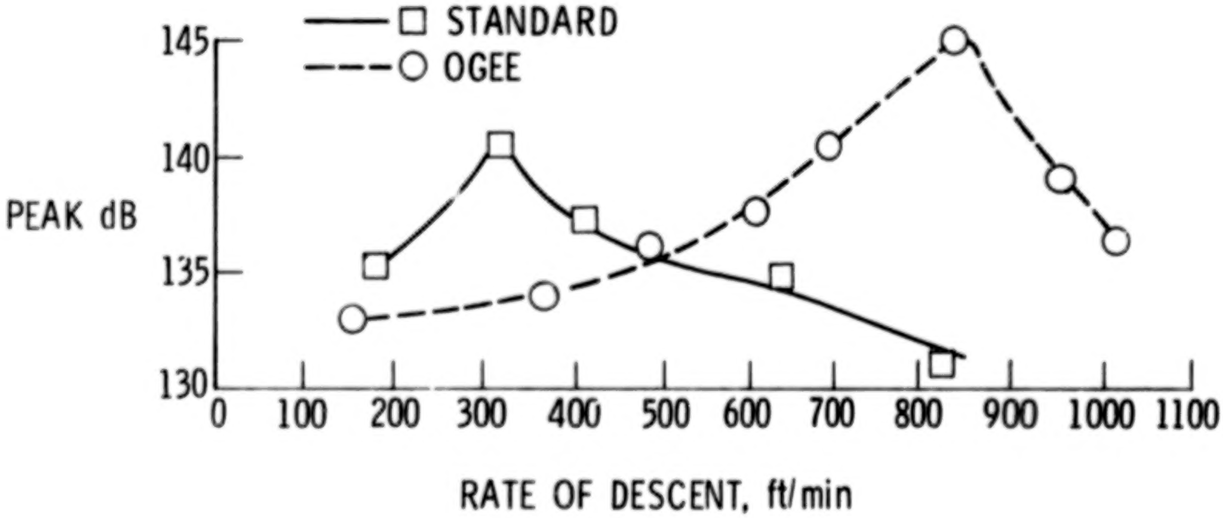

(b) $\bar{V}_t = 66.5$ knots; $\bar{C}_L = 0.00306$.

Figure 10.- Near-field peak sound pressure level variation with rate of descent at high gross weight.

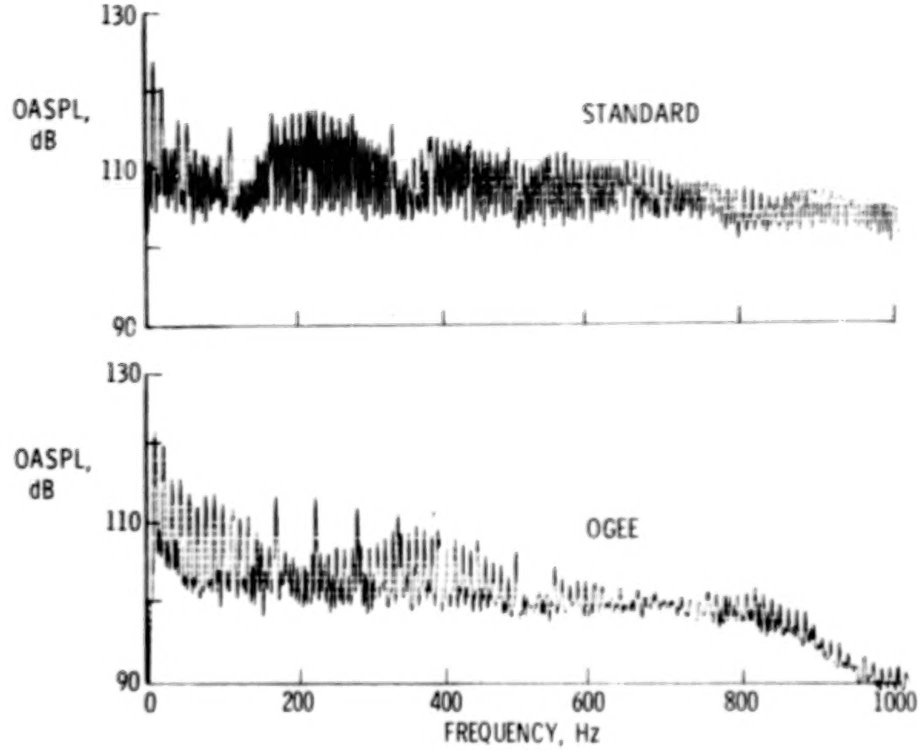

(a) Flight condition of figure 9(a).

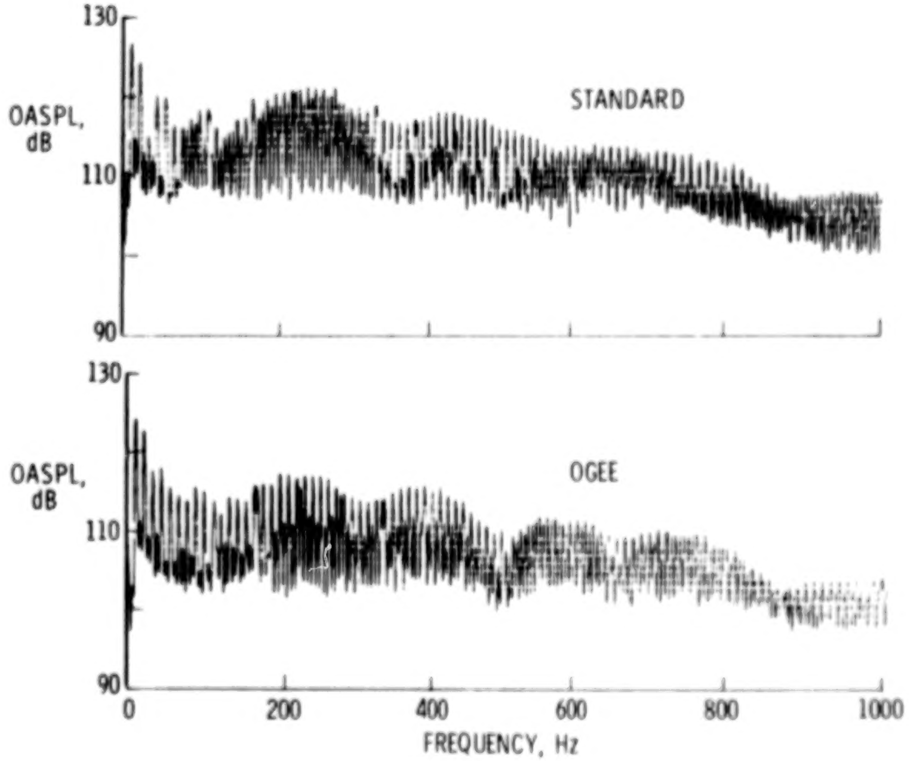

(b) Flight condition of figure 9(b).

Figure 11.- Spectra for near-field noise data.

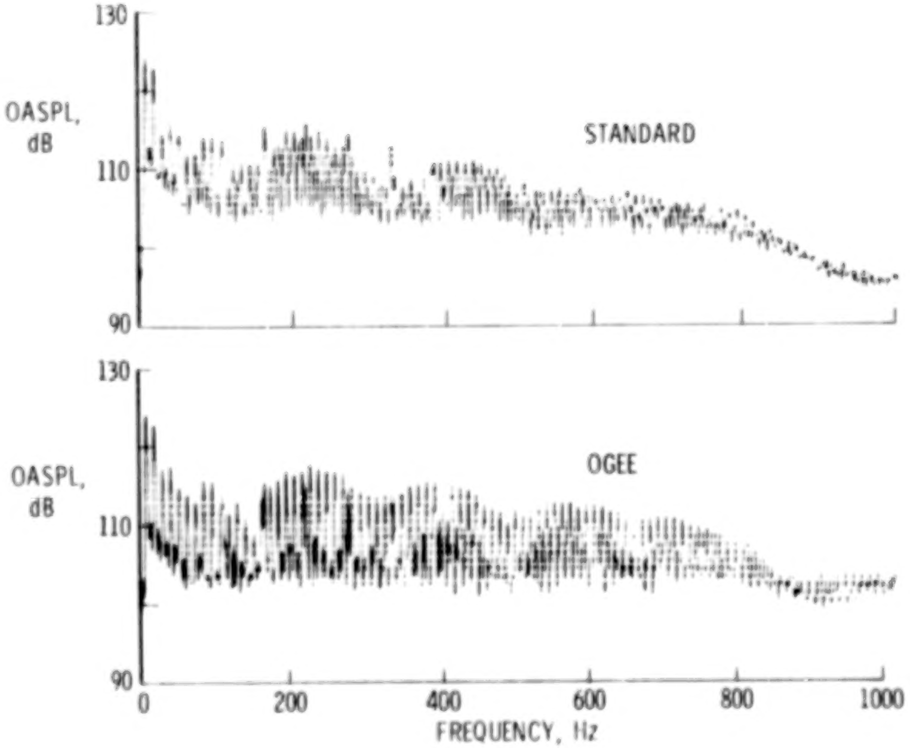

(c) Flight condition of figure 9(c).

Figure 11.- Concluded.

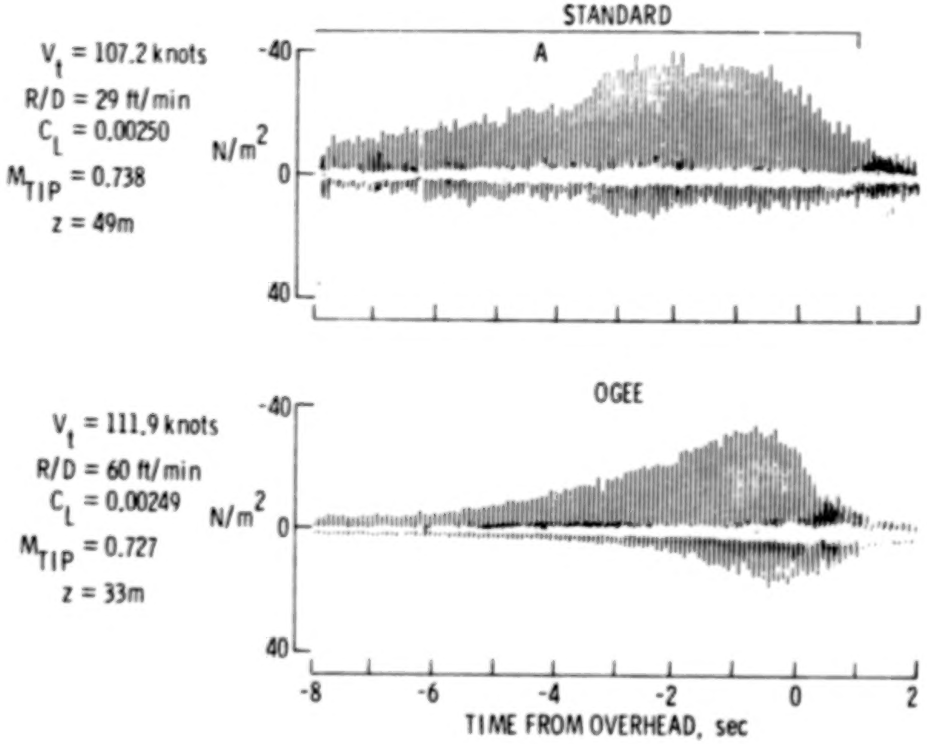

(a) High-speed level flight.

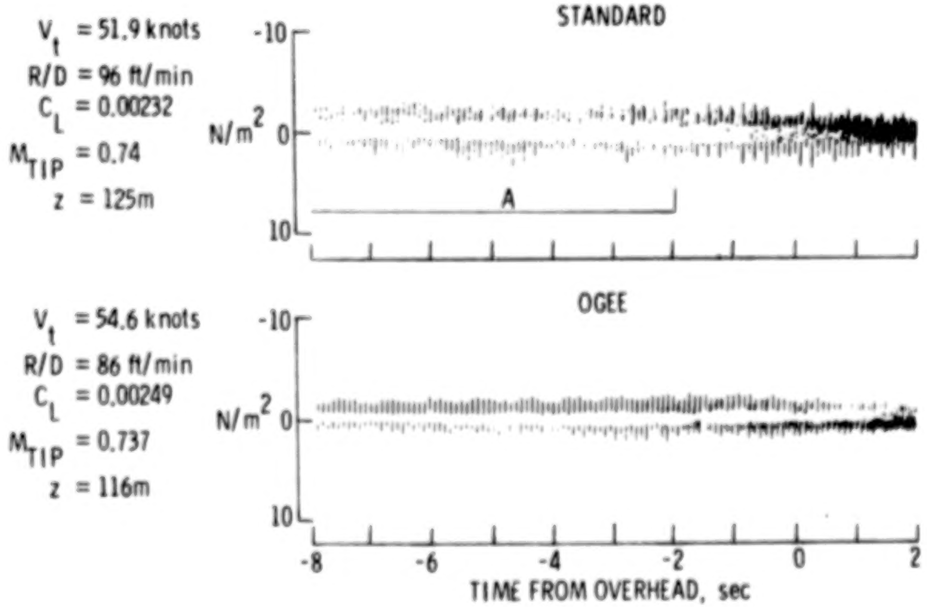

(b) Low-speed level flight.

Figure 12.- Far-field rotor noise measured by acoustic array center microphone.

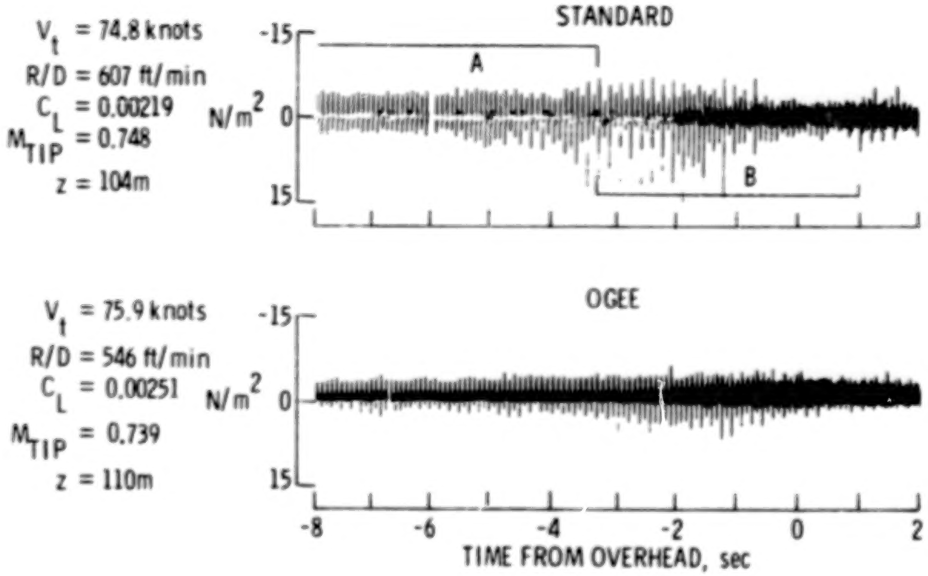

(c) Rate of descent.

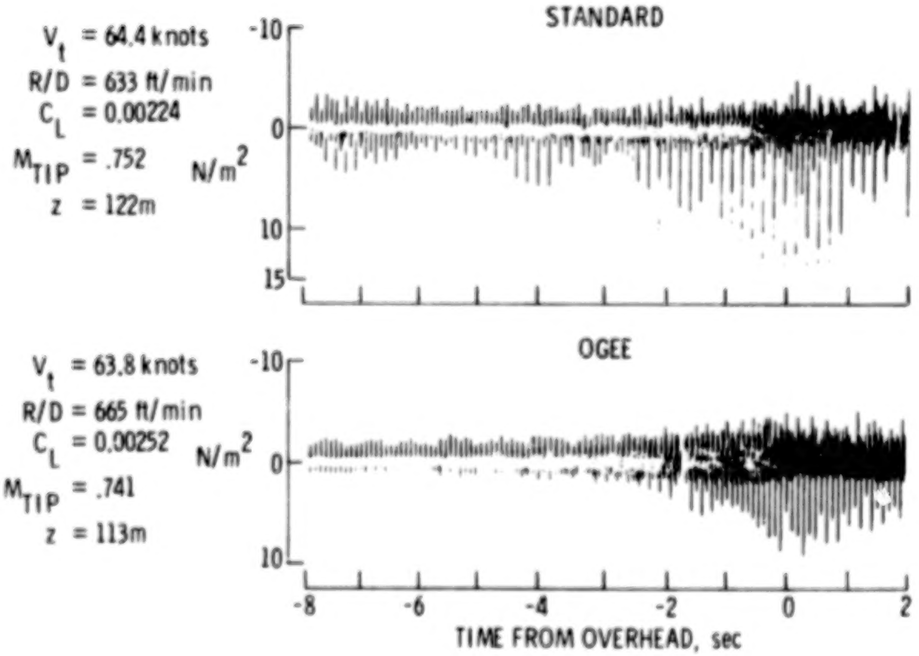

(d) Rate of descent.

Figure 12.- Continued.

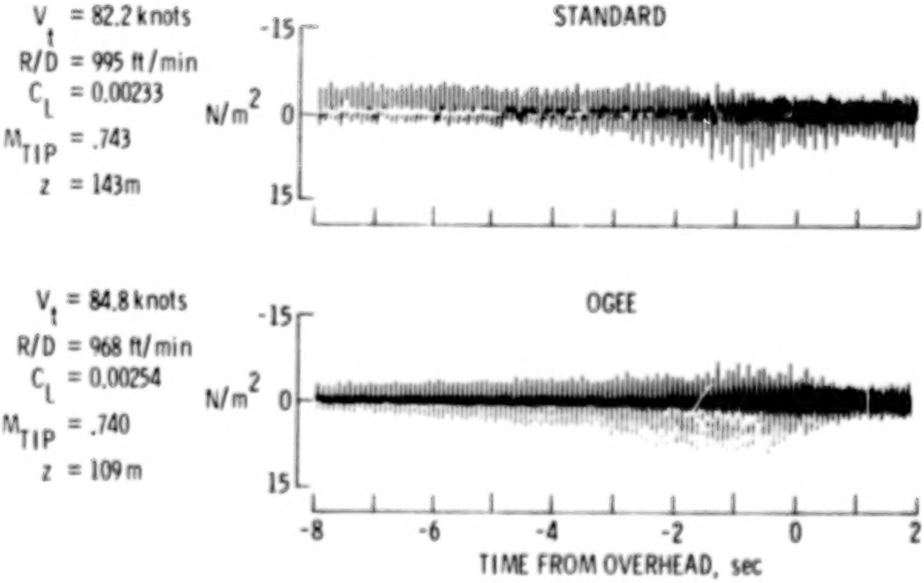

(e) High-speed high rate of descent.

Figure 12.- Concluded.

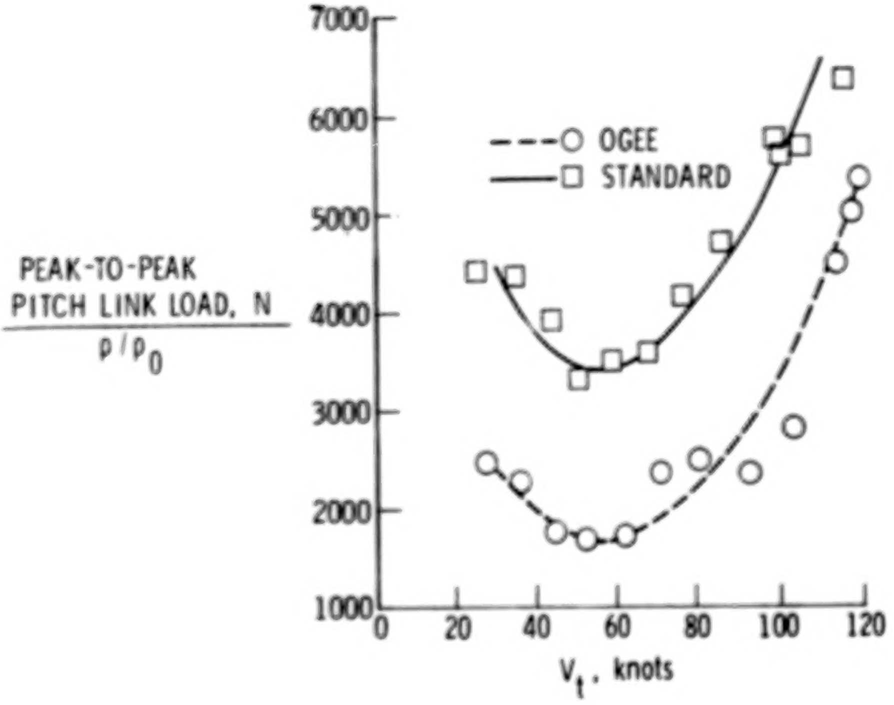

(a) $\bar{C}_L = 0.00266$; $\bar{M}_{TIP} = 0.744$.

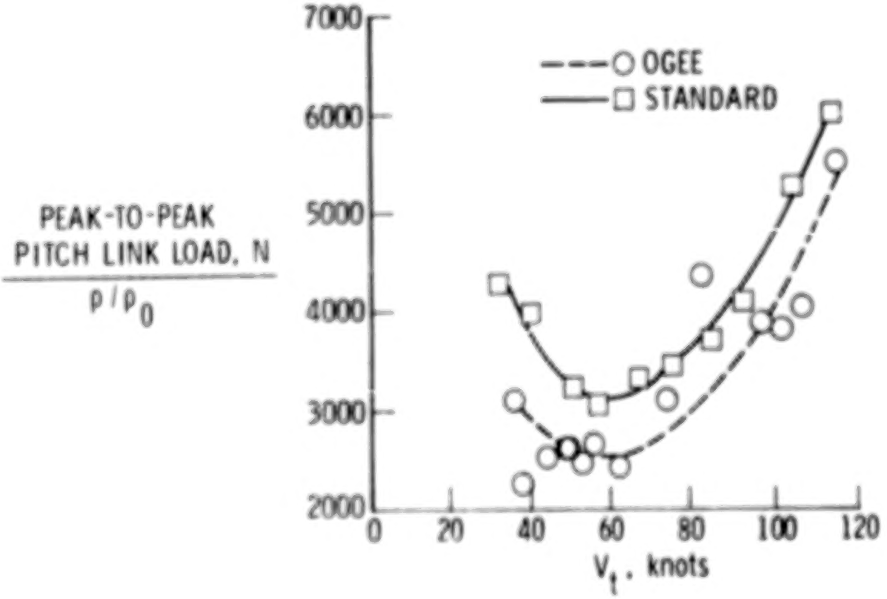

(b) $\bar{C}_L = 0.00323$; $\bar{M}_{TIP} = 0.733$.

Figure 13.- Oscillatory pitch link loads in level flight.

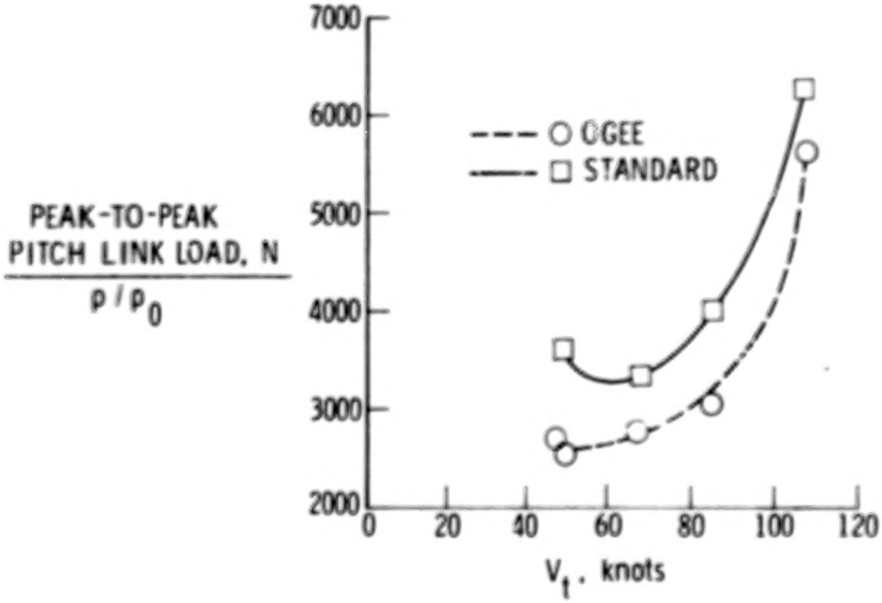

(c) $\bar{C}_L = 0.00356$; $\bar{M}_{TIP} = 0.736$.

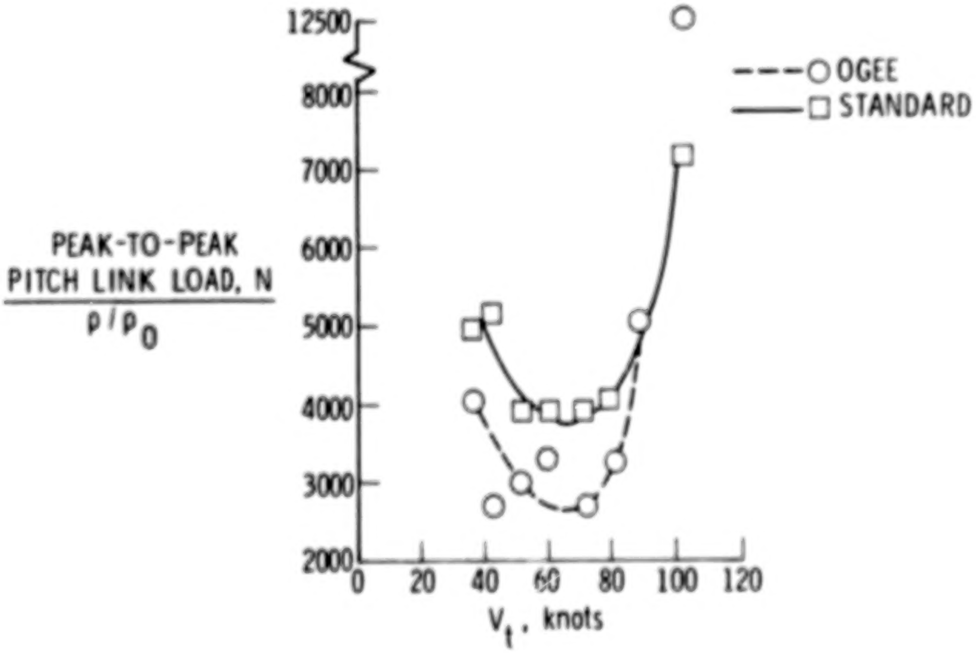

(d) $\bar{C}_L = 0.00388$; $\bar{M}_{TIP} = 0.75$.

Figure 13.- Concluded.

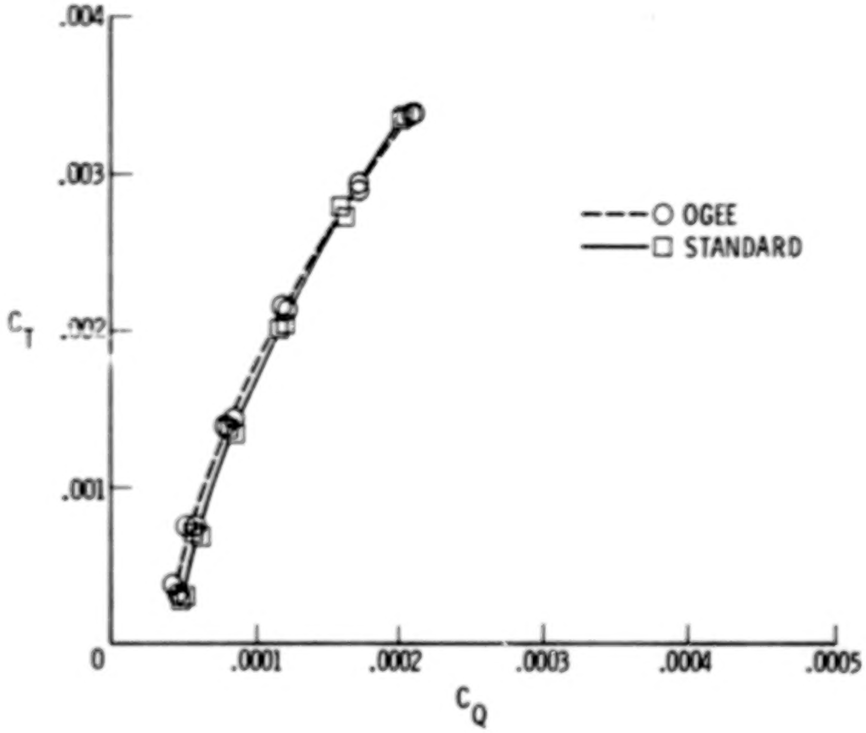

(a) $\bar{M}_{TIP}$ = 0.714.

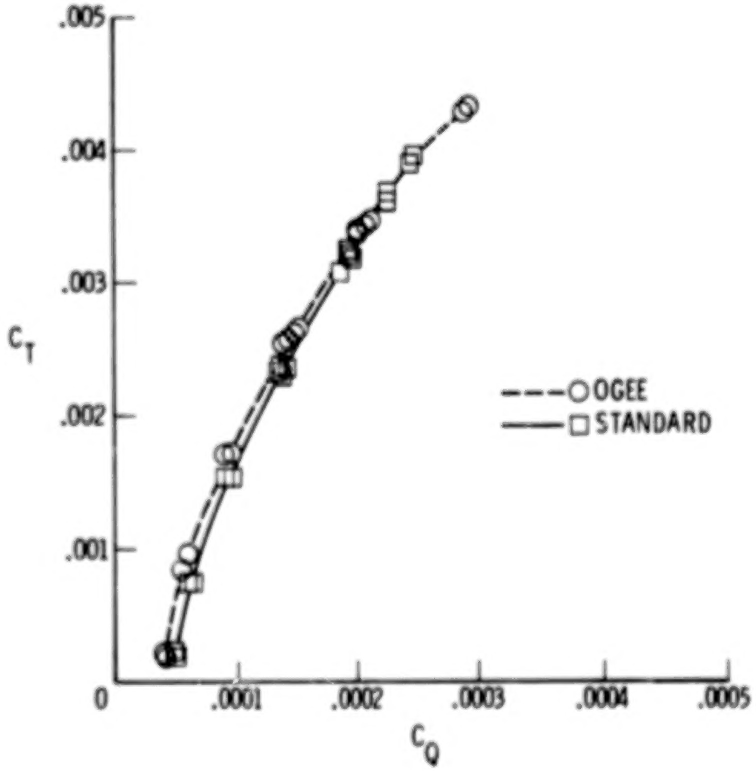

(b) $\bar{M}_{TIP}$ = 0.657.

Figure 14.- Hover performance data from whirl tower.

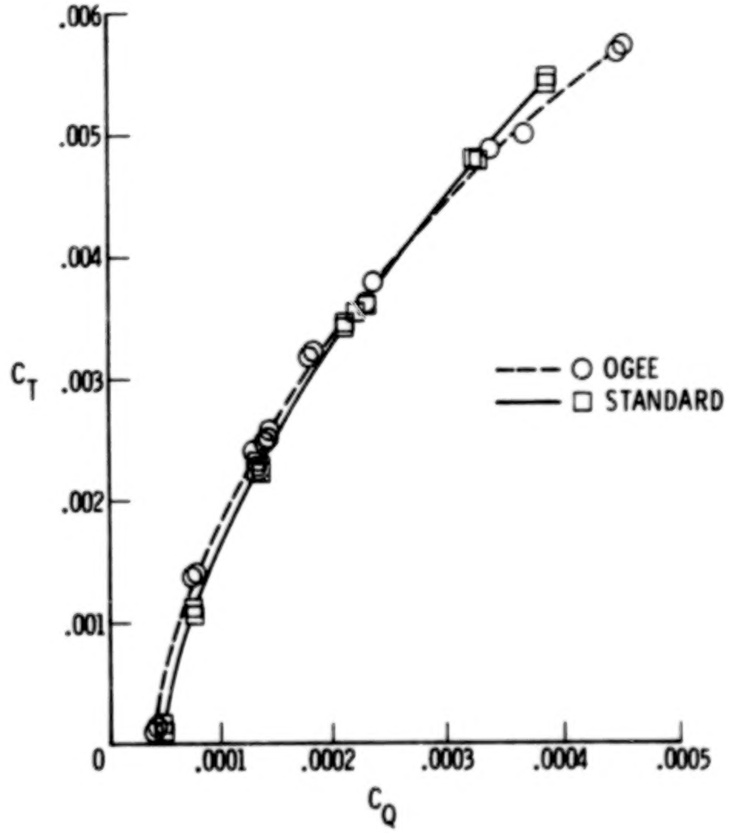

(c) $\bar{M}_{TIP} = 0.535$.

Figure 14.- Concluded.

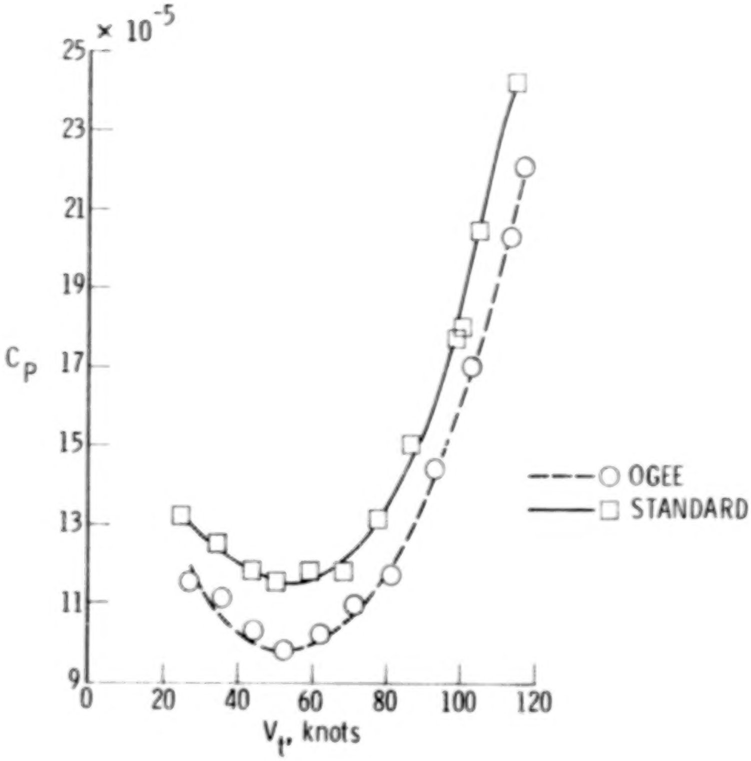

(a) $\bar{C}_L = 0.00266$; $\bar{M}_{TIP} = 0.744$.

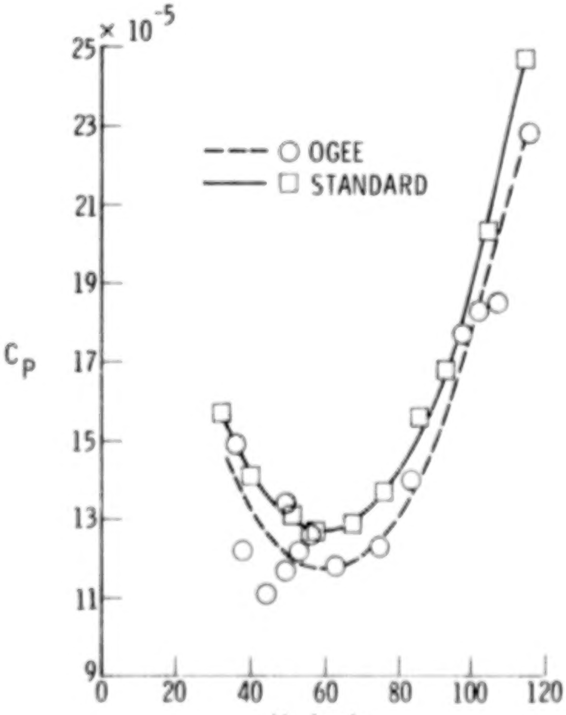

(b) $\bar{C}_L = 0.00323$; $\bar{M}_{TIP} = 0.733$.

Figure 15.- Forward-flight performance of standard and Ogee rotors.

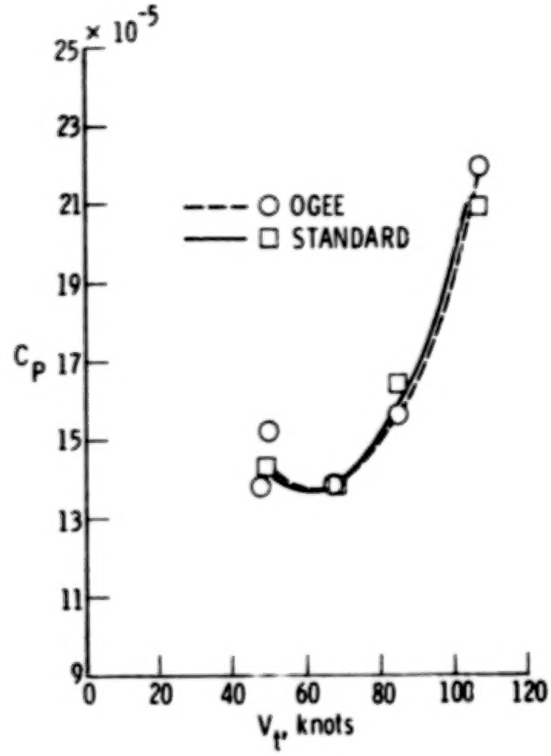

(c) $\bar{C}_L = 0.00356$; $\bar{M}_{TIP} = 0.736$.

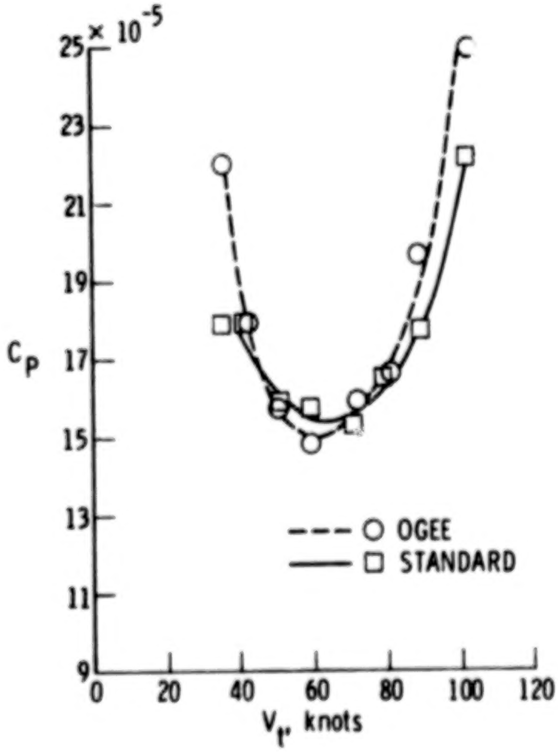

(d) $\bar{C}_L = 0.00388$; $\bar{M}_{TIP} = 0.75$.

Figure 15.- Concluded.

HOVERING IMPULSIVE NOISE

SOME MEASURED AND CALCULATED RESULTS

D. A. Boxwell, Y. H. Yu, and F. H. Schmitz
Aeromechanics Laboratory
U.S. Army R&T Laboratories (AVRADCOM)
NASA Ames Research Center

SUMMARY

In-plane impulsive noise radiating from a hovering model rotor has been measured in an anechoic environment. The hover acoustic signature was compared with existing theoretical prediction models and with previous forward flight experiments using the same model rotor. These hover tests showed good experimental consistency with forward flight measurements, both in pressure level and waveform character, over the range of Mach numbers tested (0.8 to 1.0). Generally poor correlation, however, was confirmed with current linear theory prediction efforts. Failure to predict both the peak pressure levels and the shape was reported, especially with increasing tip Mach number.

INTRODUCTION

In recent years, high-speed helicopter impulsive noise has been the subject of much acoustic research, both experimentally (refs. 1 to 6) and theoretically (refs. 5 to 11). The main motivation behind the research is the eventual mitigation, by design techniques, of this intense source of noise. The military and civilian communities will both benefit. In the first case, the detection distance of an approaching helicopter will be reduced, while in the second case, quieter helicopter operations will reduce community annoyance.

High-speed helicopter impulsive noise is quite distinctive in nature. In its milder form, it consists of a sequence of thumping sounds which, because of their low frequency character and high intensity, can often be heard for many miles. As the advancing tip Mach number of the helicopter increases the subjective quality, pulse shape, and amplitude of the noise change (refs. 1 and 4). The sequence of acoustic pulses becomes harsh sounding in character and radiates large amounts of higher frequency harmonic noise. The increasing annoyance of a developing saw-toothed pulse shape is also apparent.

Prediction and measurement of this phenomena has proceeded along several different paths. Both frequency-domain and time-domain theories have been developed which emphasize the noncompactness of the problem. Most of the theoretical approaches are derived from the work of Ffowcs Williams and Hawkings (ref. 12) for bodies in high-speed flight. The application of this approach to the rotor problem was first pursued by Farassat (ref. 8) and Hawkings and Lowson (ref. 5). Today there are several basically similar ways of calculating this impulsive noise signature (refs. 5 to 7, 9, and 11) which are in general theoretical agreement and yield numerical values which agree in pulse shape and amplitude.

Unfortunately, the agreement of any of these theoretical approaches with experimental measurements is not at all certain. The issue is often clouded by the different methods of gathering impulsive noise data. For instance, ground noise measurements have shown good agreement in pulse shape and amplitude with thickness noise theories (refs. 6 and 8). Full-scale wind-tunnel measurements of rotors operating at high tip Mach number show good theoretical agreement in the peak levels of the negative pressure pulse but generally poor agreement with theory in pulse shape (ref. 3). Scale model wind-tunnel measurements of reference 4 show generally poor agreement with predicted amplitude and pulse shapes at high advancing tip Mach numbers. Also full-scale impulsive noise measurements of the UH-1H helicopter taken by an in-flight technique (ref. 1) have shown poor agreement in amplitude and in pulse shape at high advancing tip Mach numbers. All of these different measurement techniques have inherent strengths and weaknesses, but all should yield consistent results. As judged by existing theoretical models, however, they do not.

The major purpose of this paper, therefore, is to continue to pursue the comparison between test and theory by investigating a simpler problem, high tip speed hovering impulsive noise. In particular, a 1/7-scale model of the UH-1H helicopter was tested in an anechoic hover environment over a range of Mach numbers consistent with high-speed advancing flight. By avoiding major recirculation through facility design and by testing at high tip Mach numbers, the details of high tip speed noise become clearer. It will be shown from the current tests that the acoustic characteristics highlighted in the previous in-flight full-scale and wind-tunnel scale-model investigations are again present in hover. It will also be shown that existing linear theoretical approaches do not adequately describe the event of high-speed impulsive noise.

EXPERIMENTAL SETUP

The data presented in this paper were gathered in a unique anechoic hover test facility which was designed primarily to gather acoustic and aerodynamic data on hovering rotors. The test chamber has been lined with polyurethane foam and has been designed to be anechoic (without acoustic reflections) down to 110 Hz. As illustrated in figure 1, aerodynamic recirculation is avoided by allowing quiescent air to be drawn into the room through acoustically lined ducts, collecting the wake of the hovering rotor through an annular diffuser, and exhausting the wake to the outside. In its current configuration, the test chamber can accommodate rotors from 1.5 to 2.4 m in diameter.

A final acoustic and aerodynamic calibration of this facility is concurrently being conducted. Preliminary calibrations revealed the feasibility of investigating the noise generated by a high tip speed hovering rotor in the early stages of the facility checkout. Quantitative estimates of noise due to inflow turbulence, detailed measurements of thrust and power, and final verification of the free field characteristics of the chamber are not yet available. Nevertheless, preliminary measurements indicate the room is anechoic to its design frequency and that most of the rotor's wake is captured by the annular diffuser. For the tests to be reported, a minimum amount of collective pitch control (1.5 degrees at the rotor tip) was employed to exhaust the shed wake.

The rotor chosen for the test was a 1/7-scale UH-1H main rotor. The geometrically scaled rotor had a NACA 0012 airfoil section with a root-to-tip washout of 10.9° and a full-scale twist. A teetering hub was employed with cyclic controls locked out for this pure hovering test. A high-speed stroboscopic system was used for blade tracking and visual monitoring during the test. No flutter was apparent throughout the testing matrix. Thrust and torque were monitored, but data can only be considered to be qualitative at this time.

Acoustic data were gathered using 12.7-mm (0.5 in.) "free field" condensor microphones and monitored on an oscilloscope both before and after recording on an FM tape recorder. This insured that the full dynamic range of all the electronic equipment was utilized without clipping of the impulsive signature. A double extended 60 ips mode of the FM recorder gave a transient response of at least 20 000-Hz bandwidth.

EXPERIMENTAL RESULTS

The data reported in this test have been taken with a microphone located within the tip-path plane of the rotor at a distance of 1.5 rotor diameters (r/D = 1.5) from the hub. This in-plane microphone position is consistent with previous in-flight and wind-tunnel testing (refs. 1 and 4) and is in a position to measure the most intense high-speed impulsive signature. As stated in reference 11, another benefit of utilizing an in-plane microphone is that the measured signal will only theoretically depend upon acoustic dipole sources whose major axes are in the plane of the rotor disc (i.e., the thrust dipole does not contribute, only in-plane drag forces). Therefore, comparison of theory and experiment is not dependent upon detailed measurement of rotor thrust.

Figure 2 presents the measured acoustic signature at a hover tip Mach number M_T of 0.8. Two time scales are presented. Part (a) depicts two blade passages, approximately one-half of a complete rotor revolution. Part (b) of the same figure is an expanded scale of the first acoustic pulse. The latter is used to emphasize the detailed waveform characteristics of the measured pulse.

The waveform presented in this figure (and throughout this report for all test conditions) is unaveraged and exhibits some degree of unsteadiness both in peak negative pressure level and in the finer waveform shape structure. An investigation into the sources of this unsteadiness is one of the purposes of ongoing tests. The most striking feature of the waveform at $M_T = 0.8$ is its almost symmetrical character. This same character has been observed in full-scale and scale-model forward flight testing. The only real difference when the same model rotor is tested in forward flight is that the peak negative amplitude of the pulse is higher in the hovering condition, as would be predicted.

Figure 3 illustrates the pressure time history at a hovering tip Mach number of 0.9. The peak negative amplitude of the measured pulse has increased dramatically and the pulse shape has now lost its symmetry. The resulting saw-toothed waveform is known to generate large amounts of high intensity, higher frequency noise. Again, this same type of waveform was measured on the same rotor system operating in forward flight at an advancing tip Mach number of 0.9. In this previous test, schlieren photographs were used to correlate the discontinuous increase in pressure with a radiating shock wave. It is apparent that a similar phenomenon is occurring in this controlled hover test.

At a hover tip Mach number of 0.962 (fig. 4), the saw-toothed pulse shape is firmly established and the negative peak pressure level has doubled from the $M_T = 0.9$ condition. The large, discontinuous rise in pressure resulting from a radiating shock wave exhibits some variability from blade to blade. One particularly interesting aspect of the waveform shown in figure 4(b) is the pulse width. At lower hover tip Mach numbers, the pulse width was observed to narrow with increasing rotor tip speed up to the point of waveform transition from symmetrical to sawtooth. Above this transition point, for example at $M_T = 0.962$, the pulse width has become larger. Figure 4 also shows that a positive pressure wave (bow wave) begins to form. At still higher tip Mach numbers, the classical N-wave of sonic boom research is likely.

In addition to the general increase of peak negative pressure level with increasing hover tip Mach number, the waveform transition from symmetrical to sawtooth dominates the changing acoustic signature. Figure 5 illustrates the development of the radiating waveform discontinuity as measured in hover at $r/D = 1.5$. The sequence of waveforms in figure 5 shows that transition occurs over a very small range in hover tip Mach number from 0.88 to 0.90, with $M_T = 0.89$ being the point of transition for the test rotor. Transition was found to be characterized by a simultaneous increase in negative peak pressure level and the following rapid pressure rise. Both events were observed to be highly unsteady even under controlled rotor test conditions.

It is also instructive to compare the peak negative amplitude of the measured waveform versus hover tip Mach number (fig. 6). A very rapid increase in level is noticed as M_T approaches 0.9. However, as M_T increases beyond 0.9 to $M_T = 1.0$, the increase in peak level is less or the rate of increase of this peak negative pressure level with Mach number becomes smaller. As noted on figure 6, the shaded area depicts the degree of unsteadiness (mentioned previously) in the measured data. The vertical solid bars reflect data taken with the UH-1H model twisted blades, and the "dashed" vertical bars are for the same dimension model rotor using untwisted blades. The correlation between twisted and untwisted results is good with the exception of unsteadiness at $M_T \approx 1.0$ for the twisted blades. The reason for this difference is not known at this time. No apparent flutter was visualized for either set of blades.

The peak levels versus advancing tip Mach number measured on the same model rotor in forward flight (ref. 4) are also shown in figure 6. Although the rate of increase is similar, the peak levels are much smaller in amplitude as would be expected.

COMPARISON WITH THEORY

Figures 7 to 10 compare the measured hover results with the linear non-compact acoustic models developed in the literature. In this case, the methods of reference 11 were used to calculate the pulse shape. Only monopole thickness terms were included, because local forces in the in-plane direction do little to affect the calculated signature. The linear dipole and quadrupole refinements as well as details of the often transonic flow field have been neglected. An "acoustic planform" approach (ref. 7) was used to calculate the waveform time history at or near $M_T = 1.0$ and to check theoretical computations at lower Mach numbers. There is nothing really new in these computations of "thickness noise" at the current time as there are many existing programs which could produce similar results. In the following comparisons, no exact attempt was made to phase match the theoretical and experimental acoustic signatures.

The striking features of the comparison between theory and experiment in hover at $M_T = 0.8$ (fig. 7) are the similarity in pulse shape and the discrepancy in peak pressure levels. As in forward flight (ref. 4) at advancing tip Mach numbers below 0.9, thickness noise theory misses the measured negative peak levels by a factor of approximately two.

The comparison of theory and experiment as M_T is increased to 0.88 (fig. 8) remains similar to that made at $M_T = 0.8$. The waveform shape is still generally symmetrical but the peak negative pressure level is underpredicted by slightly more than a factor of two. As was noted previously, $M_T = 0.88$ is slightly less than the critical hover tip Mach number for waveform transition, at least as measured at $r/D = 1.5$ with the test rotor.

At a hover tip Mach number of 0.9, the situation becomes even worse (fig. 9). The amplitude of the peak negative pressure pulse is again underpredicted by a factor of approximately two. However, as indicated previously, there is also a dramatic change in the waveform of the experimental data which is not predicted by the linear theory.

The comparison becomes even more intriguing at a hover tip Mach number of 0.962 (fig. 10). The theoretical waveform is still symmetrical and generally smooth in shape and thus does not compare favorably with the measured data. In addition, theory now only slightly under-predicts the peak negative pressure amplitude of the pulse. Also as previously noted, the measured pulse width is becoming wider; whereas, the linear theory predicts a more narrow pulse width with increasing hover tip Mach number. In fact, the experimental pulse width (measured at zero pressure) exceeds by at least 50% the width expected (by linear theory) from an airfoil of chord equal to the model rotor tested and traveling at sonic velocity. This pulse widening effect suggests that aerodynamic events off the rotor blade are contributing to the measured acoustic signature.

The difference in peak negative pressure levels between linear monopole theory and experiment can be seen more clearly in figure 11. Clearly, the theoretical model does not predict the rate of increase of the peak negative pressure level. However, at a hover tip Mach number of 0.97, the two curves cross. This fact may be a partial explanation for the generally good correlations between theory and experiment reported in reference 3.

The theoretical predictions utilized in this paper have only considered the linear monopole source contributions. It was shown in references 2 and 4 that forward flight in-plane impulsive noise was not (to first order) dependent upon thrust. Similarly, in this test, no first-order dependence of thrust (and therefore drag) was observed. The inclusion of in-plane quadrupoles will tend to improve the correlation. However, as pointed out in reference 11, a more sophisticated treatment of rotor transonic aerodynamics is undoubtedly necessary. For quantitative comparisons, it may be necessary to reformulate the basic acoustic equations to capture these transonic effects.

CONCLUDING REMARKS

The preliminary data taken in a controlled aerodynamic and acoustic environment on model rotors have shown that there are many fundamentals of rotor noise that are on the verge of discovery. The development of the anechoic rotor test facility is a valuable asset in that direction.

It is apparent that there exists a major discrepancy between existing linear theoretical approaches to the high-speed noise problem and experimental measurements. The use of monopole thickness and dipole drag terms in the theoretical expressions does not predict the trend of increasing noise levels with Mach number. It also only predicts the correct waveform below hover tip Mach numbers of 0.89 for the test rotor. It is concluded that the use of these theoretical approaches in the design of rotors at high tip speed is somewhat premature, their applicability has yet to be quantitively demonstrated.

The underprediction of impulsive noise at low hovering Mach numbers (0.8) is not understood. An additional large source of noise appears to be present which has been omitted from the theoretical analysis to date. The overprediction of impulsive noise at high Mach numbers ($M_T = 1.0$) is not quantitatively describable. However, as in transonic fixed-wing aerodynamics, this might qualitatively be explained by arguing that local transonic effects weaken the radiating sound wave.

REFERENCES

1. Schmitz, F. H.; and Boxwell, D. A.: In-Flight Far-Field Measurement of Helicopter Impulsive Noise. J. American Helicopter Soc., vol. 21, no. 4, Oct. 1976, pp. 2-16.

2. Tangler, J. L.: Schlieren and Noise Studies of Rotors in Forward Flight. Preprint No. 77.33-05, American Helicopter Soc., May 1977.

3. Johnson, W.; and Lee, A.: Comparison of Measured and Calculated Helicopter Rotor Impulsive Noise. NASA TM-78473, 1978.

4. Schmitz, F. H.; Boxwell, D. A.; and Vause, C. R.: High-Speed Helicopter Impulsive Noise. J. American Helicopter Soc., vol. 22, no. 4, Oct. 1977, pp. 28-36.

5. Hawkings, D. L.; and Lowson, M. V.: Noise of High Speed Rotors. AIAA Paper No. 75-450, Mar. 1975.

6. Farassat, F.; and Brown, T. J.: A New Capability for Predicting Helicopter Rotor and Propeller Noise Including the Effect of Forward Motion. NASA TM X-74037, 1977.

7. Hanson, Donald B.: Near Field Noise of High Tip Speed Propellers in Forward Flight. AIAA Paper No. 76-565, July 1976.

8. Farassat, F.: Theory of Noise Generation From Moving Bodies With an Application to Helicopter Rotors. NASA TR R-451, 1975.

9. Isom, M. P.: Theory of Sound Radiated by a Hovering Transonic Helicopter Blade. Rept. No. POLY-AE/AM 75-4, Polytech. Inst. New York, May 1975.

10. Wright, S. E.: The Relative Importance of Acoustic Sources Generated by Helicopter Rotors in High Speed Flight. Presented at the 2nd European Rotorcraft and Powered Lift Aircraft Forum, Sept. 1976.

11. Schmitz, F. H.; and Yu, Y. H.: Theoretical Modeling of High-Speed Helicopter Impulsive Noise. Paper No. 54, Presented at the 3rd European Rotorcraft and Powered Lift Aircraft Forum, Sept. 1977.

12. Ffowcs Williams, J. E.; and Hawkings, D. L.: Sound Generation by Turbulence and Surfaces in Arbitrary Motion. Philos. Trans. R. Soc. London, ser. A, vol. 264, no. 1151, May 8, 1969, pp. 321-342.

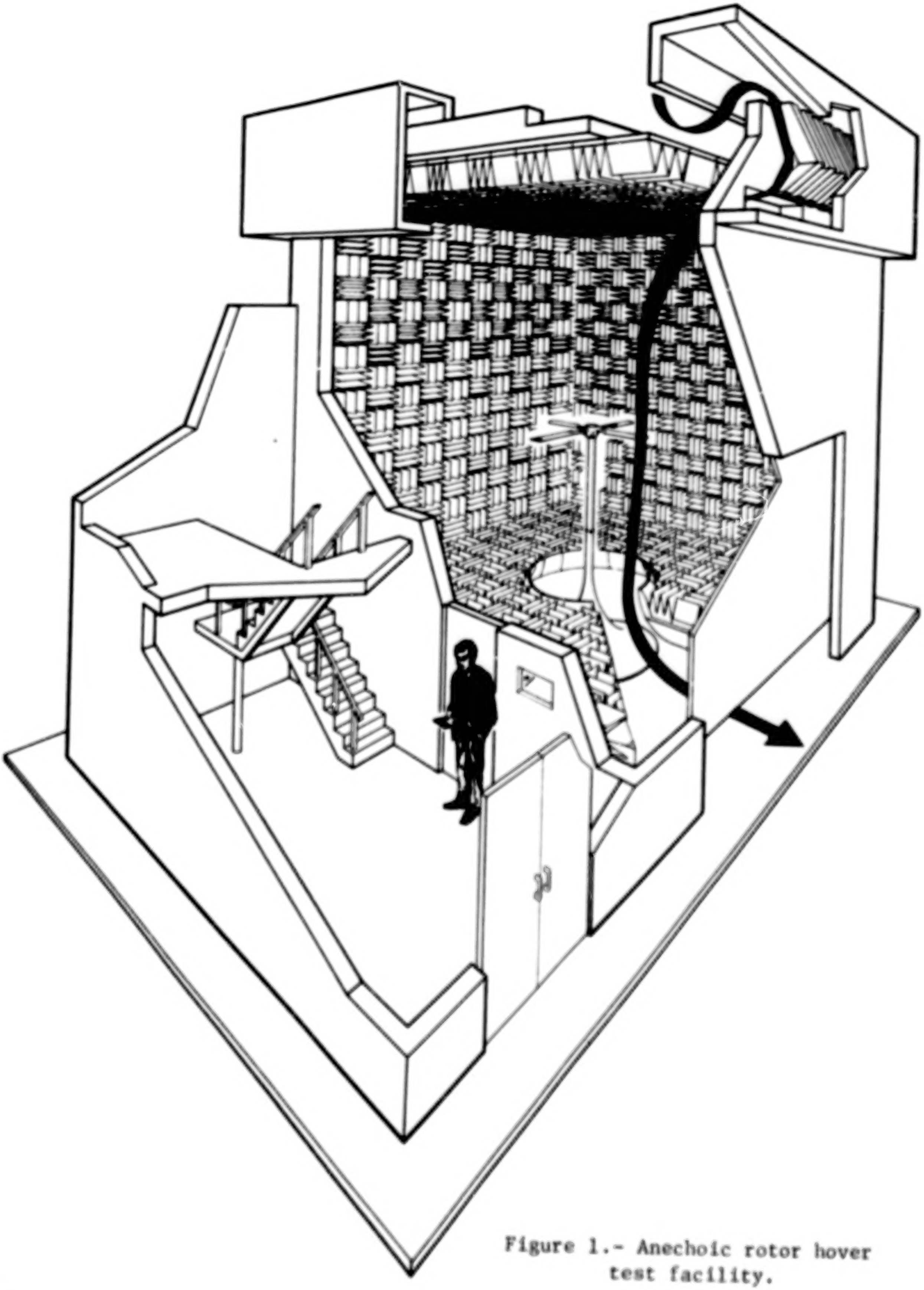

Figure 1.- Anechoic rotor hover test facility.

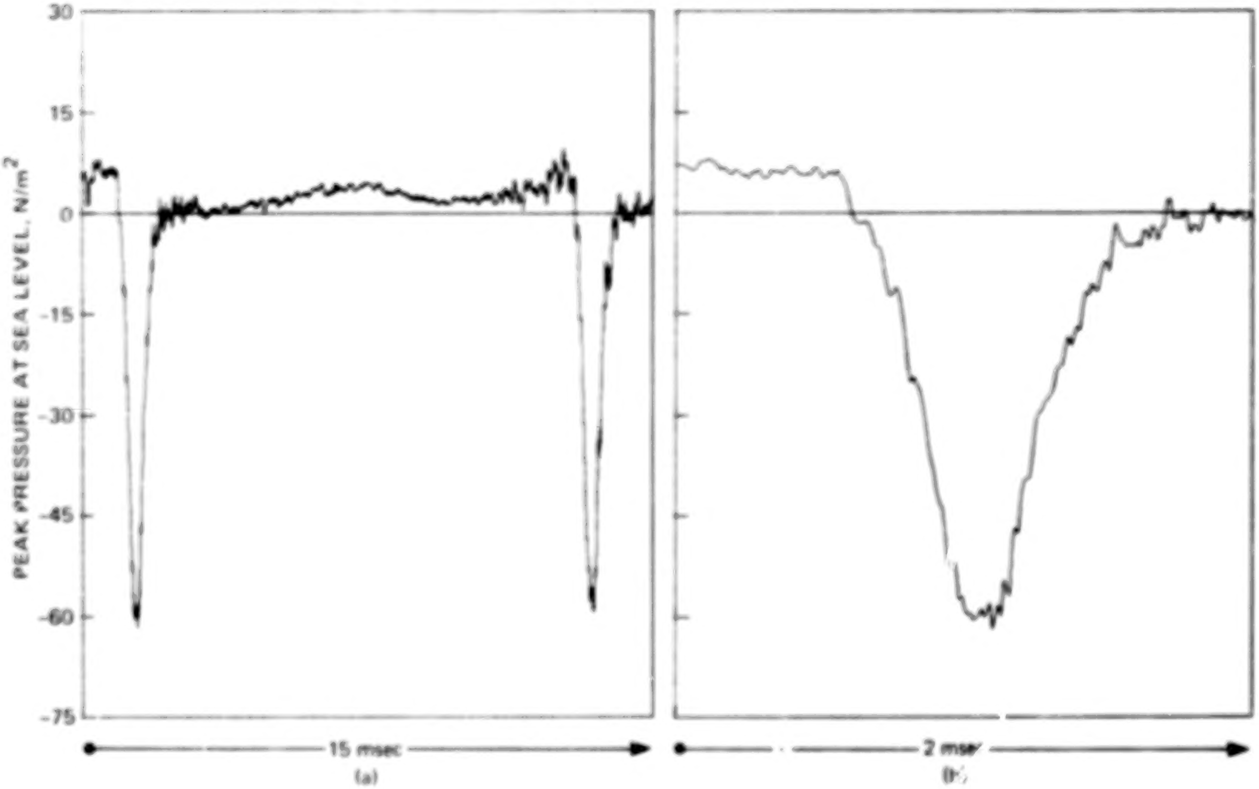

Figure 2.- Acoustic pressure-time history, in-plane, r/D = 1.5, M_T = 0.8.

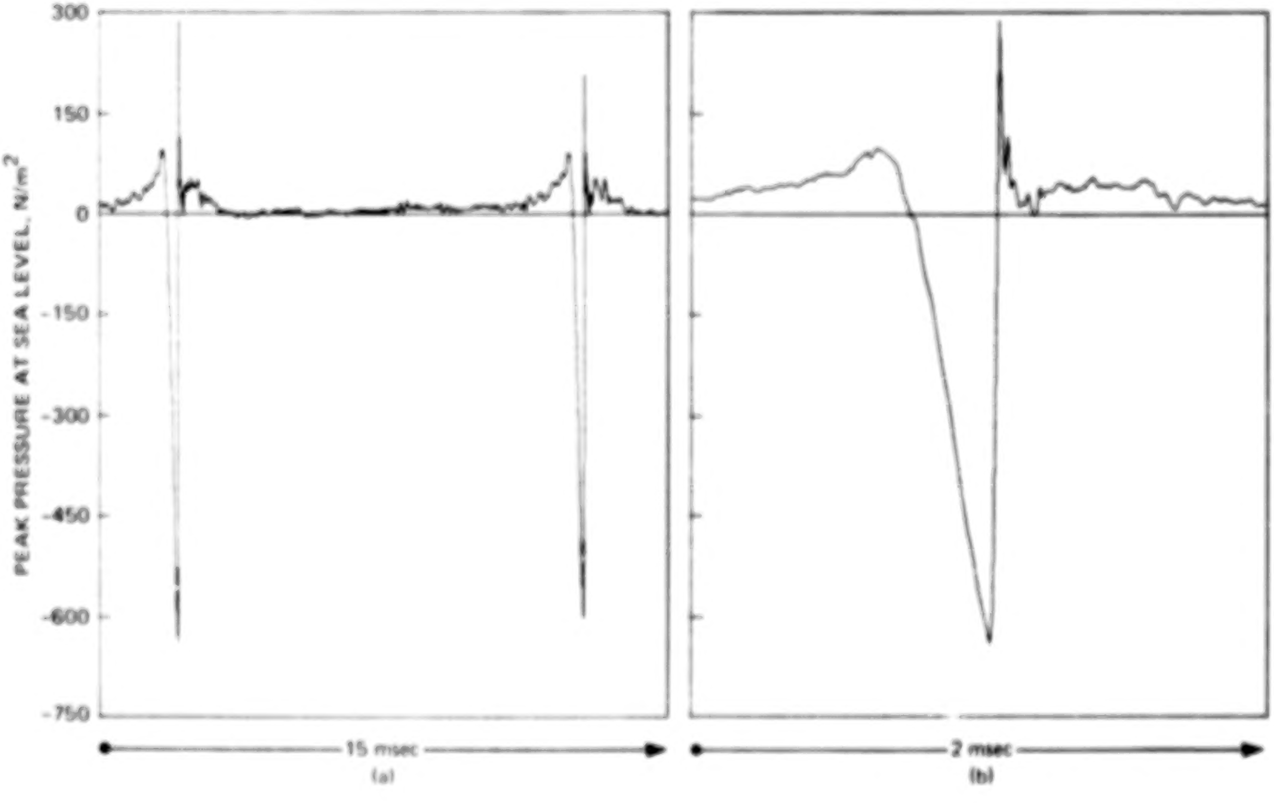

Figure 3.- Acoustic pressure-time history, in-plane, r/D = 1.5, M_T = 0.9.

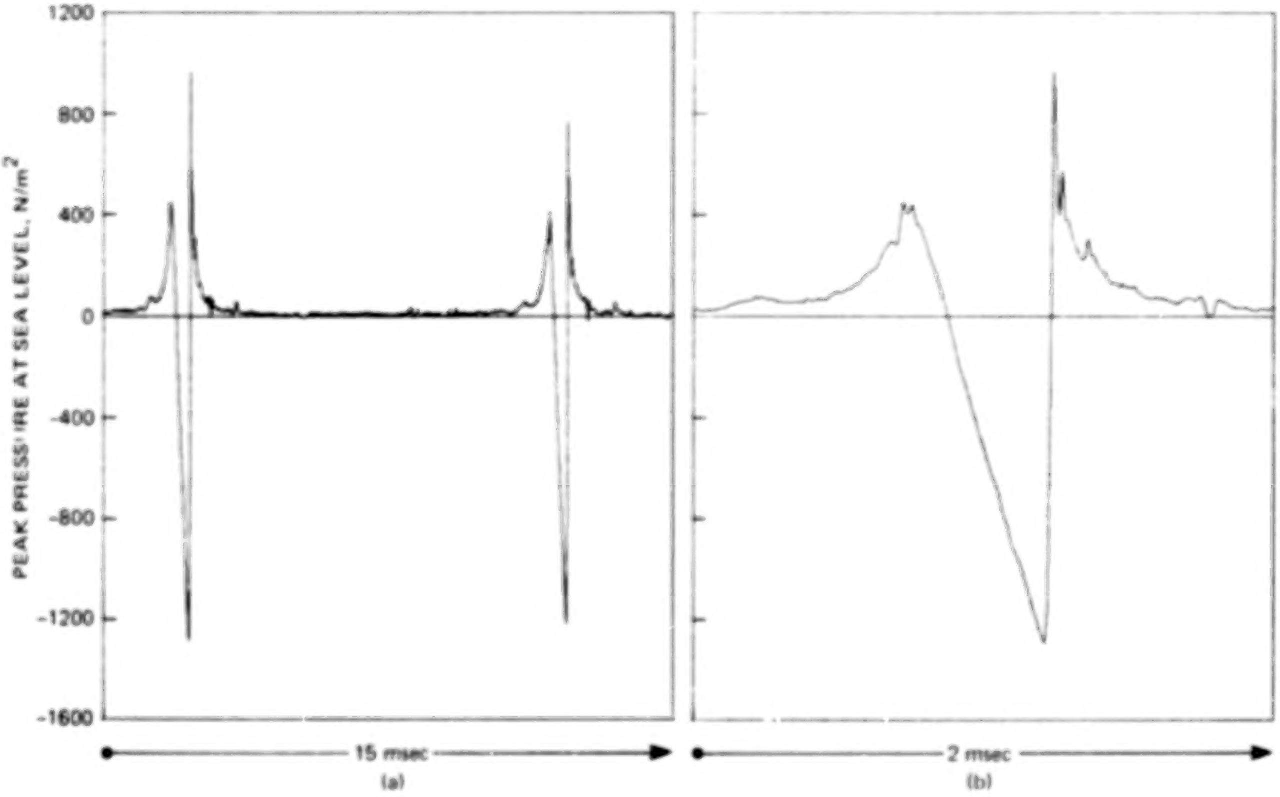

Figure 4.- Acoustic pressure-time history, in-plane, r/D = 1.5, M_T = 0.962.

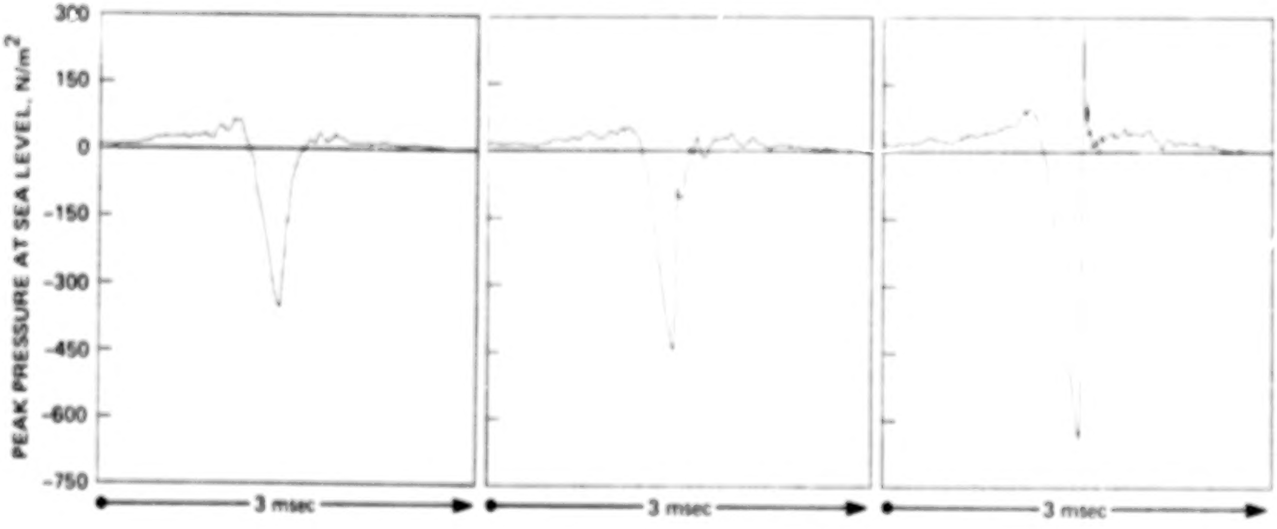

(a) M_T = 0.88. (b) M_T = 0.89. (c) M_T = 0.90.

Figure 5.- Waveform transition — the development of a radiating discontinuity, in-plane, r/D = 1.5, M_T = 0.88 to 0.90.

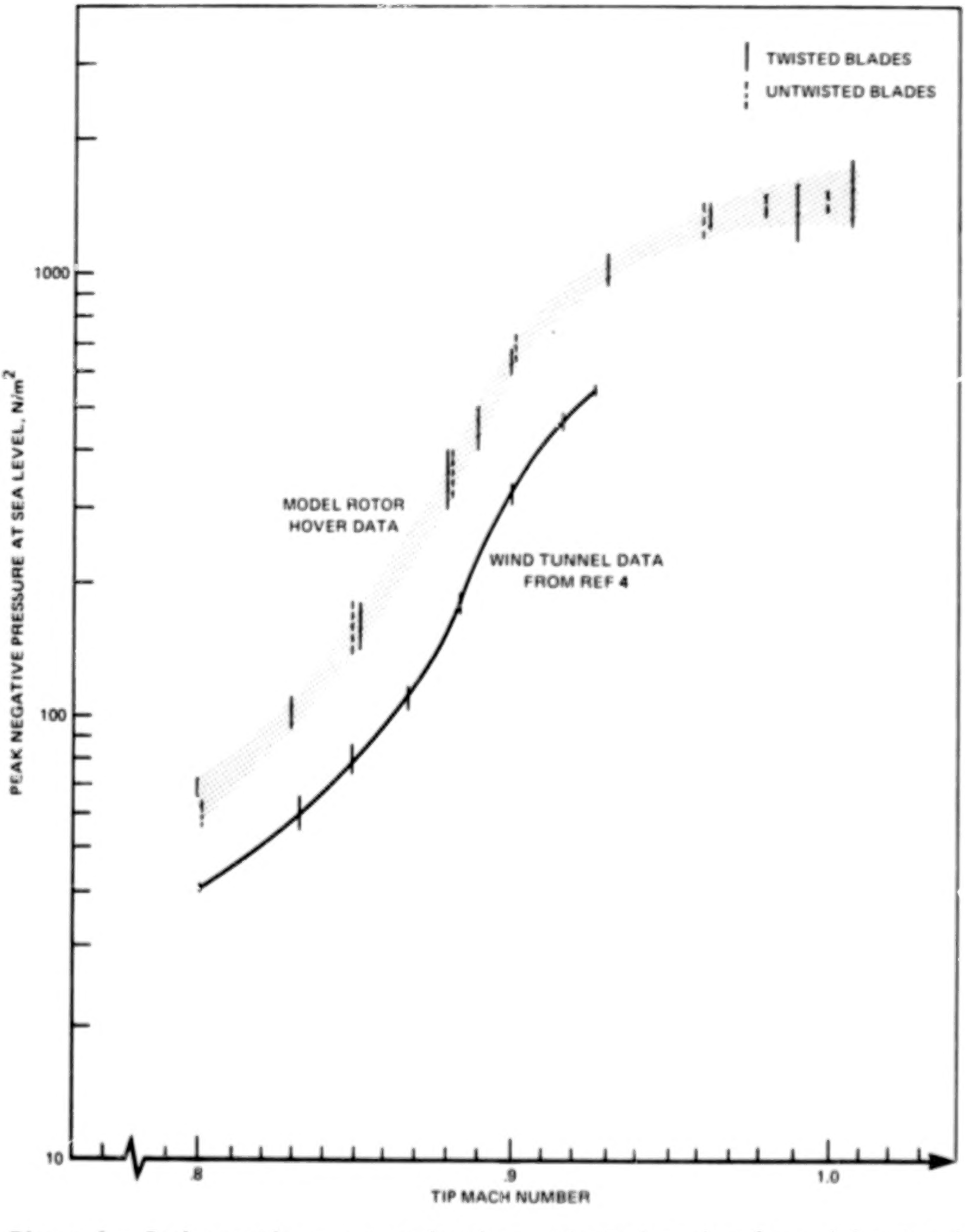

Figure 6.- Peak negative pressure level vs. tip Mach number for model rotor in hover and forward flight, in-plane, r/D = 1.5.

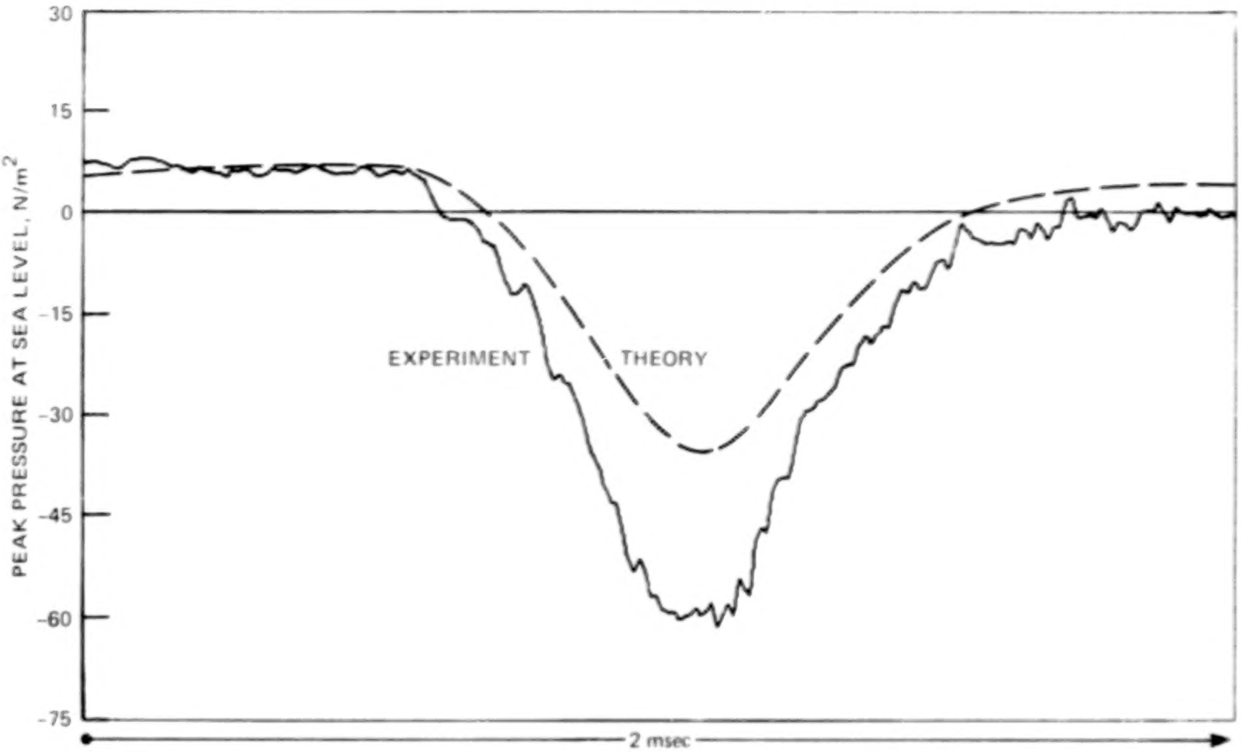

Figure 7.- Comparison of theory with experimental pressure-time history, in-plane, r/D = 1.5, M_T = 0.8.

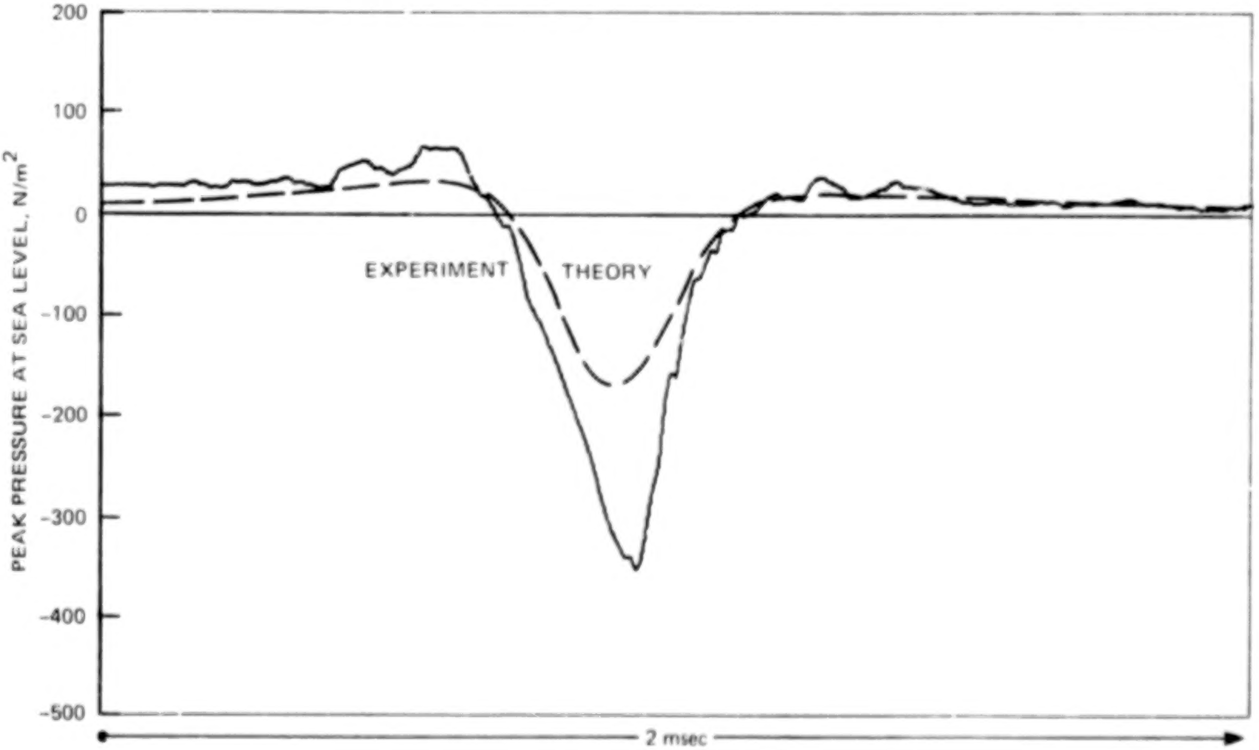

Figure 8.- Comparison of theory and experimental pressure-time history, in-plane, r/D = 1.5, M_T = 0.88.

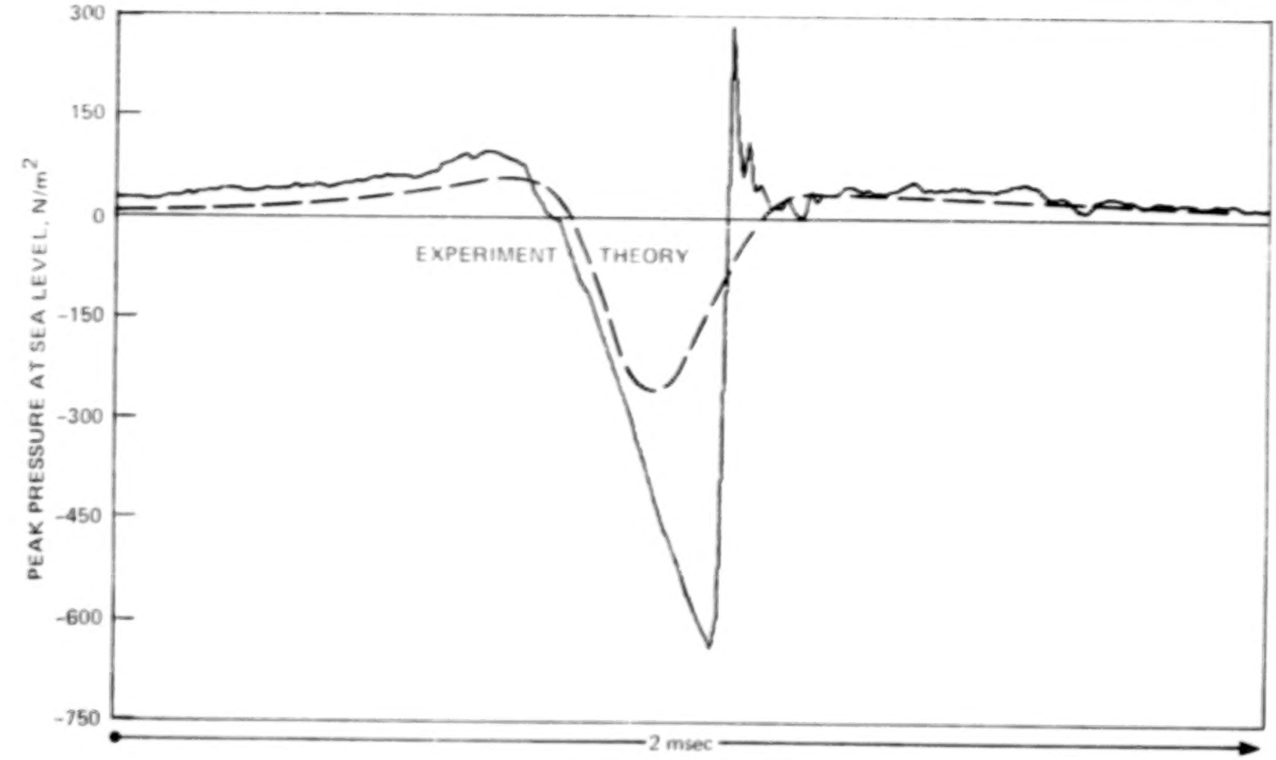

Figure 9.- Comparison of theory and experimental pressure-time history, in-plane, r/D = 1.5, M_T = 0.9.

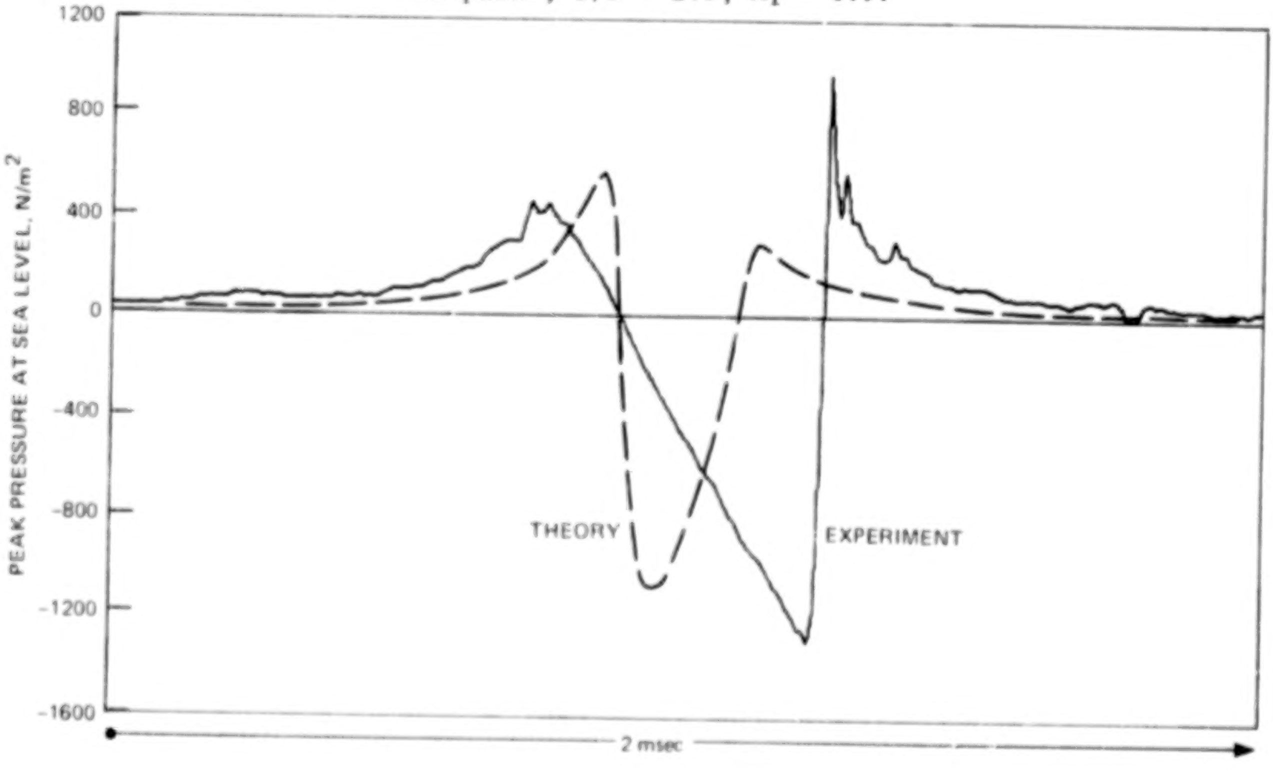

Figure 10.- Comparison of theory and experimental pressure-time history, in-plane, r/D = 1.5, M_T = 0.962.

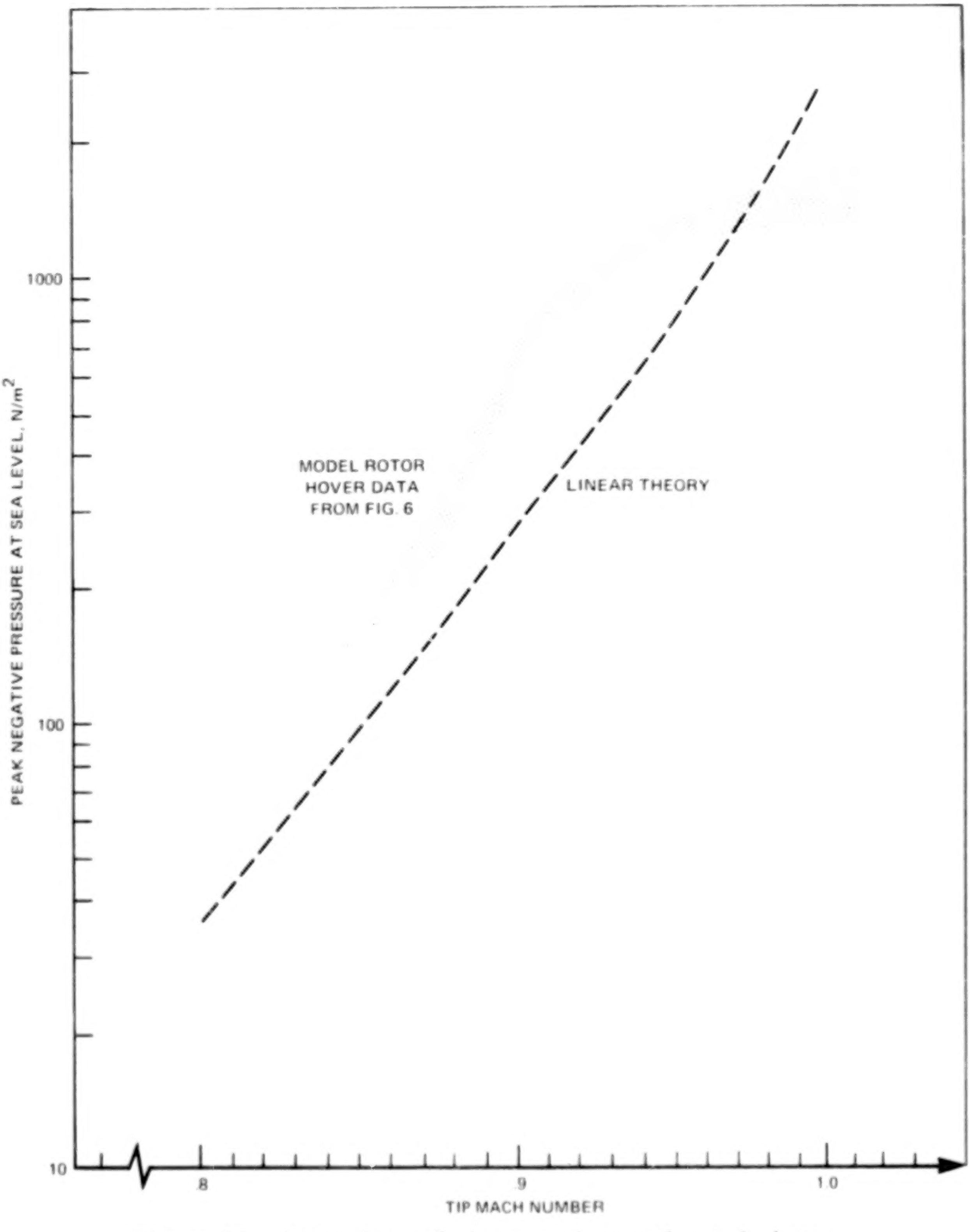

Figure 11.- Comparison of theory and experiment in hover, in-plane, r/D = 1.5.

IMPROVED METHODS FOR CALCULATING THE THICKNESS NOISE

Yoshiya Nakamura and Akira Azuma
University of Tokyo

SUMMARY

Three advanced methods to compute the rotor thickness noise which is predominant in the case of high speed rotor have been developed. These methods are deduced from a previous method by transforming the integral coordinate, commuting the order of integration and differentiation, and/or performing chordwise integration analytically with some adequate assumptions. The necessary computational times and waveforms obtained by the previous and three advanced methods were compared. It was then concluded that the advanced methods could save the computational time very much compared with the previous method in keeping the same accuracy.

INTRODUCTION

Farassat has proposed a method to calculate the thickness noise which is produced by moving bodies of finite volume or thickness normal to the moving direction and applied it to the rotor noise of helicopters (ref.1).

Based on his work, the authors made clear the cause and the characteristics of the rotor rotational noise. Through these studies (ref.2 and 3) with the concept of the "influential surface", which is an integral region at retarded time, and of the distribution of source strength, many acoustic characteristics of helicopter rotor noise have been clarified by the analytical predictions and numerical calculations, and verified by the experimental tests. It has been shown that among the rotor rotational noise components the rotor thickness effect executes a dominant roll rather than the loading effects such as thrust noise and drag noise in the case of high blade-tip speed.

In the computational process of the thickness noise, however, the calculation has the worst converging characteristics and thus needs a lot of computer time in getting solutions within enough accuracy. It has, therefore, been expected to develop an improved method of calculation for obtaining an advanced form of solution which is more convenient to get the result with less computer time and enough accuracy.

SYMBOLS

B	number of blades
c_0	sound speed, m/sec
C_h	chord length
$f=0$	equation of body surface
	$= \begin{cases} \eta_3 - h(\eta_1, \eta_2) & \text{at the upper surface} \\ -\eta_3 - h(\eta_1, \eta_2) & \text{at the lower surface} \end{cases}$
$g=0$	equation of acoustic sphere $= \tau - t + [r]_{ret}/c_0$
h	blade thickness, m
K	integrand of a modified solution of thickness noise, see equation (10)
M_r	relative Mach number
p	acoustic pressure, kg/m^2
R	rotor radius, m
R_0	blade cut-off radius, m
r	distance between source and observer, $=\lvert \mathbf{x} - \mathbf{y} \rvert$, m
r_0	distance between hub center and observer, m
$\hat{\mathbf{r}}_\eta$	unit vector in direction of propagation in blade fixed coordinate $\begin{cases} =(\hat{r}_{\eta_1}, \hat{r}_{\eta_2}, \hat{r}_{\eta_3})^T = (\partial r/\partial\eta_1, \partial r/\partial\eta_2, \partial r/\partial\eta_3)^T \\ =\left(\dfrac{r_1 \sin\psi - r_2 \cos\psi}{r}, 0, \dfrac{r_3}{r}\right)^T \end{cases}$
t	observer time
$\mathbf{V}$	rotor hub velocity, $=(V_1, V_2, V_3)^T$, m/sec
$\mathbf{V}_\eta$	$=(V_{\eta_1}, V_{\eta_2}, V_{\eta_3})^T$, m/sec
v_n	blade element velocity normal to blade surface, m/sec
$\mathbf{x}$	observer position vector, $=(x_1, x_2, x_3)^T$, m
$\mathbf{y}$	source position vector, $=(y_1, y_2, y_3)^T$, m

α	angle between radiating direction and rotor plane, rad or deg
Γ	curve of intersection of body with acoustic sphere
η	position vector in blade fixed Cartesian coordinate system
θ	angle between radiating direction and normal direction to blade surface, rad or deg
ρ	density of undisturbed fluid, kg·sec/m^4
τ	source time, sec
ψ	blade azimuth angle, rad or deg
Ω	rotor rotational speed, rad/sec
Λ	directional parameter in modified method, see equation (8)
λ	directional parameter in previous method, see equation (3)

Superscript

$(\ )^T$	transposed of ( )

Subscript

$[\ ]_{ret}$	value at a retarded time

Operator

∇	gradient operator in fluid fixed coordinate, $=\partial/\partial y_i$, 1/m

PREVIOUS ANALYSIS — METHOD (A)

According to Farassat (ref.1), the rotor thickness noise, p, for a given observer position, $\mathbf{x}$, and time, t, is given by

$$p\ (\mathbf{x},t) = \frac{\rho c_0}{2\pi}\ \frac{\partial}{\partial t}\int_{\tau_1}^{\tau_2}\int_{\Gamma}\frac{(\partial h/\partial \eta_1)V\eta_1}{r\lambda}\,d\Gamma d\tau \tag{1}$$

where $h(\eta_1)$ is the blade thickness distribution as a function of chordwise coordinate, η_1. Here the relative speed of a blade element with respect to the fluid and the directional parameter, λ, are respectively given by

$$V_{\eta_1} = V_1\sin\psi - V_2\cos\psi + \eta_2\Omega, \tag{2}$$

$$\lambda = |\nabla f|\sin\theta = |(-\partial h/\partial \eta_1,\ -\partial h/\partial \eta_2,\ \pm 1)^T|\sin\theta$$
$$= \{1-\hat{r}^2_{\eta_3}+(\partial h/\partial \eta_1)^2(1-\hat{r}^2_{\eta_1})\}^{1/2}, \qquad (3)$$

where r is the distance between the observer and the source, and ∇f means the vector outward normal to the blade surface. Other symbols related to the above equations are listed in SYMBOLS.

The integrations appearing in equation (1) may be understood as follows: In order to calculate the noise field of a moving source, the concept of retarded time designated by $[\ ]_{ret}$ must be considered, because the pressure change generated at different points and times might be received by an observer at a given time simultaneously. It is, thus, useful to know all regions of noise sources that have influence on the observer at the given time. These regions will be formed by the loci or trajectories of closed curves called "Γ-curves" for the given observer time and position with the change of the source time, $-\infty<\tau\leq t$.

An external surface of each region has been named "influential surface". All sources distributed on these surfaces must be integrated to give the instantaneous pressure of the given observer time and position. By considering the shape of the respective influential surface, many typical effects of various rotor operating parameters on each noise component have come to be predictable analytically (ref.2 and 3).

The integration $\int_{\tau_1}^{\tau_2}\int_\Gamma d\Gamma c_0 d\tau$ should be performed on the influential surfaces which are the loci of intersections between an "acoustic sphere," $g=t-\tau-[r]_{ret}/c_0=0$, and blade surfaces, $f(y,\tau)=0$, for a given observer time, t. The times specified by τ_1 and τ_2 are source times at which the acoustic sphere enters and leaves the blade respectively. With the lapse of the source time, the acoustic sphere contracts toward its center, just where the observer locates, with the speed of sound, c_0, while the blade rotates around the rotor axis. Fig.1 shows the geometric arrangements of an influential point. The influential point is given as the intersection between an acoustic line and a specified point, (η_1,η_2), on the i-th blade and is determined by the following equation:

$$F \equiv \cos\alpha\cdot(\eta_2\cos\psi-R)\Omega/c_0+\psi$$
$$-(\Omega t+2\pi(i-1)/B-\eta_1/\eta_2) = 0, \qquad (4)$$

where

$$0\leq\eta_1\leq C_h$$
$$R_0\leq\eta_2\leq R. \qquad (5)$$

The angular velocity of the influential point, $\partial\psi/\partial t$, which plays an important role in the noise calculation as will be stated later, can be derived by differentiating equation (4) as

$$\partial\psi/\partial t = \Omega/(1-M_r), \qquad (6)$$

where M_r is relative Mach number of the specified blade position with respect to an observer. Since M_r has positive peak at $\psi=90°$, $\partial\psi/\partial t$ takes maximum value at this azimuthal position.

In the numerical calculation by the previous method, factors which decide the precision level of calculation are: i) mesh dimension of the Simpson sum, ii) dimension of the observer time increment, iii) precision rank adopted in the computation. After some trial computations by using a computer, FACOM 230/75, it was concluded that the double precision was necessary and sufficient for the present calculation and that the number of integrating point for obtaining reliable results was about 10^4, which corresponded to the following dimension for one element: The tangential partition was (chord length)/20; the radial partition was (rotor radius)/300; and $\Delta\eta=0.16$. This mesh dimension required about twenty seconds to compute the total pressure value of a given observer time and position. Then it was decided that the number of discrete observer times in the one blade passing period was thirty six in order to give a total computational time within twenty minutes.

MODIFIED ANALYSES — METHODS (B) AND (C)

Undesirable defects on the accuracy in the previous computation were caused by the numerical differentiation, $\partial/\partial t$, and the numerical double integration on the influential surfaces, $\iint d\Gamma d\tau$. If the observer time differentiation, $\partial/\partial t$, can be put inside the integration, and be performed analytically, then the numerical differentiation will disappear and very much computational time can be saved.

In the previous analysis, the integration on the influential surface was performed along a contracting acoustic sphere, $d\Gamma d\tau$. Here, in the present analyses, by using a polar coordinate system associated with the rotor disk, an elemental area of the integration, $\eta_2 d\psi d\eta_2$, can be transformed as follows:

$$\frac{c_0 d\Gamma d\tau}{\lambda/|\nabla f|} = \frac{\eta_2 d\psi d\eta_2}{\Lambda} \tag{7}$$

where

$$\begin{aligned} \Lambda &= (1+M_n^2-2M_n\cos\theta)^{1/2} \\ M_n &= v_n/c_0 \\ v_n &= -\frac{\partial f}{\partial \tau}/|\nabla f| = \frac{\partial h}{\partial \eta_1} V\eta_1/|\nabla f|. \end{aligned} \tag{8}$$

Then, by using the above relation, the solution of wave equation of the rotor thickness noise can be rewritten in the new coordinate system as follows:

$$p(\mathbf{x},t) = \frac{\rho}{2\pi}\frac{\partial}{\partial t}\sum_{i}^{B}\int_{R_0}^{R}\left[\int_{\psi_2}^{\psi_1} K d\psi\right]_{ret} \eta_2 d\eta_2 \tag{9}$$

where

$$K = \frac{\partial h}{\partial \eta_1} V\eta_1 / r|\nabla f|\Lambda. \tag{10}$$

In the ranges of integrations, ψ_1 and ψ_2 are the azimuth angles of the leading edge and trailing edge of the influential surface respectively, which are functions of the span position, η_2, the observer time, t, and position, $\mathbf{x}$; and R and R_0 are the rotor radius and the blade cut-off radius respectively. The integrand, K, is considered to be a function of independent variable, η_1 or ψ, η_2, t, and $\mathbf{x}$. Thus, the double integration, $\iint \eta_2 d\psi d\eta_2$, gives an influential-surface integration of a single blade.

Fig.2 shows two different arrangements of integrating points on the same influential surface. It can be seen that the present methods have a well-fitting coordinate converging to the integral region. The method (B) is derived from equation (9) by performing numerically the differentiation and the integration.

By commuting the order of the differentiation and the integration, equation (9) becomes

$$p(\mathbf{x},t) = \frac{\rho}{2\pi}\sum_{i}^{B}\int_{R_0}^{R}\left[\int_{\psi_2(t)}^{\psi_1(t)} \frac{\partial K(\psi)}{\partial t}\bigg|_{\psi,\eta_2} d\psi - K(\psi_2)\frac{\partial \psi_2}{\partial t} + K(\psi_1)\frac{\partial \psi_1}{\partial t}\right]_{ret} \eta_2 d\eta_2, \tag{11}$$

where $\partial K(\psi)/\partial t$ should be considered as follows:

$$\begin{aligned}\frac{\partial K}{\partial t}\bigg|_{\psi,\eta_2} &= \left[\frac{\partial K}{\partial t}\bigg|_{\eta_1} + \frac{\partial K}{\partial \eta_1}\frac{\partial \eta_1}{\partial t}\right]_{\psi,\eta_2} \\ &= \left[\frac{\partial K}{\partial r}\frac{\partial r}{\partial t} + \frac{\partial K}{\partial \Lambda}\frac{\partial \Lambda}{\partial t}\right]_{\eta_1,\eta_2,\psi} + \left[\left(\frac{\partial K}{\partial(\partial h/\partial \eta_1)}\frac{\partial^2 h}{\partial \eta_1^2}\right.\right. \\ &\quad \left.\left. + \frac{\partial K}{\partial V_{\eta_1}}\frac{\partial V\eta_1}{\partial \eta_1} + \frac{\partial K}{\partial r}\frac{\partial r}{\partial \eta_1} + \frac{\partial K}{\partial|\nabla f|}\frac{\partial|\nabla f|}{\partial \eta_1} + \frac{\partial K}{\partial \Lambda}\frac{\partial \Lambda}{\partial \eta_1}\right)\frac{\partial \eta_1}{\partial t}\right]_{\eta_2,\psi} .\end{aligned} \tag{12}$$

The method (C) is derived from equation (11) by performing the numerical integration.

ANALYTIC METHOD — METHOD (D)

Consider the following case for simplicity of analysis:

(i) hovering state, $V_{\eta_1} = \eta_2 \Omega$ (13)

and

(ii) far field, $R << r$ that is $r = r_0 = \text{const.}$, $\Lambda = 1$, and $|\nabla f| = 1$.

Then the kernel given by equation (10) and the acoustic pressure can be written respectively as follows:

$$K = (\partial h/\partial \eta_1)\eta_2 \Omega / r_0 \tag{14}$$

and

$$\begin{aligned} p(x,t) &= \frac{\rho\Omega}{2\pi r_0}\int_{R_0}^{R} \eta_2^2 \left[\frac{\partial}{\partial t}\int_{\psi_2}^{\psi_1} \frac{\partial h}{\partial \eta_1} d\psi\right]_{\text{ret}} d\eta_2 \\ &= \frac{\rho\Omega}{2\pi r_0}\int_{R_0}^{R} \eta_2^2 \left[\int_{\psi_2}^{\psi_1} \left[\frac{\partial}{\partial t}\left(\frac{\partial h}{\partial \eta_1}\right)\right]_{\psi} d\psi + \frac{\partial h}{\partial \eta_1}\bigg|_{\psi_1} \frac{\partial \psi_1}{\partial t} - \frac{\partial h}{\partial \eta_1}\bigg|_{\psi_2} \frac{\partial \psi_2}{\partial t}\right]_{\text{ret}} d\eta_2 \\ &= \frac{\rho\Omega}{2\pi r_0}\int_{R_0}^{R} \eta_2^2 \left[\int_{\psi_2}^{\psi_1} \left(\frac{\partial^2 h}{\partial t \partial \eta_1} + \frac{\partial^2 h}{\partial \eta_1^2} \frac{\partial \eta_1}{\partial t}\bigg|_{\psi}\right) d\psi + \frac{\partial h}{\partial \eta_1}\bigg|_{\psi_1} \frac{\partial \psi_1}{\partial t} - \frac{\partial h}{\partial \eta_1}\bigg|_{\psi_2} \frac{\partial \psi_2}{\partial t}\right]_{\text{ret}} d\eta_2 . \end{aligned} \tag{15}$$

In a double parabolic airfoil, for example, the thickness change can be given by

$$\frac{\partial h}{\partial \eta_1} = \frac{2h_{max}}{C_h}\,(1 - 2\eta_1/C_h), \tag{16}$$

which is, at the leading edge, $\eta_1 = 0$ ($\psi = \psi_1$), and the trailing edge, $\eta_1 = C_h$ ($\psi = \psi_2$), given by

$$\frac{\partial h}{\partial \eta_1}\bigg|_{\psi_1} = -\frac{\partial h}{\partial \eta_1}\bigg|_{\psi_2} = \frac{2h_{max}}{C_h} . \tag{17}$$

Combining equations (16) and (4) yields

$$\frac{\partial h}{\partial \eta_1} = \frac{2h_{max}}{C_h} \left[1 - \frac{2\eta_2}{C_h} \left\{ \Omega t + \frac{2\pi}{B}(i-1) - \psi - \frac{\Omega}{c_0}(\eta_2 \cos\psi - R)\cos\alpha \right\} \right]. \tag{18}$$

By substituting the above two relations into equation (15), the acoustic pressure can be obtained in a decomposed form as follows:

$$p(x,t) = p_1(x,t) + p_2(x,t) + p_3(x,t)$$

where

$$\begin{aligned} p_1(x,t) &= \frac{\rho\Omega h_{max}}{\pi r_0 C_h} \int_{R_0}^{R} \eta_2^2 \left\{ - \frac{2\eta_2 \Omega}{C_h} (\psi_1 - \psi_2) \right\} d\eta_2 \\ p_2(x,t) &= \frac{\rho\Omega h_{max}}{\pi r_0 C_h} \int_{R_0}^{R} \eta_2^2 \dot{\psi}_1 \, d\eta_2 \\ p_3(x,t) &= \frac{\rho\Omega h_{max}}{\pi r_0 C_h} \int_{R_0}^{R} \eta_2^2 \dot{\psi}_2 \, d\eta_2 . \end{aligned} \tag{19}$$

As written above, the chordwise integration and the time differentiation have been performed analitically. Three components of equation (19) are corresponding to the first, second, and third terms of equation (11) exactly. An example of computed waveform is shown in Fig.3, in which solid lines show components of the respective term and a dotted line shows the total acoustic waveform obtained by summing up these three components.

As shown in Fig.4, the influential surfaces of multi-bladed rotor can be made from those of one blade at appropriate observer time. Then, once the sound pressure of one blade is computed, the acoustic pressure of the multi-bladed rotor can be easily obtained by summing up those of each blade one after another. Fig.5 shows an example of this process for three bladed rotor.

COMPUTATIONAL RESULTS

The dimensions of an exemplified rotor are given in Table I. The computational procedure is shown in Fig.6. Shown in Fig.7 is an example of the computed waveforms by four different methods, (A) through (D). It can be seen that these four methods give the very good coincidence in the waveform and the negative peak value, but a slight difference in the positive peak value. The difference between the waveforms of (B) and (C) is too small to be distinguished. It is interesting to note that the area made by the positive acoustic pressure and zero line in one period is equal to that made by the negative one.

Fig.8 shows the change of computed pressure amplitude in methods (B) and (C) in relation to the spanwise mesh size for a given chordwise mesh size by circles, and to the chordwise mesh size for a given spanwise mesh size by triangles. The difference of sensitivity of the accuracy for the number of spanwise and chordwise partitions are obvious. The insensitive tendency of the chordwise partition may result mostly from the blade contour of symmetric profile without singularity.

Fig.9 shows the computed pressure amplitudes or peak values of pressure versus the number of spanwise partitions in four methods. As the number of partitions increases the pressure converges to an expected true value whereas the computation time increases predominantly as shown in Fig.10. It can be seen that choice of proper coordinate, analytic chordwise integration, and the consequently simplified program used in the present methods saved the computational time significantly. This guarantees that the present methods (C) and (D) need respectively only one tenth and one hundredth of the computational time of the method (A) to get the acoustic pressure in the same accuracy.

CONCLUSION

Four different methods to compute the rotor thickness noise have been compared. They are (A) the previous method based on equation (1); (B) the one modified method based on equation (9) in which the surface integration is performed in the rotor-fixed-coordinate system; (C) the other modified method based on equation (11) in which the numerical differentiation is discarded; (D) the still other modified method based on equation (19) in which the numerical chordwise integration is further discarded. All methods have shown the good coincidence in both the waveform and the peak amplitude.

The introduction of the rotor-fixed-polar-coordinate system has brought better characteristics in convergence and accuracy of the numerical integration than the previous method (A) in which the observer-fixed-polar-coordinate system was adopted. Specifically, the method (D), in which the chordwise integration was performed analytically by assuming the hovering state of rotor and the far field location of observer, has saved further computational time. The computational time in the method (D) was only one hundredth of method (A) and one tenth of methods (B) and (C) in keeping the same accuracy. It can, thus, be concluded that the computing method of the rotor thickness noise was improved very much by introducing the advanced methods (C) and (D) in the accuracy and speed.

REFERENCES

1. Farassat, F.: Theory of Noise Generation From Moving Bodies With an Application to Helicopter Rotors, NASA TR R-451, Dec. 1975.

2. Nakamura, Y.: Helicopter Noise. PhD Thesis, University of Tokyo, March, 1977.

3. Nakamura, Y.: The Analysis of Helicopter Rotor Noise, ISAS Report No. 549 (Vol. 42, No. 4), Institute of Space and Aeronautical Science, University of Tokyo, Sept. 1977.

TABLE I

Dimensions:

Rotor radius; R, m	5.0
Blade cut off; R_0,m	0.7
No. of blades; B	2
Blade chord ; C_h, m	0.4
Blade thickness ratio; h_{max}/C_h	0.10
Airfoil section	NACA 0010

Operating conditions:

Forward speed; V, m/sec	0 (hovering)
Tip Mach number; M_t	0.9

Observer:

Observer position; r_0,m	50
Observer elevation angle;α_0,deg	0

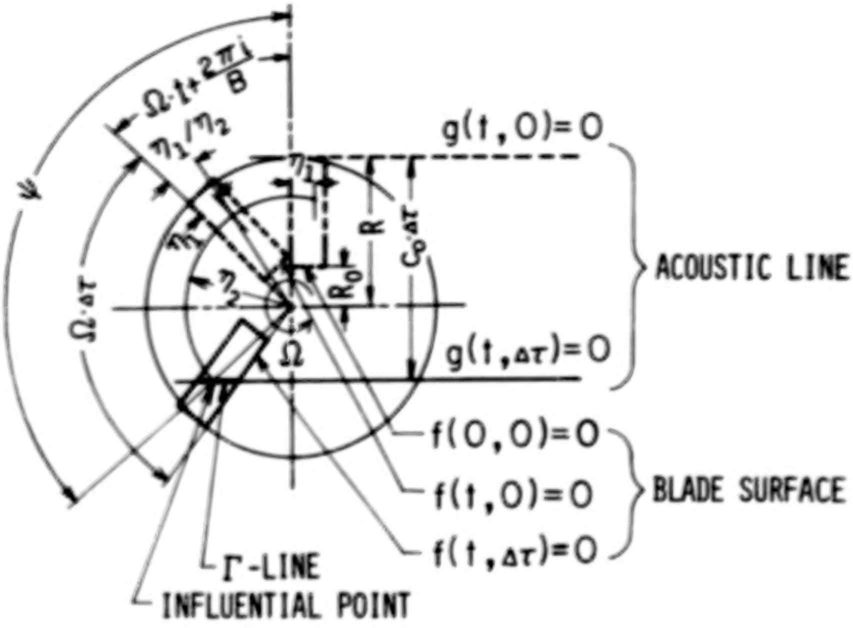
Ω·t+2πi/B
η₁/η₂
ψ
Ω·Δτ
η₁
η₂
R
R₀
c₀·Δτ
Ω
g(t,0)=0
g(t,Δτ)=0
ACOUSTIC LINE
f(0,0)=0
f(t,0)=0
f(t,Δτ)=0
BLADE SURFACE
Γ-LINE
INFLUENTIAL POINT

$$F = \cos\alpha(\eta_2\cos\psi - R)\Omega/c_0 + \psi - (\Omega t + 2\pi i/B - \eta_1/\eta_2) = 0$$

Figure 1.- Geometric arrangements of an influential point.

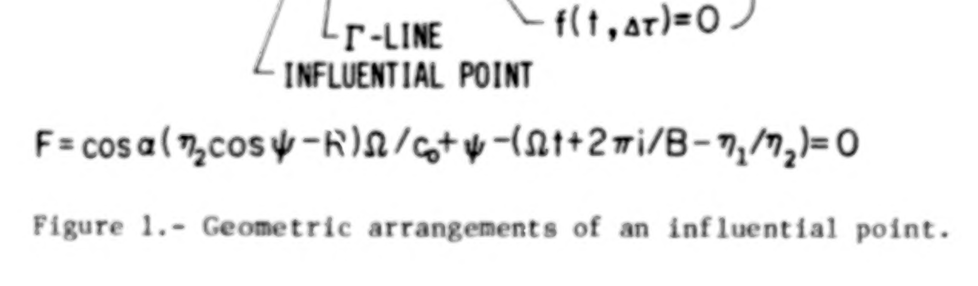
dη₁
dη₂
INTEGRATING POINTS
INFLUENTIAL SURFACE
BLADE TIP
LEADING EDGE
TRAILING EDGE
R₀
Ω
R
dΓ
c₀·dτ
ACOUSTIC LINES
Ω
LINES OF INSIGHT FROM OBSERVER

(a) Present methods. (b) Previous method.

Figure 2.- A comparison of integrating mesh between two coordinate systems

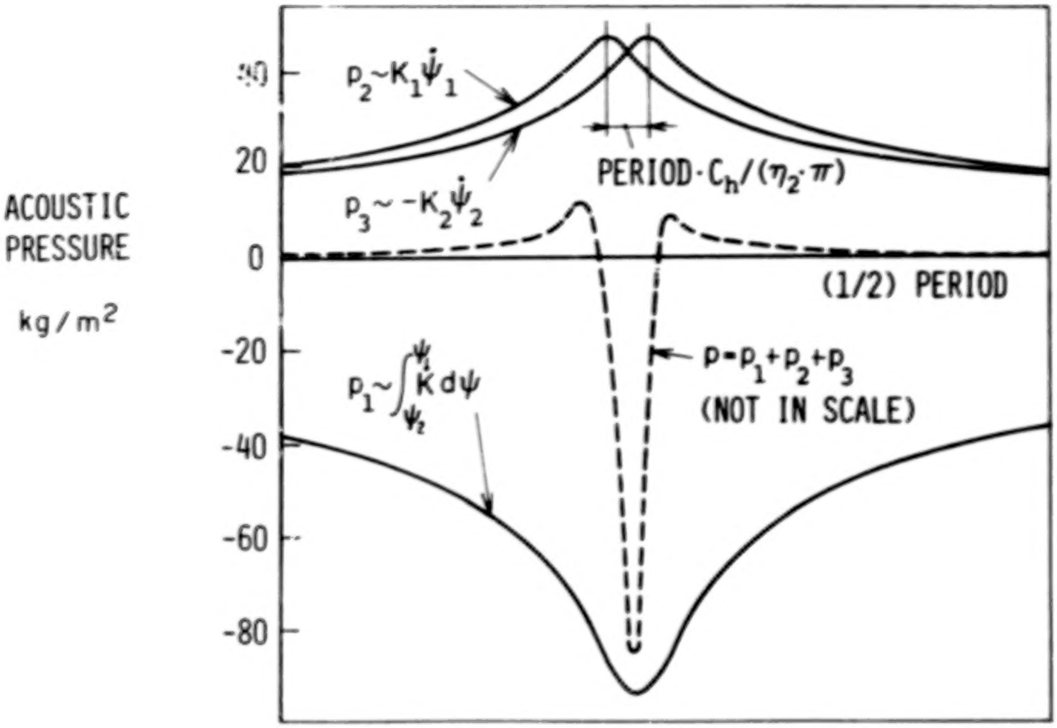

Figure 3.- Computation of waveform.

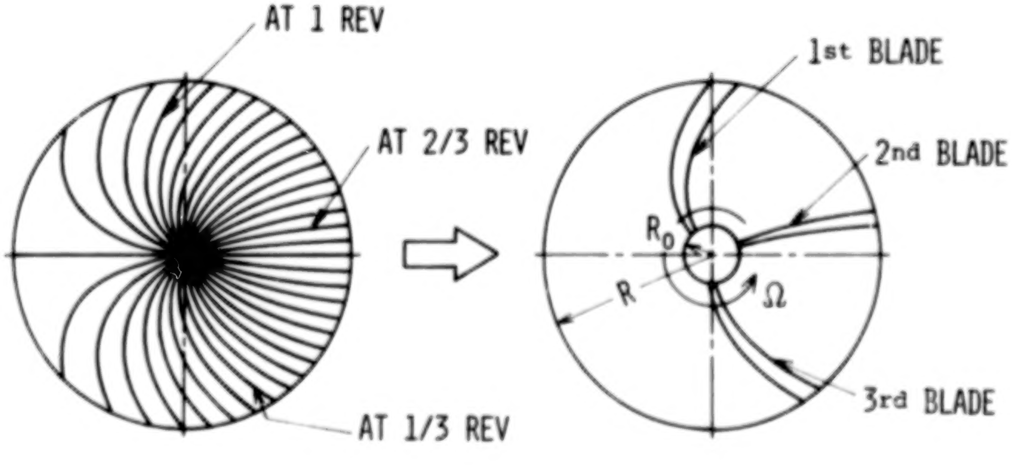
AT 1 REV
AT 2/3 REV
AT 1/3 REV
1st BLADE
2nd BLADE
3rd BLADE
R_0
R
Ω

(a) Influential lines of leading edge of one blade at each observer time.

(b) Influential surfaces of three bladed rotor at given observer time.

Figure 4.- An example to obtain influential surfaces of multi-bladed rotor from influential lines.

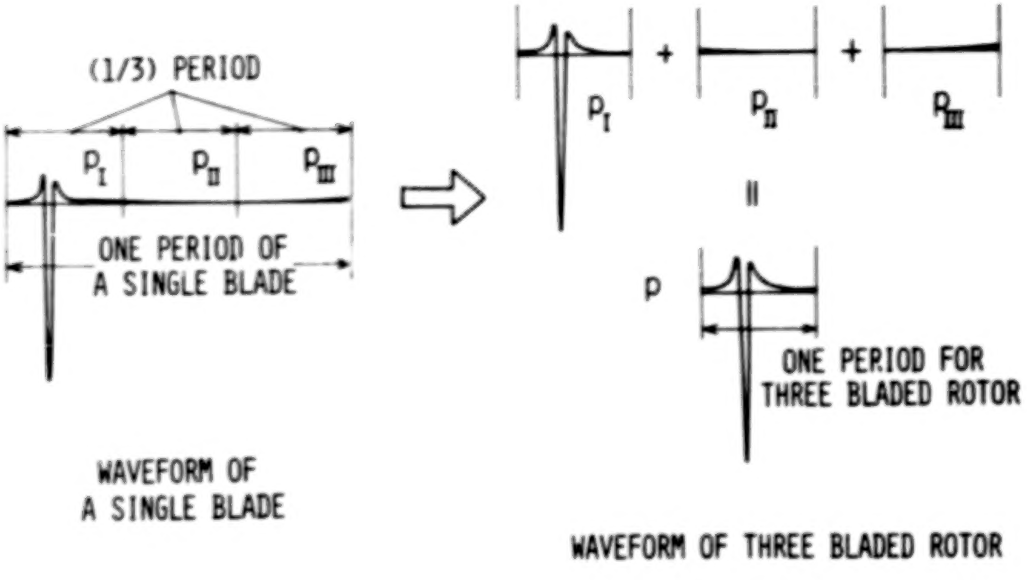

(1/3) PERIOD
P_I
P_II
P_III
ONE PERIOD OF A SINGLE BLADE
WAVEFORM OF A SINGLE BLADE
P_I
+
P_II
+
P_III
=
P
ONE PERIOD FOR THREE BLADED ROTOR
WAVEFORM OF THREE BLADED ROTOR

Figure 5.- An example to obtain waveform of multi-bladed rotor from a waveform of single blade.

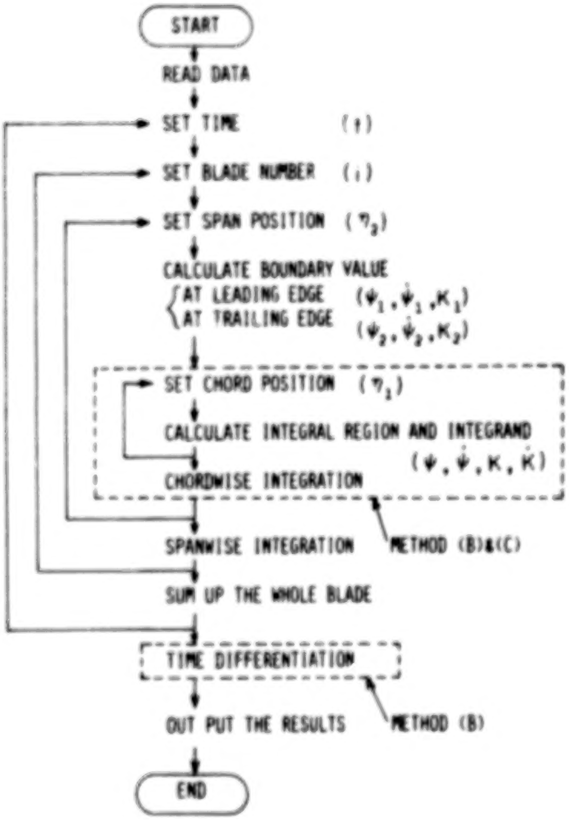

START
READ DATA
SET TIME (t)
SET BLADE NUMBER (i)
SET SPAN POSITION (η₂)
CALCULATE BOUNDARY VALUE
AT LEADING EDGE (ψ₁, ψ̇₁, κ₁)
AT TRAILING EDGE (ψ₂, ψ̇₂, κ₂)
SET CHORD POSITION (η₁)
CALCULATE INTEGRAL REGION AND INTEGRAND (ψ, ψ̇, κ, κ̇)
CHORDWISE INTEGRATION
SPANWISE INTEGRATION
METHOD (B)&(C)
SUM UP THE WHOLE BLADE
TIME DIFFERENTIATION
OUT PUT THE RESULTS
METHOD (B)
END

Figure 6.- Flowchart of modified mehtods to compute the rotor thickness noise.

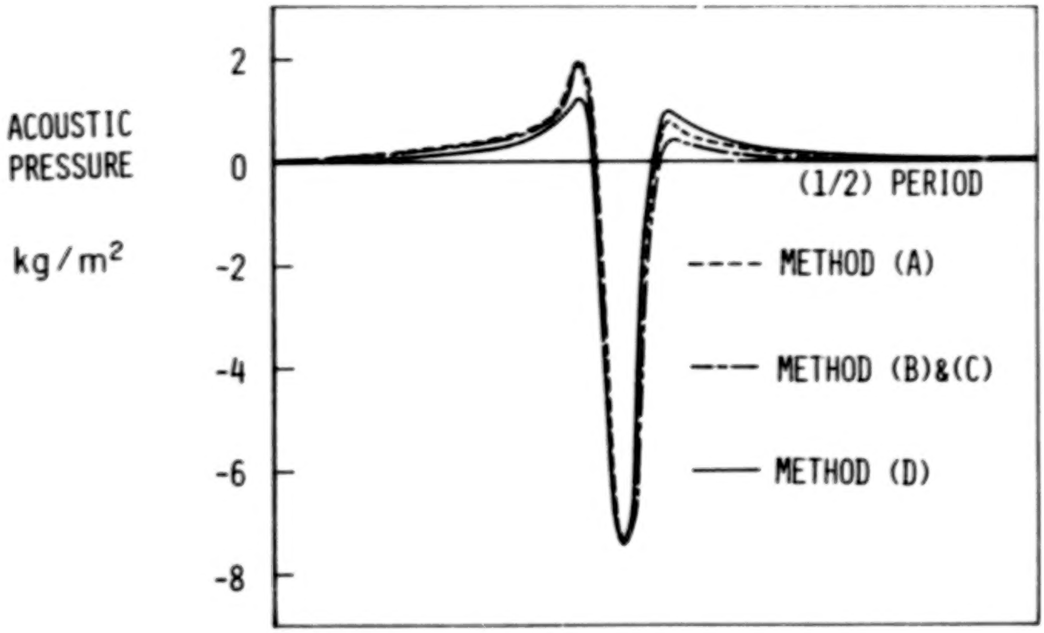

Figure 7.- Waveforms given by four methods.

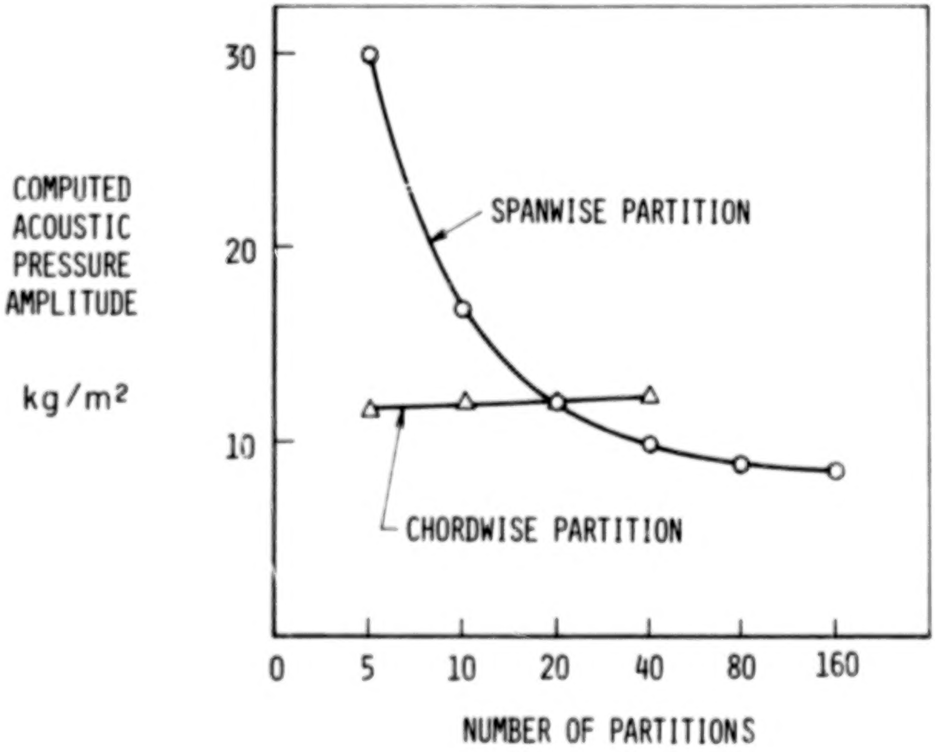

Figure 8.- Converging tendency with the number of partitions.

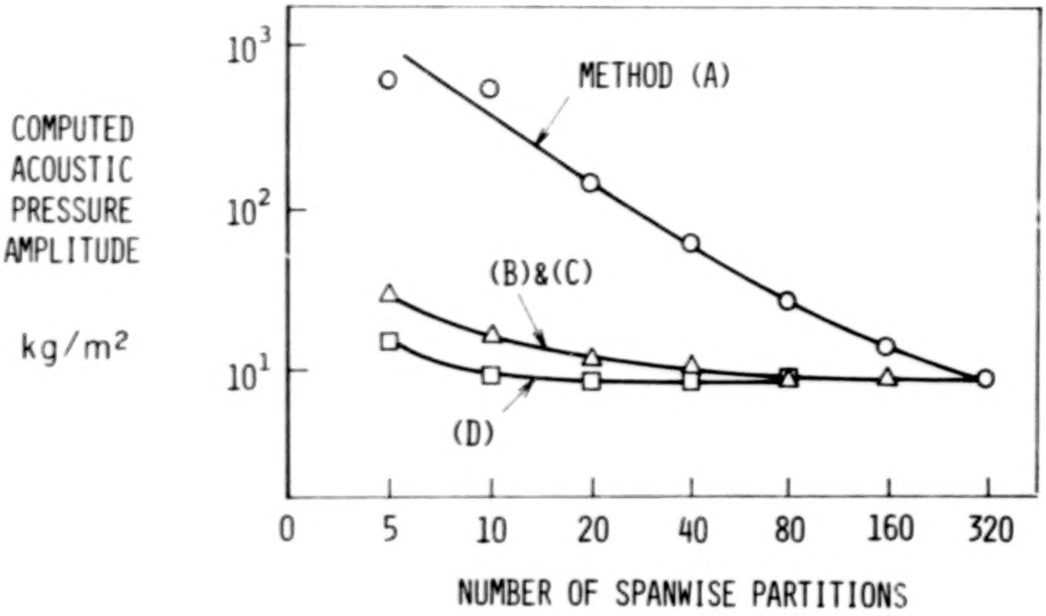

Figure 9.- Converging tendency of the four methods.

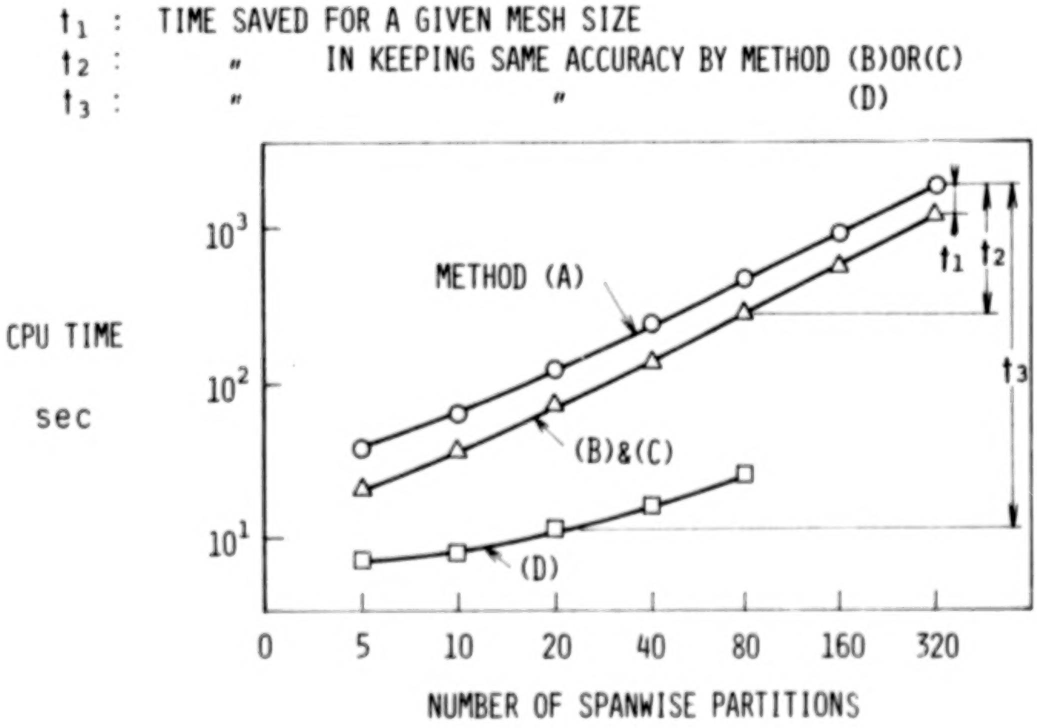

Figure 10.- A comparison of computational time between four methods.

Blank Page

THE IMPORTANCE OF QUADRUPOLE SOURCES IN PREDICTION OF TRANSONIC TIP SPEED PROPELLER NOISE

Donald B. Hanson
Hamilton Standard Division of United Technologies Corporation

Martin R. Fink
United Technologies Research Center

SUMMARY

A theoretical analysis is presented for the harmonic noise of high speed, open rotors. Far field acoustic radiation equations based on the Ffowcs-Williams/Hawkings theory are derived for a static rotor with thin blades and zero lift. Near the plane of rotation, the dominant sources are the volume displacement and the ρu^2 quadrupole, where u is the disturbance velocity component in the direction of blade motion. These sources are compared in both the time domain and the frequency domain using two-dimensional airfoil theories valid in the subsonic, transonic, and supersonic speed ranges. For nonlifting parabolic arc blades, the two sources are equally important at speeds between the section critical Mach number and a Mach number of one. However, for moderately subsonic or fully supersonic flow over thin blade sections, the quadrupole term is negligible. It is therefore concluded for thin blades that significant quadrupole noise radiation is strictly a transonic phenomenon and that it can be suppressed with blade sweep. Noise calculations are presented for two rotors, one simulating a helicopter main rotor and the other a model propeller tested at United Technologies Corporation. For the latter, agreement with test data was substantially improved by including the quadrupole source term.

INTRODUCTION

In the 1970's there has been a renewed interest in noise of open rotors, not only for helicopter application, but because of a development program in the United States for fuel conservative propulsion systems. Ffowcs-Williams and Hawkings provided a theoretical basis (ref. 1) for analyzing this type of problem by showing that, in principle, the noise can be calculated exactly if certain aerodynamic quantities (source

---

This paper was originally presented at the Spring Meeting of the Institute of Acoustics, Cambridge University, Cambridge, England, April 7, 1978. The manuscript has been submitted for possible publication in the Journal of Sound and Vibration and is reproduced herein by permission of the editor of that journal.

terms) are known on and around the blades. The surface sources are the volume displacement and the blade surface forces. The volume sources are quadrupole terms representing shear stress in the air. The propeller noise problem is an ideal application of the theory because the blades are thin and, in forward flight, the sources are essentially steady in the blade coordinate system.

Because the surface source terms are linear, considerable progress has been made in developing techniques for computing their noise (refs. 2, 3, 4). However, the quadrupoles have been neglected because they are second order in the disturbance velocities, which makes them appear small. This appeared justified because the linear theories worked reasonably well for moderate speed propellers. Also, sonic boom theory, which uses only the linear volume displacement and loading sources, is successful at supersonic aircraft speeds. However, Kitaplioglu and George (ref. 5) remarked in a recent paper that the linear theories consistently underpredict noise from rotors operating at the transonic speeds which are currently of interest. An example of this is the transonic propeller in figure 1 which was run at United Technologies Research Center. Figure 2 shows test versus linear theory from ref. 4. Maximum noise along the fuselage occurs near the plane of rotation, where noise levels predicted from the surface sources are as much as 5 dB lower than the data. After considering other mechanisms, the quadrupole source was investigated as an explanation for this underprediction.

The purpose of this report is to illustrate the role of the quadrupole sources in noise radiation from open rotors using the simplest possible meaningful example. To accomplish this, far field radiation equations are derived for a static, nonlifting rotor. The equations are cast into a form which permits direct comparison of the volume displacement and quadrupole sources inside the radiation integrals. The source terms are then evaluated using aerodynamic techniques which are valid through the subsonic, transonic, and supersonic ranges. Finally, some sample noise calculations are presented.

SYMBOLS

b	airfoil chord
B	number of blades
$B_D \equiv b/D$	chord-to-diameter ratio
c_o	ambient speed of sound
D	propeller diameter
f_i	i^{th} component of force/unit area exerted by airfoil on fluid
G	Green's function (eq. 2)
h	thickness distribution (figure 3)

H	h/b, normalized thickness distribution (figure 4)
i, j	1, 2, 3 Cartesian coordinate indices
J_n	Bessel function
k	specific heat ratio, 1.4 for air
m	harmonic of blade passing frequency
M_r	$\Omega \frac{r_o}{c_o}$, section relative Mach number
M_T	$\Omega \frac{r_T}{c_o}$, tip rotational Mach number
n	mB, harmonic of shaft frequency
p	acoustic pressure
P_n	complex Fourier coefficient of p
P_{Vn}	volume displacement portion of P_n
P_{Qn}	quadrupole portion of P_n
r	distance from origin to observer point
r_o	distance from origin to source point on blade
r_T	propeller tip radius, $D/2$
R	$\left\| \vec{x} - \vec{y} \right\|$, distance from source point to observer
S	source surface in eq. 1
t	observer time
T	integration limit for source time (τ) integration
T_{ij}	$\rho u_i u_j$, quadrupole (shear stress) source
u	component in chordwise direction of disturbance velocity
u_i	component in i^{th} direction of disturbance velocity
U	Ωr_o, local blade section speed
v	component normal to chord of disturbance velocity
V_n	normal component of airfoil surface velocity
$\vec{x}$	$(x, y, 0)$, observer coordinates (figure 3)
X	γ/b, normalized chordwise coordinate
y	observer distance from propeller axis (figure 3)
y_i	source coordinates y_1, y_2, y_3

Y	ξ/b, normalized coordinate perpendicular to chord and to radius
Z	$\frac{r_\circ}{r_T}$, normalized radial coordinate
ξ	source coordinate normal to chord (figure 3)
γ	source coordinate in chordwise direction (figure 3)
δ	Dirac delta (impulse) function
θ	angle from propeller axis to observer point
ν	source volume (volume exterior to blades)
ρ	density
$\rho_\circ$	ambient density
τ	source time variable
Ψ_V	integrated volume displacement source strength in frequency domain (eqs. 31, 34)
Ψ_{ij}	integrated quadrupole strength in frequency domain (eq. 33)
Ψ_{11}	integrated strength of ρu^2 quadrupole in frequency domain
ω	radian frequency of sound
Ω	2π times shaft rotation frequency

$\rightarrow$ indicates vector, as in $\vec{x}$

$'$ indicates differentiation with respect to argument, as in h'

ACOUSTIC THEORY

The starting point for the analysis is Goldstein's version of the acoustic analogy (eq. 3.6, ref. 6) from which the Ffowcs-Williams/Hawkings formulas (ref. 1) can be derived:

$$\begin{aligned}\rho'(\vec{x},t) = {} & \frac{1}{c_\circ^2}\int_{-T}^{T}\int_{S(\tau)}\left(-\rho_\circ V_n \frac{\partial G}{\partial \tau} + f_i \frac{\partial G}{\partial y_i}\right) dS(\vec{y})\, d\tau \\ & + \frac{1}{c_\circ^2}\int_{-T}^{T}\int_{\nu(\tau)} T_{ij}\, \frac{\partial^2 G}{\partial y_i\, \partial y_j}\, d\vec{y}\, d\tau \end{aligned} \tag{1}$$

This equation gives the disturbance density ρ' exactly for known values of the source terms. The sources to be evaluated on the moving surface $S(\tau)$ are the normal surface velocity V_n (taken to be positive outward, the opposite of Goldstein's convention) and the surface force components f_i. The quadrupole source is the

Lighthill stress tensor T_{ij} which is to be evaluated in the volume around the blades $\nu(\tau)$. The source time (τ) integration is over a range $-T \leq \tau \leq T$ large enough to include all signals from the source region which arrive at the observation point at time t. G is the Green's function

$$G = \frac{\delta(t-\tau-R/c_\circ)}{4\pi R} \tag{2}$$

where $R = |\vec{x} - \vec{y}|$ is the distance between source point $\vec{y}$ and observer point $\vec{x}$.

For a thin, nonlifting propeller blade, the surface forces f_i can be neglected. Also, we make the usual approximations that the acoustic pressure

$$p = c_\circ^2 \ \rho' \tag{3}$$

where $c_\circ$ is the ambient sound speed and

$$T_{ij} = \rho u_i u_j \tag{4}$$

where ρ is the density and u_i is the disturbance velocity component in the i^{th} direction. The pressure term in T_{ij} is neglected for now but can be added at any time in the analysis. For the static propeller, we approximate the Cartesian source coordinates with locally orthogonal curvilinear coordinates as shown in figure 3:

$$y_1 = \gamma \qquad y_2 = \xi \qquad y_3 = r_\circ$$

The observer coordinates are x, y, 0.

The distance R is given by

$$R = \sqrt{(x+\xi)^2 + y^2 + r_\circ^2 - 2yr_\circ \cos\left(\frac{\gamma}{r_\circ}\right)} \tag{6}$$

In the far field Green's function

$$G = \frac{\delta(t-\tau-R/c_\circ)}{4\pi r} \tag{7}$$

only the terms of order ξ/r and $r_\circ/r$ in a series expansion of R are retained, giving

$$R \rightarrow r + \xi \cos\theta - r_\circ \sin\theta \cos\left(\frac{\gamma}{r_\circ}\right) \tag{8}$$

where θ is the angle of the observer from the propeller axis.

Since the blades of interest are thin, we consider the surface sources to act on the mean chord line $\xi = 0$ and neglect the volume occupied by the blade. This is easily justified, for example, with blades 2% thick and a 0.15 chord-to-diameter ratio operating at a tip Mach number of 1.0 because the maximum error in point of action of the sources is less than the wavelength of the 2000th harmonic of shaft rotation frequency. To evaluate the surface integral at $\tau = 0$, we note that $V_n \, dS = \frac{1}{2} U \, h'(\gamma) \, d\gamma \, dr_\circ$ for each surface of the airfoil. Here $U = \Omega r_\circ$ is the local blade section speed, $h(\gamma)$ is the airfoil thickness distribution shown in figure 3, and the prime on h denotes differentiation with respect to the argument. The only time dependence of the sources considered here is that due to convection at speed U in the negative γ direction, so the source behavior is given simply by $h(\gamma + U\tau)$ and $T_{ij}(\gamma + U\tau)$.

From these arguments, eq. 1 reduces to

$$p(\vec{x}, t) = \int_{-\infty}^{\infty} \int_{0}^{r_T} \int_{-\pi r_\circ}^{\pi r_\circ} -\rho_\circ U h'(\gamma + U\tau) \frac{\partial G}{\partial \tau} \, d\gamma \, dr_\circ \, d\tau$$

$$+ \int_{-\infty}^{\infty} \int_{0}^{\infty} \int_{-\pi r_\circ}^{\pi r_\circ} \int_{-\infty}^{\infty} \left[T_{11}(\gamma + U\tau) \frac{\partial^2 G}{\partial \gamma^2} + 2 T_{12}(\gamma + U\tau) \frac{\partial^2 G}{\partial \gamma \partial \xi} + T_{22}(\gamma + U\tau) \frac{\partial^2 G}{\partial \xi^2} \right] d\xi \, d\gamma \, dr_\circ \, d\tau \tag{9}$$

where the integrations over upper and lower airfoil surfaces are lumped together using γ as an integration parameter and r_T is the blade tip radius. T has been set to ∞, assuming the τ integrals will converge. The sum on i and j has been performed neglecting any radial velocity disturbances so that the remaining quadrupole sources are

$$T_{11} = \rho u^2 \tag{10}$$

$$T_{12} = \rho u v \tag{11}$$

$$T_{22} = \rho v^2 \tag{12}$$

where u and v are as shown in figure 3. The great simplification brought to eq. 9 by the thin blade approximation is that the γ and ξ integration limits no longer depend on τ. Thus, the integrations may be performed in any order. Equation 9 gives the noise caused by one blade; the other blades are accounted for by superposition.

The derivatives of the Green's function with respect to τ and γ are shifted temporarily onto the source functions using integration by parts.

$$p(\vec{x},t) = \int_{-\infty}^{\infty}\int_{0}^{r_T}\int_{-\pi r_0}^{\pi r_0} \rho_0 U^2 h''(\gamma + U\tau)\, G \, d\gamma \, dr_0 \, d\tau$$
$$+ \int_{-\infty}^{\infty}\int_{0}^{\infty}\int_{-\pi r_0}^{\pi r_0}\int_{-\infty}^{\infty} \left[T_{11}''(\gamma + U\tau)\, G - 2\,T_{12}'(\gamma + U\tau)\,\frac{\partial G}{\partial \xi} + T_{22}(\gamma + U\tau)\,\frac{\partial^2 G}{\partial \xi^2}\right] d\xi \, d\gamma \, dr_0 \, d\tau \tag{13}$$

Because h' is discontinuous at the blade leading and trailing edges and because the T_{ij}'s are discontinuous across shocks, their derivatives must, at this point, be considered as generalized functions in the sense described by Farassat (ref. 7). The differentiations will shortly be removed from the sources. The derivatives $\frac{\partial G}{\partial \xi}$ and $\frac{\partial^2 G}{\partial \xi^2}$ can be evaluated explicitly from eqs. 7 and 8:

$$\frac{\partial G}{\partial \xi} = - \frac{\cos \theta}{4\pi c_0 r}\, \delta'(t - \tau - R/c_0) \tag{14}$$

$$\frac{\partial^2 G}{\partial \xi^2} = \frac{\cos^2 \theta}{4\pi c_0^2 r}\, \delta''(t - \tau - R/c_0) \tag{15}$$

Substitution of these into eq. 13 eliminates derivatives with respect to ξ. The derivatives with respect to the argument of the delta function can be removed using integration by parts on the τ integral.

$$p(\vec{x},t) = \frac{1}{4\pi r}\int_{-\infty}^{\infty}\int_{0}^{r_T}\int_{-\pi r_0}^{\pi r_0} \rho_0 U^2 h''(\gamma + U\tau)\, \delta(t - \tau - R/c_0)\, d\gamma \, dr_0 \, d\tau$$
$$+ \frac{1}{4\pi r}\int_{-\infty}^{\infty}\int_{0}^{\infty}\int_{-\pi r_0}^{\pi r_0}\int_{-\infty}^{\infty} \left[T_{11}''(\gamma + U\tau) + 2\,\frac{U\cos\theta}{c_0}\, T_{12}''(\gamma + U\tau) + \frac{U^2\cos^2\theta}{c_0^2}\, T_{22}''(\gamma + U\tau)\right] \delta(t - \tau - R/c_0)\, d\xi \, d\gamma \, dr_0 \, d\tau \tag{16}$$

Time Domain Radiation Equations

The τ integration is now trivial, simply replacing the arguments $\gamma + U\tau$ by $\gamma + Ut - M_r R$ where $M_r = U/c = \Omega r_0/c_0$ is the section relative Mach number.

$$p(\vec{x},t) = \frac{1}{4\pi r}\int_{0}^{r_T}\int_{-\pi r_0}^{\pi r_0} \rho_0 U^2 h''(\gamma + Ut - M_r R)\, d\gamma \, dr_0$$
$$+ \frac{1}{4\pi r}\int_{0}^{\infty}\int_{-\pi r_0}^{\pi r_0}\int_{-\infty}^{\infty} \left[T_{11}''(\gamma + Ut - M_r R) + 2\,M_r \cos\theta\, T_{12}''(\gamma + Ut - M_r R) + M_r^2 \cos^2\theta\, T_{22}''(\gamma + Ut - M_r R)\right] d\xi \, d\gamma \, dr_0 \tag{17}$$

The derivatives are removed from the source functions by noting that $\frac{\partial^2}{\partial t^2} h(\gamma + Ut - M_r R) = U^2 h''(\gamma + Ut - M_r R)$ and that $\frac{\partial^2}{\partial t^2}$ can be moved outside the integrals because the limits are independent of t.

$$
\begin{aligned}
p(\vec{x}, t) = \frac{1}{4\pi r} \frac{\partial^2}{\partial t^2} \int_0^{r_T} \int_{-\pi r_\circ}^{\pi r_\circ} \rho_\circ\, h(\gamma + Ut - M_r R)\, d\gamma\, dr_\circ \\
+ \frac{1}{4\pi r} \frac{\partial^2}{\partial t^2} \int_0^{\infty} \int_{-\pi r_\circ}^{\pi r_\circ} \int_{-\infty}^{\infty} \left[\frac{1}{U^2} T_{11}(\gamma + Ut - M_r R) + 2 \frac{\cos\theta}{Uc_\circ} T_{12}(\gamma + Ut - M_r R) + \frac{\cos^2\theta}{c_\circ^2} T_{22}(\gamma + Ut - M_r R) \right] d\xi\, d\gamma\, dr_\circ
\end{aligned}
\tag{18}
$$

The γ integrations in eqs. 17 and 18 run from $-\pi r_\circ$ to $\pi r_\circ$. However, $h\ (\gamma + Ut - M_r R)$ is zero except for values of γ satisfying

$$
2\pi N r_\circ - \frac{b}{2} < \gamma + Ut - M_r R < 2\pi N r_\circ + \frac{b}{2} \tag{19}
$$

where N is an integer. Finding these values of γ is equivalent to finding the acoustic planform or retarded blade location as described in ref. 4.

The first integral in eq. 18 is the traditional thickness noise which is the direct result of volume displacement at the surface of the blade. This surface integral over the rotor disc was derived previously by Hanson (ref. 4) and was shown to give the same result as Farassat's theory (ref. 2). The second integral in eq. 18 is the quadrupole thickness noise which is also a result of volume displacement but is accounted for by integrating the associated stress terms T_{11}, T_{12}, and T_{22} over the volume surrounding the rotor disc. The quadrupole term has not been calculated correctly in previous work.

Equation 18 has been presented in a form which shows that the T_{11} quadrupole (integrated over ξ) radiates exactly like the volume displacement source with regard to frequency and directivity dependence. Since T_{12} and T_{22} are multiplied by $\cos\theta$, we need only compare chordwise distributions of

$$
\frac{h}{b} \quad \text{versus} \quad \int_{-\infty}^{\infty} \frac{\rho u^2}{\rho_\circ U^2}\, d\left(\frac{\xi}{b}\right) \tag{20}
$$

to compare contributions of the two sources to noise near the plane of rotation. This is done in a later section entitled "Aerodynamic Evaluation of Quadrupole Source Term."

The time domain equations can be transformed to blade fixed coordinates by substituting $\eta = \gamma + Ut - M_r R$. Since this might be an advantage for subsonic tip speed rotors, an example is given in the appendix.

Frequency Domain Radiation Equations

It is also useful to compare these sources in the frequency domain, which is done by calculating complex Fourier coefficients from either eq. 17 or eq. 18 according to

$$P_n(\vec{x}) = \frac{\Omega}{2\pi}\int_0^{2\pi/\Omega} p(\vec{x}, t)\, e^{in\Omega t}\, dt \tag{21}$$

The volume displacement term from eq. 18 becomes

$$P_{Vn}(\vec{x}) = -\frac{\rho_\circ n^2\Omega^2}{4\pi r}\int_0^{r_T}\int_{-\pi r_\circ}^{\pi r_\circ}\frac{\Omega}{2\pi}\int_0^{\frac{2\pi}{\Omega}} h(\gamma + Ut - M_r R)\, e^{in\Omega t}\, dt\, d\gamma\, dr_\circ \tag{22}$$

where the factor $-n^2\Omega^2$ in the frequency domain comes from $\frac{\partial^2}{\partial t^2}$ in the time domain.

We change variables with

$$Xb = \gamma + Ut - M_r R \tag{23}$$

Then, because the surface source is assumed to act on the mean chordline $\xi = 0$, eq. 8 gives

$$t = \frac{Xb}{\Omega r_\circ} - \frac{\gamma}{\Omega r_\circ} + \frac{r}{c_\circ} - \frac{r_\circ}{c_\circ}\sin\theta\,\cos\left(\frac{\gamma}{r_\circ}\right) \tag{24}$$

This results in

$$\begin{aligned} P_{Vn}(\vec{x}) = -\frac{\rho_\circ n^2\Omega^2}{4\pi r}\, e^{in\frac{\Omega r}{c_\circ}}\int_0^{r_T} b\Bigg[\int_{-\frac{1}{2}}^{\frac{1}{2}} h(Xb)\, e^{in\frac{bX}{r_\circ}}\, dX \\ \cdot\frac{1}{2\pi r_\circ}\int_0^{2\pi r_\circ} e^{-in\frac{\gamma}{r_\circ} - in\frac{\Omega r_\circ}{c_\circ}\sin\theta\,\cos\frac{\gamma}{r_\circ}}\, d\gamma\Bigg]\, dr_\circ \end{aligned} \tag{25}$$

The γ integration gives Bessel functions so that eq. 25 reduces to

$$P_{Vn}(\vec{x}) = -\frac{\rho_\circ n^2\Omega^2}{4\pi r}\, e^{in\left(\frac{\Omega r}{c_\circ} - \frac{\pi}{2}\right)}\int_0^{r_T} J_n\left(\frac{n\Omega r_\circ}{c_\circ}\sin\theta\right) b\int_{-\frac{1}{2}}^{\frac{1}{2}} h(bX)\, e^{i\frac{nb}{r_\circ}X}\, dX\, dr_\circ \tag{26}$$

which is the same result derived by Hawkings and Lowson (ref. 3). Equation 26 is now normalized using

$$Z = \frac{r_\circ}{r_T} \tag{27}$$

$$M_T = \frac{\Omega r_T}{c_\circ} \tag{28}$$

$$B_D = \frac{b}{D} \tag{29}$$

and the thickness function $H(X) = h(bX)/b$ shown in figure 4 to arrive at the final form for the volume displacement noise component:

$$P_{Vn}(\vec{x}) = -\rho_\circ c_\circ^2 \frac{n^2 M_T^2}{\pi\left(\frac{r}{r_T}\right)} e^{in\left(\frac{\Omega r}{c_\circ} - \frac{\pi}{2}\right)} \int_0^1 B_D^2 \, J_n(nZ M_T \sin\theta) \, \Psi_V\left(\frac{2nB_D}{Z}\right) dZ \tag{30}$$

where

$$\Psi_V\left(\frac{2nB_D}{Z}\right) = \int_{-\frac{1}{2}}^{\frac{1}{2}} H(X) \, e^{i\frac{2nB_D}{Z}X} \, dX \tag{31}$$

is the Fourier transform of the airfoil thickness distribution. The same manipulations for the quadrupole term in eq. 18 give

$$P_{Qn}(\vec{x}) = -\rho_\circ c_\circ^2 \frac{n^2 M_T^2}{\pi\left(\frac{r}{r_T}\right)} e^{in\left(\frac{\Omega r}{c_\circ} - \frac{\pi}{2}\right)} \int_0^\infty B_D^2 \, J_n(nZ M_T \sin\theta)$$
$$\times \left(\Psi_{11} + 2Z M_T \cos\theta \, \Psi_{12} + Z^2 M_T^2 \cos^2\theta \, \Psi_{22}\right) dZ \tag{32}$$

where $Y = \xi/h$ and

$$\Psi_{ij}\left(\frac{2nB_D}{Z}\right) = \int_{-X_1}^{X_1}\int_{-\infty}^{\infty} \frac{\rho u_i u_j}{\rho_\circ U^2} \, e^{2in B_D M_T \cos\theta \, Y} dY \, e^{i\frac{2nB_D}{Z}X} dX \tag{33}$$

is the integrated quadrupole source term. The chordwise integration is over a range $\pm X_1$ equivalent to $\pm \Omega r_\circ$. Because eqs. 30 and 32 are in the same form, the two sources can be compared in the frequency domain by comparing the source terms Ψ_V and Ψ_{11}. This and the time domain comparison are the subjects of the following section.

AERODYNAMIC EVALUATION OF QUADRUPOLE SOURCE TERM

It is well known from experimental studies that noise of high speed rotors is maximum near the plane of rotation. Since $\cos\theta = 0$ in the plane of rotation, the preceding acoustic analysis shows that the volume displacement and quadrupole thickness sources can be compared by calculating

$$\Psi_V = \int_{-\frac{1}{2}}^{\frac{1}{2}} H(X)\, e^{i\frac{2mBB_D}{Z}X}\, dX \tag{34}$$

and

$$\Psi_{11} = \int_{-\infty}^{\infty}\int_{-\infty}^{\infty} \frac{\rho u^2}{\rho_0 U^2}\, e^{i\frac{2mBB_D}{Z}X}\, dY\, dX \tag{35}$$

where n has been replaced by mB and m is the harmonic of blade passing frequency. The streamwise velocity perturbation is u and ρ is the local density. The chordwire integration is shown with an infinite range because the source is now considered to be "unwrapped" to allow use of two dimensional airfoil theory for evaluation by Ψ_{11}. These source terms have been evaluated for biconvex parabolic airfoils,

$$H(X) = (1 - 4X^2)\, \frac{h_{max}}{b} \tag{36}$$

and the results are presented below.

Aerodynamic Theory

The airfoil flow field was studied using different computation schemes for fully subsonic, transonic, and fully supersonic flow as described herein. All calculations were two dimensional and assumed small disturbances so that the density ratio could be calculated from the small perturbation approximation for isentropic compressible flow

$$\frac{\rho}{\rho_0} = \left\{1 - \frac{k-1}{2} M_r^2 \left[\frac{(U+u)^2 + v^2}{U^2} - 1\right]\right\}^{\frac{1}{k-1}} \approx 1 - M_r^2 \frac{u}{U} \tag{37}$$

where k is the ratio of specific heats.

For fully subsonic flow, velocity distributions were calculated using the Spreiter and Alksne local linearization method as given in ref. 8.

For fully supersonic flow, explicit first order solutions for the supersonic flow field of a parabolic arc airfoil were taken from Caughey (ref. 9). The calculated shock wave positions for a 2% thickness ratio airfoil at a Mach number of 1.15 are plotted in figure 5. Because of the spreading shock waves, the quadrupole noise originates from an increasingly noncompact region at increasing heights above the airfoil. Streamwise perturbation velocities near the surface are predicted to vary inversely as $\sqrt{M_r^2 - 1}$, as is also predicted by linearized supersonic theory. Thus, the ratio of quadrupole to volume displacement acoustic pressure is predicted to increase as supersonic Mach number is decreased and the largest value of this ratio should occur in the transonic regime.

For transonic flow, elaborate digital computer programs are available for detailed calculation of transonic flow past two-dimensional airfoils. Rather than modify one of those programs to calculate the spatial distribution of perturbation velocity, an older approximate method for transonic flow was modified by use of information available from the newer, more rigorous solutions. This modified solution is also based on the local linearization method developed by Spreiter and Alksne (ref. 8). In that method, the streamwise velocity gradient in a locally subsonic portion of the flow field is obtained from its value for incompressible flow by

$$\frac{d}{dX}\left(\frac{u}{U}\right) = \left[1 - M_r^2 - (k+1)\, M_r^2 \,\frac{u}{U}\right]^{-\frac{1}{2}} \frac{d}{dX}\left(\frac{u}{U}\right)_{M_r = 0} \tag{38}$$

Here, the quantity in square brackets is one minus the local axial component of Mach number squared. Similarly, streamwise velocity gradient in a locally supersonic flow field is obtained from its value as calculated from linearized supersonic theory at a free stream Mach number $\sqrt{2}$ by

$$\frac{d}{dX}\left(\frac{u}{U}\right) = \left[M_r^2 - 1 + (k+1)\, M_r^2 \,\frac{u}{U}\right]^{-\frac{1}{2}} \frac{d}{dX}\left(\frac{u}{U}\right)_{M_r = \sqrt{2}} \tag{39}$$

Also, streamwise velocity gradient in an accelerating near-sonic flow was shown to be equal to its value at the same location at a free stream Mach number of one, divided by free stream Mach number to the 2/3 power.

Equations were given by Spreiter and Alksne in ref. 8 for calculating the streamwise perturbation velocity within these three regions, assuming that the value of this velocity was known at one chordwise position. This velocity, and therefore the constant of integration when integrating the above velocity derivatives, was known only for the cases of fully subsonic, near sonic, and fully supersonic flow. Fortunately, numerical solutions for the flow field of a nonlifting parabolic arc airfoil are available for transonic Mach numbers less than one (Murman and Cole, ref. 10) and greater than one (Murman, ref. 11). These numerical results can be utilized to evaluate the variations of any flow property of interest throughout the transonic range. In particular, it had been noted in ref. 8 that the equation for perturbation velocity in accelerating near-sonic flow had a denominator that went to zero at the sonic point on the airfoil surface. To obtain valid results, the numerator also had to go to zero such that their ratio remained locally constant. The analytical solutions for fully subsonic flow, fully supersonic flow, and free stream Mach numbers very near one and the numerical results in refs. 10 and 11 for the intermediate regions were utilized to prescribe the streamwise perturbation velocity at this chordwise position (for a parabolic arc airfoil, the quarter-chord).

Velocity gradients calculated from eqs. 38 and 39 should be reasonably accurate if the local Mach number is not near one. As local Mach number approaches one, the calculated gradients approach infinity. Therefore if one starts with a prescribed locally subsonic velocity at some chordwise location and numerically integrates eq. 41 in the downstream (increasing local velocity) direction, incorrect results would be obtained at nearly sonic local Mach numbers. As with the calculation method described by Fink (ref. 12) for axisymmetric transonic flow, the numerical integration has been modified to use velocity gradients calculated for accelerating near-sonic flow at the chordwise position where it gives a smaller gradient. Further downstream where the flow was locally supersonic, the velocity gradients calculated for accelerating transonic flow and for locally supersonic flow were compared, and the smaller value was used in numerical integration.

Shock wave position was prescribed by use of a curve fitted to the positions given in ref. 10 for this airfoil section. Shock wave strength in the presence of a boundary layer was obtained by an approximation to the data correlation given by Sinnott in ref. 13. The variation of perturbation velocity with distance above and below the airfoil was calculated from the Spreiter and Alksne theory (eqs. 63 and 64 of ref. 14) for positive perturbation velocities and by

$$\frac{u}{U} = \left(\frac{u}{U}\right)_{\xi = 0} \left(1 + \left|\frac{\xi}{h_{max}}\right|\right)^{-1} \tag{40}$$

for negative perturbation velocities at subsonic free stream Mach numbers.

To check the validity of this transonic theory, comparisons have been made with calculations from the exact theory of Carlson using the TRANDES computer program (ref. 15). Mach number distributions around the blade matched well enough to justify use of the approximate theory, which requires two orders of magnitude less computer time.

Calculated Aerodynamic Flow Field

Variations of streamwise perturbation velocity along the chord, as calculated for transonic Mach numbers from 0.80 to 1.04 and also for Mach numbers of 0 to 1.15, are plotted in figure 6 for a 2% thickness ratio parabolic arc airfoil. As Mach number was increased from 0 to 0.8, calculated perturbation velocities increased by approximately a factor of $\left(1-M_r^2\right)^{-\frac{1}{2}}$ as would have been predicted by linearized subsonic theory. Further increase to 0.90 caused a relatively larger increase of maximum perturbation velocity so that the velocity distribution was relatively more peaked than that for incompressible flow. This change in shape of the velocity distribution agrees with that expected for the nonlinear effect of subsonic Mach number as calculated by the Karman-Tsien compressibility correction.

Small increases of Mach number above 0.90 caused the development of locally supersonic flow followed by a shock wave. Calculated values of local velocity ratio upstream of midchord were approximately independent of free stream Mach number in the range from about 0.91 to 0.94. This range of Mach number was characterized by the change from a broad maximum of perturbation velocity near midchord to an accelerating transonic flow with large perturbation velocities.

As free stream Mach number was further increased, a general reduction in perturbation velocity ratio occurred. However, the shock wave continued to move downstream until it reached the trailing edge at a free stream Mach number of about 0.97. The calculated distribution of perturbation velocity for a Mach number of 1.04 resembles that for fully supersonic flow at a Mach number of 1.15 except for having a logarithmic singularity rather than a finite value at the leading edge. This difference corresponds to the presence of a detached shock wave and leading edge stagnation point at 1.04 but an attached shock wave at the sharp leading edge for the higher Mach number.

These velocity distributions and the corresponding densities from eq. 37 were used to calculate the normalized quadrupole strength $\rho u^2/\rho_\circ U^2$ on the airfoil surface as shown in figure 7. In fully subsonic flow the source distribution for this airfoil is symmetric about midchord with sharp peaks at the leading and trailing edges and a broad peak near midchord. Increasing the free stream Mach number increases the amplitude of this broad peak. Further increase above the critical Mach number causes the growth of a large, strong quadrupole noise-radiating region along the aft 2/3 of the chord. As free stream Mach number is increased through one, the acoustic strength of this aft region decreases and the sharp peak near the leading edge strengthens. Finally, at supersonic Mach numbers large enough to maintain an attached leading edge shock wave, the source strength is concentrated near the leading and trailing edges. The integration of the quadrupole source in the vertical direction is described below; however, if the effective extent of the source above the surface were temporarily assumed to be 1 chord, then the curves in figure 7 would represent $\int (\rho u^2/\rho_\circ U^2)\, dY$.

This permits the shape and general level of these chordwise quadrupole distributions to be compared with those of the one-sided volume displacement source distribution $H(X)/2$, also plotted in the figure. For subcritical Mach numbers the two distributions are similar. This may explain observations by Schmitz and Yu (ref. 16) and others that the linear theories predict waveshapes like the test data but with levels too low. At supercritical speeds, the downstream shift of the quadrupole will result in a substantially different noise waveform.

Figure 8 shows the vertical distribution of the quadrupole source Ψ_{11} for a combination of B_D, Z, and mB of interest for advanced turbopropeller applications. The ordinate,

$$\frac{1}{\Psi_{11}} \int \frac{\rho u^2}{\rho_\circ U^2} e^{i \frac{2mBB_D}{Z} X} dX \tag{41}$$

is normalized such that each curve has unit area. It can be seen that the quadrupole source extends farther from the airfoil at a Mach number of 0.95 than at 0.90 or 1.00. This, coupled with the trends in $\rho u^2/\rho_\circ U^2$ on the surface as shown in figure 7, leads to a strong peaking of the integrated quadrupole source Ψ_{11} at transonic speeds as shown below.

Figure 8 shows that the effective vertical extent of the quadrupole is about one chord. This means that the two-dimensional aerodynamic theory is probably adequate except near blade tips. It also means that for out of plane noise calculations, noncompactness in the Y direction has to be accounted for with the Y exponential in eq. 33.

Comparison of Volume Displacement and Quadrupole Source Terms

The aerodynamic methods described above are now used to compare the integrated quadrupole source Ψ_{11} with the integrated volume displacement source Ψ_V as functions of radius (i.e., as functions of section relative Mach number, which varies as radius). For the biconvex parabolic airfoil, eqs. 34 and 36 can be integrated analytically to give

$$\Psi_V(\omega_c) = \left[\frac{16}{\omega_c^3} \sin\left(\frac{\omega_c}{2}\right) - \frac{8}{\omega_c^2} \cos\left(\frac{\omega_c}{2}\right) \right] \frac{h_{max}}{b} \tag{42}$$

which is plotted in figure 9. The frequency parameter

$$\omega_c = \frac{2\,m\,B\,B_D}{Z} \tag{43}$$

is a measure of noncompactness. In the limit as $B_D \rightarrow 0$, $\Psi_V \rightarrow \frac{2}{3} \frac{h_{max}}{b}$ which (multiplied by b^2) is just the cross-sectional area of the airfoil. The effect of increasing the harmonic order, or increasing the chord at constant section area, is to reduce the noise via chordwise phase interference. The example chosen here for comparison with the quadrupole is the advanced turboprop mentioned above with $B_D = 0.14$ and $B = 8$. For the blade passing frequency fundamental $(m = 1)$, figure 9 gives $\Psi_V(2.24) = 0.587 \; h_{max}/b$, which is only slightly reduced due to noncompactness.

The quadrupole source was integrated numerically in the X direction from leading edge to trailing edge for the subsonic and transonic cases and from the bow shock to trailing shock for the supersonic case. Integrations in the Y direction were carried out to 20 chords, which figure 8 shows to be well within 1% of the total. The calculated ratios of Ψ_{11} to Ψ_V for a 2% thickness ratio airfoil section are plotted versus section relative Mach number in figure 10 for the 3 speed ranges. The fully subsonic calculations and the transonic calculations are shown to blend well in their range of overlap. The transonic calculations show a peak at $M_r = 0.95$ and then start to decay with increasing Mach number. The increase in calculated values of Ψ_{11} starting at $M_r = 1.05$ is caused by the incorrect assumption that velocity perturbations decay along vertical lines rather than along Mach waves, so that phase cancellation is not correctly represented. The fully supersonic calculations are also shown to diverge at Mach numbers below about 1.15 because the leading edge shock would not be attached as assumed in the theory. Thus, the transonic and supersonic calculations are faired together as shown by the dashed line in figure 10.

The faired curve from figure 10 is replotted in figure 11 as $20 \log_{10} \left| \frac{\Psi_{11} + \Psi_V}{\Psi_V} \right|$ which is the number of decibels added to the volume displacement thickness source by the quadrupole thickness source. Two features are immediately apparent. First, the peak value of 5.7 dB shows clearly that quadrupole radiation is an important factor in high speed rotor noise. Second, the quadrupole source is important only at or very near transonic section speeds. The acoustic results in figure 11 correspond to the well known aerodynamic results from thin airfoil theory in which linear sources and doublets give good performance predictions except near a Mach number of one. It also shows in a unified way why the linear source terms have been adequate for prediction of rotor noise at subcritical tip speeds, why linear source terms are adequate for sonic boom calculations $(M_r > 1.5)$, and why linear source models fail for the transonic speeds of interest for advanced propellers and helicopter rotors.

Now that quadrupole noise is recognized as a transonic flow phenomenon, one can ask how to suppress it. Sweep in wings is known to decrease adverse effects of transonic flow if the effective Mach number (product of the relative Mach number and the cosine of the sweep angle) is less than the section critical Mach number. These favorable effects of sweep have also been shown (ref. 17) to occur for rotating blades. Thus, by analogy figure 11 shows for 2% thickness ratio propeller sections, that the additional noise due to the ρu^2 quadrupole should be reduced to less than 1 dB by sweeping the blade to obtain an effective Mach number of 0.85.

ROTOR NOISE CALCULATIONS

In the preceding section, volume displacement and quadrupole sources were compared at relative Mach numbers corresponding to various radii on a blade. It remains to integrate these sources over the blade radius to find the net effect of the quadrupole on radiated noise. This section presents noise calculations for two rotors. The first is a model propeller for which transonic tip speed test data are available and the second is a rectangular planform helicopter rotor previously studied by Farassat (ref. 2).

Transonic Propeller

Figure 2 compared near field data from a transonic tip speed propeller with noise predicted using Hanson's near field theory (ref. 4) for volume displacement and dipole noise surface sources. These data and predictions are replotted in figure 12 along with the noise predicted using a near field version of the present theory for the ρu^2 quadrupole added to the other sources. Including the quadrupole substantially improves the agreement with test data, particularly in, and forward of, the plane of rotation. The remaining underprediction is probably caused by omission of lift effects. Lift is expected to increase the ρu^2 quadrupole and will be the major contributor to the ρuv quadrupole, which can be shown to radiate with the same directivity as the lift dipole. These effects are now being evaluated at United Technologies.

Farassat Rotor

In ref. 2 Farassat predicted thickness noise for a rectangular planform helicopter rotor with 10% thickness ratio parabolic arc blades and a 4% chord-to-diameter ratio. In ref. 4, Hanson showed that the volume displacement term from eq. 18 gave results equivalent to those of Farassat. Figure 13 shows the radial distribution of the additional source strength due to the ρu^2 quadrupole for a tip rotational Mach number of 1.1. As in figure 11, the ordinate is $20 \log_{10} \left|(\Psi_{11} + \Psi_V)/\Psi_V\right|$. For this thick blade, the peak occurs at a lower section speed $(M_r = 0.88)$ as would be expected because of the reduced critical Mach number. However, the peak increase of 6.2 dB is nearly the same as for the thinner airfoil (as well as intermediate thicknesses). Since this result was a surprise, it was verified by using an exact inviscid-flow transonic airfoil computer program (ref. 15). It was found that, while the surface values of the quadrupole grow roughly as $(h_{max}/b)^3/2$ as predicted by transonic similarity laws, the decay rate with vertical distance increases roughly as $(h_{max}/b)^{\frac{1}{2}}$. The net effect is that the peak value of the quadrupole source Ψ_{11} grows approximately as (h_{max}/b), like the surface source. However, as can be seen by comparing figures 11 and 13, the quadrupole is significant compared to the volume displacement over a wider range of relative Mach numbers for the thicker airfoil.

The effect of the quadrupole integrated over the full radius of the Farassat blade has been checked with eq. 32. For the first several harmonics the noise increase is 3.8 to 4.0 dB in the plane of rotation. However, many more harmonics would have to be evaluated to find the overall effect on the waveform because of the impulsive nature of the sound from this blade.

CONCLUSIONS

An analysis has been presented for the far field harmonic thickness noise of a nonlifting rotor. The acoustic radiation equations are essentially exact except for the thin blade approximation. The ρu^2 quadrupole has been evaluated using two-dimensional aerodynamic theory valid through the transonic speed range. Comparison of this quadrupole with the volume displacement sources has led to the following conclusions.

1. The ρu^2 quadrupole is an important thickness noise source at transonic blade section speeds. For any thickness ratio, the maximum contribution is roughly 6 dB above the volume displacement thickness noise.

2. For thin propeller blades the quadrupole becomes negligible outside the transonic speed range, which explains why linear source acoustic theories are successful for subcritical propellers and for sonic boom calculations.

3. As thickness ratio is increased, the quadrupole contributes significantly in the range of transonic section speeds found in current helicopter designs.

4. The comparison of theory with test data for a transonic tip speed propeller was substantially improved by adding the ρu^2 quadrupole to the linear source terms.

5. Quadrupole radiation should be reduced to the negligible point if the blades are swept so that their effective Mach number is subcritical.

APPENDIX

Blade-Fixed Coordinates for Time Domain Calculations

As was explained in ref. 4, the time domain equations can be transformed to blade-fixed coordinates by substituting

$$\eta = \gamma + Ut - M_r R \tag{44}$$

For example, the ρu^2 quadrupole pressure from eq. 17 can be written

$$p_{11}(\vec{x}, t) = \frac{1}{4\pi r} \frac{\partial}{\partial t} \iiint \frac{1}{U} T'_{11} (\gamma + Ut - M_r R) \, d\xi \, d\gamma \, dr_o \tag{45}$$

Differentiation of eq. 44 gives

$$d\eta = d\gamma - M_r \frac{\partial R}{\partial \gamma} d\gamma \tag{46}$$

But $M_r \dfrac{\partial R}{\partial \gamma} = M_{or}$ is the Mach number of the source relative to the observer so that $d\gamma$ can be expressed $d\gamma = d\eta / \left| 1 - M_{or} \right|$. Substitution into eq. 45 gives

$$p_{11}(\vec{x}, t) = \frac{1}{4\pi r} \frac{\partial}{\partial t} \int \frac{1}{U} \left[\frac{\frac{\partial}{\partial \eta} (\rho u^2)}{\left| 1 - M_{or} \right|} \right]_{ret} d(\text{vol}) \tag{47}$$

where $d(\text{vol}) = d\xi \, d\eta \, dr_o$. Equation 47 would be practical for numerical computation for subcritical rotors where $1 - M_{or}$ never goes to zero and there are no shock waves to cause discontinuities in ρu^2.

REFERENCES

1. J. E. Ffowcs-Williams and D. L. Hawkings, "Sound Generated by Turbulence and Surfaces in Arbitrary Motion," Philosophical Transaction of the Royal Society of London, Series A, Vol. 264, 1969.

2. F. Farassat, "Theory of Noise Generation from Moving Helicopter Blades with an Application to Helicopter Rotors," NASA TR-R-451, National Aeronautics and Space Administration, Washington, D.C. 1975.

3. D. L. Hawkings and M. V. Lowson, "Theory of Open Supersonic Rotor Noise," J. Sound and Vibration, Vol. 36, No. 1, 1974.

4. D. B. Hanson, "Near Field Noise of High Tip Speed Propellers in Forward Flight," AIAA Paper No. 76-565, 1976.

5. C. Kitaplioglu and A. R. George, "A Study of the Far Field Sound Due to Unsteady Shocks on Rotors," AIAA Paper No. 77-1360, 1977.

6. M. Goldstein, Aeroacoustics, McGraw-Hill, New York, 1976.

7. F. Farassat, "Discontinuities in Aerodynamics and Aeroacoustics, the Concept and Application of Generalized Derivatives," Journal Sound and Vibration, Vol. 55, No. 2, 1977.

8. J. R. Spreiter and A. Y. Alksne, "Thin Airfoil Theory Based on Approximate Solution of the Transonic Flow Equation," NACA Report 1359, 1958.

9. D. A. Caughey, "Second-Order Wave Structure in Supersonic Flows," NASA CR-1438, September 1969.

10. E. M. Murman and J. D. Cole, "Calculation of Plane Steady Transonic Flows," AIAA Journal, Vol. 9, No. 1, January 1971, pp. 114-121.

11. E. M. Murman, "A Relaxation Method for Calculating Transonic Flows With Detached Bow Shocks," Presented at the Third International Conference on Numerical Methods in Fluid Dynamics, Paris, France, July 3-7, 1972.

12. M. R. Fink, "Calculated Transonic Flow Past Slender Fuselages and Afterbodies," Journal of Aircraft, Vol. 8, No. 9, September 1971, pp. 710-716.

13. C. S. Sinnott, "On the Prediction of Mixed Subsonic/Supersonic Pressure Distributions," Journal of the Aerospace Sciences, Vol, 27, No. 10, October 1960, pp. 767-778.

14. J. R. Spreiter and A. Y. Alksne, "Theoretical Prediction of Pressure Distributions on Nonlifting Airfoils at High Subsonic Speeds," NACA Report 1217, 1955.

15. L. A. Carlson, "TRANDES: A Fortran Program for Transonic Airfoil Analysis or Design," NASA CR-2821, June 1977.

16. F. H. Schmitz and Y. H. Yu, "Theoretical Modeling of High Speed Helicopter Impulsive Noise," Paper presented at the Third European Rotorcraft and Powered Lift Aircraft Forum," Aix-en-Provence, France, September 7-9, 1977.

17. W. F. Ballhaus and F. X. Caradonna, "The Effect of Planform Shape on Transonic Flow Past Rotor Tips," AGARD Proceedings #111, Aerodynamics of Rotary Wings. Feb. 1973.

18. R. K. Amiet, "Refraction of Sound by a Shear Layer," AIAA Paper No. 77-54, January 1977.

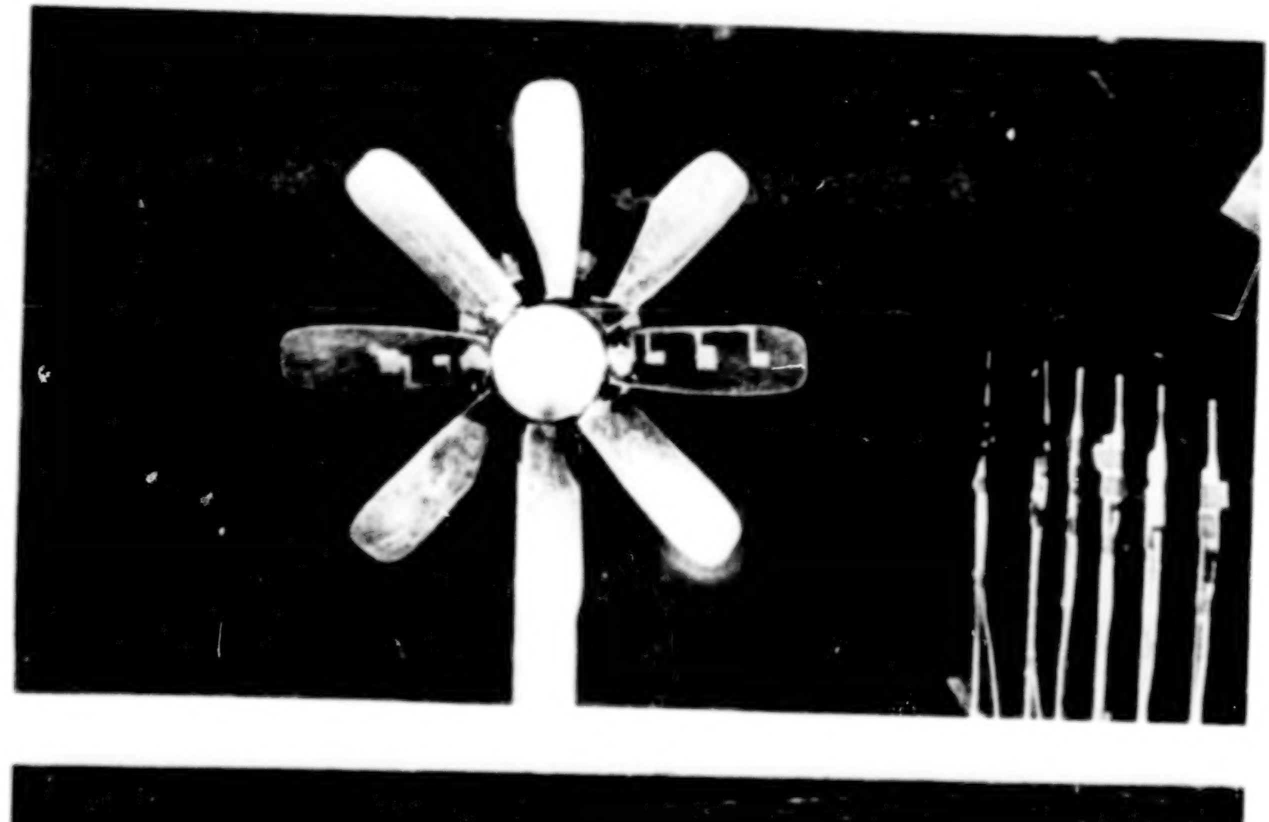

Figure 1.- Transonic tip speed propeller tested in United Technologies Research Center Acoustic Wind Tunnel. Model diameter = 0.62 m (2.04 ft).

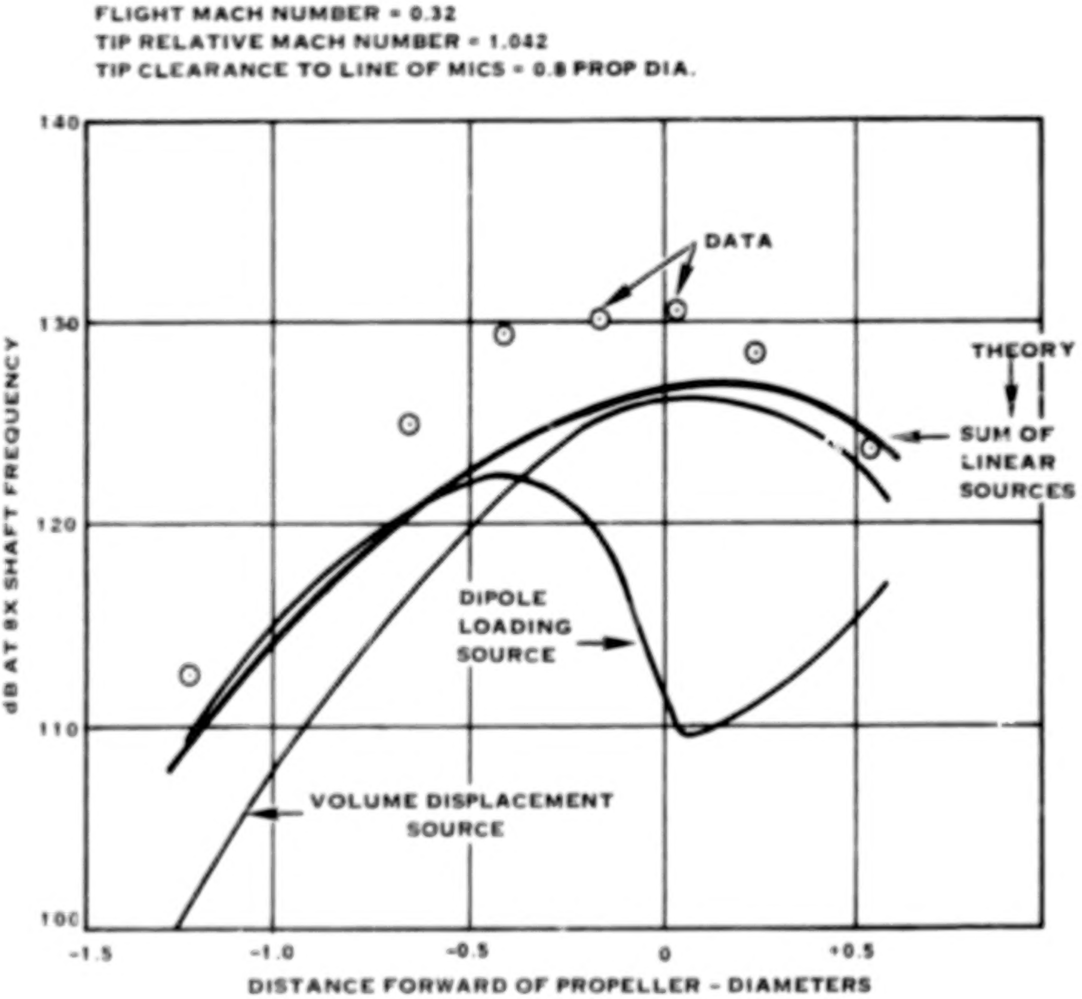

Figure 2.- Comparison of data with noise predicted for linear sources data from model shown in figure 1 tested with 2 blades. (Data corrected with Amiet's theory for tunnel shear layer refraction, ref. 18.)

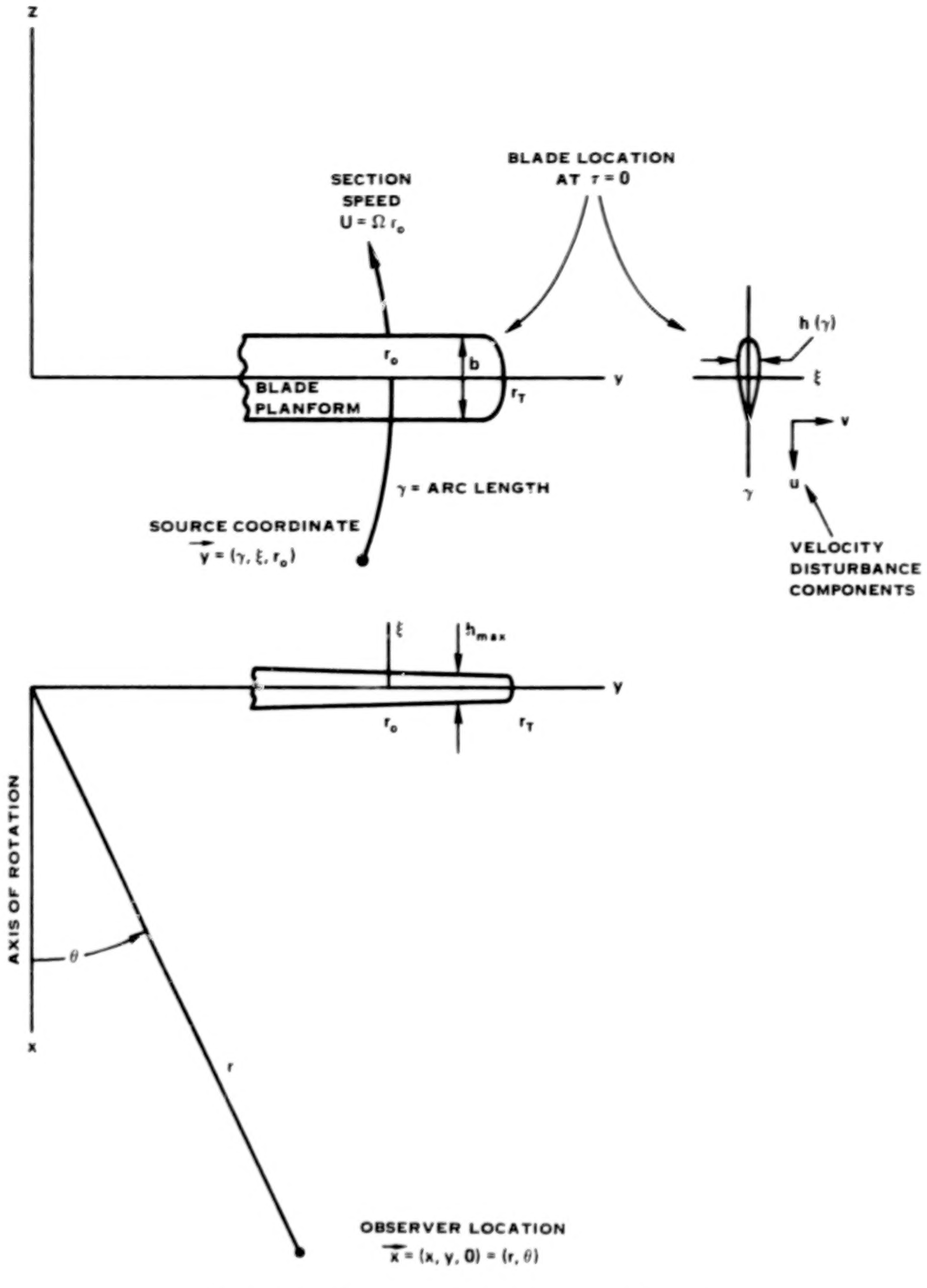

z
SECTION SPEED
U = Ω r_o
BLADE LOCATION AT τ = 0
h (γ)
r_o
b
y
ξ
BLADE PLANFORM
r_T
v
u
γ = ARC LENGTH
γ
SOURCE COORDINATE
y = (γ, ξ, r_o)
VELOCITY DISTURBANCE COMPONENTS
ξ
h_max
y
r_o
r_T
AXIS OF ROTATION
θ
x
r
OBSERVER LOCATION
x = (x, y, 0) = (r, θ)

Figure 3.- Source and observer coordinates.

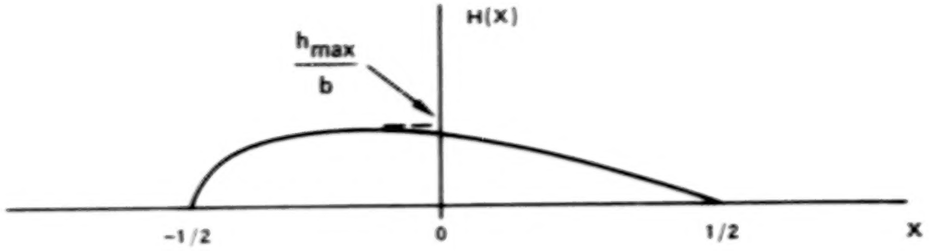
H(X)
$\frac{h_{max}}{b}$
-1/2
0
1/2
X

Figure 4.- Normalized airfoil thickness function.

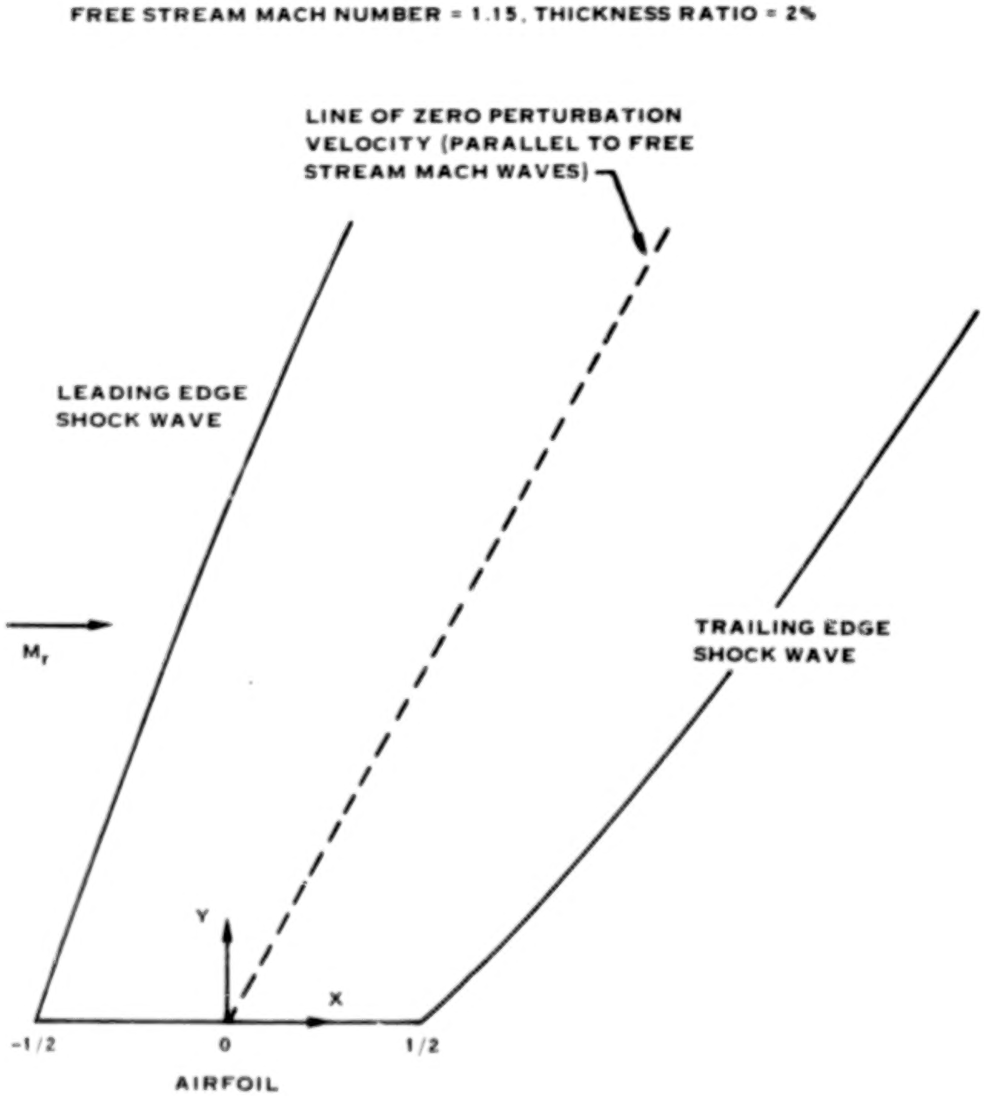
FREE STREAM MACH NUMBER = 1.15, THICKNESS RATIO = 2%
LINE OF ZERO PERTURBATION VELOCITY (PARALLEL TO FREE STREAM MACH WAVES)
LEADING EDGE SHOCK WAVE
TRAILING EDGE SHOCK WAVE
M_r
Y
X
-1/2
0
1/2
AIRFOIL

Figure 5.- Calculated shock wave pattern for parabolic arc airfoil in fully supersonic flow.

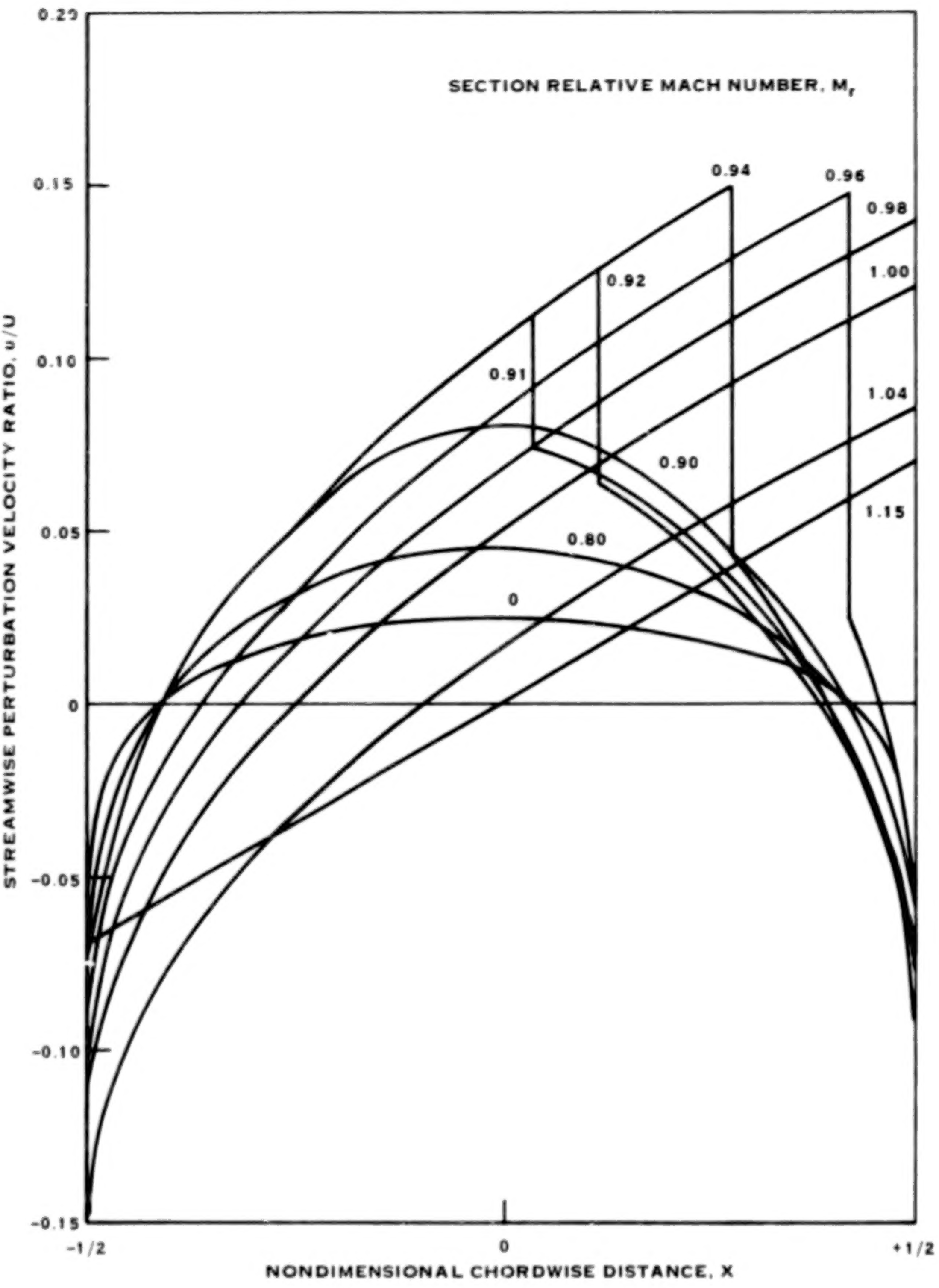

Figure 6.- Calculated chordwise velocity distributions for 2% thickness ratio parabolic arc airfoil.

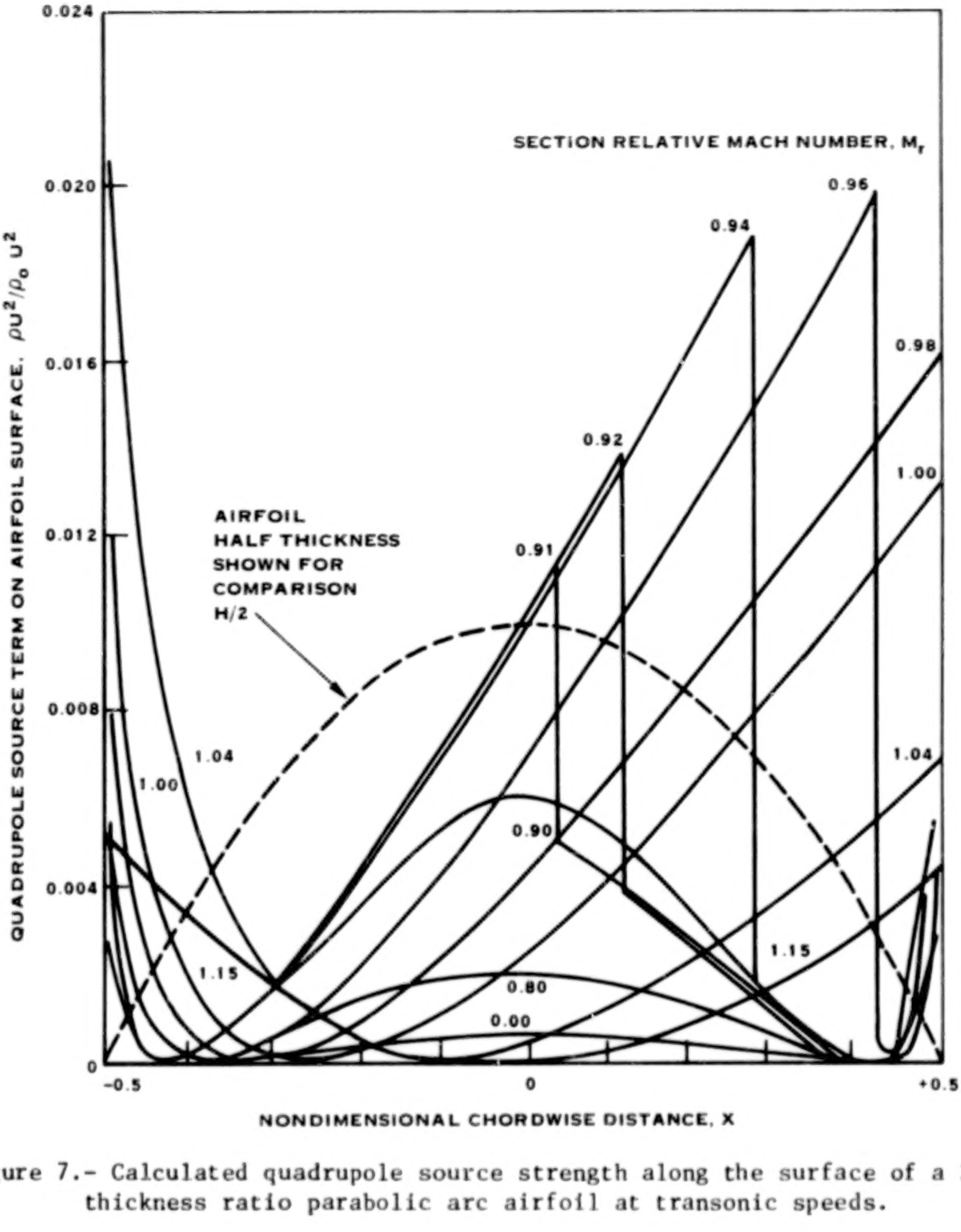

Figure 7.- Calculated quadrupole source strength along the surface of a 2% thickness ratio parabolic arc airfoil at transonic speeds.

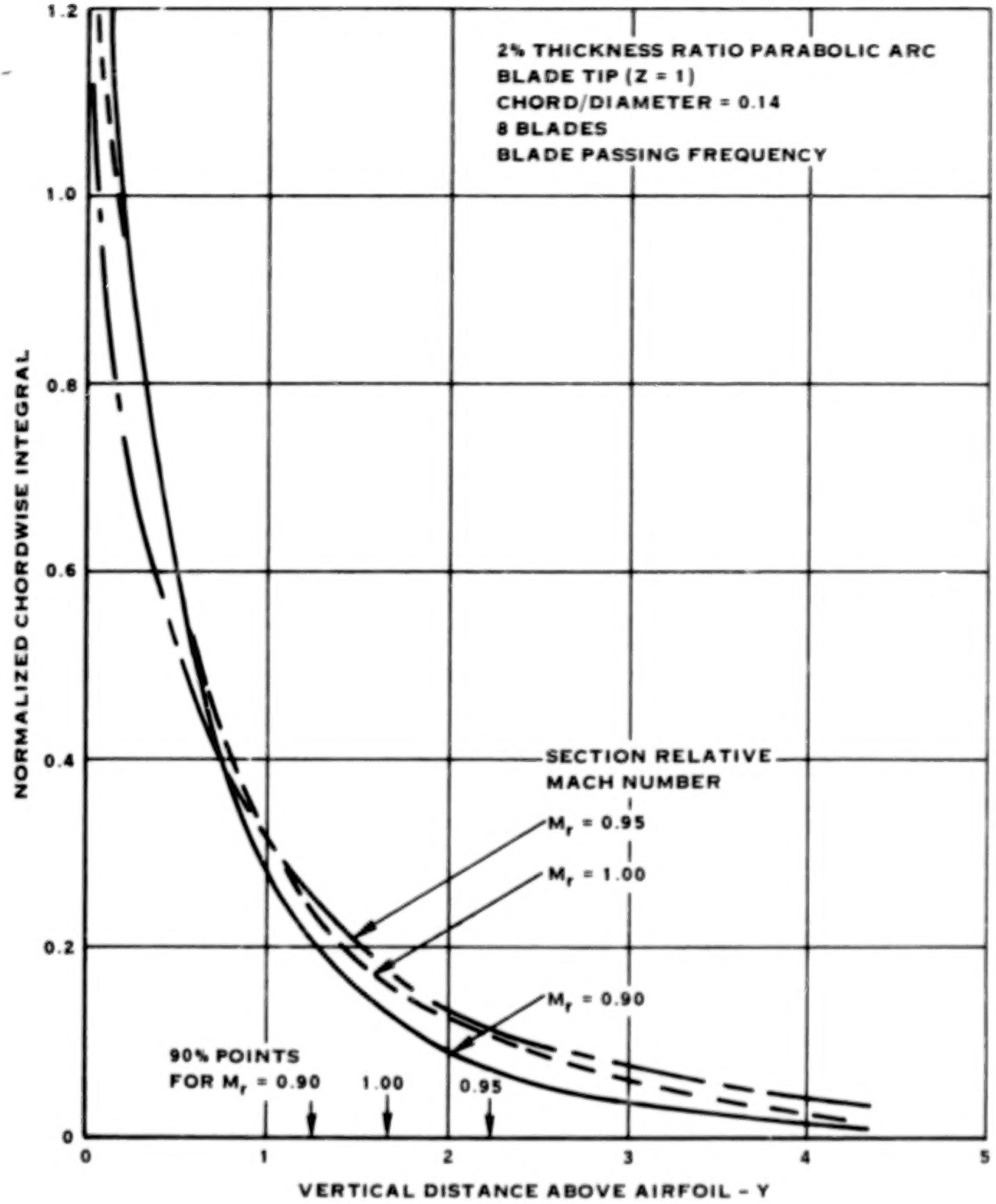

Figure 8.- Vertical distribution of quadrupole source strength. 90% points indicate value of Y which includes 90% of the quadrupole integral.

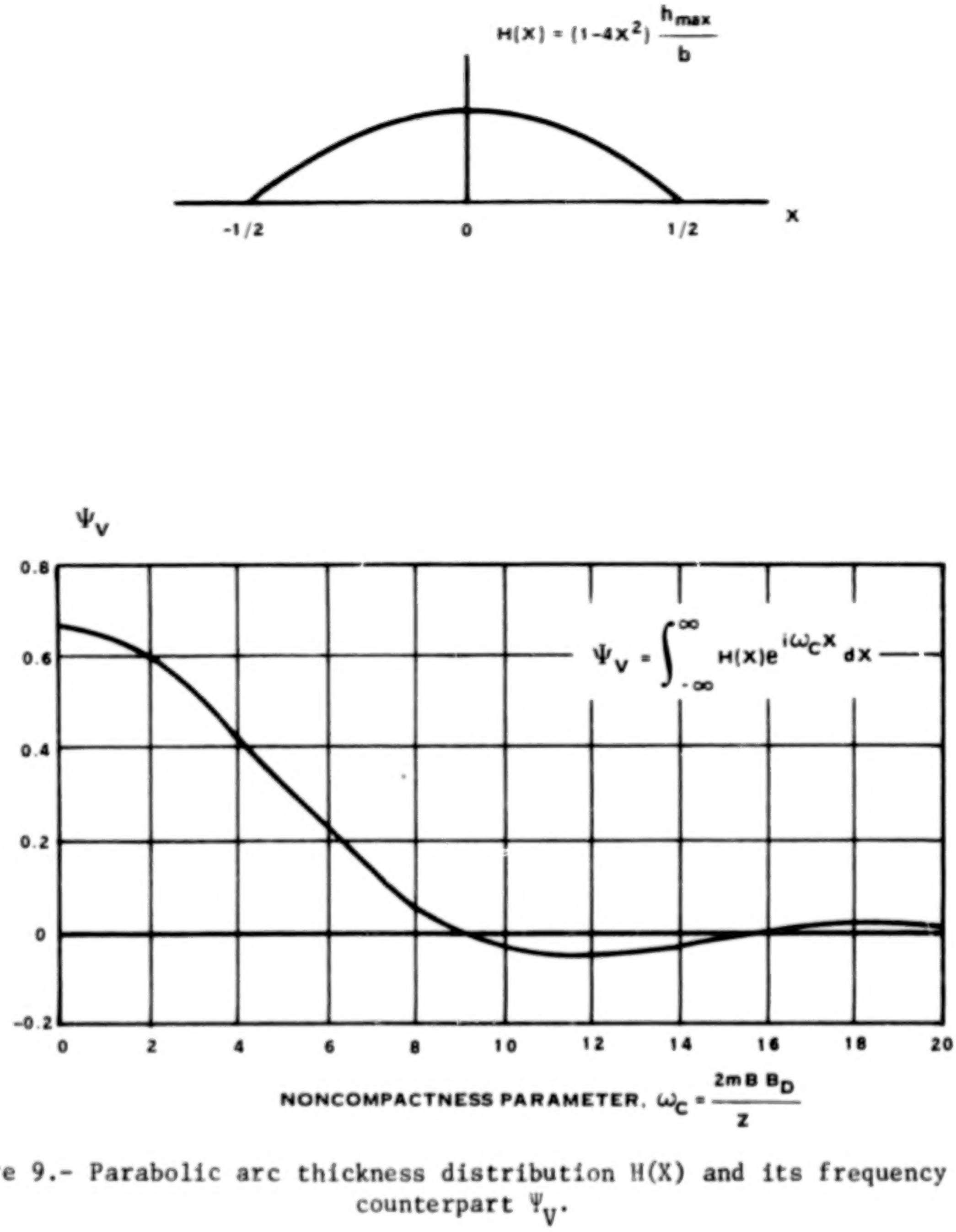

Figure 9.- Parabolic arc thickness distribution H(X) and its frequency domain counterpart Ψ_V.

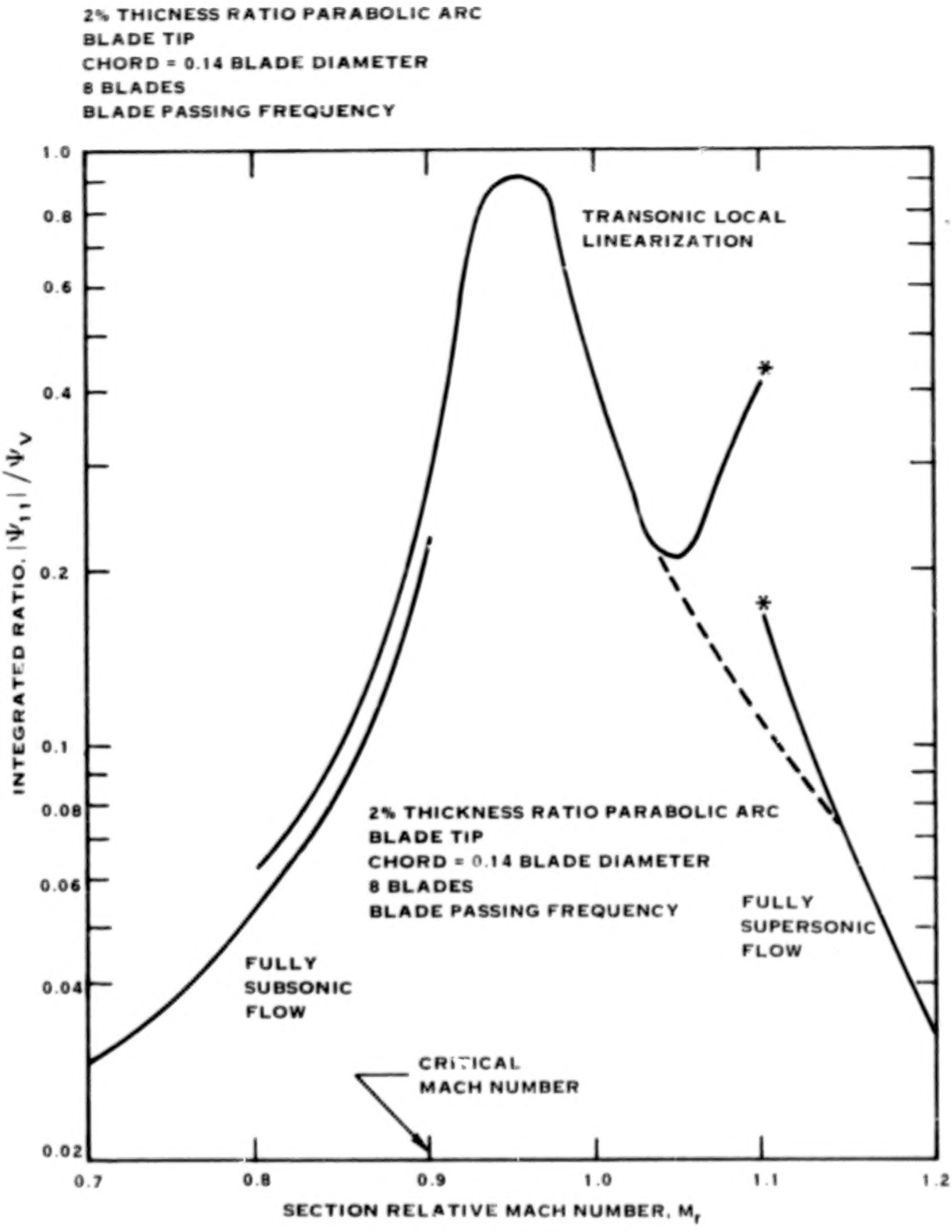

Figure 10.- Calculated ratio of integrated quadrupole strength $|\Psi_{11}|$ to integrated surface source strength Ψ_V. (Theory breaks down in regions denoted by *.)

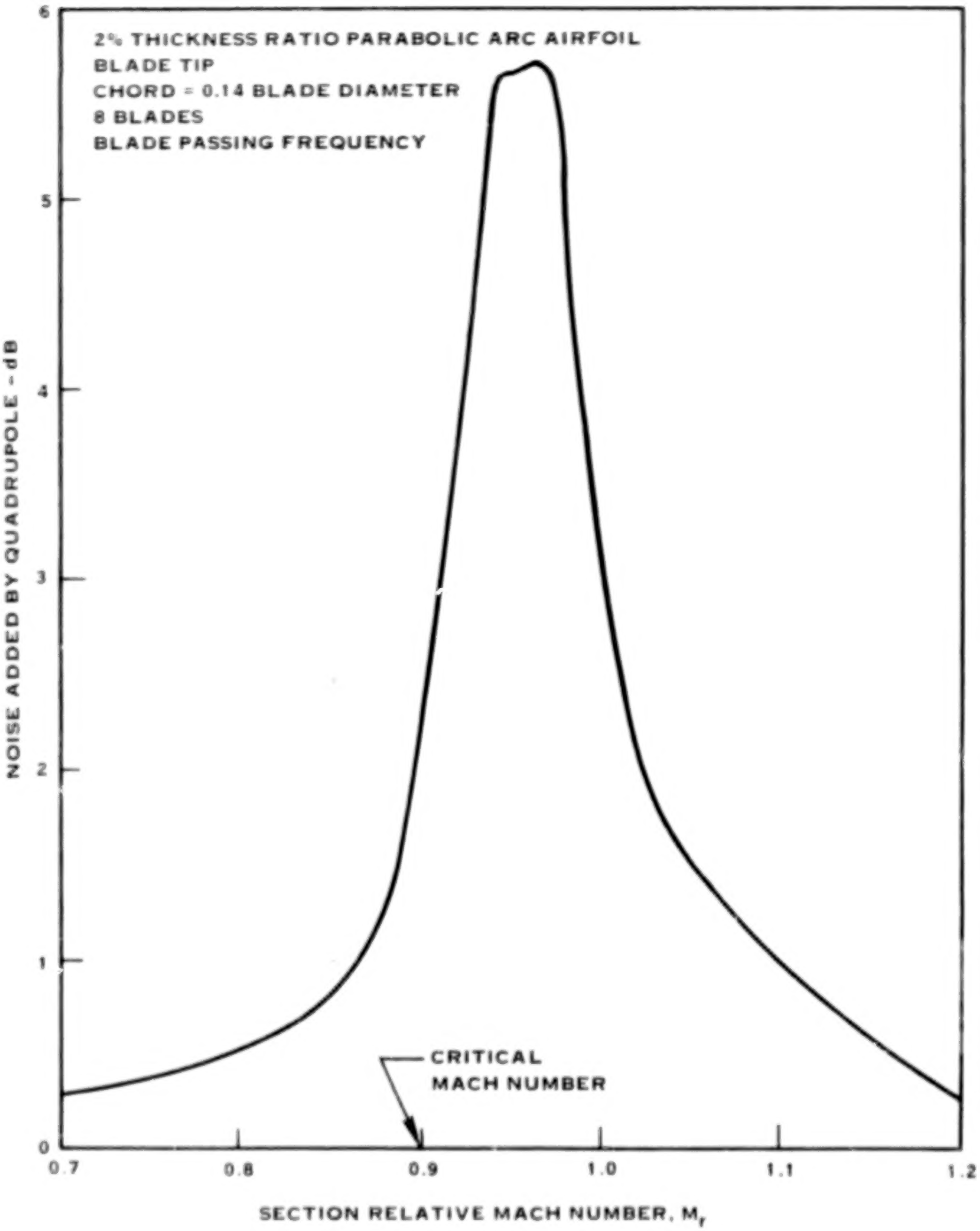

Figure 11.- Increase of blade thickness sound pressure level caused by including quadrupole noise.

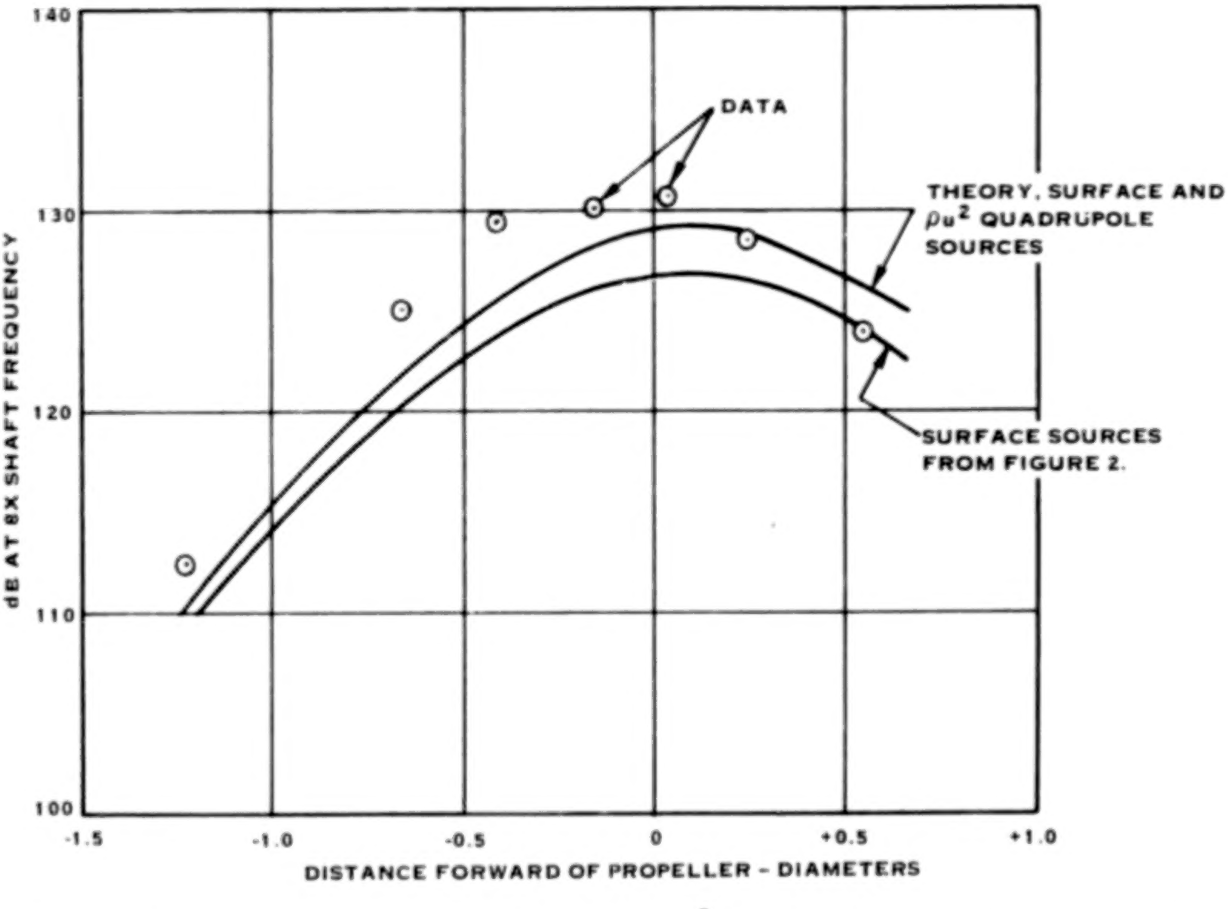

Figure 12.- Increase in noise caused by ρu^2 quadrupole and comparison with data. Same test conditions as figure 2.

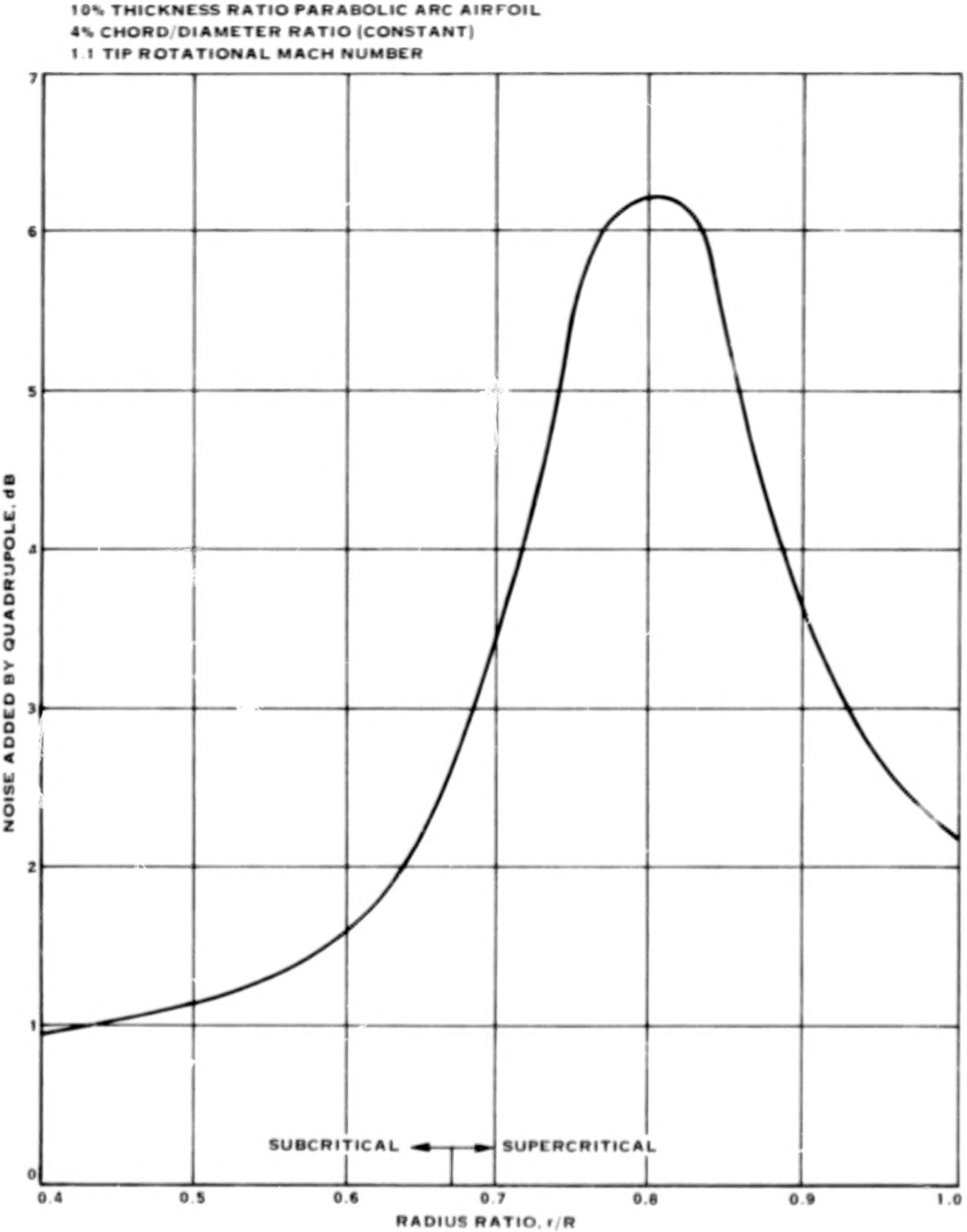

Figure 13.- Radial distribution of the quadrupole source on a helicopter blade.

Blank Page

BOUNDS ON THICKNESS AND LOADING NOISE OF ROTATING BLADES AND THE FAVORABLE EFFECT OF BLADE SWEEP ON NOISE REDUCTION

F. Farassat[+] and Paul A. Nystrom[*]
The George Washington University
Joint Institute for Advancement of Flight Sciences

Thomas J. Brown
Structures Laboratory, U.S. Army R$T Laboratories (AVRADCOM)

SUMMARY

In this paper the maxima of amplitudes of thickness and loading noise harmonics are established when the radial distribution of blade chord, thickness ratio, and lift coefficient is specified. It is first shown that only airfoils with thickness distribution and chordwise loading distributions which are symmetric with respect to midchord need be considered for finding the absolute maxima of thickness and loading noise. The resulting chordwise thickness and load distributions for these maximum noise conditions require infinite slope at some points along the chord but otherwise are uniform. It is shown that sweeping the blades reduces the thickness and loading noise, but there is no optimum sweep which generates the lowest noise.

INTRODUCTION

In the design of a high tip-speed rotating blade such as a helicopter rotor or a propeller, one important acoustic question is: given radial (spanwise) load distribution, thickness ratio, and chord distribution of the blade, can the maximum of the level of each of the sound harmonics be established? These maxima, of course, correspond to the worst possible acoustic design. If these maximum levels are kept within acceptable limits, then neither the chordwise load distribution nor the airfoil shape would be of concern in the acoustic design. Another question which comes to mind next is whether sweeping the blade tips appropriately can result in the lowest possible noise. In this paper both of the above questions are studied and answered.

The starting point of our analysis is the following equation. Let S be the mean surface of the blade, h and p be the local thickness and load distribution on this surface, respectively. Then, the acoustic pressure $p'(\vec{x},t)$ in the far field is given by the equation

---

[+] Work supported by U.S. Army Research Office (Durham).
[*] Work supported under NASA Research Grant NSG 1474.

$$4\pi r_o p'(\vec{x},t) = \rho_o \frac{\partial^2 \Psi}{\partial t^2} + \frac{\hat{r}_i}{c} \frac{\partial L_i}{\partial t} \tag{1-a}$$

$$\Psi(\vec{x},t) = \int_S \left[\frac{h}{|1-M_r|}\right]_{ret} dS \tag{1-b}$$

$$L_i(\vec{x},t) = - \int_S \left[\frac{pn_i}{|1-M_r|}\right]_{ret} dS \tag{1-c}$$

The first term in eq. (1-a) is called the thickness noise. This formulation of thickness noise was derived by Hanson (ref. 1) and by Farassat (ref. 2), using a different approach. The second term in eq. (1-a) is the loading noise.

It is assumed that the blade system, lying in y_1y_2-plane, is not in motion as a whole. That is, only hovering rotors and static propellers are considered here. It is also assumed that unsteady loading noise is negligible. For high-speed rotating blades, this assumption is justified for observer positions where the sources on the blades appear noncompact. Under this assumption, the acoustic pressure will be periodic with fundamental frequency based on blade passage frequency. For simplicity one blade is considered in the analysis.

The nth Fourier component of the noise, $p_n'(\vec{x})$, is found from eq. (1-a) to be

$$4\pi r_o p_n'(\vec{x}) = - \rho_o n^2 \omega^2 \Psi_n(\vec{x})$$

$$- ikn \hat{r}_i L_{in}(\vec{x}) \tag{2}$$

In the following analysis, the surface integrals with respect to S, used in evaluation of $\Psi_n(\vec{x})$ and $L_{in}(\vec{x})$, are written in an unconventional manner in chordwise direction. Written in this form, the effect of sweep can be introduced easily. The bounds are obtained in two stages as follows. First, it is shown that if the airfoil shape is deformed in such a way that the chordwise distance between the points of equal thickness on the airfoil surface is not changed, then the thickness noise is maximum if the airfoil is made symmetric with respect to a radius of the blade disc at each radial position. A similar result holds for the chordwise loading distribution. Therefore to obtain the absolute maxima of thickness and loading noise, only airfoil shapes and chordwise loading with midchord symmetry should be considered. These and the related result concerning sweep do not apply at high frequencies due to the mathematical limitations of some of the inequalities used in their derivation. The range of applicability of these results is, however, wide, particularly in the case of helicopter rotors and conventional propellers.

In all the examples in this paper a rotor blade of 5-m radius and uniform chord of 0.4 m is used. The number of blades is two and the tip Mach number is 0.95.

SYMBOLS

A	function of η (used in eq. (12))
B	function of η (used in eq. (14)), number of blades
b	chordwise variable (see fig. 1), m
b'	mean chord in blade tip region, m
b_o	blade chord (function of η), m
b_p	value of $b \leq b_o$ where $\sin(nb/2\eta)$ achieves its peak, m
C	coefficient used in eq. (5)
c	speed of sound, m/sec
c_ℓ	section lift coefficient (a function of η)
$g(\vec{y}), g(\vec{y}')$	arbitrary positive functions
h	blade section thickness variable (see fig. 1), m
h_m	maximum thickness of blade section (function of η), m
I, I_γ	integrals defined in eq. (7)
J_n	Bessel function of first kind on nth order
k	wave number, ω/c
L_i, L_{in}	surface integral used in calculation of loading noise, and its amplitude of the nth Fourier component of L_i (see eq. (1-c) and (2)), $i=1,2,3$
M_r	Mach number along radiation direction
M_t	tip Mach number of the blade
n	harmonic number
n_i	unit normal to surface S, direction from pressure to suction side of the blade. $i=1,2,3$
p	load distribution of the blade, Pa
p_m	peak section load (function of η), Pa
p'	acoustic pressure, Pa
p'_n	amplitude of the nth Fourier component of p', Pa

CONTENTS

Part I

PREFACE . . . . iii 1/A6

REGULATIONS

1. HELICOPTER EXTERNAL NOISE REQUIREMENTS - FAA PERSPECTIVE 1 1/A8
Charles R. Foster

2. HELICOPTER NOISE REGULATIONS: AN INDUSTRY PERSPECTIVE 17 1/B10
R. A. Wagner

3. NOISE REQUIREMENTS FROM A MILITARY POINT OF VIEW 33 1/C12
Charles C. Crawford, Jr.

4. THE IMPACT OF URBAN OPERATIONS ON HELICOPTER NOISE REQUIREMENTS . . . 45 1/D10
Stanley R. Spector

ROTOR NOISE

5. PREDICTION AND REDUCTION OF ROTOR BROADBAND NOISE 61 1/E12
Richard E. Hayden and Krishna S. Aravamudan

6. THEORETICAL MODELS OF HELICOPTER ROTOR NOISE 89 1/G12
D. L. Hawkings

7. NOISE DUE TO ROTOR-TURBULENCE INTERACTION 109 2/B6
R. K. Amiet

8. THEORY ON ACOUSTIC SOURCES 127 2/C10
S. E. Wright

9. POTENTIAL ACOUSTIC BENEFITS OF CIRCULATION CONTROL ROTOR 149 2/E5
Robert M. Williams and Ian C. Cheeseman

10. HELICOPTER NOISE RESEARCH AT THE LANGLEY V/STOL TUNNEL 181 2/G9
Danny R. Hoad and George C. Greene

11. EXPLORATORY WIND-TUNNEL INVESTIGATION OF THE EFFECT OF THE MAIN ROTOR WAKE ON TAIL ROTOR NOISE 205 3/B7
Robert J. Pegg and Phillip A. Shidler

12. WIND TUNNEL INVESTIGATIONS OF MODEL ROTOR NOISE AT LOW TIP SPEEDS . . . 221 3/C9
K. S. Aravamudan, A. Lee, and W. L. Harris

13. HELICOPTER EXTERNAL NOISE PREDICTION AND CORRELATION WITH FLIGHT TEST 263 3/F11
Bharat P. Gupta

14. FULL-SCALE TESTING OF AN OGEE TIP ROTOR 277 3/G11
Wayne R. Mantay, Richard L. Campbell, and Phillip A. Shidler

15. HOVERING IMPULSIVE NOISE - SOME MEASURED AND CALCULATED RESULTS 309 4/C4
D. A. Boxwell, Y. H. Yu, and F. H. Schmitz

16. IMPROVED METHODS FOR CALCULATING THE THICKNESS NOISE 323 4/D4
Yoshiya Nakamura and Akira Azuma

17. THE IMPORTANCE OF QUADRUPOLE SOURCES IN PREDICTION OF TRANSONIC TIP SPEED PROPELLER NOISE 339 4/E6
Donald B. Hanson and Martin R. Fink

18. BOUNDS ON THICKNESS AND LOADING NOISE OF ROTATING BLADES AND THE FAVORABLE EFFECTS OF BLADE SWEEP ON NOISE REDUCTION 373 4/G12
F. Farassat, Paul A. Nystrom, and Thomas J. Brown

19. A STUDY OF THE NOISE RADIATION FROM FOUR HELICOPTER ROTOR BLADES . . . 387 5/A14
Albert Lee and Marianne Masher

$Q_n(\vec{x})$	function defined in eq. (10-a)
r	$\lvert\vec{x}-\vec{y}\rvert$, m
r_o	observer distance from center of rotation, m
$\hat{r}_i$	$(x_i-y_i)/r$, radiation vector
R, R_i	blade outer and inner radius, respectively, m
S	mean surface of the blade
t	observer time, sec
$\tilde{t}$	thickness ratio of the blade (a function of η)
$T_n(\vec{x})$	function defined in eq. (10-b)
T	period of the sound, sec
$\vec{x}$	observer position vector, origin at rotation center
$\vec{y}$	source position vector, origin at rotation center
α	geometric angle of attack (function of η), deg
β	azimuthal angle, rad
β_c	$(\beta_t+\beta_\ell)/2$ azimuthal angle of point C midway points A and B in fig. 1, rad
β_t, β_ℓ	functions of η and h or p indicating azimuthal angles of points A and B in fig. 1, rad
$\gamma(\vec{y})$	arbitrary function (see eq. 8)
$\delta(b-b_p)$	Dirac delta function
ϵ	angle between axis of rotation and $\vec{x}$, rad
η	radial position variable, m
μ	variable defining the degree of blade sweep
ρ_o	density of the undisturbed medium, kg/m^3
τ	source time, sec
Ψ	surface integral used in calculation of thickness noise (see eq. (1-b))
Ψ_n	amplitude of the nth Fourier component of Ψ
ω	angular velocity of the blade, rad/sec

DERIVATION OF THE BOUNDS

In this section, our attention will be focused on Ψ_n. The manipulations for L_{in} are identical to those of Ψ_n. If T is the period of the sound, then

$$\Psi_n(\vec{x}) = \frac{1}{T}\int_0^T \Psi(\vec{x},t)e^{in\omega t}\,dt \tag{3}$$

For our purpose, the volume $\Psi(\vec{x},t)$ will be written as

$$\Psi(\vec{x},t) = \int_{R_i}^{R} \eta\,d\eta \int_0^{h_m} dh \int_{\beta_t}^{\beta_\ell} [|1-M_r|]^{-1}_{ret}\,d\beta \tag{4}$$

where η is the radial position and h_m is the maximum thickness of the airfoil. The azimuthal angle is denoted by β. The angles β_t and β_ℓ are the azimuthal angles of points A and B, respectively, in fig. (1). Note that $h_m=h_m(\eta)$ $\beta_t=\beta_t(\eta,h)$, and $\beta_\ell=\beta_\ell(\eta,h)$. The only dependence on $\vec{x}$ and t in eq. (4) comes through the integrand so that the time integral in eq. (3) commutes with all the integrals in eq. (4).

We now introduce the source time τ in a manner used by Hawkings and Lowson (ref. 3). Since $dt=[|1-M_r|]_{ret}\,d\tau$, the Doppler singularity in eq. (4) is cancelled. Writing $t=\tau+r/c$ and using the well-known integration with respect to τ which results in a Bessel function of first kind (ref. 3), we get

$$\Psi_n(\vec{x}) = C\int_{R_i}^{R} \eta\,d\eta \int_0^{h_m} dh \int_{\beta_t}^{\beta_\ell} e^{-in\beta} J_n(nk\eta\sin\epsilon)\,d\beta \tag{5}$$

where $C=(i)^n e^{iknr_o}$ is a constant. Let $\beta_c=(\beta_t+\beta_\ell)/2$ and use $\beta_\ell-\beta_t\approx b/\eta$ where $b=b(\eta,h)$ is the chordwise distance between points A and B in fig. (1). Then integrating eq. (5) with respect to β results in

$$\Psi_n(\vec{x})=-2iC\int_{R_i}^{R}\int_0^{h_m} \eta J_n(nk\eta\sin\epsilon)\,e^{-in\beta_c}\sin\left(\frac{nb}{2\eta}\right)dh\,d\eta \tag{6}$$

We note that the angle $\beta_c=\beta_c(\eta,h)$. We will show that the maximum of Ψ_n when only β_c varies corresponds to β_c=constant, that is at each radial station and for all $0\leq h\leq h_m$, points A and B should be located symmetrically with respect to one and the same radius of the blade disk. We need the following result. If $g(\vec{y}) \geq 0$ and $\gamma(\vec{y})$ is an arbitrary function, then in any region D

$$I_\gamma = \left| \int_D e^{i\gamma} g \, d\vec{y} \right| \leq \int_D g \, d\vec{y} = I \qquad (7)$$

To prove this, we note that

$$I^2 - |I_\gamma|^2 = \int_D \int_D 2 \sin^2 \frac{1}{2} [\gamma(\vec{y}) - \gamma(\vec{y}\,')] g(\vec{y}) g(\vec{y}\,') d\vec{y} d\vec{y}\,' \geq 0 \qquad (8)$$

In fact, strict inequality $I_\gamma < I$ holds in most cases since the integrand in eq. (8) has to be non-zero only in a small region in DxD. Note that if $\gamma(\vec{y})=$ constant, $|I_\gamma| = I$.

In eq. (6), $J_n(nk\eta\sin\varepsilon) \geq 0$ even for transonic and low supersonic speeds, since $nk\eta\sin\varepsilon \leq nM_t$ where M_t is the tip Mach number. If $\sin(\frac{nb}{2\eta}) \geq 0$, then we can apply the result proved above. This would require $nb/2\eta \leq \pi$ or $n \leq 2\pi\eta/b$. Since for high-speed blades, the tip region is responsible for the generation of the noise, a reasonable value for n is $n \leq 2\pi\vec{x} \cdot 7R/b' = 4.4R/b'$ where b' is the mean chord in the blade tip region. For blades with B blades; we must have $nB \leq 4.4R/b'$. For two-bladed helicopter rotor blades the following result typically holds up to twenty fifth harmonics of the blade passage frequency. Applying eq. (7) to eq. (6), we get

$$|\Psi_n(\vec{x})| \leq 2 \int_{R_i}^{R} \int_0^{h_m} \eta J_n(nk\eta\sin\varepsilon) \sin(\frac{nb}{2\eta}) \, dh \, d\eta \qquad (9)$$

In exactly similar fashion, we can show that

$$|Q_n(\vec{x})| \equiv |\hat{r}_1 L_{1n} + \hat{r}_2 L_{2n}| \leq \frac{2}{k} \int_{R_i}^{R} \int_0^{p_m} J_n(nk\eta\sin\varepsilon) \sin(\frac{nb}{2\eta}) \sin\alpha(\eta) \, dp \, d\eta \; , \qquad (10\text{-a})$$

and

$$|T_n(\vec{x})| \equiv |\hat{r}_3 L_{3n}| \leq 2 |\cos\varepsilon| \int_{R_i}^{R} \int_0^{p_m} \eta J_n(nk\eta\sin\varepsilon) \sin(\frac{nb}{2\eta}) \cos\alpha(\eta) \, dp \, d\eta \qquad (10\text{-b})$$

where $p_m = p_m(\eta)$ is the peak chordwise loading and $\alpha(\eta)$ is the geometric angle of attack. Equations (10) and (11) describe bounds on torque and lift or thrust noise, respectively, when they are used in eq. (2).

We have shown above that, if we are only allowed to deform the airfoil shape or the chordwise loading in such a way that the chordwise distance between points of equal thickness or equal loading is kept fixed, the maximum thickness and loading noise correspond to symmetrical positioning of such points with respect to the same radius. Incidentally, in this case the thickness noise and loading noise are 90 degrees out of phase.

To find the absolute maxima of thickness and loading noise, eqs. (9) and (10) will be used. It is assumed that the airfoil thickness and load distribution functions are monotonic with respect to variable b. This assumption is satisfied in most cases of interest. To be specific, thickness noise will be considered first. The right side of eq. (9) can be written as

$$\int_{R_i}^{R}\int_{0}^{h_m} \eta J_n(nk\eta\sin\epsilon)\sin(\frac{nb}{2\eta})\ dh\,d\eta$$

$$= -\int_{R_i}^{R}\int_{0}^{b_o} \eta J_n(nk\eta\sin\epsilon)\sin(\frac{nb}{2\eta})\frac{dh}{db}\ db\,d\eta \qquad (11)$$

where $b_o = b_o(\eta)$ is the blade chord. To maximize the last integral, take

$$\frac{dh}{db} = -\ A\delta(b-b_p) \qquad (12)$$

where A is a function determined by the maximum thickness of the airfoil and $b_p = b_p(\eta)$ is the value of $b \leq b_o$ where $\sin(nb/2\eta)$ achieves its peak. If $\tilde{t}(\eta)$ is the thickness ratio of the airfoil, then $A(\eta) = b_o(\eta)\tilde{t}(\eta)$. Using eqs. (9), (11) and (12), we find that

$$|\Psi_n(\vec{x})|_{max} = 2\int_{R_i}^{R} \eta b_o\ \tilde{t}\ J_n(nk\eta\sin\epsilon)\sin(\frac{nb_p}{2\eta})\ d\eta \qquad (13)$$

Similarly, to maximize the integrals in eqs. (10-a) and (10-b), take

$$\frac{dp}{db} = -\ B\delta(b-b_p) \qquad (14)$$

where B is a function determined by spanwise loading of the blade. If $c_\ell(\eta)$ is section lift coefficient of the blade, then $B = \rho_o b_o\ \eta^2\omega^2 c_\ell/2b_p$. Equations (10-a) and (10-b) then give

$$|Q_n(\vec{x})|_{\max} = \frac{\rho_o \omega^2}{k} \int_{R_i}^{R} \frac{b_o \eta^2 c_\ell}{b_p} J_n(nk\eta\sin\epsilon)\sin\left(\frac{nb_p}{2\eta}\right)\sin\alpha(\eta)d\eta \qquad (14\text{-a})$$

$$|T_n(\vec{x})|_{\max} = \rho_o \omega^2 \, |\cos\epsilon| \int_{R_i}^{R} \frac{b_o \eta^3 c_\ell}{b_p} J_n(nk\eta\sin\epsilon)\sin\left(\frac{nb_p}{2\eta}\right)\cos\alpha(\eta) \, d\eta \qquad (14\text{-b})$$

We have shown that for all blades with a given thickness ratio $\tilde{t}(\eta)$ at each radial station, the rms amplitude of the nth harmonic of thickness noise has the following bound

$$4\pi r_o |p_n'(\vec{x})| \leq \sqrt{2} \ \rho_o n^2 \omega^2 |\Psi_n(\vec{x})|_{\max} \qquad (15)$$

Similarly for all blades with a given section lift coefficient $c_\ell(\eta)$, the rms amplitude of the nth harmonic of torque and thrust (lift) noise have the bounds

$$4\pi r_o |p_n'(\vec{x})| \leq \sqrt{2} \ nk \ |Q_n(\vec{x})|_{\max} \qquad (16\text{-a})$$

$$4\pi r_o |p_n'(\vec{x})| \leq \sqrt{2} \ nk |T_n(\vec{x})|_{\max} \qquad (16\text{-b})$$

respectively.

Equations (12) and (14) show that the thickness function and chordwise load distribution function which generate maximum noise have infinite slope at the same two points which are symmetrically located with respect to the mid-chord. The corresponding thickness and chordwise load distributions are rectangular. Note also that $|p_n'|$ is maximized by different thickness and load distributions for different n. In general, therefore the results of equations (15) and (16) are expected to be too pessimistic.

Figure 2 shows some spanwise aerodynamic data for a two-bladed helicopter rotor. These performance data were calculated by a strip theory-momentum analysis described in reference 4. The blade thickness ratio is 8 percent, the blade radius is 5 m and the chord is 0.4 m. The blade planform is rectangular. The rotor rpm is 626. Figure 3 shows the calculated thickness and loading noise with the theoretical bounds obtained above. The chordwise load distribution at each radial position was obtained from the Garabedian-Korn program (ref. 5). The airfoil section used is NACA 0008. The observer position is 50 m from the rotor center and 30° below the rotor (ϵ=120°). The bound for loading noise is obtained by adding the right sides of eqs. (16-a) and (16-b). It is seen that both bounds are very coarse although the bound on loading noise is not as pessimistic as that of thickness noise. For the first harmonic level of loading noise, the reason for the theoretical bound being lower than the calculated level is not known. It may be due to the fact that the drag force (skin friction and wave drag) obtained from the Garabedian-Korn program has a component normal to the chord which was used in the acoustic calcualtions.

For B blades, substitute nB in all the equations derived above.

THE EFFECT OF BLADE SWEEP

We have shown that $|\Psi_n(\vec{x})|$ is maximum when $\beta_c(\eta,h)$=constant. One way of reducing the level of the thickness and loading noise is blade sweep. This can be seen from eq. (8). The question arises whether a blade sweep can be selected which generates the least noise. We will show that among the blades with gradually increasing sweep towards the tip, there is no optimal sweep.

To be specific, we take $\beta_c=-\mu\eta^2$ where $\mu>0$. The same argument holds as long as $\partial\beta_c/\partial\eta < 0$. From eq. (6), we have

$$\Psi_n(\vec{x}) = \int_{R_i}^{R} \eta\, J_n(nk\eta\sin\varepsilon)\, e^{in\mu\eta^2/2}\, d\eta \int_0^{h_m} \sin(\tfrac{nb}{2\eta})\, dh$$

$$= \int_{R_i}^{R} g(\eta)\, e^{in\mu\eta^2/2}\, d\eta \tag{17}$$

where $g(\eta)>0$ is defined as

$$g(\eta) = \eta\, J_n(nk\eta\sin\varepsilon) \int_0^{h_m} \sin(\tfrac{nb}{2\eta})\, dh \tag{18}$$

It is assumed, as before, that $nb/2\eta\leq\pi$. We note that as μ increases, so does the blade sweep. We have

$$\frac{d|\Psi_n(\vec{x})|^2}{d\mu} = \frac{d}{d\mu}\int_{R_i}^{R}\int_{R_i}^{R} g(\eta)g(\eta')\cos[\tfrac{n\mu}{2}(\eta^2-\eta'^2)]d\eta d\eta'$$

$$= -n\mu \int_{R_i}^{R}\int_{R_i}^{\eta'} (\eta^2-\eta'^2)g(\eta)g(\eta')\sin[\tfrac{n\mu}{2}(\eta^2-\eta'^2)]d\eta d\eta' \tag{19}$$

If it is assumed that $\sin[\frac{n\mu}{2}(R^2-R_i^2)]>0$, that is $n\leq 2\pi/\mu(R^2-R_i^2)$, then

$$\frac{d|\Psi_n(\vec{x})|^2}{d\mu} < 0 \tag{20}$$

For all practical angles of sweep, the above restriction on n is less strict than previously obtained restriction $n\leq 2\pi\eta/b$. The above result indicates that the levels of harmonics of the thickness noise decreases as the blade sweep increases. This result is also valid for loading noise.

To test the validity of the above result, figure 4 shows the thickness noise spectra of three blades with increasing sweep. The tip Mach number is 0.95 and the thickness ratios of all the blades are 8 percent. The observer is in the rotor plane and 50 m from the rotor center. It is seen that the above conclusion is indeed correct and should hold up to the 22nd harmonic. In fact it holds for much higher harmonics. The airfoil section used in the calculations is NACA 0008.

CONCLUSIONS

In this paper, bounds are established on thickness and loading noise of rotating blades. Only steady loading noise is considered which restricts the results to high tip speeds. It is shown that only chordwise thickness and load distributions with midchord symmetry need be considered to establish these bounds. The resulting thickness and load distributions have infinite slopes at two points symmetrically located with respect to the midchord. Due to the fact that the amplitude of each harmonic of the spectrum is maximized, the resulting bounds are too coarse. A more appropriate approach may be to search for chordwise thickness and load distributions which maximize overall acoustic level.

It is also shown that sweeping the blade tips is beneficial in reducing the radiated noise. Also for blades with sweeps that increase towards the tip, there is no optimal sweep for minimum noise level.

REFERENCES

1. Hanson, D. B.: Near Field Noise of High Tip Speed Propellers. AIAA Paper No. 76-565, July, 1976.

2. Farassat, F.: Discontinuities in Aerodynamics and Aeroacoustics: The Concept and Applications of Generalized Derivatives. Jour. Sound and Vib., vol. 55, no. 2, Nov. 1977, pp. 165-193.

3. Hawkings, D. L.; Lowson, M. V.: Theory of Open Supersonic Rotor Noise. Jour. Sound and Vib., vol. 36, no. 1, Sep. 1974, pp. 1-20.

4. Mantay, W. R.; Shidler, P. A.; Campbell, R. L.: Some Results of the Testing of a Full-Scale Ogee Tip Helicopter Rotor; Acoustics, Loads, and Performance. AIAA Paper No. 77-1340, Oct. 1977.

5. Bauer, F.; Garabedian, P.; Korn, D.; Jameson, A.: Supercritical Wing Sections II, A Handbook. Lecture Notes in Economics and Mathematical Systems, No. 108. Springer-Verlag, 1975.

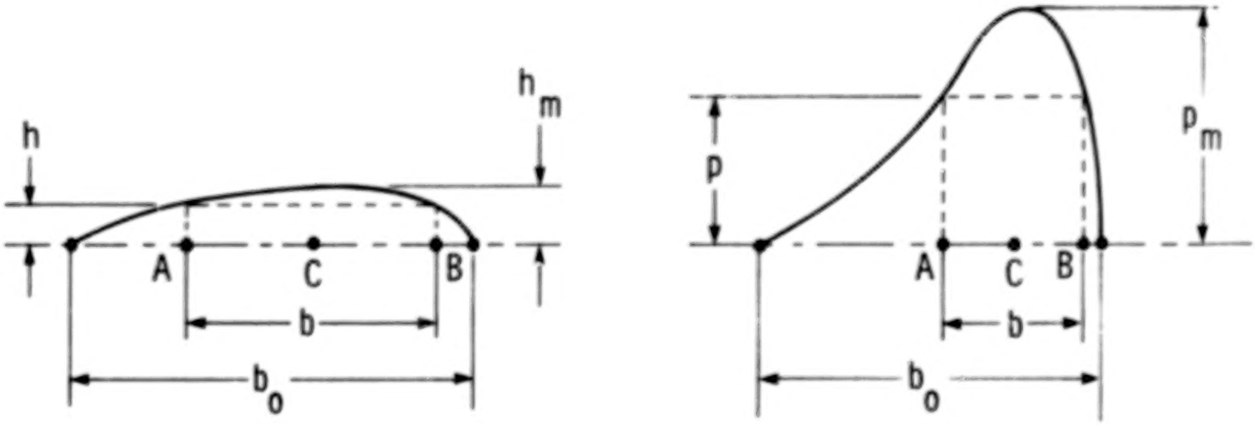
h
h_m
A
C
B
b
b_o
p
p_m
A
C
B
b
b_o

(a) Thickness.

(b) Load.

Figure 1.- Chordwise distributions.

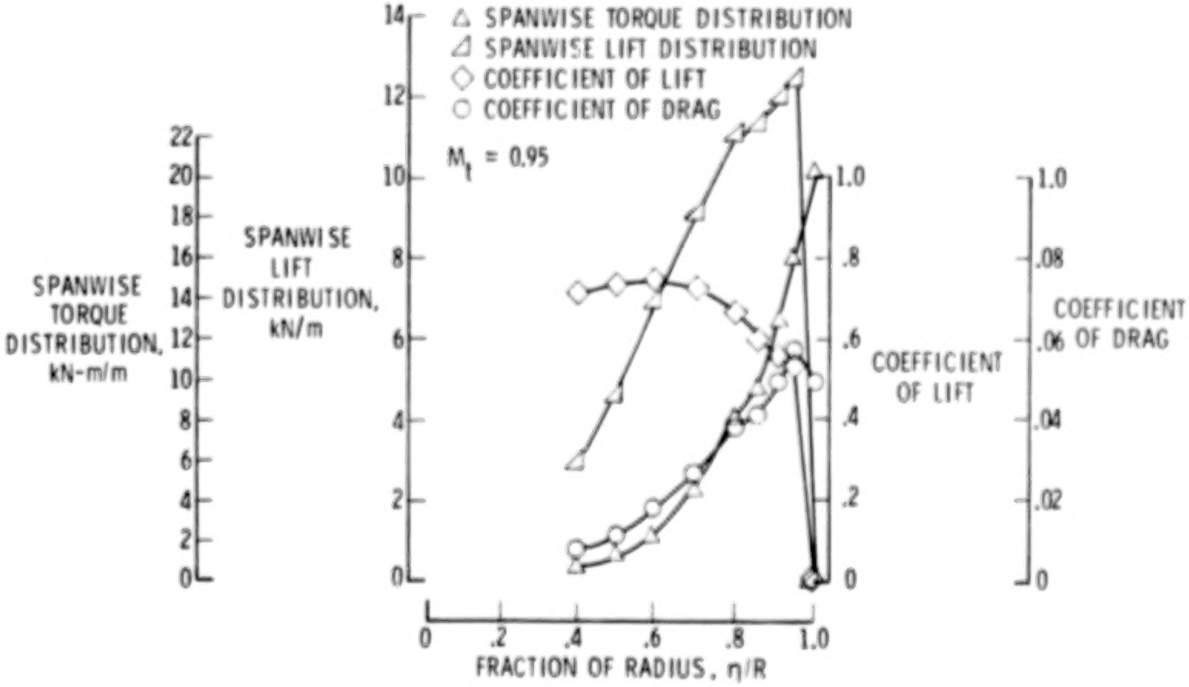

Figure 2.- Performance curves for two-bladed helicopter.

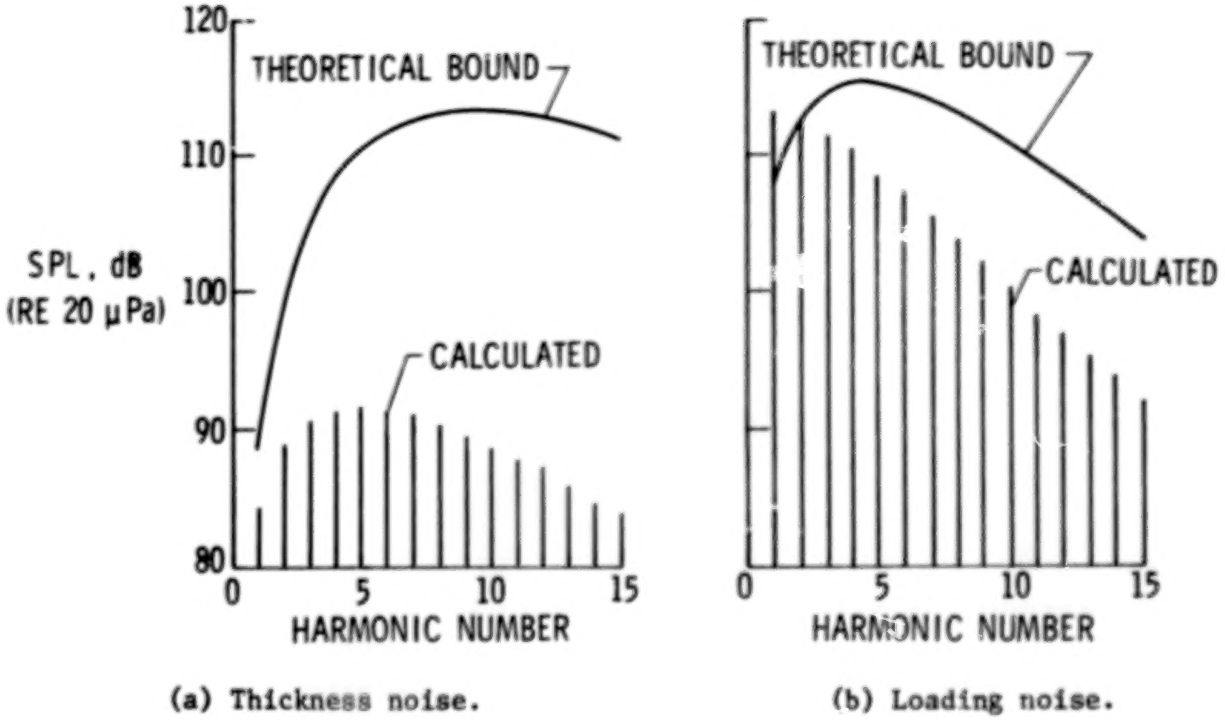

(a) Thickness noise.

(b) Loading noise.

Figure 3.- Comparison of theoretical bound with calculated thickness and loading noise spectra.

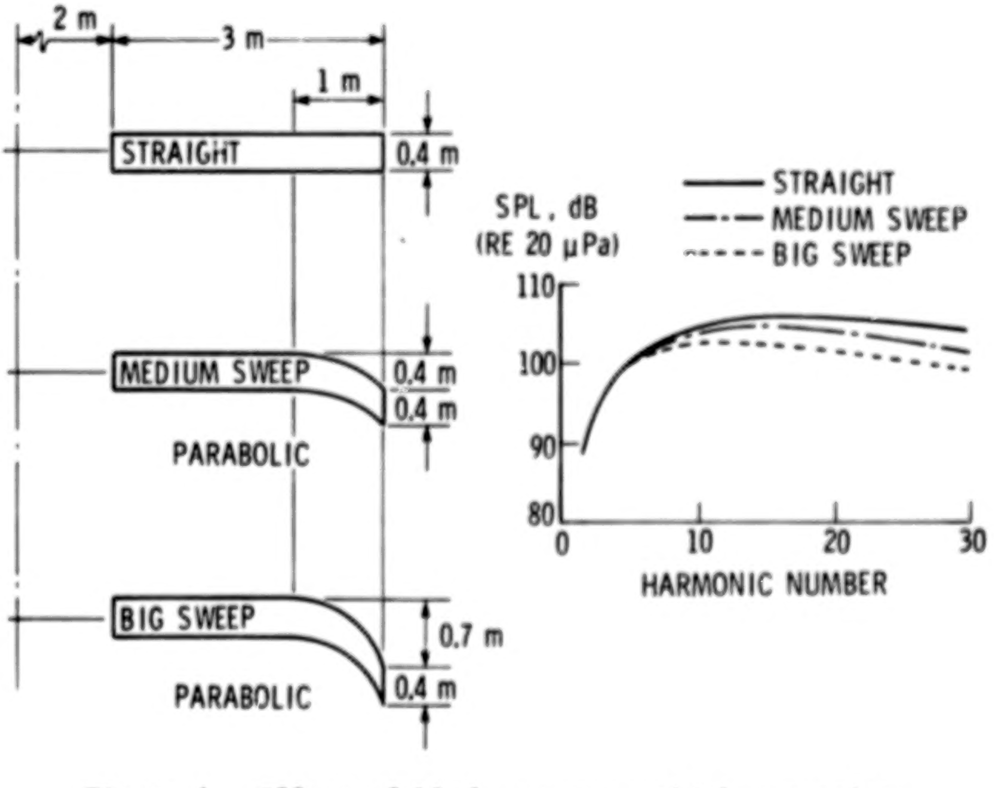

Figure 4.- Effect of blade sweep on thickness noise.

Blank Page

A STUDY OF THE NOISE RADIATION FROM FOUR HELICOPTER ROTOR BLADES

Albert Lee
Beam Engineering, Inc.

Marianne Mosher
NASA Ames Research Center

SUMMARY

Acoustic measurements were taken of a modern helicopter rotor with four blade-tip shapes in the NASA Ames 40-by-80-Foot Wind Tunnel. The four tip shapes are: rectangular, swept, trapezoidal, and swept-tapered in planform. Acoustic effects due to tip shape changes were studied based on the dBA level, peak noise pressure, and subjective rating. The swept-tapered blade was found to be the quietest above an advancing tip Mach number of about 0.9, and the swept blade was the quietest at low speed. The measured high-speed impulsive noise was compared with theoretical predictions based on thickness effects; good agreement was found.

INTRODUCTION

The helicopter rotor blade tip region is one of the most important sources of helicopter noise, and the effects of shaping the tip on the noise generation are complicated because of the many phenomena involved in the tip aerodynamics. For different tip shapes, the blade aerodynamic loading distributions and the resulting tip vortices are different. Due to the combined effects of tip vortex changes and different aerodynamic response at the tip region, the blade/vortex interaction noise will be changed. Because of the change in unsteady blade loading, the rotational noise radiation will also be changed. At high speed, blade thickness can be a significant noise source (refs. 1-4). The thickness noise is directly related to the tip planforms and to their thickness distributions. Noise will also be generated when the tip region experiences strong compressibility effect (ref. 5), which is closely related to blade tip shapes.

Because of the complexity of the tip-shape effects on rotor noise generation, no complete analytical method has been developed. Lyon, Mark, and Pyle (ref. 6) conducted a theoretical study of the rotor tip sound radiation and tried to synthesize rotor tips for less noise. Lowson, Whatmore, and Whitfield (ref. 7) found that cutting off one corner of rectangular fan tips can significantly reduce the high frequency broadband noise. Farassat and Brown (ref. 2) and Farassat (ref. 8) found, in a theoretical study, that airfoil thickness distribution and planform sweep of the blade tip region have significant effects on noise radiation. Since theoretical predictions cannot completely determine the acoustic effects of tip shapes, experiments have been performed to evaluate several tip shapes, either in a wind tunnel or in flight. Recently, a full-scale, ogee-tip helicopter rotor was tested on a whirl tower and in flight (ref. 9). Favorable effects on acoustics, performance, and loads were found.

It is expected, therefore, that suitable design of rotor tip shapes could reduce noise and improve performance. To investigate this possibility, a wind-tunnel experiment was conducted using a modern helicopter rotor, 13.4-m in diameter, with interchangeable tips. The rotor test encompassed an advance ratio range of 0.2 to 0.375 and an advancing tip Mach number range of 0.72 to 0.97. Four tip shapes were tested. The test data were used to determine the acoustic effects of the specific tip shapes and to establish a data base for theoretical modeling and predictions of high-speed rotor impulsive noise.

SYMBOLS

C_{LR}/σ	lift coefficient to solidity ratio
$M_{1,0}$	blade rotational tip Mach number
$M_{1,90}$	blade advancing tip Mach number
P	acoustical pressure, N/m^2
V	wind-tunnel speed, m/sec
α_s	rotor shaft angle, deg
ΩR	blade rotational tip speed, m/sec

EXPERIMENT

A 13.4-m-diameter, four-bladed rotor with interchangeable tips constructed by Sikorsky Aircraft was tested in the NASA-Ames 40-by 80-Foot Wind Tunnel. Four different tip shapes were tested (fig. 1). The tip shapes are: rectangular, swept, tapered (trapezoidal), and swept-tapered. The rectangular tip serves as a baseline; the other three tips were used to systematically evaluate the effects of taper and sweep. The rotor blades had a constant chord and 9.5% thickness ratio airfoil inboard of 95% radius. The rectangular tip maintained the constant chord and thickness out to 100% radius. The trapezoidal tip was tapered to 60% of the baseline chord at the tip, with a constant thickness ratio and an unswept quarter chord line. The swept tip had constant chord and thickness with 20° sweepback. The swept-tapered tip had 35° sweep of the leading edge, a 10° sweep of the trailing edge, and a constant thickness ratio.

The investigation covered a wide range of operating conditions. The range of advancing tip Mach number was 0.72 to 0.96, and the advance ratios were from 0.2 to 0.375. The rotor performance is given in reference 10.

Seven 13-mm (1/2-in.) B & K condenser microphones with cathode followers were used for the acoustical measurements. Each microphone was equipped with a nose cone to reduce the wind-induced noise. The microphone locations are given in table 1 and shown in figure 2. The microphones were calibrated daily with a B & K pistonphone. Conventional acoustic power supply and amplifier units were used for data conditioning. The acoustical signals as well as 1/rev and 256/rev voltage pulses were recorded on an Ampex 1300A, 14-track FM tape recorder. The recorder setting was IRIG wide-band 1 and 19.05 cm/sec (7.5 ips), with a center frequency of 27 kHz, and a bandwidth of 5 kHz. An acoustical polarity calibration device, which generated a strong positive pressure pulse, was used to calibrate the polarity of the acoustical data system.

The A-weighted SPL was obtained by using a B & K audio frequency analyzer, type 2107. The acoustical waveforms were reduced by a minicomputer-based time series analyzer. The noise signal was sampled at a rate of 5120/sec for 0.2 sec, beginning with the trigger of 1/rev pulses. The resulting frequency resolution was 5 Hz with a Nyquist frequency of 2.56 kHz. A 2 kHz anti-aliasing filter was used. By averaging 50 records in a synchronized fashion, the nonperiodic noise was significantly reduced. A discrete Fourier transform was then applied to obtain the amplitude and phase relationship of each frequency component. By zeroing out the frequency components below 25 Hz and applying inverse Fourier transform, an averaged, 25 Hz high-passed, phase distortion-free acoustical waveform was obtained. These waveforms are particularly useful in the study of helicopter impulsive noise. A complete set of noise waveforms is given in reference 11.

EXPERIMENTAL RESULTS

dBA Levels

The acoustical data measured in the wind tunnel were contaminated by the background noise and reverberations. The background noise data were measured at various wind-tunnel speeds with the rotor hub turning (without blades). The A-weighted SPL of background noise is proportional to the 5.6th power of the wind-tunnel velocity. The A-weighted SPL of rotor noise was corrected for the background noise. These corrected dBA quantities should not be considered to be the absolute values because of reverberations from the hard wind-tunnel walls. Nevertheless, these data are useful for comparisons of the different tip shapes.

Figure 3 shows the dBA noise levels of Mic (microphone) 3 as a function of C_{LR}/σ, for the rotor operating at $V/\Omega R = 0.2$, $M_{1,0} = 0.6$, and $\alpha_s = -5°$. No data for the trapezoidal tip are available at these conditions. The noise of the swept blade is about 2 dBA lower than that of the rectangular blade or swept-tapered blade over most of the range of blade loading. The difference is small at high blade loading. Figure 4 shows the noise level of Mic 3 at $V/\Omega R = 0.375$, $M_{1,0} = 0.65$ and $\alpha_s = -5°$. The dBA levels of swept blades are the lowest, with the swept-tapered blades second. The rectangular blade and trapezoidal blades are loudest. Similar trends were observed at Mic 6.

The advancing tip Mach number is an important parameter defining the rotor noise. Figure 5 shows the noise levels of the four blades over a Mach number range. Below about $M_{1,90} = 0.9$ the swept blades have the lowest dBA. When the advancing tip Mach number is above 0.9, the swept-tapered blades have the lowest dBA. Similar trends were found at Mic 6.

Waveforms

The noise waveforms may be more useful in studying the rotor noise when impulsive components are dominant. The noise waveforms in the different stages of data reduction are shown in figure 6. The background noise and rotor broadband noise are reduced or eliminated by averaging 50 times, as seen in figure 6(b). The 25 Hz high-pass filtering mainly eliminated the first blade passage harmonic of the thrust- and drag-generated rotational noise. The averaged and filtered waveforms are useful in the study of rotor impulsive noise. Although the tunnel background noise and rotor broadband noise can be averaged out, the reflected noise from the tunnel surfaces are still present in the processed waveforms. However, if the time lag of reflections is larger than the incident pulse width, the reflections will not mask the impulsive noise. For the test configuration considered here, it was verified experimentally that the first reflection (from the wind-tunnel floor) arrives about 4 msec after the direct wave. The sound pressure pulse width was found to be much less than 4 msec, particularly at high speed. Actually, there was little evidence of impulsive noise reflections in the measured sound pressure signal (see fig. 6). A probable factor in the absence of strong reflections is the location of the microphone (Mic 3) nearly in the rotor tip-path plane, where the impulsive noise directivity is greatest. The pulse reflected off the tunnel floor or ceiling thus has much smaller magnitude than the pulse traveling directly from the rotor to the microphone.

Figure 7 shows the acoustical waveforms (averaged 50 times) of the four tips at $V/\Omega R = 0.375$, $M_{1,0} = 0.65$ ($M_{1,90} = 0.90$), and $\alpha_s = -5°$. The swept-tapered tip blades produce the lowest impulsive noise. This is also true for the advancing Mach number greater than 0.90. However, the dBA results of figure 5 show the swept tip blade to be the lowest among four tip shapes at $M_{1,90} = 0.90$. This is because dBA is an overall rating of noise with an emphasis on the high frequencies (around 3 kHz); rotor noise contains many components in addition to impulsive noise. At high advancing tip Mach number, both the dBA and impulse peak indicate the swept-tapered tip blades are quietest.

Subjective Rating of High Speed Impulsive Noise

Subjective rating of rotor high-speed impulsive noise (with its complicated waveform) cannot be immediately discerned based on dBA measurements of the noise. An ordering based on dBA measurements will not necessarily agree with an ordering based on peak pressure levels. To find subjective ratings of the four blade sets of this investigation, a subjective evaluation was conducted.

Twenty subjects were used for this test. Each subject was presented with the noise from a pair of rotors, first one and then the other, separated by a 3-sec gap. Ten seconds later, another pair was presented. All possible pairs were thus presented (in scrambled order) and the subjects were asked to judge which of the two rotors of each pair was loudest.

For all samples, the advance ratio was 0.375, the rotational Mach number was 0.65 (corresponding to an advancing tip Mach number of 0.90), and C_{LR}/σ was 0.07. Recordings from Mic 3 were used. The recordings were played back to the subjects in an anchoic chamber. The recordings were band-pass filtered from 25 Hz to 2.5 kHz, and played to the subjects at a reduced but constant level. The physical measurements of the original signals are shown in table 2.

A subjective ordering of the loudness of the different rotor tips presented can be derived from the frequencies with which the various tip shapes were judged loudest. The rectangular tip was judged loudest the most often, followed by the swept tip, then the trapezoidal tip. The swept-tapered tip was judged loudest the least often (see table 2). A standard statistical test (t-test) showed that the differences in responses between different tip shapes was significant for all pairs except between the trapezoidal tip and swept-tapered tip.

The ordering derived from the subjects' responses agrees with the ordering derived from the peak negative impulses but not the ordering from the dBA measurements. This indicates that when this impulse is presented in the rotor noise, perception of loudness correlated more with impulsive peak level than with the dBA level of the noise. It should not, however, be assumed that the peak level of impulsive noise is the only relevant factor determining subjective loudness. More extensive testing would have to be done to determine precisely what affects subjective loudness.

COMPARISON OF MEASURED IMPULSIVE NOISE WITH THEORY

Time histories of the measured impulsive noise are shown in figure 8 for the trapezoidal tips, at three advancing tip Mach numbers. The negative pressure pulse increases in amplitude with Mach number so that it dominates the sound pressure signal at high speed. At very high speeds a positive pressure spike closely follows the negative pulse. Similar results were found from flight measurement of a UH-1 helicopter noise (ref. 12). Calculations were made based on the thickness noise theory which was developed by

Johnson (ref. 13). Calculations based on the theory of Farassat and Brown (ref. 2) or the theory of Schmitz and Yu (ref. 3) can result in similar predictions. There is more to the periodic rotor noise than just the thickness noise component, but the impulse is well accounted for by the thickness noise theory. More comparisons can be found in reference 4.

Figure 9 compares the measured and calculated peak impulsive noise pressure for four different blades over the range of advancing tip Mach number. The advance ratio is 0.375 for all cases. The overall correlation is quite good. It can be seen that the impulsive noise can be reduced by the cross-sectional area of the blade tip. Sweeping the blade tip without changing the chord or thickness has little effect on the thickness noise. Figure 10 shows the directivity in the elevation plane for the swept-tapered rotor at an advancing tip Mach number of 0.90. As can be seen, the impulsive noise is quite directional. Good agreement between the experimental data and calculation is found.

CONCLUSIONS

The acoustic data of a 13.4-m rotor with four blade-tip shapes were obtained in a wind-tunnel test. These tip shapes are rectangular, swept, trapezoidal (tapered), and swept-tapered. Below an advancing tip Mach number of about 0.9, the dBA data appear to indicate that the swept tip is the quietest, the swept-tapered tip second, the trapezoidal tip third, and the rectangular tip the most noisy. Above an advancing tip Mach number of about 0.9, a distinct negative acoustical pulse, which occurs once per blade passage, was observed. The amplitudes of these pulses are strongly dependent on the advancing tip Mach number. Based on the amplitude of impulsive noise, the data indicate the swept-tapered tip is the quietest, the trapezoidal tip second, the swept tip third, and the rectangular tip loudest.

The overall comparisons show good agreement between measured impulsive noise and calculated results based on thickness noise theory. This correlation suggests that the rotor high-speed impulsive noise is thickness noise dominated. Changing blade chord or thickness has significant effects on the noise radiation. Simply sweeping alone has little effect on high-speed impulsive noise. A complete prediction of helicopter noise will, of course, require an accurate treatment of all noise components.

REFERENCES

1. Lowson, M. V.; Hawkings, D. L.: Noise of High Speed Rotors. AIAA Paper 75-450, AIAA 2nd Aeroacoustics Conference, 1975.

2. Farassat, F.; and Brown, T. J.: A New Capability for Predicting Helicopter Rotor and Propeller Noise Including the Effect of Forward Motion. NASA TM X-74037, 1977.

3. Schmitz, F. H.; and Yu, Y. H.: Theoretical Modeling of High Speed Helicopter Impulsive Noise. European Rotorcraft and Powered Lift Aircraft Forum, France, Sept. 1977.

4. Johnson, W.; and Lee, A.: Comparison of Measured and Calculated Helicopter Rotor Impulsive Noise. NASA TM 78473, 1978.

5. Arndt, R. E.; and Borgman, D. C.: Noise Radiation from Helicopter Rotors Operating at High Tip Mach Numbers. 29th Annual National Forum of American Helicopter Soc., Preprint No. 402, June 1970.

6. Lyon, R. H.; Mark, W. D.; and Pyle, R. W., Jr.: Synthesis of Helicopter Rotor Tips for Less Noise. Helicopter Noise Symposium, ARO-Durham, September 1971.

7. Lowson, M. V.; Whatmore, A.; and Whitfield, C. E.: Source Mechanisms for Rotor Noise Radiation. TT7202, Department of Transportation Technology, Loughborough University of Technology, March 1972.

8. Farassat, F.: Theory of Noise Generation from Moving Bodies with an Application to Helicopter Rotors. NASA TR R-451, 1973.

9. Mantay, W. R.; Shidler, P. A.; and Campbell, R. L.: Some Results of the Testing of a Full-Scale Ogee Tip Helicopter Rotor; Acoustics, Loads, and Performance. AIAA Paper 77-1340, AIAA 4th Aeroacoustics Conference, 1977.

10. Stroub, R. H.: Full Scale Wind Tunnel Test of a Modern Helicopter Main Rotor – Part A and Part B. Thirty-fourth Annual National Forum of American Helicopter Soc., Preprint No. 3, May 1978.

11. Lee, A.: Acoustical Effects of Blade Tip Shape Changes on a Full Scale Helicopter Rotor in a Wind Tunnel. NASA CR-152082, April 1978.

12. Schmitz, F. A.; and Boxwell, D. A.: In-Flight Far-Field Measurement of Helicopter Noise. J. American Helicopter Soc., October 1976.

13. Johnson, W.: Helicopter Theory. Princeton University Press, Princeton, New Jersey, 1978.

TABLE 1. - MICROPHONE LOCATIONS

Mic. no.	X		Y		Z		Above floor		Angle below horizontal plane, deg
	m	ft	m	ft	m	ft	m	ft	
1	-19.8	-65	0.61	2	5.30	-17.4	1.22	4	15
2	-2.65	-8.7	1.89	6.2	3.08	-10.1	3.02	9.9	43.6
3	-19.2	-63	0	0	4.21	-13.8	2.29	7.5	12.4
4	-18.6	-61	0.61	-2	2.62	-8.6	3.90	12.8	8
5	-19.0	-62.3	5.5	18.2	4.18	-13.7	2.35	7.7	11.9
6	-3.47	-11.4	3.60	11.8	3.90	-12.8	2.19	7.2	38
7	-19.0	-62.3	5.55	-18.2	4.18	-13.7	2.35	7.7	11.9

TABLE 2. - RATINGS OF IMPULSIVE ROTOR NOISE

	Rectangular	Swept	Trapezoidal	Swept-tapered
dBA	117.2	115.1	116.7	115.9
Peak pressure, N/m^2	90	70	60	50
Possible number of responses	180	177	177	180
Number of times judged louder	153	107	51	46

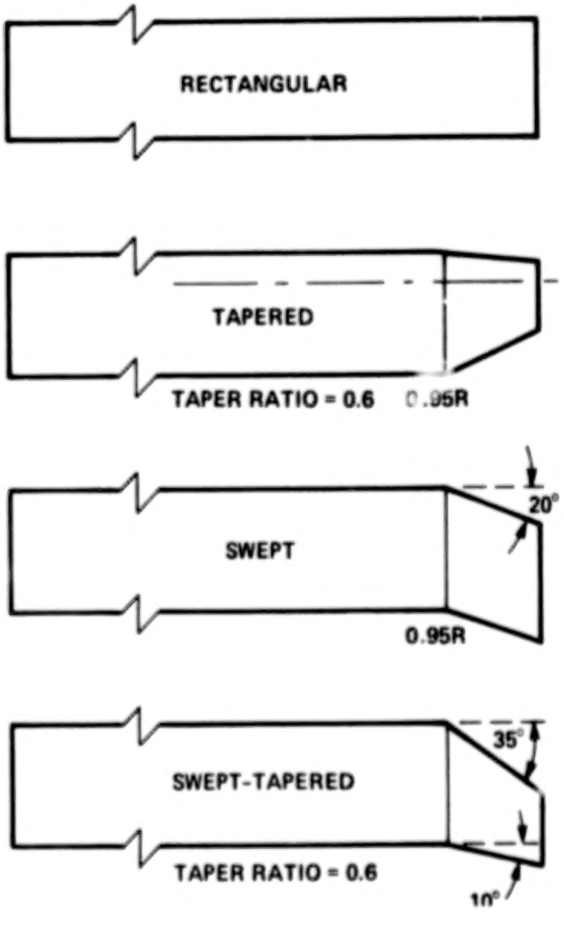
RECTANGULAR
TAPERED
TAPER RATIO = 0.6
0.95R
SWEPT
20°
0.95R
SWEPT-TAPERED
35°
TAPER RATIO = 0.6
10°

Figure 1.- Four tip shapes tested.

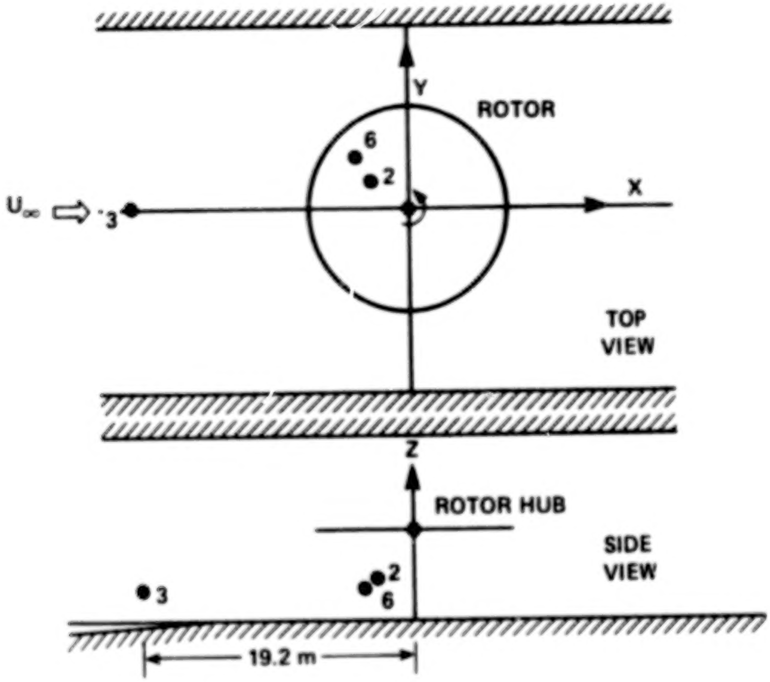
Y
ROTOR
6
2
X
U∞
3
TOP VIEW
Z
ROTOR HUB
SIDE VIEW
2
6
3
19.2 m

Figure 2.- Microphone locations.

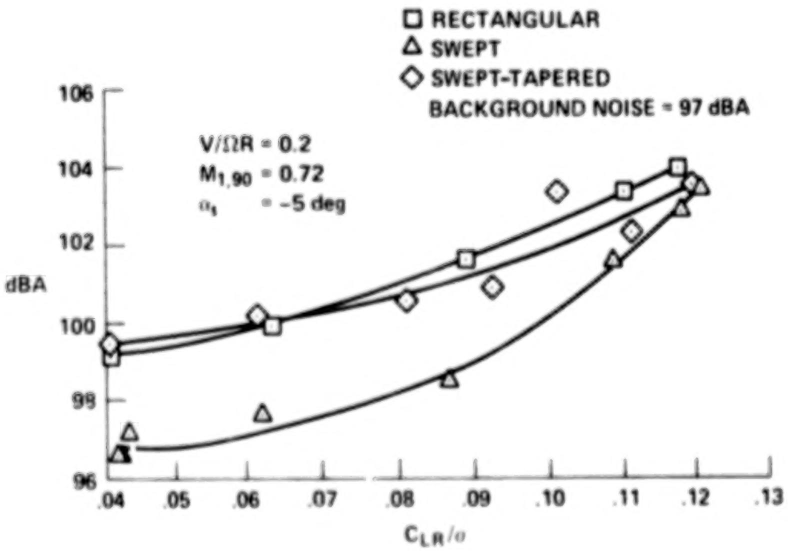

Figure 3.- dBA noise levels as a function of C_{LR}/σ. Mic 3; $\alpha_s = -5^{\circ}$; $V/\Omega R = 0.2$; $M_{1,90} = 0.72$.

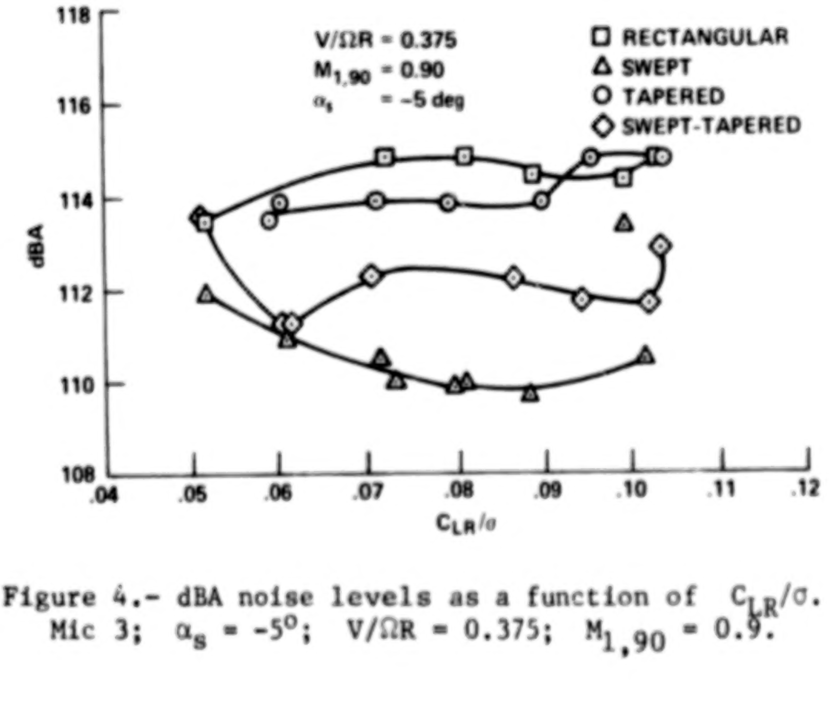

Figure 4.- dBA noise levels as a function of C_{LR}/σ. Mic 3; $\alpha_s = -5^{\circ}$; $V/\Omega R = 0.375$; $M_{1,90} = 0.9$.

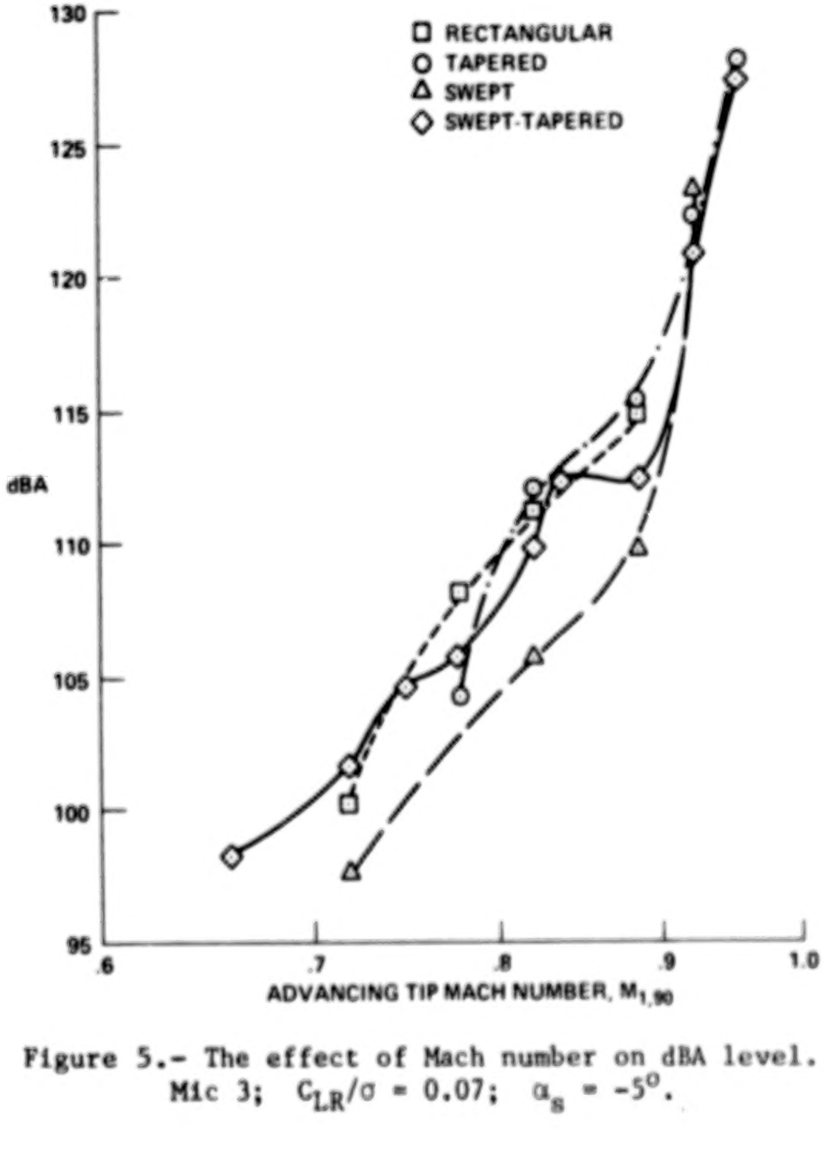

Figure 5.- The effect of Mach number on dBA level.
Mic 3; $C_{LR}/\sigma = 0.07$; $\alpha_s = -5^{\circ}$.

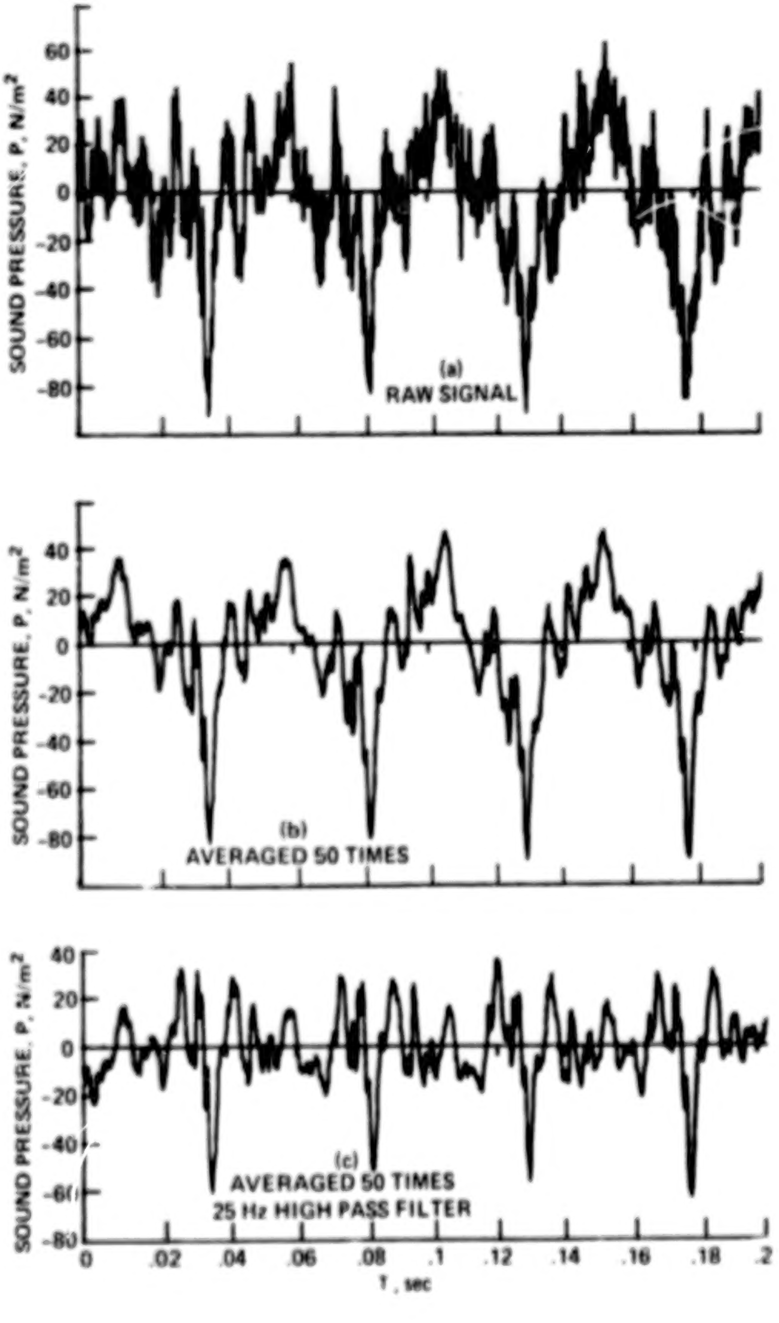

Figure 6.- Example of the noise signal processing. Trapezoidal tips; $M_{1,90} = 0.9$; $V/\Omega R = 0.375$.

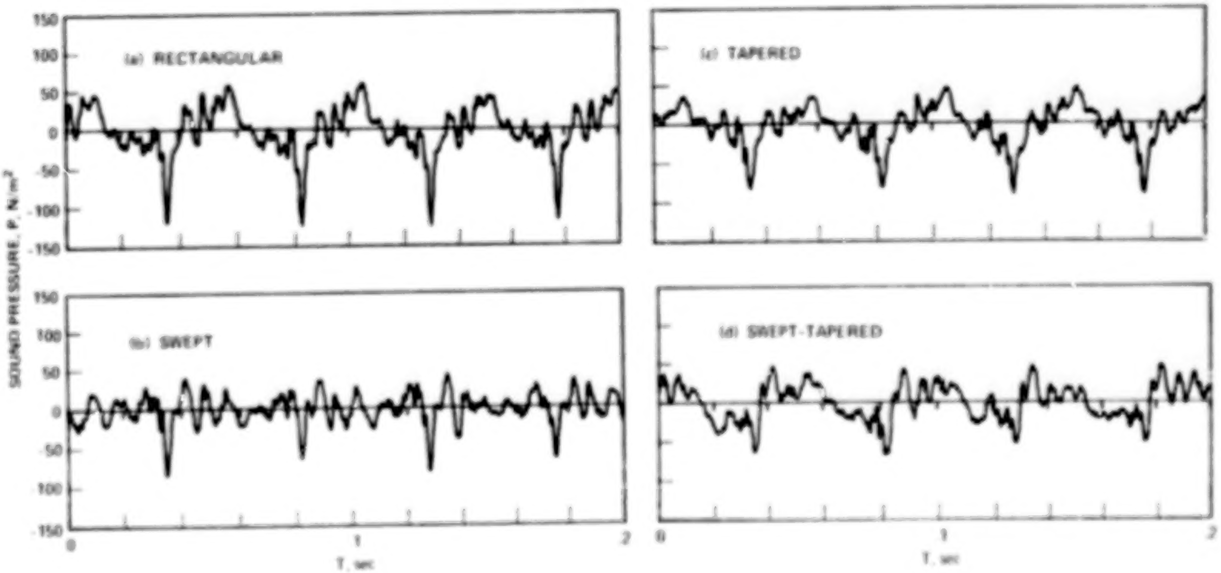

Figure 7.- Waveforms of four blades. $V/\Omega R = 0.375$; $M_{1,0} = 0.65$; $M_{1,90} = 0.9$; $\alpha_s = -5^o$.

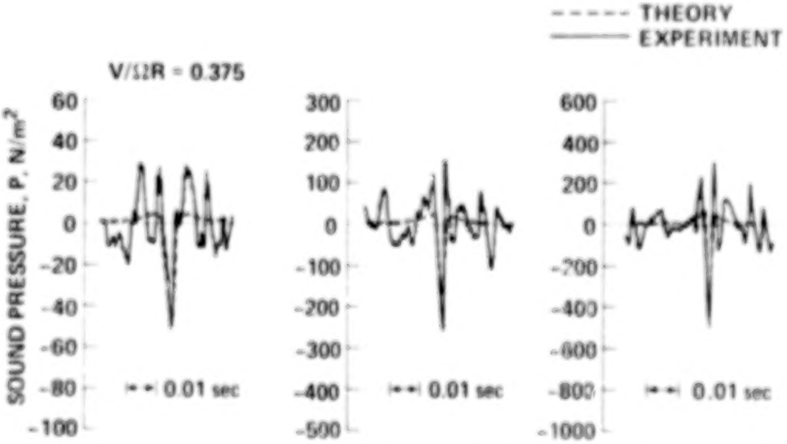

(a) $M_{1,90} = 0.9$ (b) $M_{1,90} = 0.939$ (c) $M_{1,90} = 0.966$

Figure 8.- Comparison of measured and calculated thickness noise time histories at several advancing tip Mach numbers. Trapezoidal tips; $V/\Omega R = 0.375$.

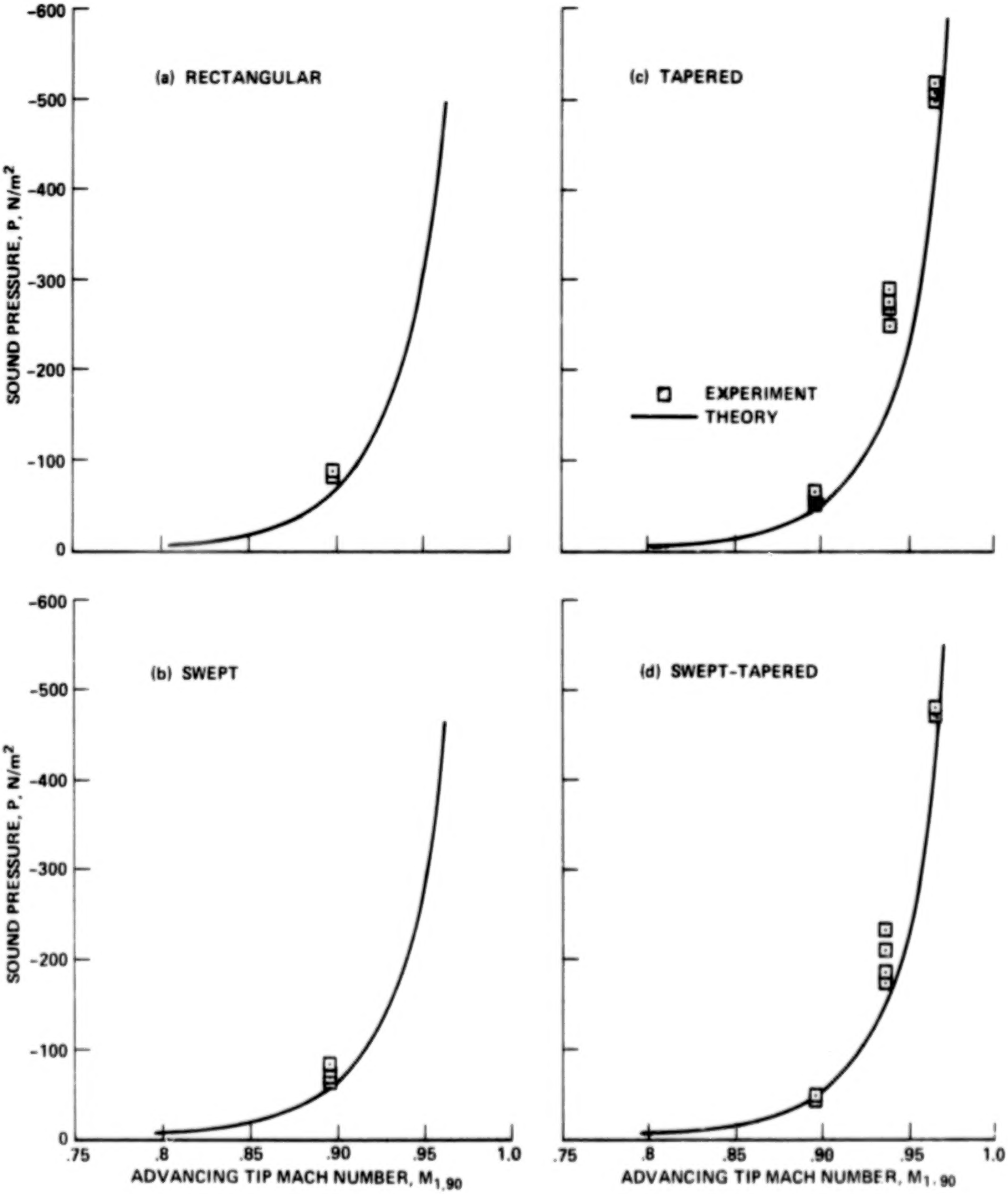

Figure 9.- Comparison of measured and calculated impulsive noise peak pressures. $V/\Omega R = 0.375$.

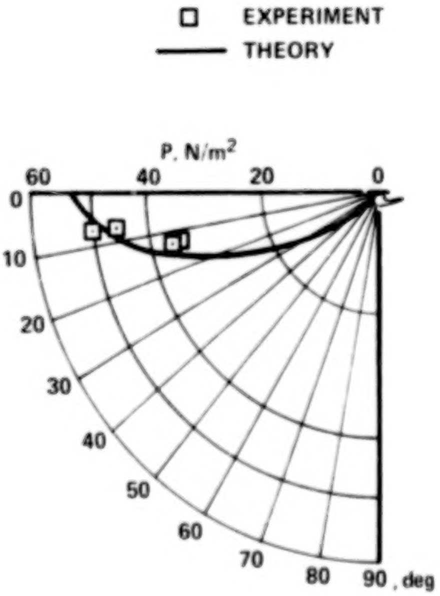

Figure 10.- Impulsive noise peak pressure in the vertical plane forward of the rotor disk. $V/\Omega R = 0.375$; $M_{1,0} = 0.65$; $M_{1,90} = 0.90$.

1. Report No.
NASA CP-2052, Part I

2. Government Accession No.

3. Recipient's Catalog No.

4. Title and Subtitle
HELICOPTER ACOUSTICS

5. Report Date
August 1978

6. Performing Organization Code

7. Author(s)

8. Performing Organization Report No.
L-12339

10. Work Unit No.
505-03-13-15

9. Performing Organization Name and Address
NASA Langley Research Center
Hampton, VA 23665

11. Contract or Grant No.

13. Type of Report and Period Covered
Conference Publication

12. Sponsoring Agency Name and Address
National Aeronautics and Space Administration
Washington, DC 20546

14. Sponsoring Agency Code

15. Supplementary Notes

16. Abstract

This report is a compilation of papers presented at the International Specialists Symposium on Helicopter Acoustics, jointly sponsored by the American Helicopter Society, the U.S. Army Research Office, and the NASA Langley Research Center on May 22-24, 1978. Included in the topics covered are noise regulation concepts; human factors and criteria; rotor noise generation and control; design, operation and testing for noise control; helicopter noise prediction, and research tools and measurements. Exterior and interior noise problems are addressed both from the physics and engineering as well as the human factors points of view.

17. Key Words (Suggested by Author(s))
Helicopters
Acoustics
Noise control
Human factors
Noise regulations

18. Distribution Statement
Distribution - Unlimited

Subject Category 71

19. Security Classif. (of this report)	20. Security Classif. (of this page)	21. No. of Pages	22. Price*
Unclassified	Unclassified	410	$13.25

* For sale by the National Technical Information Service, Springfield, Virginia 22161

403

90

50

END

DEC 8 1978